NASA
TT
F-346
c.1

S. M. Gorlin and I. I. Slezinger

WIND TUNNELS AND THEIR INSTRUMENTATION

LOAN COPY: RETURN
AFWL (WLIL-2)
KIRTLAND AFB, N MEX

TECH LIBRARY KAFB, NM
0068829

TRANSLATED FROM RUSSIAN

Published for the National Aeronautics and Space Administration, U.S.A.
and the National Science Foundation, Washington, D.C.
by the Israel Program for Scientific Translations

TECH LIBRARY KAFB, NM
0068829

S. M. GORLIN and I. I. SLEZINGER

WIND TUNNELS AND THEIR INSTRUMENTATION

(Aeromekhanicheskie izmerenia. Metody i pribory)

Izdatel'stvo "Nauka"
Moskva 1964

Translated from Russian

Israel Program for Scientific Translations
Jerusalem 1966

NASA TT F-346
TT 66-51026

Published Pursuant to an Agreement with
THE U.S. NATIONAL AERONAUTICS AND SPACE ADMINISTRATION
and
THE NATIONAL SCIENCE FOUNDATION, WASHINGTON, D.C.

Copyright © 1966
Israel Program for Scientific Translations Ltd.
IPST Cat. No. 1680

Translated by P. Boltiansky, E.E.
Edited by IPST Staff

Printed in Jerusalem by S. Monson

Binding: Wiener Bindery Ltd., Jerusalem

Price: $ 9.00

Available from the
U.S. DEPARTMENT OF COMMERCE
Clearinghouse for Federal Scientific and Technical Information
Springfield, Va. 22151

XII/13/4.5

TABLE OF CONTENTS

FOREWORD v

INTRODUCTION 1

Chapter I. THE DESIGN OF MODELS FOR AERODYNAMIC EXPERIMENTS . . 3
§ 1. Criteria of similarity 3
§ 2. Coordinate axes. Aerodynamic coefficients 8

Chapter II. WIND TUNNELS AND INSTALLATIONS 13
§ 3. Operating principles of wind tunnels 13
§ 4. Subsonic wind tunnels. Open-circuit tunnels 24
§ 5. Transonic tunnels 48
§ 6. Supersonic wind tunnels 63
§ 7. Hypersonic wind tunnels 86
§ 8. Wind tunnels for testing aircraft engines 115

Chapter III. WIND TUNNEL DESIGN CALCULATIONS 122
§ 9. Design of subsonic tunnels 122
§10. Gas dynamics of supersonic tunnels 142

Chapter IV. MEASUREMENT OF FLOW PARAMETERS IN WIND TUNNELS . . 156
§11. Pressure measurement 160
§12. The measurement of the Mach number and flow velocity . . 173
§13. The measurement of flow direction 195
§14. Measurement of temperature in flow 207
§15. Measurement of density: humidity corrections 219
§16. Boundary-layer measurements 223
§17. Instruments for mapping distributions 232
§18. Visual and optical methods of flow distributions 239

Chapter V. INSTRUMENTS AND APPARATUS FOR PRESSURE MEASUREMENT . 255
§19. Liquid-column manometers 257
§20. Mechanical manometers 270
§21. Electrical pressure transducers and micromanometers . . . 281
§22. Equipment for measuring pressure distribution. Multiple manometers 294
§23. Transmission lag in manometric systems 310
§24. Manometric instruments for determining dimensionless characteristics 314

Chapter VI. WIND-TUNNEL BALANCES 326
§25. Wind-tunnel balances located outside the model 328
§26. Design examples of wind-tunnel balances 357
§27. Balance elements of wind-tunnel balances 362
§28. Wind-tunnel balances located inside the model 379
§29. The errors of wind-tunnel balances. Calibration 425

Chapter VII. TECHNIQUES AND METHODS OF AERODYNAMIC MEASUREMENTS 438
§30. Adjustment of wind tunnels 438
§31. Techniques and methods of balance measurements . . . 445
§32. Determination of pressure and velocity distributions . . . 451
§33. The testing of propellers 458
§34. Testing of blade cascades 476
§35. Testing of fans 490
§36. Experimental determination of local resistances 496
§37. Testing of wind turbines 503
§38. Testing of ejectors 508
§39. Determining rotational derivatives 510

Chapter VIII. PROCESSING THE RESULTS OF WIND-TUNNEL TESTS . . . 527
§40. Interference between tunnel and model 527
§41. Interference between model and supports 547
§42. Accuracy and reproducibility of tests 555

Chapter IX. AUTOMATIC DATA RECORDING AND PROCESSING OF WIND-TUNNEL MEASUREMENTS 564
§43. Methods of automatically processing measured data . . . 564
§44. Digital conversion of measured values. Digital conversion of angles 569
§45. Processing the measured data on computers 586

FOREWORD

Aerodynamic measuring techniques and theoretical aerohydrodynamics have developed together. The connection is seen vividly in the works of N. E. Joukowski and S. A. Chaplygin, who established the basis of modern aerodynamic theory, and founded the aerodynamics laboratories of the Soviet Union.

Although the relationship between theory and experiment has changed as aerodynamics developed, there has always been a paucity of experimental data from which to develop the theory.

Some of the measuring techniques and instruments described in this book are mentioned in the well-known books of A. K. Martinov, "Eksperimental'naya aerodinamika" (Experimental Aerodynamics) (1950), S. G. Popov, "Nekotorye zadachi eksperimental'noi aeromekhaniki" (Some Problems in Experimental Aeromechanics) (1952), and N. A. Zaks, "Osnovy eksperimental'noi aerodinamiki" (The Basis of Experimental Aerodynamics) (1957). In these textbooks for advanced students measuring techniques and instruments are necessarily described only briefly and in passing. R. C. Pankhurst and D. W. Holder discuss a wide range of experimental problems in their textbook "Wind-Tunnel Technique" (1952), but the treatment is general and sometimes superficial. Since the publication of these works the technology of aerodynamics has advanced greatly.

We try in this book to treat systematically certain modern techniques of aerodynamic measurement, formerly described only in periodicals. We have made wide use of experience in the USSR and abroad, selecting material to enable readers with a knowledge of theoretical aerodynamics to become familiar with experimental practice and with the instruments and apparatus used in practice.

The book is intended mainly for experimental-research workers in aerodynamics and for those using their results and also for students of fluid dynamics. We think that engineers and technicians designing and constructing aerodynamic installations, and developing measuring equipment, will also find the book useful.

Chapters I, II, III, VII, and VIII were written by S. M. Gorlin and Chapters IV, V, VI, IX and Sections 7 and 34 by I. I. Slezinger.

S. M. G.
I. I. S.

INTRODUCTION

The development of fluid mechanics involves observation and study of the physical phenomena which form the basis of the theory. Experimental aerodynamics serve to check the existing theory, and also its extension. On the other hand, theoretical developments strongly influence experimental techniques, installations and measuring equipment.

Since aircraft first appeared aerodynamics have been directed toward the study of increasingly large flight speeds. There has been a corresponding development of equipment and techniques for experimental research and for measurement. The type of installation and the techniques currently used depend on the flight speed in the five ranges:

1. Low subsonic speeds [Incompressible flow].
2. High subsonic speeds [Subsonic compressible flow].
3. Transonic speeds.
4. Supersonic speeds.
5. Hypersonic speeds.

Experimental aerodynamics are at low speeds are based on the fundamental work of N. E. Joukowski, L. Prandtl, and other leading scientists. This speed range is still important for research in industrial aerodynamics, surface vehicles, and the take-off and landing characteristics of aircraft. There are low-speed wind tunnels, of comparatively low power, in almost every university and institute of advanced learning. For simulating natural conditions in the testing of aircraft, large aerodynamics laboratories of scientific research institutes possess low-speed wind tunnels whose powers extend to tens and even hundreds of megawatts. The techniques for measuring forces, pressures, and speeds, and for visual observation of the flow around bodies at low speeds, are widely used in research at higher speeds, and have merited extensive treatment in this book.

The study of flight at high subsonic speeds, which first became important about 1930, demands considerably more power and complicated equipment, because as speed increases, the compressibility of the air becomes as important as its viscosity. Variable-density wind tunnels are therefore used which must have automatic instrumentation and control and permit measurements of a wide range of parameters. The optical techniques developed for this speed range are even more important at still higher speeds.

We have paid special attention to transonic techniques because of the acoustic effects of aircraft flying at speeds near the velocity of sound. Important techniques are described for measuring parameters and calculating effects which cannot be neglected in experiments in this speed range. We also describe the design of instrumentation for transonic installations.

Even more involved are supersonic wind tunnels, where the power may reach tens, and even hundreds, of megawatts. Measuring techniques, developed for use at lower speeds, can still, with care, be used, but optical techniques become more important, and supplementary techniques must be introduced. The installations are far more expensive; a considerable part of the book is devoted to the use of automatic measuring and data-processing techniques which thus become economical.

Hypersonic speeds, only lately being studied, involve high temperatures and physicochemical processes in gases. They demand a new approach to wind-tunnel design; techniques and instrumentation are being evolved rapidly, and their full description would justify a separate volume. Here we have merely reviewed this aspect of the subject in order to acquaint readers with the trends.

Within each of the five speed ranges it is impossible to separate sharply measuring techniques and use of equipment from installation design. We have therefore alloted individual chapters to the description of aerodynamic research installations, to the measurement of the various flow parameters, to wind-tunnel balances, etc. We hope that this method of presentation will permit the reader to study each problem in detail, while avoiding the repetition which would inevitably follow from a division of the material by speed range. An exception has been made in the chapter on hypersonic speeds, which combines a brief description of experimental installations and common measuring techniques.

Chapter I

THE DESIGN OF MODELS FOR AERODYNAMIC EXPERIMENTS

§ 1. CRITERIA OF SIMILARITY

It is very difficult to reproduce flight conditions exactly in aerodynamic experiments, whether the body is moving through a stationary gas or the gas past a stationary body. Models are therefore commonly used in wind tunnels of limited dimensions, to predict the behavior of prototypes in flight.

The accuracy of predictions from tests on models depends on the fidelity with which flow around the model or in a channel of limited size reproduces the flow around the full-scale body or in the full-scale channel, i. e., it depends on the fulfilment of "criteria of similarity."

As L. I. Sedov /1/ has pointed out, scaling-down will be sucessful if we are able to substitute for the phenomena which interest us, closely analogous phenomena on another scale. Scale-model testing is thus based on studying physically similar phenomena. Geometric similarity* is fundamental to aerodynamic experimentation. The coefficient of geometric similarity, i. e., the geometric scale factor of the model, is the ratio of the dimensions of the model to the dimensions of the (geometrically similar) natural object. Mechanical or physical similarity implies that we should be able to calculate physical effects from observations on a different scale. However, certain conditions must be fulfilled if this similarity is to be achieved.

We define two systems as being similar to each other if all the physical characteristics at corresponding points** in the two systems have the same relationship. The relationship between masses, velocities, viscosities, and other parameters in two such systems can be derived by considering the conditions and relationships within each system at any instant.

For the flow of viscous, incompressible fluids such considerations /2/ show that at corresponding points within the systems mechanical similarity demands that

$$\frac{t_2 V_2}{l_2} = \frac{t_1 V_1}{l_1}; \quad \frac{Z_2 l_2}{V_2^2} = \frac{Z_1 l_1}{V_1^2};$$

$$\frac{\nu_2}{V_2 l_2} = \frac{\nu_1}{V_1 l_1}; \quad \frac{p_2}{\rho_2 V_2^2} = \frac{p_1}{\rho_1 V_1^2}.$$

* Two bodies are "geometrically similar" if the ratio of all corresponding linear dimensions is uniform.

** By corresponding points of similar systems we understand points which are similarly placed geometrically in relation to geometrically similar bodies within the two systems.

Here t is a representative time, l a representative length, ρ the density, ν the coefficient of kinematic viscosity, Z the body force [gravity, centrifugal force, etc.; Z has the dimensions of acceleration], V is the velocity, p the pressure; the subscripts 1 and 2 refer to the first and second system respectively.

The first of these relationships is the condition for kinematic similarity. The other expressions define the conditions of dynamical similarity, i.e., the similarity of forces arising during motion.

To ensure similarity when studying rotational motion of liquids or bodies (the flow of liquid around a rotating propellor, or the velocity fluctuations in a wake) the [dimensionless] coefficient $\frac{tV}{l}$ must be the same for both model and prototype. In practice, for cyclic phenomena, we use Strouhal's criterion that

$$\frac{nl}{V} = \mathrm{Sh} ,$$

be constant, n being the frequency and V the free-stream velocity of the flow. For example, when comparing performance and efficiencies of propellers we maintain constancy of the advance ratio

$$\lambda = \frac{V}{n_c D} .$$

Here n_c is the number of revolutions of the screw; the advance ratio, relating the flight speed to the circumferential velocity of the blade tips, is a form of the Strouhal number, which ensures similarity of the systems.

For steady flow of viscous, incompressible liquids two conditions of similarity apply. Both the Froude number

$$\frac{V_2^2}{gl_2} = \frac{V_1^2}{gl_1} = \mathrm{Fr},$$

and the Reynolds number

$$\frac{V_2 l_2}{\nu_2} = \frac{V_1 l_1}{\nu_1} = \mathrm{Re}$$

must be the same for the two systems.

Thus, in a viscous, compressible liquid under the action of the force of gravity only, two systems which have the same Reynolds and Froude numbers are similar. Whenever we mention "similarity" phenomena, we consider geometrically similar bodies, similarly oriented with respect to the flow.

When there are no body forces the criteria of similarity are greatly simplified; two flows will then be similar if the Reynolds numbers are the same. The aerodynamic forces on a body depend in this case only on the Reynolds number and the orientation of the body to the flow.

When allowance is made for inertia, viscosity, compressibility, and thermal conductivity*, the conditions for the mechanical similarity of motion in fluids, of geometrically similar, similarly placed solid bodies, are more complicated. It is then necessary to maintain equality of the

* Neglecting buoyancy and radiant heat transfer.

following dimensionless parameters in the two systems:

$$\mathrm{Re}=\frac{Vl}{\nu};\ \mathrm{M}=\frac{V}{\sqrt{\varkappa gRT}};\ \mathrm{Pr}=\frac{\mu c_p}{\lambda};$$
$$\varkappa=\frac{c_p}{c_v};\ \frac{T_1}{T}\text{ and }\frac{C}{T}.^{*}$$

Here **M** is the Mach number, which relates flight speed to the velocity of sound $a=\sqrt{\varkappa gRT}$, Pr is the Prandtl number; C is Sutherland's constant (which has the dimensions of temperature, and for air is about 113°C)**; λ is the coefficient of thermal conductivity; μ is the ratio of the specific heat c_p at constant pressure to the specific heat c_v at constant volume; T_1 is the absolute temperature at the surface of the body; and T is the absolute temperature of the gas.

In some cases $T_1 \approx T$, and the parameter T_1/T may be ignored. It is often permissible to ignore C/T, which expresses the influence of the temperature on the viscosity and thermal conductivity†. Thus, in studying motion through gases of equal compressibility and atomicity, and for which the values of $\frac{c_p}{c_v}$ and Pr are therefore the same, similarity will be ensured if the Reynolds and Mach numbers are the same in both gases. These two magnitudes are the most important similarity criteria in aerodynamics.

For an ideal, incompressible fluid, the criterion of similarity for the pressures at corresponding points is expressed by

$$\frac{p_2}{\rho_2 V_2^2}=\frac{p_1}{\rho_1 V_1^2}.$$

It thus follows that the ratio of the reactions R_1 and R_2 of the fluid on geometrically similar (and similarly oriented) bodies is

$$\frac{R_1}{R_2}=\frac{\rho_1 V_1^2 l_1^2}{\rho_2 V_2^2 l_2^2}=\mathrm{Nw},$$

where **Nw** is Newton's [dimensionless] number.

Newton's number defines the similarity in this case.

Thus in an ideal, incompressible fluid, the hydrodynamic forces on a body are proportional to the square of the relative velocity (Square Law).

* The criterion C/T is important when the gases have different numbers of atoms per molecule. For gases of the same atomicities the values of $\varkappa$ and Pr will be the same.

** Sutherland's Criterion can be written

$$\frac{\lambda}{\lambda_0}=\frac{\mu}{\mu_0}=\frac{1+\frac{C}{273,1}}{1+\frac{C}{T}}\sqrt{\frac{T}{273,1}},$$

where λ_0 and μ_0 correspond to $T = 273,1°$.

† This may be done by using the criterion

$$\frac{\lambda}{\lambda_0}=\frac{\mu}{\mu_0}=\sqrt{\frac{T}{273,1}}.$$

which does not contain the dimensional constant C.

This law is exact only when the fluid displays ideal behavior during the experiment.

For viscous flow of a fluid at sufficiently high Reynolds number this law is a good approximation. At very low velocities, corresponding to small values of **Re**, the influence of the viscous forces increases. When inertia forces become negligible in comparison with the viscous drag, the force on a body is proportional to the velocity, to the linear dimensions of the body, and to the coefficient of viscosity (Stokes Law). At very high Reynolds numbers viscosity effects decrease while compressibility effects increase. As the flow velocity increases, the forces due to the elasticity of the gas, which depend on its pressure, become comparable with the forces of friction, inertia etc. This causes not only a quantitative change in the aerodynamic characteristics of the body (e.g., drag), but also in the nature of the flow around the body. In particular, as **M** approaches unity, the flow becomes locally supersonic in several regions around the body; this causes shock waves and dissipation of energy. The pressure distribution over the body and the moments due to the applied forces will change, and the drag will increase sharply. It may, therefore, be best to accept variations of the Reynolds number in experiments, to avoid changes in the Mach number

Attainment of full similarity i.e., similarity of all parameters, may in practice be impossible. If we choose the same medium for the two systems (e.g., water or air) at the same temperature and pressure, then for equality of **Fr**, **Re**, and **M** we must have $\rho_1 = \rho_2$, $\nu_1 = \nu_2$, , and $g_1 = g_2$; so that $V_1 = V_2$ and $l_1 = l_2$, i.e., it is impossible to obtain similar motions in the same medium for two bodies of different sizes. Although in principle it is possible to achieve similarity using two different liquids, it is in practice difficult to select satisfactory values of ν and a.

For these reasons it is possible to obtain only partial similarity in most aerodynamic experiments, and we must select those criteria on which the phenomena of interest most strongly depend.

In practice, geometric similarity is fully maintained only when testing full-scale prototypes under field conditions, or when a full-scale model is much smaller than the test section of the wind tunnel. In most cases the full-scale prototype is much larger than the tunnel, and tests must be made on a reduced scale, at which it is difficult to reproduce faithfully the shape of small projections and the surface finish of the prototype. This unavoidably introduces inaccuracy, especially at high test velocities. Dimensional tolerances in scale-model production are therefore sometimes tenths or hundredths of millimeters. Often, we model only the main elements of a prototype: during comparative wing tests the ailerons and flaps are not modelled.

In current practice the orientation of bodies in space can be reproduced with sufficiently high accuracy (0.1 to 0.2°). The Reynolds number is an adequate criterion of similarity at low velocities. At Mach numbers above 0.3 or 0.4 (depending on the shape of the body and its orientation in the fluid) compressibility becomes increasingly important, and the Mach number must be reproduced in the model test. Aerodynamic characteristics will still, however, be considerably influenced by viscosity, and for accuracy in such tests it is necessary to reproduce both Reynolds and Mach numbers.

When compressibility effects predominate (e.g., in a jet airplane or rocket) it is sufficient to consider only the Mach number. In the same

medium at equal temperatures, similarity then requires only that $V_2 = V_1$.

The Reynolds number can be reproduced in a small-scale model by increasing the velocity in inverse proportion to the geometric scale factor, or by increasing the density of the test medium in inverse proportion to the product Vl *. It is technically difficult to increase the velocity, since the power required is proportional to V^3. Even when adequate power is available, it must be remembered that as the velocity increases, compressibility effects become increasingly important, so that by maintaining the Reynolds number constant we may cause changes in the Mach number. It is therefore common practice to reproduce the Reynolds number by increasing the density, using variable-density wind tunnels, the flow velocity being sufficient to permit simultaneous reproduction of the Mach number.

Reproduction of the Mach number requires reproduction of the ratio of the flow velocity to the velocity of sound. Since the velocity of sound is $a = \sqrt{\varkappa g R T}$ it can be altered by varying either T or the product $\varkappa R$.

The use of other gases instead of air /3/ (e.g., Freon, which has a lower value of $\varkappa R$, and requires much less power for a given **M**) is technically difficult.

In this discussion of similarity criteria we have assumed that other things being equal the same velocities in the two systems corresponded to equal forces. However, there are usually velocity fluctuations superimposed on the mean velocities in a wind tunnel. The effect of these fluctuations on the flow and on the forces acting on the model, is in many ways analogous to the effect of increasing the Reynolds number. The ratio of the r.m.s. fluctuating velocity to the mean velocity of the undisturbed flow is the turbulence level ε of the undisturbed flow. It is necessary to reproduce the value of ε as closely as possible in the model, since there is no practical way of calculating its effect on the aerodynamic characteristics. In few wind tunnels are the values of ε as low as in nature. Wind tunnels in which ε exceeds 0.5 to 1% are unsuitable for physical aerodynamic research** and for these purposes it is usual to build special low-turbulence tunnels.

When studying the flow of rarified gases, an important criterion of similarity is the Knudsen number δ, which is the ratio of the molecular mean free path L to a representative length of the body or the thickness of the boundary layer. Molecular motion is important to a decreasing extent /4/ in free molecule flow and slip flow, and can be ignored generally in gas dynamics (Figure 1.1).

Other characteristics of the gas or body, which may play an important part in the motion, will each involve new criteria and similarity conditions. For instance, in the study of a vibrating wing in a gas stream, dynamic similarity depends on the dimensionless parameters $\rho V^2/E$; G/E and $m/\rho l^3$ where E is Young's modulus, G the shear modulus, and m, the mass of the wing.

In experimental work our problem is to select those similarity criteria which most influence the test results. Imperfect similarity will lead to

* It should be remembered that the coefficient of dynamic viscosity μ is independent of density, and therefore of pressure. The coefficient of kinematic viscosity $\nu = \mu/\rho$ depends on density, and thus on pressure.

** Investigations of the structure of the boundary layer, the position of the transition point from laminar to turbulant flow, etc.

errors which must be evaluated when making predictions of prototype behavior from results of tests on models. This is a particular case of the basic problem of aerodynamics, i.e., to determine the criteria and similarity conditions relevant to particular aerodynamic characteristics; methods, instruments, and technology of all aeromechanical measurements depend on the solution of this problem.

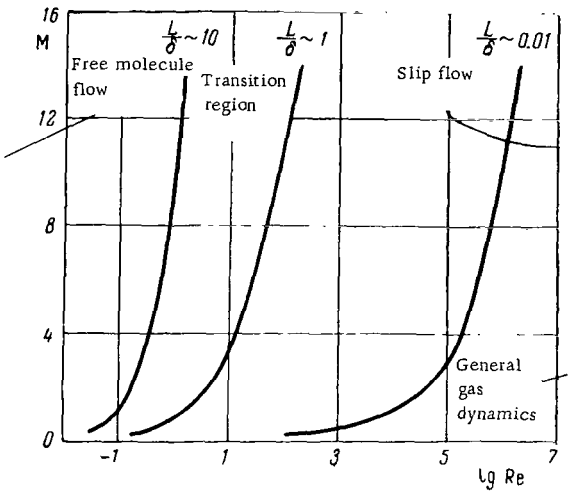

FIGURE 1.1. Flow regimes in fluids.

§ 2. COORDINATE AXES. AERODYNAMIC COEFFICIENTS

In experimental aerodynamics and aircraft design we use (as specified in GOST 1075-41) one of the following coordinate systems: velocity, fixed, or semifixed. All these are right-hand systems, in which positive rotation about any axis appears clockwise to an observer placed at the origin. All these systems of coordinates have a common origin at the center of gravity of the aircraft. In the velocity system of coordinates $Oxyz$ (Figure 1.2) the x-axis is positive in the direction of flight. The y-axis lies in the plane of symmetry of the body; its direction is parallel to the lift on the aircraft, being positive upwards. The z-axis is normal to the Oxy plane, and is positive to starboard (toward the right when looking forward).

The fixed system of coordinates $Ox_1y_1z_1$ corresponds to the geometric axes of the aircraft; the x_1-axis is directed forward parallel to the horizontal center line or the wing chord which determines the angle of attack. The semifixed system of coordinates coincides with the velocity system when there is no sideslip or drift ($\beta = 0$).

When the angle of sideslip changes, the semifixed system rotates with the body around the y-axis. The velocity system of coordinates differs from the the semifixed system by the angle of attack. The angle of attack thus defines the orientation of the body with respect to the semifixed axes.

In wind-tunnel tests of fixed models, the free-stream velocity is opposed to the velocity of free flight; to avoid having negative drag forces we sometimes use a flow coordinate system in which we replace the x-axis of the velocity system by an axis OQ in the opposite direction. The directions of positive rotations in the flow system of coordinates are the same as in the velocity system. In the literature the OQ axis is often denoted by Ox for simplicity; the reader should be aware of this.

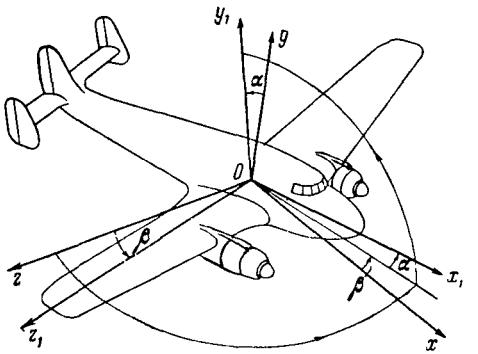

FIGURE 1.2. Velocity and fixed systems of coordinates

In wind-tunnel tests in which the angles of attack and sideslip both vary it is usual to apply not the flow system of coordinates but a modified semifixed system in which the positive direction of the x-axis is reversed. When there is no sideslip ($\beta = 0$) this semifixed "tunnel" system coincides with the flow system, but when the sideslip angle changes the semifixed system follows the model, rotating about Oy by the angle β. In wind tunnels the primary measurements of forces and moments are usually made in the so-called "weight system of coordinates" (Chapter VI), while the results are expressed in the flow or "tunnel" systems. This is very important when determining moment coefficients. The signs of moments and angles of rotation of the control surfaces are shown in Figure 1.3 for a velocity system of coordinates.

The total aerodynamic force which acts on a body moving in a fluid is proportional to the density, the square of the velocity, and the square of the linear dimensions: $R = c_R \rho V^2 l^2$. The constant of proportionality c_R depends on the shape of the body, its orientation in the flow, and the conditions of similarity; it is called the coefficient of total aerodynamic force.

In experimental aerodynamics we often use a representative area S (for instance, the wing area of an aircraft, or the cross section of a body) rather than l^2; and the velocity head ρV^2 of the flow instead of $\rho V^2/2$ The total aerodynamic forces is then

$$R = c_R \rho \frac{V^2}{2} S, \qquad (1.1)$$

where c_R is the coefficient of total aerodynamic force.

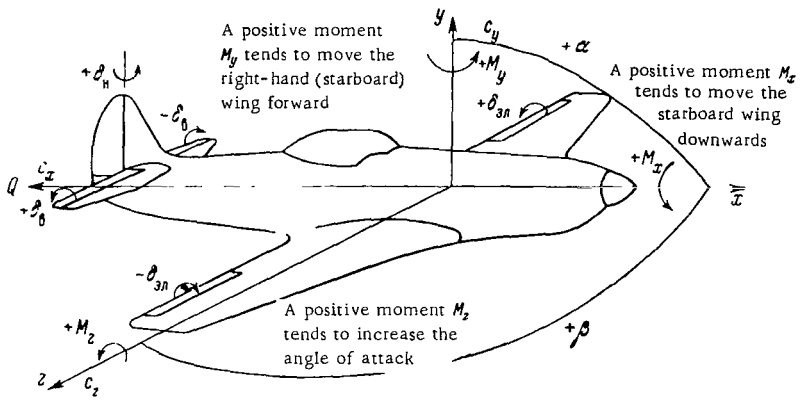

FIGURE 1.3. Signs of angles and moments in the velocity system of coordinates

The moment $M = RL$ due to the total aerodynamic force is taken about a specified point, usually the center of gravity of the body; it can be expressed expressed as

$$M = m_M \rho \frac{V^2}{2} SL, \tag{1.2}$$

where m_M is the coefficient of total aerodynamic moment.

The projections of the total aerodynamic force on the velocity axes are:

The lift (c_y is the coefficient of lift)

$$Y = c_y \rho \frac{V^2}{2} S, \tag{1.3}$$

The force parallel to the direction of flight ($-c_x$ is the coefficient of chordwise force for velocity axes)

$$X = -c_x \rho \frac{V^2}{2} S, \tag{1.4}$$

The side force (c_z is the coefficient of side force)

$$Z = c_z \rho \frac{V^2}{2} S. \tag{1.5}$$

The components of the moments, due to the total aerodynamic force, with respect to the coordinate axes are:

The heeling moment (m_x is the coefficient of heel)

$$M_x = m_x \rho \frac{V^2}{2} SL, \tag{1.6}$$

The yawing moment (m_y is the coefficient of yaw)

$$M_y = m_y \rho \frac{V^2}{2} SL, \tag{1.7}$$

The pitching moment (m_z is the coefficient of pitching)

$$M_z = m_z \rho \frac{V^2}{2} SL. \tag{1.8}$$

In the flow system of coordinates we use the concept of drag $Q = -X$, positive in the direction of the undisturbed flow; correspondingly, the coefficient of drag is c_x. The positive directions of the forces Y and Z coincide respectively with the positive directions of the y and z axes.

In the fixed system of coordinates $Ox_1y_1z_1$ the total aerodynamic force R has the following components:

Tangential force

$$X_1 = -c_{x1} \rho \frac{V^2}{2} S, \tag{1.9}$$

or drag

$$Q_1 = -X_1 = c_{x1} \rho \frac{V^2}{2} S; \tag{1.10}$$

Normal force

$$Y_1 = c_{y1} \rho \frac{V^2}{2} S, \tag{1.11}$$

and transverse force

$$Z_1 = c_{z1} \rho \frac{V^2}{2} S. \tag{1.12}$$

The symbols for the components of the total moment and their coefficients are the same in the flow and fixed systems, the subscript "1" denoting the fixed system. We can determine the signs of the moments by the following rule: the origin of coordinates is at the center of gravity of the model. To an observer placed at the distant end of an axis, a positive moment will tend to turn the model about that axis in a counterclockwise direction.

A detailed description of the coordinates systems used in experimental aerodynamics, and the formula for transformation from one system to another will be found in /5/ and /6/.

BIBLIOGRAPHY

1. Sedov, L.I. Metody podobiya i razmernosti v mekhanike (Similarity Methods and Dimensions in Mechanics). — GTTI. 1957.
2. Kochin, N.E., I.A. Kibel' and N.V. Roze. Teoreticheskaya gidromekhanika (Theoretical Hydromechanics). — Gostekhizdat, 1948.
3. Pankhurst, R.C. and D.W. Holder. Wind-Tunnel Technique. — Pitman, London. 1952. [Russian translation, 1955.]
4. Tsien, H.S. Aerodinamika razrezhennykh gazov (Aerodynamics of Rarified Gases). — Review of "Gas Dynamics", IL. 1950.

5. Martynov, A.K. Eksperimental'naya aerodinamika (Experimental Aerodynamics). — Oborongiz. 1958.

6. Zaks, N.A. Osnovy eksperimental'noi aerodinamiki (Fundamentals of Experimental Aerodynamics). — Oborongiz. 1953.

7. [Pankhurst, R.C. Dimensional Analysis and Scale Factors. Institute of Physics and the Physical Society, London. 1964. (Especially Chapter VII)].

Chapter II

WIND TUNNELS AND INSTALLATIONS

§ 3. OPERATING PRINCIPLES OF WIND TUNNELS

The effects of air on a body moving in it can be studied by imparting to the body a velocity in relation to the stationary air, or imparting to the air a velocity in relation to a stationary body.

Most problems of experimental aerodynamics are connected with the study of motion of a body in relation to a stationary fluid (direct problem). However, we can reverse the problem and study the motion of a fluid in relation to a stationary body (inverse problem). When the conditions of motion reversal are strictly maintained, and all effects are excluded which are due to the wind-tunnel boundaries, which are commensurable with the body investigated, full agreement of the laws of fluid flow around a body is obtained between the direct and the inverse problem.

Nowadays, direct investigations with complex equipment and special measuring techniques are undertaken in different types of flight and airfield tests of flying machines (airplanes, rockets, etc.) and their models, and for testing separate elements of these machines.

Airfield and flight tests make it possible to maintain full dynamic similarity, but their main drawback is that in addition to the high cost and complications, research on many types of machines, the study of the interaction of separate elements (e.g., of wing and tail, or propeller and fuselage), testing under similar operating conditions, etc. present difficult problems, sometimes impossible to solve. Therefore, aerodynamic full-scale tests supplement and complete the tests made in wind tunnels.

Aerodynamic measurements are also possible on a whirling arm (Figure 2.1), where the tested body moves together with the rotating arm of the machine. However, the body is in this case moving in air agitated by the arm of the machine. This affects both in magnitude and in direction the flow velocity relative to the model. Thus, in tests on the whirling arm, similar conditions are not obtained, and this method is only used in special problems, e.g., for finding the heeling and yawing moments acting on an airplane, which are due to the continuous rotation about a vertical axis.

The main method of research, which determines the success of aerodynamics as a science and its wide application in many fields of technology, is the testing in wind tunnels. The wind tunnel is a physical instrument, which makes it possible to obtain in one of its elements, i.e., in the test section where the body under test is placed, uniform

rectilinear steady air flow at a given velocity. A simple wind tunnel for low subsonic speeds (low-speed tunnel) is shown in Figure 2.2.

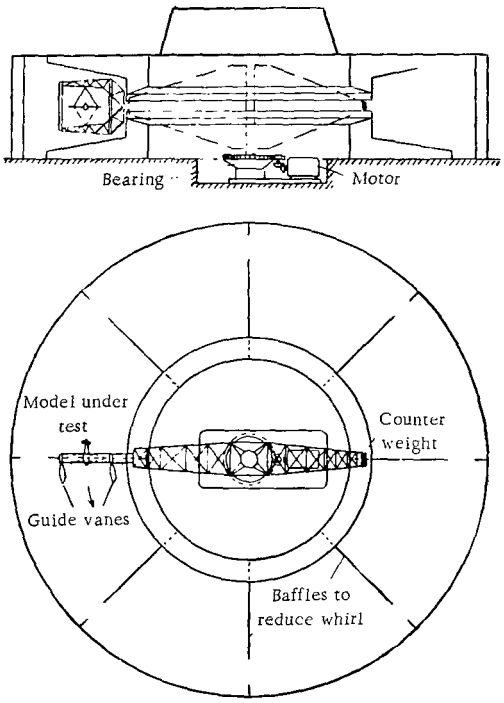

FIGURE 2.1. Whirling arm.

Air from the outside is drawn in by a fan at the end of the tunnel. The air enters first a nozzle whose cross section gradually decreases in the flow direction. The flow velocity is thus increased. After attaining its maximum velocity in the narrowest section of the nozzle, the air enters the test section, whose cross section is constant. The test section contains

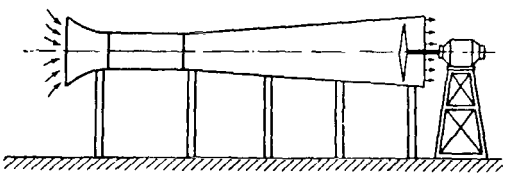

FIGURE 2.2. Simple wind tunnel.

the body to be tested around which the air flows uniformly at constant velocity. Behind the test section there is the diffuser, whose gradually increasing cross section permits a gradual reduction of the flow velocity.

The fan is installed at the end of the diffuser. The flow velocity in the tunnel is changed by adjusting the rotational speed of the fan.

The tunnel shown in Figure 2.2 operates on the open-circuit principle with closed test section. In this tunnel the flow around the model is confined between solid walls. If in such a tunnel we increase the diffuser length, providing a return duct, and connect it to the nozzle, we obtain a closed-circuit wind tunnel with closed test section in which the air circulates continuously in a closed cycle. If we remove the walls of the test section, we obtain a closed-circuit tunnel with open test section, in which the air also circulates in a closed cycle.

If in the open-circuit tunnel (Figure 2.2) we remove the walls of the test section, the latter has to be surrounded by a hermetically sealed chamber (Eiffel chamber) in order to obtain correct air flow through the tunnel.

Design requirements for wind tunnels

Already invented at the end of the 19th century, wind tunnels are nowadays widely used in developed countries. The dimensions of existing tunnels vary over a wide range — from tunnels with test sections whose cross-sectional areas are a few cm^2, to tunnels which enable modern bombers to be tested in full-scale size. The power, necessary to operate such a tunnel, may attain hundreds of thousands of kw. However, despite the great variety of types, dimensions, and designs of wind tunnels, their principal characteristics are the same; and differences are due only to the specific requirements which a given wind tunnel must fulfil.

The main requirement of a wind tunnel is the possibility of obtaining a translational uniform rectilinear air flow. The fulfillment of this requirement is very difficult. To a first approximation linearity and flow uniformity are provided by the geometry of the tunnel walls and by internal constructional elements. *

Figure 2.3 shows the velocity distribution in the test section. As can be seen, over a large part of the cross section the velocity is uniform and rectilinear, forming a large "core" in which the tested body can be placed. Outside this core the velocity decreases to zero at the boundaries or walls. The core should be as large as possible.

The velocity distribution should not vary greatly over the length of the test section, in which the static pressure should be constant; otherwise, the wing of an airplane would be tested under different conditions than the tail. The flow velocity in the test section** should not deviate from the

* Special attention should be paid to the shape of the nozzle, test section, and diffuser. The linear dimensions of transonic tunnels should be accurate to within ± 1/200 to 1/1000, while the straightness of the tunnel axis and the blade angles of the fan, should be exact to within ± 0.25° to ± 0.5°.

In supersonic wind tunnels the contour coordinates of the nozzles are practically accurate to within ± 0.05 mm. Especially in the case of a high-speed tunnel, the inner walls must be not only smooth (the permissible roughness is ± 0.01 to 0.3 mm), but also sufficiently strong and elastic to withstand damage by broken parts of the model and its supports in the test section and at the leading edges of the blades of high-speed fans and compressors. For this reason, in closed-circuit high-speed tunnels, provision must be made for systematic dust removal.

** The flow conditions in other parts of the tunnel are important only in as much as they affect the flow conditions in the test section and the operation of the fan.

mean value by more than ± 0.5 to 0.75%, while the flow direction in the horizontal or vertical plane should not deviate from the axial direction by more than ± 0.25°.

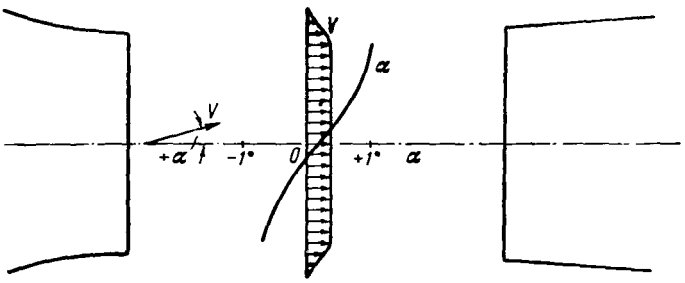

FIGURE 2.3. Velocity distribution in the test section of a wind tunnel.

Usually the static pressure varies linearly along the test section in low-speed tunnels ($V \approx 100$ m/sec); with open test sections* $\frac{d\bar{p}}{dx} = 0.01\ \text{m}^{-1}$ (where $\bar{p}$ is the difference between the static pressure of the flowing medium and atmospheric pressure, divided by the velocity head).

No less important, but more difficult is the maintenance of low initial turbulence in the test section of the tunnel. The air flow in the tunnel is always turbulent to a certain degree. A high level of turbulence or vorticity affects the test results, due to changes in the flow pattern, caused by premature transition from laminar to turbulent flow in the boundary layer around the tested body. Strong turbulence also causes the transition region to be displaced forward along the body, changes the frictional resistance, etc. Thus, an increase in turbulence is to a certain degree analogous to an increase of the Reynolds number.

The influence of initial turbulence in the tunnel depends on the test conditions. In air at rest, under normal conditions of free flight or motion of a body, turbulence is small and can even be ignored. To determine the influence of the Reynolds number, turbulence in the test section should be reduced as far as possible. The turbulence level is $\varepsilon = \frac{\bar{v}}{V_{av}}$ where $\bar{v} = \sqrt{\frac{1}{t}\int_0^t V^2 dt}$ is the root-mean square of the velocity and t is a time interval during which a large number of velocity fluctuations occur. The value ε is given in %. Since conventional tunnels are most frequently equipped with measuring instruments giving averaged velocities, the turbulence level must be taken into account when analyzing and interpreting the test results.

For indirect evaluation of the turbulence level in a wind tunnel we use the results of measuring the drag of a sphere. Such tests in wind tunnels having different turbulence levels, give different values of drag. Figure 2.4 shows the results of such tests.

* In tunnels with closed test sections, steps are also taken to reduce the pressure gradient (see below).

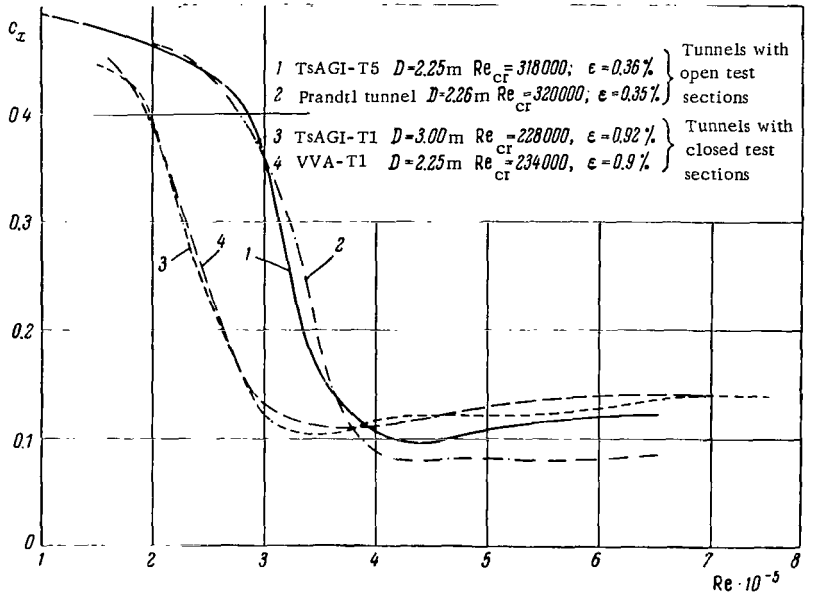

FIGURE 2.4. Drag of a sphere, obtained by tests in different tunnels.

Knowing the turbulence level we can plot the diagram in Figure 2.4 as a functional relationship $\varepsilon\% = f(\mathrm{Re}_{cr})$ where Re_{cr} is the Reynolds number for which c_x is 0.3*. In Figure 2.5, the curve $\varepsilon\% = f(\mathrm{Re}_{cr})$ is very smooth and agrees well with the results of various experiments. To find the turbulence level in a newly built tunnel, the drag of a sphere should be determined at different flow velocities (or of spheres of different diameter at a constant velocity) and the relationships $c_x = f(\mathrm{Re})$ plotted.

Determining from this diagram the Reynolds number at which $c_x = 0.3$, we find from Figure 2.5 the value of $\varepsilon\%$. According to flight tests, the critical Reynolds number for a sphere under atmospheric turbulence conditions is 385,000.

In properly designed wind tunnels the critical Reynolds number for a sphere does not exceed 360,000 — 375,000 ($\varepsilon = 0.2$ to 0.3%). The critical Reynolds number can also be determined from the pressure difference between the frontal stagnation point and the point of flow separation from the sphere. It was shown experimentally that the value $c_x = 0.3$ corresponds to a ratio of 1.22 between this pressure difference and the velocity head in the undisturbed flow.

An important requirement for wind tunnels is the absence of flow-velocity fluctuations, which are mainly caused by the periodical shedding of vortices from poorly streamlined elements of the tunnel, (fans, fairings, protruding parts, etc.), and by the poor streamlining of the tunnel in general, especially in the nozzle (in tunnels with open test sections), diffuser, and

* At $c_x = 0.3$ there is an abrupt change in $c_x = f(\mathrm{Re}, \varepsilon)$; this presents a more accurate determination of $\mathrm{Re}_{cr} = f(\varepsilon)$.

and corners. As a rule, such fluctuations do not cause considerable changes in the aerodynamic characteristics of the test body, but lengthen the time required for measuring the aerodynamic forces, and cause damage to the tunnel.

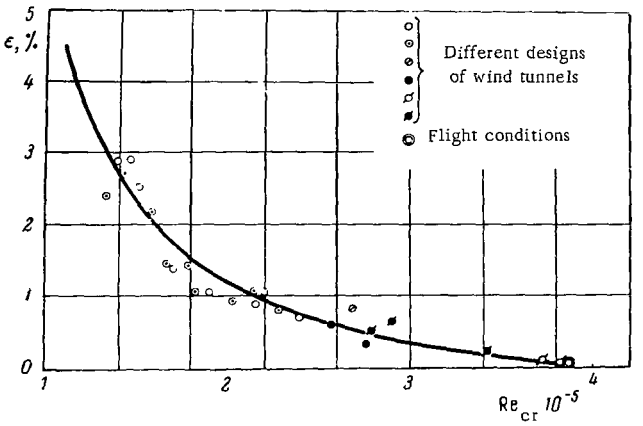

FIGURE 2.5. Dependence of Re_{cr} for a sphere on turbulence in tunnels.

Velocity fluctuations can be eliminated by proper streamlining of the tunnel and installing special devices for breaking up vortices (outlets in the diffuser, etc.).

Requirements of wind-tunnel instruments

Wind-tunnel test instruments can be divided into 3 main groups.

The first group comprises instruments for measuring the flow parameters of the air — velocity, density, temperature, and humidity. The second group comprises instruments to determine the aerodynamic forces on the test models. The third group consists of instruments for determining the pattern of airflow around models.

Instruments and devices for controlling and monitoring the operation of the tunnel itself and of the auxiliary installations, are not discussed here.

The main requirements of wind-tunnel instrumentations are as follows:

1. Stability in the period between instrument calibrations and test checks; the systematic (instrument) errors must be constant.
2. Minimum flow perturbation by instruments both near the instrument and near the test object.
3. Small random errors of measurement.

To fulfill this last requirement it is essential, before making any measurements in the tunnel, to determine carefully, with the aid of the error theory, the accuracy anticipated in the tests. The error ΔF in a function F of a number of arguments x_i respectively subject to random errors Δx_i

(i.e., the error of indirect measurement) can be expressed in terms of the partial derivatives of the functions /1/

$$\Delta F = \pm \sqrt{\Sigma_i \left(\frac{\partial F}{\partial x_i} \overline{\Delta x_i} \right)^2},$$

taking the random errors Δx_i as the errors in a single measurement, as determined by static calibration of the instrument. Although no definite conclusion can be drawn in this way on the accuracy of the whole experiment, which is affected by the dynamic characteristics of the instruments and by other factors, the method does permit evaluation of the effects of the various errors on the total error ΔF, and provides an adequate basis for selecting measuring instruments and equipment. For instance, four instruments are used in wind tunnel investigations of propeller efficiency, viz. of wind-tunnel balance for measuring the thrust P and the torque M, a tachometer to measure the rotational speed n_c of the propeller, and a manometer to measure the flow velocity of the air.

If the test results are to be used for predicting to an accuracy of 1%, the flight speed of an aircraft equipped with this propeller, and if we assume that all the errors are of a random nature and arise from the determination of the propeller efficiency, the latter has to be determined with a random error of not more than ±3%, since the flight speed V is proportional to the cube root of the propeller efficiency

$$V = \sqrt[3]{\frac{75N\eta}{\rho c_x S}}.$$

Each of the four instrument systems used in determining the efficiency must therefore have a random error considerably smaller than ±3%. It can be shown that the relative error of the efficiency measurement is

$$\frac{\Delta\eta}{\eta} = \sqrt{\left(\frac{\Delta P}{P}\right)^2 + \left(\frac{\Delta M}{M}\right)^2 + \left(\frac{\Delta n_c}{n_c}\right)^2 + \overline{\left(\frac{\Delta V}{V}\right)^2}},$$

so that if each of the instruments has the same accuracy, the limit of the permissible random error for each of them can be found from the expression

$$\pm 3\% = \pm \sqrt{4\Delta^2},$$

whence

$$\Delta = \pm \frac{3}{2}\%.$$

However, the flight speed of the aircraft is a function not only of the propeller efficiency but also of the drag coefficient c_x of the airframe and the power N of the engine. If we suppose that each of these is subject to the same random error as the efficiency, the latter will have to be measured to an accuracy of $\pm\sqrt{3}\%$. Hence, the permissible random error in each of the four measuring systems used to determine magnitude of η is $\pm\frac{\sqrt{3}}{2}\%$. In aerodynamic research the accuracy of standard instruments is thus likely to be inadequate.

The accuracy of experiments depends not only on the accuracy of the instruments but also on the degree to which similarity conditions are maintained in the experiment, the exactness of boundary-layer corrections, the allowance made for the interference between the model and its supports, etc.

Types of wind-tunnel tests

Tests in wind tunnels can be divided into the following kinds:

1. Investigating the effects of the shape of the model on its aerodynamic characteristics as functions of the free-stream velocity and the attitude of the model. Such experiments are, as a rule, carried out in two stages; the effect of various shapes is first investigated at a constant flow velocity (usually in a low-speed tunnel), and, having selected the optimum shape, further tests are carried out at different flow velocities in a high-speed* tunnel.
2. Testing of gas turbines, compressors, propellers, fans, etc.
3. Testing the characteristics of aircraft engines (piston engines, turbojets, ramjets, etc.).
4. Investigations of flight dynamics.
5. Investigations of the effects of aerodynamic forces on the elastic characteristics of structures of flying machines (for instance, the study of wing flutter).
6. Physical testing concerned with the flow of air under different conditions. Studies of the boundary layer and of supersonic flow, etc.
7. Methodological research involving wind tunnels as physical instruments, the development of test methods, and the processing of derived data.

Although the techniques used in all these investigations have much in common, it is necessary as a rule to build wind tunnels with facilities specifically designed for a limited range of investigations.

This has led to the creation of the many types and designs of modern wind tunnels.

The effect of experimental conditions in wind tunnels

Application of the results of wind-tunnel tests to bodies moving under actual flow conditions is possible only if experimental and actual conditions are completely similar. However, even then (similarity conditions will be discussed below) the results of tests in any wind tunnel require corrections specific to the experimental conditions of testing a particular model in a given wind tunnel.

These corrections are chiefly concerned with the following parameters of the experiment:

* High- and low-speed tunnels require models of different strengths and designs.

1. **Effect of flow quality.** This is the effect of nonuniformities of velocity distribution and of flow direction in the empty tunnel, i.e., when its test section contains no model and is devoid of obstructions to the flow.

After determining the characteristics of the tunnel, we can introduce a correction for the nonuniformity of flow velocity, using for processing the experimental results the arithmetic mean velocity at the point where the model has its maximum span. Flow inclinations smaller than 0.25° can be neglected since the relevant correction will be only 1 to 1.5% of the measured value. However, if the total flow inclination in the tunnel is as high as ±1°, the correction for the inclination must take into account the fact that as a rule, wind-tunnel balances measure the components of the aerodynamic forces in directions parallel and perpendicular to the constructional axis of the tunnel, while the components to be measured are parallel and perpendicular to the flow direction.

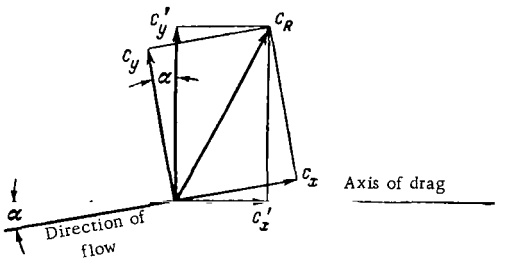

FIGURE 2.6. Effect of flow inclination on force coefficients.

Figure 2.6 shows the influence of the angle of flow inclination α on the magnitude of the coefficients of lift c_y and of drag c_x of the model. Since α is small we may write

$$c_y = c_y' - \alpha c_x',$$
$$c_x = c_x' + \alpha c_y',$$

where α is measured in radians. For modern airfoils, which have small drag, $\alpha c_x'$ is small (of the order 2 to 3% of the value of c_y'); the magnitude of $\alpha c_y'$ is comparable with that of c_x'. For instance, the correction in c_x when $\alpha = 1°$ and $c_y = 0.25$ (corresponding to an angle of attack of about 2°) is approximately 0.0045, whereas the true magnitude of c_x under these conditions is 0.015.

2. **The effect of the model supports and struts.** The components used to support the model obstruct the flow, and cause a general change in velocity and pressure distributions around them; this, in turn, affects the magnitude of the aerodyhamic forces acting on the model. The supports also cause interference with nearby components of the model. Furthermore, the aerodynamic forces acting on the supports are partially transmitted to the wind-tunnel balance used for measuring the aerodynamic forces acting

on the model. All these effects must be taken into account and eliminated from the test results. Methods for eliminating the effects on the supports, and deriving test results referring to the "clean" model are described below (Chapter VIII).

3. Wall effects. Under actual conditions of tests in wind tunnels the flow boundaries have an important influence on the experimental results. In general, this effect consists in that the model is surrounded by air moving at a different velocity than that in a tunnel of infinite dimensions or in free space, while the streamlines near the model are distorted.

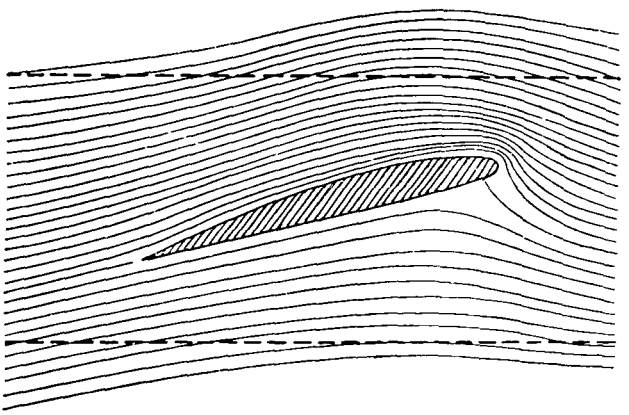

FIGURE 2.7. Wall effects in a closed test section of a wind tunnel. The solid lines show the streamlines corresponding to infinite flow; the broken lines represent the tunnel walls which constrain the flow.

Figure 2.7 shows flow around an airfoil in a tunnel with closed test section. It can be seen that the upper and lower walls of the test section constrain the streamlines near the model; this affects in particular the lift of the airfoil. In addition, the flow velocity at the model is greater than the velocity upstream. Since the mass flow rate is constant throughout the test section, this change in velocity at the model leads to a change in the static pressure. This cannot be avoided in practice, since the walls of the test section cannot be shaped strictly to conform to the streamlines in an infinite medium for models tested at various angles of attack. Wall-effect in a tunnel with open test section will differ from those in a tunnel with closed test section.

The most important factor determining wall effects is the magnitude of the velocity in the test section. At velocities approaching the speed of sound, the nature of the wall effects changes sharply. Due to the complexity of the phenomena related to bounded flow around models in wind tunnels, the correction of the test results consists in allowing separately for each kind of interference.

Flow blockage. The degree of blockage, as well as its effect, depend on the angle of attack and on the free-stream velocity. At low flow velocities the blockage effect is small, but it becomes considerable

at large subsonic velocities, when supersonic regions of flow and shocks appear in the vicinity of the model.

In low-speed tunnels, the permissible degree of blockage by the model and its supports is 5 to 6%. In transonic tunnels the permissible degree of blockage is only 2 to 3%.

Figure 2.8 illustrates the blockage effect in a tunnel at large subsonic velocities. The data have been calculated assuming $M = 1$ at the model and its supports, although the velocity of the undisturbed flow is considerably less than the speed of sound. Figure 2.8 shows that the permissible dimensions of the model and supports (their cross-sectional area F) rapidly decrease with increasing free-stream velocity; at $M = 0.9$ F is only about 1% of the cross-sectional area of the test section /2/. Additional effects are due to the increasing thickness of the boundary layer, so that it is very difficult to correct adequately the results of tests made at near-sonic flow velocities.

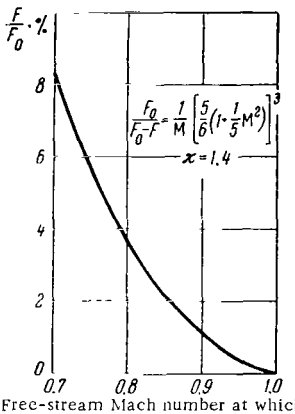

FIGURE 2.8. The influence of the blockage effect in the test section on the onset of supersonic flow. F_0 is the cross-sectional area of the test section; F is the cross-sectional area of the model and supports.

In addition to flow blockage by the model, the blockage effect of wakes in closed-section wind tunnels is also important. Because of pressure losses in the flow around a model the total pressure in the wake is smaller than the total pressure outside it, while the static pressures in and outside the wake are practically the same: thus, by Bernoulli's Law, the velocity head and the velocity in the wake will be less than outside the wake. Because the mass flow rate remains constant, the wake causes a local increase in velocity near the model.

Wakes appear in the test section not only downstream of the model, but also downstream of structural tunnel elements situated upstream of the test section. Such elements include air coolers, supports, vanes, etc.

Static-pressure gradient. Because of the velocity increase near the model, the static pressure in the flow decreases and a horizontal buoyancy force appears, giving rise to spurious drag in measurements with wind-tunnel balances or with manometers used for measuring the static-pressure distribution on the surface of the model*.

If, however, the form drag is determined by measuring the total pressures upstream and downstream of the model, the static-pressure gradient in the test section has no effect.

An axial static-pressure gradient can also be caused by an increase in boundary-layer thickness along the walls of the test sections or the nozzles since this causes a reduction in the effective cross section of the tunnel; the resulting velocity increase in the flow core leads to a decrease in static pressure. This effect can be greatly reduced by gradually increasing the cross section of the tunnel by amounts calculated to compensate for the gradual increase in boundary-layer thickness. For this purpose the test section is slightly conical (diverging at an angle of 0.5 to 0.75°).

* When the static pressure increases toward the diffuser, the horizontal buoyancy force will reduce the value of the drag as measured by the wind tunnel.

Lift effect. Lift effect is due to the constraints to flow around a lift-producing airfoil, caused by the boundary layer. The resulting increase in velocity, and thus in lift, is apparent even in models whose dimensions are very small in relation to those of the tunnel. The effect disappears completely for airfoils of zero lift.

It is necessary to reduce the dimensions of models in wind tunnels operated at near-sonic velocities in order to avoid local velocity increases and shocks. This reduction in size causes a corresponding reduction in the corrections for the lift effect.

Energy ratio and economical design of wind tunnels

The energy ratio of a wind tunnel was defined by Joukowski as the ratio of the power available in the test section to the installed power N. The power available is measured in terms of the rate of flow of kinetic energy in the test section, and is

$$\frac{mV^2}{2} = \frac{1}{2}\rho FV^3,$$

where ρ is the density and V the flow velocity of the air in the test section whose cross-sectional area is F. The energy ratio is thus

$$\lambda = \frac{\frac{1}{2}\rho FV^3}{N}.$$

The energy ratio λ may attain a value of 4 or more in a well-designed tunnel, since part of the kinetic energy of the air in the test section is derived in the nozzle from the potential energy of pressure.

However, the economical design of wind tunnels is not merely a matter of maximizing λ; the installation must be designed as a whole to provide uniform flow through the test section, ease of testing with the highest possible mass flow rate and careful maintenance of the similarity conditions.

§ 4. SUBSONIC WIND TUNNELS. OPEN-CIRCUIT TUNNELS

In this type of wind tunnel the air is ejected to atmosphere after passage through the tunnel. The velocity distribution in open-circuit wind tunnels (Figure 2.2) is uniform to within 3 to 5%, while the flow inclination may be as low as $\pm 2-3°$. The critical Reynolds number for a sphere is about 200,000 in such tunnels; this corresponds to a turbulence level of about 1.5%.

The velocity distribution and flow inclination in open-circuit tunnels can be improved, and the turbulence level reduced, by using a two-stage nozzle and by installing special straightening grids (honeycombs)*.

* The absence of wake from recirculated air in an open-circuit wind tunnel enables a very low initial-turbulence level be obtained in specially constructed low-turbulence tunnels of this type.

Figure 2.9 shows schematically the layout of the TsAGI-T1;2 tunnel /3/, built in 1926. The tunnel has two octagonal closed test sections whose widths are 3 and 6 m, and in which maximum flow velocities of 75 and 30 m/sec respectively are obtained with a 600 h.p. fan.

In open-circuit tunnels with closed test sections the pressure is lower than in the surrounding medium. This makes it more difficult to carry out tests, and introduces inaccuracies into the determination of the forces acting on the model, since atmospheric air leaks through the glands where the model supports pass through the walls of the test section. For these reasons,

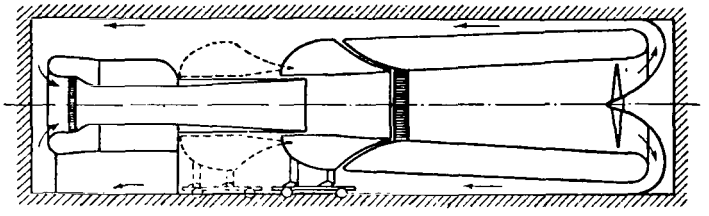

FIGURE 2.9. The TsAGI-T1;2 tunnel.

tunnels with open test sections came into use; such tunnels are surrounded by so-called Eiffel chambers (Figure 2.10). In such a chamber, which is usually sufficiently large to provide working space for personnel and test equipment, the pressure is equalized to that of the flow. Although the total-pressure losses in the test section of such a chamber are about 20% higher than those in closed test sections, tunnels with Eiffel chambers are successfully used.

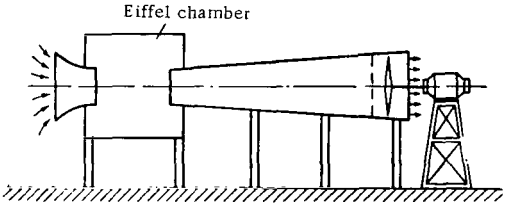

FIGURE 2.10. Wind tunnel with Eiffel chamber.

The Eiffel chamber surrounding the open test section permits tests of larger models and reduces the wall effects in comparison with a closed test section, but when an Eiffel chamber is provided, open-circuit tunnels have a nonuniform velocity distribution and a relatively large power consumption (low energy ratio).

The siting of the tunnel in the tunnel house, especially its height above the floor and the distance of the air intake from the wall, as well as absence of obstacles to flow, such as roof pillars, all affect the quality of the flow in the test section.

If the tunnel-house cross section is large compared with the cross section of the tunnel (e.g., a tunnel-house width of about 5 or 6 times the tunnel diameter), the velocity distribution in the tunnel will be satisfactory. Air should not be drawn directly from atmosphere into an open-circuit tunnel, since this leads to instability and nonuniformity of flow in the test section.

The TsAGI-T1;2 tunnel (Figure 2.9) is of a type, intermediate between the open-circuit and the closed-circuit type, which is most widely used.

A characteristic feature of the T-1;2 tunnel is the fact that the tunnel house forms a reverse diffuser, so that the flow velocity in this tunnel is uniform to within 1%; the energy ratio is 3.5, when a honeycomb is provided.

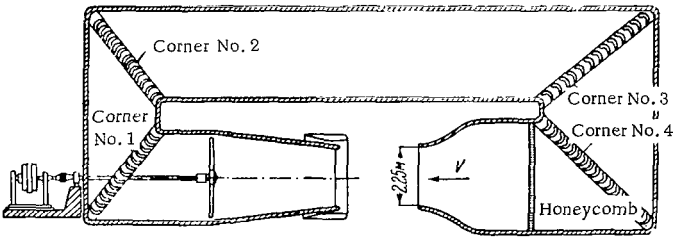

FIGURE 2.11. TsAGI T-5 tunnel ($V_{max}=60$ m/sec).

Closed-Circuit-Tunnels

In this type of tunnel a gradually widening diffuser leads the air back into the nozzle, so that the air continually recirculates in a closed loop. Typical closed-circuit tunnels with open and closed test sections are shown in Figures 2.11 and 2.12.

Figure 2.13 shows the test section of a closed-circuit full-size tunnel (NASA, U.S.A.). The main elements of such tunnels are: nozzle, test

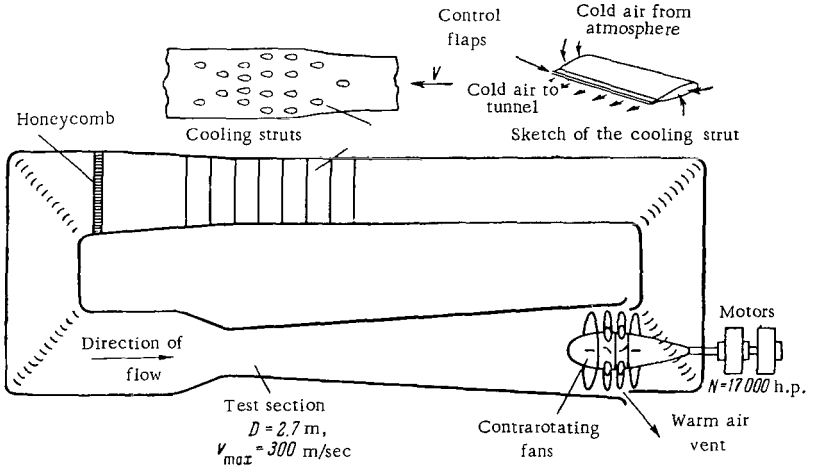

FIGURE 2.12. PVL tunnel.

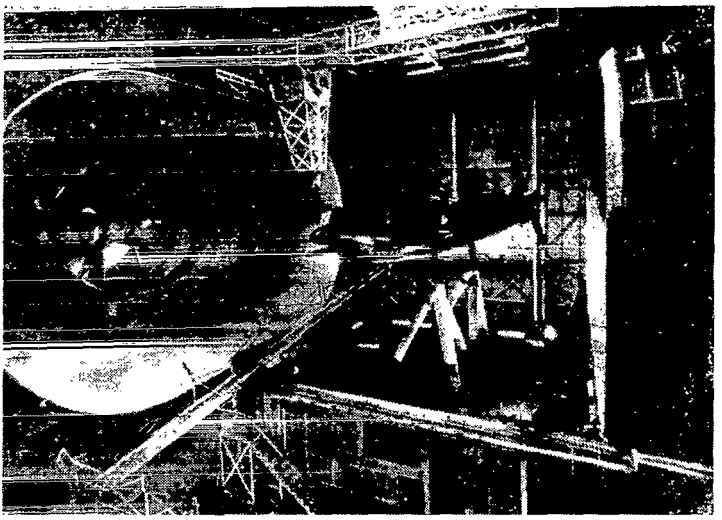

FIGURE 2.13. Test section of large NASA tunnel. Dimensions 18 m· 9.1 m; $V = 53$ m/sec; $N = 8000$ h.p.

section, diffuser, fan, corners with vanes, return duct, and settling chamber with straighteners.

These elements are essential not only in low-speed tunnels, but also in tunnels for large subsonic and supersonic velocities. Their use in subsonic wind tunnels will be discussed below. The further discussion of transonic or supersonic tunnels will deal specifically with those characteristic features which arise from the presence of sonic and supersonic flow in certain regions in certain regions of the tunnels.

Nozzle

The principal function of the nozzle is the acceleration of the low-speed air entering it from the settling chamber to the velocity required in the test section. In addition, because of its gradually decreasing cross section, the nozzle reduces the velocity nonuniformity. The shape and dimensions of the nozzle determine not only the magnitude of the velocity, but also its uniformity, and affect the energy loss in the nozzle mainly due to friction at the walls. These losses are expressed as a fraction of the velocity head or of the total head $p + \rho\frac{V^2}{2}$ in design calculations, where p is the static pressure and V the flow velocity in the test section.

The working principle of the nozzle is as follows:

Suppose that the air moves with velocity V_1 at one point of the cross section I, at the nozzle inlet, and with velocity $V_1 + \Delta V_1$ at another point of this cross section. The pressure can be considered constant at all points of this cross section where the flow velocities are considerably less than the speed of sound at which pressure perturbations are propagated. Let the velocities at two points of a cross section II in the test section be V_2 and $V_2 + \Delta V_2$. Neglecting the squares of the small quantities ΔV_1 and ΔV_2 we obtain from Bernoulli's equation for the two streamlines, we obtain

$$V_1 \Delta V_1 = V_2 \Delta V_2 \quad \text{or} \quad \Delta V_1 = \Delta V_2 \frac{V_2}{V_1}.$$

If the fractional velocity variation at the nozzle inlet is $a_1 = \frac{\Delta V_1}{V_1}$, and that in the test section is $a_2 = \frac{\Delta V_2}{V_2}$, we may write

$$a_1 = \Delta V_2 \frac{V_2}{V_1^2} = \Delta V_2 \frac{V_2}{\left(\frac{V_2}{n}\right)^2} = n^2 a_2,$$

where $n = \frac{V_2}{V_1} = \frac{F_1}{F_2}$ is the nozzle contraction ratio. Thus, the velocity variations in the test section are n^2 times less than the velocity variations at the nozzle inlet.

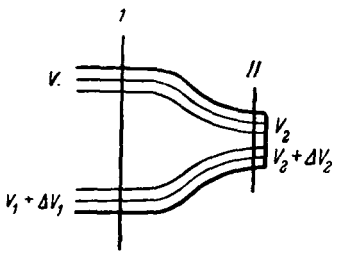

FIGURE 2.14. Velocity equalization in a nozzle.

The reduction of velocity variations in the nozzle leads also to a reduced turbulence in the test section. Figure 2.15 shows the results of

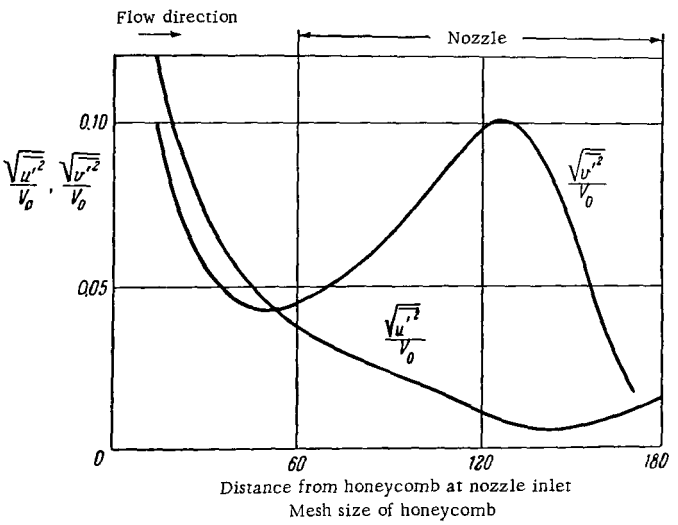

FIGURE 2.15. Variation of the components of the velocity fluctuation along a nozzle.

measurements of the r.m.s. longitudinal component $\left(\sqrt{\overline{u'^2}}\right)$ and transverse component $\left(\sqrt{\overline{v'^2}}\right)$ of the velocity fluctuation expressed as fractions of the velocity V_0 upstream of the nozzle and plotted as functions of the distance from the nozzle inlet. The contraction ratio n of this nozzle was 10 : 1, and the air had first to pass through a honeycomb and a gauze screen. Figure 2.16 shows the critical Reynolds number for a sphere as a function of the contraction ratio n (as measured by Horner) / 4/.

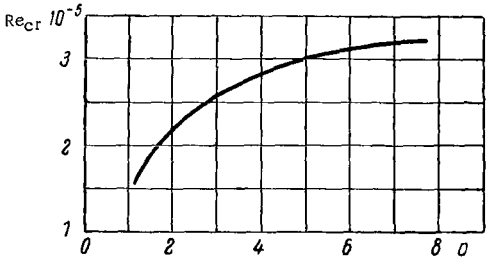

FIGURE 2.16. Effect of nozzle contraction ratio on the critical Reynolds number for a sphere.

It can be seen that with increasing contraction ratio of the nozzle, the critical Reynolds number increases; this proves the reduction in turbulence. A high contraction ratio reduces the tunnel-power requirements considerably, since it permits low velocities almost throughout the tunnel, causing small energy losses. In modern tunnels the contraction ratio varies between 4 and 25, depending on the type of tunnel.

The nozzle contraction ratio is determined, in designing the tunnel, from the required velocity in the test section and from constructional consideration. To avoid unnecessary losses, the designed velocity of the air entering the nozzle is held within the limits of 10 to 25 m/sec in low-speed tunnels (maximum flow velocity, 100 to 150 m/sec) and 20 to 50 m/sec in tunnels for large subsonic speeds (maximum flow velocity 250 to 300 m/sec). For a test section of given size, any increase in nozzle contraction ratio necessitates a considerable increase of all other tunnel dimensions which complicates construction and adds to the cost.

The nozzle profile is designed to provide uniform velocity distribution at the outlet. The velocity variation along the walls must be such that no boundary layer separation occurs, although this is inevitable under real conditions of gas flow. From this point of view a longer nozzle is to be preferred. However, a very long nozzle not only causes a large increase in the boundary-layer thickness, but is also inadmissible because of the design considerations mentioned above. It is standard practice based on operating experience to make the nozzle length equal to about 1.5 to 2.5 times the diameter.

At the outlet of the nozzle there is usually a straight cylindrical section 0.1 to 0.2 nozzle inlet diameters long, to provide a gradual transition from the nozzle to the test section.

The nozzle profile is usually designed to follow the curve (due to Vitoshinskii)

$$r = \frac{r_0}{\sqrt{1 - \left[1 - \left(\frac{r_0}{r_1}\right)^2\right] \frac{(1 - 3z^2/a^2)^2}{(1 + 3z^2/a^2)^3}}},$$

where r is the radius of the nozzle cross section at a distance z along the axis from the inlet, and the inlet and outlet radii are denoted by r_1 and r_0 respectively (when $z = \frac{a}{\sqrt{3}}$ $r = r_0$). The values of r_1 and r_0 are given, and a is usually taken as $4r_0$.

Since the settling chamber is often of square or rectangular cross section, and the nozzle-outlet section (test-section inlet) is an ellipse, transition pieces are provided between them in order to ensure streamline flow. If the settling chamber is rectangular and the nozzle is of eliptical section it is sufficient to have eight such pieces for each quarter of the ellipse. The shape of the nozzle walls thus obtained is usually corrected for the effect of boundary-layer thickening*.

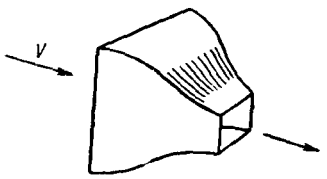

FIGURE 2.17. Nozzle with four curved walls.

Frequently, the nozzles are not axisymmetric. Either the two vertical walls are plane and the upper and lower walls curved, or all four walls may be curved, as shown in Figure 2.17. This shape is dictated by production considerations, since it is difficult to manufacture a large (axisymmetrical) nozzle with a high degree of accuracy, and also because of the general layout of the tunnel. The side ratio of the nozzle is governed by the intended function of the tunnel. If, for instance, the tunnel is intended for testing airfoils at small angles of attack, it is best to have a wide test section and thus to remove the central cross section of the airfoil, which is the section most frequently tested, from the tunnel walls which might otherwise affect the experiment. In wind tunnels for testing models of complete aircraft, the test section should be wider than its height (usually 1.5 times as much), so as to permit testing aircraft of large wing span in a tunnel of given cross-sectional area, thus improving the conditions of similarity.

In tunnels for large subsonic velocities, the nozzle outlet is made square or round, to facilitate three-dimensional studies.

If tests at large angles of attack are intended, the model should be installed at some distance from the upper and lower walls of the test section. In such cases the height of the nozzle is much larger than the width, side ratios of 3 : 1 being common.

Before building large and expensive wind tunnels, models of the tunnels are tested for nozzle-outlet flow quality, so that the design may be corrected.

* Particularly in supersonic tunnels, since a quite small change in the effective cross section of the nozzle (due to boundary layer thickening) causes a considerable change in velocity. For instance, a 1% reduction in the nozzle cross section near the throat will cause a velocity increase of 9% at M = 1.

Test section

The test section has the same cross section as the nozzle outlet, and may be either open or closed.

An open test section has the great advantage of providing freer access to test models and instruments. Open test-section tunnels are sometimes subject to severe low-frequency flow pulsation which can endanger the tunnel structure; they arise from eddies at the nozzle outlet and at the free jet boundaries. Pulsations can be damped out by providing the diffuser inlet with several rows of vents, and by mounting triangular or parabolic tabs, bent outward from the flow axis at an angle of 20° (Figure 2.18),

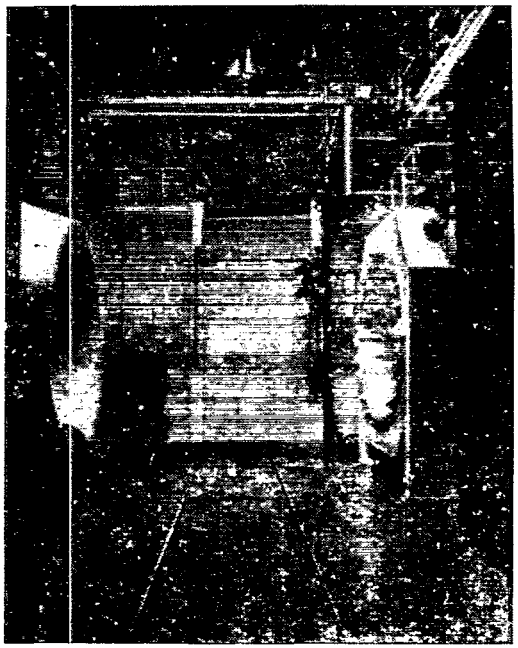

FIGURE 2.18. Open test section with tabs at the nozzle outlet.

at the periphery of the nozzle outlet. Sometimes "knives" [spoilers] are installed for this purpose around the edge of the nozzle, projecting slightly into the jet. In spite of these drawbacks, most modern wind tunnels for flow velocities below 100 to 150 m/sec have open test sections. This is especially true for large tunnels, for which the ease of mounting and adjusting models is of decisive importance in choosing the type of test section.

At higher maximum flow velocities in the tunnel the required fan power may be reduced by enclosing the test section. The length of the closed section is designed to permit tests of different types of models. For tunnels

designed for testing models of wings, aircraft, etc., a 1.5 to 2 diameters long test section is sufficient. In tunnels intended for testing elongated bodies, such as rockets and hulls of submarines and ships, the length of the test section is 2 to 4 diameters. To maintain a constant axial flow velocity, the cross-sectional area of a closed test section should gradually increase in the flow direction to compensate for the thickening of the boundary layer. Despite the dependence of this phenomenon on the velocity, pressure and temperature, which all vary in space and time, in practice, a constant taper of the test section is sufficient. For instance, in circular test sections /5/ the taper should be between 0.1 and 0.25° for large Reynolds number ($Re = 10^7$ to 10^8) and between 0.25 and 0.5° for small Reynolds numbers ($Re = 10^5$ to 10^6). The static pressure can be maintained constant throughout very long test sections by providing vents to atmosphere. Such a test section, whose length equals 5 diameters, is used in the wind tunnel of the Hamburg Shipbuilding Institute.

Some experiments require exceptionally long test sections. In particular, a special wind tunnel for studying low-speed rising air currents (5 to 15 cm/sec) has a conical test section some 10 diameters long (Figure 2.19). The test section is equipped with a fan for boundary-layer removal.

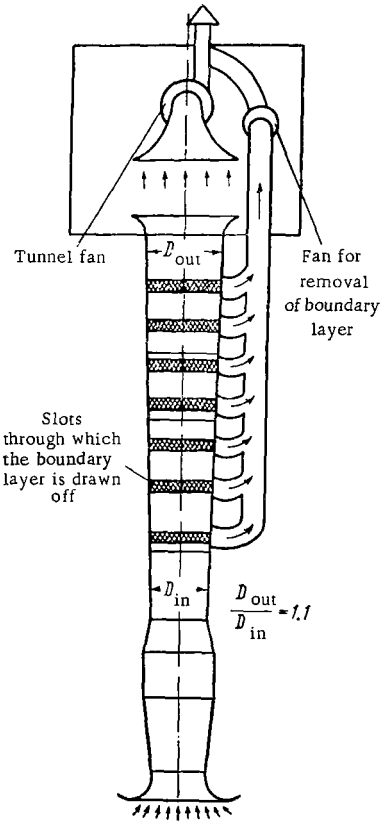

FIGURE 2.19. Tunnel with very long test section.

Diffuser

The diffuser of the tunnel is a gradually widening duct downstream of the test section and serving for the more efficient conversion of the kinetic energy of the air into pressure energy. In closed-circuit tunnels a diffuser is also necessary to prevent excessive friction (and large power requirements) due to high flow velocities which would also cause poor flow quality in the test section and render impossible the reliable measurements of aerodynamic forces. The performance of a diffuser, i.e., its capability of converting the kinetic energy into pressure energy, is mainly influenced by the magnitude and distribution of the velocity at its inlet, its divergence angle, and the expansion ratio.

The total-pressure losses in the diffuser (Figure 2.20) are conveniently expressed as fractions of the velocity head at its outlet and inlet, where the flow parameters are respectively V_d, ρ_d, and ρ_{0d} and V_{ts}, ρ_{ts}, and ρ_{0ts}, respectively.

Thus:

$$\Delta p = \zeta_d \rho_{0d} \frac{V_d^2}{2} = p_{0\,ts} - p_{0\,d},$$

where ζ_d is the resistance coefficient of the diffuser, and is related to the total-pressure recovery coefficient ν_d of the diffuser by the expression /6/:

$$\frac{(p_0)_d}{(p_0)_{ts}} = \nu_d = 1 - \frac{\varkappa}{\varkappa+1}\zeta_d \lambda_d^2,$$

where $\lambda_d = \frac{V_d}{a_{kp}}$ is the reference Mach number in the diffuser outlet and $\varkappa$ is the ratio of specific heats.

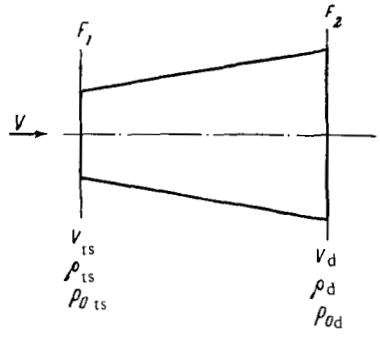

FIGURE 2.20. A diffuser.

The resistance coefficient ζ_d greatly depends on the Reynolds number at the diffuser inlet, especially when Re is less than 10^7 (Figure 2.21).

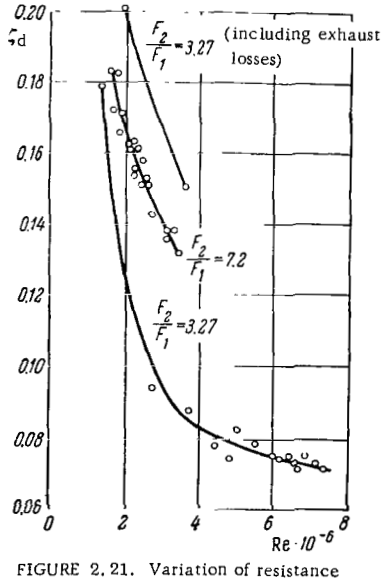

FIGURE 2.21. Variation of resistance coefficient of a diffuser at low Reynolds numbers.

The resistance coefficient of the diffuser is virtually constant above $Re = 10^7$ (Figure 2.22). It has been shown experimentally that the Mach number of the diffuser inlet has little influence at subsonic flow velocities.

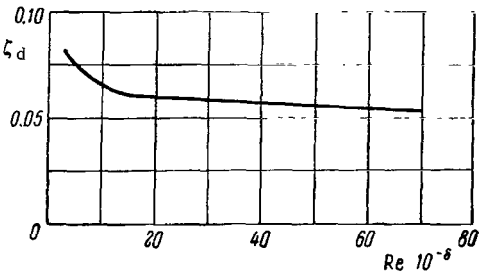

FIGURE 2.22. Variation of resistance of a conical diffuser with Reynolds number.

The coefficient ζ_d depends on the diffuser divergence and on the expansion ratio in it. The optimum divergence angle at which α is minimum, is about 6°.

At smaller divergence angles ζ_d increases because of the consequent increase in the diffuser length. At divergence angles above 8°, losses increase due to nonuniform velocity distribution across the diffuser.

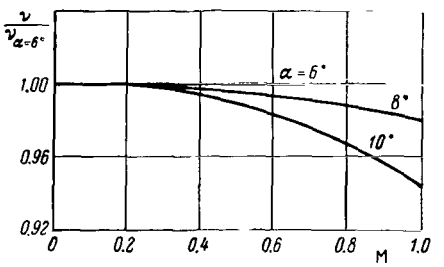

FIGURE 2.23. Influence of divergence angle of a conical diffuser on total-pressure recovery coefficient.

Figure 2.23 shows the influence of the divergence angle on the total-pressure recovery coefficient of the diffuser /7/.

In practice ζ_d is frequently determined in a simpler manner. Experimental evidence shows that the expression

$$\zeta_d = \psi_{div}\left(1 - \frac{F_1}{F_2}\right)^2,$$

is a satisfactory approximation of the losses in a diffuser.

For conventional diffusers with divergence angles below 10°, at which no flow separation occurs at the diffuser walls, $\psi_{div} = 0.15$ to 0.20. When the air from the diffuser is discharged into a large chamber, additional losses have to be taken into account in determining the total-pressure recovery

coefficient. These losses are due to the finite velocity of the air leaving the diffuser, whose kinetic energy is not recovered, since the static pressure at the diffuser outlet is equal to the total pressure in the chamber. These losses are usually called exhaust losses. At the diffuser outlet

$$p_d = p_{0d}\left(1 - \frac{\varkappa - 1}{\varkappa + 1}\lambda_d^2\right)^{\frac{\varkappa}{\varkappa - 1}},$$

where p_d, p_{0d} and λ_d are the static pressure, total pressure, and Mach number at the diffuser outlet. However, $p_d = p_c$, where p_c is the pressure in the chamber. Hence

$$\nu_{exh} = \frac{p_c}{p_{0d}} = \left(1 - \frac{\varkappa - 1}{\varkappa + 1}\lambda_d^2\right)^{\frac{\varkappa}{\varkappa - 1}}.$$

Taking into account exhaust losses, the total-pressure recovery coefficient of the diffuser is

$$\nu_d' = \nu_d \nu_{exh}.$$

The length of the diffuser is determined, on the one hand, by its divergence angle, and on the other, by the overall dimensions of the tunnel and the tunnel house.

Actually, the whole return circuit of the tunnel between test section and settling chamber forms a diffuser with small cylindrical portions in the zones where the fan is installed and at the corners which are difficult to construct in tapering form. In practice the term "diffuser" is applied to the first part of the circuit situated between the test section and the first corner (Figure 2.11). Between the first and second corners there is usually a short cylindrical portion. The portion between the second and third corners (the "return duct") is, with the exception of the fan mounting, also a diffuser with a slightly larger divergence angle (8° to 10°) than that of the diffuser after the test section. In a tunnel with an open test section the dimensions of the diffuser inlet are selected to enable the diffuser to collect most of the air emerging from the nozzle in a diverging stream.* The half-width and half-height of the diffuser inlet should therefore exceed the corresponding dimensions of the nozzle exit by an amount kl, where k is the tangent of the angle between the free jet boundary and the test section axis, and l is the distance between the nozzle outlet and the diffuser inlet /8/. The measurements by G. N. Abramovich suggest that $k = 0.045$.

Fan installation

It is necessary to supply energy to replace losses and maintain the air flow in a wind tunnel. In closed-circuit tunnels this is provided by means of fans or blowers; subsonic tunnels usually employ single- or two-stage fans.

The power required by the fan is a function of the fan head, which is calculated from the aerodynamic design data for the tunnel, by considering

* The fitting of a collar to the inlet of the diffuser (Figure 2.11) reduces the static-pressure gradient in the test section.

the hydraulic losses as the air passes through it. The details will be explained below.

The maximum angular velocity and the diameter of the fan are limited by the fan tip speed, which must not exceed 180 to 200 m/sec.

A net of 25 to 50 mm mesh is mounted upstream of the fan to protect it from mechanical damage, by trapping any components which may accidentally break loose from the model or its supports in the test section.

Straightening vanes are installed behind the fan impeller to reduce turbulence. In a two-stage fan an intermediate flow straightener, placed between the impellers of the first and the second stage, creates the necessary flow conditions at the inlet to the second stage.

Generally, the flow velocity is adjusted by altering the fan speed, the fan motor being provided with continuously variable speed control.

The multistage compressors of transonic and supersonic tunnels usually have fixed air-straightening vanes fitted with a feathering mechanism, either on the vanes themselves or on flaps attached to them, for controlling the delivery and compression ratio of the compressor to suit different operating conditions (values of Re and M) of the tunnel. The ARA (Great Britain) tunnel compressor is shown in Figure 2.24.

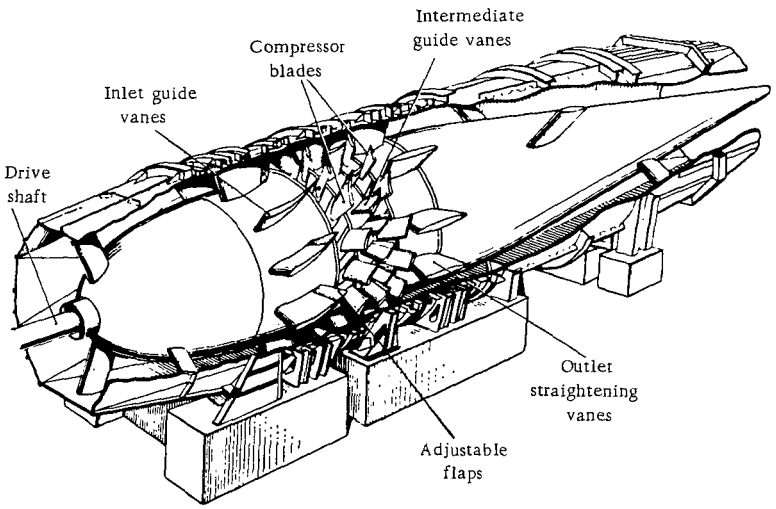

FIGURE 2.24. Two-stage compressor for the ARA (Great Britain) tunnel.

In large high-speed tunnels, designed for operation over a large range of Mach numbers, it is sometimes more suitable to regulate the flow velocity in the test section by switching off some stages of the compressor, or to use separate compressors part of which can be bypassed. Such a system is used, for instance, in the AEDC supersonic tunnel (U.S.A.), which has a power consumption of 216,000 h.p., the test-section Mach number being variable from 1.4 to 3.5 by de-energising some of the compressors. In several tunnels the velocity is controlled by feathering the fan or compressor blades at constant speed. However, the complications of such a design are hardly justified.

The characteristics of the fan depend strongly on the clearance between the blade tips and the tunnel wall, which should be as small as possible. There is some danger of breaking the blades, and the clearance should be between 30 and 40 mm when the fan diameter exceeds 5 m, although a 20 or 30 mm clearance is suitable for fans having diameters of 2 to 5 m, and 5 to 15 mm for smaller fans. At these clearances the fan efficiency will not decrease more than 1 or 2%. To avoid destructive vibrations, the fan must be balanced statically to an accuracy better than 5 or 10 grams per meter diameter, and the blade angles must be set with a tolerance not exceeding $\pm 0.25°$.

Corners

In closed-circuit tunnels the air which emerges from the test section must be returned to the nozzle, i. e., must circulate through 360°. The turn is made in four corners, each of 90°.

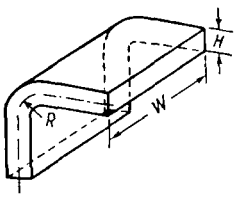

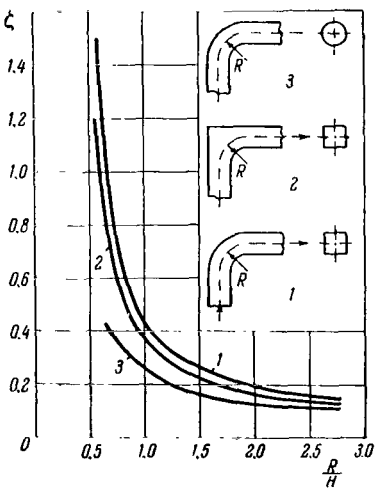

FIGURE 2. 25. Variation of resistance coefficient with radius of bend.

The shape of the return corners, and especially of the fourth (Figure 2. 26) should not cause uneven or turbulent flow. Rounded corners are aerodynamically better than sharp right angles. It is, however, structurally easier to make corners of small curvature.

The resistance coefficient of corners and thus, the flow uniformity, depend on the ratios R/W and R/H, where R is the radius of curvature, W the width, and H the height of the corner. The higher these ratios (up to certain limits), the smaller the losses. Figure 2. 25 shows the resistance coefficient ζ of corners as a function of R/H:

$$\zeta = \frac{\Delta p_0}{\rho V^2/2}.$$

Here Δp_0 is the total-pressure loss in the corner and $\rho V^2/2$ is the velocity head at the inlet. Low flow velocities are conducive to small energy losses at the corners, and should be adhered to whenever possible.

The wind-tunnel design will generally permit an increase in R/H by increasing R, but there is little freedom in selecting W/H whose value is intimately related to the test-section dimensions. The effective value of W/H can be increased by reducing H; a cascade of turning vanes is installed at the corner to divide the corner into a set of smaller corners.

The vanes used in wind tunnels are either airfoil sections or thin sheet-steel baffles bent into arcs of circles. Airfoil sections accommodate

internal braces inside them whose surfaces can be used to cool the air.

Figure 2.26 shows corner vanes and bends for the A-6 MGU closed-circuit wind tunnel which has a rated flow velocity of 100 m/sec. To reduce turbulence the number of vanes in the fourth corner is larger, and their chord length is less than in other corners.

In order to adjust the flow direction downstream, vanes with adjustable flaps are sometimes fitted at the corners.(in particular the fourth), the axes of the flaps being perpendicular to the vane chords. In large tunnels these flaps also provide structural support for the vanes, it being difficult to manufacture and mount vanes of very large span. The effect of corner vanes is illustrated in Figures 2.27 and 2.28. When vanes of airfoil section are fitted, the velocity distribution becomes approximately uniform at a distance of 1 to 1.5 widths from the corner, whereas without vanes the velocity distribution is still nonuniform at a distance of about 4 widths downstream.

Settling chambers

The settling chamber serves to straighten and smooth the flow downstream of the fourth corner; it is normally 1.5 to 2 widths long. A honeycomb

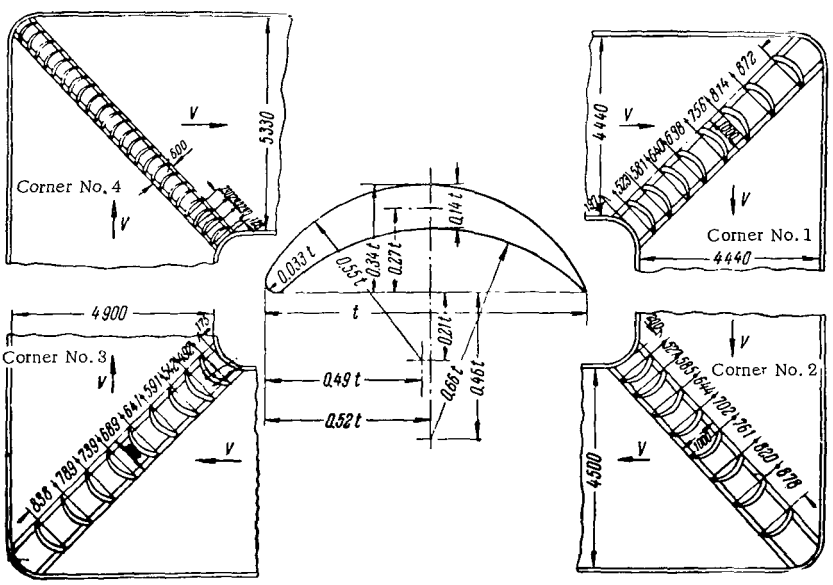

FIGURE 2.26. Vanes fitted to the corners of a wind tunnel.

and gauze anti-turbulence screens are fitted at the inlet for straightening the flow.

A honeycomb consists of a grid with cells of 0.5 to 2 mm* wall thickness, the thickness of the honeycomb being some 5 to 10 times the mean cell width. The honeycomb straightens the flow by breaking up large eddies, and also reduces the spread of longitudinal velocities. At the same time, the honeycomb itself causes a certain turbulence due to the wake formed by the cell walls. In settling chambers, therefore, where the honeycomb is the only fitting, the overall length of the chamber must be increased so that this turbulence decays before the nozzle inlet.

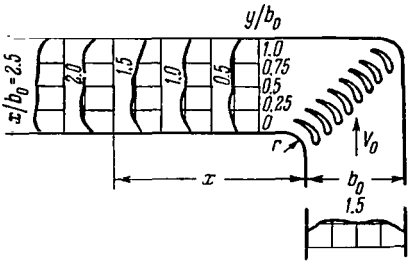

FIGURE 2.27. Velocity-head distribution downstream of a corner fitted with guide vanes. $\left(\frac{r}{b_0}=0.1;\ \frac{t}{b_0}=0.25\right)$.

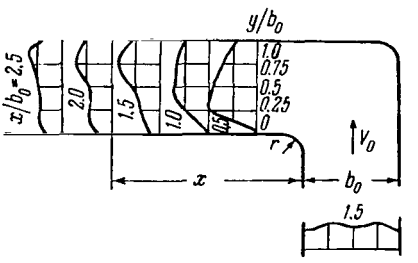

FIGURE 2.28. Velocity-head distribution downstream of a corner without guide vanes. $\frac{r}{b_0}=0.1$.

In recent years it has become common practice to install a wire net behind the honeycomb, in order to dampen turbulence and to increase the uniformity of the velocity distribution. Such a screen must be made of small-gage wire and be of fine mesh. Figure 2.29 shows the effect of screens having different resistance coefficients, on the evenness of the flow /9/.

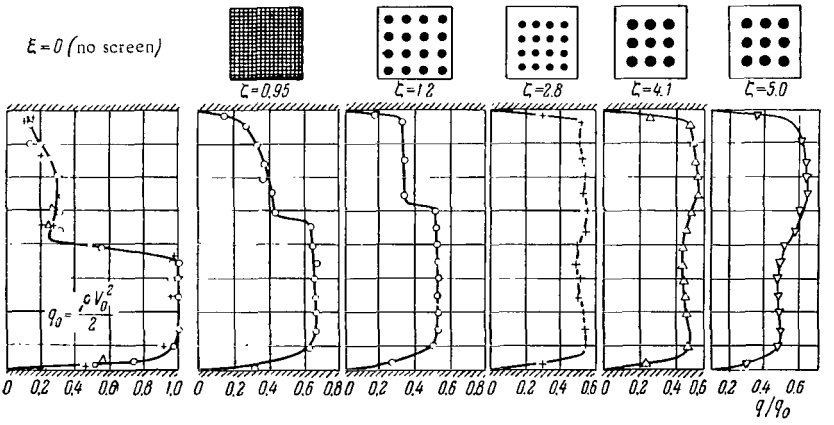

FIGURE 2.29. The smoothing effect of screens having different resistance coefficients.

* The mean cell width is normally between 1% and 2% of the mean width of the settling chamber.

The smoothing action of screens is based on the fact that losses are proportional to the square of the velocity [so that the relative velocity reduction of the faster moving particles is much greater]. Theory suggests that a velocity perturbation ΔV_1 upstream of the screen will produce a corresponding perturbation ΔV_2 downstream, where $\Delta V_2 = \frac{2-\zeta}{2+\zeta}\Delta V_1$, and ζ is the resistance coefficient of the screen. When $\zeta = 2$, the perturbation downstream should be zero. Tunnel experiments amply confirm this prediction.

A screen, fitted over the whole cross section of the tunnel, acts as a distributed [nonlinear] hydraulic resistance, and completely smooths out flow irregularities.

To minimize the turbulence caused by the screen, it is necessary to use a net made from wire of very light gage, and to install it at the section of minimum velocity. The Reynolds number with thus be low $\left(\mathrm{Re} = \frac{dV}{\nu} = 50\right)$ and turbulence arising from the screen will be so slight that it will decay completely, upstream of the test section. The principal function of settling-chamber screens is, however, to reduce the free-stream turbulence in the test section. They serve to reduce both the intensity of the initial turbulence in the test section, and the scale of turbulence L defined by the formula /10/

$$L = \frac{\varepsilon_{in}}{\varepsilon} M,$$

where $\varepsilon_{in} = \sqrt{\frac{\varepsilon_0}{\frac{1}{\varepsilon_0} + 2A\frac{x_{eff}}{M}}}$ is the calculated value and ε the turbulence level when a screen of aperture size M is in position, x_{eff} is the distance downstream to the point where turbulence is effectively damped out; ε_0 is the turbulence level without a screen, and A is a dimensionless constant. Experiments by Dryden /11/ suggest that the constant A has a value of 0.206. The scale of turbulence at the plane of the honeycomb or screen is equal to the size of its apertures. The net effect of the intensity and the scale of turbulence is given by Taylor's complex parameter

$$\mathrm{T} = \varepsilon\left(\frac{D}{L}\right)^{1/2},$$

where D is a typical dimension of the test body (for instance the diameter of a sphere). Test results of the reduction in the turbulence level, caused by the installation of a screen, agree with calculations of the corresponding decrease in the magnitude of the parameter T.

Figure 2.30 shows the dependence of the ratio of the turbulence level in the test section to the free-stream turbulence level ε_0 on the distance x_{eff} needed to reduce turbulence to negligible proportions . As can be seen, the turbulence is substantially reduced at a distance of only 5000 aperture sizes downstream of the screen. The screen selected should have an aperture size between 2 and 5 mm and a resistance coefficient ζ between 1.8

and 2.2, and should be installed as far as possible from the test section.

In selecting screens the following expression /12/ obtained from tests of screens at Reynolds numbers between 500 and 2000 may be used:

$$\zeta = (1-\bar{f}) + \left(\frac{1-\bar{f}}{\bar{f}}\right)^2,$$

where ζ is the resistance coefficient of the screen and

$$\bar{f} = \frac{F_1 - F_3}{F_1} = \frac{F_2}{F_1},$$

F_3 denoting the projected area of the screen wires.

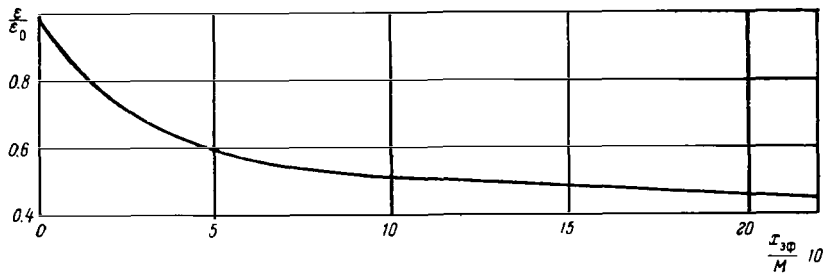

FIGURE 2.30. Influence of screen location on turbulence in test section.

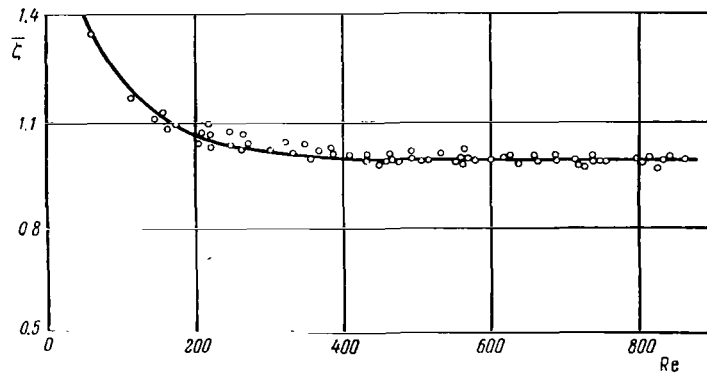

FIGURE 2.31. Influence of Reynolds number on [hydraulic] resistance of screen.

At Reynolds numbers below 500, a correction must be made whereby

$$\zeta_{Re} = \bar{\zeta}\zeta,$$

the coefficient $\bar{\zeta}$ being determined from Figure 2.31. The Reynolds number at the screen should be calculated from the free-stream velocity and the mean wire diameter.

Variable-density wind tunnels

Variable-density wind tunnels were originally developed as a means for increasing the Reynolds number without increasing either the tunnel dimensions or the power required. Later such tunnels were built also for large velocities.

Comparing the formulas for the power required

$$N = \lambda \rho \frac{V^3 F}{2},$$

and for the Reynolds number in the test section

$$\mathrm{Re} = \frac{\rho}{\mu} Vl,$$

we see, that if the Reynolds number is increased by raising the flow velocity, the power required will increase as the cube of the velocity; if the Reynolds number is increased by increasing the linear dimensions, the power required will increase as the square of the linear dimensions, but when the Reynolds number is increased by raising the density, the power required will be directly proportional to the density of air. The expressions for N, Re, and $\mathbf{M} = \frac{V}{\sqrt{\varkappa p/\rho}}$ show that at the same values of Re and $\mathbf{M}$ the power required is inversely proportional to the static pressure p in the test section:

$$N = \frac{1}{2} \lambda \frac{F}{l^2} \mathbf{M} \frac{\mu^2 a^3}{\varkappa p} \mathrm{Re}^2 \ * .$$

Raising the tunnel pressure complicates its design and adds to the difficulty of experimental work because of the need for remote measurements and monitoring. However, this is compensated by increased accuracy and lower power requirements.

The earliest variable-density tunnels operated at comparatively high pressures; the contraction ratios of the nozzles were small, so that the velocity distribution was very nonuniform. Later, tunnels with initial pressure of 4 to 8 atm and high nozzle-contraction ratios were increasingly used. Figure 2.32 shows a variable-density tunnel at the California Institute of Technology** .

This tunnel features a decompression sphere containing the test rig. Entry to the tunnel to alter or adjust the model is through airlocks which isolate the decompression sphere from the rest the tunnel, whose pressure need not be released.

* The properties and temperature of the medium are assumed constant.

** The tunnel has now been modernized. Its power has been increased from 12,000 h. p. to 40,000 h. p. at $\mathbf{M} = 1.8$. [See Millikan, C. B, High Speed Testing in the Southern California Co-operative Wind Tunnel. Aeromechanical Conference, London 1947, p. 137.—Roy. Aero. S. 1948.] The tunnel is equipped with 3 test sections, for subsonic, transonic and supersonic velocities.

Variable-density wind tunnels can be operated at pressures either above or below atmospheric. The maximum free-stream velocity can thus be obtained in the tunnel for any given power. This facility is useful when

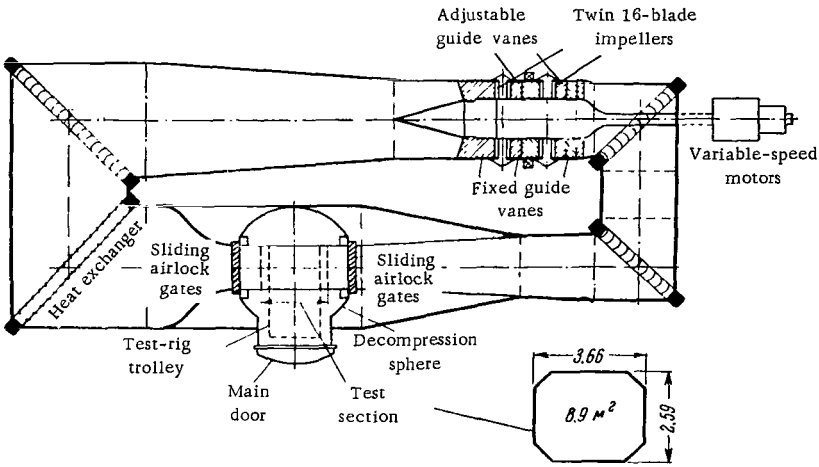

FIGURE 2.32. California Institute of Technology variable density wind tunnel ($p = 0.2$ to 4 atm, $M = 0.7$ to 1.3; dimensions of test section $2.59 \times 3.66\ m^2$.

only compressibility effects are being studied, although the Reynolds number decreases with the density. Variable-density tunnels are particularly useful when testing the combined influence of Reynolds and Mach numbers on aerodynamic characteristics. Figure 2.33 shows another variable-density tunnel (U.S.A.)

Special low-speed tunnels

Certain aerodynamic problems demand special wind tunnels adapted to particular kinds of tests. Such tunnels include airspin tunnels, free-flight tunnels, low-turbulence tunnels, wind-gust tunnels, vertical-flow tunnels, tunnels for cooled and humidified media, radiator-type , and other tunnels.

All these tunnels have much in common with standard wind tunnels, but differ from them considerably in design, equipment, and testing techniques.

Airspin tunnels

Airspin tunnels were developed to assist in solving problems of non-steady motion of aircraft, and especially of spin. They are also used for tests of helicopters, parachutes, bodies of small resistance, etc.

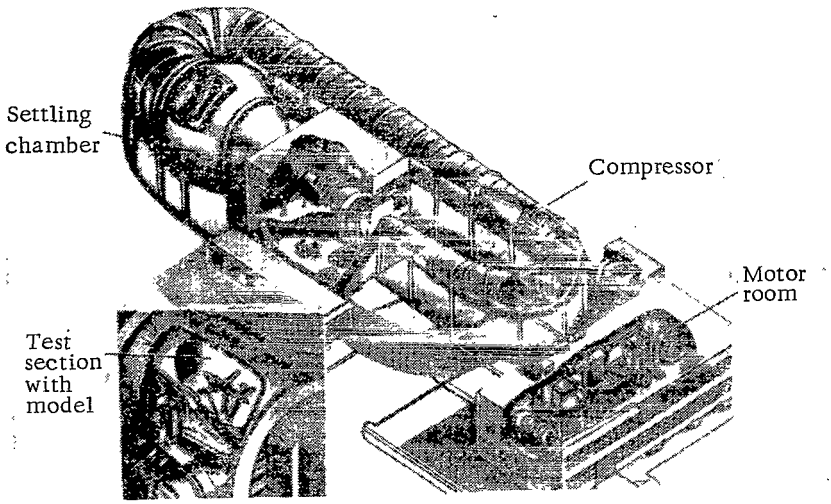

FIGURE 2.33. NASA variable-density tunnel.

(N= 11,000 h.p.; M= 0.97; $D_{l.c.}$ = 3.66 m; p = 0.17—6 atm)

Airspin tunnels are installed vertically with the air flowing upwards as shown in Figure 2.34. One of the largest airspin tunnels is the vertical NASA tunnel which has a dodecagonal test section 6.1 meters across, and a rated flow velocity of 30 m/sec at a power of 400 h.p. Figure 2.35 shows the test section of this tunnel.

Free-flight photographs in the test section of this tunnel permit the spin characteristics of the model to be investigated. In the nozzle and diffuser, and around the test section, nets are installed for catching the model when the flow is stopped.

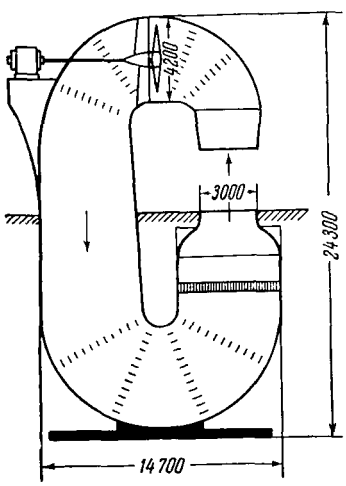

FIGURE 2.34. Airspin tunnel at the Monticelli laboratory (Italy), N = 150 h.p., V_{max} = 25 m/sec.

Free-flight tunnels

Models for free-flight testing in tunnels must, like the models for airspin tunnels, have mass and rigidity characteristics similar to those of the full-scale aircraft. The model is usually provided with a light-weight electrical motor driving a small propeller. The control surfaces of the model (rudder and ailerons) are adjusted by electromagnetically operated remote controls.

Figure 2.36 shows schematically a large free-flight tunnel of NASA. The octagonal closed test section has an inscribed-circle diameter of 3.66 m; the maximum flow velocity is 27.5 m/sec, and the power required

is 600 h.p. To adjust the Reynolds number, which considerably affects the characteristics of flight stability, the tunnel is housed in a steel sphere of 18.3 m diameter, which can be either evacuated, or pressurized to 4 atm.

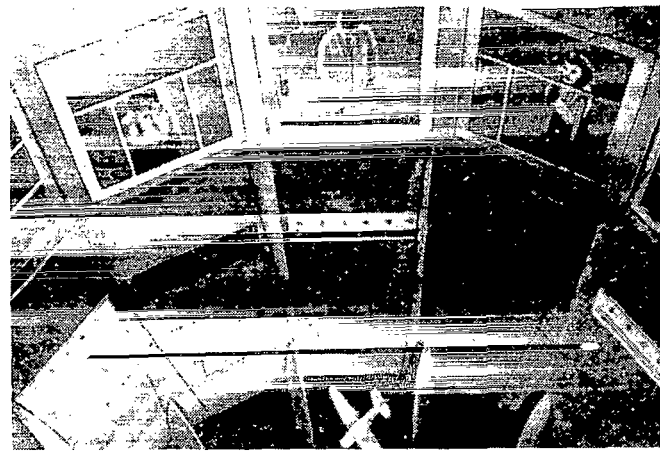

FIGURE 2.35. Test section of the vertical NASA tunnel.

At the beginning of the test the model is installed stationary on the horizontal floor of the test section. The flow velocity is then increased, and at the appropriate instant the elevators are operated so that the model rises from the floor. Free-flight tests are begun when the model has risen almost to the axis of the tunnel, photographs under various flight conditions being taken with a movie camera from which the characteristics of the motion of the model can be determined.

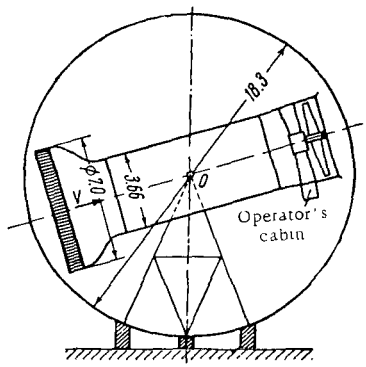

FIGURE 2.36. NASA Free-flight tunnel. O is the axis of rotation of the tunnel.

Low-turbulence wind tunnels

A turbulence level, approximating the turbulence of the free atmosphere, can be obtained by using a nozzle having a very high contraction ratio, which may exceed 25 : 1. In the long settling chamber upstream of the nozzle of such a tunnel, perforated-sheet turbulence screens are commonly fitted. Low-turbulence tunnels usually have squat test sections (the height may be only half of the width) to accommodate wings. The chord of the model airfoil section is sometimes equal to its span, or even 2 or 3 times as much, in order to increase the Reynolds number*; the sides of the airfoil may be

* In certain low-turbulence tunnels the Reynolds number may be increased by reducing the free-stream pressure.

mounted on the vertical side walls of the tunnel, so that the flow at the center line of the model closely approximates the flow around a wing of infinite span. Low-turbulence tunnels are used mainly for studying the boundary-layer structure of the air flow around variously shaped bodies and for investigating the influence of turbulence and the state of the surfaces of bodies on their aerodynamic characteristics.

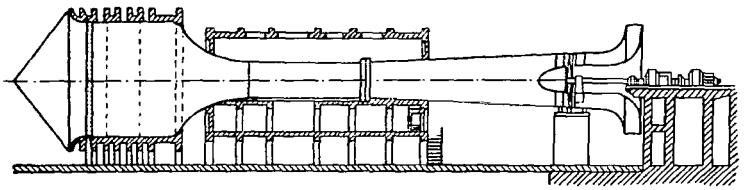

FIGURE 2.37. A.V.A. low-turbulent wind tunnel

Figure 2.37 shows schematically the low-turbulence A.V.A. open-ciruit wind tunnel Göttingen, (Germany).

Air from the large room in which the tunnel is housed is drawn through a conical cloth filter. A honeycomb is fitted at the entrance of the settling chamber, and a series of wire-gauze screens inside the settling chamber. The nozzle contraction ratio is 27 : 1. The diameter of the test section is 3 m, but flat side-walls 1.5 meters apart can also be installed. The maximum flow velocity is 100 m/sec at a rated power of 1000 KW.

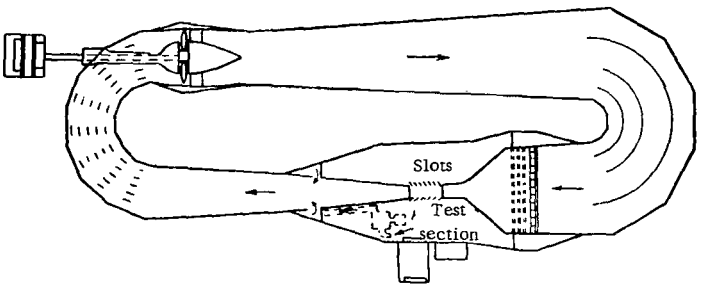

FIGURE 2.38. NASA low-turbulence variable-density tunnel.

Figure 2.38 shows a plane low-turbulence variable-density tunnel of the NASA*. The test section measures 0.91 m × 2.29 m; [3' × 7 ½ ']; the maximum velocity is 150 m/sec at a maximum fan power of 2000 h.p. and operating pressures up to 10 atm. Screens are fitted to reduce turbulence in the test section, and the boundary layer is extracted from the walls of the test section, the air being reinjected into the diffuser. Special corners are also provided.

* [von Doenhoff, A.E. and L.H. Abbot. The Langley Two-Dimensional Low-Turbulence Pressure Tunnel. — N.A.C.A. Technical Note 1283. 1947.]

Thermal and altitude tunnels

A number of special tunnels have been built for the study of cooling, heat exchange, heat transfer from air to water and oil, wing icing, and the operational effects of high altitudes and low temperatures on the components of fin-stabilized ballistic missiles and their instruments.

The wind tunnel shown in Figure 2.39 is intended for the study of icing (NASA. Cleveland, U.S.A.). It has a closed test section measuring 2.74 m by 1.83 m. The maximum flow velocity is 180 m/sec, and the minimum temperature is -55°C. The power is 4,160 h.p. The return duct of the tunnel is also used for testing propellers, etc. A cooler is installed between the third and fourth corners, and water-spray nozzles are located in the settling chamber.

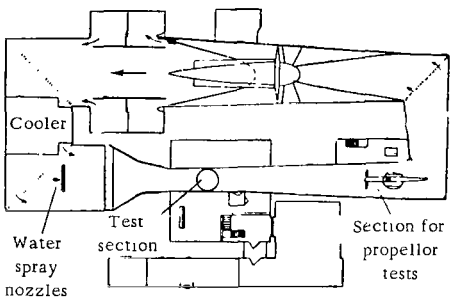

FIGURE 2.39. Tunnel for studying icing (NASA).

A large chamber has been built by Vickers Armstrong Ltd. (U.K.) for testing aircraft components and equipment under different temperature and altitude conditions. The chamber is actually a closed-circuit tunnel. With four return ducts, each 2.05 m in diameter. The test section is circular, with a diameter of 7.6 m and a length of 15.2 m. The maximum flow velocity in the tunnel is 31 m/sec. The refrigeration plant, to provide air cooling down to -65°C, consists of four 150 h.p. two-stage ammonia compressors. The coolant is methyl alcohol, which circulates inside the copper guide vanes of the 16 tunnel elbows. Cooling from +15°C to -65°C requires about 300 hours.

Altitude conditions for pressure-effect studies are obtained with the aid of a 140 h.p. two-stage vacuum pump so that various rates of ascent and altitudes of level flight can be simulated.

At an air temperature of -60°C, ascent conditions to a height of 18,000 m (pressure, 56 mm Hg) can be simulated with a climbing rate of 300 m/min. Special release valves permit the simulation of a descent from 15,000 m to ground level in 160 seconds. The tunnel permits various kinds of aerodynamic tests: study of cold starting of engines and control of turbine starters, wear of the slipring brushes of generators, high-altitude behavior of aircraft and guided missiles and their control surfaces, and investigation of electronic equipment of radar installations, radio probes , hermetically sealed cabins, etc.

In wind-tunnel tests of radiosondes, the use of infrared and ultraviolet radiation makes it possible to simulate solar radiation and to maintain inside the probes a temperature of +40°C, despite ambient tunnel-air temperatures of −60°C.

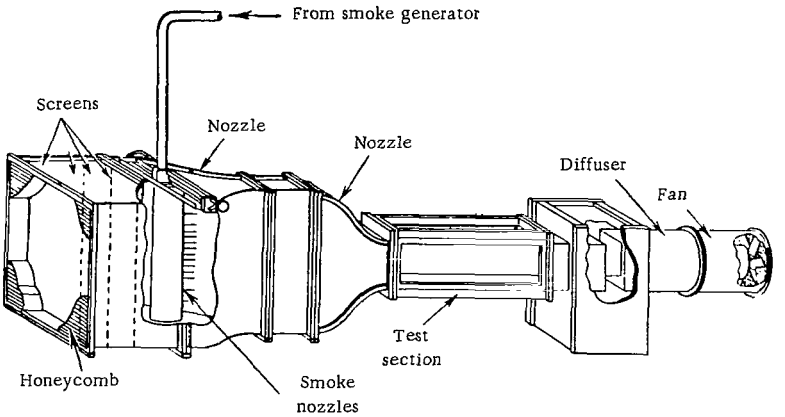

FIGURE 2.40. Smoke-jet wind tunnel.

Smoke-jet tunnels are used for visualizing the pattern and characteristics of flow around bodies at small velocities. The principle of such a tunnel is shown in Figure 2.40.

§ 5. TRANSONIC TUNNELS

In transonic tunnels the test-section Mach number ranges from 0.85 to 1.4. Tests in transonic tunnels may be of short or long duration. In continuous-operation tunnels the pressure difference is created by a fan or a compressor, which is rated for continuous operation over an extended period.

In intermittent-operation tunnels, flow is caused by the pressure difference between the settling chamber and the diffuser outlet, a compressed-air or vacuum chamber being used. The air is highly compressed before each test and discharged through a reduction valve to the settling chamber and thence through the test section to the atmosphere. In vacuum-chamber tunnels the "high" pressure is the atmospheric pressure at which air is drawn through the tunnel by virtue of the lower pressure in the vacuum chamber.

The test duration in intermittent-operation tunnels usually depends on the reserve of compressed air or on the volume of the vacuum chamber, and varies between 1 and 5 minutes.

For $M < 1$ the shape of the tunnel may be almost the same as for conventional subsonic tunnels. Because the flow becomes unstable at $M \cong 1$, facilities for studies at these velocities should be provided.

As the free-stream velocity increases, a critical value is reached at which the local velocity at certain points on the surface of the test model becomes sonic, although the flow is subsonic everywhere else. The Mach number corresponding to this critical free-stream velocity is denoted by M_{cr}; its value depends on the shape of the model; for airfoils and streamlined fuselages it varies between 0.8 and 0.85. When the free-stream velocity approaches the velocity of sound the whole model, except, perhaps, a very small area beneath the lower surface of a thin airfoil (Figure 2.41),

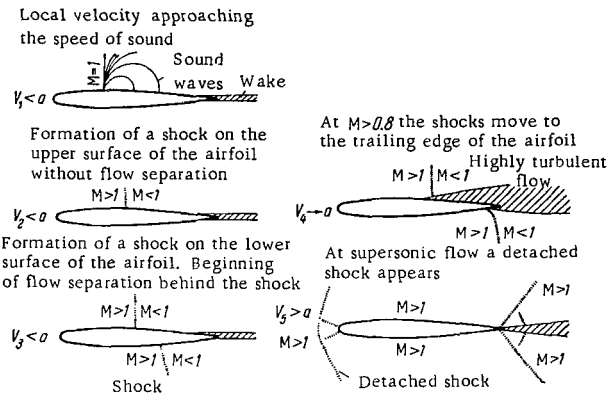

FIGURE 4.21. Variation with increasing Mach number of the position of shocks on airfoil.

is in a region of supersonic flow. At such velocities, shocks will propagate from the model in the test section toward the tunnel walls, reaching them as soon as the free-stream velocity becomes sonic. Further increase of flow velocity in the tunnel is impossible, irrespective of upstream pressure; the tunnel becomes choked. Further pressure increase will only cause the shocks to be displaced toward the trailing edge of the model, becoming oblique and distorted; finally, further shocks will appear (from the supports of the model to the walls of the tunnel etc.). Choking is also likely to occur in an empty tunnel when the velocity in a particular cross section becomes sonic, at the outlet of the test section because of boundary-layer thickening, or because of the wake. When the tunnel is choked, different parts of the model and its supports are under completely different flow conditions. Part of the model is in a subsonic region, and part in a supersonic region. The lack of methods for taking into account the different flow patterns makes it practically impossible to process the results of measurements, and tunnel choking should therefore be prevented.

An important factor in tunnel choking is the extent to which flow is impeded by the model and its supports. Reduction in the dimensions of the model (and correspondingly of the supports) is possible only to a limited extent. Even if the model is made from high-quality steel (with an ultimate strength of 120 to 130 kg/mm^2), rigidity requirements lead to a minimum blockage of 1.5 to 2%, or taking the supports into account, between 2.5 and 3%, even if the supports are of the arrow type.

Therefore, endeavors have been made to work out methods for model tests at transonic velocities in conditions where tunnel choking is prevented. One method is to increase considerably the flow area of the test section or the dimensions of the test model, so that blockage by the model will be less than 1%. However, an enlargement of the test section necessitates more power; thus, for instance, for testing an aircraft model having a wing span of 1.5 to 1.6 m, the diameter of the test section would have to be at least 4.5 m and the required power to obtain sonic flow in such a tunnel would be 50,000 kw.

Another method of eliminating tunnel choking is to provide an open test section. Choking is far less pronounced in such tunnels, and the corrections for its effect are much smaller than in tunnels with closed test sections. This method was used in several high-speed tunnels of early design, but was abandoned later because of the large power requirements, and the difficulties in obtaining a satisfactory velocity distribution. All high-speed tunnels have at present closed test sections.

The best method to prevent choking is to provide a test section with perforated walls. A steady flow, increasing in velocity from rest to supersonic speed, can be obtained in a Laval nozzle which consists of a converging (inlet) part, a throat — the narrowest section of the nozzle, where the free-stream velocity is equal to the local velocity of sound, i.e., to the critical velocity * — and a diverging part in which the velocity continues to increase. However, a Laval nozzle is not the only device for obtaining supersonic flow velocities. Supersonic flow can also be obtained in a cylindrical duct /13/, if we remove from it part of the medium.

Supersonic wind tunnels generally have divergent nozzles provided with extraction sections where part of the medium is exhausted from the test sections. Bypassing the medium, even when a conventional rather than a Laval nozzle is used, permits velocities close to, or even slightly in excess of, the speed of sound to be obtained in the test section in the presence of a model. The bypass consists of openings or slots (Figure 2.42) in the walls of the test section, through which the medium from the nozzle can expand, so that sonic flow is preserved throughout almost the entire length of the test section provided that the pressure drop is sufficient. The bypassed medium may reenter the tunnel at the end of the test section, and is mixed with the remainder flowing into the diffuser. However, the velocity distribution in the test section is improved by forced extraction through the walls of the test section.

In certain tunnels, air is extracted from the test section and reinjected into the diffuser to restore the total pressure in the boundary layer. This is done in the above-mentioned NASA low-turbulence tunnel (Figure 2.38). Numerous tests have shown that interference between model and tunnel in the region of transonic flow can be reduced in test sections with perforated or slotted walls.

Figure 2.43 shows comparative measurements of the resistance coefficient of a system of wings and fuselage, obtained in free flight (rocket tests) and in a transonic tunnel of the Langley Laboratory (NASA, U.S.A.)

* The critical velocity, which depends on the characteristics of the gas and its stagnation temperature T_0, is $a_* = \sqrt{\frac{2\varkappa}{\varkappa+1} g R T_0}$.

with a slotted test section measuring 2.44 m × 2.44 m. . It is seen that the slots in the test section permit reliable measurements in transonic tunnels.

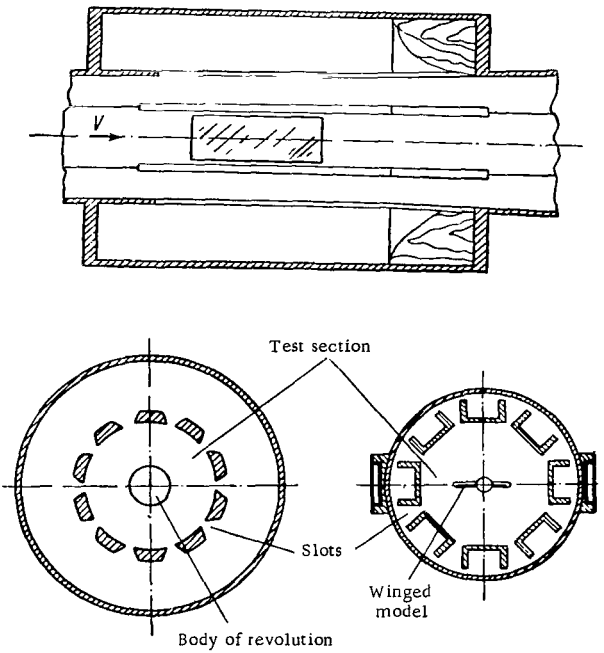

FIGURE 2.42. Test section with slotted walls.

The ratio of the area of the openings to the total area of the walls (degree of perforation) depends on the Mach number in the test section.

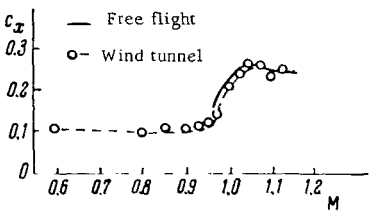

FIGURE 2.43. Comparative values of the resistance of a system of wings and fuselage obtained in free flight and in a transonic tunnel with slotted test-section walls.

Figure 2.44 shows this dependence. The use of perforated wall is feasible up to $M = 1.3$ to 1.5. Such walls, and the forced extraction of air, also permit a better utilization of the test section. Longer models can be tested,

since the shock waves are not reflected from the perforated walls toward the model, as happens when the walls are solid (Figure 2.45).

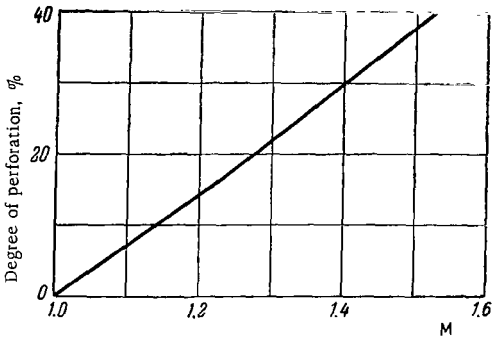

FIGURE 2.44. Variation with Mach number of the optimum degree of perforation.

The extraction of air from the test section makes it possible not only to obtain transonic velocities, and to reduce the interference between tunnel and model, but also to reduce the losses in the diffuser, since the boundary layer at the diffuser inlet will be thinner.

Diffusers in transonic tunnels

The diffuser plays a very important role in transonic tunnels when the Mach number exceeds unity since it is then necessary to reduce, with minimum energy loss, the flow velocity downstream of the test section to subsonic before contraction takes place again in the nozzle (of closed-circuit tunnels) or release to atmosphere (in open-circuit tunnels). The simplest method of reducing the flow velocity in the diffuser is to permit normal shocks to occur in the diffuser. The quality of a diffuser is very often characterized by its isentropic efficiency η_d,

$$\eta_d = \frac{2}{\varkappa - 1} \frac{1}{M_1^2} \left[\left(\frac{p_2}{p_1} \right)^{\frac{\varkappa - 1}{\varkappa}} - 1 \right],$$

where M_1 is the Mach number at the diffuser inlet, and p_1 and p_2 are the pressures at the inlet and outlet of the diffuser. The full line in Figure 2.46 shows the dependence of the diffuser efficiency η_d on the Mach number; the relationship was obtained using the standard equations for normal shocks. Such values of η_d are impossible in practice because of the pressure losses due to the interaction between shock and boundary layer at the wall. The same figure shows experimental values of the efficiency of such diffusers. Despite the considerable scatter of the experimental points, we see clearly that the losses in a normal-shock diffuser are still very high. Nevertheless such low-divergence diffusers (from 3 to 5°) are used in most transonic wind tunnels.

In modern transonic continuous-operation tunnels the test section may be as large as 5 m × 5 m. Very often the static pressure can be varied in such tunnels: underpressure is used for operating at high Mach numbers,

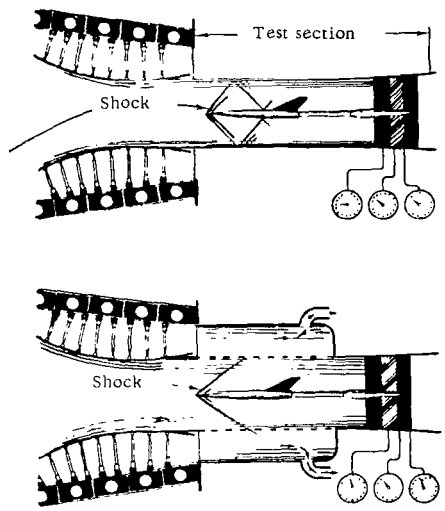

FIGURE 2.45. Reflection of shocks from the walls of wind tunnels with solid and perforated test-section walls.

and high pressure for obtaining large Reynolds numbers. Mostly, the test section is rectangular (with the width larger than the height); less often it is square or round.

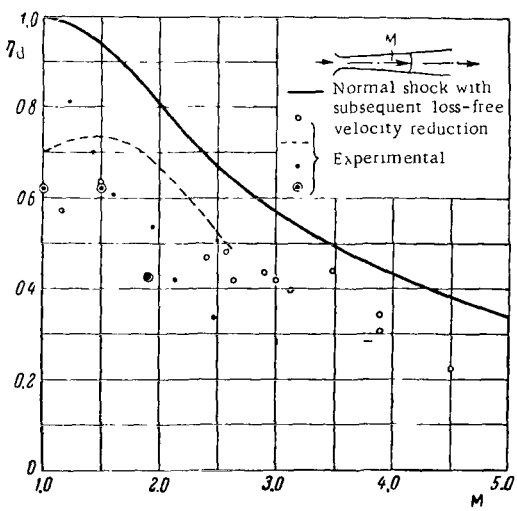

FIGURE 2.46. Variation with Mach number of isentropic diffuser efficiency.

Figures 2.47 to 2.49 show conventional modern transonic tunnels for continuous operation.

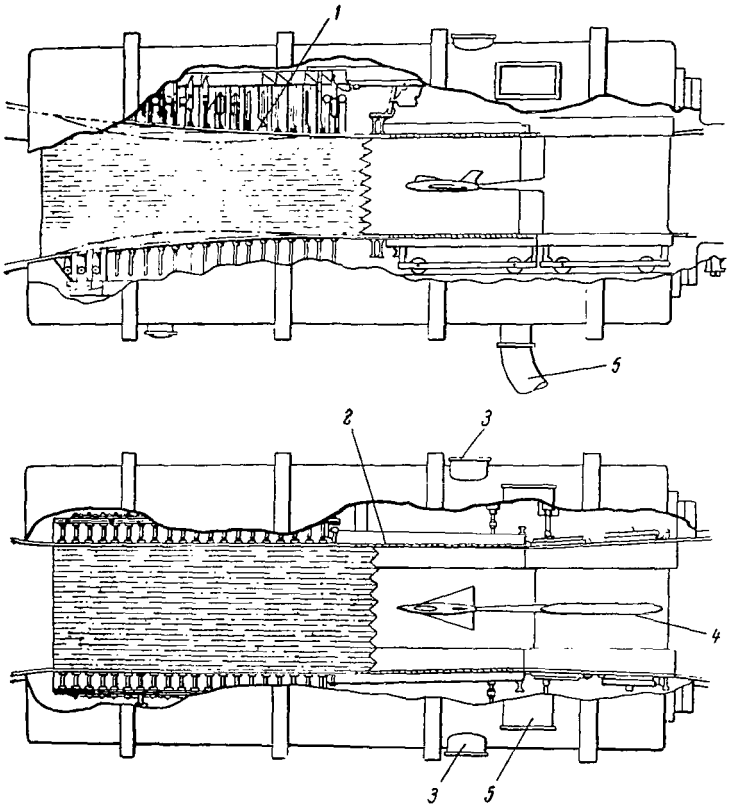

FIGURE 2.47. Test section of transonic tunnel (ARA-Great Britain). 1 — Adjustable nozzle; 2 — perforated test-section walls; 3 — observation windows; 4 — model carriage; 5 — pipes for air extraction through test-section walls.

Figure 2.47 shows the 2.74 m × 2.44 m test section of the ARA tunnel (Great Britain). Velocities up to M 1.3 can be obtained in this tunnel in which the pressure can be varied between 0.8 and 1.2 atm. The Reynolds number for a test at $M = 1$ on a model of 1.1 m wing span is 6×10^6. The tunnel is equipped with an adjustable nozzle and a test section with perforated walls. A 13,750 h.p. eleven-stage axial compressor extracts air through the perforated walls at a rate of up to 8500 m^3/min, thus effectively reducing interaction between model and boundary layer and preventing choking of the tunnel. The model in the test section of the tunnel is installed on a telescopic support mounted on a carriage at the diffuser inlet, so that it can easily be withdrawn from the tunnel for calibration adjustment.

The carriage supports a wind-tunnel balance and a cradle for adjustment of the angle of attack. The tunnel is equipped with a radiation air cooler

which maintains the tunnel air temperature below 50°C. An absorption-type dryer reduces the water content to a level of 1 g of water per kilogram of air, which is equivalent to a relative humidity of 10% at 50°C. The air is impelled through the tunnel by two tandem-mounted 20-blade fans with an impeller diameter of 6.5 m, driven at a maximum speed of 485 r.p.m. by a 25,000 h.p. motor. The guide vanes before the first fan stage and between the stages, have flaps (25% of the chord) which during tunnel operation can be rotated to angles between 10 and 20° from the normal position, to supplement velocity regulation by fan-speed adjustment. The test results are processed in an electronic computer.

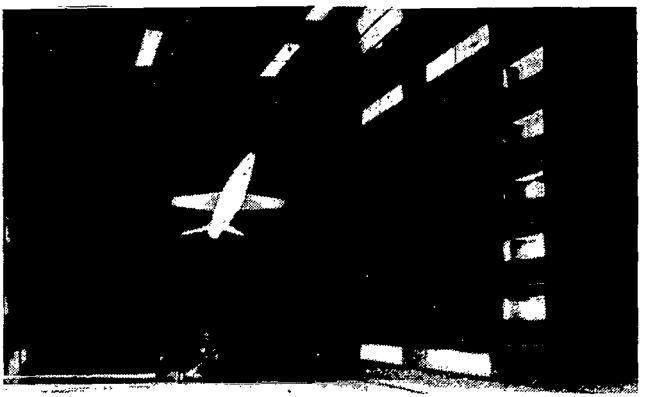

FIGURE 2.48. Test section of a transonic tunnel (NASA) with slotted walls. The dimensions of the test-section flow area are 4.28 m × 4.28 m. $M \leqslant 1.2$.

Figure 2.48 shows a test section with slotted walls in a NASA transonic tunnel, while Figure 2.49 shows the HLL transonic tunnel (Netherlands).

Modern transonic (and supersonic) tunnels are equipped with sliding test-beds for easy withdrawal of the model (Figure 2.50), television monitoring of model and tunnel, automatic test equipment, and remotely controlled tunnel facilities. The powers required are very large, and a single drive unit may be designed to serve several tunnels. For instance, in the Moffett Field Laboratory (NASA) the 216,000 h.p. drive serves 3 tunnels (Figure 2.51).

Intermittent-operation transonic tunnels

A typical tunnel of this type is shown in Figure 2.52. High-pressure air is discharged from a system of gas bottles* through a manifold into the settling chamber of the tunnel. After passing through the settling chamber, the test section, and the diffuser, the air is exhausted to atmosphere.

* In some tunnels a single gas reservoir is used instead of a number of bottles. For instance, in the AEDC gas dynamics laboratory (U.S.A.) the E-1 unit operates from a gas reservoir 220 m long and 0.9 m in diameter, which can hold about 50 tons of air at a pressure of 283 kg/cm^2.

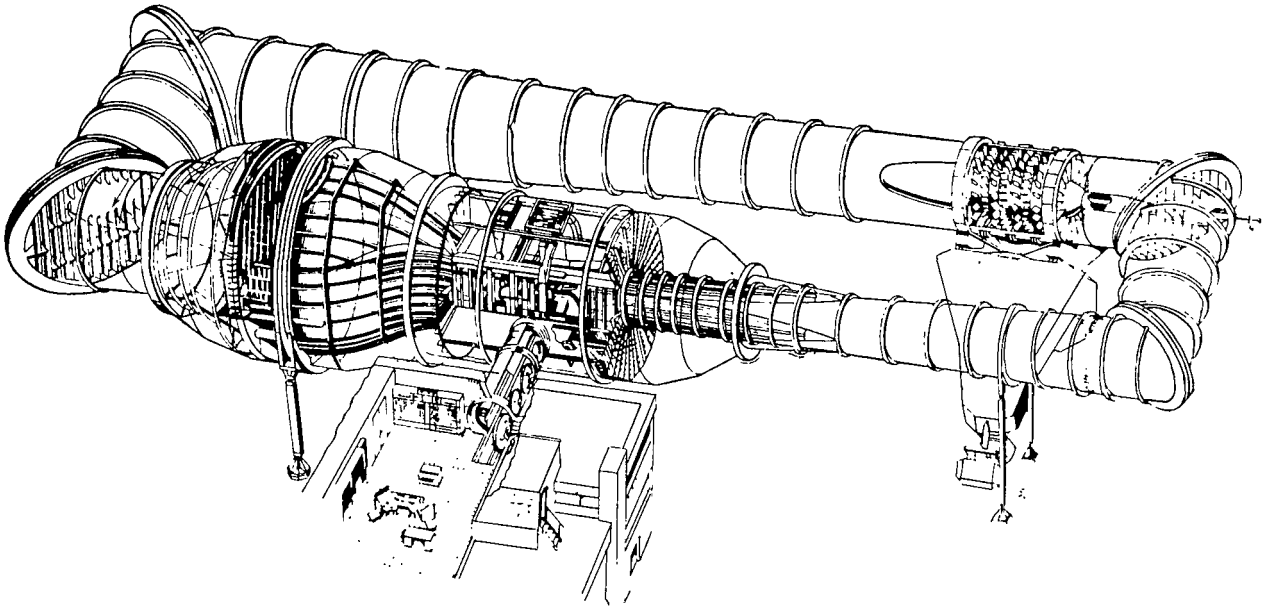

FIGURE 2.49. HLL variable-density transonic tunnel (Netherlands): p = 0.125 to 4 atm; M = 0 to 1.3; test-section dimensions: 2 m × 1.6 m; power: N = 2000 h. p.

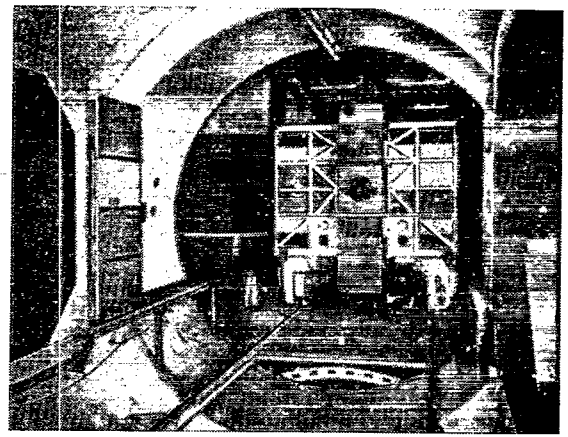

FIGURE 2. 50. Sliding test bed of the California Institute of Technology wind tunnel ($M = 1.8$); test-section dimensions: 2.6 m × 3.4 m).

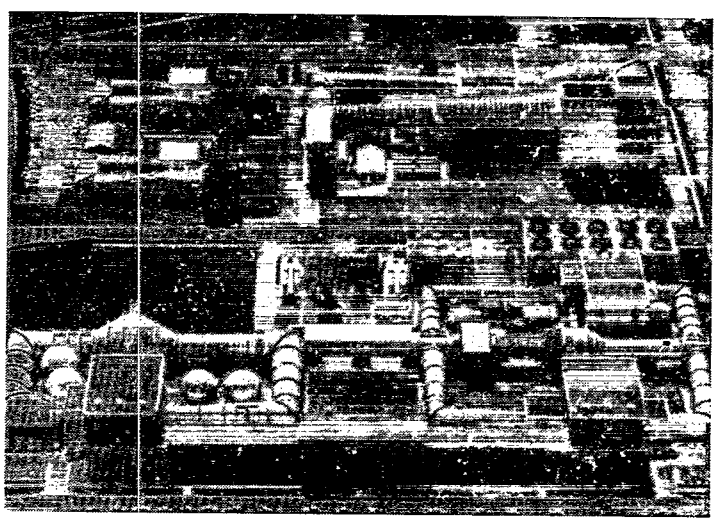

FIGURE 2. 51. General view of a triple tunnel (Moffett Field). The 216,000 h. p. drive (with booster) serves 3 tunnels; test section: 3.35 m × 3.35 m, $M = 0.07$ to 1.5; test section (2): 2.13 m × 2.74 m, $M = 1.4$ to 2.7; test-section (3): 2.13 m × × 2.74 m, $M = 2.4$ to 3.

To obtain velocities up to $M = 1.4$ in the test section of such a tunnel, its settling-chamber pressure must be between 1.5 and 1.7 atm. To extend the duration of tunnel operation the reservoir pressure should be much higher. A butterfly control valve is installed between the reservoirs and the settling chamber; it is operated by a pressure regulator to maintain constant pressure in the settling chamber, so that tests can be performed at constant Reynolds numbers. The designed operating duration of the tunnel depends on the measuring facilities available and on the kind of test undertaken. If an automatic wind-tunnel balance is used, a minimum of 15 to 30 seconds will be required for equilibrium conditions to be attained before each observation. Several readings could be made within this interval with a strain-gage balance, but a high-speed attitude cradle would be required.

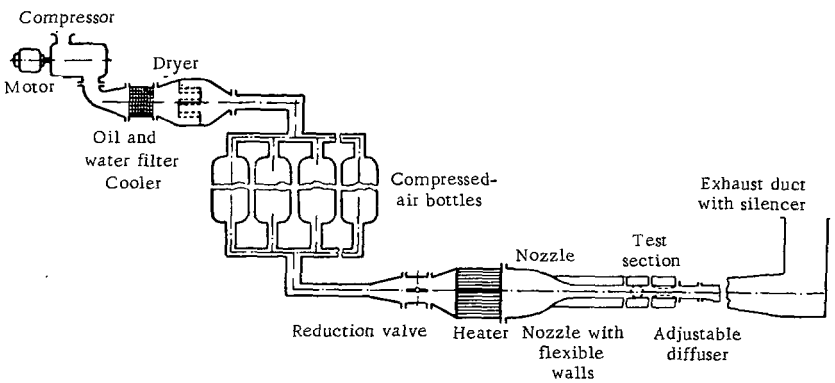

FIGURE 2.52. Intermittent-operation wind tunnel supplied with compressed air from bottles.

The design mass flow through the test section depends on the dimensions of the latter, the flow velocity, and the flow deceleration, and can be calculated from the formula for mass flow rate through unit area

$$\rho u = M a_0 \rho_0 \left[\frac{2}{2 + (\varkappa - 1) M^2}\right]^{\frac{\varkappa+1}{2(\varkappa-1)}}.$$

Figure 2.53 shows how the operating duration t (expressed as a fraction of the operating duration at $M = 1$) of a reservoir-type tunnel depends on M. Figure 2.54 shows how the reservoir capacity for unit operating duration at $M = 1$ depends on the pressure when the flow area of the test section is $1\ m^2$. These results have been confirmed by experiments, and can be used to calculate the number and capacity of the compressed-air bottles needed for intermittent-operation tunnels. As the diagram shows, the required reservoir volume decreases sharply as reservoir pressure increases. However, experience in the construction and use of reservoir-powered intermittent-operation tunnels has shown that the pressure in the bottles should not exceed 20 atm, since the weight of the bottles cannot be substantially reduced further, while the rated power of the compressor must be increased. In addition, high pressures complicate design and

operation of the equipment. It is therefore usual to operate this type of wind tunnel at a maximum pressure in the bottle of 8 to 20 atm.

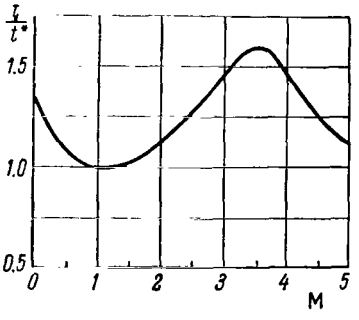

FIGURE 2.53. Mach-number dependence of operating duration of wind tunnels supplied with compressed air from storage bottles.

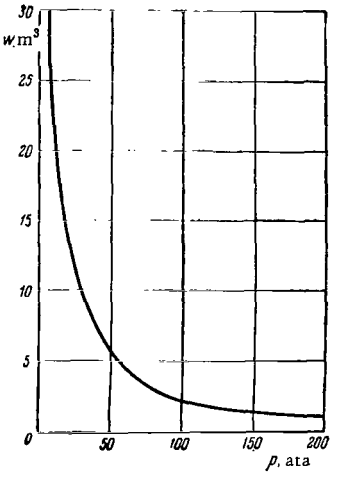

FIGURE 2.54. Pressure dependence of the reservoir volume at $M = 1$, $t = 1$ sec, flow area of test section = 1 m^2.

Intermittent-operation induced-flow wind tunnels

Transonic intermittent-operation tunnels may also function on the induced-flow principle. In such tunnels, high-pressure air is supplied to ejectors installed at the test section outlet. The air flows at high velocity through annular or axial slots in the walls of the ejector, so that it entrains low-pressure tunnel air and induces air flow through the test section to atmosphere. In comparison with continuous-operation tunnels, induced flow tunnels have the advantage, shared by reservoir-type tunnels, of great simplicity of design. Their drawbacks are low efficiency in comparison with continuous-operation tunnels, and the necessity to regulate the pressure at the ejector inlet or to adjust the flow area of the inlet slot of the ejector as the reservoir pressure decreases.

Induced-flow tunnels may also have semi-closed circuits, in which the surplus air is removed through outlet slots in the return duct (Figure 2.55). Such tunnels are more economical, since part of the air is recirculated; the duration of their operation is 30 to 50% longer than that of ordinary induced-flow tunnels.

Jet-engine exhaust is sometimes used to induce transonic flow. Figure 2.56 shows a tunnel powered by the exhausts of three jet engines. A feature of this tunnel is the use of part of the hot air, which is circulated through the tunnel to heat the cold atmospheric air. The cross-sectional area of the test section is 0.23 m^2, and a maximum velocity of $M = 1.2$ can be obtained.

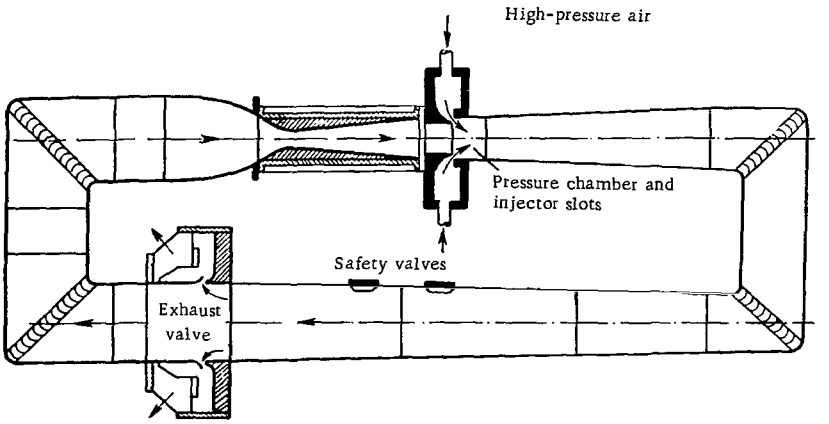

FIGURE 2.55. NPL induced-flow transonic tunnel; M = 0 to 1.8; test section dimensions: 0.23 m × 0.077 m.

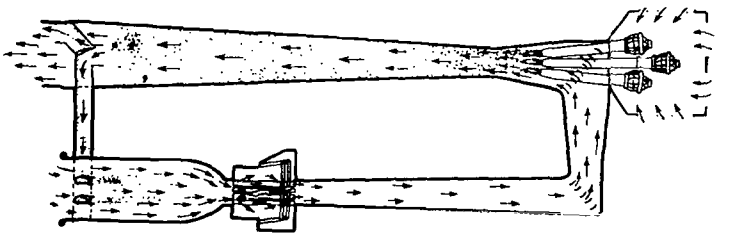

FIGURE 2.56. Induced-flow transonic tunnel operated by jet-engine exhaust.

When sufficient reserves of air are available at only a limited pressure it is better to supply air to the settling chamber, and the remainder to an ejector usually placed immediately downstream of the test section. In this case the required test-section velocity can be obtained at a considerably lower settling-chamber pressure. The operating duration of induced-flow tunnels is proportional to the induction coefficient, i.e., to the ratio of the exhaust-air flow rate to the air injection rate.

Figures 2.57 and 2.58 show the dependence of the induction coefficient on the relative flow areas of slot and test section, and on the ratio of total pressures of injected and induced air for various numbers.

As can be seen from Figure 2.57 the induction coefficient decreases sharply with increasing Mach number; for this reason intermittent-operation induced-flow tunnels, of the type shown in Figure 2.55, are less widely used than tunnels in which the ejectors serve only to reduce the pressure at the test-section outlet. In certain induced-flow tunnels, steam is used instead of compressed air.

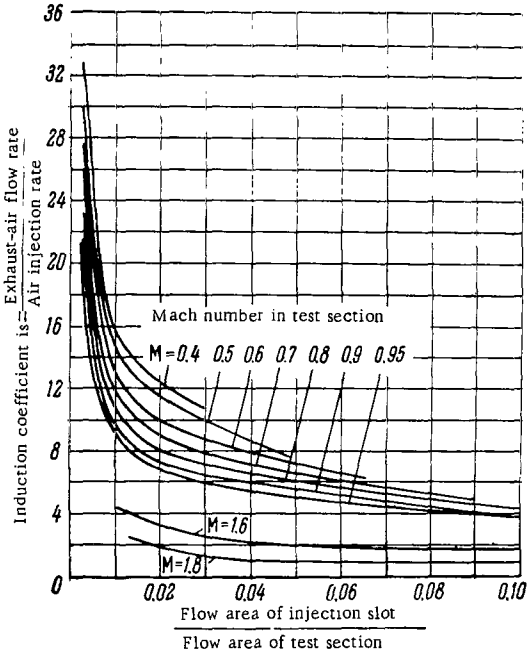

FIGURE 2. 57. Dependence of induction coefficient on flow areas of ejector slot and test section, and Mach number.

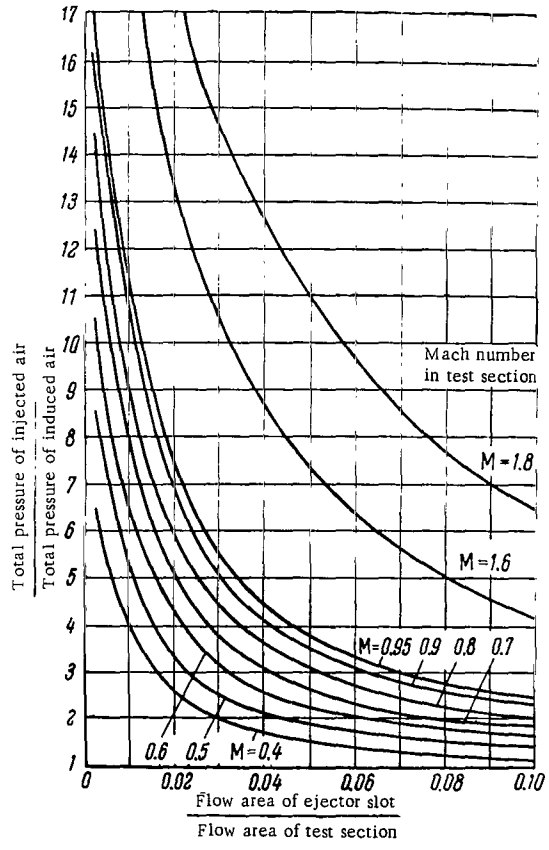

FIGURE 2. 58. Dependence of the ratio of total pressure of injected air to total pressure of induced air on flow areas of ejector slot and test section at various Mach numbers.

Vacuum-powered tunnels

An intermittent-operation vacuum-powered wind tunnel is shown in Figure 2.59. Atmospheric air is drawn through the dryer, settling chamber, nozzle, test section, and diffuser into the vacuum reservoir (usually a sphere), from which air is either evacuated beforehand, or continuously exhausted to atmosphere by means of a vacuum pump. The pressure drop in these tunnels may be varied within very wide limits by changing the pressure in the evacuated reservoir.

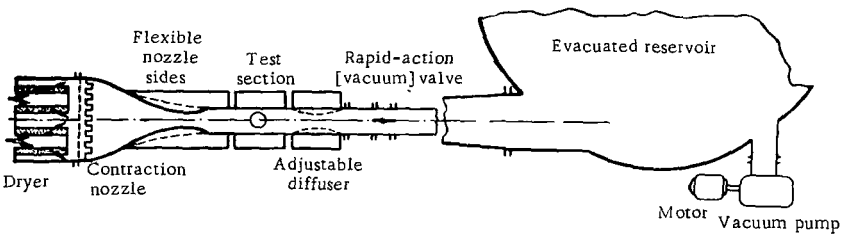

FIGURE 2.59. An intermittent operation, vacuum-powered wind tunnel.

Figure 2.60 shows the pressure-dependence of the capacity required of the evacuated reservoir for 1 second operation of a tunnel with a test section 1 m^2 in cross-sectional area at $M = 1$. It can be seen that even at a very low reservoir pressure, the volume required for the conditions stated exceeds 250 m^3 per second of operation.

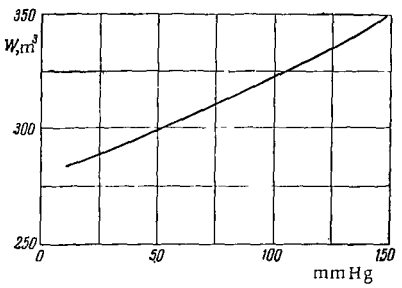

FIGURE 2.60. Required reservoir capacity as function of the pressures in it, for $M = 1$, operation duration, t = sec, flow area of test section is 1 m^2.

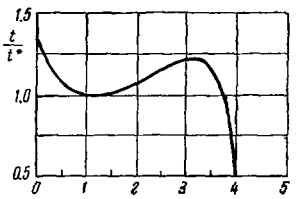

FIGURE 2.61. Mach number-dependence of the operating duration of a vacuum-powered tunnel (initial reservoir pressure is 100 mm Hg).

Figure 2.61 shows the Mach number-dependence of the ratio of the operating duration of a vacuum-powered tunnel to the operating duration at $M = 1$. The very high reservoir capacities required considerably restrict the use of such tunnels.

The need to dry the atmospheric air drawn through the tunnel is a serious problem in intermittent-operation vacuum-powered tunnels. If the tunnel is operated at a rated moisture content of 0.1 g water per kg of air, the designed surface area of the dryer amounts to about 400 m^2 per square meter of test-section flow area.

§ 6. SUPERSONIC WIND TUNNELS

Supersonic wind tunnels are by convention, tunnels with operational Mach numbers above 1.4 or 1.5. Like transonic tunnels these tunnels may either be for continuous or for intermittent operation, and are designed and equipped accordingly. However, the aerodynamic profile of supersonic tunnels, from settling chamber to diffuser, is independent of operating method and type of drive. In general, the test section of supersonic tunnels is rectangular to facilitates optical studies and simplify tunnel design.

Nozzle

Modern design methods permit uniform straight axial supersonic flow to be obtained at the nozzle outlet and test-section inlet. The designed nozzle profile can usually be realized. The tolerances for the internal surface of supersonic nozzles are quite fine (as little as ± 0.01 to 0.05 mm with a polished surface). Existing production methods permit such tolerances to be achieved even in the manufacture of nozzles of considerable dimensions.

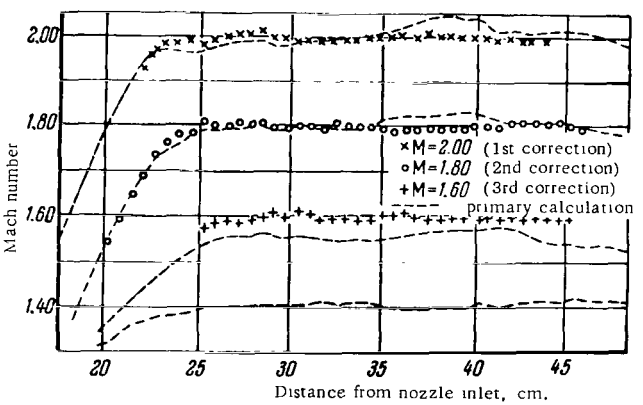

FIGURE 2.62. Velocity distribution in nozzles.

Design techniques are sometimes inadequate to ensure a sufficiently uniform flow over the entire test section, and in practice nozzles require experimental "tuning."

Figure 2.62 shows the velocity distribution in a test section before and after tuning of the nozzle /2/. For large supersonic tunnels the design is checked and adjusted on models. In modern well-tuned tunnels we can obtain a test-section velocity distribution uniform to within less than ±1%.

FIGURE 2.63. Interchangeable nozzle ("insert") of a supersonic wind tunnel.

The Mach number in rectangular test sections of supersonic tunnels can be varied by fitting interchangeable nozzles ("inserts", Figure 2.63) or by using adjustable nozzles (Figure 2.64), in which the lower and upper

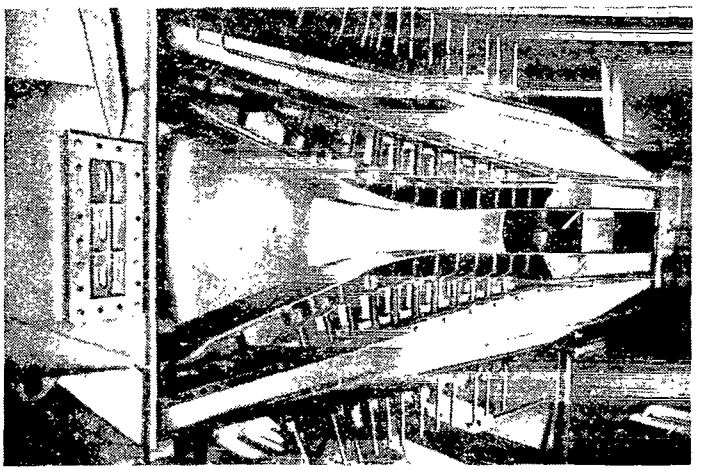

FIGURE 2.64. Adjustable nozzle of a supersonic tunnel ($M < 4$) NASA (Pasadena).

walls forming the nozzle profile can be deformed at will. Interchangeable nozzles for very large tunnels are mounted on carriages weighing several tons and sliding on rails. Such a design necessitates a large tunnel-house, and special devices for connecting the nozzle to the settling chamber and test section. It is for these reasons that in recent years many supersonic

tunnels have been equipped with adjustable nozzles, in which the profile needed is obtained through elastic deformation of tunnel floor and roof.

There are many designs of adjustable nozzles differing in the degree to which the flexible wall can be made to approximate the required nozzle profile. The perfection depends mainly on the number of adjusting jacks used to determine the profile (Figure 2.64). Modern tunnels may have as many as 25 to 30 jacking points. In the supersonic wind tunnel of the Lewis laboratory, which has a test section measuring 3.05 m × 3.05 m, the adjustable nozzle has 27 jacks and Mach numbers ranging from 2 to 3.5 can be obtained.

Although at the same Mach number, rigid interchangeable nozzles produce a better velocity distribution than the corresponding adjustable nozzles, the latter are being increasingly used, since with careful design they do produce a sufficiently uniform velocity distribution while their use considerably reduces the cost of tests and increases the testing capacity of the tunnel.

Plane nozzles are only adequate up to $M = 7$. Beyond this their critical cross section becomes very small, so that they are difficult to manufacture, and the slot is subject to appreciable thermal deformation, with resulting deterioration in the flow uniformity. Axisymmetric or three-dimensional nozzles should therefore be used at high Mach numbers. It is common practice to use nozzles whose shapes can be automatically adjusted by remote control during tunnel operation, so that the Mach number can be varied swiftly. This is especially important in tests of fixed models at different flow velocities in intermittent-operation tunnels, and recent designs permit adjustment for small Mach-number changes to be completed in a few seconds. This is achieved with a programming mechanism at the control panel, consisting, for example, of a series of templates reproducing the nozzle profile, appropriate to each Mach number, very accurately to a small scale. Push-button selection of a template causes depression of a series of spring-loaded cordinate rods, equal in number to the jacking points. A selsyn system operates each jack so that it follows the movements of its cordinate rod, thereby setting up the desired tunnel profile.

Recent designs employ digital control of the nozzle profile, using either punched cards or tapes on which the nozzle profiles for various Mach numbers are programmed.

When the program card is inserted, the control device automatically moves the adjusting jacks into the appropriate positions.

A simpler system of nozzle control is used in certain tunnels to permit Mach-number changes of 0.05 to 0.10, e.g., from $M = 1.5$ to $M = 1.6$. Such a change can be achieved without seriously impairing the quality of flow in the test section by adjusting the throat section and suitably deforming nearby parts of the nozzle.

In the design of adjustable nozzles careful attention must be paid to the rigidity of the adjustable walls, and to hermetical sealing between the walls and the housing of the nozzle ("nozzle box").

If the adjustable wall is not sufficiently rigid, it will "flap" and the distortion of the nozzle profile will impair the flow in the test section. Hermetical sealing of the space behind the flexible wall of the nozzle is very important to prevent large loads on the wall when the tunnel is started up or when operating conditions are changed; the position of the

shock may change so rapidly that the pressures inside and outside the wall do not have time to become equalized. In designing supersonic tunnels special attention must also be paid to the connection between the nozzle and the test section. The slightest projections give rise not only to nonuniform velocity distributions, but also to serious inclinations of the flow in the test section. For example, a 1.5 mm projection at the inlet to a 1000 mm × 1000 mm test section operating at Mach numbers between 1.5 and 3 will cause a flow inclination of up to ± 3°.

The optimum results in terms of uniform supersonic flow with a thin boundary layer may be obtained by using porous nozzle walls, so that boundary-layer thickening can be abated by controlling the flow through the walls, and a more uniform pressure distribution obtained at the test-section inlet.

Porous nozzle walls are used in high-vacuum supersonic tunnels where the boundary layer would otherwise occupy a considerable part of the test section.

Test section

Closed test sections are generally used in supersonic tunnels, largely because of the considerably greater power needed for tunnels with open test sections (Figure 2.65). The test section is, as a rule, not more than 1.5 to 2 widths in length, and sometimes an even shorter test section is adequate. This is because very small models are used in supersonic tunnels,

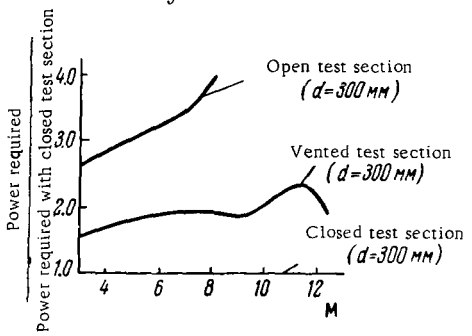

FIGURE 2.65. Dependence of the power of supersonic tunnels on the type of test section.

a practice enforced by the need to place the model in the test section in such a way that the shock from its nose will not be reflected from the tunnel walls onto either the tail itself or the wake immediately downstream. The test section of a modern high-speed tunnel is a complicated structure equipped with a variety of mechanisms and devices. Its inner surface must be polished and the liners, frames of optical glass ports, etc., must be made of stamped parts polished flush with the tunnel walls. Figures 2.66 to 2.68 show test sections of different supersonic wind tunnels.

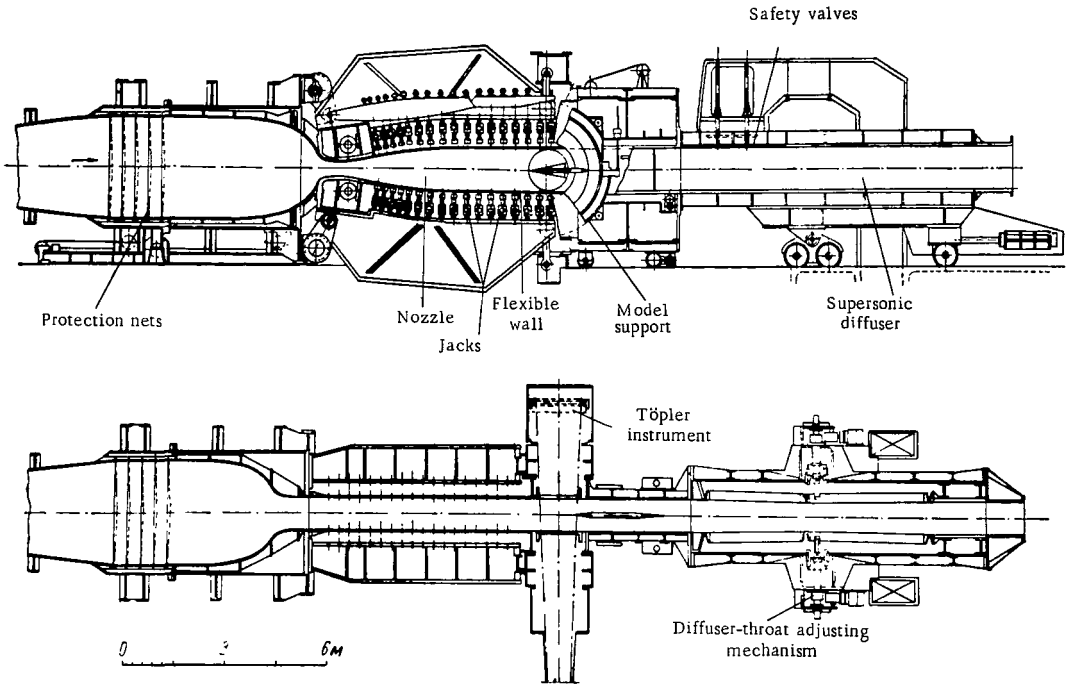

FIGURE 2.66. Test section of an RAE tunnel (Great Britain). Dimensions 1.2 m × 0.9 m; $p = 5$ to 14 atm; $M = 2.5$ to 5; $N = 88{,}000$ h. p.

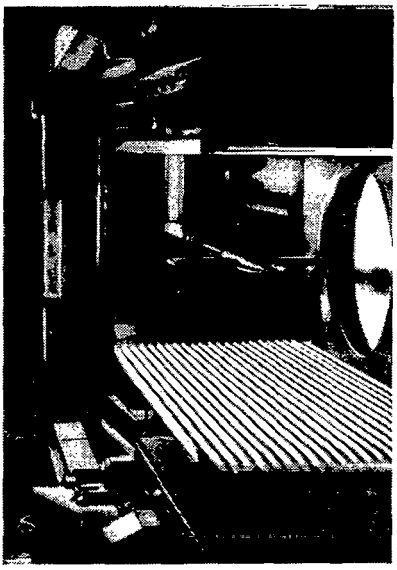

FITURE 2.67. Test section of the FFA supersonic vacuum-powered tunnel (Stockholm). Test-section dimensions 0.9m x 1.15m; M = 1 to 2.5; Vacuum-reservoir volume = 9,000 m^3; Operating duration = 30 sec.

FIGURE 2.68. External view of the test section of the FFA supersonic tunnel.

Diffuser for supersonic tunnels

Efficient deceleration from supersonic velocities is a very difficult problem not only in wind tunnels but in other fields of aerodynamics. Deceleration by means of a normal shock might be acceptable for test-section velocities up to M = 1.3 or 1.4, but the energy losses become excessive at large velocities, and an adjustable diffuser with a series of oblique shocks is then often used.

At inlet Mach numbers greater than 1, standard subsonic diffusers are subject to large energy losses, which exceed the losses due to deceleration to subsonic velocities by means of normal shocks. Figure 2.69 illustrates the effectiveness of flow deceleration in standard diffusers of various angles /17/. Pressure losses are least for small divergence angles, but even then they still exceed the losses in normal shocks. With further increase in inlet Mach number the pressure losses in a standard diffuser rise sharply: the pressure ratio exceeds 100 at M = 6 (Figure 2.70).

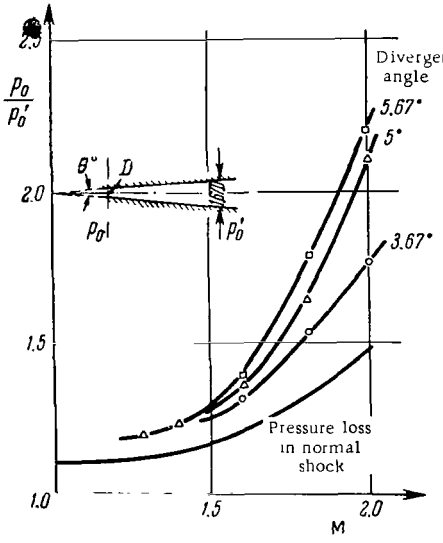

FIGURE 2.69. The influence of Mach number and divergence angle on the effectiveness of flow deceleration by shocks.

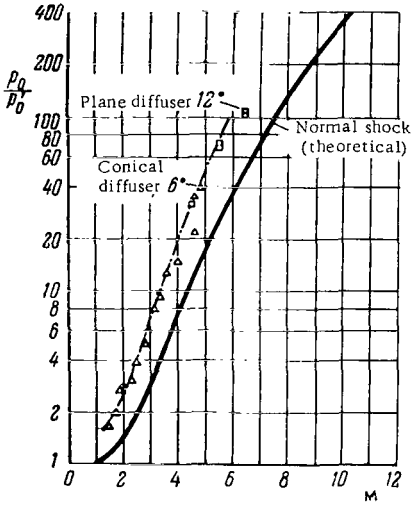

FIGURE 2.70. Mach number dependence of pressures in diffuser without contraction.

The diffusers used in supersonic tunnels are therefore fitted with either fixed or adjustable throats /18/. In a converging duct with supersonic flow, a nearly normal shock will form in the narrowest section, downstream of which the velocity will be subsonic. The velocity can then be further reduced in a subsonic diffuser. This method of decelerating a supersonic flow considerably reduces the losses in the diffuser, as can be seen, for example, in Figure 2.71. In the adjustable diffuser (Figure 2.72) supersonic flow can be obtained throughout the test

section by widening the diffuser throat during start-up so as to ensure that the shock travels the full length of the test section and is swallowed by the diffuser as the inlet Mach number is gradually increased. After start-up,

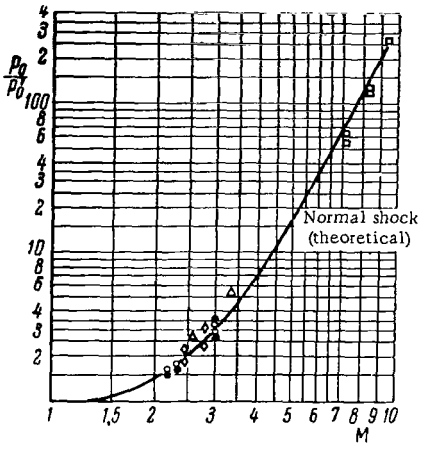

FIGURE 2.71. The Mach-number dependence of pressures in diffuser with fixed contraction ratio. Experimental points refer to divergence angles between 3 and 20° at $Re = 3.0 \times 10^6$.

the throat area is reduced so that the shock is stabilized at the diffuser throat; a high pressure-recovery coefficient can be obtained in this way.

Adjustable supersonic diffuser.

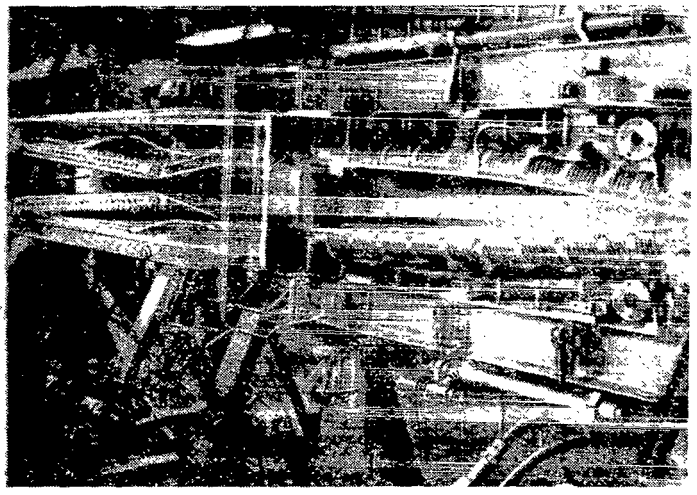

FIGURE 2.72. Test section of tunnel with adjustable supersonic diffuser. $M = 4.5$ to 8.5; test section dimensions 0.53 m × 0.53 m. (California Institute of Technology).

Figure 2.73 shows the Mach-number dependence of the ratio of throat area to inlet area of the diffuser, for start-up and for operation of the tunnel.

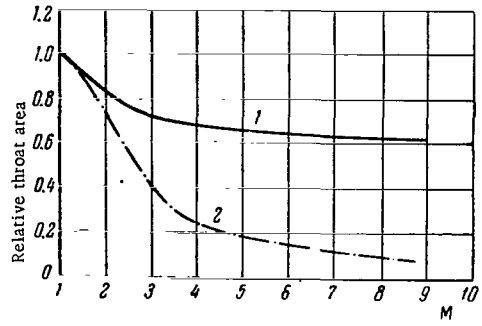

FIGURE 2.73. Mach-number dependence of relative throat area, required for start-up (1) and operation (2).

At $M = 6$, the ratio of inlet to outlet total pressure is 100 for diffusers without contraction, 35 for a diffuser with fixed contraction ratio, and 15 for an adjustable diffuser.

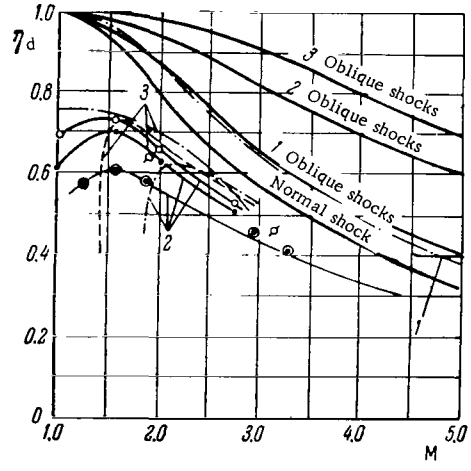

FIGURE 2.74, Variations of isentropic efficiency with Mach number in a diffuser employing various alternative means of flow deceleration. 1 — diffuser throat with maximum relative contraction and subsequent complete (loss-free) deceleration of subsonic flow; 2 — experimental results for diffuser with contraction; 3 — experimental results for diffuser with wedge.

At $M = 3$ the corresponding pressure ratios are 5 to 6, 3.5, and 2.5. Thus, adjustable diffusers are preferable even at small supersonic velocities.

However, a better method of decelerating supersonic flow in the diffuser is by means of several oblique shocks. It has been shown both theoretically and experimentally that this method is more efficient than the use of a single normal shock. Deceleration by oblique shocks is successfully employed at the inlet to jet engines, in which the flow velocity must be subsonic although the flight speed is supersonic.

The same principle is used for supersonic diffusers in wind tunnels, and consists of fitting a wedge into an ordinary diffuser. Figure 2.74 shows the values of the isentropic efficiency of a diffuser in which deceleration from supersonic to subsonic velocities was carried out in different ways /14/. This was done most efficiently by means of oblique shocks. The diffuser wedge is also sometimes used as a base for the model, which in this case is installed on a telescopic support connected to the wedge.

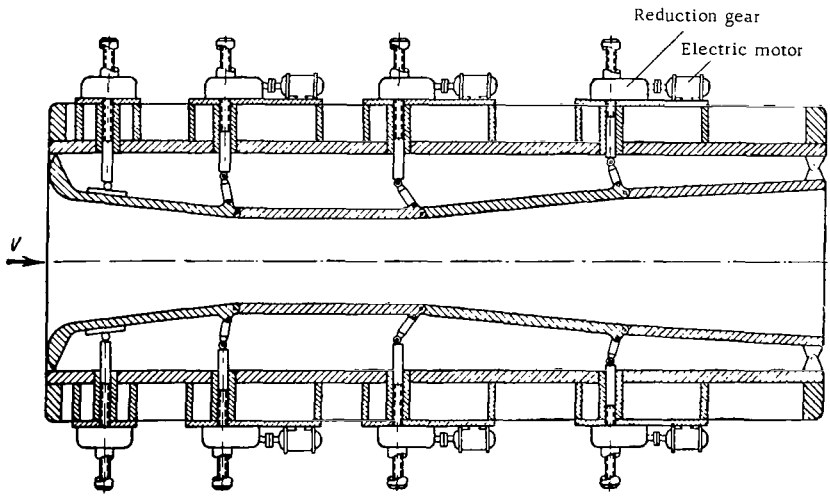

FIGURE 2.75. Variation of diffuser geometry, using rigid adjustable wall sections.

The design of a supersonic diffuser can be further improved by extracting the boundary layer through the walls of the diffuser, so as to prevent choking of the diffuser throat, with consequent transfer of the shock to the test section. A better effect is obtained if the boundary layer is extracted through the walls of both test section and diffuser.

Boundary-layer extraction in the test section not only assists the development of supersonic flow and reduces the interference between model and tunnel, but it also considerably reduces the boundary-layer thickness at the diffuser inlet.

In certain supersonic tunnels (usually for intermittent operation), the necessary pressure drop is obtained by ejectors installed immediately upstream and downstream of the diffuser. Velocities up to $M = 10$ are

possible in such tunnels without any further devices in the diffuser if two ejectors are installed. In such a diffuser shocks form, as a rule, behind the second ejector, where the supersonic velocity is not large.

Despite many theoretical and experimental studies, there remains a paucity of design data and methods on diffusers for high-speed tunnels; the power consumption of supersonic tunnels could be reduced by a more rational design of diffusers in which the main operating losses of the tunnel occur.

The design of a supersonic diffuser is considerably simpler than that of an adjustable nozzle, since the aerodynamic requirements for diffusers are less severe.

It is simpler in practice to design diffusers with adjustable walls than with adjustable wedges, so that the latest designs of supersonic tunnels favor the principles of diffuser regulation by altering the geometry of successive diffuser cross sections in the manner illustrated in Figure 2.75. The position of the wall sections of such a diffuser is usually adjusted by remote control. Electric motors, installed outside the tunnel and remotely controlled, adjust the wall sections through hinged lead screws. The positions of the wall sections and the geometry of the adjustable diffuser are determined with the aid of limit switches, which de-energise the electric motors when the programmed position of the lead screws, appropriate to preset operating conditions, has been reached.

The hermetic sealing of the joints between the wall sections of the diffuser and the vertical walls of the tunnel is very important when the supply of air is limited. Unless the joints are properly sealed leaks will occur, and high settling-chamber pressures will be required to obtain the designed supersonic velocities in the test section.

Air drying and preheating

Acceleration of the moist air entering a wind tunnel causes a reduction in its temperature and pressure, and may lead to saturation, supersaturation, and condensation of water vapor. Figure 2.76 shows the Mach numbers at which saturation occurs in the test section, plotted as a function of the relative humidity at the tunnel inlet /14/.

Condensation does not always take place immediately after saturation occurs, but only when a supersaturated condition is reached, generally corresponding to a strong adiabatic supercooling, and to a large difference between the dew point and the true air temperature. Condensation of water vapors occurs suddenly as a shock accompanied by liberation of the latent heat of vaporization. The consequent change in the behavior of the medium affects the test characteristics of the model.

In supersonic tunnels, condensation, which very often takes place near the nozzle throat, impairs the flow uniformity and reduces the test-section Mach number in comparison with the calculated value for dry air. In subsonic tunnels condensation begins, as a rule, in regions of large local velocities near the model and very often, condensation and compression shocks are formed together around the model, changing the flow-pattern.

Figure 2.77 gives the results of tests of the Mach-number distribution along the half-section of a thick symmetrical airfoil in a tunnel at a free-stream Mach number of 0.72 and with a relative humidity $r = 61\%$ /19/. The shocks shown in the diagram changed their position, and one of them disappeared, when the relative humidity decreased, demonstrating the pronounced effect of condensation on the aerodynamic characteristics of the airfoil. The aim in modern supersonic tunnels is therefore to prevent moisture condensation and limit the absolute humidity.

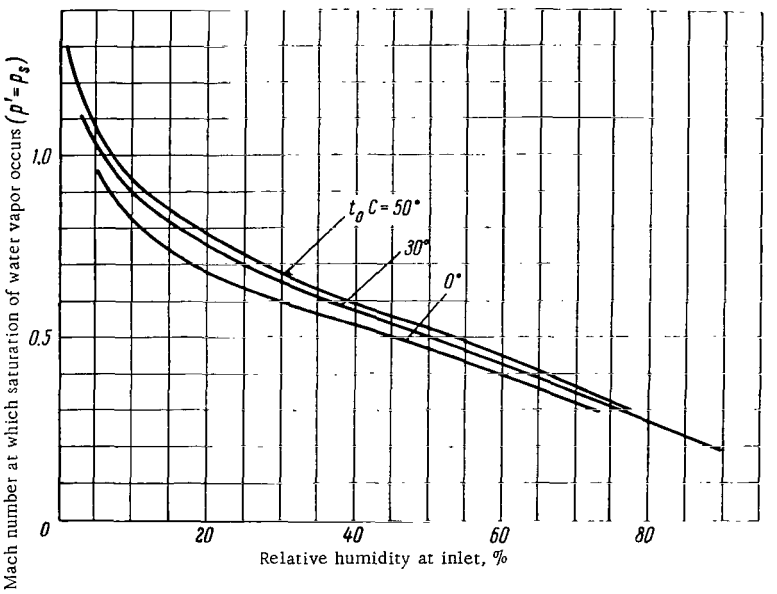

FIGURE 2.76. Dependence of Mach number at which saturation occurs on relative humidity at tunnel inlet. p' is the partial pressure of water vapor; p_s is the saturation water-vapor pressure; t_0 is the dry-bulb temperature at the inlet.

thereby reducing the maximum amount of heat that can be liberated during condensation. If the quantity of water vapor in the air is limited to 0.5 grams per kilogram* of vapor-air mixture, the effects of condensation become negligible below $M = 4$.

Since the saturation vapor pressure increases with temperature, condensation can be prevented by heating the air so that its relative humidity is reduced. Although this process does not remove moisture, and leaves the absolute humidity unchanged, it does reduce the effects of condensation, should it still occur, by virtue of the increased heat content of air. Increase of the stagnation temperature is particularly necessary to prevent condensation at high Mach numbers ($M > 4$) of other gases in the air. In continuous-operation tunnels, however, the stagnation

* Current practice is to reduce the inlet humidity even further down to 0.1 grams water vapor per kilogram of air-vapor mixture in order to ensure uniform air flow at the outlet of supersonic tunnels.

temperature can only be increased to a limited extent, since although the increase can be achieved very easily by reducing the cooling, no great increase is permissible in the temperatures of the model and instruments; in particular, dangerous overheating of the compressor bearings might occur, since the ambient air temperature reaches 200° to 350°C in their vicinity, even without air heating. Air heating is therefore only used in intermittent-operation tunnels, the air passing through heaters (see below) as it enters the settling chamber.

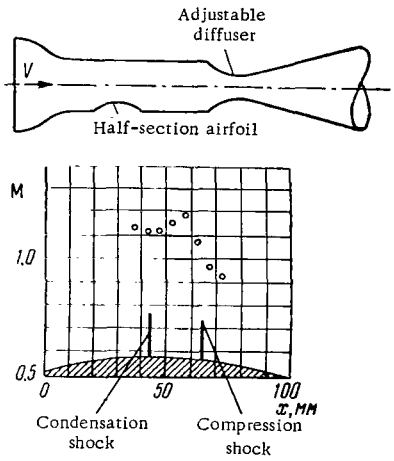

FIGURE 2.77. Mach-number distribution along half-section of an airfoil in the presence of a condensation shock.

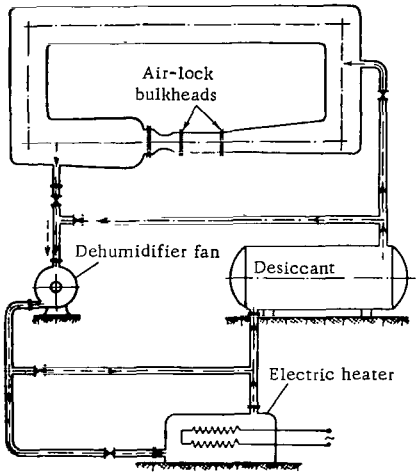

FIGURE 2.78. Wind-tunnel dehumidifier. The dash-and-dot lines and arrows show the circuit used for drying the tunnel air, and the broken lines, the circuit for desiccant regeneration.

In continuous-operation supersonic closed-circuit tunnels, condensation is prevented by slightly increasing the temperature of the air, from which much of the moisture has been removed by absorption. The inlet air is forced by the dehumidifier fan to pass at low velocity* over layers of a desiccant, usually silica gel or alumina (Al_2O_3). The desiccant is afterwards regenerated by passing hot air through the dehumidifier (Figure 2.78). This method of drying is necessarily slow, and to avoid reprocessing all the air in the tunnel after each adjustment or instrument calibration in the test section, the latter is often isolated by means of bulkheads.

The compressed air used in intermittent-operation high-pressure tunnels, supplied from reservoirs, is dried both by absorption and by refrigeration condensation of the moisture. Heat exchangers (usually the refrigerant is ammonia) are installed between the air compressors and the reservoirs to cool the air to between −20° and − 25°C, sufficient to remove the moisture. This is more effective than drying with desiccants. The multistage compressors usually employed for filling the reservoir should have inter- and aftercoolers fitted with water-separating columns and draincocks so that much of the moisture is removed during compression of the air.

* The air velocity in the dryer must not exceed 0.5 to 1.5 m/sec.

Drying the air in vacuum-powered intermittent-operation is very difficult, since the entire air drawn in through the tunnel in each test must first pass through absorption-type dryers. This is one reason why such tunnels have comparatively small test sections which require only small mass flow rates and hence, small dryers. A tunnel of this type with a test section measuring 1.8 m × 1.8 m would require a dryer having a surface area of about 1700 m^2, the weight of desiccant (alumina gel) being 410,000 kg. With such a dryer the tunnel could be operated three times per hour for 20 sec. The dimensions and weight of the dryer can be reduced by collecting the used dried air in a special reservoir. However, the capacity of the latter would not be much less than the volume of the vacuum reservoir, amounting to about 200 m^3 per square meter of test-section flow area in a tunnel operating at $M = 1$ for 1 sec, (assuming the dry-air reservoir to be at atmospheric measure).

It is no less difficult to dry the air in tunnels for testing jet engines, where clean dry air must be supplied to the engine in very large quantities. The dryers needed are large and rather complicated in design. Thus, for instance, the drying installation of a continuous-operation tunnel for testing jet engines (see below) is 25 m high, and its desiccant charge of 1200 tons can absorb up to 1500 kg/min of moisture. The installation is equipped with heaters and fans for regeneration of the alumina gel.

Tunnel air-cooling systems

The air temperature in closed-circuit wind tunnels rises continuously because of the heat generated by the fan. The process cannot be allowed to continue indefinitely, because it increases the difficulties in aerodynamic measurement leading to thermal distortion of the model and interference with the normal operation of the motor and fan. This is especially important in hypersonic wind tunnels, where the compression ratios are large, and where the temperature in the last compressor stages may rise to between 350 and 370°C. At test-section velocities of 100 to 150 m/sec the rate of stagnation-temperature increase is about 1°C/min, so that forced cooling of the air is necessary to prevent differences of 30 or 40°C between the temperatures at the beginning and end of a test.

As the velocity increases, the higher powers required necessitate installation of the drive outside the tunnel. The air can be cooled in liquid-filled heat exchangers, or by the continuous withdrawal of a fraction of the hot air, and its replacement by cool air.* (Figures 2.79 and 2.12) Liquid-filled honeycomb or tubular coolers are most widely used, being installed across a whole section of the return duct. Water is most commonly employed as coolant, though less frequently a saline solution is used. In some tunnels the coolant circulates through the corner vanes or through cooling jackets lining the tunnel walls. The latter method is more complicated and less easy to operate. The total amount of heat to be extracted by the heat exchanger is calculated from the shaft power

* This method is also used to replace the air contaminated by the combustion products of engines being tested in special tunnels.

of the fan or compressor, but the heat content of the tunnel shell and heat transfer through the walls should be neglected, because the inside and outside of the tunnel are usually coated with several layers of oil-bound or nitro-cellulose paint, which has negligible heat conductivity. Thus, for instance, in a special test at a tunnel stagnation temperature of +60°C, and an ambient air temperature of +10°C, the external temperature of the tunnel shell was found to be +20°C. The temperature rise during an experiment should preferably not exceed 10 to 20°C.

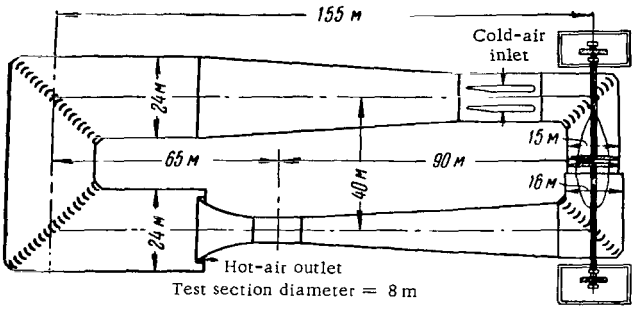

FIGURE 2.79. Air cooling system of the ONERA tunnel ($M = 0.95$, $N = 100{,}000$ h.p.).

Aerodynamically, the most suitable heat exchangers are honeycomb radiators of the aircraft type (in a number of tunnels these serve simultaneously as flow-straightening honeycombs) or tubular radiators. The installation of radiators involves additional pressure losses, which however, comprise only a negligible fraction (2% to 5%) of the total losses.

In modern tunnels the air-cooling system is a complicated installation, because a large flow rate of cooling water is needed; thus, for instance, in the above-mentioned ARA transonic tunnel (see page 54) which requires 25,000 kw to operate at $M = 1.6$ in its 2.74 m × 2.44 m test section, the radiator installation measures 9 m × 11 m and requires 27 m^3 of water per minute. The system maintains the air temperature below 50° C.

A modern supersonic tunnel for continuous operation necessarily incorporates the following components: adjustable inlet nozzle, supersonic diffuser, cooler, air-drying installation, heater*, and variable-speed electric motors driving (usually) multistage compressors.

Figure 2.80 shows a continuous-operation supersonic tunnel.

Drives for continuous-operation supersonic tunnels

The proper choice of drives for supersonic tunnels is based on the aerodynamic design calculations of the tunnel, which determine the losses in the tunnel circuit and the required ratio of the pressures before and after the compressor in order to obtain the desired range of Mach numbers in the test section.

* A heater is necessary when the Mach number exceeds about 4 or 5.

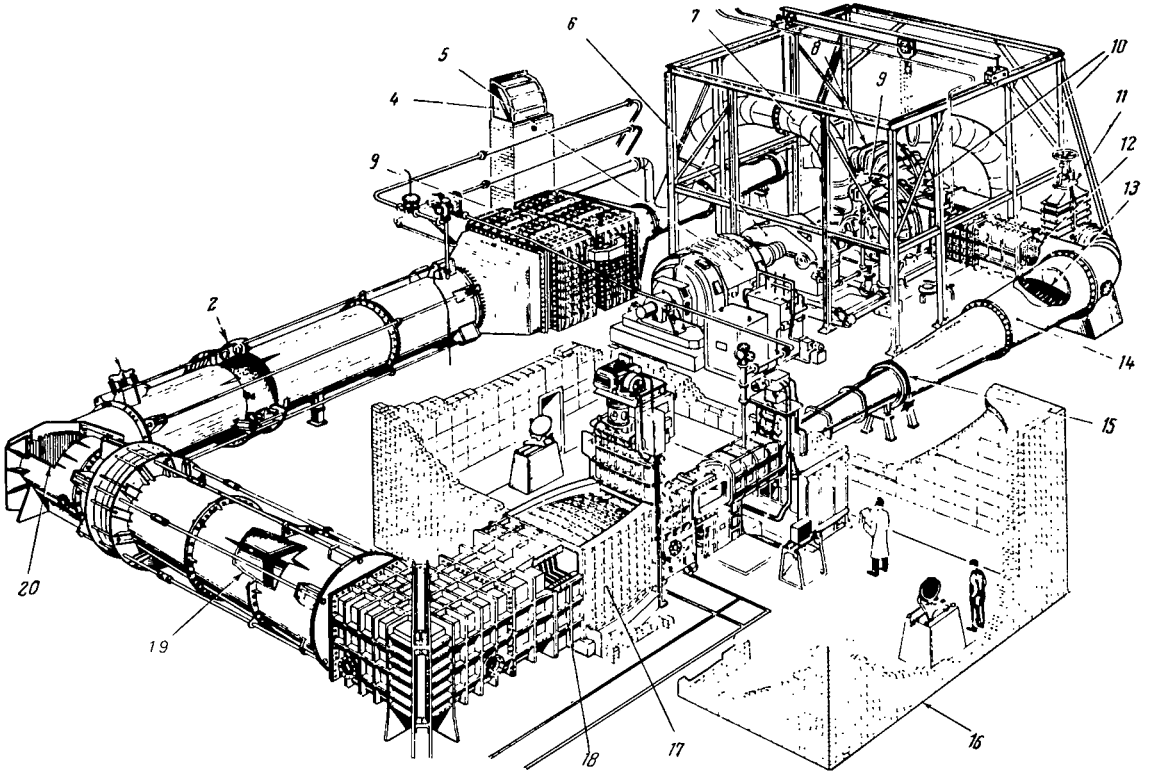

FIGURE 2.80. Variable-density supersonic wind tunnel of Armstrong-Whitworth Ltd. (U. K.). The tunnel has six interchangeable test sections (0.5 m×0.5 m); N = 10,000 h. p. M = 1 to 3. 1 — safety valve; 2 — expansion joint; 3—radiator; 4—air intake for motor-cooling system; 5 — 10,000 h. p. motor; 6 — reduction gear; 7 — movable bend; 8 — small compressor; 9 — large compressor; 10 — adjustable vanes; 11 — gate valve; 12 — screen; 13 — protection net; 14 — diffuser; 15 — expansion point; 16 — control cabin; 17 — nozzle; 18 — turbulence screens; 19—transfer section; 20 — corner.

Supersonic velocities in a closed-circuit tunnel with closed test section demand pressure ratios beyond the capabilities of normal fans, and multi-stage compressors are therefore used. The AEDC supersonic tunnel (U.S.A.) is equipped with four tandem axial-flow compressors, three having two stages, and the fourth having six stages, to a total power of 216,000 h. p.

Such an arrangement of the compressors provides for flexibility and effective operation of the compressor plant over a wide range of compression ratios and air flow rates, the latter changing with test-section Mach number from 37,000 m^3/min at **M** = 1.4 to 20,000 m^3/min at **M** = 3.5. This compressor is a rather complicated engineering structure with a rotor weighing 5000 tons. The rated shaft end-thrust is 1100 tons, while the temperature in the final compression stages is 350 to 370°C. The centrifugal force on the blades is 800 tons. Such a machine requires special starting and braking systems. This tunnel has two asynchronous 25,000 kv starting motors, which bring the compressor up to the synchronous speed of the two main 83,000 kw motors, and are then switched out. After the required output of 166,000 h.p., has been reached the starting motors may be switched in again to increase the total power of the tunnel to 216,000 h.p. Start-up of motors and tunnel requires about 10 minutes. Figure 2.81 shows the compressor of the NASA supersonic tunnel.

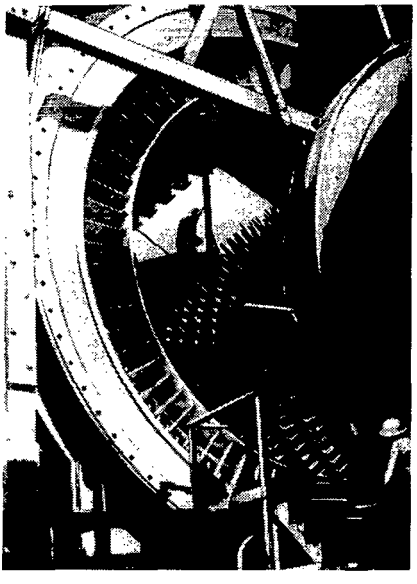

FIGURE 2.81. Multi-stage compressor of the supersonic tunnel of the NASA Ames Research Center, Moffett Field, California. Rotor diameter = 6.6 m; delivery = 90 tons/min; compression ratio = 3.5; n = 720 rpm; N = 216,000 h. p.

Intermittent-operation supersonic tunnels

Such tunnels may be operated by pressure, vacuum, or by a combination of the two. Pressure-powered tunnels have high inlet pressures and exhaust to atmosphere, whereas the inlet pressure of vacuum-powered tunnels is atmospheric and the exhaust is below atmospheric. In combination vacuum-pressure tunnels, the inlet pressure is above, and the outlet below, atmospheric. Intermittent-operation tunnels do not require coolers; they are very often equipped with ejectors fitted just downstream of the test section. High-speed instrumentation and control systems are essential, and this is particularly true of the rapid-action valve, normally operated from the pressure regulator in the settling chamber.

Pressure-powered tunnels. Preheating of the air supplied to pressure-powered tunnels working at Mach numbers up to 3.5 or 4 is unnecessary if the air is dried before storage in the reservoir. Reservoir pressure for tunnels operating at Mach numbers up to 4 does not usually exceed 8 to 10 atm.; in tunnels for higher velocities the reservoir pressure

may be as much as 100 or 200 atm, although the settling-chamber pressure is only 30 or 40 atm. Large wind tunnels are, as a rule, supplied with air through manifolds from batteries of standard industrial gas cylinders, which are recharged by powerful (up to 500 m^3/min) compressors. Compressors designed for metallurgical industries lend themselves well to this type of continuous duty; high-pressure compressors are needed, however, for the charging of high-pressure reservoirs. Figure 2.82 shows the flowsheet of a compressor plant for charging a cylinder storage unit. In both transonic and supersonic tunnels it is very important to maintain p_0 and T_0 constant at the tunnel inlet (settling chamber). Current types of pressure regulators, acting through special control valves, permit stabilization of settling-chamber pressure to an accuracy of about 10 mm Hg; this ensures adequate constancy of Reynolds number and minimum expenditure of air to establish the required conditions in the test section.

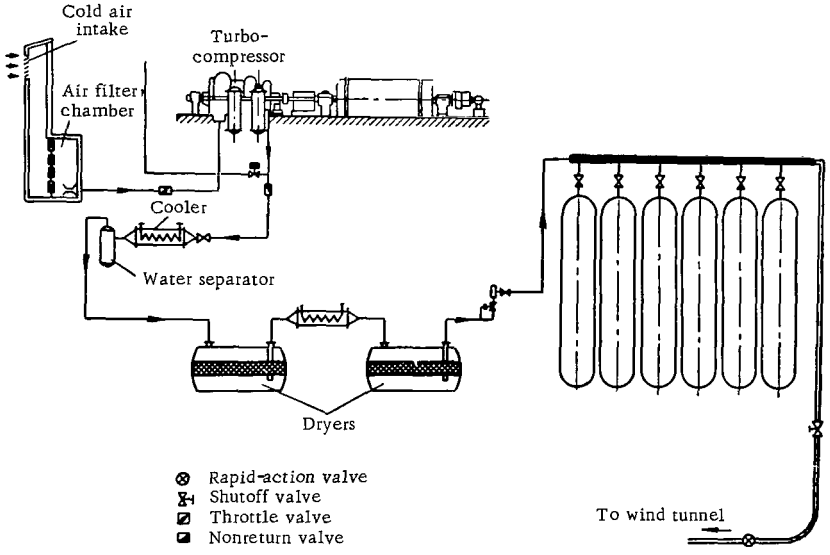

FIGURE 2.82. Flowsheet of air-compressor plant.

It is important to maintain the stagnation temperature of small-volume high-pressure reservoirs constant; as the air in the tanks is used up the pressure drop may be accompanied by a rapid lowering of the temperature to the point where the air becomes supercooled and even liquified. Heat storage has recently gained favor as a means to overcome this problem: metal tubes of high thermal capacity release their stored heat to the air and reduce its cooling rate to about 0.5°C/sec. This is not necessary when low-pressure high-volume reservoirs are used, since the temperature drop is then negligible. Thus, when cylinders of 5000 m^3 volume with pressures of 8 to 10 atm are used for a wind tunnel with a 0.3 m × 0.4 m test section, the settling-chamber temperature falls at the rate of only 0.1°C/sec, so that experiments lasting 100 to 150 seconds can be performed without additional air heating.

The operating duration of a pressure-powered tunnel depends on the dimensions of the test section, the flow velocity, and the reserve of air. Most tunnels of this type, used for model testing, can operate for periods ranging between 1/2 or 1 minute and 3 or 4 minutes.

Larger pressure drops, and often longer operating durations, can be achieved in pressure-powered tunnels by injecting air at the diffuser inlet, permitting a reduction in the rated settling-chamber pressure.

Supersonic vacuum-powered intermittent-operation tunnels. The principle of this type of tunnels is shown in Figure 2.59; nozzle, test section, and diffuser are similar to those in other types of supersonic wind tunnel, and a dryer is usually installed before the settling chamber.

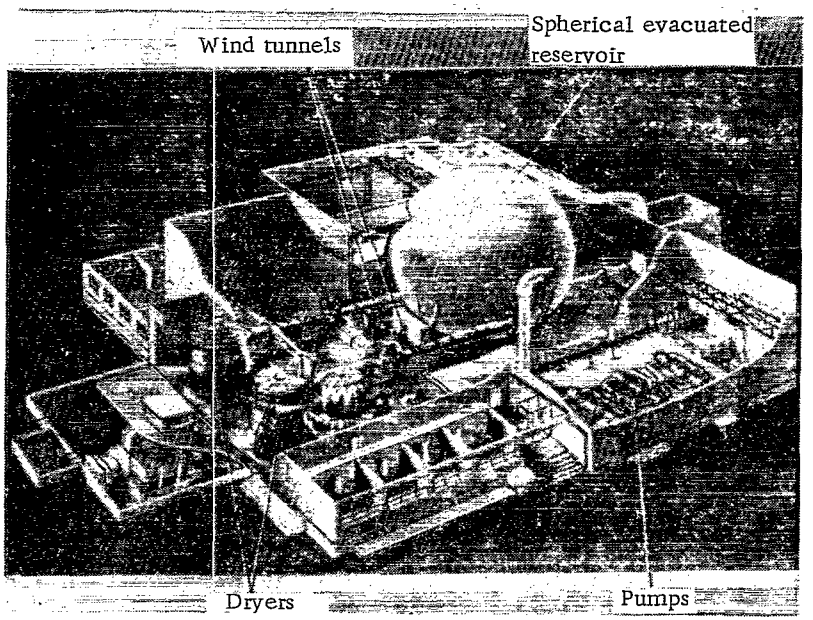

FIGURE 2.83. Vacuum powered supersonic wind tunnel.

The test section is limited in size by the complications introduced by the air dryer and by the very large capacity required of the evacuated reservoir. The Reynolds-number range is also restricted, in contrast to pressure-powered tunnels in which the Reynolds number of the experiment can be raised by increasing the pressure (density) in the settling chamber and test section. The pressure in the test section of vacuum-powered tunnels is necessarily low, and the Reynolds number can therefore only be increased by enlarging the test section. This is a distinct disadvantage.

Figure 2.83 shows the NOL (U.S.A.) vacuum-powered tunnel installation, in which three wind tunnels having test sections measuring up to 0.4 m × 0.4 m, are operated at Mach numbers up to 6.5 from a single spherical evacuated reservoir.

reservoir. The vacuum pumps are driven by motors of 300 h.p. total output.

The principle of a combination vacuum-pressure tunnel is illustrated in Figure 2.84. The flow through the 0.28 m × 0.25 m test section is created by compressed air from an 11 m^3, 50 atm reservoir. After traversing the test section and the supersonic diffuser the air is collected in a 340 m^3 reservoir at about 0.01 ata, so that pressure ratios of 5000 are possible. Using air as the working fluid, test-section velocities corresponding to $M = 7$ can be attained, but larger Mach numbers are possible by using gases having smaller velocities of sound; $M = 11$ is possible with xenon, and $M = 17$ with krypton. The air is heated to 425°C before reaching the test section in which its temperature decreases to − 180°C. Without supersonic diffuser the tunnel can be operated for up to 25 seconds; if a supersonic diffuser and a radiator are installed at the inlet of the evacuated reservoir, the operating duration increases to 1 or 1.5 minutes.

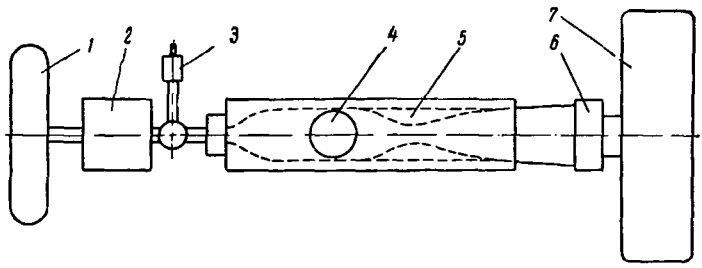

FIGURE 2.84. Principle of the combination vacuum-pressure, intermittent-operation supersonic tunnel. 1 — High-pressure storage tank; 2 — air heater; 3 — rapid-action valve; 4 — test section; 5 — adjustable supersonic diffuser; 6 — cooler; 7 — evacuated reservoir.

To obtain Mach numbers above 15 or 20 both high temperatures and large pressure drops are required. The technical difficulties of solving these problems, using air as the working fluid, are so great that the operation of conventional wind tunnels is currently limited to $M = 10$ or 12.

Selection of type of supersonic tunnel

If no limitations are imposed on the maximum instantaneous power available for operating the wind tunnel, continuous operation is the best solution, despite its much higher capital cost in comparison with intermittent operation. The total power required for a continuous-operation supersonic tunnel (including the dryers, coolers, etc.) at $M = 3.5$ is no less than 12,000 to 15,000 h.p. per square meter of test-section flow area.

Continuous-operation tunnels having test-section flow areas less than 0.5 to 0.6 m^2 are of limited usefulness because of the difficulties in accurate scaling and the reduced Reynolds numbers of the tests. If no more than 5000 or 10,000 kw is available a pressure-powered intermittent-operation tunnel, using compressed air at 6 to 10 atm, is preferable. A single

4000 kw compressor charging a 4000 to 5000 m^3 battery of cylinders can provide one start-up every 2 or 3 hours for a tunnel having a 0.4 to 0.5 m^2 test-section and operating at $M = 4$.

Although intermittent-operation tunnels require far less installed power (Figure 2.85) than continuous-operation tunnels /20/, their capital cost has tended to increase as larger test sections have become necessary to meet the requirements of even larger models and even lower Reynolds numbers, adding to the complexity and size of the installation. It is becoming standard practice, however, to compensate for the increased size of the test section by reducing the operating duration in such tunnels to 30 or 40 seconds or less, and to use high-speed automatic test equipment to measure forces and pressures over a considerable range of model attitudes during the brief test period available. The cost advantage of intermittent-operation tunnels is thus maintained, and even a rapid change in model attitude does not affect the measurements, since the translational velocity of a point on the periphery of the model is still only about 1 part in 10,000 of the free-stream velocity. Using strain-gage transducers and high-speed self-balancing potentiometer recorders, forces and pressures can be measured within fractions of a second.

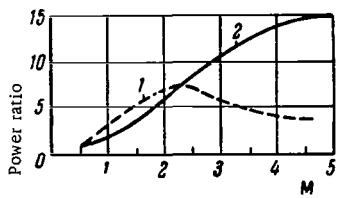

FIGURE 2.85. Power requirements of continuous- and intermittent-operation tunnels at equal Reynolds numbers. 1—ratio of installed powers of continuous-operation and vacuum-powered tunnels; 2— ratio of installed powers of continuous-operation and pressure-powered tunnels.

If the available power is less than 1000 or 1500 kw it is better to build an intermittent-operation pressure-powered tunnel with high-pressure reservoirs. A tunnel with a 0.4 to 0.5 m^2 test section for $M = 4$ requires three or four 250 kw high-pressure compressors discharging into a 200 to 250 m^3 battery of 200 atm gas cylinders.

If the available power is only 100 kw or less, a vacuum-powered tunnel is more suitable, the only difficulties being the construction of the spherical vacuum tank and of the dryer.

Notable cost advantages over a continuous-operation tunnel are possible when a group of intermittent-operation tunnels can be served by a central compressor plant, especially since it is fairly easy to modernize existing tunnels if their compressor plants need not be enlarged.

Low-density wind tunnels

Wind tunnels for large flow velocities and low gas densities are increasingly being used for investigations of high-speed rarified-gas flow. Problems of the forces acting on high-speed rockets at large altitudes, and of the heat exchange between them and the surrounding medium, are particularly important. Low-density wind tunnels have specific features, and involve test methods which take account of the flow properties of rarified gases at pressures of the order of a few mm Hg (absolute) or less. Consequent upon a reduction in pressure or increase

in altitude, the number of molecules per unit volume of a gas decreases and the distance mean free path — the average distance travelled by an individual molecule before colliding with another — increases. For instance, at a height of 120 km, the mean free path is about 0.3 m; for bodies whose

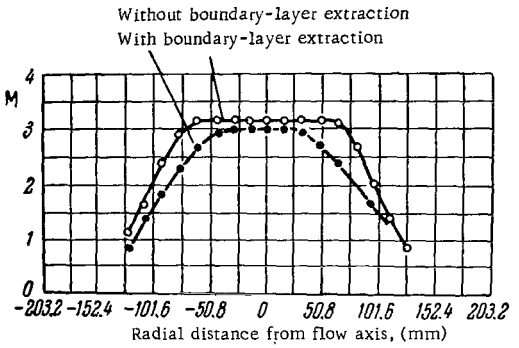

FIGURE 2.86. Nozzle-exit velocity distribution of a low-density high-speed tunnel.

dimensions are comparable to this, the atmosphere cannot be considered as a continuous medium.

Rarified gases can be investigated under natural conditions in the upper layers of the atmosphere and in special installations, such as "altitude" chambers, into which a model is projected. However, supersonic wind tunnels adapted for low-pressure operation provide much better experimental conditions /21/.

There are two main difficulties in designing low-density tunnels, namely, achieving the required low pressure and a sufficiently uniform velocity distribution in the test section of the tunnel. An oil-diffusion pump and a backing pump are necessary to obtain the required high vacuum (10^{-3} to 10^{-6} mm Hg). Although the boundary layer can be extracted to obviate a nonuniform velocity distribution in the test section, it is not good practice to attempt to evacuate the tunnel through porous walls; it is far better to use a tunnel whose large dimensions make allowance for the thickening of the boundary layer, the required range of uniform velocities being obtained in the central flow core.

Figure 2.86 shows the nozzle-exit velocity distributions in an axisymmetrical wind tunnel (Hyams Laboratory, (NASA) U.S.A.) operated at a static pressure of 115 m Hg with and without boundary-layer extraction. The nozzle-exit diameter of this tunnel is 50.8 mm [2 inches].

Figure 2.87 shows this tunnel schematically. The gas is supplied to the receiver of the tunnel from cylinders via a throttle valve. From the receiver the gas flows into a nozzle to which the (Eiffel-type) test section is connected. Beyond this is a plenum tank, continuously evacuated by four oil-diffusion pumps connected in parallel and discharging to backing pumps exhausting to atmosphere. The gas inlet rate into the system can

be adjusted to obtain the required pressure and Mach number; Mach numbers up to 2.75 can be obtained by using interchangeable nozzles. The total pressure in the receiver and the static pressure in the test section are measured by McLeod gages.

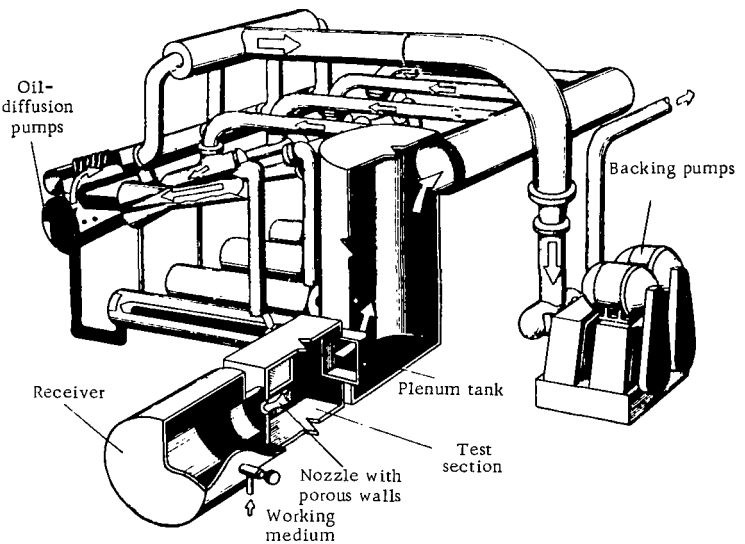

FIGURE 2.87. Supersonic low-density tunnel.

Boundary-layer growth at low pressures causes a considerable reduction in Mach number in comparison with the Mach numbers obtained for given pressure ratios at higher pressures. It is therefore necessary to control in each test both the pressure ratio and the magnitudes of the pressures themselves. The higher the static pressure in helium-and nitrogen-filled wind tunnels, the closer the Mach number approaches its calculated valve. The distribution of static and total pressures across a test section is shown in Figure 2.88. Low-density tunnels are equipped with special microbalances for determining drag.

Low-density wind tunnels demand special care in the choice of the equipment for measuring the gas parameters and for visualizing the flow. McLeod, Pirani, and other types of vacuum gages are used for measuring the pressure. The flow pattern at pressures below a few mm Hg cannot be studied with standard optical techniques, using Töpler instruments or interferometers. Instead, the flow pattern is visualized and the positions of shocks established by using either the afterglow of nitrogen which has been ionized by passage through a grid connected to an a.c. supply, or with the aid of a monochromator. The latter is used in conjunction with a source of ultraviolet radiation (for instance a Xenon pulse lamp) and special photographic plates*.

* The absorption of ultraviolet radiation by oxygen is a function of the density of the oxygen. The intensity of radiation transmitted through a region of low density will be higher than that of radiation transmitted through a region of high density, and the flow pattern can be judged from the shadows thus formed.

The design, construction, and operation of low-density wind tunnels demand special techniques, and many unusual features are involved in both their construction and their instrumentation. The high-vacuum technology

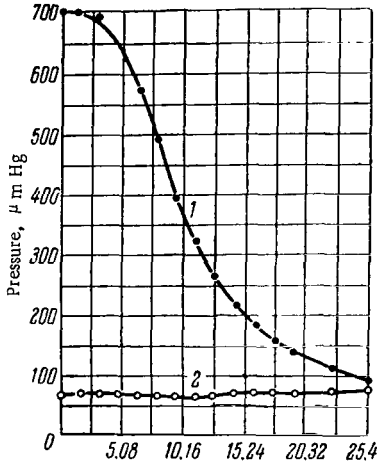

FIGURE 2.88. Variation in total and static pressure across a nitrogen-filled test section. 1 — total pressure; 2 — static pressure.

and exact physical measurements are very demanding, so that such tunnels are comparatively few in number, and experimental techniques are still in process of development.

§ 7. HYPERSONIC WIND TUNNELS

In the supersonic wind tunnels described in the preceding sections, velocities up to M = 4 or 4.5 could be obtained. This range of velocities is sufficient for tests of supersonic aircraft and ballistic missiles. However, the rapid expansion of rocket technology in recent years has made it necessary to study phenomena of flight through the earth's atmosphere at velocities greater than 10 km/sec, i.e., 20 or more times the velocity of sound. Entirely new physical phenomena arise when vehicles move at such hypersonic velocities through a gas, caused by the rise in temperature of the gas layer close to the surface of the vehicle. For instance, at a flight velocity of 6 km/sec in the stratosphere the compression of the gas in the shock preceding the nose of the vehicle, and friction in the boundary layer, cause a temperature rise of the order of 10,000°K. At temperatures above 1500 to 2000°K, the dissociation of the gases composing the air and the excitation of molecular vibrations increasingly change the physical and chemical characteristics of the air.

After the onset of gas dissociation the air can no longer be considered as a perfect gas, for which the equation of state $pv = RT$ holds true and the ratio $\varkappa$ of the specific heats is constant. Typical changes in the properties of air are shown in Figure 2.89, where the ratio pv/RT (which can be considered as the degree of dissociation) is shown as a function of velocity for the conditions behind normal and oblique shocks at sea level and at 75 km altitude. The value of $\varkappa$ at a velocity of 7 km/sec and at altitudes of 30 to 60 km decreases /22/ from 1.4 to 1.13.

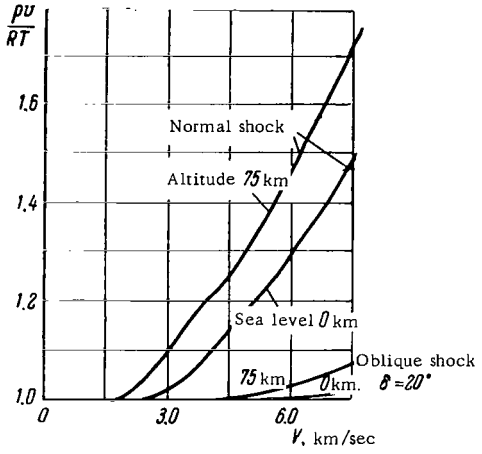

FIGURE 2.89. Change of air properties behind normal and oblique shocks at an altitude of 75 km and at sea level.

Ionization of the components of the atmosphere becomes increasingly pronounced at temperatures above 2000 to 3000°K, corresponding to flight velocities above 6 km/sec, and large numbers of positively and negatively charged particles appear. New gas species, such as NO, are also formed by chemical reactions.

The presence of ionized particles makes the gas conductive, so that at speeds close to the gravitational escape velocity, electromagnetic forces might become considerable at least in the boundary layer. The interaction of the flow of the conducting medium with a magnetic field, which is the subject of a new branch of hydrodynamics — magnetohydrodynamics — affects the forces acting during flight, and influences the heat transfer in the boundary layer. The degree of dissociation and, therefore, the temperature of air at velocities above 2.5 to 3 km/sec, depends on the pressure: the lower the pressure, the higher the degree of dissociation, and the higher the divergence from perfect-gas conditions. Figure 2.90 shows the stagnation temperature as a function of flight velocity of a body, calculated for different conditions of compression /26/. For isentropic compression at constant ratio of specific heats, the variation of temperature with velocity is shown in curve 1, which is plotted from the equation

$$T_0 = T + \frac{V^2}{2gJc_p}.$$

At velocities greater than 1500 m/sec the curve for isentropic compression of the real gas diverges considerably from the curve for $\varkappa = 1.4$ (curve 2).

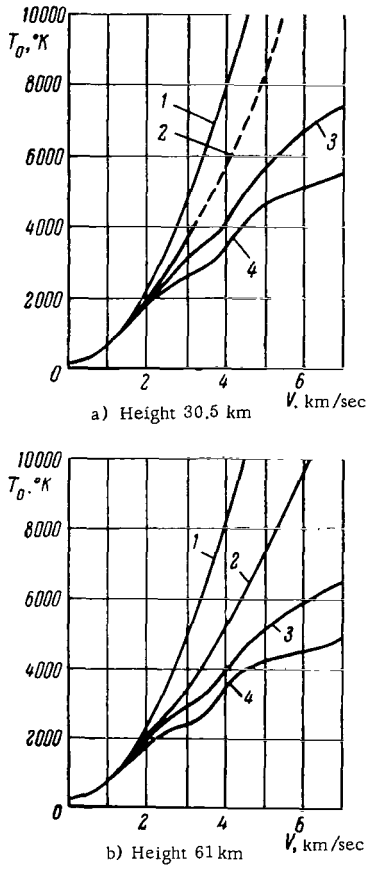

FIGURE 2.90. Variation of stagnation temperature with conditions of compression at altitudes of 30.5 km and 61 km. 1 — isentropic compression of air $\varkappa = 1.4$; 2 — isentropic compression of real gas; 3 — temperature at stagnation point of a blunt-nose body; 4 — temperature on the surface of a plate.

Curve 3 illustrates the temperature increase across the nose shock in front of a thermally insulated body from which there is no radiation. Compression in the nose shock is followed by isentropic compression at the stagnation point of the body. Because of the shock, the total pressure is less than with isentropic compression, while the degree of dissociation is higher and the temperature is lower at a given heat content of the gas. Curve 4 shows the temperature on the surface of a flat plate having a perfectly sharp leading edge when there is no heat exchange and the coefficient of temperature recovery is unity. In this case the pressure at the surface of the plate equals the surrounding pressure and the temperature is much lower [than with isentropic compression]. We see that when dissociation occurs the stagnation temperature depends strongly on the pressure, and thus on the altitude. The first inflexion point of curve 4, corresponding to a velocity of about 3 km/sec, is the result of the dissociation of oxygen, which is completed before the next inflexion point (4.5 to 6 km/sec), which is caused by the dissociation of nitrogen.

These considerations are important in the design of wind tunnels. To provide the necessary conditions in the test section the gas must expand isentropically from rest in the settling chamber to full flow in the test section. Thus, for instance, if the density and temperature in the test section are to correspond to flight at 4.5 km/sec at altitudes of 30 and 60 km, the stagnation temperature should be about 7500 and 6500°K, and the total pressures 10^4 and 10^3 atm respectively.

The changes in the properties of the gas make it difficult to simulate the flow around bodies at hypersonic velocities. In aerodynamics of steady flow at velocities above $\mathbf{M} = 7$ or 8, similarity is achieved by reproducing the Reynolds and Mach numbers, corresponding to natural conditions (similiarity for $\varkappa$ is maintained automatically if the tests are made in air). In hypersonic tests new similarity criteria have to be introduced because the ratio of specific heats and other properties of the air change at high temperatures.

In addition to measuring forces and pressure distributions, it becomes necessary to study the heat exchange between the medium and the body, so that the relevant process in the model must be exactly similar to the natural phenomena. Special installations and experimental techniques are used for the investigation of heat exchange in the boundary layer. In many cases reliable results can be achieved by testing at the natural values of stagnation temperature and total pressure, while carefully maintaining the thermodynamic equilibrium.

However, it is in practice impossible to achieve full similarity of all the conditions in the laboratory, so that in the installations described below full similarity conditions are observed only for the phenomena most strongly affecting the parameters of immediate interest, the influence of each separate parameter being studied in turn. Thus, heat transfer depends strongly on the flow regime in the boundary layer, whose transition from laminar to turbulent flow depends on the Reynolds number; hence, in heat-transfer studies at hypersonic velocities a wide range of Reynolds numbers must be obtainable. This is possible in wind tunnels, where hypersonic velocities are achieved by isentropic expansion of the gas in a Laval nozzle, at comparatively small Mach-numbers changes by adjustment of the nozzle divergence (or the area of the tunnel). Thus, for a test-section velocity of 4.5 km/sec (corresponding to $M \approx 15$ at an altitude of 60 km) a 32-fold increase of the divergence angle of the nozzle will increase the 60 km-altitude Reynolds number by a factor of 10; the Mach number will be reduced only to about 1/2 of its previous value, while the change in flow velocity is only 4% because the total-heat content of the air is very large in comparison with its static-heat content.

New types of wind tunnels have been developed during the past ten years for high-temperature hypersonic tests. These include:

1) hypersonic wind tunnels with air heaters;
2) installations with adiabatic compression;
3) shock tubes of various types;
4) electric plasma wind tunnels;
5) installations for free flight of the model (ballistic ranges).

Of these devices only the installations of the first type are capable of providing steady flow lasting seconds or minutes. All the others enable high-temperature high-speed flow to be obtained only for periods of micro- or milliseconds.

Wind tunnels with air heaters

It is impossible to obtain Mach numbers greater than 4 or 4.5 in standard supersonic wind tunnels at normal stagnation temperatures since cooling of the air during expansion causes liquefaction at the nozzle outlet. The Mach number can only be further increased by using a gas, such as helium, which has a lower boiling point than air, or by heating the air before it reaches the nozzle outlet. The minimum stagnation temperatures to prevent condensation of air are shown in Figure 2.91.

Mach numbers of 20 or 30 can be obtained in helium-filled wind tunnels without external gas heating. Whereas similarity as regards Mach and Reynolds numbers can be achieved in helium-filled tunnels, the fact that helium is a monatomic gas precludes its use in the study of phenomena associated with the properties of air at high temperatures. A further drawback of helium-filled tunnels is the need for perfectly pure helium, since the large amount of latent heat, released during condensation of impurities, considerably impairs the flow uniformity.

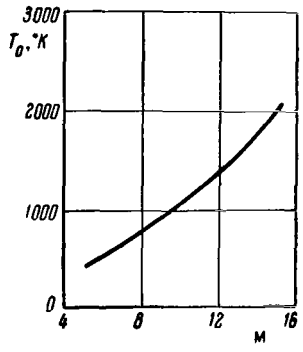

FIGURE 2.91. Stagnation temperature required to prevent condensation of air in a wind tunnel.

Mach numbers greater than 4.5 can be obtained in intermittent-operation pressure-powered tunnels fitted with heaters upstream of the settling chamber. By these means, Mach numbers up to $M = 10$ can be obtained. It is difficult to obtain Mach numbers above 5 or 5.5 in continuous-operation tunnels, since the high stagnation temperatures greatly impair the operating conditions and reduce the mechanical strength of the components, especially of the compressor. An example of such a tunnel is the hypersonic tunnel of the RAE. It has a 1.2 m × 1.2 m test section operated at velocities up to $M = 5$ and stagnation temperatures up to 130°C, using 88,000 h.p. compressors.

The total pressure in the test section of pressure-powered wind tunnels must be kept very high (up to 350 atm) lest the Reynolds number become too low. The air can be heated by:

1) combustion of fuel
2) use of storage heaters
3) use of continuously operating electric heaters
4) use of electric plasma heaters.

Fuel combustion can be easily arranged by installing a jet engine at the settling-chamber inlet of a continuous-operation tunnel to provide simultaneously heat and mechanical energy. The drawback of this arrangement is that the jet-engine combustion products have physical properties quite different from those of air.

TABLE 1

	ThO_2	$ZrO_2 + 5\%$ CaO	MgO	Al_2O_3
Melting point, °K	3240	2550	2880	2200
Maximum permissible temperature in still air, °K	2700	2500	2400	1400
Density, g/cm^3	9.7	5.4	3.65	4.0
Specific heat at 1300. K, Kcal/kg·°K)	0.04	0.09	0.17	0.16

Thermal-storage units in hot-air tunnels are made from special refractory materials heated by combustion of a fuel or by means of electric resistance heaters. Hydrocarbon fuels can be used to provide temperatures up to 2400°K, or, if burned in pure oxygen, up to 3000°K.

When the refractory has reached its maximum permissible temperature (the values of which for various refractory materials are shown in Table 1) air is led from cylinders through the thermal-storage unit into the settling chamber, whence it flows through the nozzle and test section of the tunnel in the usual way. The temperature T_0, attained by the air after it has absorbed heat from the thermal-storage unit, depends on the temperature, dimensions, and heat-transfer coefficient of the unit.

A section through the thermal-storage air heater, used in a wind tunnel at the Brooklyn Polytechnic Institute (U.S.A.), is shown in Figure 2.92. The air passes through a 600 mm - diameter tube made of refractory material and charged to a depth of 1.8 m with 9.5 mm-diameter zirconia balls. The tube is surrounded by a pressure chamber which is preheated by passing an electric current through heating rods containing silicon carbide. This storage heater will heat 4.4 kg/sec of air at 40 atm, to 1600°K.

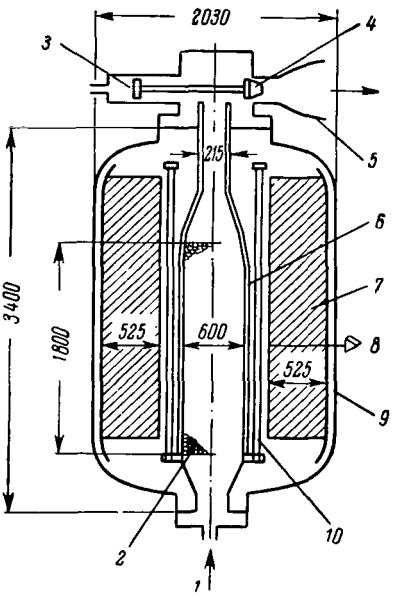

FIGURE 2.92. Thermal-storage air heater. 1 — air inlet; 2 — refractory balls; 3 — operating mechanism; 4 — valve to start wind tunnel; 5 — nozzle; 6 — ceramic tube; 7 — thermal insulation; 8 — thermocouple; 9 — high-pressure chamber; 10 — heating elements.

It is more common to heat the air entering the settling chamber by passing it over electric resistance heaters switched in throughout the operating period of the tunnel. Metallic or graphite resistors are installed for this purpose in a tube upstream of the settling chamber, so that the air must pass over their heated surfaces. Much trouble has been experienced with metal failure and insulator breakdown at these high operating temperatures and pressures, and low-voltage systems are now favored. Table 2 shows the characteristics of the air heaters used in several U.S. wind tunnels; it is seen that the performance of low-voltage systems is superior in terms of heat flow rate per unit surface area and volume of heating element. Graphite, whose melting point is above 4000°K at 100 atm, is the best material for the heating elements, but special coatings must be used to prevent rapid oxidation and crumbling of its surface. Figure 2.94 shows, as an example of a hypersonic heated wind tunnel, the AEDC tunnel in the U.S.A. It has a test section diameter of 1270 mm, in which velocities corresponding to $M = 7$ can be reached at stagnation temperatures of 600°K and total pressures of 30 atm.

The most vulnerable part of a high-temperature wind tunnel is the nozzle inlet, which undergoes large stresses at high temperatures. Heat transfer from the nozzle walls can be improved by making them thin and by cooling them externally with high-speed air or water; nevertheless, the throat tends to burn out very quickly, and is usually made of exchangeable inserts.

Table 2

Type of Heater	High voltage		Medium voltage	Low Voltage			
Supply voltage, (v.) . . .	2300	230	250	56	24 5	90	90
Material of heater element .	Nichrome	Cantal alloy	Cantal alloy	Graphite	Stainless steel	Stainless steel	Stainless steel
Max. power (kw)	4500	5000	600	2200	25.5	3000	3270
Heat exchange surface area (m^2)	32.2	38.0	3.25	1.70	0.033	1.64	6.0
Heat flow rate per unit surface area of heating element (kw/m^2)	140	132	185	1300	770	1830	545
Heat flow rate per unit volume of heat-exchange chamber (kw/m^3) . . .	1730	2360	1430	102000	-	39000	42700
Chamber volume, m^3 . . .	2.6	2.1	0.42	0.02	-	0.077	0.077
Air outlet temp. ^0K	1070	1530	1550	2480	1090	1090	1090
Heater Construction . . .	Two concentric circular cylinders	Circular pipes in groups of seven	1.1 mm-dia wire wound on silica rod formers	Shown in figure 2.93	Rectangular tubes, 12.7X X 25.4 mm	Rectangular slots 1.3X12.7 mm	Rectangular slots 1.9X25.4 mm

Many difficulties are experienced in the construction of thermal-storage units and electric heaters rated for operating temperatures in the region of 1000°K at powers of hundreds of megawatts. Figure 2.91 shows that

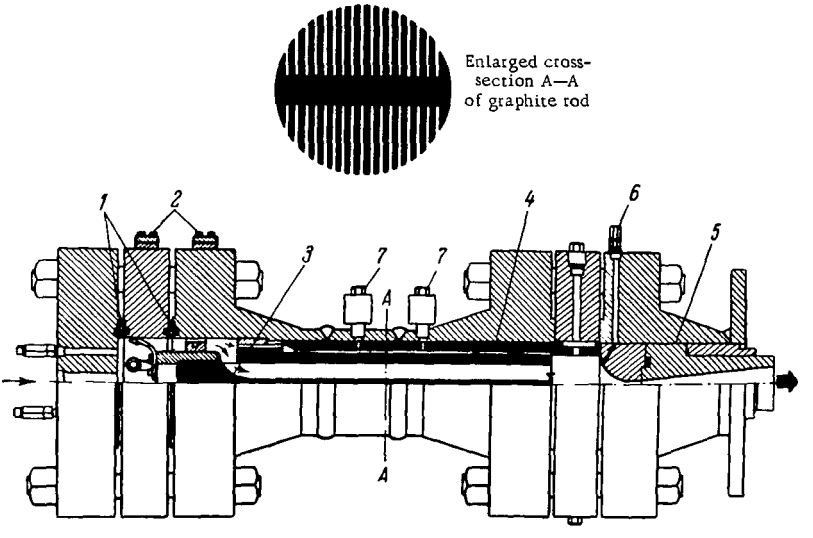

FIGURE 2.93. Electric heater with graphite resistor element. 1—insulators; 2 — busbars; 3 —graphite heating element; 4 — insulation; 5 — nozzle; 6 — thermocouples; 7 — radiation pyrometer fittings.

this temperature is only sufficient to prevent liquefaction of air at velocities up to $M = 10$; simulation of the far larger velocities of space craft reentering the earth's atmosphere requires much higher temperatures of the order of 4000 to 8000°K.

Modern engineering has solved these problems by the use in wind tunnels of electric-arc heaters (plasma generators), and by shock tubes.

The electric-arc (plasma) wind tunnel is the only type in which high-temperature hypersonic flow can be realised for extended periods. The plasma generator (Figure 2.95) consists of a cylindrical chamber along whose axis a cylindrical cathode either solid or hollow, and a tubular or conical anode forming a nozzle, are installed.

The working medium, generally air, is led into the chamber tangentially through openings in the walls. An arc forms between the electrodes when a high potential difference is applied across them, and this is stabilized by the turbulent flow of the gas, electrode erosion being abated by rotation of the arc about the electrodes. The discharge is maintained by thermal ionization in the discharge duct and by emission from the electrodes. The ionized gas in the discharge duct is called plasma. The gas stream cools the outside of the plasma jet, so that there is less ionization and reduced conductivity at its surface. The electric current becomes concentrated in the central hot region of the plasma, increasing its temperature and conductivity, and, at the same time its pressure. Under the influence of the electromagnetic force and of this pressure the plasma is ejected from the nozzle as a jet.

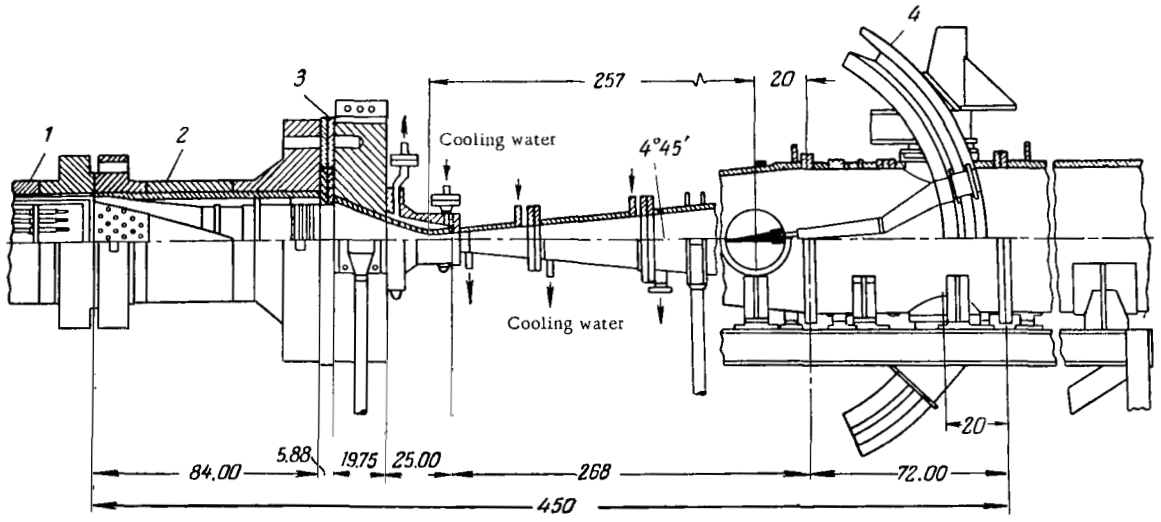

FIGURE 2.94. AEDC hypersonic wind tunnel with heater. 1 — electric heater; 2 — mixing section; 3 — annulus with pressure and temperature points; 4 — radial cradle for adjustment of angle of attack.

A more uniform flow is obtained if the jet is led initially into a settling chamber where flow fluctuations are damped out. The gas then passes into a second nozzle. (Figure 2. 96), in which it expands and is accelerated to a high speed.

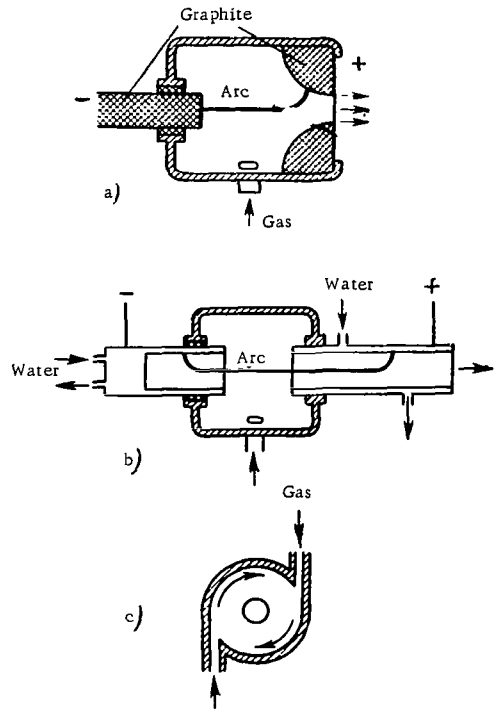

FIGURE 2.95. Principle of the electric-arc heater (plasmatron). a—with graphite electrodes; b—with metal electrodes.

The model under test is placed in the free jet or in the test section at the end of the nozzle. The shock in front of the model reionizes the gas, which had cooled during the expansion in the nozzle, transforming it again into a plasma and reheating it approximately to its former temperature.

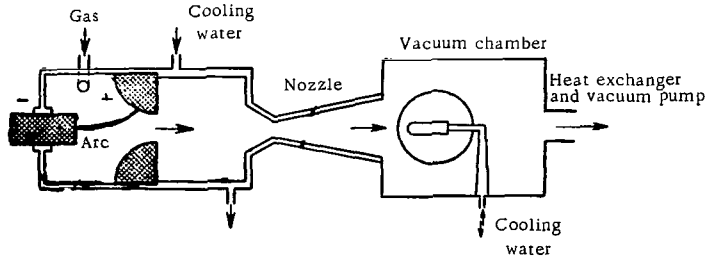

FIGURE 2.96. Wind tunnel with electric-arc heater.

The gas is sometimes accelerated in the test section by evacuating the latter, the gas being cooled in a heat exchanger before passing to the vacuum pump.

Temperatures of 6000 to 10,000°K can be obtained with plasma generators, the main operational difficulties being rapid nozzle erosion and burning away of the electrodes, which limits the period for which the installation can be continuously operated and contaminates the jet with combustion products. The contaminants themselves may abrade or corrode the model.

The electrodes are made of graphite, copper, steel, or tungsten. Graphite can withstand very high temperatures for brief periods. However, at very high powers, particles tend to become detached from the graphite mass, contaminating the plasma. The flow velocity can be increased by reducing the cross section of the nozzle throat; however, the smaller the throat, the more is it subject to erosion and to blockage by electrode fragments.

Contamination is less serious if metal electrodes are employed. Thus, a 12.7 mm graphite cathode rod and a hollow thin-walled water-cooled anode are used in the AVCO tunnel /23/. The walls of the second nozzle and the chamber are similarly water cooled. The AVCO tunnel has an installed power of 130 kw. The throat diameters of the first and second nozzles are 15.2 and 7.6 mm respectively. The chamber is spherical with a diameter of 76.2 mm. The diameter of the test section is 152.4 mm. The nose of the model is 6.5 mm upstream of the nozzle outlet.

Plasma tunnels are chiefly used for the study of heat-exchange problems of blunt axisymmetrical bodies, and for the investigation of surface fusion and mass removal from bodies in hypersonic flight. Studies of mass removal from bodies re-entering the earth's atmosphere can only be carried out in plasma tunnels because shock-tube tunnels can be operated only for brief periods.

Free-stream velocities up to 3600 m/sec can be attained in plasma tunnels with Laval nozzles; the maximum velocity is limited chiefly by erosion of the nozzle throat. Although the arc is comparatively small, its power may be many thousands of kw. The specific power in the nozzle throat may be of the order of tens of kilowatts per square millimeter, which is many times the specific power of the heat flow of a liquid-fuel jet engine.

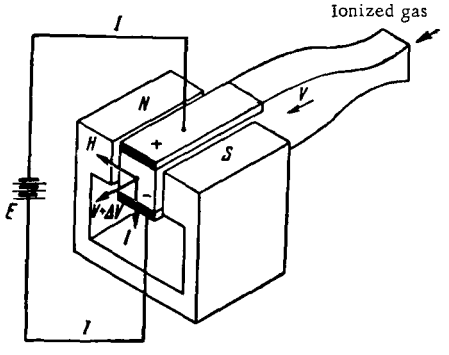

FIGURE 2.97. A magnetohydrodynamic plasma accelerator.

It is proposed to increase the flow velocity in plasma tunnels still further, up to between 5000 and 9000 m/sec, by accelerating the plasma, as shown in Figure 2.97, through the interaction of a current passing through it and an applied magnetic field.

A voltage E is applied between the two electrodes forming opposite walls of a rectangular duct, so that a current I flows through the plasma in the direction shown by an arrow in Figure 2.97. A magnetic field of strength H is applied in a direction perpendicular both to the direction of plasma flow and to that of the electric current, so that a force (Lorentz force), proportional to H and to I acts on the plasma, accelerating it along the tunnel axis from the initial velocity V to a velocity $V + \Delta V$.

The nozzle throat of a hypersonic tunnel is the most highly stressed part and is most difficult to make. At free-stream velocities corresponding to $M = 3$ to 5, the simplest structural solution is a plane-parallel nozzle. When M exceeds 10, however, even in a large wind tunnel, the throat height of a plane nozzle is only tenths or hundredths of a millimeter, being several thousand times smaller than the nozzle width. In such a narrow nozzle heat transfer from the gas to the walls is very high, and it becomes difficult to maintain the height uniform over the full nozzle width because of the high thermal stresses.

Axisymmetric nozzles are of the optimum shape from the viewpoint of heat transfer and dimensional stability, and can be efficiently water-cooled. The axisymmetric nozzles can be formed by turning, precision casting, or electroforming in dies previously machined to the required nozzle profile.

Shock tubes

The shock tube was the first apparatus in which research demanding simultaneously high temperatures and high flow velocities could be carried out. The simplest form of shock tube (Figure 2.98) is a long cylindrical tube closed at both ends and separated into two unequal parts (chambers) by a [frangible] diaphragm. The smaller left-hand chamber is filled with high-pressure gas "propellant", while the right hand chamber is filled with the working gas at low pressure. In the equations below initial states of the propellant and working gases are indicated by the subsripts 4 and 1 respectively. The diaphragm is ruptured, so that the propellant gas expands to state 3 (Figure 2.98b). A rarefaction wave is formed in the high-pressure chamber, and a compression shock moves into the low-pressure chamber at a propagation velocity u_s [in relation to the tube at rest].

As the shock moves through the tube, the working gas behind it is compressed, heated, and forced to flow in the direction of the shock wave. If the shock-propagation velocity in the tube is constant, a region of steady high-temperature flow forms behind the shock (stage 2). Under these conditions, the flow around models installed in the right-hand part of the tube, nonsteady aerodynamic processes, the kinetics of chemical reactions, etc. can be studied. The column of the working gas moving at a constant velocity V_2 is delimited by the so-called contact discontinuity, which separates the regions at states 2 and 3, and defines the propellant-gas front.

The propagation velocity u_s of the shock wave is higher than the particle velocity V_2 of the gas, which equals the velocity with which the contact discontinuity moves along the tube. The duration Δt of steady flow past point A of the tube where the test model is installed can be calculated approximately from the difference between these velocities; $\Delta t = l(1/V_2 - 1/u_s)$, where l is the distance from the diaphragm to point A (Figure 2.98c).

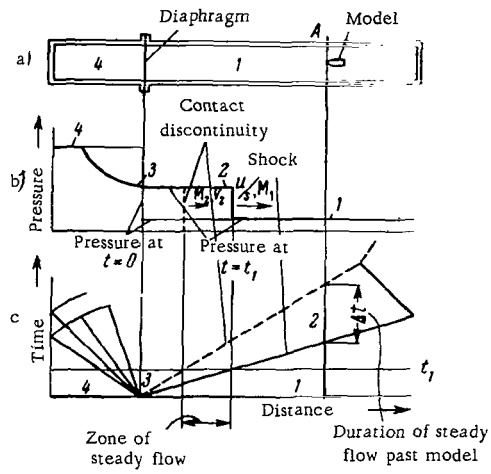

FIGURE 2.98. Principle of the shock tube.

Given the Mach number $M_1 = u_s/a_1$ of the shock it is possible to determine the parameters of the moving gas. Here, a is the velocity of sound in the undisturbed working gas in front of the shock M_1. Assuming the propellant and working fluids to be perfect gases with constant specific heats, and neglecting the influence of viscosity and turbulence on the contact discontinuity, M_1 is given by /24/:

$$\frac{p_4}{p_1} = \left[\frac{2\varkappa_1 M_1^2}{\varkappa_1+1} - \frac{\varkappa_1-1}{\varkappa_1+1}\right]\left[\frac{1}{1-\frac{\varkappa_4-1}{\varkappa_1+1}\frac{a_1}{a_4}\left(M_1-\frac{1}{M_1}\right)}\right]^{\frac{2\varkappa_4}{\varkappa_4-1}}. \qquad (2.1)$$

For an infinitely high ratio of propellant pressure to working-gas pressure we have

$$M_1 = \frac{\varkappa_1+1}{\varkappa_4-1}\frac{a_4}{a_1}. \qquad (2.2)$$

Knowing M_1 we can find the flow velocity and Mach number behind the shock:

$$\frac{V_2}{a_2} = M_2 = \frac{2}{\varkappa_1+1}\left(M_1 - \frac{1}{M_1}\right)\frac{a_1}{a_2} \qquad (2.3)$$

The pressure ratio across the shock is

$$\frac{p_2}{p_1} = \frac{2\varkappa_1 M_1^2 - (\varkappa_1 - 1)}{\varkappa_1 + 1} \approx \frac{2\varkappa_1 M_1^2}{\varkappa_1 + 1} = \frac{2\varkappa_1 (\varkappa_1 + 1) a_4^2}{(\varkappa_4 - 1)^2 a_1^2}. \qquad (2.4)$$

while the ratio of the temperature in the region of steady flow to the temperature of the propellant gas is:

$$\frac{T_2}{T_4} \approx \frac{\varkappa_4 (\varkappa_1 - 1)}{2\varkappa_1} \left(\frac{\varkappa_1 + 1}{\varkappa_4 - 1}\right)^2 \frac{\mu_1}{\mu_2}, \qquad (2.5)$$

where μ is the molecular weight of the gas. From (2.5) we can see, that at a given propellant-gas temperature, the temperature of the working gas can be increased by using a heavy working gas and a lighter propellant gas.

The force of the shock and the temperature of the moving gas can be raised further by increasing the ratio of the velocities of sound a_4/a_1 through heating the propellant gas. The most widely applied method is to use as propellant gas a combustible mixture of oxygen and hydrogen, to which helium is added to reduce the risk of detonation. After igniting the mixture electrically (for instance, by an ordinary automobile spark plug), the temperature in the chamber rises to 1500—2000°C. In some shock tubes maximum shock-propagation velocities of 18 km/sec have been observed after rupture of the diaphragm, with temperatures behind the shock of 16,000°K. Another method of increasing the shock-propagation velocity at a given pressure ratio is to use a shock tube with more than one diaphragm. The rupture of the first diaphragm causes propagation of a shock through an intermediate chamber filled with argon; after rupturing a second diaphragm the shock reaches the working gas. Shock-propagation velocity is increased in this case at the expense of a reduction in the duration of steady flow.

Since the shock-propagation velocity exceeds the velocity at which the contact discontinuity moves, the region of steady flow between the shock and the contact discontinuity increases with tube length. In fact, viscosity causes an increase in the velocity at which the contact discontinuity moves, often to a degree where any further increase in tube length increases the region of steady flow only slightly. Usually, the duration of steady flow is a few milliseconds. The parameters of the steady flow are determined from the shock-propagation velocity and the initial states of the propellant and working gases.

This type of shock tube cannot be used for complete simulation of atmospheric-re-entry conditions of rockets or space craft. The ratio of sound velocities in front and behind the shock is

$$\frac{a_1}{a_2} \approx \sqrt{\frac{(\varkappa_1 + 1)^2}{2(\varkappa_1 - 1)\varkappa_1}} \frac{1}{M_1}.$$

Substituting this value into (2.3), we obtain for high shock-propagation velocities

$$M_2 \approx \sqrt{\frac{2}{\varkappa_1 (\varkappa_1 - 1)}}.$$

For air the Mach number of the flow cannot thus exceed 1.89, so that shock tubes of this simple type are only used when it is not very important to reproduce M, but high temperatures corresponding to the actual conditions must be achieved (for instance, when studying heat exchange at the nose of a blunt body).

Shock wind tunnels

The velocity of steady flow in shock tubes may be increased by expanding the gas, moving behind the shock wave, in a nozzle. Distinct from cylindrical shock tubes, those with diverging nozzles (Figure 2.99) are called shock wind tunnels. The time interval required for the passage of the shock waves formed during the initial flow in the nozzle can be reduced, by installing a low-strength auxiliary diaphragm at the nozzle inlet. However, when a diverging nozzle is fitted the duration of steady uniform flow is less than in a cylindrical shock tube. Figure 2.100 shows the principle of a shock wind tunnel similar in design to the below-mentioned tunnel, in which adiabatic compression is employed. In addition to increasing the flow velocity up to $M = 20$ to 25, this system permits the period of tunnel operation to be

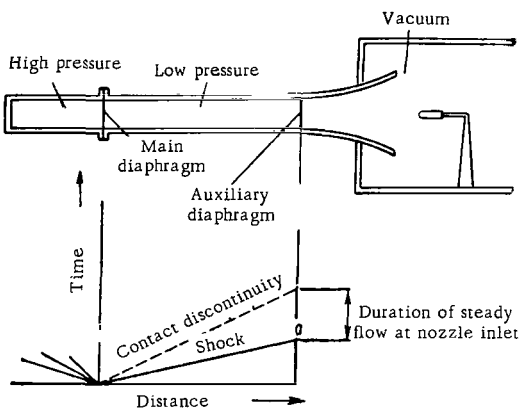

FIGURE 2.99. A simple shock wind tunnel.

increased. At the end of the chamber containing the working gas, which forms the inlet of a converging-diverging [Laval] nozzle, a second, low-strength diaphragm is installed. After bursting the first diaphragm, the shock reaches the nozzle inlet and is reflected from it, leaving between the nozzle inlet and the reflected shock a region of almost stationary hot gas which, after rupturing the second diaphragm, flows through the nozzle into the partially evacuated test section.

When the reflected shock reaches the contact discontinuity, it is reflected as a secondary shock moving towards the nozzle. The velocity,

at which the contact discontinuity moves, is sharply decreased so that the duration of steady flow, which ends at the instant when the contact discontinuity reaches the nozzle inlet, is increased considerably (Figure 2.100b). The perturbations caused by the secondary reflected shock must be attenuated in order to obtain uniform flow at the nozzle inlet.

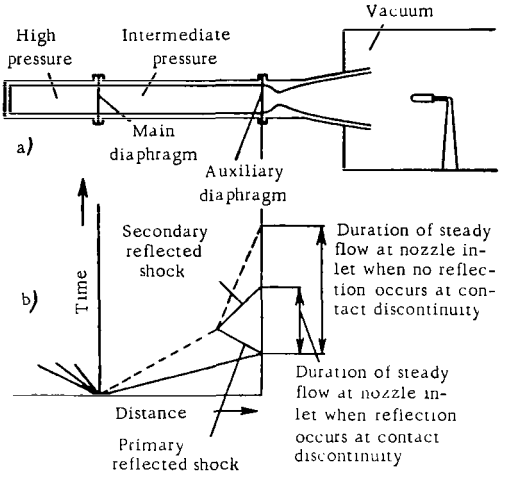

FIGURE 2.100. A shock wind tunnel using a reflected shock.

Formation of a secondary reflected shock can be prevented by a so-called "matched" contact discontinuity /25/. The initial state of the working and propellant gases is chosen so that the primary reflected shock passes through the contact discontinuity without interaction. The operating time of the tunnel can thus be increased 8 to 60 times.

In order to find the flow conditions behind the reflected shock, which determine the initial state at the nozzle inlet, the following parameters have to be measured: propellant-gas pressure at instant of diaphragm rupture; initial working-gas pressure; time variation of pressure behind shock; propagation velocities of incident and reflected shocks. Detailed data for shock tunnels are given in /36/.

Electromagnetic shock tunnels

A powerful recently-developed source of shocks whereby temperatures up to tens of thousands of degrees may be achieved, relies on the spark discharge of the electrical energy stored in a bank of large capacitors, some 30 to 50% of which can be released as Joule heat close to the electrodes. The electric current flowing through the instantaneously ionized gas induces a magnetic field, and this, together with thermal expansion, accelerates the gas, causing a strong shock to be propagated at a velocity

of tens, and even hundredths, of kilometers per second. This shock is employed in electromagnetic shock tunnels in exactly the same way as in pneumatic shock tunnels; but the transit time of the steady flow behind the shock wave is usually no more than 20 or 30 microseconds, while the Mach number is not more than 3 or 4 because of the high velocity of sound in a very hot gas.

The high levels of ionization of the very hot gases in such tunnels are suitable for experiments in magnetohydrodynamics. Figure 2.101 shows an installation of this type /27/. The tunnel is a glass tube of 76 mm inside diameter with the spark generator fitted at one end which forms a truncated cone; the test model is installed, with test probes, at the other flat end. The central spark-gap electrode is mounted at the narrowest part of the truncated cone, the other, annular electrode is placed at the intersection of the conical and cylindrical sections of the tube.

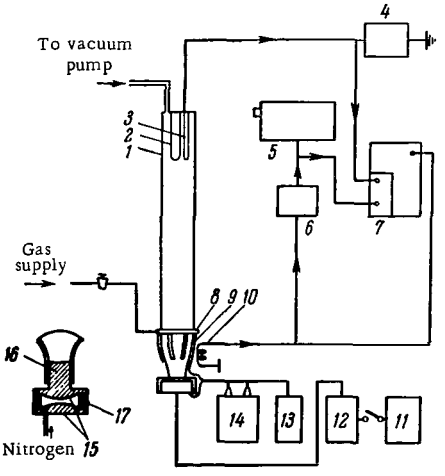

FIGURE 2.101. Diagram of an electromagnetic shock tunnel. 1 — glass tube; 2 — test model; 3 — ionization-sensing element. 4 — battery, 67.5 v; 5 — movie camera; 6 — variable delay; 7 — oscillograph; 8 — annular electrode 9 — conducting strips (6 #); 10 — oscillograph trigger pickup coil; 11 — battery, 300 v; 12 — auxiliary trigger supply unit (30 kv); 13 — 30 kv. supply unit; 14 — capacitor bank, 630 μF; 15 — trigger electrodes; 16 — central electrodes; 17 — insulator.

The discharge is initiated by means of an auxiliary spark gap, consisting of two convex copper electrodes. One of these is formed by the back of the central electrode; the other, mounted coaxially, is separated from it by a ceramic insulator, so as to form a chamber filled with nitrogen at 100 mm Hg to reduce erosion of the auxiliary electrodes.

The tunnel itself is evacuated to a pressure of 25 to 300 μm Hg before each test. The auxiliary gap, which is electrically in series with the main gap, shields the central electrode, preventing it

from discharging to the annular electrode until a 15 kv trigger pulse is applied to the auxiliary gap. As soon as this gap is ionized the main capacitor (formed a bank of 6 μF capacitors) discharges through the auxiliary gap and the main gap in series, the return path from the annular electrode of the main gap being provided by six copper strips equally spaced around the outside of the truncated cone.

High-speed movie cameras can be used for observing the shock; the cameras available in Soviet laboratories permit speeds of 2.5 million frames per second /33/.

Test models, and probes for measuring ionization intensity and air conductivity are placed in the test section of the tunnel. Figure 2.102 shows a model used for studying the interaction between an air stream and a magnetic field. A solenoid is placed inside a 20 mm-diameter cylinder having a blunt nose of 1 mm-thick Pyrex glass. A 40,000 gauss magnetic field can be instantaneously created in front of the model by discharging a 100μF, 1500 volt capacitor bank through the solenoid. The field is timed to synchronize with the passage of the shock, and photographs demonstrate how the shock moves further away from the nose as the magnetic-field intensity increases.

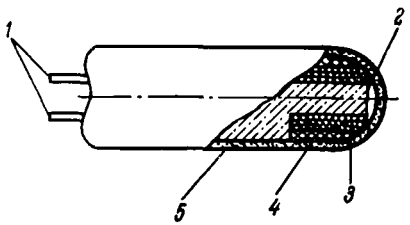

FIGURE 2.102. Model to test interaction between magnetic field and air stream. 1—current supply; 2—Plexiglas core; 3—solenoid; 4—glass-fiber reinforced plastic; 5—Pyrex glass.

Adiabatic shock tunnels

Tunnels in which high temperatures are obtained by adiabatic compression of the air before it enters the tunnel are known as adiabatic shock tunnels. Such a tunnel, shown in Figure 2.103, incorporates a long tube (generally a gun barrel) down which a freely-fitting lightweight piston travels at supersonic speed, impelled by the air pressure released by the rupture of a diaphragm sealing off a high-pressure chamber at one end. The shock formed ahead of the piston is repeatedly reflected from a diaphragm at the far end of the tube back onto the piston, until the piston is brought to rest. By this time the gas enclosed between the piston and the second diaphragm has (virtually adiabatically) attained a high temperature and pressure, so that rupture of the second diaphragm releases hot gas at very high velocity into the partially evacuated wind tunnel of which this second diaphragm forms the inlet. Stagnation

temperatures up to 3000°K can thus be obtained in steady flow persisting for 0.1 second.

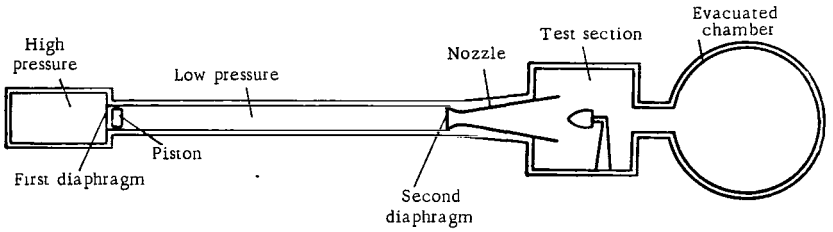

FIGURE 2.103. Principle of the adiabatic shock tunnel.

Spark-operated wind tunnels

Electric-arc heating is increasingly replacing shock-wave compression heating in hypersonic wind tunnels. Such a tunnel (Figure 2.104) has a Laval nozzle in which the gas attains a supersonic velocity, and a cylindrical test section upstream of a pumped vacuum-chamber. A high-pressure chamber, corresponding to the reservoir and settling chamber of a pressure-powered tunnel, is directly heated by an electric discharge.

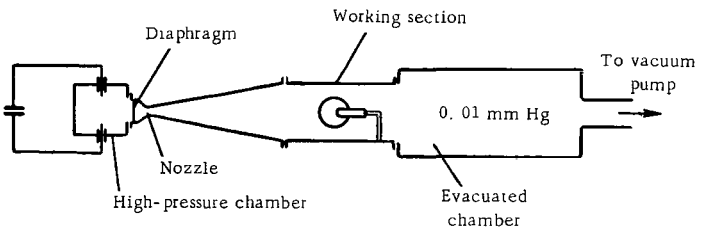

FIGURE 2.104. Spark-operated wind tunnel.

This chamber is initially filled with air or other gas at a pressure of 100 to 200 atm, the remainder of the tunnel being evacuated to a pressure of 0.01 mm Hg. Electrodes inside the chamber are connected to a large reservoir of electrical energy which can be liberated as a powerful pulse discharge when the tunnel is started. The discharge is brief (a few microseconds) and the current intensity is 10^6 amp, so that the temperature and pressure rise virtually instantaneously to burst a diaphragm separating the chamber from the Laval nozzle. After a short transition period, quasi-steady flow conditions are established in the test section.

To determine the flow parameters of the gas passing through the test section, it is necessary to know the volume of the pressure chamber and to measure the initial and variable temperatures and pressures in it.

The total- and static-pressure changes in the test section are also determined. From these data, and from the stagnation temperature and total pressure at the nozzle inlet, the velocity and state of the gas flowing through the test section can be calculated.

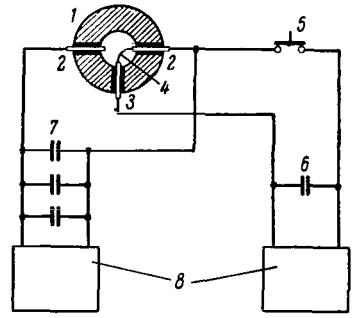

FIGURE 2.105. Capacitive storage unit for spark-operated wind tunnel. 1 — high-pressure chamber; 2 — main electrodes; 3 — auxiliary electrode; 4 — fusible link to trigger main discharge; 5 — contactor to apply trigger pulse; 6 — auxiliary capacitor bank; 7 — main capacitor bank; 8 — control panel.

Electrical energy to power spark-operated wind tunnels can be stored either capacitively or inductively. The capacitive storage system used in a wind tunnel at the Arnold Aerodynamic Center (U. S. A.) is shown in Figure 2.105. This tunnel has a test section of about 400 mm diameter for the simulation of flight conditions at 4.5 km/sec at 50 km altitude /22/.

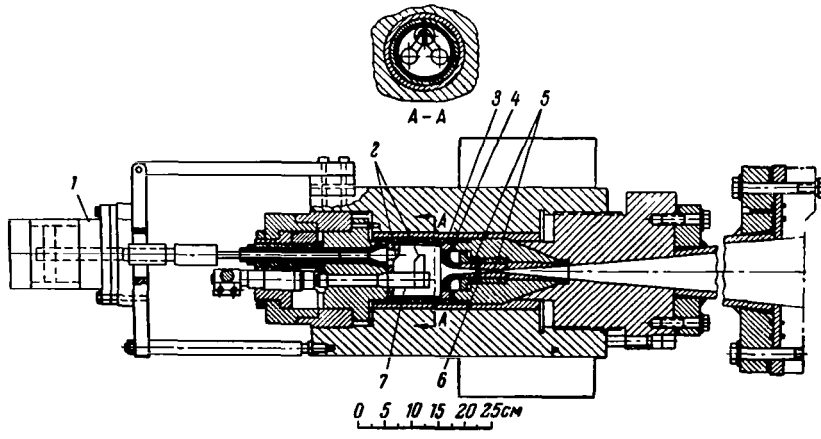

FIGURE 2.106. Discharge chamber of spark-operated wind tunnel. 1—pneumatic cylinder for advancing of electrode; 2—tungsten electrode; 3—Plexiglas screen; 4—graphite screen; 5—tungsten nozzle-throat liner; 6—diaphragm; 7—beryllium-bronze electrode.

The 10^6 joule discharge (10^5 kg · m) of a bank of one thousand 225 μF capacitors raised to 4000 volts is initiated by means of an auxiliary circuit, whereby a very much smaller capacitor is discharged through a [fusible] thin wire joining one of the principal electrodes to an auxiliary electrode.

The inductive storage system employs a very large coil fed from the rotor of a single-pole generator with a high-inertia flywheel mounted on its shaft, which is driven by an electric motor. The coil stores an energy amounting to tens of millions of joules, a substantial proportion of which is liberated in the arc formed when the coil is switched over from the generator to the spark gap in the chamber.

Figure 2.106 shows the design of a 700 cm^3 chamber intended for the AEDC wind tunnel with a 1270 mm-diameter test section. The chamber pressure during discharge is 3400 atm. The chamber is a cylindrical pressure vessel into which a cartridge, containing the electrodes, pressure and temperature transducers, a metal or plastic diaphragm, and a hard-metal interchangeable nozzle-throat liner, is inserted. The electrodes are supported externally by the tunnel, so that their insulators do not have to bear the full pressure load. Although the nozzle is made of tungsten, it burns out after a very few experiments, and the cartridge arrangement permits its rapid replacement.

Spark-operated wind tunnels have slightly longer operating periods than shock tunnels of comparable dimensions; steady conditions can be maintained for several tens of milliseconds. Spark-operated tunnels have the further advantage of reproducing natural conditions more closely, since the operating pressure, and therefore the Reynolds number, can be higher.

Ballistic ranges

A further method of studying hypersonic flows is to observe the motion of bodies in free flight. This can be done in the laboratory by using "ballistic ranges" consisting of long tubes into which the test model is launched from a special gun. Full-scale values of M and temperature can be obtained by projecting the model at the actual free-flight velocity; the required Reynolds number can be obtained by appropriately adjusting the pressure in the tunnel.

Special guns, with muzzle velocities up to 4.5 km/sec, are used in which light gas propellants are burned or heated by adiabatic compression or electrical discharge. The maximum velocity obtained when using gunpowder is about 2.4 km/sec. The most promising method is electrical discharge heating, using capacitive or inductive storage systems as in a spark-operated wind tunnel (Figure 2.107).

The gas is heated at constant volume by the spark discharge, so that its temperature and pressure rise sharply. At a given release of energy into the gas, the final pressure is independent of the gas density, the final temperature varying inversely with gas density. The gas density should therefore be as low as possible if the maximum velocity is to be obtained. The Arnold Research Center (U. S. A.) has a tunnel in which the high-pressure chamber is initially filled with hydrogen at 35 atm pressure,

and in which an electrical discharge causes the pressure to rise to 2600 atm, corresponding to a temperature of 14,000°K.

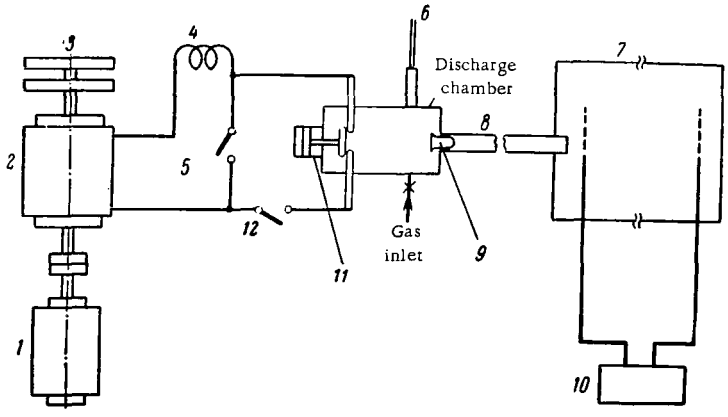

FIGURE 2.107. Gas gun with inductive electrical-energy storage system. 1 — motor; 2 — generator; 3 — flywheel; 4 — energy-storing solenoid; 5 — main contactor; 6 — pressure transducer; 7 — evacuated chamber; 8 — barrel; 9 — missile; 10 — electronic timer; 11 — electrodes, and pneumatic system for adjusting spark gap; 12 — auxiliary contactor.

It is theoretically possible to obtain velocities of the order of 10 to 12 km/sec with a spark-fired gas gun, but this involved great technical difficulties because of the heat losses and the erosion of the barrel at these high temperatures.

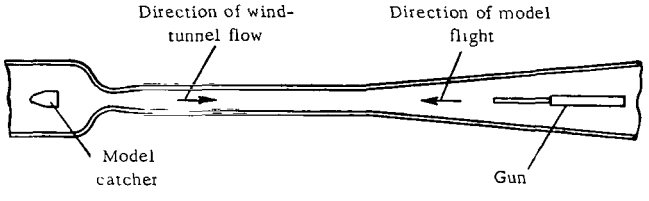

FIGURE 2.108. Ballistic range with air flow.

It is in practice easier to obtain very high relative velocities of model and medium by combining the wind tunnel and the ballistic range, projecting the model upstream from the diffuser of a wind tunnel. (Figure 2.108).

In ballistic tests the position and trajectory of the model are determined in space and time by observing the model at a number of points along its flight path. The aerodynamic characteristics of the model can then be calculated. Ballistic ranges are the only type of installation which permit the study of the steady process connected, for instance, with the stability of

flight at hypersonic velocities. To find the drag, it is necessary to measure the time of flight of the body between several points.

Figure 2.109 shows the CARDE ballistic installation /35/. It consists of a gas gun and a long vacuum chamber whose wall has windows for the schlieren photography of the model and for measuring its flight velocity with photomultipliers and oscillographs. Pulses from the photomultipliers are also used to trigger the schlieren arcs at the instant the model passes the window. The photographs thus obtained provide data not only on the position of the model during flight, but also on the flow in the boundary layer of the model and on the shape of the shock, so that the pressure and density distributions near the model can be calculated.

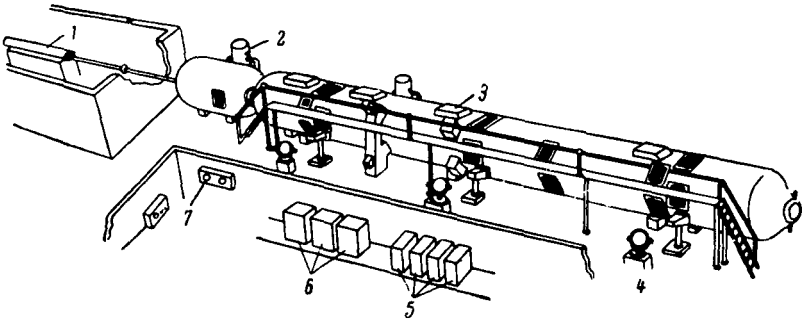

Figure 2.109. Ballistic installation. 1 — gas gun; 2 — vacuum pump; 3 — window for illumination and for photomultipliers; 4 — schlieren instrument; 5 — oscillographs; 6 — chronographs; 7 — vacuum gages.

Recently, radio telemetering equipment has been increasingly used for measurements connected with the flight of models. A series of antennas are installed along the trajectory to intercept the signals radiated by a transmitter inside the model. All the components of the transmitter, including its battery, are cast in epoxy resin which forms the body of the model. The transmitter can thus withstand high accelerations.

Experiments in ballistic tunnels are considerably more labor-consuming, and require more complicated instrumentation, than work in the more usual types of tunnel. The advantages of a ballistic range are the higher Mach and Reynolds numbers obtainable, the absence of interference from model supports, and the directness of the measurements of flight velocity and gas parameters.

Measurements in hypersonic tunnels

Experiments at the high temperatures and during the brief duration of the steady flow in hypersonic wind tunnels demand special measurement techniques. Slightly deviating from the sequence adopted in this book (the measurements in wind tunnels are described in later chapters), we shall discuss briefly several features of measurements in hypersonic tunnels.

Measurement of forces. In air-heated hypersonic tunnels, where the flow durations are measured in seconds or minutes and the stagnation temperature may obtain 800°K, the technique of measuring forces is practically the same as in supersonic tunnels. Aerodynamic forces can be measured by wind-tunnel balances of the mechanical and strain-gage type. The influence of temperature on the strain gages is reduced by cooling the sensitive elements with water or air.

In spark-operated wind tunnels and adiabatic shock tunnels, which permit test durations from 10 to 100 msec, it is possible to measure the aerodynamic forces with the aid of strain-gage transducers if the rigidity of their elastic members is high and the mass of the model small. The natural frequency of the measuring elements of the balances must be of the order of 1000 cycles/sec.

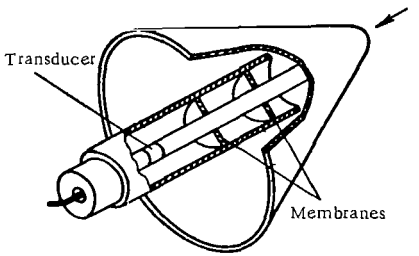

FIGURE 2.110. Wind-tunnel balance for drag measurements in a shock wind tunnel.

In the General-Electric (U.S.A.) shock wind tunnel the drag of the model is measured with a piezoelectric quartz transducer (Figure 2.110). The model is supported by a rod, mounted on metal diaphragms in a holder and forced against the transducer at its free end. It is also possible to use accelerometers to measure the drag. Attempts have also been made to measure the aerodynamic forces acting on a model during acceleration in free flight in a tunnel, in which it was suspended initially on thin strings, broken by the action of the flow. The motion of the model can be photographed with high-speed movie cameras. Knowing the displacement δ of the model from examination of the movie film, its acceleration can be determined from the expression

$$\delta = vt + \frac{at^2}{2},$$

with an accuracy of about 3%. The force $Q = ma$ acting on a model of mass m can be determined with the same accuracy. Using the value of the velocity head $q = \frac{\rho v^2}{2}$ determined during the calibration of the tunnel, the drag coefficient is determined as

$$c_x = \frac{Q}{qS}.$$

The accuracy of this method of measuring c_x is not high, because of the difficulty of making accurate measurements of q, which varies substantially along the axis of the test section /30/.

Measurement of pressures. Measurements of total and static pressures in wind tunnels with conventional heaters can be performed by the usual methods. In tunnels with plasma heaters water-cooled tubes are used to measure the total pressure.

In intermittent-operation tunnels the pressures on the walls and on the surface of the model are measured mainly with piezoelectric (quartz) and barium-titanate transducers having natural frequencies of up to 100,000 cycles/sec. Barium-titanate transducers are far more sensitive than quartz transducers, but they cannot be used for long periods at high temperatures and have a very low mechanical strength. Piezoelectric transducers permit measurements of pressures from fractions of an atmosphere to thousands of atmospheres. For the measurements of high pressures (for instance, that of the propellant gas) transducers can be equipped with devices to reduce their effective area. After fitting a transducer to the model, it can be calibrated dynamically by placing the model in a shock tube of constant cross section, through which a shock of known characteristics is propagated. Some types of transducers respond unduly to vibrations of the wall to which they are attached, and anti-vibration mountings must be used (Figure 2.111). The tests in adiabatic shock and spark-operated tunnels are of comparatively long duration, and strain-gage, inductive, and capacitive pressure transducers can then be used.

Measurement of temperature and density. Thermocouples can be used for the measurement of wind-tunnel gas temperatures up to 1000°C.

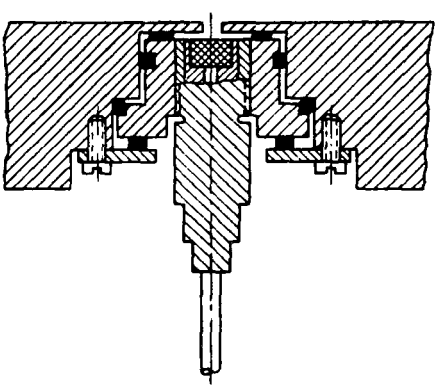

FIGURE 2.111. Anti-vibration mounting for a pressure transducer.

Various types of fittings are available (see Chapter IV). Higher temperatures are measured spectrometrically. Optical interferometers are used for density measurements, supplemented, at low densities, by measurements of the absorption of electrons or X-rays. Quartz windows are provided in the walls of the tunnels for this purpose.

Special techniques are required for optical investigations in hypersonic tunnels, because of the very short time intervals during which the measurements must be made, and because of the luminescence of the very hot gases. The schlieren systems used employ microsecond-spark light sources. Optical filters are installed near the slot to reduce the influence of gas luminescence. Often the luminescence at the shock provides clear photographs of the nose shock in front of the model.

Measurement of shock-propagation velocity. The shock-propagation velocity in shock tubes can be measured with ionization transducers or film-resistance thermometers. The ionization transducer consists of an insulated electrode inside the tunnel at a short distance from the wall, which forms the second electrode. A potential of some tens or hundreds of volts is applied to the electrode and the change of resistance of the air gap at the instant when the passage of the shock ionizes the air is picked up and displayed on an oscilloscope with a crystal-controlled time-base generator. A series of transducers, installed at known distances along the tunnel, feed a single oscilloscope, so that the shock-propagation velocity in different parts of the tunnel can be determined. In electromagnetic shock tunnels the shock-propagation velocity is measured with ultrahigh-speed movie cameras and photorecorders which photograph the motion of the luminescent front.

Film-resistance thermometers are used to detect comparatively weak shocks, which are accompanied by ionization of air (see p. 113). The shock-propagation velocity is measured by recording the sudden temperature increases as the shock passes two successive film-resistance thermometers installed a known distance apart.

Measurement of heat transfer. In continuous-operation wind tunnels, having comparatively long operating durations, the amount of heat transferred convectively by the gas to unit surface during unit time can be determined with the aid of models having cooled (or heated) walls.

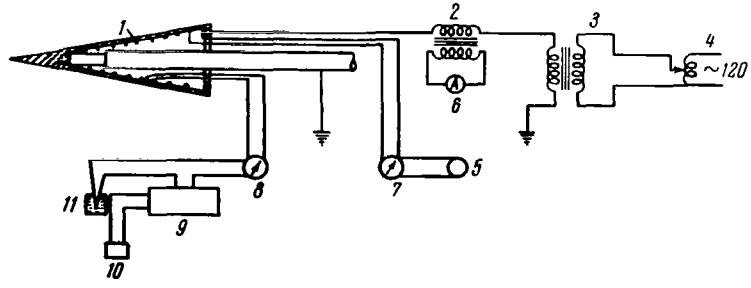

FIGURE 2.112. Measurement of heat transfer from a heated cone. 1 — voltage-measurement points; 2 — current-measurement transformer; 3 — power transformer; 4 — autotransformer; 5 — electron-tube voltmeter; 6 — ammeter; 7 — voltage-point selector switch; 8— thermocouple-selector switch; 9 — potentiometer; 10 — galvanometer; 11 — thermocouple cold junction

Figure 2.112 shows the measurement of the heat transfer from a cone, the walls of which are heated by low-voltage high-intensity a.c. /28/.

The body of the model is made from stainless steel, which has high ohmic resistance; all other parts are made from copper. The temperature distribution at a number of points on the surface of the cone is determined by means of thermocouples connected through a selector switch to a potentiometer. Nearby points on the wall of the cone are connected by wires through another selector switch to a voltmeter with which the potential gradient along the cone can be measured. The supply voltage is adjusted to maintain the temperature of the wall constant; the measured values of temperature, voltage and current intensity determine the local heat input to the wall of the model. The stagnation temperature, static pressure, and humidity of the undisturbed air are measured at the same time.

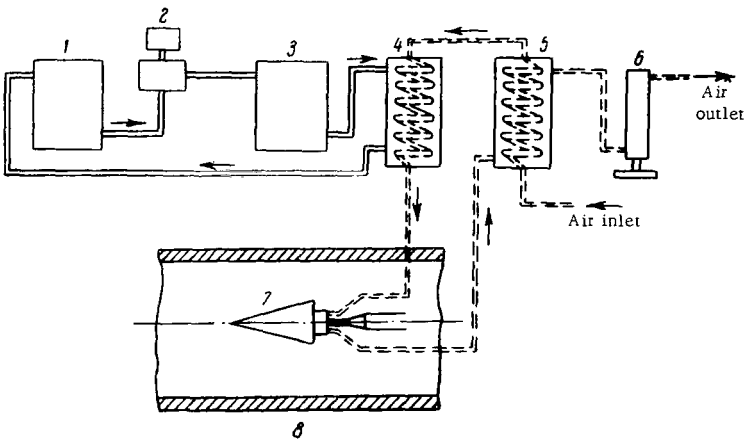

FIGURE 2.113. Measurement of heat transfer from a cooled model. 1 — container; 2 — pump; 3 — cooling vessel containing alcohol and solid carbon dioxide; 4 — air heat exchanger; 6 — flow meter; 7 — model; 8 — wind tunnel.

The measurement of heat transfer by cooling the wall of the model is illustrated in Figure 2.113. The outer wall of the model is continuously cooled by air flowing in an annular gap between the wall and the body of the model. To obtain a sufficiently uniform distribution of the cooling-air temperature, the Reynolds number in the gap should be high. At a given model-surface temperature, the temperature rise of the cooling air (as measured by thermocouples), and its flow rate determine the heat input Q per unit time.

Knowing Q, the surface area F of the model, the recovery temperature T_r, and the temperature T_w of the wall, the coefficient of heat transfer can be determined from the expression

$$\alpha = \frac{Q}{F(T_r - T_w)}.$$

The recovery temperature can be found by measuring the surface temperature of a heat-insulated model of the same shape.

Heat transfer can also be studied under transient conditions, for instance, by suddenly inserting a model at known initial temperature into a stream of hot air. In the AEDC tunnel (Figure 2.94), a pair of cooling shrouds is

installed for this purpose on telescopic mountings attached to the walls of the test section. The model is held within these shrouds at zero angle of attack and is air-cooled to the required temperature until the tunnel flow is established. The shrouds are then hydraulically retracted into the walls of the test section (Figure 2.114), the model is turned to the required attitude, and the temperature of the model wall is measured at 0.25 second intervals by 100 thermocouples. Heat conduction parallel to the surface can be neglected in a thin-walled model, and the local coefficient of heat transfer can be found from the thermal capacity of the wall and the rate of change of its temperature.

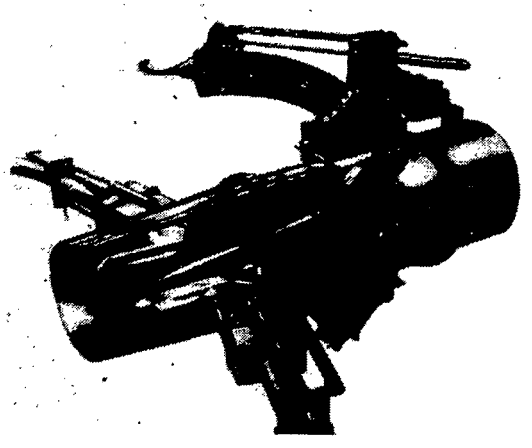

FIGURE 2.114. Shrouds for model precooling in a wind tunnel.

The coefficient of heat transfer is

$$\alpha = \frac{mc}{F}\frac{dT_w}{dt}\frac{1}{T_r - T_w},$$

where m is the mass of the wall, c its specific heat, and t denotes time. The shrouds serve also to protect the model from overloads caused by shocks during start-up and shut-down of the tunnel.

In both shock and conventional wind tunnels, surface heat exchange at the model nose can be investigated with film-resistance thermometers which have very small time constants. On the surface of the model, which is made from quartz or refractory glass, a 0.01 to 0.1 μ thick film of platinum, gold, or rhodium, is applied by evaporation or sintering. After deposition the metal film is heat-treated at a temperature of 610 to 670°C, and then slowly cooled to ensure better penetration of the metal into the surface of the model and to increase the wear resistance of the film. The electric resistance of the film is

$$R = R_i[1 + k(T - T_i)].$$

where R_i is the resistance of the film at initial temperature $T = T_i$, and k is a constant. For platinum or gold films k lies between 0.0015 and 0.002 degree^{-1}. The resistance will be about 4 to 40 ohm, depending on the dimensions of the thermometer. A current of the order of 20 to 50 ma is passed through the thermometer to generate an output signal (usually measured by an oscillograph) of 1.5 to 2.5 mV per degree; the time constant is about 1 microsecond.

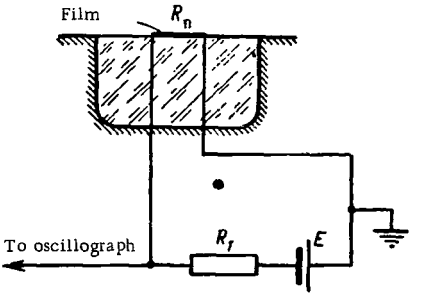

FIGURE 2.115. Film temperature transducer.

Figure 2.115 shows the diagram of a film temperature transducer, used for the study of heat transfer at the wall of a shock tube /34/. The transducer consists of a glass cylinder of 5 mm diameter and 6 mm height. Platinum leads, welded to the body of the transducer, are at their ends polished flush with the surface before the film is deposited. The film is sintered to the face in the form of a 3 mm long and 1.5 mm wide strip.

When the temperatures are so high that gas becomes ionized, the metal film is covered with a very thin layer of insulating material, such as silica, which prevents short-circuiting of the metal film by the conductive gas, without seriously increasing the time constant. The surface of the metal film is first covered by evaporation with a film of SiO having a thickness of the order of 0.01μ. The model is then heat-treated in a furnace at a temperature of about 540°C, so that the SiO is oxidized to SiO_2, which is a better insulator /32/. Such a film can withstand a potential difference of up to 12 v, corresponding to a breakdown voltage of about 1000 kV/em.

Heat flux is measured with film-resistance thermometers as follows. Neglecting the lag due to the thermal capacitance of the film, the instantaneous value of the specific heat flux $\overline{Q}$ is

$$\overline{Q}(t) = \sqrt{\frac{\rho\lambda c}{\pi}} \int_0^t \frac{1}{\sqrt{t-\tau}} \frac{dT}{d\tau} d\tau \frac{\text{cal}}{\text{m}^2\,\text{sec}},$$

where ρ, λ, and c are density, coefficient of thermal conductivity, and specific heat of the film substrate while τ is the variable time.

The specific heat flux can also be expressed in terms of the voltage u, measured by the film-resistance thermometer

$$\overline{Q}(t) = \frac{\sqrt{\rho\lambda c}}{IR_i k\sqrt{\pi}} \int_0^t \frac{1}{\sqrt{t-\tau}} \frac{du}{d\tau} d\tau,$$

where R_f is the electrical resistance of the film and I is the current flowing through it.

Thus, to determine $\overline{Q}$ from the time-voltage oscillogram we must know the constant

$$A = \frac{\sqrt{\rho\lambda c}}{k},$$

which is evaluated by passing through the film a rectangular current pulse, using the discharge of a capacitator, so that a predetermined quantity of heat flows into the surface of the model. By comparing the theoretical relationships between the temperature and time with the time-voltage oscillogram, we can find A.

§8. WIND TUNNELS FOR TESTING AIRCRAFT ENGINES

Tests in which similarity of velocity and flight altitude is maintained are important in the study of aircraft take-off and the interaction between the aircraft and its propeller or jet stream.

Full-scale aircraft and propeller-testing tunnels were built in several countries in the thirties for solving these problems. In the NASA laboratory at Moffett Field a full-scale aircraft tunnel with a test section having a flow area of 24.4 m × 12.2 m and a length of 24.4 m was built. The maximum velocity in the tunnel is 90 m/sec, and the drive power 40,000 h. p. Full-scale tunnels usually have six-component wind-tunnel balances on which the aircraft is installed, traversing cradles for investigating the pressure and velocity distributions and the flow inclination, and also a centralized system of fuel supply to the engines of the aircraft, since it is hazardous to supply fuel directly to the engines from the tanks within the aircraft.

Periodical changes of air and removal of combustion products are necessary when an engine is run in the tunnel, because even with intermittent operation of the engine (15—20 min), the air circulating in the tunnel becomes contaminated so that the engine power is reduced, and the accuracy of measurements suffers; there is also a hazard to the operators. In closed-circuit full-scale tunnels with open test sections, partial natural exchange takes place between the tunnel air and that of the room around the test section, and a powerful ventilation system is required (Figure 2.116).

In tunnels with closed-test sections, contaminated air is bled off in the return duct, using additional fans or compressors, or as shown in Figure 2.79.

In these full-scale tunnels pressures corresponding to high altitudes cannot be simulated, and tests are made only for ground conditions. The advent of jet engines made necessary special wind tunnels for large test-section velocities and variable pressures and temperatures to approximate altitude conditions; these tunnels are equipped with systems for cleaning and renewing the air.

For the study of problems in gas dynamics related to engine intake, air flow in engines, and combustion, special engine-testing tunnels and rigs of various types are required.

One of the largest tunnels for testing the characteristics of jet engines in aircraft or rockets is the high-speed AEDC wind tunnel mentioned on p. 79.

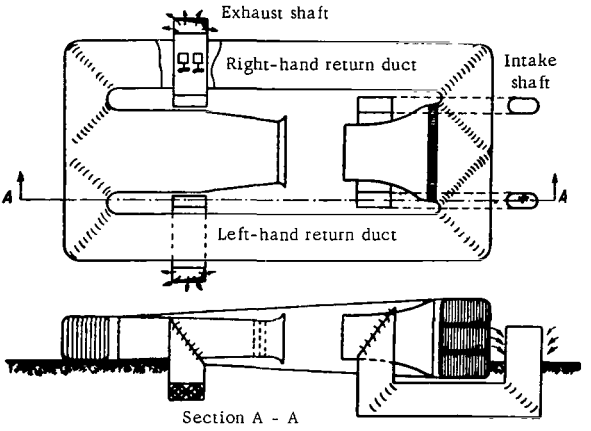

FIGURE 2.116. Wind-tunnel ventilation system.

The jet engines tested in this tunnel have high fuel consumptions, and a powerful system of compressors and extractors is required to supply the tunnel with fresh dry air and remove contaminated air at rates up to 210 kg/sec, meanwhile maintaining a tunnel pressure appropriate to flight at altitudes of about 30 km.

The large dimensions of the test section of this tunnel (4.88 m × 4.88 m) permit investigations of the flows both around the jet engines and, simultaneously, within it. The flow rate of air through the engine is so great as to influence substantially the external resistance and stability of the aircraft or missile.

A modern continuous-operation wind tunnel for jet-engine testing exists at the Lewis Laboratory of NASA (Figure 2.117).

This tunnel has a test section of 3.05 m × 3.05 m flow area in which a maximum velocity corresponding to $M = 3.5$ can be obtained. The total electric drive power of the tunnel is about 250,000 h.p. (or 300,000 h.p. when the booster is used). The main compressor of the tunnel is an eight-stage unit with a diameter of 6.1 m of 131,000 m^3/min capacity, with a compression ratio of 2.8 and requiring 150,000 h.p. With this compressor Mach numbers of 2.5 can be obtained. A booster compressor, used when higher Mach numbers (up to $M = 3.5$) are needed, has ten stages; it has a compression ratio of 2.8, a capacity of 38,200 m^3/min, and requires 100,000 h.p.

The tunnel can be operated either as closed-circuit tunnel, or as open-circuit tunnel, exhausting to atmosphere. The ranges of tunnel pressures and velocities possible in either case are shown in Figure 2.118 (shaded areas). The tunnel has an adjustable nozzle, a supersonic diffuser, an installation for air cooling and drying, extractors to reduce the initial

pressure, automatic instrumentation, and a remote-control system for the model and for tunnel operation. Data processing is fully automatic, employing computers and automatic curve-plotting equipment.

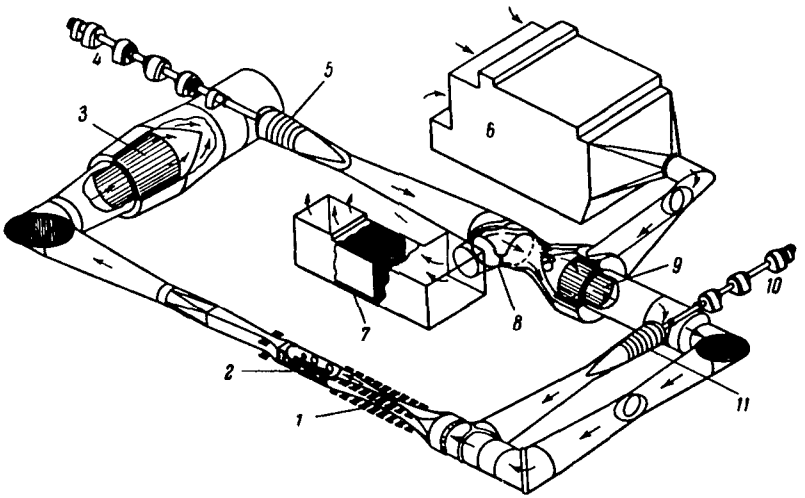

FIGURE 2.117. NASA tunnel for testing jet engines (Lewis Laboratory). 1 — adjustable nozzle; 2 — test section, 3 — cooler No. 1, 4 — main motor, 5 — main compressor, 6 — air drier; 7 — extractor; 8 — valve, 9 — cooler No. 2, 10 booster motor, 11 — booster compressor.

Specially built exhaust-test rigs are used for testing internal components of jet engines. A compressor supplies air to a container or settling chamber, and thence to a nozzle, whence it passes directly to the jet-engine intake. If it is not desired to measure thrust, the engine may be flanged directly to the nozzle, to avoid leakages and pressure losses. The air flow rate through the test rig is arranged to equal the flow rate through the engine under the corresponding flight conditions, taking into account altitude and mixture composition.

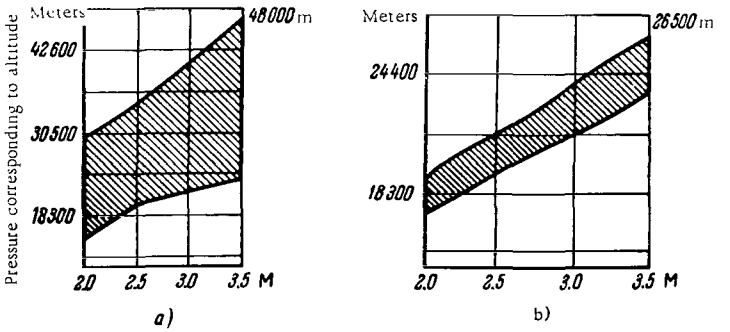

FIGURE 2.118. Pressures obtainable in the test section. a — closed-circuit tunnel; b — open-circuit tunnel.

Conventional test rigs permit tests under ground conditions or under conditions of flight at low altitudes, since the rarefaction from flow acceleration in the nozzle up to $M = 0.85$ to 0.95 is not high.

For simulating conditions at higher altitudes a diffuser can be connected to the engine exhaust. It is better, however, to exhaust the engine into a separate diffuser, so that the jet thrust can also be measured. The equivalent altitude of such test rigs can be further increased by fitting one or more extractors. Using a diffuser and two extractors the pressure at the nozzle inlet is substantially reduced, so that by changing the pressure in the settling chamber, the internal gas dynamics of the engine and the combustion conditions at different densities and Reynolds numbers can be investigated.

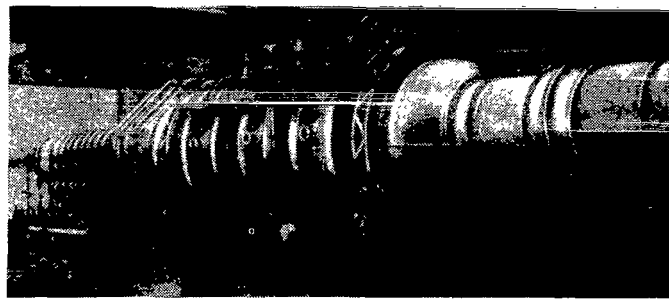

FIGURE 2.119. Turbo-jet engine test facility (AEDC test rig T-1).

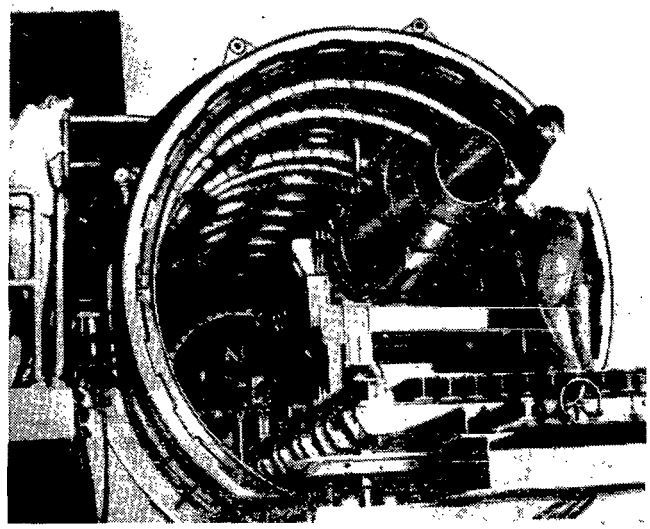

FIGURE 2.120. Mounting a jet engine on the test rig.

With the increase of jet-engine power, velocity, and altitude of flight it has become necessary to build test rigs, in which full-scale engines are supplied with clean, dry, and heated air in the state and velocity corresponding to flight conditions. The test rigs constructed in recent years for studying jet engines and their equipment are not, therefore, very different from supersonic tunnels for engine testing. The power of the compressors supplying air to the engines and removing the exhaust gases may attain 50,000 to 100,000 h.p., and jet-intake Mach numbers of 4 to 5 are obtained.

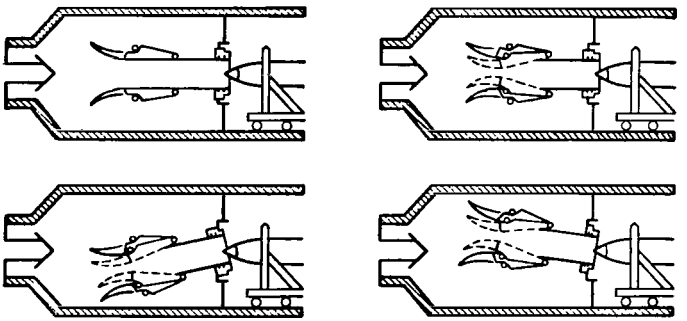

FIGURE 2.121. Adjustable nozzle system used in the AEDC jet-engine test rig.

Figure 2.119 shows the AEDC (USA) T-1 test rig for turbo-jet engines. Figure 2.120 shows a jet engine being installed for tests, and Figure 2.121, the adjustable nozzle system used by AEDC, which permits the angle of attack of the engine to be varied.

When engines are tested, the following magnitudes are measured: jet thrust, air flow rate, air pressures and temperatures at engine intake and exhaust, fuel flow rate and pressure, velocity distribution at inlet and exit of engine diffuser and at outlet nozzle, parameters related to fuel atomization and combustion.

Bibliography II.

1. Malikov, M.F. Osnovy metrologii (Fundamentals of Metrology). Moskva. 1959.
2. Howarth, L. (Editor) (Modern State of High-Speed Aerodynamics, Vol. 2). [Russian translation. 1956].
3. Spravochnik aviakonstruktora Vol. I. Aerodinamika samoleta (Handbook of Aircraft Design, Vol. I. Aircraft Aerodynamics). — Izdanie TsAGI, Moskva. 1937.

4. Hoerner, S. Versuche mit Kugeln betreffend Kennzahl, Turbulenz und Oberflächenbeschaffenheit.— Luftfahrforschung, Vol. XII, No. 1. 1935.
5. Solodkin, E.E. and A.S. Ginevskii. Turbulentnoe techenie vyazkoi zhidkosti v nachal'nom uchastke osesimmetrichnykh i ploskikh Kanalov (Turbulent Flow of Viscous Liquids in the Initial Length of Axisymmetrical and Plane Ducts).— Trudy TsAGI, Vol. 701. 1957.
6. Abramovich, G.N. Prikladnaya gazovaya dinamika (Applied Gas Dynamics).— GTTI. 1953.
7. Szilard, K.S. Issledovanie diffuzorov aerodinamicheskikh trub bol'shikh skorostei (Testing Diffusers of High-Speed Wind Tunnels). Tekhnicheskie zametki TsAGI No. 160. 1938.
8. Abramovich, G.N. Aerodinamika potoka v otkrytoi chasti aerodinamicheskoi (Aerodynamics of Flow in the Open Test Section of Wind Tunnels).— Trudy TsAGI No. 218. 1935.
9. Taganov, G.I. Vyravnivayushchee deistvie setki v potokakh zhidkosti i gazov (The Smoothing Effect of Screens Inserted in Streams of Fluids).— Trudy TsAGI No. 604. 1947.
10. Minskii, E.M. O gashenii turbulentnosti sponioshch'yu setochnykh fil'trov (Smoothing of Turbulence with the Aid of Screens).— Tekhnicheskie zametki TsAGI, No. 63. 1946.
11. Dryden, H.L. A Review of the Statistical Theory of Turbulence.— Quart. of Appl. Math., Vol. 1, No. 1. 1943.
12. Idel'chik, I.E. Spravochnik po gidravlicheskim soprotivleniyam (Handbook of Hydraulic Resistances).— Gosenergoizdat. 1960. [Translated by IPST, Cat. No. 1505.— AEC - tr - 6630.]
13. Vulis, L.A. O prekhode cherez skorost' zvuka v gazovom techenii (Passage of a Gas Flow Through the Sound Barrier).— Doklady AN SSSR, Vol. 54, No. 8. 1946.
14. Pankhurst, R.C. and D.W. Holder. Wind Tunnel Technique. 1954 [Russian translation. 1955.)
15. Holder, D. and North. The 9 × 3 in. NPL Induced - Flow High - Speed Wind Tunnel.— Rep. ARC, No. 12, 387. 1949.
16. Holder, D. The High - Speed Laboratory of the Aerodynamics Division NPL.— R. a. M., ARC, No. 2, 560. 1946.
17. Lukasiewicz, J. Diffuzory dlya sverkhzvukovykh aerodinamicheskikh trub (Diffusers for Supersonic Wind Tunnels). Collection of translations and reviews of foreign periodical literature.— "Mekhanica", No. 5 (28).— IL. 1954.
18. German, R. Sverkhzvukovye vkhodnye diffuzory (Supersonic Intake Diffusers).— Fizmatgiz. 1960.
19. Andreev, V.A. and S.Z. Belenkii. Vliyanie kondensatsii parov vody na sverkhzvukovye techeniya (The Influence of Condensation of Water Vapors on Supersonic Flow).— Trudy TsAGI, No. 579. 1946.
20. Lukasiewicz, J. Razvitie bol'shikh aerodinamicheskikh trub kratko vremennogo deistviya (Development of Large Intermittent - Operation Wind Tunnels).— Collection of translations and reviews of foreign periodical literature "Mekhanica", No. 6 (34).— IL. 1955.

21. Tsien, H.S. Problemy issledovanii po aerodinamike razrezhennykh gazov v trubakh (Investigation of the Aerodynamics of Rarefied Gases in Wind Tunnels). Collection of papers "Gas Dynamics".— IL. 1950.
22. Lukasiewicz, J. Experimental Investigations in Hypervelocity Flight.— Advances in Aeronautical Sciences, Vol. II, Pergamon Press, London, N.Y. 1959.
23. Brogan, T.R. The Electric Arc Wind Tunnel . A Tool for Atmospheric Reentry Research. — ARS J., Vol. 29. No. 9. 1959.
24. Resler, E.L. The Production of High Temperature Gases in Shock Tubes.— J. Appl. Phys., Vol. 23, No. 12. 1952.
25. Wittliff, C.F. The Tailored-Interface Hypersonic Shock Tunnel.— J. Aero/Space Sciences, Vol. 26, No. 4. 1959.
26. Monoghan, R.J. Features of Hypersonic Heat Transfer.— Advances in Aeronautical Sciences, Vol. I. Pergamon Press, London, N.Y. 1959.
27. Ziemer, R.W. Experimental Investigations in Magneto-Aerodynamics.— ARS J., Vol. 29, No. 9. 1959.
28. Scherrer, J.R. Comparison of Theoretical and Experimental Heat-Transfer Characteristics of Bodies of Revolution at Supersonic Speeds.— NACA Rept. No. 1055. 1951.
29. Hall, J. and A. Hertzberg. Recent Advances in Transient Surface Temperature Thermometry.— Jet Propulsion, Vol. 28, No. 11. 1958.
30. Bloxom, D.E. Supersonic Aerodynamic Experiments Using Very High Temperature Air Wind Tunnels.— Jet Propulsion, Vol. 28, No. 9. 1958.
31. Bloom, M.H. A High Temperature-Pressure Air Heater.—ASME Paper, No. 59-A-233. 1959.
32. Marrone, P.V. Thin-Film Thermometer Measurements in Partially Ionised Shock-Tube Flows.— Phys. of Fluids, Vol. 2, No. 6. 1959.
33. Borzunov, N.A., D.V. Orlinskii and S.M. Osovets. Issledovanie moshchnogo impul'snogo razryuda v konicheskikh kamerakh (Investigation of Intense Pulse Discharges in Conical Chambers).— Zhurnal Eksperimental'noi i Teoreticheskoi Fiziki, Vol. 36, No. 3. 1959.
34. Polyakov, Yu.A. and E.A. Mit'kina. Tonkoplenochnyi termometr soprotivleniya (Film-Resistance Thermometers).— Pribory i Tekhnika Eksperimenta, No. 4. 1961.
35. Bull, G.V. Reentry Studies in Free Flight Ranges. — JAS Paper, No. 143. 1959.
36. Udarnye truby (Shock Tubes). Collection of translated papers.— IL. 1962.

Chapter III

WIND-TUNNEL DESIGN CALCULATIONS

The design calculations of wind tunnels involve the determination of the velocities, pressures, densities, and temperatures throughout the tunnel circuit in terms of the test-section velocity. Aerodynamic calculations begin from a draft tunnel layout based on the required test-section dimensions, Mach number, and Reynolds number.

The type of test section (open or closed) is selected by considering the available power and the requirements of the tests. In addition, the contraction ratio of the nozzle must be chosen. For a given test-section velocity and with maximum permissible diffuser divergence, the contraction ratio determines the velocity distribution throughout the tunnel circuit, the tunnel length and the geometry of all elements forming the return circuit.

Aerodynamic calculation determines the compression ratio, discharge capacity, and power of the compressor or the fan* necessary for obtaining the flow in the test section, and also the pressure loads on all the elements of the tunnel.

§ 9. DESIGN OF SUBSONIC TUNNELS

The influence of compressibility may be ignored in the design of subsonic wind tunnels, because the flow throughout the tunnel circuit is at velocities considerably less than that of sound. Energy losses in the airstream are due mainly to frictional resistance and to pressure losses due to eddies, in the diffusers, in the turning vanes at the corners, etc.

The total hydraulic resistance ΔH_{tot} of the wind tunnel, which defines the loss of energy (of total head) when air flows in it, can be divided arbitrarily into two components: the frictional resistance ΔH_{fr}, which depends on the flow regime (i.e., Reynolds number) and on the degree of roughness ε of the wall, and the local resistance ΔH_{loc}, caused by local flow separation and turbulent mixing, which depends on the geometry of the tunnel elements. The resistance of the duct is usually expressed in terms of the velocity head

$$\Delta H_{tot} = \zeta_{tot} \rho \frac{V^2}{2} \text{ kg/m}^2,$$

where $\zeta_{tot} = \zeta_{fr} + \zeta$ is the coefficient of total hydraulic resistance. Here

* Or the required pressure gradients and air flow rates for intermittent-operation tunnels.

$\zeta = \frac{\Delta H_{loc}}{\rho V^2/2}$ is the coefficient of local resistance; $\zeta_{fr} = \frac{\Delta H_{fr}}{\rho V^2/2}$ is the coefficient of frictional resistance* and V is the mean velocity in the section considered. Thus, the first stage of aerodynamic design consists of determining the magnitudes of the coefficients ζ and ζ_{fr} for each tunnel element.

To facilitate calculations and comparisons of losses in each element of the tunnel, the values of ζ and ζ_{fr} are expressed in terms of the velocity head in the test section, by multiplying the calculated values of the coefficients ζ and ζ_{fr} by the factor $\left(\frac{F_{t.s.}}{F}\right)^2$ where F is the cross-sectional area of the tunnel element considered, and $F_{t.s.}$ that of the test section. The magnitudes of ζ and ζ_{fr} are estimated from measured data for the local and frictional resistances of various tunnel elements of different shapes**.

The hydraulic resistance of parts of ducts depends not only on their geometry, but also on certain external factors, including:

1) The velocity distribution at the inlet to the element considered, which in turn is related to the flow conditions, the shape of the inlet, the influence of upstream elements of the tunnel, and the length of straight duct immediately preceding the element considered.

Design handbooks generally give the hydraulic-resistance data for elements through which air flows at uniform velocity, except where the contrary is stated.

2) The Reynolds number $\left(\mathrm{Re} = \frac{VD}{\nu}\right)$, which affects the frictional-resistance coefficient, and also the local-resistance coefficient at comparatively low values ($\mathrm{Re} < (0.1 - 0.2) \cdot 10^6$), though only slightly at large values; when the Reynolds number at which the measurement was made is not quoted in the handbook, it can be assumed that the value of ζ is independent of Re even at small Reynolds numbers.

3) The Mach number $\mathrm{M} = \frac{V}{a}$, which influences the local resistance (and the frictional resistance) considerably, although this effect has been little studied. Since large velocities are not usual in the ducts ($\mathrm{M} \leqslant 0.3$ to 0.4), data in the handbooks, compiled from low-velocity ($\mathrm{M} < 0.3$) tests, can generally be used in practice.

4) The roughness of internal surfaces, which strongly affects the frictional resistance, and should be considered in each individual case on the basis of the experimental data available. Where design handbooks fail to specify the degree of surface roughness it should be assumed that the coefficient of friction quoted relates to smooth walls.

5) Shape of the cross section. For noncircular sections (square or rectangular with side ratios between 0.6 and 1.7), the coefficient of resistance can often be taken as for circular sections.

* As distinct from the coefficient $\lambda = \frac{\Delta H_{fr}}{(\rho V^2/2)\,(l/D)}$ of the frictional resistance per unit length of duct of constant cross section.

** The data below for local and frictional resistances are due to Idelchik, I.E. Spravochnik po gidravlicheskim soprotivlenam (Handbook of Hydraulic Resistances). — Gosenergoizdat M.-L. 1960. [English translation, IPST, Cat. No. 1505; AEC tr-6630.]

Frictional resistance

In general the pressure drop per unit length due to friction in a duct is

$$\Delta H_{\text{fr}} = \frac{\lambda}{4} \frac{S}{F_0} \rho \frac{V_0^2}{2},$$

where λ is the coefficient of frictional resistance per unit of length of the duct (usually called the friction coefficient), V_0 is the mean flow velocity, F_0 is the cross-sectional area of the duct, and S is the friction surface area. This formula can also be written

$$\Delta H_{\text{fr}} = \lambda \frac{l}{D_{\text{h}}} \rho \frac{V_0^2}{2}.$$

Here, l is the length of the duct whose resistance is being determined, and D_{h} is the hydraulic diameter of the duct cross section; for a circular section $D_{\text{h}} = D_0$; for a rectangular section whose sides are a_0 and b_0,

$$D_{\text{h}} = \frac{4F_0}{U_0} = 2 \frac{a_0 b_0}{a_0 + b_0},$$

where U_0 is the perimeter.

The coefficient λ depends mainly on the Reynolds number and the roughness. The roughness is characterized by the average height k of the surface irregularities (projections), called the absolute geometrical roughness; the ratio of the average projection height to the hydraulic diameter $\varepsilon = \frac{k}{D_{\text{h}}}$ is the relative geometrical roughness.

Since the geometrical roughness characteristics are an inadequate measure of the resistance of the tunnel, we introduce the concept of hydraulic roughness, based on resistance measurements. The presence of a laminar sub-layer determines the effect of surface roughness on the hydraulic resistance. When the thickness of the laminar sub-layer exceeds the height of the projections, air flows uniformly over them at the low velocities characteristic of the sub-layer, and the height of the projections has no influence. The frictional-resistance coefficient λ therefore decreases as **Re** increases. However, as **Re** increases the thickness of the laminar sub-layer decreases, until it is smaller than the largest projections, which thus intensify the turbulence. The consequent increase in pressure loss is reflected in the increasing value of λ as **Re** rises further.

Tunnels can be considered smooth (both hydraulically and technically), if the height of the projections is less than the thickness of the laminar sub-layer. The corresponding limiting value of the relative [geometrical] roughness is

$$\varepsilon' \approx \left(\frac{k}{D_{\text{h}}}\right)' \approx 17.85 \mathbf{Re}^{-0.875}.$$

Figure 3.1 shows the value of the friction coefficient as a function of the Reynolds number for tunnels of uniform roughness (obtained by sprinkling the surface with sand of fixed grain size). This relationship is used when calculating the frictional losses in the elements of wind tunnels.

Determination of λ for laminar flow (Re < 2000).

1) Circular section:

$$\lambda = \frac{64}{Re}.$$

2) Rectangular section of side ratio $\frac{a_0}{b_0} \leqslant 1.0$:

$$\lambda_1 = \lambda\varphi_1,$$

where φ_1 is determined from Figure 3.2.

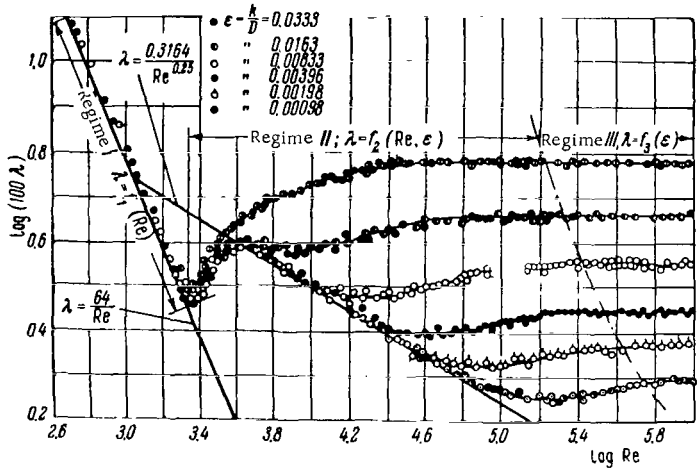

FIGURE 3.1. Friction coefficient λ as function of Reynolds number for tunnels of uniform roughness. Regime no. 1 — laminar; regime no. 2 — transitional, regime no. 3 — turbulent.

Determination of λ for tunnels with smooth walls (Re > 2000).

1) Circular section:

$4000 < Re < 100{,}000 \quad \lambda = \frac{0.3164}{\sqrt[4]{Re}}$ (Figure 3.3a),

$Re > 4000 \quad \lambda = \frac{0.303}{(\lg Re - 0.9)^2}$ (Figure 3.3b).

2) Rectangular section $\left(\frac{a_0}{b_0} = 0.7 - 1.0\right)$:

$$\lambda_1 = \lambda\varphi_2,$$

where φ_2 is found from Figure 3.4.

Determination of λ for tunnels with uniform wall roughness (Re > 2000).

1) Circular section:

$$\lambda = \frac{1}{\left[a_1 + b_1 (Re \lg \sqrt{\lambda}) + c_1 \lg \frac{k}{D_h}\right]^2}.$$

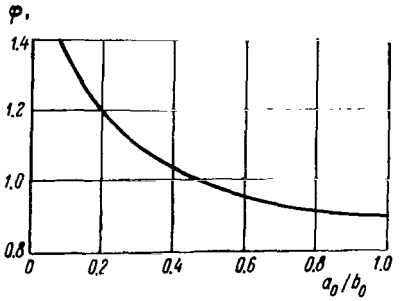

FIGURE 3.2 Correction coefficient for rectangular tunnel section (Re < 2000).

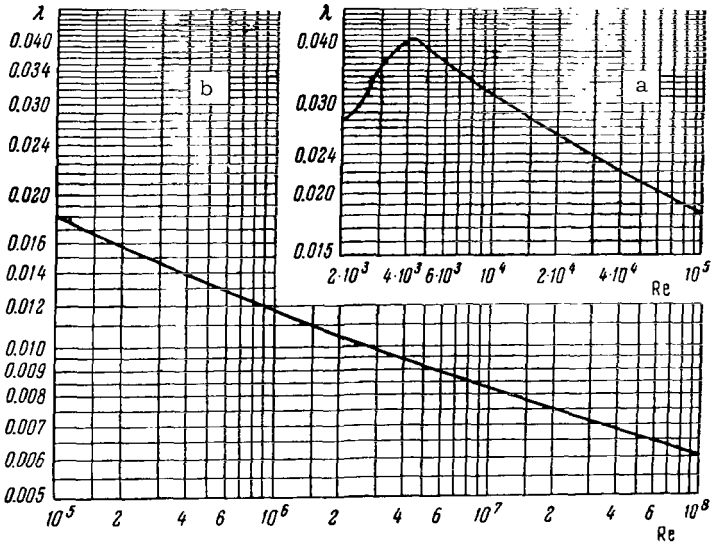

FIGURE 3.3 Variation of friction coefficient with Reynolds number for tunnels with smooth walls (Re > 2000, transitional regime).

The values of a_1, b_1, c_1, are given in Table 3. The value of λ can be determined from Figure 3.5.

2) Rectangular section $\left(\frac{a_0}{b_0} = 0.7 \text{ to } 1.0\right)$:

$$\lambda_1 = \lambda\varphi_3,$$

where $\varphi_3 = \varphi_2$ (Figure 3.4).

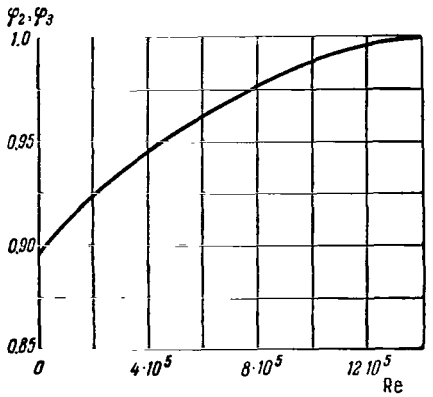

FIGURE 3.4 Correction coefficient for rectangular tunnel sections.

Determination of λ for tunnels with rough walls (turbulent regime).

1) Circular section:

$$\lambda = \frac{1}{\left(2\lg 3.7\frac{D_h}{k}\right)^2} \text{ (Figure 3. 6).}$$

2) Rectangular section $\left(\frac{a_0}{b_0} = 0.7 \text{ to } 1.0\right)$:

$$\lambda_1 = \lambda\varphi_2 \text{ (Figure 3. 4).}$$

The Reynolds number is

$$\mathrm{Re} = \frac{V_0 D_h}{\nu},$$

where $\nu = \mu/\rho$ depends on the temperature and pressure (for $p = 1$ atm, the value of ν is found from Figure 3. 7). The temperature dependence of μ is

$$10^6\mu = 1.712\sqrt{1 + 0.00366t}\,(1 + 0.0008t)^2,$$

where t is in °C.

Table 3. Values of a_1, b_1, c_1 for determining the coefficient λ for tunnels of circular section and uniform wall roughness (Re > 2000).

$\varepsilon\mathrm{Re}\sqrt{\lambda}$	a_1	b_1	c_1
3.6 — 10	—0.8	2.0	0
10 — 20	0.068	1.13	—0.87
20 — 40	1.538	0	—2.0
40 — 191	2.471	—0.588	—2.588
191	1.138	0	—2.0

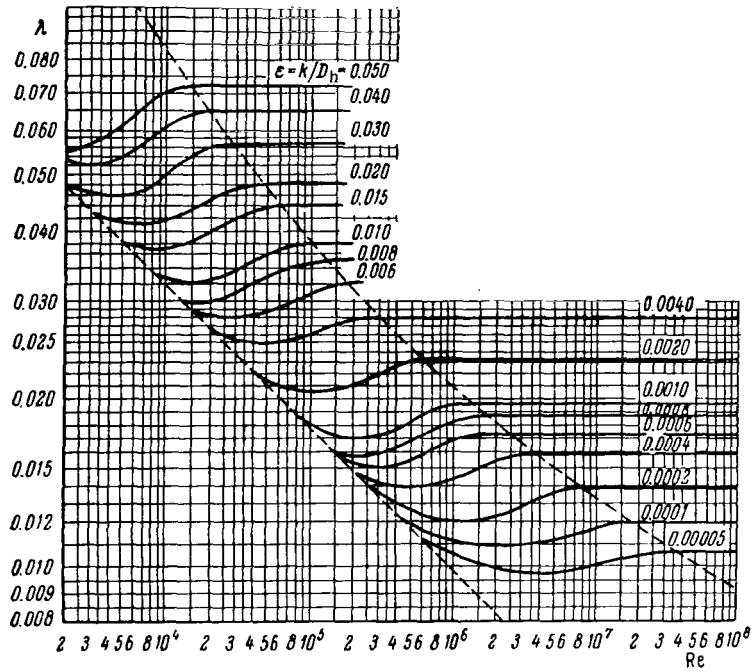

FIGURE 3.5. Variation of friction coefficient with Reynolds number for tunnels of uniform wall roughness; transitional regime (Re >2000).

The following values of the projection height k (mm) can be assumed for materials generally used in the construction of wind tunnels.

Clean seamless brass, copper, or lead pipes	0.0015-0.001
New seamless steel pipes	0.04-0.17
Galvanized iron pipes	0.39
New cast-iron pipes	0.25-0.42
Birch plywood	0.025-0.05
Pine plywood	0.1
Wooden pipes	0.25-1.25
Planed-wood flumes	0.25-2.0
Clean cement surfaces	0.25-1.25
Plaster with cement mortar	0.45-3.0
Concrete ducts	0.8-9.0
Glazed ceramic tubes	0.25-6.0
Glass tubes	0.0015-0.01
Oil paint applied on a priming coat	0.1

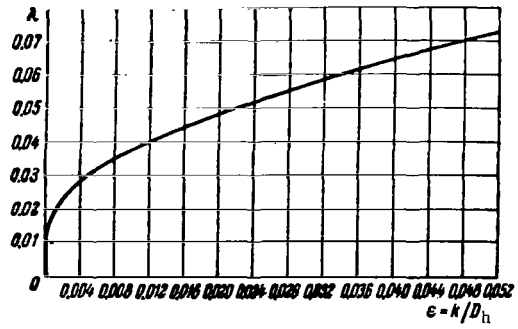

FIGURE 3.6. Variation of resistance coefficient of tunnel with wall roughness in turbulent regime.

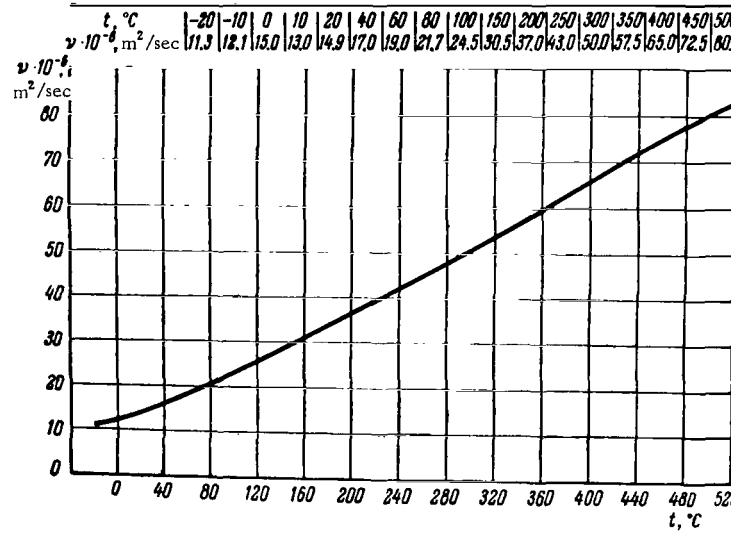

FIGURE 3.7 Variation with temperature of kinematic coefficient of air viscosity (p = 1 atm).

Losses in the nozzle

Losses in the nozzle are mainly due to friction, and can thus be calculated for a given nozzle profile from the expression

$$\zeta_{fr} = \frac{\lambda}{8} ef,$$

where $\lambda = f_1(\mathrm{Re}, \varepsilon)$ is calculated from the formulas and graphs above,

while e and f are coefficients by which allowance is made for the contraction ratio.

$$e = 1 - \left(\frac{F_{t.s.}}{F_\Phi}\right)^2 = 1 - \frac{1}{n^2},$$

$$f = \frac{1}{\sin \alpha/2} \text{ *)},$$

$$\zeta_{fr} = \frac{\lambda}{8 \sin \alpha/2}\left[1 - \frac{1}{n^2}\right].$$

The frictional resistance of the nozzle can be more accurately calculated from the expressions

$$\zeta_{fr} = \frac{\lambda}{4}\frac{1}{n^2-1}\frac{l}{a_0}\left(\frac{a_0}{b_0}\frac{n^4-1}{n^2} + \frac{4}{5}\frac{n^5-1}{n^3}\right) \text{ for a plane nozzle and}$$

$$\zeta_{fr} = \frac{4}{9}\lambda\frac{l}{D_h}\frac{n^{3/2}-1}{n^{5/2}(n-1)} \text{ for a nozzle of circular or rectangular section.}$$

Losses in the test section

Open test section:

1) circular or rectangular cross section

$$\zeta_{tot} = 0.0845\frac{l_{t.s.}}{D_h} - 0.0053\left(\frac{l_{t.s.}}{D_h}\right)^2 \text{ (Figure 3.8);}$$

2) elliptical cross section

$$\zeta_{tot} = 0.08\frac{l_{t.s.}}{D_h} - 0.0015\frac{l_{t.s.}^2}{a_c \cdot b_c} \text{ (Figure 3.9).}$$

Here $l_{t.s.}$ is the length of the test section while a_c and b_c are lengths of the major and minor semi-axes of the ellipse.

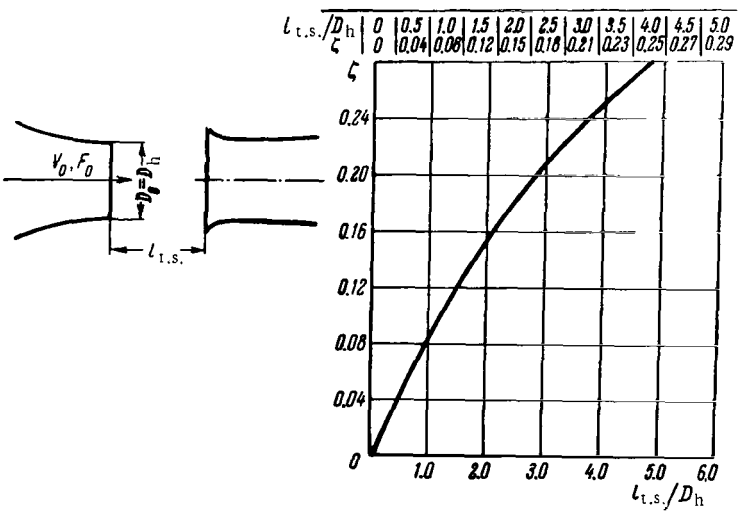

FIGURE 3.8. Resistance coefficient of open circular or rectangular test sections as function of the test-section dimensions.

* The angle α is the convergence angle of a conical nozzle equivalent to the given curvilinear nozzle.

In a closed test section the frictional losses can be determined from the values of Re and ε.

Resistance of a model in the test section

The resistance of the model and its supports in the test section forms a considerable part of the total resistance of the wind tunnel, and depends on the degree of blockage $\frac{S_{med}}{F_{t.s.}}$ by the model and the supports, and their streamlining. The resistance can be found from the expression

$$\zeta = c_x \frac{S_{med}}{F_{t.s.}} \frac{1}{\left(1 - \frac{S_{med}}{F_{t.s.}}\right)^3},$$

where c_x is the drag of the model and its supports, given in handbooks of aerodynamics as a function of the Reynolds number (calculated in terms of the velocity in the tunnel); S_{med} is the area of the median section of the model and its supports.

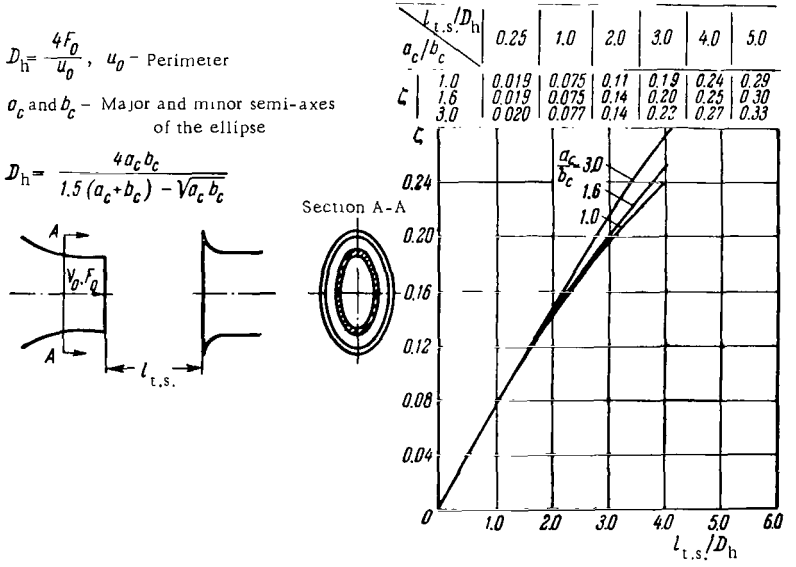

FIGURE 3.9 Variation of resistance coefficient of an open elliptical test section with test-section dimensions.

Losses in the diffuser

The resistance coefficient of a subsonic diffuser is arbitrarily separated into the coefficient of the resistance due to cross-section enlargement, and

the friction coefficient, i.e.,

$$\zeta = \zeta_{enl} + \zeta_{fr},$$

where

$$\zeta_{enl} = \varphi_{enl}\, k\left(1 - \frac{F_0}{F_1}\right)^2.$$

Here φ_{enl} is the shock coefficient, i.e., the ratio of the expansion losses to the theoretical losses at a sudden change from a narrow to a wide flow section:

$$\varphi_{enl} = \frac{\Delta H}{\frac{\rho}{2}(V_0 - V_1)^2},$$

V_0 and V_1 are the mean velocities in the inlet and exit sections respectively; k is a correction factor for the nonuniformity of the velocity distribution at the diffuser inlet or for the boundary-layer regime; and $\left(1 - \frac{F_0}{F_1}\right)^2 = d$ is a coefficient which takes into account the effect of the diffuser divergence.

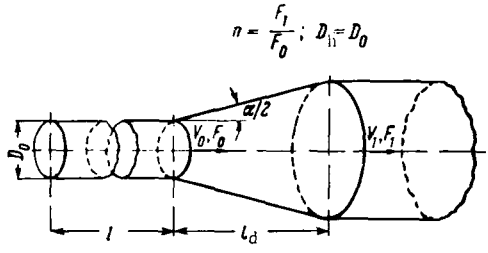

FIGURE 3.10. Conical diffuser.

For conical or plane diffusers with divergence angles α between 0° and 40° (Figure 3.10)

$$\varphi_{enl} = 3.2\left(\operatorname{tg}\frac{\alpha}{2}\right)^{1/4}.$$

In a diffuser with square or rectangular cross sections in a pyramidal or wedge-shaped diffuser (Figure 3.11), for which $0° < \alpha < 25°$,

$$\varphi_{enl} = 6.2\left(\operatorname{tg}\frac{\alpha}{2}\right)^{1/4}.$$

The coefficient k is determined from Figure 3.12 as a function of $\frac{V_{max}}{V_0} = f\left(\frac{l}{D_h}\right)$.

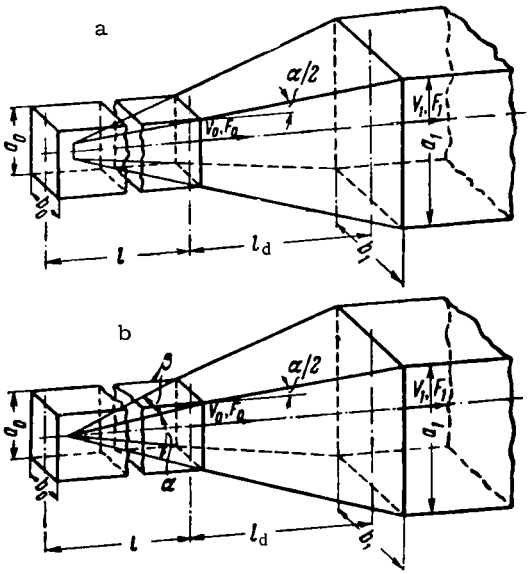

FIGURE 3.11. Diffusers with square and rectangular cross sections. a — wedge-shaped; b — pyramidal.

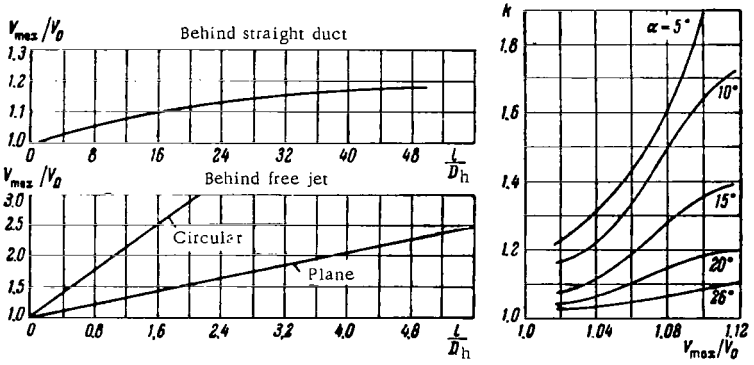

FIGURE 3.12. Effect of velocity nonuniformity at diffuser inlet (V_{max}/V_0) on diffuser resistance (coefficient ζ).

The friction coefficient for conical and wedge-shaped diffusers (with square or rectangular cross sections) is

$$\zeta_{fr} = \frac{\lambda}{8} ef,$$

where λ, e and f are found in the same way as for a nozzle. For a pyramidal diffuser (with square or rectangular cross sections) the resistance coefficient is

$$\zeta_{fr} = \frac{\lambda}{16} e(f+f'),$$

where

$$f=\frac{1}{\sin\alpha/2},\quad f'=\frac{1}{\sin\beta/2},\quad e=1-\left(\frac{F_0}{F_1}\right)^2,$$

Here α and β are respectively the divergence angles of the pyramidal diffuser in the two orthogonal planes. The additional resistance of slots, provided in the diffuser wall in order to dampen pulsations, can be determined from Figure 3.13. The flow area of the slots is assumed to be about 25 to 35% of that of the diffuser inlet, and the flow velocity past the slots as equal to the velocity in the test section; the velocity immediately downstream of the slots is taken as 0.8 times the velocity immediately upstream.

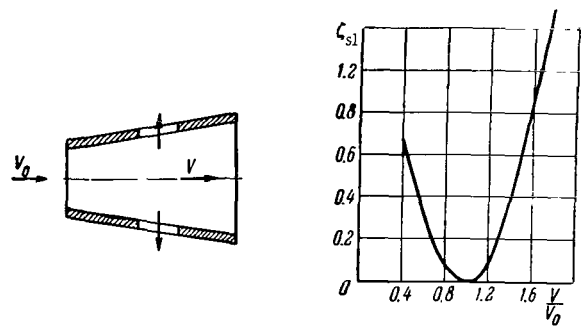

FIGURE 3.13. Dependence of resistance coefficient ζ_{sl} of slots on velocity immediately downstream.

Resistance of corners

The corners of wind tunnels are fitted with turning vanes, which may be circular or airfoil sections, subtending arcs of 95 to 107°. The corners may be curved or sharp. For the corner shapes and radii, and the numbers and types of vanes generally used, the resistance coefficients are given in Table 4, expressed in terms of the velocity head at the corner inlet.

Resistance of the fan installation

The resistance of the fan installation (motor casing, shaft bearings, etc.) can be determined in the same way as the resistance of the model in the test section, using the expression

$$\zeta_f=c_{xf}\frac{S_{med\,f}}{F_f}\frac{1}{\left(1-\frac{S_{med\,f}}{F_f}\right)^3}.$$

TABLE 4. Resistance coefficients for corners of different types ($Re \geq 0.2\ 10^6$; $\Delta = 0.0003$).

Type of corner	Cross-section shape	Type of vane	Number of vanes	Radius of curvature of corner	ζ							Remarks
					$\frac{r}{b_0} = 0$	01	02	03	04	05	06	
90°	square			varying	1.3	0.8	0.5	0.36	0.3	0.27	0.25	
90°	rectangular	airfoil section	$2.12\frac{b_0}{r}-1$	"	0.33	0.23	0.17	0.16	0.17	0.22	0.31	
90°	"	"	$1.4\ \frac{b_0}{r}$	"	0.33	0.23	0.15	0.11	0.13	0.19	0.30	
90°	"	thin, curved to subtend arc	5 — 7	r_0			0.15					$\alpha_d = 45 \div 50°$
90°	circular	airfoil section, uniform gap width	$\frac{3D_0}{t}-1$	$\frac{r}{D_0} = 0.18$			0.26					$\frac{t}{D_0} = 0.25$ t — vane chord $\alpha_d = 48°$
90°	"	"		0			0.33					"

D_0 — corner inlet-section diameter

h — corner height

r — radius of curvature of corner, when $r_1 = r_0$

b_0 — width of corner inlet

Here c_{xf} is the drag coefficient of the fan installation, expressed in terms of the velocity immediately upstream (generally c_{xf} is 0.25), $S_{med\,f}$ is the median section of the fan installation ($S_{med\,f}$ is usually about 0.4 F_f), and F_f is the flow area at the fan.

The resistance coefficient of the safety net in front of the fan is $\zeta = 0.02$.

Resistance of the return duct. When the return duct is cylindrical its resistance is entirely frictional, and can be calculated from the frictional-resistance formulas above. When the return duct is of variable cross section its resistance is calculated in the same way as for a diffuser.

Resistance of radiators

The total resistance of a radiator, installed in the return duct for cooling the tunnel air, consist of:

1) losses at the inlet to the radiator tubes;
2) losses due to friction of the air against the tube walls;
3) losses due to sudden expansion of the air leaving the tubes.

For a honeycomb coefficient (Figure 3.14) with hexagonal or round tubes, the resistance coefficient is

$$\zeta_{rad} = \frac{\Delta H}{\rho V_1^2/2} = \lambda\left(0.3 + \frac{l}{d_h}\right)\left(\frac{F_1}{F_0}\right)^2 + \left(\frac{F_1}{F_0} - 1\right)^2,$$

where V_1 is the flow velocity in the tunnel immediately upstream of the radiator, $\frac{F_0}{F_1}$ is the flow-area ratio of the radiator, l is the length of the radiator tubes (radiator depth), d_h is the hydraulic diameter of the radiator tubes, λ is the resistance coefficient per unit length of a radiator tube (λ depends on the local Reynolds number $\mathbf{Re}^* = \frac{V_0 k}{\nu}$ where V_0 is the flow velocity in the radiator tubes), and k is the mean height of the roughness peaks of the tube walls.

The relationship $\lambda = f(\mathbf{Re}^*, \varepsilon)$ is shown in Figure 3.14. For $35 < \mathbf{Re}^* < 275$,

$$\lambda = 0.375(\mathbf{Re}^*)^{-0.1}\varepsilon^{0.4}.$$

For $275 \leqslant \mathbf{Re}^* \leqslant 500$, λ is practically independent of the Reynolds number:

$$\lambda = 0.214\varepsilon^{0.4}.$$

For a hot radiator, the resistance coefficient is higher by an amount

$$\Delta\zeta = \left(1.7 + \lambda\frac{l}{d_h}\right)\theta,$$

where $\theta = \frac{T_1 - T}{T}$ is the ratio of the difference of the air temperatures at the outlet and inlet to the absolute air temperature at the inlet. For the

radiators shown in Figures 3.15 and 3.16, the resistance coefficient is

$$\zeta = \left(n\gamma + \lambda \frac{l}{d_h}\right)\left(\frac{F_1}{F_0}\right)^2.$$

Here $\gamma = 1.5\left(1 - \frac{F_0}{F_0'}\right)^2$ is a coefficient which takes into account the losses due to the constriction and expansion of the air stream between the tubes,

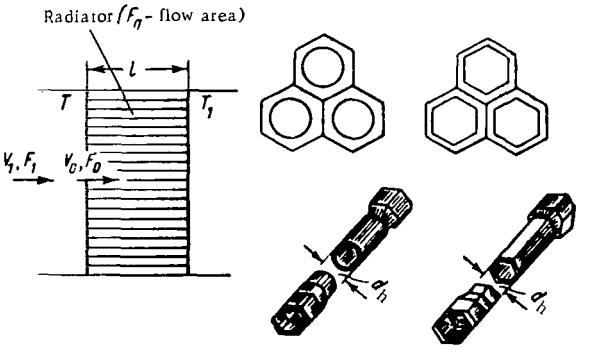

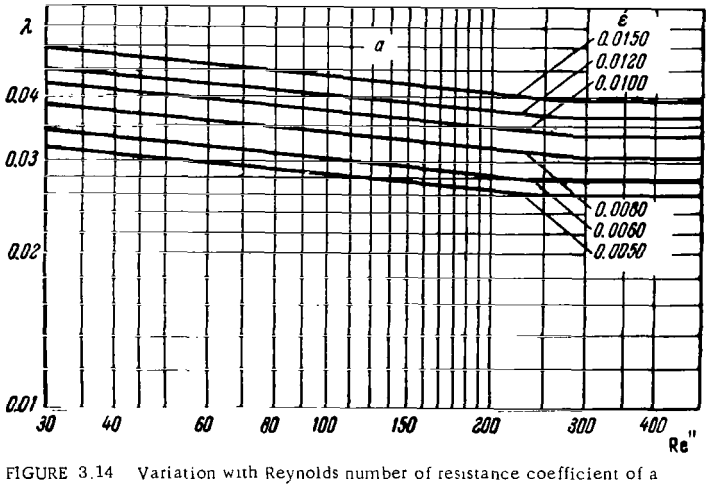

FIGURE 3.14 Variation with Reynolds number of resistance coefficient of a honeycomb radiator.

F_0 is the total projected area of the gaps between the radiator tubes at the point where the gap is narrowest, F_0' is the total projected flow area between two adjacent plates, F_1 is the overall area of the radiator front, and n is the number of rows of radiator tubes.

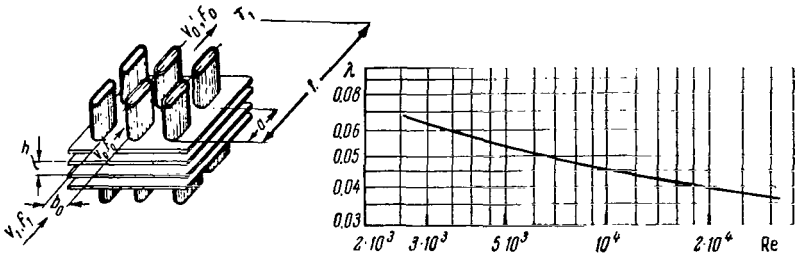

FIGURE 3.15 Variation with Reynolds number of the resistance coefficient of tube-and-plate radiators.

The friction coefficient λ must be calculated in terms of the Reynolds number $\mathrm{Re}=\frac{V_0 d_h}{\nu}$, where $d_h=\frac{2hb_0}{h+b_0}$. For tube-and-plate radiators

$$\lambda=\frac{0.77}{\sqrt[3]{\mathrm{Re}}} \quad (3{,}000<\mathrm{Re}<25{,}000) \quad \text{(see Figure 3.15).}$$

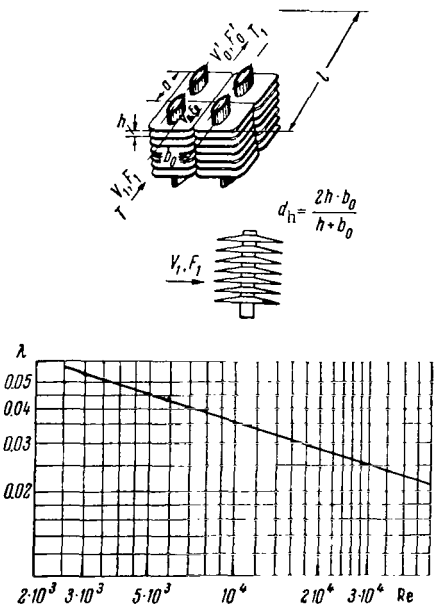

FIGURE 3.16. Variation with Reynolds number of resistance coefficient of ribbed-tube radiators.

For ribbed-tube radiators:

$$\lambda=\frac{0.98}{\sqrt[3]{\mathrm{Re}}} \quad (4{,}000 \leqslant \mathrm{Re} \leqslant 10{,}000)$$

and

$$\lambda = \frac{0.21}{\sqrt[6]{\mathrm{Re}}} \quad \text{for} \quad \mathrm{Re} > 10{,}000 \quad \text{(see Figure 3.16).}$$

The additional resistance of hot tube-and-plate and ribbed-tube radiators is found in the same way as for honeycomb radiators.

Resistance of settling chambers fitted with turbulence screens and honeycombs

The resistance of the settling chamber is frictional. For a honeycomb it is found in the same way as for a honeycomb radiator.

The resistance coefficient of turbulence screens is

$$\zeta = \sum_{1}^{n} \left[1.3\left(1 - \frac{F_0}{F_1}\right) + \left(\frac{F_1}{F_0} - 1\right)^2\right],$$

where F_1 is the cross-sectional area of the tunnel, F_0 is the flow area, and n is the number of turbulence screens selected to obtain $\zeta = 2.0$.

Head and capacity ratings for a wind-tunnel fan

Table 5 shows the values of the resistance coefficients, referred to the velocity head in the test section, of the various elements of a wind tunnel for a maximum test-section velocity of 100 m/sec (Figure 3.17).

The head and capacity of the fan required for this tunnel can be calculated from the data given in Table 5. The required fan head is

$$H = \sum_{i} \zeta_i \rho \frac{V^2}{2} = \rho \cdot \frac{V^2}{2} \sum_{i} \zeta_i \quad \mathrm{kg/m^2}$$

where V is the flow velocity in the test section and ζ_i is the resistance coefficient of a tunnel element, referred to the velocity head in the test section.

The required fan capacity is

$$Q = F_{t.s.} V \quad \mathrm{m^3/sec}$$

The power of the fan motor is

$$N = \frac{QH}{102\eta} = \frac{\rho}{2} \cdot \frac{F_{t.s.} V^3}{102\eta} \sum \zeta_i \quad \mathrm{kw}$$

where η is the fan efficiency (usually about 0.65 to 0.75).

TABLE 5

Tunnel element			ζ*
Nozzle			0.01
Open test section	Circular or elliptical	Test section	0.11
		Slotted diffuser	0.15
	Rectangular	Test section	0.11
		Slotted diffuser	0.10
Closed test secton	Circular or elliptical	Test section	0.014
		Diffuser	0.10
	Rectangular	Test section	0.016
		Diffuser	0.10
Model in a test section			0.030
Four corners			0.05
Fan			0.02
Radiator			0.02
Settling chamber and return circuit			0.05
Honeycomb			0.02
Turbulence screens			0.08

* Referred to velocity head in the test section: $\zeta = \zeta_i \left(\frac{F_{t.s.}}{F_i}\right)^2$.

The energy ratio λ of the tunnel (see p. 24), which depends on the tunnel resistance and the fan efficiency, is

$$\lambda = \frac{\eta}{\Sigma \zeta_i}.$$

Calculation of velocities, pressures, and temperatures

The velocities, pressures, and temperatures must be calculated in order to forecast the loads on tunnel elements, the operating conditions of equipment installed in the tunnel, and the extent to which air cooling is necessary. The velocity distribution varies along the tunnel in accordance with the changing tunnel cross section since the mass flow rate is constant throughout the tunnel.

The static-pressure and velocity-head distributions at various sections of the tunnel are determined from Bernouilli's law

$$p_i + \rho \frac{V_i^2}{2} = p_{i+1} + \rho \frac{V_{i+1}^2}{2} + \zeta \rho \frac{V_i^2}{2},$$

where the subscripts i, $i+1$ correspond to the inlet and exit respectively of the tunnel element considered, whose total-resistance coefficient is ζ.

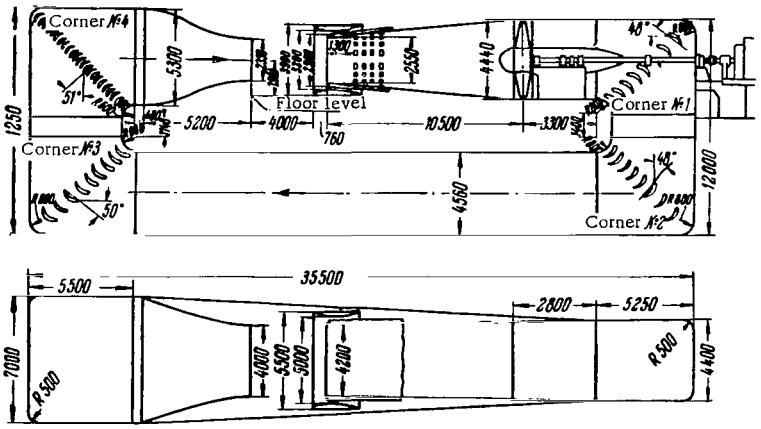

FIGURE 3.17. Geometry of subsonic wind tunnel.

Since the velocity is low, compressibility can be neglected, and we can assume that $\rho_i = \rho_{i+1}$.

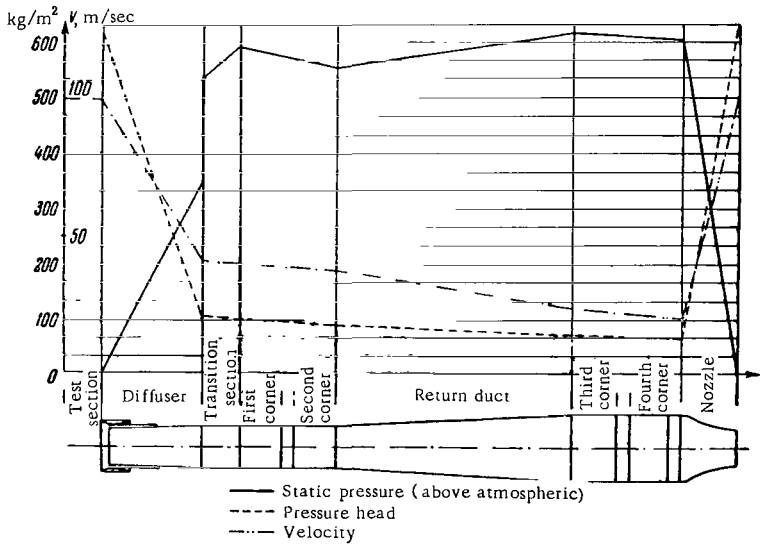

FIGURE 3.18 Distribution of velocities and pressures in a closed-circuit wind tunnel (V_{max} = 100 m/sec).

Pressures in tunnels with open test sections are best determined by beginning with the test section, where the total pressure is

$$p_a + p\frac{V_{t.s.}^2}{2};$$

the calculations are best begun with the fan outlet for tunnels with closed test sections. Figure 3.18 shows the distribution of velocities and pressures for the tunnel shown in Figure 3.17.

The temperatures in low-speed closed-circuit tunnels can be calculated by assuming that the entire power of the drive is converted into heat. In tunnels with open test sections and slots in the diffuser it should be assumed that about 10% of the tunnel air will be drawn from the room which surrounds the tunnel.

§ 10. GAS DYNAMICS OF SUPERSONIC TUNNELS

The design problem of subsonic and supersonic wind tunnels consists in calculating the pressure, density and temperature in the test section in terms of the velocity, and in determining the capacity, compression ratio, and power of the compressor needed (in a continuous-operation tunnel) to provide the required Reynolds and Mach numbers in the test section. In an intermittent-operation tunnel, corresponding calculations must yield the minimum reservoir volume and pressure to obtain the required values of **Re** and **M** during the operating period t.

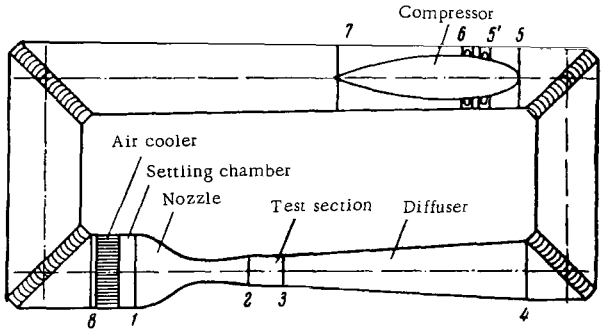

FIGURE 3.19. Supersonic wind tunnel.

The design of supersonic tunnels differs considerably from that of subsonic tunnels by virtue of the large variations of pressure, density, and temperature throughout the tunnel. Furthermore, the losses due to the resistance of tunnel elements are small compared with the losses in the diffuser and in the test section when the model is installed.

Design calculations of continuous-operation tunnels

Consider a closed-circuit continuous-operation wind tunnel (Figure 3.19). The calculations for supersonic tunnels are most easily carried out if the pressure and temperature in any part of the tunnel are expressed in terms

of the total pressure p_{01} and stagnation temperature in the settling chamber, which, in tunnels of this type, approximate the pressure and temperature respectively of the still air in the tunnel when the fan is at rest. The values of the velocity λ_2 [referred to the critical speed] at the test-section inlet, and of the corresponding Mach number $M = M_2$, are assumed to be given.

We designate the ratio of total pressures at the inlet and outlet of any tunnel element as its coefficient of pressure recovery $\nu_i = \frac{p_{0i+1}}{p_{0i}}$ while the corresponding ratio of stagnation temperatures is $\vartheta_i^2 = \frac{T_{0i+1}}{T_{0i}}$.

The ratio of stagnation densities is

$$\frac{\rho_{0i+1}}{\rho_{0i}} = \frac{\nu_i}{\vartheta_i^2}.$$

The static temperatures, pressures, and densities are found from the expressions

$$\frac{T_i}{T_{0i}} = 1 - \frac{\varkappa - 1}{\varkappa + 1}\lambda_i^2,$$

$$\frac{p_i}{p_{0i}} = \left(1 - \frac{\varkappa - 1}{\varkappa + 1}\lambda_i^2\right)^{\frac{\varkappa}{\varkappa - 1}},$$

$$\frac{\rho_i}{\rho_{0i}} = \left(1 - \frac{\varkappa - 1}{\varkappa + 1}\lambda_i^2\right)^{\frac{1}{\varkappa - 1}}$$

The velocities at the inlet section F_i and outlet section F_{i+1} of any tunnel element are related to each other by the equation of continuity

$$q(\lambda_{i+1}) = \frac{\vartheta_i^2}{\nu_i}\frac{F_i}{F_{i+1}} q(\lambda_i),$$

where

$$q(\lambda_i) = \left(\frac{\varkappa + 1}{2}\right)^{\frac{1}{\varkappa - 1}} \lambda_i \left(1 - \frac{\varkappa - 1}{\varkappa + 1}\lambda_i^2\right)^{\frac{1}{\varkappa - 1}}$$

The function $q = f(\lambda)$ is given in Figure 3.20 and in Table 6 (for $\varkappa = 1.4$).

Table 6. Values of $q(\lambda)$

λ	$q(\lambda)$	λ	$q(\lambda)$	λ	$q(\lambda)$	λ	$q(\lambda)$
0	0	0.65	0.8541	1.25	0.9271	1.85	0.3527
0.05	0.0787	0.70	0.8920	1.30	0.8965	1.90	0.2999
0.10	0.1570	0.75	0.9246	1.35	0.8629	1.95	0.2494
0.15	0.2343	0.80	0.9515	1.40	0.8213	2.00	0.2021
0.20	0.3101	0.85	0.9726	1.45	0.7775	2.05	0.1586
0.25	0.3841	0.90	0.9877	1.50	0.7902	2.10	0.1196
0.30	0.4555	0.95	0.9967	1.55	0.6802	2.15	0.0854
0.35	0.5242	1.00	1.0000	1.60	0.6278	2.20	0.0569
0.40	0.5895	1.05	0.9965	1.65	0.5737	2.25	0.0342
0.45	0.6512	1.10	0.9877	1.70	0.5182	2.30	0.0174
0.50	0.7088	1.15	0.9728	1.75	0.4625	2.35	0.0065
0.55	0.7621	1.20	0.9528	1.80	0.4070	2.40	0.0012
0.60	0.8105						

Let us now consider the changes in velocity, pressure, and air temperature in different parts of the tunnel.

Settling chamber and nozzle (ν_1). The air flow in the settling chamber and nozzle is approximately adiabatic. The losses in the nozzle are relatively small in comparison with those in other tunnel elements, and are due mainly to friction. At supersonic velocities, the nozzle losses $\delta = 1 - \nu$ are less than 0.01 to 0.02, i.e., the total-pressure loss is about 1 to 2%. It is safe to assume in calculations that $\nu_1 = 0.98$.

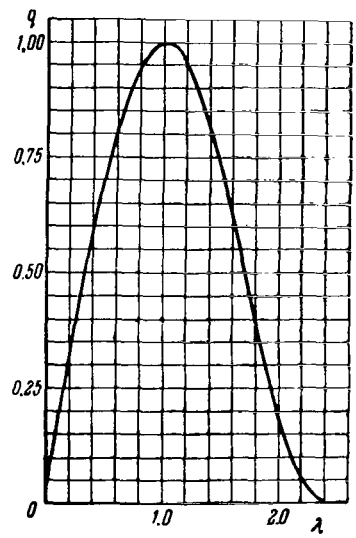

FIGURE 3.20 Values of $\tau(\lambda)$.

Since heat transfer through the walls of the settling chamber and nozzle (as well as of other tunnel elements) is negligible, we can write

$$\vartheta_1^2 = \frac{T_s}{T_0} = 1.$$

Test section and model (ν_2). Total-pressure losses in the test section are due to friction at the rigid walls and to the resistance of the model and its supports. In an open test section, a large resistance is caused by the intense turbulence at the free jet boundary.

The coefficient of pressure recovery in a closed cylindrical test section can be calculated from the ratio of the velocities at its inlet and outlet:

$$\nu_2 = \frac{q(\lambda_2)}{q(\lambda_3)}.$$

At velocities close to the speed of sound

$$\nu_2 \approx 1 - \frac{\varkappa + 1}{2} \Delta^2,$$

where Δ is found from $\lambda_2 = \lambda_3(1-\Delta)$. The relation between the λ_3 and Δ is given approximately by the expression

$$(1-\lambda_3^2)\Delta + (2-\lambda_3^2)\Delta^2 = \frac{\varkappa}{\varkappa+1}\lambda_3^2\left(\zeta_2\frac{l_{t.s.}}{D_{t.s.}} + c_x\frac{F_{mod}}{F_{t.s.}}\right)^*.$$

For given values of $\frac{l_{t.s.}}{D_{t.s.}}$, ζ_2 and c_x we obtain the relationships between λ_3 and Δ (or, which is the same, between λ_3 and λ_2) and can find $q(\lambda_2)$, $q(\lambda_3)$ and ν_2.. In supersonic tunnels, $\frac{l_{t.s.}}{D_{t.s.}} = 1$ to 3. The resistance coefficient of the test section is calculated in the same way as for subsonic tunnels. For a closed test section $\zeta_2 = 0.014$, while for an open test section $\zeta_2 = 0.1$.

Thus, the parameter $\zeta_2\frac{l_{t.s.}}{D_{t.s.}}$ varies between 0.014 and 0.042 (0.03 on the average). The drag coefficient c_x of the model and supports is maximum at velocities close to $M = 1$ ($c_x = 0.2$). The ratio $\frac{F_{mod}}{F_{t.s.}} = \frac{F_{mod}}{F_2}$ is generally between 0.1 and 0.15. In designing the test sections of supersonic tunnels, we can assume

$$\zeta_2\frac{l_{t.s.}}{D_{t.s.}} = \zeta_2\bar{l} = 0.03,$$
$$c_x\frac{F_{mod}}{F_{t.s.}} = 0.02,$$

where $\bar{l} = l_{t.s}/D_{t.s.}$.

If the walls have perforations or slots, the resistance of the test section is higher. The increase in resistance depends on the degree of perforation, i.e., the ratio of the area of the perforations to the total wall area of the test section; this ratio varies from about 0.10 for $M = 1.2-1.3$ to about 0.40 for $M = 1.7-1.8$. The resistance of a test section with perforated walls can be assumed to be about 50% higher than that of a test section with unperforated walls $\left(\zeta_{2p}\frac{l_{t.s.}}{D_{t.s.}} = 0.045\right)$. The range of the transonic velocities obtainable at the inlet of a closed test section is limited because the model and its supports block the tunnel and thus increase the velocities.

Using the continuity equation, the dependence of the test-section inlet velocity (λ_2) on the cross-sectional area (F_{mod}) of the model can be found by assuming that the velocity at the median section of the model is sonic ($\lambda_3 = 1$). In this case,

$$1 - \frac{F_{mod}}{F_{t.s.}} = q(\lambda_2) = q(1-\Delta) \approx 1 - \frac{\varkappa+1}{2}\Delta^2.$$

* This formula is derived from the momentum equation:

$$\rho_2 V_2 F_2 (V_3 - V_2) = (p_2 - p_3)F_2 - c_x\frac{\rho_2 V_2^2}{2}F_{mod} - \zeta_2\frac{\rho_2 V_2^2}{2}\frac{l}{D}F_2$$

By dividing both sides by $\rho_2 V_2 F_2 a_* = \rho_3 V_3 F_3 a_*$ and substituting

$$\frac{p}{\rho} = \frac{\varkappa+1}{2\varkappa}a_*^2\left(1 - \frac{\varkappa-1}{\varkappa+1}\lambda^2\right)$$

It thus follows that the referred velocity at the test-section inlet will be less than unity by an amount

$$\Delta = \sqrt{\frac{2}{\varkappa+1}\frac{F_{\text{mod}}}{F_{\text{t.s.}}}}.$$

Expressing the referred velocity λ_2 in terms of the Mach number, we obtain (neglecting Δ^2 by comparison with Δ)

$$\Delta \mathbf{M} = 1 - \mathbf{M}_2 = \sqrt{\frac{\varkappa+1}{2}\frac{F_{\text{mod}}}{F_{\text{t.s.}}}}.$$

For air ($\varkappa = 1.4$)

$$\Delta \mathbf{M} = 1.1\sqrt{\frac{F_{\text{mod}}}{F_{\text{t.s.}}}}.$$

If the area of the median section comprises 2% of the cross section of the tunnel, then $\Delta \mathbf{M} = 0.15$, i. e., the maximum velocity at the inlet of the cylindrical test section will be 0.85 times the velocity of sound*.

In modern transonic tunnels this obstacle to the increase of the free-stream Mach number is overcome, as we have seen, by perforating the walls, or by forced extraction of air through the walls.

For an open test section $p_2 = p_3$, and we obtain from the momentum equation

$$\lambda_3 = \lambda_2\left[1 - \frac{1}{2}\left(c_x\frac{F_{\text{mod}}}{F_{\text{t.s.}}} + \zeta_2\bar{l}\right)\right],$$

where $\zeta_2 = 0.1$ is the resistance coefficient of the free jet.

It should be noted that $\lambda_3 < \lambda_2$, i. e., the velocity decreases along an open test section.

The pressure-recovery coefficient is

$$\nu_2 = \frac{p_{03}}{p_{02}} = \left[\frac{1 - \frac{\varkappa-1}{\varkappa+1}\lambda_2^2}{1 - \frac{\varkappa-1}{\varkappa+1}\lambda_3^2}\right]^{\frac{\varkappa}{\varkappa-1}}.$$

Assuming that in an open test section $\lambda_3 = \lambda_2(1-\Delta)$ we have approximately**

$$\nu_2 = 1 - \frac{\frac{2\varkappa}{\varkappa+1}\lambda_2^2\Delta}{1 - \frac{\varkappa-1}{\varkappa+1}\lambda_2^2};$$

when $\lambda_2 = 1$

$$\nu_2 = 1 - \varkappa\Delta$$

* The value $\Delta \mathbf{M}$ is called the velocity induction correction of the tunnel, and should be taken into account when testing models at transonic velocities in a closed test section

** For cylindrical closed test sections the outlet velocity is

$$\lambda_3 = \frac{\lambda_2}{1-\Delta}.$$

or

$$\nu_2 = 1 - \frac{\varkappa}{2}\left(c_x \frac{F_{\text{mod}}}{F_{\text{t.s.}}} + \zeta_2 \bar{l}\right).$$

For $\zeta_2 = 0.1; c_x \frac{F_{\text{mod}}}{F_{\text{t.s.}}} = 0.02;\ \bar{l} = 2$, we obtain

$\nu_2 = 0.846$ (model in test section)
$\nu_2 = 0.86$ (no model in test section).

For open test sections we can assume that $\nu = 0.85$.

Losses in the diffuser

The value of the pressure-recovery coefficient ν_3 in a diffuser is inferred from test results of diffusers of design similar to that projected. The pressure-recovery coefficient can be estimated approximately from the total pressure and equivalent test-section velocity, using the data of Figure 3.21.

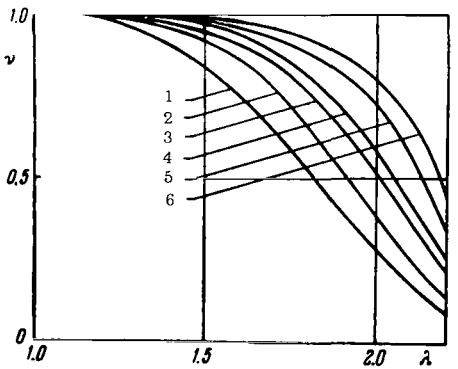

FIGURE 3.21. Theoretical pressure-recovery coefficient of a diffuser as a function of total pressure and referred velocity. 1 — normal shock; 2 — oblique shock; 3 — normal+oblique shocks; 4 — two oblique shocks; 5 — three oblique shocks; 6 — four oblique shocks.

Losses in the return duct

In the section between the diffuser and compressor the velocity is low, so that changes in the air density and temperature may be ignored. The change in total pressure is

$$p_{0i} - p_{0i+1} = \zeta_i \rho_{0i} \frac{V_i^2}{2}$$

or

$$\nu_i = 1 - \zeta_i \frac{V_i^2}{2} \frac{\rho_{0i}}{p_{0i}}.$$

But

$$\frac{p_{0i}}{\rho_{0i}} = gRT_{0i} = \frac{\varkappa+1}{2\varkappa} a_*^2,$$

whence

$$\nu_i = 1 - \zeta_i \frac{\varkappa}{\varkappa+1} \lambda_i^2.$$

The values of ζ_i are calculated by the method used for low-speed tunnels.

For the duct between the diffuser and the compressor (two corners + second diffuser + two cylindrical parts, etc.), the value of ζ_i, expressed in terms of the velocity head in these elements, is about 0.75.

The respective velocities are calculated using the mass flow-rate equation

$$\lambda_{i+1} = \lambda_i \frac{F_i}{F_{i+1}} \frac{1}{\nu_i}.$$

For velocities below 45 m/sec λ is generally less than 0.15.

In these conditions, the total-pressure losses between the diffuser and the compressor are, for air,

$$\nu_4 = 1 - 0.75 \frac{1.4}{2.4} 0.15^2 = 0.99.$$

A considerable velocity increase takes place between sections 5 and 5' (Figure 3.19) since the compressor rotor occupies a considerable part of the tunnel cross section. The velocity increase can be calculated from the equation

$$q(\lambda_{i+1}) = \frac{\vartheta_i^2}{\nu_i} \frac{F_i}{F_{i+1}} q(\lambda_i),$$

by assuming that

$$\vartheta_5 = \nu_5 = 1.$$

Selection of compressor. The total pressure immediately upstream of the compressor depends on the resistance of the tunnel return duct between the compressor and the settling chamber*. In the settling chamber and air cooler λ is small (generally below 0.1), so that we can assume that

$$\frac{q(\lambda_1)}{q(\lambda_8)} = \frac{\lambda_1}{\lambda_8}.$$

Setting $\nu_8 = 1$, we have $\lambda_8 = \frac{1}{\vartheta_8^2} \frac{F_1}{F_8} \lambda_1$. Here $\vartheta_8^2 = \frac{T_{01}}{T_{08}}$ is the stagnation-temperature ratio across the air cooler.

* For Mach numbers below 2, the total-pressure recovery coefficient ν_7 in this part, allowing for the resistance of radiator, corners, honeycomb, and turbulence screens, is about 0.98

Assuming that the air cooler removes all the heat generated from the mechanical-energy output of the compressor, we have

$$T_{06} - T_{05} = T_{08} - T_{01},$$

but since $T_{05} = T_{01}$, and $\frac{T_{05}}{T_{05}} = \vartheta_5^2$, it follows that $\vartheta_5 = \frac{1}{\vartheta_8}$.

Here, $\vartheta_5^2 = \varepsilon^{\frac{\varkappa-1}{\eta\varkappa}}$ where ε is the compression ratio of the compressor (which depends on the resistance of the entire tunnel) and η is the compressor efficiency. The compression ratio must be equal to the total-pressure ratio between the beginning and end of the tunnel:

$$\varepsilon = \frac{p_{06}}{p_{05}} = \frac{1}{\nu_1\nu_2 \ldots \nu_7} = \frac{1}{\nu},$$

where ν is the pressure-recovery coefficient for the entire tunnel. The compression ratio is found to a first approximation by assuming that $\nu_8 = \nu_7 = \nu_6 = 1$. Using the value of ε thus determined we calculate λ_8 from the expressions $\vartheta_5^2 = \varepsilon^{\frac{\varkappa-1}{\eta\varkappa}}$, $\vartheta_8 = \frac{1}{\vartheta_5}$ and $\lambda_8 = \frac{1}{\vartheta_8^2}\frac{F_1}{F_8}\lambda_1$, and also determine ν_7 and ν_6 from which a more exact value of ε is then calculated. The mass flow rate at the inlet of the compressor is

$$\frac{Q}{\rho_5'} = F_5'\lambda_5' a_{*1}.$$

Expressing Q in terms of the referred velocity in the test section and the total pressure and stagnation temperature in the settling chamber, taking into account that

$$\rho_2 = \rho_0\left(1 - \frac{\varkappa-1}{\varkappa+1}\lambda_2^2\right)^{\frac{1}{\varkappa-1}} = \rho_0 q(\lambda_2)\left(\frac{2}{\varkappa+1}\right)^{\frac{1}{\varkappa-1}} \text{ and } \rho_0 = \frac{p_0}{gRT_0},$$

we obtain

$$Q = F_2 q(\lambda_2)\frac{p_{01}a_{*1}}{gRT_0}\left(\frac{2}{\varkappa+1}\right)^{\frac{1}{\varkappa-1}}.$$

The power of the compressor will thus be

$$N = \frac{1}{102}\frac{\varkappa}{\varkappa-1}\left(\frac{2}{\varkappa+1}\right)^{\frac{1}{\varkappa-1}} F_2 q(\lambda_2)\left(\varepsilon^{\frac{\varkappa-1}{\eta\varkappa}} - 1\right)p_{01}a_{*1}$$

In hermetically sealed tunnels, it is necessary to take into account the variation with test-section velocity of the total pressure in the settling chamber. Let the initial pressure and temperature at zero flow be p_{in} and T_{in}; assuming that $T_{in} = T_{01}$, we have

$$p_{01} = \frac{W}{\sum(\rho_i/\rho_{0i})W_i}p_{in},$$

where W is the volume of the tunnel, and W_i the volume of the i-th element of the tunnel where the density is ρ_i.

Figure 3.22 shows the compressor power required per square meter of the test-section flow area as a function of the referred velocity in the test section. It is assumed that $p_{01} = 1$ atm and $T_{01} = 288°\,K$, and examples are given of different systems of pressure recovery in the diffuser.

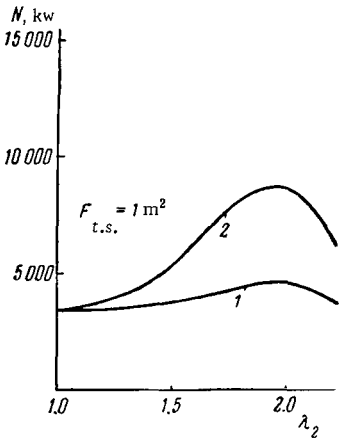

FIGURE 3.22. Variation of rated compressor power with referred velocity in the test section of a wing tunnel ($F_{t.s.} = 1m^2$). 1 — normal + oblique shock; behind the shocks $\nu = 0.93$; 2 — normal shock; behind the shock $\nu = 0.93$

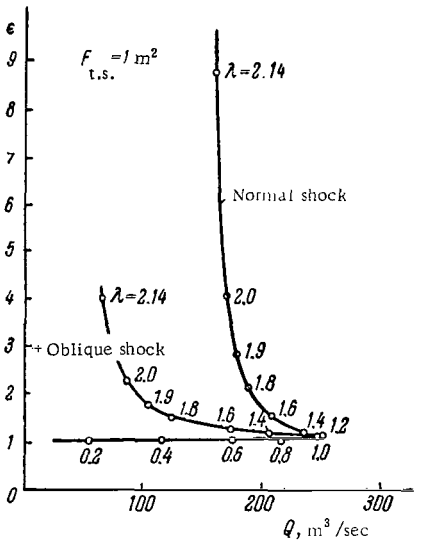

FIGURE 3.23 Theoretical variation of compression ratio with mass flow rate at compressor inlet for different systems of pressure recovery in the diffuser.

For the same initial conditions Figure 3.23 shows the variation of compression ratio ε with mass flow rate at the compressor inlet for different systems of pressure recovery in the diffuser (at $T = 288°\,K$). Figure 3.24 shows how the minimum required compression ratio varies with the mass flow rate and the Mach number of a continuous-operation tunnel /1/*.

Figure 3.25 shows comparative values of the loss coefficients ($\delta_i = 1 - \nu_i$) in different parts of the tunnel. As can be seen, at high test-section velocities the losses are mainly concentrated in the diffuser. The losses throughout the return circuit are negligible; the losses in the test section (or the model-resistance losses in a closed test section) are several times as great as the losses (δ_6) in the return circuit . Thus, in supersonic tunnels attention should be paid to the correct design of the diffuser and the test section.

The relationship between **M** and **Re** in the test section is the main criterion of the testing capacity of the tunnel. The determination of this

* Experimental values for the minimum required compression ratio are given for fixed-geometry diffusers up to **M** = 2.5, and for variable-geometry diffusers at **M** > 2.5 (see /2/).

relationship is the final stage in the tunnel design. The Mach number in the test section is

$$M = \sqrt{\frac{2}{\varkappa+1}}\ \frac{\lambda_2}{\sqrt{1-\frac{\varkappa-1}{\varkappa+1}\lambda_2^2}},$$

and the Reynolds number

$$Re = \frac{\rho_2 b V_2}{\mu^*)} = \frac{b}{\mu}\sqrt{\frac{\varkappa}{gRT_0}}\,p_{01}\ \frac{M}{\left(1+\frac{\varkappa-1}{2}M^2\right)^{\frac{\varkappa+1}{2(\varkappa-1)}}}.$$

For air $\varkappa = 1.4$, and

$$M = 0.91\ \frac{\lambda_2}{\sqrt{1-0.166\lambda_2^2}},$$

$$Re = \frac{b}{\mu}\frac{0.07}{\sqrt{T_{01}}}\,p_{01}\ \frac{M}{(1+0.2M^2)^3},$$

where b is a typical linear dimension of the model.

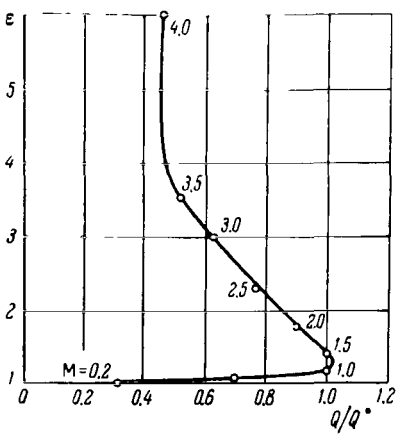

FIGURE 3.24. Variation of the minimum required compression ratio with mass flow rate and Mach number of a continuous-operation tunnel. $\bar{Q}^*$ is the mass flow rate at $M = 1$ in the test section.

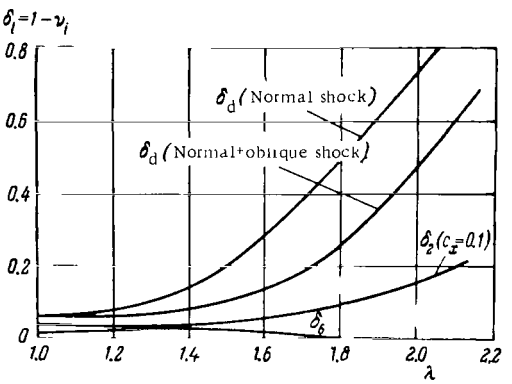

FIGURE 3.25. Comparative values of loss coefficients in different parts of the tunnel.

Design calculation of intermittent-operation tunnels

Pressure-powered tunnels (Figure 3.26). The calculation consists in determining: a) the minimum pressure $p_{0\,min}$ in the storage cylinders necessary to obtain the required Mach and Reynolds numbers in the test

* Here μ is the viscosity coefficient of the air temperature in the test section (see p. 5).

section, and b) the volume W required for given operating duration t and initial pressure p_{in}.

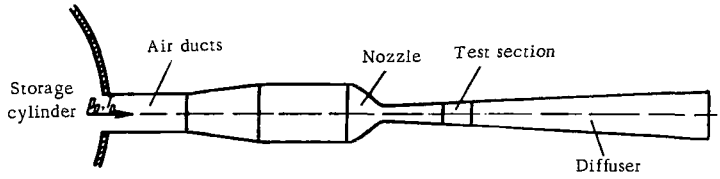

FIGURE 3.26. Intermittent-operation pressure-powered wind tunnel

The values of $p_{0\,min}$ for given Mach numbers are found from the total-pressure losses in the tunnel, in the air duct between the cylinder and the tunnel (ν_a) and from the exhaust losses to atmosphere. The total-pressure losses in the air duct (ν_a), the settling chamber and nozzle (ν_1), the test section (ν_2), and the diffuser (ν_3) are found from the above formulas. The exhaust losses can be found from the expression /3/

$$\nu_4 = \frac{p_a}{p_{0d}} = \left(1 - \frac{\varkappa - 1}{\varkappa + 1}\lambda_d^2\right)^{\frac{\varkappa}{\varkappa - 1}},$$

where p_a is the atmospheric pressure, p_{0d} is the total pressure at the diffuser exit and λ_d is the referred velocity at the diffuser exit.

Assuming that the pressure at the tunnel exit is atmospheric, we obtain

$$p_{0\,min} = \frac{p_a}{\nu_a\nu_1 \ldots \nu_4\left(1 - \frac{\varkappa - 1}{\varkappa + 1}\lambda_4^2\right)^{\frac{\varkappa}{\varkappa - 1}}}.$$

The Reynolds number in the test section is

$$\mathrm{Re} = \frac{b}{\mu}\sqrt{\frac{\varkappa}{gRT_{01}}}\left(\frac{2}{\varkappa + 1}\right)^{\frac{\varkappa + 1}{2(\varkappa - 1)}}\nu_a\nu_1 p_{0\,min} q(\lambda_2).$$

When Re is given

$$p_{0\,min} = \left(\frac{\varkappa + 1}{2}\right)^{\frac{\varkappa + 1}{2(\varkappa - 1)}}\frac{\mu \mathrm{Re}}{q(\lambda_2) b \nu_a \nu_1}\sqrt{\frac{gRT_{01}}{\varkappa}},$$

with $\varkappa = 1.4$, assuming $T_{01} = T_{in}$(in the storage cylinders) we obtain

$$p_{0\,min} = 24.4\frac{\mu \mathrm{Re}}{q(\lambda_2) b \nu_a \nu_1}\sqrt{T_{in}}.$$

The operating duration of the tunnel is

$$t = \frac{2}{\varkappa + 1}\frac{m_{in}}{Q_{in}}\left[1 - \left(\frac{p_{0\,min}}{p_{0in}}\right)^{\frac{\varkappa + 1}{2\varkappa}}\right],$$

where

$$Q_{in} = q(\lambda_2) F_2 \left(\frac{2}{\varkappa+1}\right)^{\frac{1}{\varkappa-1}} \nu_a \nu_1 a_{*in} \frac{p_{0\,min}}{gRT_{01}},$$

m_{in} is the mass of air initially in the cylinders, Q_{in} is the initial mass flow rate of the air.

When the storage-cylinder pressures fall rapidly*, we must replace $\varkappa$ by $\eta\varkappa$ (where $\eta < 1$). For air $\eta \approx 0.8$.

If the storage cylinder pressure falls slowly** the expansion of the stored air is virtually isothermal, because of heat transfer to the walls. We then have

$$Q = \text{const}$$

and

$$t = \frac{m_{in}}{Q}\left[1 - \frac{p_{0\,min}}{p_0}\right].$$

Vacuum-powered tunnel (Figure 3.27). In this case the air mass flow rate is constant:

$$Q = q(\lambda_2) F_2 \left(\frac{2}{\varkappa+1}\right)^{\frac{1}{\varkappa-1}} \nu_a \nu_1 a_{*in} \frac{p_a}{gRT_a}.$$

The operating duration of the tunnel is

$$t = \frac{W}{QgRT_a}(p_{p\,min} - p_{p\,in}),$$

where $p_{p\,min} = p_a \nu_a \nu_1 \ldots \nu_4 \left(1 - \frac{\varkappa-1}{\varkappa+1}\lambda_4^2\right)^{\frac{\varkappa}{\varkappa-1}}$ is the final, and p_{pin} the initial pressure in the evacuated reservoir [whose volume is W].

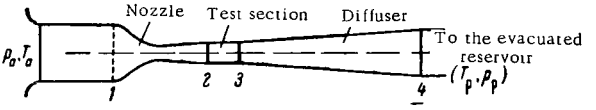

FIGURE 3.27 Vacuum-powered wind tunnel.

Induced-flow tunnel (Figure 3.28). Air from high-pressure cylinders (p_0, T_0) is supplied to an ejector provided with a mixing chamber at whose outlet the total pressure of the compressed air is p_0' and its stagnation temperature is T_0'. The inlet area of the mixing chamber is F'.

* Tunnel-operating duration 1 to 2 min

** Tunnel-operating duration 10 to 15 min

The values of p_{01} and T_{01} of the low-pressure air flowing through the test section are known from the design calculations for the tunnel (from its inlet to the location of the ejector). The total pressure p_{02} at the mixing-chamber outlet (i.e., diffuser inlet in the considered system) is determined from the total-pressure recovery factor of the diffuser.

$$p_{02} = \frac{p_a}{\nu_d}.$$

The compressed-air pressure p_0' can be held constant with the aid of a pressure regulator. It is, however, better to supply high-pressure air to the ejector without throttling by slowly increasing the area F' to compensate for the decrease in total pressure p_0'. For the design calculations of ejectors, cf. /3/.

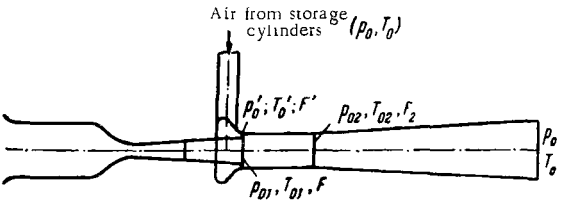

FIGURE 3.28 Induced-flow tunnel

The operating duration of a tunnel in which the area F' (and thus the area F) is adjustable, so that the compressed-air pressure is variable, is in the case of adiabatic expansion*

$$t = \frac{m_{in} q(\lambda_1)}{Q(p_{02}/p_{01} - 1)} \sqrt{\frac{T_{0in}}{T_{01}}} \left\{ \frac{2}{\varkappa - 1} \left[1 - \left(\frac{p_{0\,min}}{p_{0\,in}} \right)^{\frac{\varkappa+1}{2\varkappa}} \right] - \frac{2p_{02}}{(\varkappa - 1)\nu_a p_{0\,in}} \left[\left(\frac{p_{0in}}{p_{0\,min}} \right)^{\frac{\varkappa-1}{2\varkappa}} - 1 \right] \right\},$$

where $Q = Fq(\lambda_1) \frac{p_{01} a_{*1}}{gRT_{01}} \left(\frac{2}{\varkappa + 1} \right)^{\frac{1}{\varkappa - 1}}$ is the mass flow rate of air through the test section p_{0in} is the initial (total) pressure in the storage cylinders, T_{0in} is the initial (stagnation) temperature in the storage cylinders, m_{in} is the mass of air initially contained in the cylinders, and $p_{0\,min} = \frac{p_0'}{\nu_a}$ is the minimum pressure at which the tunnel can operate.

In tunnels operated at constant compressed-air pressure, the operating duration of the tunnel is

$$t = \frac{2}{\varkappa + 1} \frac{m_{in} q(\lambda_1)}{Q\left(\frac{p_{02}}{p_{01}} - 1\right)} \sqrt{\frac{T_{0in}}{T_{01}}} \left(1 - \frac{p_{02}}{p_{0\,min}\nu_v} \right) \left[1 - \left(\frac{p_{0\,min}}{p_{0\,in}} \right)^{\frac{\varkappa+1}{2\varkappa}} \right].$$

* Here p_{02} and ν_a are assumed to be constant.

Some remarks on the design of hypersonic tunnels

As we have seen (Chapter II), a characteristic feature of hypersonic tunnels is the provision of a heater and a nozzle-cooling system, whose effects on the temperature and the resistance to flow have to be taken into account.

The resistance of the heater, which is located in a region of low velocities, can be determined from its geometry. The change of resistance in the nozzle, due to its cooling, can be accounted for by considering flow with heat removal.

The main difficulty is the design of hypersonic tunnels arises in the determination of the resistance of the diffuser and the test section with the model in it. The resistance of these tunnel elements is an important factor in selecting the compression ratios required to obtain the rated velocity in the test section. The resistance is determined more exactly by experiment than by calculation.

BIBLIOGRAPHY

1. Lukasiewicz, J.D. Razvitie bol'shikh aerodinamcheskikh trub krateovreniennogo deistviya (The Development of Large Intermittent-Operation Wind Tunnels). [Russian Translation.] Collection of Translations and Reviews, "Mekhanika", No. 6 (34). —IL. 1955.
2. Lukasiewicz, J.D. Diffuzory sverkhzvukovykh aerodinamicheskikh trub (Diffusers of Supersonic Wind Tunnels). [Russian Translation.] Collection of Translations and Reviews, "Mekhanika" No. 5 (28). —IL. 1954.
3. Abramovich, G.N. Prikladnaya gasovaya dinamika (Applied Gas Dynamics). —Gostekhizdat. 1953.

Chapter IV

MEASUREMENT OF FLOW PARAMETERS IN WIND TUNNELS

In this chapter we will consider test methods in wind tunnels where conditions are steady, i.e., the flow parameters are constant in time. The most important parameters in aerodynamic experiments are pressure, temperature, velocity, and direction of flow.

Pressure is defined as force per unit surface area. It results from the collision of gas molecules with a surface. The magnitude of the pressure exerted by a perfect gas on a wall is determined by the mean velocity of these molecules and by the number of collisions with the wall in unit time. The number of the colliding molecules depends on the gas density, while the velocity of the molecules is a function of the absolute temperature, and is thus determined by the kinetic energy of the molecules in their translational, rotational, and vibratory motion. The pressure p, temperature T, and density ρ of a perfect gas are related by the equation of state

$$p = \rho g R T, \tag{4.1}$$

where R is the gas constant (for air $R = 29.27$ m/degree).

Steady flow in wind tunnels can generally be considered to be one-dimensional and adiabatic (no heat exchange with the outside). It is also often permissible to neglect the viscosity and thermal conductivity of the gas and to consider the gas as a perfect fluid. Continuous adiabatic flow of a perfect gas is isentropic because in the absence of internal friction and heat transfer, all processes in a perfect gas are reversible.

The energy equation for adiabatic flow between two regions 1 and 2, where the velocities are V_1 and V_2, is

$$i_2 + \frac{V_2^2}{2gJ} = i_1 + \frac{V_1^2}{2gJ}. \tag{4.2}$$

This equation is also valid for a real gas, in which viscosity and heat transfer affect the flow.

The quantity (4.2) is called heat content or enthalpy. For gas with specific heats c_p and c_v, satisfying the equation of state (4.1), $i = c_p T$. The mechanical equivalent of heat J is equal to 427 kg · m/kcal.

If $V_2 = 0$ the energy equation takes the form:

$$c_p T + \frac{V^2}{2gJ} = c_p T_0; \tag{4.3}$$

where $c_p T_0 = i_0$ is the heat content of the stagnant gas.

The local velocity of sound at any point in the gas is given by

$$a^2 = \varkappa g R T, \tag{4.3a}$$

also

$$R = J(c_p - c_v).$$

We can thus use (4.3) to relate the stagnation temperature to the static temperature of the gas and the Mach number $\mathbf{M} = V/a$,

$$\frac{T_0}{T} = 1 + \frac{\varkappa - 1}{2}\mathbf{M}^2. \tag{4.4}$$

In subsonic and supersonic tunnels, heating is negligible or zero, and $\varkappa = c_p/c_v$ can be assumed to be constant (for air, $\varkappa = 1.4$).

From (4.4) and the equation of adiabatic expansion of a perfect gas,

$$\frac{p}{p_0} = \left(\frac{\rho}{\rho_0}\right)^{\varkappa} = \left(\frac{T}{T_0}\right)^{\frac{\varkappa}{\varkappa - 1}},$$

we obtain the relationships between the pressures and densities and the Mach number for isentropic flow,

$$\frac{p_0}{p} = \left(1 + \frac{\varkappa - 1}{2}\mathbf{M}^2\right)^{\frac{\varkappa}{\varkappa - 1}}. \tag{4.5}$$

$$\frac{\rho_0}{\rho} = \left(1 + \frac{\varkappa - 1}{2}\mathbf{M}^2\right)^{\frac{1}{\varkappa - 1}}. \tag{4.6}$$

The pressure p_0, the temperature T_0, and the density ρ_0, which correspond to a gas isentropically brought to rest, are called stagnation parameters, and are the most important characteristics of the gas. The stagnation parameters are fully determined by (4.1) if any two of them are known. The stagnation pressure p_0 is also called total pressure.

The parameters p_0 and ρ_0 are constant everywhere in an isentropic flow. The stagnation temperature is constant everywhere in a one-dimensional adiabatic flow, in which there is no heat exchange with the outside, although there may be internal dissipation of energy, as, for example, in a shock wave. Equations (4.4) through (4.6) are used in measuring and determining the gas-flow parameters in wind tunnels. Different conditions apply when shock waves occur, and we then use relationships, whose derivation can be found in textbooks on aerodynamics (e.g., /1/), between the flow parameters upstream and downstream of the shock wave.

The Rankine-Hugoniot equations (4.7 and 4.8) relate the pressures and densities upstream (unprimed symbols) to those downstream (primed) of a normal plane shock wave (see Figure 4.1).

$$\frac{p'}{p} = \frac{\frac{\varkappa + 1}{\varkappa - 1}\frac{\rho'}{\rho} - 1}{\frac{\varkappa + 1}{\varkappa - 1} - \frac{\rho'}{\rho}}, \tag{4.7}$$

$$\frac{\rho'}{\rho} = \frac{1 + \frac{\varkappa + 1}{\varkappa - 1}\frac{p'}{p}}{\frac{\varkappa + 1}{\varkappa - 1} + \frac{p'}{p}}. \tag{4.8}$$

The change of velocity in passing through the shock wave is given by

$$VV' = a_*^2, \tag{4.9}$$

where

$$a_* = \sqrt{\frac{2\varkappa}{\varkappa+1} gRT_0} \tag{4.10}$$

is the critical velocity of sound, which depends only on the initial gas temperature. The critical velocity of sound also determines a further parameter, similar to the Mach number:

$$\lambda = \frac{V}{a_*}. \tag{4.11}$$

The ratio of velocities upstream and downstream of a shock wave can conveniently be expressed in terms of the upstream value of λ.

$$\frac{V}{V'} = \lambda^2. \tag{4.12}$$

The ratios of static pressures, of densities, and of total pressures upstream and downstream of a shock wave can be expressed as follows in terms of the Mach number:

$$\frac{p'}{p} = \frac{2\varkappa}{\varkappa+1} M^2 - \frac{\varkappa-1}{\varkappa+1}, \tag{4.13}$$

$$\frac{\rho'}{\rho} = \lambda^2 = \frac{(\varkappa+1) M^2}{(\varkappa-1) M^2+2}, \tag{4.14}$$

$$\frac{p_0}{p_0'} = \left(\frac{2\varkappa}{\varkappa+1} M^2 - \frac{\varkappa-1}{\varkappa+1}\right)^{\frac{1}{\varkappa-1}} \left[\frac{(\varkappa-1) M^2+2}{(\varkappa+1) M^2}\right]^{\frac{\varkappa}{\varkappa-1}}. \tag{4.15}$$

The relationship between the Mach numbers upstream and downstream of the shock wave is

$$M'^2 = \frac{1 + \frac{\varkappa-1}{2} M^2}{\varkappa M^2 - \frac{\varkappa-1}{2}}. \tag{4.16}$$

For an oblique shock wave, the ratios of static pressures, densities, and total pressures are given by formulas in which the angle β between the shock wave and the upstream flow direction (Figure 4.2), depends on the angle θ through which the flow direction changes. These equations differ from those for a normal shock wave only in that they contain the component of the Mach number in the direction perpendicular to the shock wave.

$$\frac{p_1}{p} = \frac{2\varkappa}{\varkappa+1} M^2 \sin^2\beta - \frac{\varkappa-1}{\varkappa+1}, \tag{4.17}$$

$$\frac{\rho_1}{\rho} = \frac{(\varkappa+1) M^2 \sin^2\beta}{(\varkappa-1) M^2 \sin^2\beta+2}, \tag{4.18}$$

$$\frac{p_0}{p_{01}} = \left(\frac{2\varkappa}{\varkappa+1} M^2 \sin^2\beta - \frac{\varkappa-1}{\varkappa+1}\right)^{\frac{1}{\varkappa-1}} \left[\frac{(\varkappa-1) M^2 \sin^2\beta+2}{(\varkappa+1) M^2 \sin^2\beta}\right]^{\frac{\varkappa}{\varkappa-1}}. \tag{4.19}$$

The Mach number downstream of an oblique shock wave is

$$M_1 = \frac{1 + \frac{\varkappa - 1}{2} M^2}{\varkappa M^2 \sin^2 \beta - \frac{\varkappa - 1}{2}} + \frac{M \cos^2 \beta}{1 + \frac{\varkappa - 1}{2} M \sin^2 \beta}. \qquad (4.20)$$

In (4.17) through (4.20) the subscripts 1 refer to the parameters downstream of the shock wave.

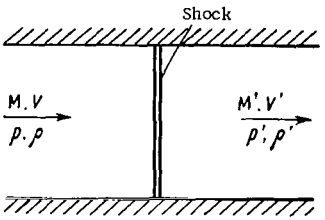

FIGURE 4.1. Normal plane shock.

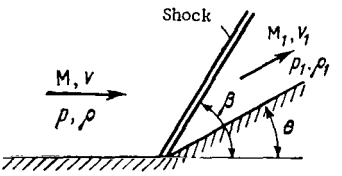

FIGURE 4.2. Oblique shock.

The test method used determines which of these formulas apply in any particular case. The method of measurement will, in turn, depend on the equipment used and on the type of problem. It is important in all measurements to know the parameters of the undisturbed flow. Quantitative measurements, such as the determination of the aerodynamic coefficients of a scale model in a wind tunnel, demand that these parameters be known to a much higher degree of accuracy than when merely investigating the nature of the flow around the model. Measurements in the region where the flow is disturbed by the model and is no longer isentropic are more difficult than measurements upstream of the model. Miniature test probes may have to be mounted in such regions when testing blade and wing cascades, determining the drag by pulse techniques, studying the boundary layer, etc.

The pressure and temperature of a gas, which can be directly measured, fully determine its state, and permit calculation of the density, viscosity, thermal conductivity, and other physical quantities, whose direct measurement may be difficult or impossible.

In a stationary medium the direct measurement of pressure and temperature is not difficult, since the results are unlikely to be affected by changes in the attitude of the sensors. When the medium is moving, the measurement of pressure and temperature is considerably more difficult. Depending on its orientation, and in some cases on the design of the instrument, the indicated pressure or temperature can range from the "static" value, which corresponds to the true flow velocity, up to a value corresponding to stagnation conditions. Due to its finite size, a sensor will disturb the moving medium. In designing probes, pick-ups, and transducers for measuring pressures and temperatures, it is therefore important to minimize the disturbances they cause by making them of small size and correct shape.

Measurement methods not requiring the insertion of probes into the medium are commonly used. Thus, for instance, if the flow between the settling chamber and the test section of a tunnel is isentropic, the velocity, pressure, and temperature of the flow in the test section can often be calculated from the initial data (stagnation pressure and temperature in the settling chamber), supplemented by measurements of the pressure at the wall. If the nature of the gas flow (e.g., possible heat transfer to the gas) is uncertain, it will be necessary to measure the temperature or density in addition to the pressure. The density is commonly determined by optical methods, which are very important in the study of compressible gas flow in boundary layers where the insertion of probes might substantially distort the flow pattern.

§ 11. PRESSURE MEASUREMENT*

Pressure measurement in experimental aerodynamics is important not only for determining the state of the gas. From the pressure distribution on a body we can determine the forces acting on it; by measuring the pressures at appropriate points on the surface of the model or the wall of the wind tunnel, we can determine the local velocity and the velocity of the undisturbed flow.

The above formulas are based on absolute pressures. Pressure measurements are often made with manometers, which measure the difference in pressure between two regions. Only if in one of these there exists perfect vacuum, will the manometer measure the absolute pressure; if the reference region is at atmospheric pressure the instrument will indicate gage pressure; to determine the absolute pressure, an additional barometer must be used. In aerodynamic experiments it is often useful to measure the difference between a given pressure and the static pressure in the undisturbed flow; a differential manometer is employed for this purpose.

When studying the motion of a liquid, knowledge of the static and total (stagnation) pressures is very important. The static pressure in the undisturbed flow may be defined as the pressure acting on the wall of a body imagined to be moving at the same velocity as the medium. The stagnation pressure is the pressure of the fluid imagined to be brought to rest isentropically.

Measurement of static pressure

It is virtually impossible to use a probe moving with the stream to measure static pressure. A common technique is to connect a stationary probe to an orifice drilled perpendicularly to the wall of the test model at a point where the streamlines are undistorted and parallel to the streamlines in the undisturbed flow. Neglecting minor disturbances caused by the orifice the pressure sensed by the manometer is equal to the static pressure in the flow.

* [For pressure-measurement devices see Chapter V.]

The static pressure in a flow can only vary between points in a plane, normal to the undisturbed flow, if the streamlines are curved. If the streamlines are straight, transverse velocity gradients do not affect the static pressure. It is therefore best to measure the static pressure in an undisturbed flow at a point where the medium moves parallel to a wall (Figure 4.3a), and all the streamlines are straight (neglecting boundary-layer disturbances). The (effectively constant) pressure difference across a thin boundary layer at a curved wall does not affect the static pressure acting at the sensor orifice.

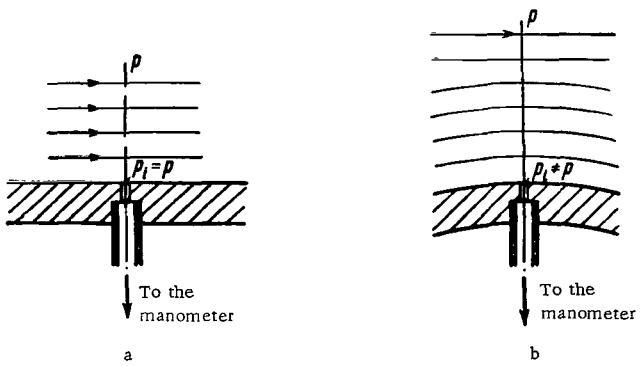

FIGURE 4.3. Measurement of static pressure. a — at a flat wall; b — at a curved wall.

The static pressure in the undisturbed flow in a wind tunnel is often measured with the aid of orifices in the flat or cylindrical walls at the entrance to the test section.

The static pressure at an orifice drilled perpendicularly to a curved wall, past which the streamlines are curved (Figure 4.3b), differs in general from the normal pressure at this point.

If the static pressure across the wind tunnel is not constant it can be mapped using a static-pressure sensor consisting of a body placed in the stream. Sensing holes drilled at certain points of this body are connected to the manometer. At the nose of a body (of any shape) the streamlines are always curved. At one point at the nose, the medium is stationary, and the pressure at this point of the sensing body is equal to the total or stagnation pressure. At other points of the surface of the body the pressures differ in general from both the stagnation and static pressures in the undisturbed flow.

Static-pressure sensors can be divided into two groups. The first group comprises sensors having the form of short tubes inserted in the flow direction. In such tubes the sensing orifices are placed at points where the pressure is close to the static pressure, but where a considerable pressure gradient exists along the surface. Thus, on the surface of a circular cylinder whose axis is perpendicular to the flow, such points are located at angles of about 30° to the flow direction (Figure 4.4).

The characteristics of a static-pressure sensor are expressed in terms of the parameter (determined by calibration)

$$\zeta = \frac{p_i - p}{\frac{\rho V^2}{2}} \quad \text{or} \quad \zeta' = \frac{p_i - p}{p},$$

where p is the true static pressure in the undisturbed flow, and p_i is the pressure measured by the manometer connected with the sensor.

For tubes of the first group the values of ζ and ζ' are usually influenced considerably by the values of **Re** and **M**. A further drawback is that small errors in the position of the orifices considerably influence the calibration. They are therefore seldom used for measuring the static pressure in the undisturbed flow in wind tunnels. However, due to their small cross section, these tubes are often combined with sensors for measuring the total pressure in the flow direction, when the flow is very disturbed and space is limited (for instance, in the clearances between the discs of axial turbomachines).

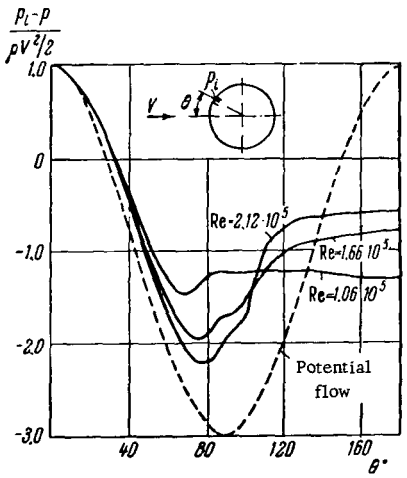

FIGURE 4.4. Pressure distribution on the surface of a cylinder placed transversely to the flow.

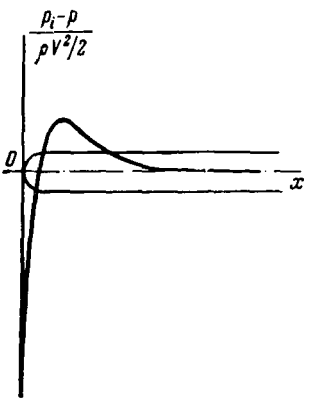

FIGURE 4.5. Pressure distribution on the surface of a cylinder with a faired nose, aligned parallel to the stream.

The second group includes tubes parts of whose surfaces are cylindrical with generatrices parallel to the direction of the undisturbed flow. The orifices are sufficiently downstream, so that the initial disturbances are already attenuated and the streamlines are practically parallel to the direction of the undisturbed flow. Usually such probes are axisymmetrical or disc-shaped. The pressure distribution at the surface of a cylindrical body, with streamlined flow around its nose, is shown in Figure 4.5. On the cylindrical part of the body, at a certain distance from the nose, there is always a region where the pressure at the wall is equal to the static pressure in the undisturbed flow.

The static pressure at points inside wind tunnels for low subsonic speeds are usually measured by means of Prandtl tubes (Figure 4.6a), which have

semispherical noses. The tube is inserted into the stream so that its axis lies in the direction of the undisturbed flow. The static pressure is transmitted into the tube through openings or slots located between the nose and the stem used for mounting the tube and connecting it to a manometer. The stem disturbs the flow [stem effect], and causes a local increase in the static pressure near the orifices. On the other hand, the disturbances at the nose cause a local velocity increase and a pressure decrease. Figure 4.7 shows the influence of the position of nose and stem of a Prandtl tube on the error in measuring the static pressure. The difference between the indicated pressure p_i and the true pressure p,

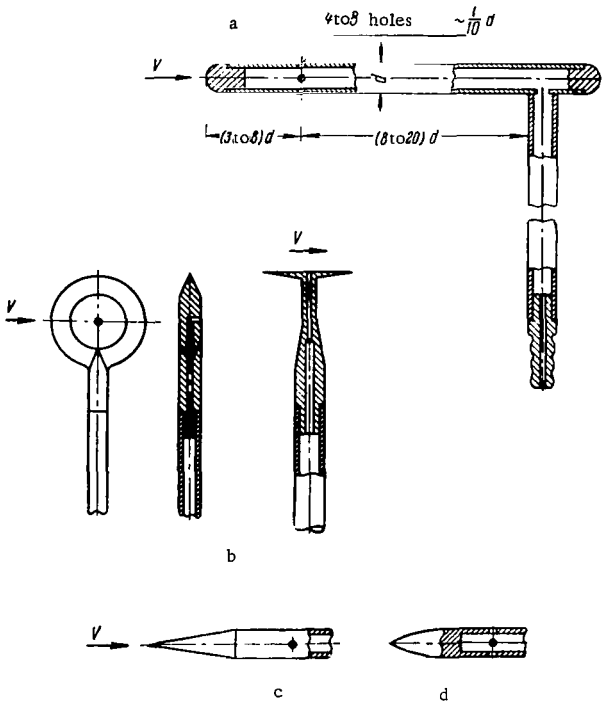

FIGURE 4.6. Tubes for measuring static pressure. a — Prandtl tube; b — disc tube; c — tube with conical nose; d — tube with ogival nose.

expressed as a percentage of the velocity head, is plotted as a function of the distances of the orifice from the nose and from the stem axis. The most suitable position for the orifice is where the effects of both nose and stem are small, or balance each other. For subsonic measurements the orifices are usually placed at a distance of 3 to 8 diameters from the nose.

The dimensions of the tube depend on its purpose. In large wind tunnels, tubes of diameters up to 10 mm may be used. For measuring the static pressure in very narrow channels and in the boundary layer the external diameter may be from 0.3 to 2 mm.

Disc tubes (Figure 4.6b), have orifices drilled in the center of one side of the disc, and are inserted into the stream so that the surface of the disc is parallel to the flow direction These tubes are very sensitive to the orientation of the disc in the stream.

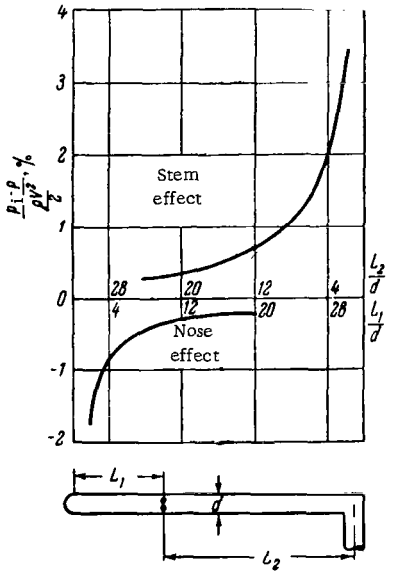

FIGURE 4.7. Influence of nose and stem on errors in measuring static pressure.

The orifices in the walls of the tube or tunnel cause certain disturbances in the flow close to the wall; the medium flowing past the orifices is partially mixed with the stagnant medium inside them. This and the centrifugal forces acting on the fluid, causes the streamlines adjacent to the orifices to become curved, so that the pressure inside the tube is not exactly equal to the static pressure in the flow. The principal errors in static-pressure measurements by means of orifices arise from the viscosity of the fluid which manifests itself in the boundary layer. The pressure in fairly deep orifices exceeds the true pressure, the error decreasing as the diameter of the orifice is reduced.

If the orifice diameter is small compared with the thickness δ of the boundary layer, the difference between the orifice pressure and the true static pressure can be expressed as follows in dimensionless form /2/:

$$\frac{\Delta p}{\tau_0} = c\,\mathrm{Re}^{\frac{1}{4}}.$$

Here, τ_0 is the frictional shearing stress at the wall:

$$\tau_0 = \mu\left(\frac{dV}{dy}\right)_{y=0},$$

where μ is the viscosity coefficient of the fluid and Re is the Reynolds number, calculated from the orifice diameter d and the velocity V_1 at a distance $y = d$ from the wall, assuming a linear velocity distribution in the boundary layer. Thus,

$$\mathrm{Re} = \frac{\rho V_1 d}{\mu} = \frac{dV}{dy}\frac{d^2}{\nu},$$

where $\nu = \mu/\rho$. The Reynolds number can also be expressed in terms of τ_0:

$$\mathrm{Re} = \frac{d^2}{\nu^2}\frac{\tau_0}{\rho}.$$

The coefficient c depends on the ratio of the orifice depth l to the diameter d, and varies from 1.0 (for $l/d = 1.75$) to 2.16 (for $l/d = 0.1$), with $3.0 < \mathrm{Re} < 1000$.

Figure 4.8 shows the values of this error determined in dimensionless form as a function of Reynolds number from turbulent-flow measurements /2/. For orifices drilled perpendicular to the wall and connected to the manometer through a tube of diameter $2d$, the error is independent of l/d when $1.5 < \frac{l}{d} < 6$. The orifice diameter is generally between 0.25 and 2 mm, the ratio l/d being not less than 2.

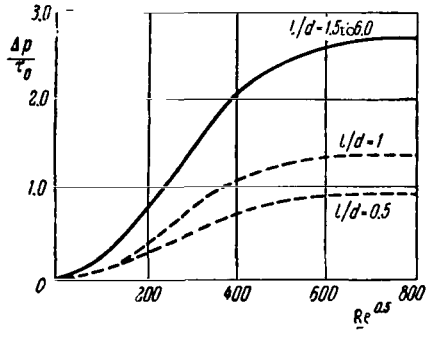

FIGURE 4.8. Orifice error (expressed in dimensionless form) in static-pressure measurements.

In practice, the error caused by the orifice is small. Thus, for instance, Figure 4.9 shows the errors in measuring the static pressure for both water and air in a 25.4 mm-bore pipe, polished internally /3/. For orifice diameters less than 0.5 mm the error does not exceed 0.3% of the velocity head of the flow.

Compressibility effects on the readings of a hemispherical-nose static-pressure tube become noticeable when the free-stream Mach number **M** rises above 0.8. At large subsonic velocities local supersonic regions appear on the cylindrical part of the probe, which are accompanied by shock waves. These regions are upstream of the orifices, so that the pressure measured exceeds the true static pressure. As **M** approaches unity, the zone of supersonic flow spreads over the orifices, which thus experience pressures below that in the undisturbed flow.

When **M** is greater than 1, a detached shock appears upstream of the tube. Near the tube the shock wave is normal to the tube axis; the static pressure directly downstream of the shock is related to the static pressure upstream of it by (4.13).

If we move the orifices along the tube so that they are well downstream of the shock wave, the measured static pressure will tend towards the value for the undisturbed flow. This is clearly seen in Figure 4.10, which shows the errors in static-pressure measurement for various distances between the hemispherical nose and the orifices /4/. We can also see from Figure 4.10 that the errors in measuring the static pressure at high subsonic velocities are even smaller with conical nozzles (Figure 4.6c).

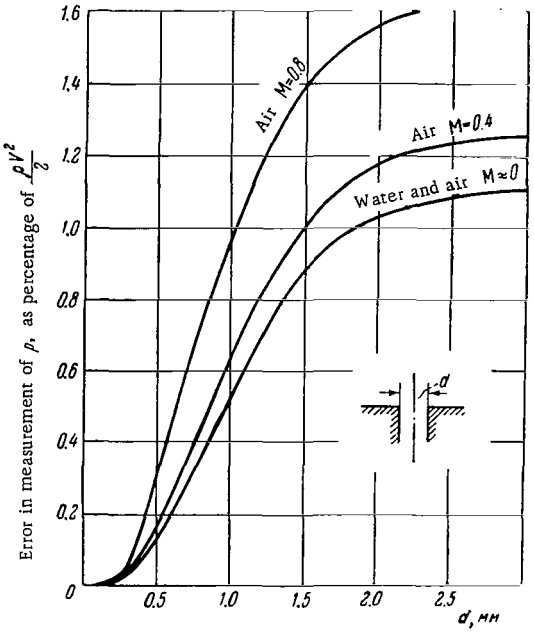

FIGURE 4.9. Effect of orifice dimensions on indicated static pressure.

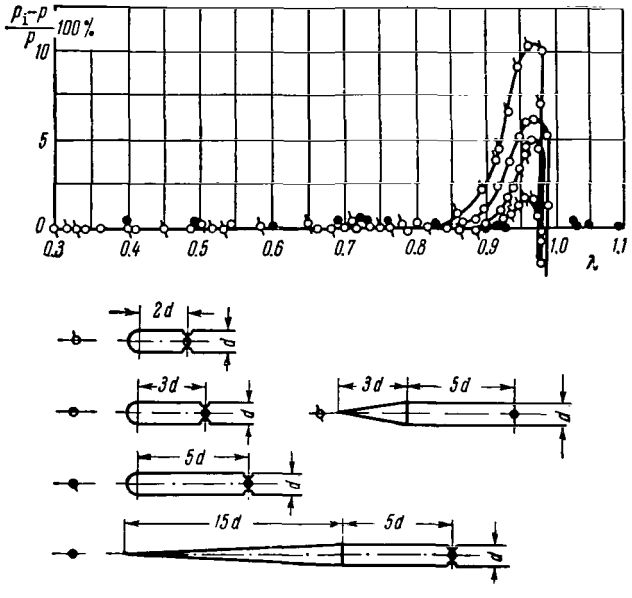

FIGURE 4.10. Errors in static-pressure measurement at transonic velocities.

Good results are also obtained with ogival tubes (Figure 4.6d). The tube shown in Figure 4.11 has a systematic error not exceeding 1% /4/.

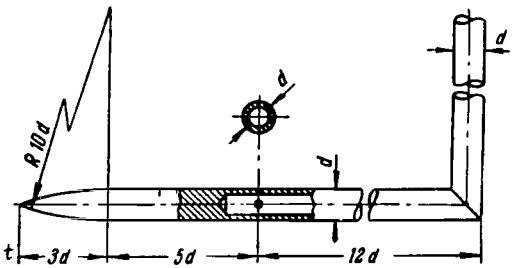

FIGURE 4.11. Ogival tube.

Conical or ogival tubes must be used at supersonic velocities to reduce the strength of the shock wave. The taper angle of the conical nose should be less than the angle at which the shock wave becomes detached from the cone (Figure 4.12). The orifices must be placed at a distance not less than 10 to 15 diameters from the beginning of the cylindrical part of the tube. Special care should be taken when drilling these holes since at supersonic velocities the smallest roughness at the edges may cause large errors in the pressure measurement.

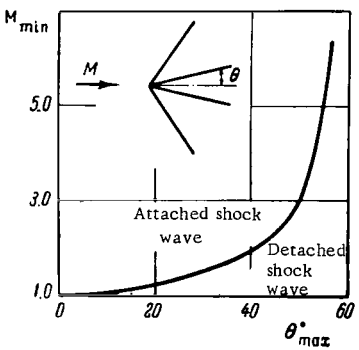

FIGURE 4.12. Conditions for attachment and detachment of a shock wave in front of a cone.

Pointed tubes are also necessary because the shock waves propagated from the noses may be reflected from the tunnel wall and affect conditions near the orifices (Figure 4.13). The pressure increase behind the shock wave will then propagate upstream in the subsonic part of the boundary layer, so that the pressure at the orifices may exceed the static pressure in the undisturbed flow.

If a tube is inserted at an angle to the undisturbed-flow direction, the streamlines near the orifices will be distorted and the pressure

measurements become inaccurate. The dependence of its calibration coefficient on yaw (α) is therefore an important characteristic of a tube.

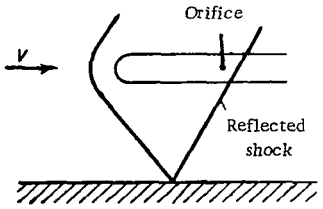

FIGURE 4.13. Effect of tube measurements in supersonic flow.

Figure 4.23 shows this dependence for a Prandtl tube (curve 1). The effect of yaw is reduced by arranging several orifices so that the pressure inside the tube is an average value. Usually the tube has from 4 to 8 orifices whose diameters are about 1/10th of the outside diameter of the tube.

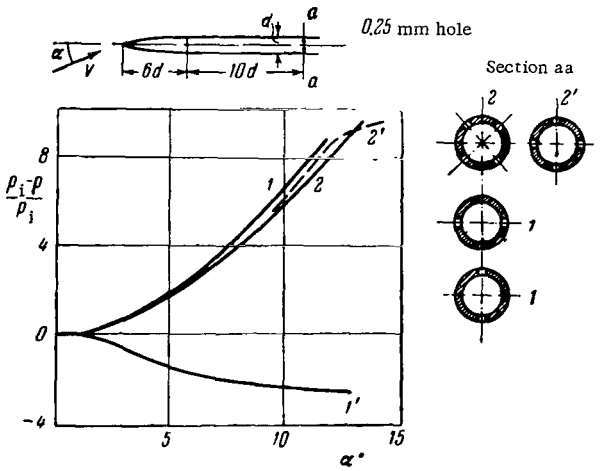

FIGURE 4.14. Effect of yaw on the indication of a tube at M = 1.6.

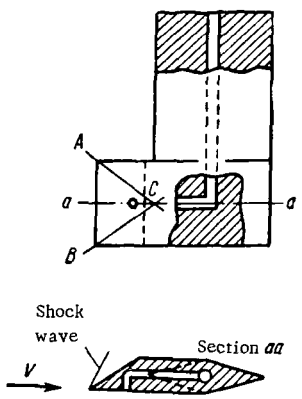

FIGURE 4.15. Static-pressure tube for supersonic flow.

Figure 4.14 shows the effect of yaw on the indications of a tube with a long ogival nose at $M = 1.6$ /5/. The different curves correspond to different orientations of the orifices. The error is least for a tube with two openings situated in the plane of yaw, since the pressure increase at one orifice is then compensated by the pressure decrease at the other.

The static pressure at transonic or supersonic velocities may be measured with a wedge-shaped tube (Figure 4.15). The orifice should be inside the triangle ABC formed by the leading edge AB and the shock waves propagated from the corners A and B.

Measurement of total pressure

The gas particles come to rest so quickly at the stagnation point of a body, that heat transfer and friction losses are negligible. In subsonic flow the gas therefore undergoes only isentropic changes, and the total pressure at the stagnation point is almost exactly equal to the initial stagnation pressure in the settling chamber of the tunnel. This pressure is related to the static pressure of the undisturbed flow by (4.5). Friction losses take place in the boundary layer only downstream of the stagnation point. The flow velocity at the surface of a body is also equal to zero, but here this is due to friction, and the change is not isentropic.

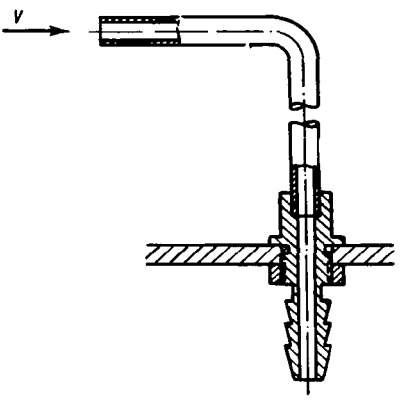

FIGURE 4.16. Total-pressure tube.

Total pressure is measured with a cylindrical tube having an orifice pointing toward the flow. The shape of the nose and the ratio of the orifice diameter to the external diameter of the tube do not influence the total-pressure measurements over a wide range of velocities, provided that the axis of the tube coincides with the flow direction. It is therefore standard practice to use tubes with blunt ends (Figure 4.16) which are insensitive to yaw at angles of up to ±10 to 12°.

At supersonic velocities, a shock wave appears upstream of the tube nose; behind this shock wave the gas moves at subsonic velocity, so that the tube measures only the total pressure behind the shock wave, which differs from the free-stream total pressure because of energy dissipation in the shock. The ratio of the total pressures upstream and downstream of the shock wave can be calculated from (4.15). In order to measure the total pressure more exactly, the tube orifice is made much smaller than the outside diameter of the tube. This ensures that the orifice is completely behind the normal part of the shock wave. The total-pressure loss in shock waves at velocities between $M = 1.0$ and $M = 1.25$ is less than 1%. If such an error is acceptable, the readings of the pressure tube can be used without correction.

Viscosity has a negligible effect on the readings of total-pressure tubes over a very wide range of Reynolds numbers. Viscosity can indeed generally be ignored in aerodynamic experiments, since it affects flow at atmospheric pressure only when the velocity is well below 1 m/sec. This happens only in boundary layers at walls. It has been experimentally shown /3/ that the correction for the effect of Reynolds-number variation on the indication of thin-walled cylindrical tubes is given by

$$\frac{p_{0i} - p}{\frac{\rho V^2}{2}} = 1 + \frac{5.6}{\mathrm{Re}}. \qquad (4.21)$$

where Re is calculated from the radius of the orifice. In supersonic-flow experiments at $2.3 < M < 3.6$, viscosity can be neglected at Reynolds numbers

above 200 /6/; in measuring p_0 the error is only 2 or 3% when $Re = 100$.

Total-pressure tubes are less sensitive to yaw than static-pressure tubes. The influence of yaw on the readings of tubes of various nose shapes is shown in Figures 4.17 through 4.19, where $p_{0i} - p_0$ is the error due to yaw.

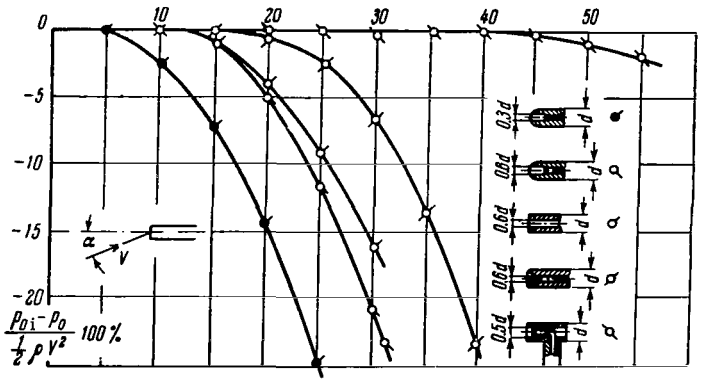

FIGURE 4.17. Error in measuring the total pressure, as a function of the angle of yaw.

We see from Figure 4.17 that the accuracy of a total-pressure tube with a hemispherical nose depends on the angle of yaw and varies inversely with the ratio of the orifice diameter to the outer tube diameter. Figure 4.18

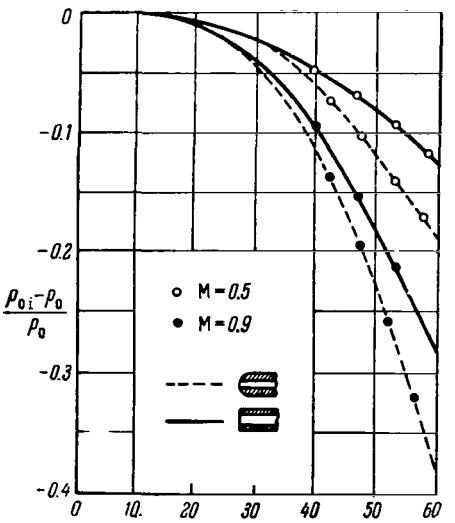

FIGURE 4.18. Error in measuring the total pressure, as a function of angle of yaw for tubes with rounded and plane noses.

shows the results of comparative tests at two values of M for two tubes, one with a hemispherical head, the other cut off at a right angle.

Blunt-nosed tubes are less sensitive to yaw than tubes with rounded-off noses. Comparison between tubes with conical noses and tubes with orifices conical inward (Figure 4.19) shows that the latter are less affected by yaw.

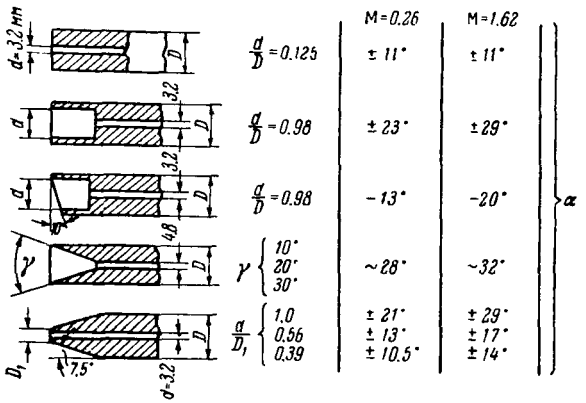

FIGURE 4.19. Types of total-pressure tube, showing yaw at which the error in measuring the total pressure is 1 % of the velocity head.

When measuring the total pressure in a strongly converging flow, devices are used in which the tube is placed inside a shield which guides

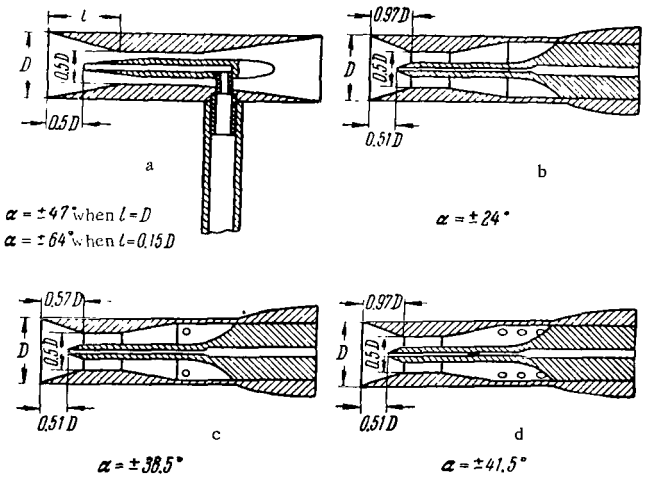

FIGURE 4.20. Shielded total-pressure tubes. α is the yaw angle below which the error in measuring the total pressure is less than 1 %. a — shield with open outlet; b — shield with closed outlet; c — shield with a single row of outlet openings; d — shield with 3 rows of outlet openings.

the air flow to the orifice (Figure 4.20). The sensitivity to yaw of such tubes depends on the taper of the inlet cone of the shield and on the

cross-sectional area of the openings through which the air leaves the shield. Best results are obtained with shields whose outlet cross sections are equal to or slightly exceed the inlet cross sections. If the inlet taper angle is large the angle of yaw may attain ±64° before the error in measuring the total pressure exceeds 1% of the velocity head. Simplified shielded miniature tubes for measuring the total pressures in turbo-machines are shown in Figure 4.21. The orifices of total-pressure tubes are placed near the apex of the shield cone. At subsonic flow such tubes /4/, /7/, /8/ show errors of less than 0.5% at yaw angles of ±30 to 40°.

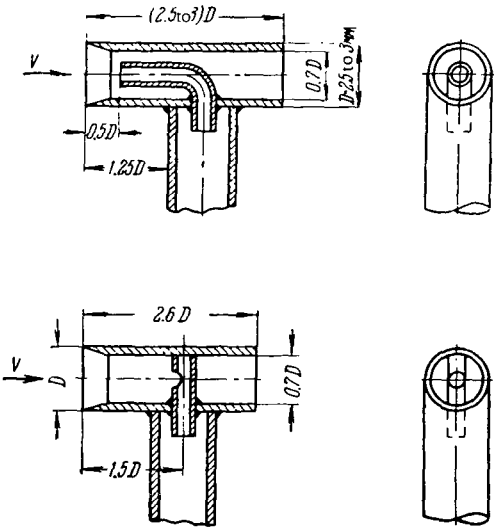

FIGURE 4.21. Shielded miniature tubes.

The compressibility of the gas affects the range of permissible angles of yaw. For unshielded total-pressure tubes this range increases with the Mach number, but for shielded tubes it decreases slightly.

Care must be taken when measuring the total pressure in flows with large transverse velocity gradients, e.g., in turbine-blade cascades, and in boundary layers. A transverse velocity gradient causes the "effective" center of total pressure of the tube (i.e., of the point at which the local velocity V' corresponds to a velocity head equal to the measured total pressure) to move from the tube axis toward the region of higher velocity. The magnitude δ of this displacement depends on the inside and outside diameters of the total-pressure tube (Figure 4.22) and is for subsonic flow determined by /9/

$$\frac{\delta}{D} = 0.131 + 0.082\frac{d}{D}, \qquad (4.22)$$

applicable for

$$\frac{D}{q}\frac{dq}{dy} = 0.1 \text{ to } 1.2,$$

where

$$q = \frac{\rho V^2}{2}.$$

This displacement of the effective center causes an increase in the total pressure indicated by the tube. For this reason the width of the wake behind a turbine blade will appear to be smaller than it really is.

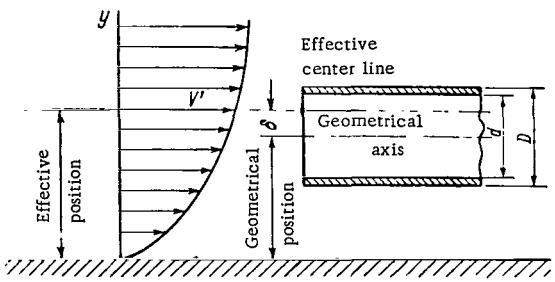

FIGURE 4.22. Displacement of the effective center of a total pressure tube in a flow with transverse velocity gradient.

The efficiency of a turbine-blade cascade determined from such measurements is thus excessive.

§ 12. THE MEASUREMENT OF THE MACH NUMBER AND FLOW VELOCITY

The flow velocity of a liquid or gas can be measured directly by observing the displacement of tracer particles. Either the time to travel a measured distance or the distance moved in given time can be measured. Different investigators have used ions, alpha particles, fluorescent, or light-reflecting particles in tracer experiments of this kind. Such methods are in practice seldom used, because although they demand very accurate physical measurements they yield only the average velocity, and give no information about its local variations. Flow-velocity measurements are therefore generally indirect, being based either on physical effects resulting from the movement of the medium, or on the relationship between the velocity or Mach number and other more easily measured flow parameters. Thus, for instance, hot-wire anemometers (see p. 192) are based on the relationship between flow velocity and rate of heat removal from a body. In isentropic flow the Mach number can be found, using (4.4), (4.5), or (4.6), from a knowledge of static and stagnation values of either temperature, density, or pressure. The stagnation parameters p_0 and T_0 of the fluid remain unchanged in isentropic flow; they can easily be measured directly, for instance in the settling chamber of the wind tunnel, where the flow velocity is small. Knowing p_0 and T_0, ρ_0 can be found from the equation of state (4.1). On the other hand, if there is any exchange

of heat with the surroundings upstream of the point where the flow velocity or Mach number is to be determined the local value of p_0 can be found with the aid of a total-pressure tube, while the local value of T_0 can be determined by a static-pressure tube, as described in § 14. At present no method exists for direct measurement of the static temperature T of the gas. It can be determined indirectly by measuring the velocity of sound in the fluid; for a given gas, the velocity of sound depends only on temperature ($a^2 = \varkappa gRT$). However, there must be a finite distance between the sound source and the receiver used for this measurement, so that an average, rather than a local, temperature value is obtained.

Measurement of the density ρ in a stream of compressible fluid is considerably easier, using indirect methods based on the relationships between the density and the coefficients of refraction, absorption, and radiation of the medium. The refraction method (described in § 18) permits density measurements even in regions where the flow is not isentropic.

By measuring ρ at different points we can determine the local Mach number at these points from the known value of ρ_0, using (4.6).

Of the three static parameters, T, ρ, and p, only the static pressure can generally be measured directly. Hence the "pneumometric" method, based on the measurement of pressures, has become the principal, and the most accurate, method of Mach-number determination, and is used up to hypersonic velocities. Mach number in an isentropic flow can be calculated from (4.5), which may be rewritten in the form

$$\mathrm{M} = \sqrt{\frac{2}{\varkappa - 1}\left[\left(\frac{p_0}{p}\right)^{\frac{\varkappa-1}{\varkappa}} - 1\right]}. \qquad (4.23)$$

From this expression we can also find the local flow velocity. Expressing the local velocity of sound in terms of the temperature, and remembering that $V = a\mathrm{M}$, we obtain

$$V = \sqrt{\frac{2\varkappa gRT}{\varkappa - 1}\left[\left(\frac{p_0}{p}\right)^{\frac{\varkappa-1}{\varkappa}} - 1\right]}. \qquad (4.24)$$

From this expression it can be seen that for determining the velocity in terms of pressure, the local values of three parameters, p, p_0, and T are needed. Since direct measurement of T is difficult, the local temperature is determined by measuring the local value of T_0.

$$T = \frac{T_0}{1 + \frac{\varkappa - 1}{2}\mathrm{M}^2}.$$

This is then substituted in (4.24). Since no heat is transferred to the medium between the settling chamber and the test section of a wind tunnel, the free-stream velocity in the heat section (excluding the boundary layer) can be found by measuring p in the test section, and p_0 and T_0 in the settling chamber. The velocity in the boundary layer is found from the local value of T_0. The pressure p is constant throughout the boundary layer, and can be measured with the aid of an orifice in the wall.

Expanding the right-hand side of (4.5) as a binomial series we have

$$\frac{p_0}{p} = 1 + \frac{\varkappa}{2}\mathrm{M}^2(1 + \varepsilon), \qquad (4.25)$$

where

$$\varepsilon = \frac{M^2}{4} + \frac{(2-\varkappa)M^4}{24} + \frac{(2-\varkappa)(3-2\varkappa)M^6}{192} + \ldots \qquad (4.26)$$

Since

$$\frac{\varkappa M^2}{2} = \frac{\varkappa V^2}{2a^2} = \frac{\varkappa V^2}{2\varkappa\frac{p}{\rho}} = \frac{\rho V^2}{2p},$$

we can write (4.25) in the form

$$p_0 = p + q(1+\varepsilon). \qquad (4.27)$$

The quantity $q = \rho V^2/2$, is called the velocity head; it is often used in experimental aerodynamics. The local values of the various dimensionless aerodynamic coefficients are usually determined by expressing the forces and pressures acting on the test model in terms of the velocity head of the undisturbed flow in the tunnel.

For sufficiently small Mach numbers, (4.27) becomes Bernoulli's equation for an incompressible fluid.

$$p_0 - p = \frac{\rho V^2}{2}. \qquad (4.28)$$

As will be shown below, the value $p_0 - p = \Delta p$ can be measured with the aid of a dual-purpose tube and a differential manometer. We can thus determine the aerodynamic coefficients (for instance, $c_x = Q/qS$) without resorting to indirect measurements of ρ and V. The coefficient c_x thus is determined by directly measuring Δp and the drag Q of the model (with a wind-tunnel balance).

In compressible fluids the value of Δp exceeds the velocity head which must be determined from

$$q = \frac{\rho V^2}{2} = \frac{\rho}{2}a^2M^2 = \frac{\rho}{2}\left(\varkappa\frac{p}{\rho}\right)M^2 = \frac{1}{2}\varkappa pM^2. \qquad (4.29)$$

Thus, for a compressible fluid, the velocity head depends on the static pressure and Mach number of the flow.

Measurements of velocity in incompressible fluids

Dual-purpose tubes

Equation (4.28) shows that the free-stream velocity of an incompressible fluid is

$$V = \sqrt{\frac{2(p_0 - p)}{\rho}} = \sqrt{\frac{2\Delta p}{\rho}}; \qquad (4.30)$$

for its determination it is necessary to know the difference between the total and static pressures and the density of the fluid. Methods of determining the density are described in § 15.

In general, for measuring the free-stream velocity, orifices at two points on the surface of a streamlined body are connected to a differential manometer. One of these orifices is usually arranged at the stagnation point of the body so that the total pressure acts on the corresponding leg of the manometer. The pressure difference between these two points is expressed through the free-stream velocity head

$$\Delta p_i = \frac{\rho V^2}{2} \frac{1}{\xi}. \qquad (4.31)$$

where ξ is the tube coefficient. At a given orientation in the flow, its value depends on the geometry of the tube and the position of the orifices. In general, ξ depends on Re and M (and also on several other similarity criteria, which are, however, of secondary importance).

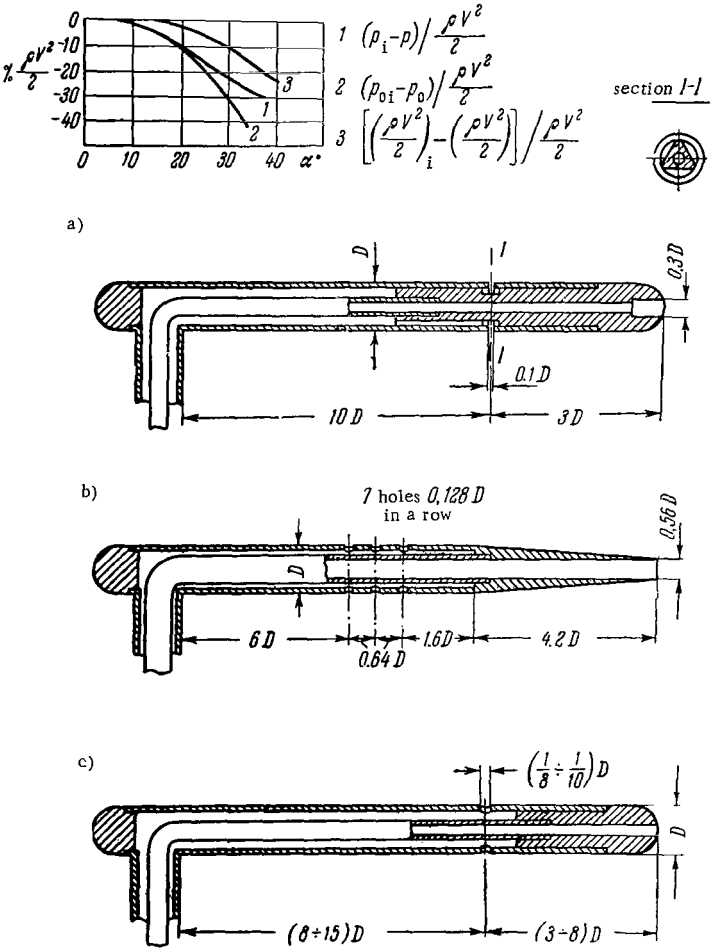

FIGURE 4.23. Dual-purpose tube. a — Pitot-Prandtl tube and its characteristics at various angles of yaw; b — NPL tube; c — tube with circular lateral orifices.

For velocity measurements in wind tunnels, dual-purpose tubes are used. They are shaped in such a way as to provide a coefficient as close to unity as possible. Such a tube consists of a static-pressure tube which measures p, and a total-pressure tube which measures p_0, combined as a single device.

Figure 4.23 shows the Pitot-Prandtl and NPL tubes. The NPL tube has circular orifices to sense the static pressure, while the Pitot-Prandtl tube has slots.

Slots are less liable to clogging, but the measured static pressure is more sensitive to the geometry of the slot. Circular orifices are therefore generally used in hemispherical-nose tubes (Figure 4.23c).

There is a simple relationship between the pressure difference Δp_i, measured by a differential manometer connected across the dual-purpose tube, and the true value Δp:

$$\Delta p_i = p_{0i} - p_i = \frac{1}{\xi}(p_0 - p) = \frac{1}{\xi}\Delta p, \tag{4.32}$$

so that if we know ξ, the velocity can be determined from

$$V = \sqrt{\frac{2\Delta p_i}{\rho}}\,\xi. \tag{4.33}$$

For dual-purpose tubes the coefficient ξ is constant and close to unity over a wide range of Reynolds numbers. For standard NPL (and geometrically similar) tubes, $\xi = 1$ for Reynolds numbers between 330 and 360,000, where **Re** is calculated from the outside diameter of the tube.

The lower limit of velocities which can be measured by dual-purpose tubes in tunnels with atmospheric-pressure test sections, is in the region of 1 to 2 m/sec. Below these velocities, measurements of total pressure are affected by viscosity and ξ is no longer unity (Figure 4.24). A further

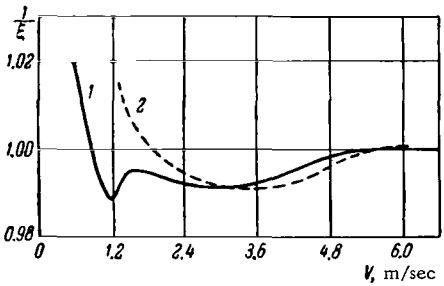

FIGURE 4.24. Variation of the tube coefficient at small free-stream velocities. 1—NPL tube; 2—Pitot-Prandtl tube.

difficulty is the extremely high sensitivity required of micromanometers used at such low velocities. To measure a velocity of 2 m/sec with an accuracy of 1%, the micromanometer error must be less than 0.005 mm W.G. The flow direction affects the readings of a Pitot-Prandtl tube when the yaw angle exceeds 5° (Figure 4.23).

The velocity is sometimes measured with tubes for which ξ is not unity, e.g., when using dual-purpose tubes for yaw measurements. Usually, variations in Re and M considerably affect the value of ξ of such tubes, and they are less accurate than standard tubes.

The advantage of dual-purpose tubes is that the value of ξ can be reproduced in a new tube if its geometry is a good replica of the original. However, calibration against a reference tube is recommended if accuracies better than 1 or 2% are required. Reference tubes are calibrated on a rotary-arm machine (see § 3). A reference tube which has been carefully calibrated on a rotary-arm machine is then used for the secondary calibration of other tubes in a special wind tunnel having uniform flow in the test sections.

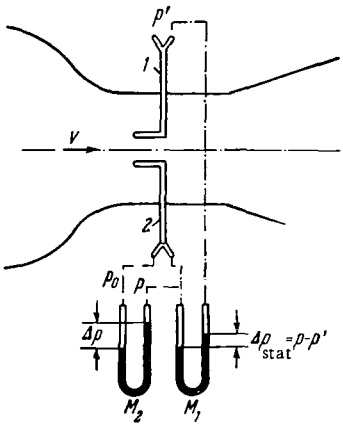

FIGURE 4.25. Calibration of tubes in a wind tunnel. 1—tube to be calibrated; 2 — reference tube.

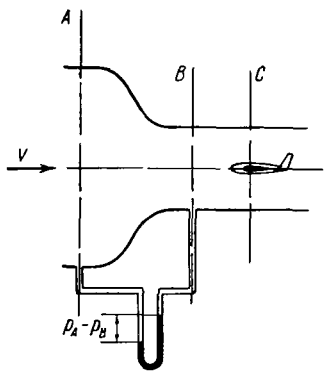

FIGURE 4.26. Determination of velocity from the static-pressure gradient in a tunnel with closed test section.

For calibration in a wind tunnel, the tube is installed beside the reference tube (Figure 4.25). The static-pressure arms of both tubes are connected to opposite legs of a sensitive differential manometer M_1. The difference of the static pressures Δp_{stat}, measured by the two tubes, is then determined at various flow velocities. Thereafter, the tubes are interchanged and the measurements repeated at the same velocities. By taking the average of the two pressure differences the effects of any static-pressure nonuniformity in the wind tunnel are eliminated.

The average static-pressure difference, measured by the manometer M_1 is

$$\Delta p_{\text{stat av}} = \left(\frac{1}{\xi} - \frac{1}{\xi_{\text{ref}}}\right)\left(\frac{\rho V^2}{2}\right)_{\text{av}},$$

where ξ and ξ_{ref} are the tube coefficients of the tube being calibrated and of the reference tube respectively.

The manometer M_2 is connected to both arms of the reference tube in order to determine the difference between total and static pressure:

$$\Delta p_{\text{av}} = \frac{1}{\xi_{\text{ref}}}\left(\frac{\rho V^2}{2}\right)_{\text{av}}.$$

Eliminating the velocity head , we obtain an expression for the tube coefficient of the tube being calibrated.

$$\frac{\xi_{\text{ref}}-\xi}{\xi}=\frac{\Delta p_{\text{stat av}}}{\Delta p_{\text{av}}}.$$

It is assumed, that in this method there is no error in measuring the total pressure by either tubes. We have already seen that a high accuracy of measuring p_0 can be obtained with tubes of very different nose shapes.

Measurement of operational velocity in low-speed wind tunnels

In wind tunnels with closed test sections the free-stream velocity can be measured by the static-pressure drop between two sections of the tunnel. These sections are most conveniently chosen in such a way that one is in the settling chamber of the tunnel (section A, Figure 4.26), while the other is at the entrance to the test section, far enough away from the model to be unaffected by its presence (section B). By Bernoulli's equation the total-pressure difference between these two sections will be equal to the losses between them:

$$p_A+\frac{\rho V_A^2}{2}=p_B+\frac{\rho V_B^2}{2}+\zeta_1\frac{\rho V_B^2}{2},$$

where ζ_1 is the loss coefficient, and p_A, p_B, V_A, and V_B are the static pressures and velocities in sections A and B, respectively. If the cross sections at A and B, and the area of the test section at C (where the model is located) are F_A, F_B, and F_C respectively, then according to the continuity equation for an incompressible fluid

$$F_AV_A=F_BV_B=F_CV_C.$$

Substituting in Bernoulli's equation the values of the velocity heads in sections A and B, expressed through the velocity head in the test section [section C], we obtain

$$p_A-p_B=\zeta\frac{\rho V_C^2}{2},$$

where

$$\zeta=\left(\frac{F_C}{F_B}\right)^2\left[1+\zeta_1-\left(\frac{F_B}{F_A}\right)^2\right].$$

With the aid of this last equation we can obtain the velocity head in the test section of the tunnel, by measuring the static-pressure drop between sections A and B. For this purpose we must also know the value of ζ. This is determined by calibrating the empty tunnel with a dual-purpose tube. At different flow velocities the average value of the velocity head in section C is determined simultaneously with the pressure drop p_A-p_B. The value of ζ can be found from these measurements. Setting $1/\zeta=\mu$ we obtain

$$V=\sqrt{\frac{2(p_A-p_B)}{\rho}}\mu,$$

where μ is the pressure-drop coefficient. For more accurate measurement of the pressure-drop, sections A and B are provided with several openings (usually from 4 to 8), which are interconnected by tubes, thus forming "piezometric" rings.

The operational flow velocity of a wind tunnel is usually specified as the average flow velocity in the empty tunnel, at the point in the test section where models are installed, and at the same mass flow rate as when a model is present. This condition ensures equal pressure drops $p_A - p_B$ with and without the model.

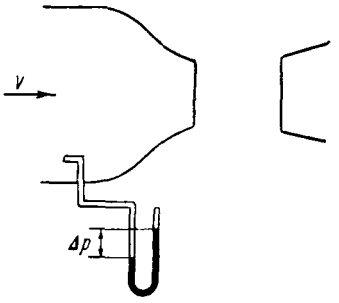

FIGURE 4.27. Velocity measurement in a tunnel with an open test section.

The static pressure in an open test section is equal to the static pressure in the surrounding space. Therefore, the operational flow velocity in the test section can be established, after calibrating the tunnel, from the difference between the total pressure in the settling chamber and the room pressure (Figure 4.27).

Measurement of high subsonic velocities

Equation (4.27) shows that in a compressible fluid the difference Δp between the total and static pressures exceeds the velocity head. In order to determine the latter (and therefore the velocity) it is necessary to find the compressibility correction ε. If the value of Δp were measured with a dual-purpose tube placed in the test section of the wind tunnel, a shock wave would appear upstream of the tube at supersonic free-stream velocities. The pressure at the orifice in the tube nose would then not be equal to the total pressure p_0. Equations (4.25) and (4.27) are therefore only fully applicable to dual-purpose tubes at subsonic flow velocities, for which

$$M = \sqrt{\frac{2\Delta p_i}{\varkappa p (1+\varepsilon)}}\,\xi, \tag{4.34}$$

$$V = \sqrt{\frac{2\Delta p_i}{\rho (1+\varepsilon)}}\,\xi. \tag{4.35}$$

Here Δp_i is the pressure difference across a differential manometer connected to the dual-purpose tube.

In compressible gas flow the value of ξ is no longer constant, as was the case at low flow velocities. As can be seen from Figure 4.28 (curve No. 1), at high subsonic free-stream velocities the total-pressure arm of a Pitot-Prandtl tube functioned correctly up to $M \approx 1$, whereas the appearance of local shock waves affected the readings of the static-pressure arm even at Mach number of 0.8 to 0.85 (curve No. 2). Thus, the overall tube coefficient ξ at high subsonic velocities differs considerably from unity (curve No. 3).

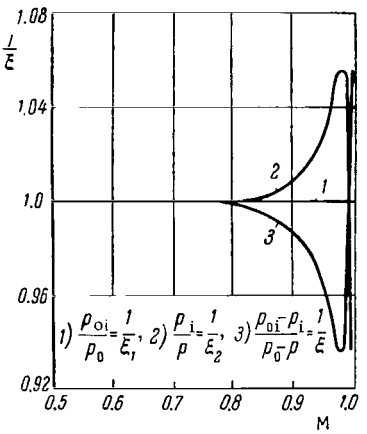

FIGURE 4.28. Effect of local shock waves on pressure measurement with a Pitot-Prandtl tube.

At low flow velocities the nose and the stem effects compensate mutually even when the orifices are quite near to the nose and the stem (Figure 4.7). At high flow velocities these effects must be reduced; this is usually done by increasing the distance of the orifices from both nose and stem. Hence, dual-purpose tubes for high-velocity measurements are usually long.

The accuracy of dual-purpose tubes at high subsonic velocities can be improved by the use of pointed noses. Figure 4.29 shows a miniature TsAGI-type tube. The needle-shaped tube nose gradually merges into the cylindrical part. At the stagnation point the nose has an orifice for measuring the total pressure. Static-pressure orifices are drilled in the assumed plane of yaw. These tubes are widely used in investigations of compressor and turbine-blade cascades, and narrow channels.

The first term of the general correction formula (4.26) for the compressibility effect gives a 0.5% velocity correction at $M = 0.2$, as calculated from tube measurements. The error caused by neglecting the second term amounts to 0.5% at $M = 0.8$, so that in practice, we can use the correction for $0 < M < 0.8$.

$$\varepsilon = \frac{M^2}{4}.$$

We can determine M and V either from (4.34) and (4.35), or from (4.23) and (4.24). The latter are used when, instead of measuring the pressure difference Δp, separate manometers are used to determine p_0 and p. In this case the magnitude p_0/p in (4.23) and (4.24) must be replaced by $p_{0i}\xi_1/p_i\xi_2$, where ξ_1 and ξ_2 are the tube coefficients for the total- and static-pressure arms of the dual-purpose tube (Figure 4.28).

However, at high velocities Δp itself can be measured very accurately by a sensitive differential manometer, so that (4.34) and (4.35) are ordinarily used. The value of p is then measured by a separate manometer connected to the static-pressure arm of the dual-purpose tube, and the value of $p_i\xi_2$ is substituted for the value of p in (4.34). In addition to Δp_i and p_i, (4.34) and (4.35) also contain the compressibility correction ε. The value of ε is determined directly from Δp and p by noting that in (4.5),

$$\frac{p_0}{p} = 1 + \frac{\Delta p}{p}.$$

Expanding $\left(\frac{p_0}{p}\right)^{\frac{\varkappa-1}{\varkappa}}$ as a series in powers of $\frac{\Delta p}{p}$, and writing

$$\varepsilon' = \frac{1}{2\varkappa}\frac{\Delta p}{p} - \frac{\varkappa+1}{6\varkappa^2}\left(\frac{\Delta p}{p}\right)^2 + \frac{(\varkappa-1)(2\varkappa+1)}{24\varkappa^3}\left(\frac{\Delta p}{p}\right)^3 - \ldots,$$

we obtain

$$M = \sqrt{\frac{2}{\varkappa}\frac{\Delta p}{p}(1-\varepsilon')}, \tag{4.36}$$

$$V = \sqrt{2gRT\frac{\Delta p}{p}(1-\varepsilon')}. \tag{4.37}$$

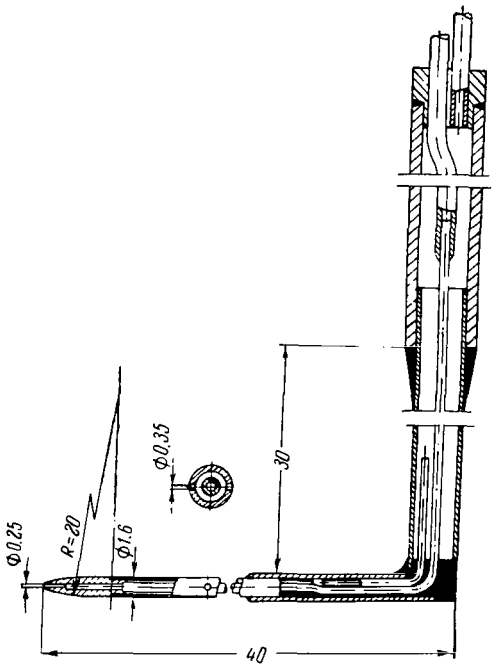

FIGURE 4.29. Miniature needle-nosed TsAGI-type tube.

Values of $\varepsilon' = \varepsilon/(1+\varepsilon)$ as function of $\Delta p/p$ are given in Table 7.

During experiments it is not good practice to use measuring tubes mounted in the test section, since they considerably affect the flow around the model. The average values of the operational free-stream velocity and of the operational Mach number in the test section are usually found by substituting in (4.36) and (4.37) the difference between the total pressure p_0 in the settling chamber of the tunnel and the static pressure p at the wall of the test section; p is measured

Table 7

M	$\frac{\Delta p}{p}$	ε'	M	$\frac{\Delta p}{p}$	ε'	M	$\frac{\Delta p}{p}$	ε'
0	0	0	1.1	1.1349	0.2537	2.1	8.1491	0.6212
0.1	0.0070	0.0025	1.2	1.4248	0.2925	2.2	9.6952	0.6506
0.2	0.0283	0.0099	1.3	1.7716	0.3323	2.3	11.315	0.6780
0.3	0.0644	0.0222	1.4	2.1827	0.3714	2.4	13.620	0.7040
0.4	0.1166	0.0395	1.5	2.6711	0.4104	2.5	16.094	0.7282
0.5	0.1862	0.0602	1.6	3.2517	0.4489	2.6	18.960	0.7504
0.6	0.2753	0.0846	1.7	3.9383	0.4863	2.7	22.310	0.7712
0.7	0.3872	0.1141	1.8	4.7471	0.5222	2.8	26.100	0.7897
0.8	0.5244	0.1457	1.9	5.7024	0.5568	2.9	30.646	0.8079
0.9	0.6915	0.1800	2.0	6.8247	0.5897	3.0	35.765	0.8239
1.0	0 8932	0.2163						

separately. The static pressure over the whole cross section is then assumed to equal the pressure at the wall. In the control stretch at the beginning of the test section, orifices are drilled for static-pressure tubes connected in parallel.

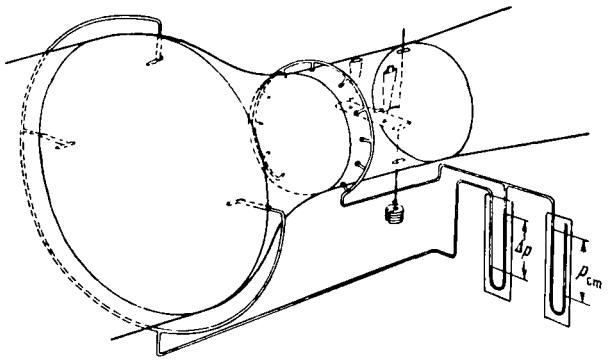

FIGURE 4.30. Layout for measuring the operational velocity and Mach number in wind tunnels.

The total pressure in the settling chamber is determined with one or several similarly interconnected tubes (Figure 4.30). Due to the considerable flow contraction at the entrance to the test section the presence of measuring tubes in the settling chamber causes practically no flow disturbance.

A subsonic wind tunnel is calibrated by comparing the pressure drop between the settling chamber and the test section (Figure 4.30) with the average pressure drop at different points of one or several different cross sections of the test section; this pressure drop is measured either with a dual-purpose tube or with separate total- and static-pressure tubes. At flow velocities close to the speed of sound, the cross-sectional area of the tube should be small in relation to the cross-sectional area of the test section. The relative change in flow velocity due to the local reduction of the tunnel cross-sectional area F by the area ΔF of the measuring tube

can be found from

$$\frac{\Delta V}{V} = \frac{\Delta F}{F}\,\frac{1}{M^2-1},$$

$$\frac{\Delta M}{M} = \frac{\Delta F}{F}\,\frac{1+\frac{\varkappa-1}{2}M^2}{M^2-1}.$$

Thus for $M = 0.95$ the error in measuring the velocity and the Mach number, due to the presence of a tube whose cross-sectional area is 0.1% of that of the test section, is about 1%.

Measurement of supersonic velocities

The Mach number is one of the most important parameters of supersonic flow and must often be determined with maximum possible accuracy. It can be determined optically by observing the inclination angles of the shock waves. A shock wave of infinitely small intensity lies along the Mach line

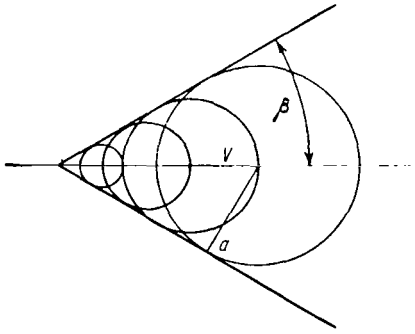

FIGURE 4.31. Mach lines.

whose angle of inclination (Figure 4.31) is

$$\beta = \arcsin\frac{1}{M}.$$

It is not possible to observe Mach lines directly, but shock waves of finite intensity (caused, for instance, by irregularities on solid walls) can be observed. The value of M found in this way is slightly less than its actual value, since the propagation velocity of weak shocks is slightly greater than the velocity of sound; the shock-wave envelope observed will thus be inclined to the flow direction at an angle slightly greater than β.

The Mach number is best determined by measuring the inclination angle of the shock wave appearing at a wedge- or a cone-shaped obstacle placed with its apex at the test point and with its axis in the flow direction. We may then use the relationship between the Mach number, the inclination angle β of the shock wave, and the taper angle 2θ of the obstacle.

For a wedge we have

$$\sin^2\beta - \frac{\varkappa+1}{2}\,\frac{\sin\beta\cos\beta}{\cos(\beta-\theta)} = \frac{1}{M^2}; \qquad (4.38)$$

for a cone the curves in Figure 4.32 may be used.

It should be remembered, however, that if the taper angle of the obstacle is higher, or the Mach number lower, than a certain limiting value, the shock wave will be detached from the apex of the obstacle, and will become curved, so that the measurement will be incorrect. The limiting values of β as function of Mach number for cones of various angles are shown in Figure 4.32, and for wedges, in Figure 4.33.

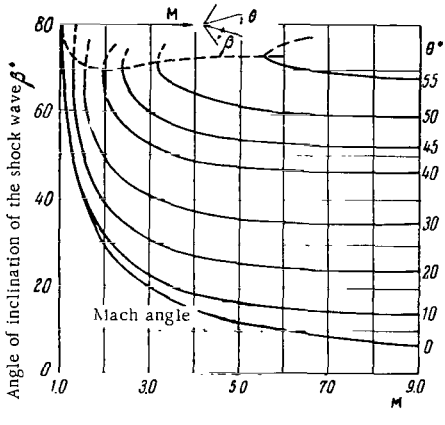

FIGURE 4.32. Variation with Mach number of angle of inclination of the shock wave at a cone apex.

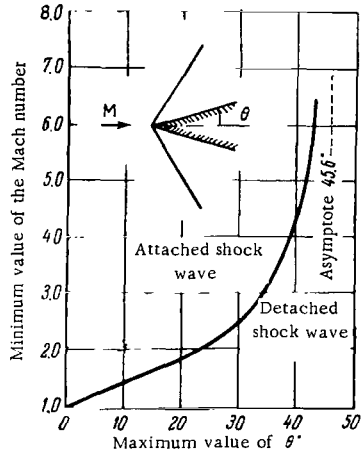

FIGURE 4.33. Conditions for detachment of the shock wave in front of a wedge.

In order to eliminate any influence of the rarefaction waves at the trailing edge of the obstacle on the shape of the nose shock wave, the angle of inclination of the latter must be determined near the nose.

The optical method of measuring Mach numbers is time-consuming and requires complicated equipment. Wind-tunnel Mach numbers are therefore generally determined on the basis of pressure measurements. Supersonic flow in the nozzle of a supersonic wind tunnel is attained isentropically. The total pressure throughout the test section, excluding the boundary layer and the region downstream of the shock caused by the model, can be considered equal to the total pressure in the settling chamber. Hence, the operational velocity and Mach number in the test section of a supersonic tunnel can be determined by the same method (Figure 4.30), using (4.5), as for subsonic velocities. At subsonic velocities $\Delta p = p_0 - p$, is small, and can be measured with high accuracy by a sensitive micromanometer. At supersonic velocities Δp is of the same order of magnitude as p_0, and we can measure p_0 and p separately without loss of accuracy.

In order to find the Mach-number distribution across the test section of the wind tunnel (i.e., to calibrate the test section), it is necessary to use a tube in turn at each test point. In principle, we can use for this purpose a Pitot-Prandtl tube and measure with separate manometers the total pressure p_0' at a given point behind the normal shock and the static pressure p of the undisturbed flow. The Mach number can then be found from Rayleigh's formula, obtained from (4.5) and (4.15):

$$\frac{p}{p_0'} = \frac{\left(\frac{2\varkappa}{\varkappa+1}\mathrm{M}^2 - \frac{\varkappa-1}{\varkappa+1}\right)^{\frac{1}{\varkappa-1}}}{\left(\frac{\varkappa+1}{2}\mathrm{M}^2\right)^{\frac{\varkappa}{\varkappa-1}}}. \tag{4.39}$$

However, this formula is reliable only when the nose orifice of the tube is in its entirety behind the shock. The tube with which the total pressure p_0' is measured must therefore have a blunt nose. On the other hand, considerable errors arise in measuring the static pressure p with a blunt-nose tube; these errors cannot always be eliminated by locating the side orifices away from the tube nose. Hence, total and static pressures in supersonic flow are usually measured by separate tubes: p_0' with a tube having a blunt nose, and p with a tube having a sharp conical or ogival tip.

When calibrating the test section we can also use (4.5); it is then necessary to measure the total pressure in the settling chamber, and the static pressure in the test section separately (Figure 4.34a).

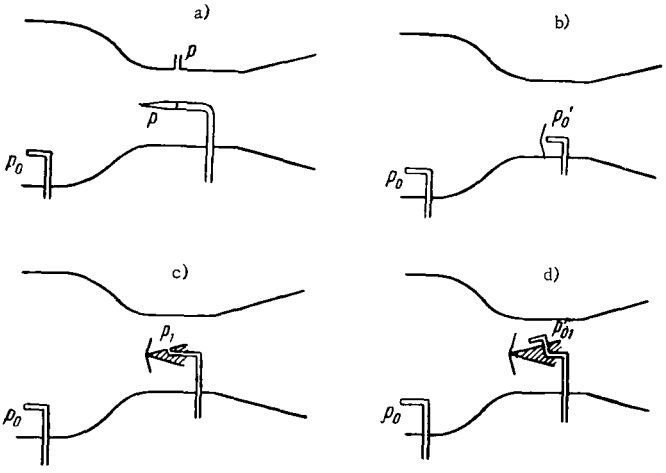

FIGURE 4.34. Measuring the Mach number in the test section of a supersonic wind tunnel by determining the total pressure p_0 in the settling chamber and the following in the test section: a — static pressure p; b — total pressure p_0'; c — static pressure p_1 on the surface of a wedge; d — total pressure p_{01}' in inclined flow.

A further method of measuring M is by mounting one total-pressure tube in the test section and another in the settling chamber (Figure 4.34b).

From the ratio of the total pressures in front of and behind the shock, given by (4.15), we then find the Mach number. Equations (4.5), (4.15), and (4.39) enable us to determine the Mach number by various methods with the aid of total-pressure and static-pressure tubes. Rayleigh's formula (4.39) is to be preferred when measuring the distribution of M in the boundary layer of a supersonic flow. In this case (4.5) cannot be used because due to friction losses, the total pressure in the boundary layer is not equal to the total pressure in the settling chamber. The total pressure p_0' in the boundary layer is therefore measured by means of a miniature total-pressure tube, and the static pressure with the aid of an orifice in the wall (Figure 4.35) or a pointed probe.

Further methods of determining the Mach number in supersonic flow consist in measuring the static pressure p_1 at the surface of a wedge and the total pressure p_{10}' behind the oblique shock, formed at the sharp corner of a wedge (Figure 4.36). For an oblique shock M is determined directly from the angle β between the shock wave and the flow direction. The relationship between β and the Mach number in the undisturbed flow is given by (4.38) for different taper angles of the wedge, while the relationships between the pressures in front of, and behind an oblique shock are given by (4.17) and (4.19).

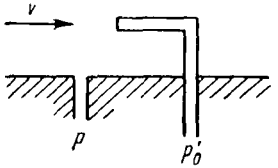

FIGURE 4.35. Determining the Mach number in the boundary layer.

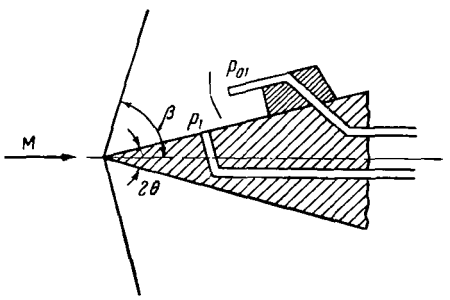

FIGURE 4.36. Wedge-shaped obstacle for measuring Mach number.

Thus the Mach number can be found by measuring any two of the following pressures: p_0, p, p_1', p' p_{01}' and p_1. The accuracy of determination depends on which different pressures are chosen, and we can use the error theory /10/ to select those pressures p_1 and p_2, which will give the least error in the calculated value of M. When $\varkappa$ = const, the ratio of any of these pressures must be a function of M only,

$$\bar{p} = \frac{p_1}{p_2} = f(\mathrm{M}).$$

Differentiating both sides of this equation, we obtain

$$d\mathrm{M} = \frac{f(\mathrm{M})}{f'(\mathrm{M})} \frac{d\bar{p}}{\bar{p}}. \qquad (4.40)$$

If the standard deviations σ_{p_1} and σ_{p_2} of the pressures p_1 and p_2 are governed by the Gaussian law of random error distributions we may use the

error summation formula to determine the standard deviation of the pressure ratio

$$\sigma_{\bar{p}} = \sqrt{\left(\frac{\partial \bar{p}}{\partial p_1}\sigma_{p_1}\right)^2 + \left(\frac{\partial \bar{p}}{\partial p_2}\sigma_{p_2}\right)^2}.$$

whence

$$\frac{\sigma_{\bar{p}}}{\bar{p}} = \sqrt{\left(\frac{\sigma_{p_1}}{p_1}\right)^2 + \left(\frac{\sigma_{p_2}}{p_2}\right)^2}.$$

Since the measuring errors are considered to be small, the error in the calculated standard deviation value of **M** can be approximated by substituting $\sigma_{\bar{p}}$ for the differential $d\bar{p}$ in (4.40).

If p_1 and p_2 are measured by manometers with the same error throughout the whole range:

$$\sigma_{p_1} = \sigma_{p_2} = \sigma_p,$$

the error by indirectly measuring will be /10/

$$\sigma_M = g\frac{\sigma_{\bar{p}}}{\bar{p}}. \qquad (4.41)$$

where

$$g = \frac{f(M)}{f'(M)}\sqrt{\left(\frac{\bar{p}}{p_1}\right)^2 + \left(\frac{\bar{p}}{p_2}\right)^2}.$$

Equation (4.41) shows that the error in determining **M** is inversely proportional to the rate of change of $\bar{p}$ with **M**. Figure 4.37 shows the values of the coefficient g for three pressure ratios measured in head-on flow.

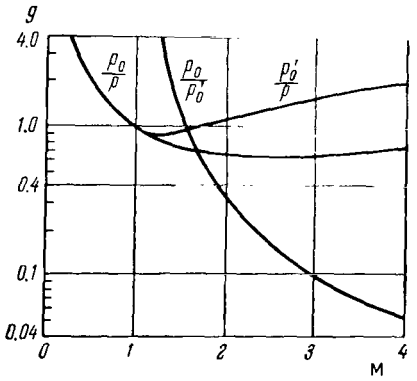

FIGURE 4.37. Errors in Mach-number determination by various methods (coefficient g).

Using (4.5) and (4.41) we can also find the errors in determining the operational value of M in the test section when p_0 is measured in the

settling chamber and p at the wall of the test section:

$$\sigma_M = \frac{1+\frac{\varkappa-1}{2}M^2}{\varkappa M}\sqrt{\left(\frac{p_0}{p}\right)^2+1}\,\frac{\sigma_p}{p_0}. \qquad (4.42)$$

The error in determining M is thus inversely proportional to the pressure p_0 in the settling chamber. Figure 4.38 shows the relative error in M if the manometer used for measuring p_0 and p is accurate to 1 mm Hg. From the graphs, simple calculation gives σ_M for other errors in measuring p_0 and p.

If the pressures p_1 and p'_{01} are measured with a wedge-shaped obstacle (Figure 4.36) the error in M is

$$\sigma_M = g_1\frac{\sigma_p}{p}. \qquad (4.43)$$

where the coefficient g_1, whose values are shown in Figure 4.39, depends on the wedge angle θ.

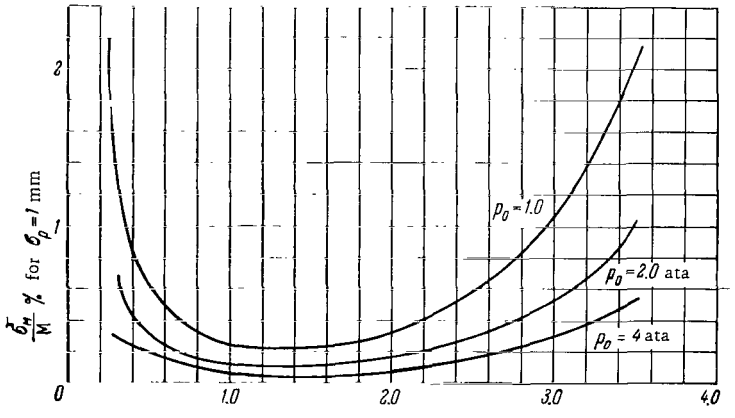

FIGURE 4.38. Relative error in determination of Mach number by measuring p_0 and p.

Technically most suitable for determining M are those methods in which the total pressure in the settling chamber is one of the measured pressures. The other may be the static pressure, the total pressure downstream of a normal shock, or the total or static pressure behind the oblique shock at a wedge (Figure 4.34). For determining the Mach number and the true velocity in subsonic flow, static pressure is usually measured. This method (Figure 4.34a) is suitable up to M = 1.6 to 1.8. At larger Mach numbers the static pressure in the test section falls sharply; because the manometer error remains the same, the accuracy of determining M will be greatly reduced.

Determination of the Mach number from measurements of the total pressure p'_0 behind a normal shock, (Figure 4.34b) is inaccurate at velocities only slightly higher than the sound velocity, because the pressure p'_0 then

differs only slightly from p_0. However, as M increases, the shock losses increase, and when M = 1.6 the accuracy of the methods using the static pressure p and the total pressure p_0' is the same. This point corresponds to the intersection of the curves $g = f\left(\frac{p_0}{p}\right)$ and $g = f\left(\frac{p_0}{p_0}\right)$ in Figure 4.37.

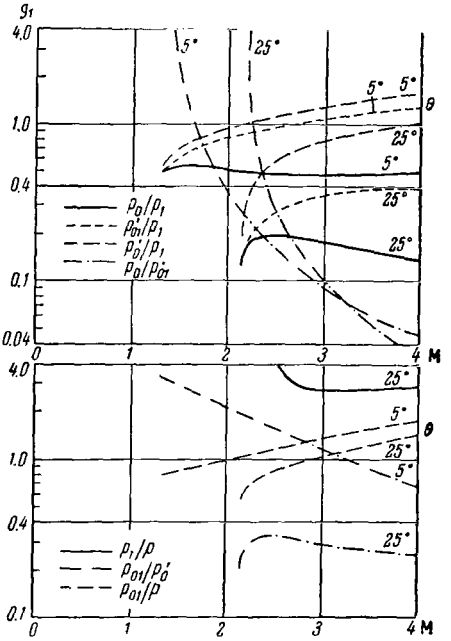

FIGURE 4.39. Errors in measuring M with a wedge (values of g_1).

When M is greater than 1.6 the measuring method shown in Figure 4.34b is preferable. When the Mach number exceeds 3 an even higher accuracy is obtained by measuring the total full pressure p_{01} behind an oblique shock (Figure 4.34d), though in practice measurement of p_0' provides sufficient accuracy.

This analysis has so far dealt only with random errors of pressure measurements. The systematic errors demand further consideration. For instance, at high Mach numbers there can be considerable total-pressure losses by condensation in the shock, and the determination of M from the values of p_0/p_0' or p_0/p_{01} can be unreliable. Systematic errors can be caused also by the tubes themselves; for instance, static-pressure tubes are sometimes affected by shocks forming at a small distance downstream of the orifices. In this case, the measured pressure may be too high since the pressure increase in the shock is transmitted upstream within the boundary layer.

When using a wedge-shaped tube, a systematic error can be caused by the boundary layer on the surface of the tube which changes the effective value of the angle θ and therefore of the pressure p_{01}. This error can be allowed, for instance, by measuring the angle of inclination of the oblique shock by the schlieren method. The curve of the total pressure p_{01}

downstream of an oblique shock as a function of the angle θ has a maximum for each value of M. Near this maximum p_{01} is almost independent of θ. Wedge-shaped tubes should be used at the optimum value of θ (i.e., the angle which corresponds to the indicated maximum) so that no great accuracy is required in measuring the angle β. For instance, when $M = 3.5$ an error of $\pm 0.5\%$ in the measurement of β causes an error in M of about ± 0.001.

The true flow velocity in a high-speed wind tunnel is a less important parameter than the Mach number, but it is necessary to determine it, for instance, for calculating the operational Reynolds number. When determining aerodynamic coefficients we use the velocity head, and no direct determination of V is required. The velocity is related to the Mach number by

$$V = M\sqrt{\varkappa g R T}.$$

Instead of the temperature in the flow we measure the total temperature in the settling chamber of the tunnel and determine T from (4.4). Thus, the velocity can be expressed in terms of the Mach number and the total temperature:

$$V = M\sqrt{\frac{\varkappa g R T_0}{1+\frac{\varkappa-1}{2}M^2}}. \tag{4.44}$$

Using the error-summation formula, we can find the absolute and relative errors in determining V :

$$\sigma_V = \sqrt{\left(\frac{\partial V}{\partial M}\sigma_M\right)^2 + \left(\frac{\partial V}{\partial T_0}\sigma_{T_0}\right)^2}, \tag{4.45}$$

$$\frac{\sigma_V}{V} = \sqrt{\frac{1}{\left(1+\frac{\varkappa-1}{2}M^2\right)^2}\left(\frac{\sigma_M}{M}\right)^2 + \left(\frac{\sigma_{T_0}}{2T_0}\right)^2}, \tag{4.46}$$

where σ_{T_0} is the error in measuring T_0.

The error in determining M thus depends on the error of the manometers and on the type of pressure being measured. Usually p_0 and p are measured. The error in the mean operational velocity in the test section of the wind tunnel, obtained by inserting into (4.46) the value of σ_M from (4.42), becomes

$$\frac{\sigma_V}{V} = \sqrt{\frac{1}{\varkappa^2 M^4}\left(\left(\frac{p_0}{p}\right)^2 + 1\right)\left(\frac{\sigma_p}{p_0}\right)^2 + \frac{1}{4}\left(\frac{\sigma_{T_0}}{T_0}\right)^2}. \tag{4.47}$$

In subsonic and supersonic flow, the coefficient of the first term within the square root is large compared with that of the second; hence, accuracy of pressure measurement is most important. At hypersonic velocities these coefficients differ very little: hence, the total temperature must be measured accurately.

The hot-wire anemometer method of measuring the flow velocity

The principle of the hot-wire anemometer is based on the variation in the rate of cooling of electrically-heated wires, with the flow velocity of fluid streaming past them. The rate of heat transfer from the heated wire to the particles of the moving fluid depends on the diameter and composition of the wire and the physical characteristics of the flowing medium. Since the electrical resistance of the wire depends on its temperature, a simple electrical-resistance measurement can be used to determine the velocity. The dependence of the anemometer resistance on the velocity is determined by calibration in a wind-tunnel against a reference instrument.

The main advantage of hot-wire anemometers over pneumometric devices is their rapid response. Change of pressure causes the flow of a finite mass of fluid between the orifices of a tube and the manometer, which therefore registers the change only after a finite time lag [transmission lag]. Except at resonance, the amplitude of pressure oscillations will be underestimated in manometer measurements; the error will depend on the amplitude and frequency of the pulsations and on the geometry of the tube (primarily on the dimensions of the orifices and on the diameters of the connecting pipes). Considerable difficulty is experienced in measuring the amplitudes of pressure and velocity fluctuations at frequencies higher than a few cycles per second. A more exact knowledge of the complex laws of gas flow depends on the instantaneous measurement of velocities. The hot-wire anemometer is thus the principle instrument for measuring turbulence.

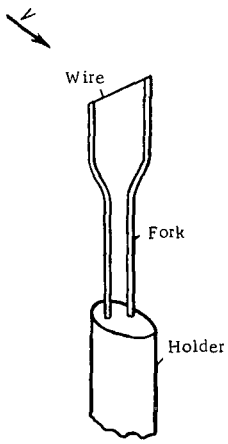

FIGURE 4.40. Hot-wire anemometer.

Another important advantage of the hot-wire anemometer is its high sensitivity. Whereas the sensitivity of the pneumometric method of velocity measurement decreases with velocity decrease, that of the hot-wire anemometer increases, so that the latter is more suitable for measuring velocities below 5 to 10 m/sec in spite of the more complicated measuring equipment required.

A further important advantage of hot-wire anemometers is that they can be incorporated in very small probes for the study of the boundary layer at a solid wall.

The design of a hot-wire anemometer is shown schematically in Figure 4.40. The wire, of a pure, chemically inert metal (platinum, tungsten, or nickel) is silver-soldered or welded to two electrodes which form a fork. The wire has a diameter of 0.005 to 0.15 mm, and is from 3 to 12 mm long. It is installed at right angles to the direction of flow.

The rate of heat loss per unit length of wire and per degree of the temperature difference between the surrounding medium and the wire is according to King /12/,

$$Q = B\sqrt{V} + C,$$

where B and C are functions of the temperature difference and of the properties of medium and wire. For a wire of given dimensions and with a constant excess temperature above that of a particular medium (e.g., air). B and C are constants which can be determined for the particular conditions. The above equation agrees well with the experimental data for velocities up to about 30 m/sec, and down to about 0.1 m/sec, which is comparable to the velocity of convection currents around the hot wire.

At equilibrium the wire will transmit heat to the surrounding medium at the rate of I^2R/J cal/sec, where J is the mechanical equivalent of heat in joules/cal. Hence

$$\frac{I^2R}{J} = B\sqrt{V} + C.$$

If the temperature of the wire is held constant, its electrical resistance is also constant. For a particular wire in a given medium we then obtain

$$I^2 = k\sqrt{V} + I_0,$$

where k is a constant, and I_0 is the current at zero free-stream velocity of the given medium. An example is given in Figure 4.41, which shows

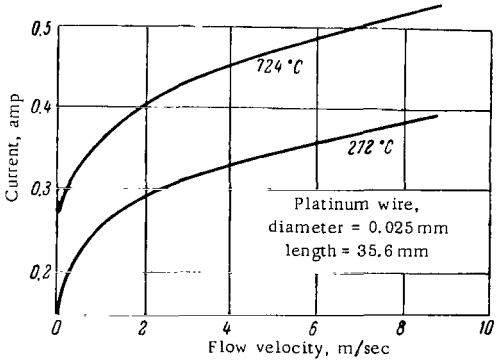

FIGURE 4.41. Relationship between the current in a hot-wire anemometer and the flow velocity, at constant wire resistance (temperature).

the main characteristic of the hot-wire anemometer, namely its high sensitivity at low flow velocities. At constant resistance the current changes with velocity most rapidly at small free-stream velocities. Sensitivity increases with the wire temperature throughout the velocity range. The temperature of the wire is, however, limited by aging and strength considerations and should not exceed 400 to 500°C.

If the current through the wire is held constant, the changes in temperature and resistance of the wire can be predicted. Hot-wire anemometers may therefore be used to measure velocity either at constant resistance or at constant current, as shown in Figure 4.42.

For measurements at constant resistance the wire forms one arm of a Wheatstone bridge, the other arms being resistors (e.g., manganin)

having a negligible temperature coefficient. A change in the velocity causes the temperature and resistance of the wire to change; this unbalances the bridge. In order to restore the balance of the bridge the wire temperature is restored to its initial value by adjusting the resistance of the adjacent arm or of an auxiliary resistor (4.42a). Velocity is measured in terms of the current in the wire, as indicated, for instance, by an ammeter connected in an external circuit.

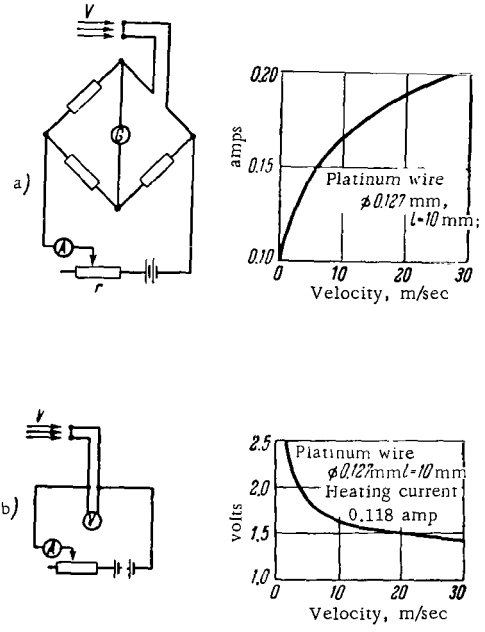

FIGURE 4.42. Circuits and calibration curves for hot-wire anemometers. a — by the constant-resistance method; b — by the constant-current method.

Higher sensitivity is obtained by a potentiometric method (Figure 4.43) in which the wire current is determined in terms of the voltage drop across a constant resistance R having a negligibly small temperature coefficient. Thus, in the constant-resistance method the velocity is determined in terms of the current (or voltage) needed to maintain a constant temperature, and thus constant resistance, of the wire.

The circuit for constant-current measurements is shown in Figure 4.42b. In this case the velocity is determined from the value of the resistance of the wire. The current in the wire is adjusted to the required constant value by means of a rheostat in series with the supply battery. The wire resistance is measured by a voltmeter of high internal resistance, connected in parallel. The constant-resistance method is more widely used, because it involves simpler measuring equipment. Complex electronic amplifiers are used to study turbulence.

In recent years, shielded hot-wire anemometers have been used to measure low velocities in steady flow (Figure 4.44). A wire heater made from nichrome (which has a low temperature coefficient of resistance) is

placed in one of the bores of a twin-bore ceramic tube of 0.8 to 1 mm outside diameter*. A copper-constantan thermocouple in the other bore serves to measure the temperature of the hot tube. The heater current is held constant, so that the temperature of the ceramic tube depends on the flow velocity. By measuring the thermoelectric emf of the thermocouple with a potentiometer or galvometer we can determine the temperature of the tube, and thus the flow velocity.

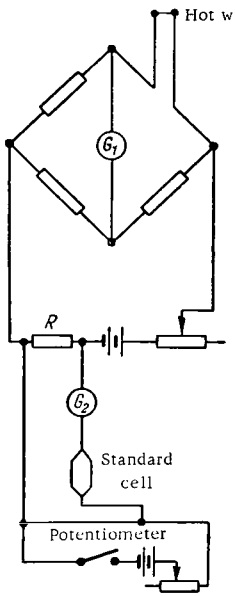

FIGURE 4.43. Potentiometric method for measuring current in a hot-wire anemometer at constant resistance.

Figure 4.45 shows a circuit for maintaining a constant current in the heater wire. An auxiliary hot-wire anemometer B, which is an exact replica of the principal anemometer A, is placed in an enclosure in which the velocity is zero and the temperature is constant. The heaters of the anemometers are connected in series. Under these conditions, the thermal emf E_B developed accross the thermocouple of B depends only on the current I passing through both heaters. A rheostat R is used to maintain this current constant in accordance with the indications of the thermocouple B. [For Figures 4.44 and 4.45 see p. 196.]

§ 13. THE MEASUREMENT OF FLOW DIRECTION

It was mentioned before that the total- and static-pressure readings by tubes are affected by the flow direction. The best instruments are, therefore, those which depend least on yaw. Exactly the contrary is true for tubes which are used for measuring the flow direction.

Usually yawmeters also measure other flow characteristics. An ideal tube would be suitable for measuring independently four quantities: the angles α and β of the inclination of the three-dimensional flow to two mutually perpendicular planes, the total pressure p_0, and static pressure p. The first pair of measurements determines the directions, and the second, the magnitude, of the velocity vector.

All-purpose tubes of this kind find wide application in investigations of turbomachines. They are, however, less accurate than dual-purpose tubes in the measurement of the magnitude of the velocity vector, due to the difficulty of measuring the static pressure accurately.

Pressure-sensing instruments for measuring the flow direction can be divided into two groups. The first group consists of devices in which the yaw is measured in terms of the pressure difference between two tubes whose orifices are arranged at a fixed angle with respect to each other.

* [Simmons, L. F. G. A Shielded Hot-Wire Anemometer for Low Speeds. — J. S. I. Vol. 26, p. 407. 1949.]

A total-pressure tube cut at a right angle to its axis is not very sensitive to variations of the yaw angle α between its axis

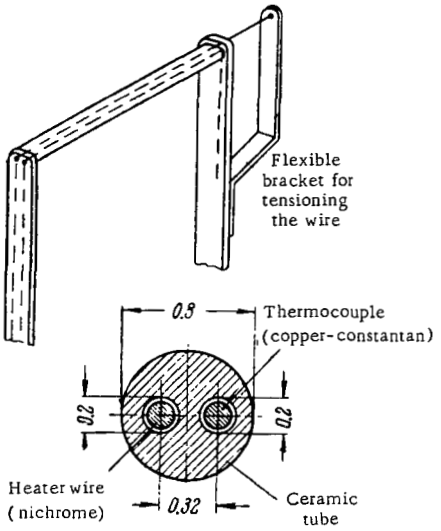

FIGURE 4.44. Shielded hot-wire anemometer.

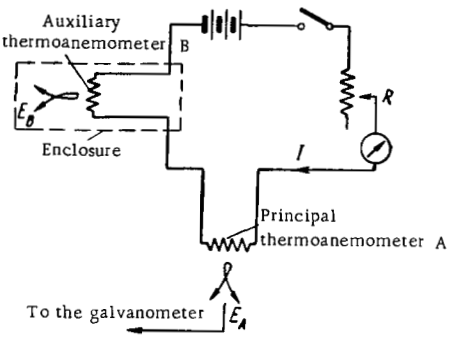

FIGURE 4.45. Circuit diagram of shielded hot-wire anemometer.

and the flow direction when α is less than 15 to 20°. The sensitivity increases sharply when α is between 40° and 60°; if the tube is cut at an angle to its axis, the same order of sensitivity can be obtained /3/ when $\alpha = 0$ (Figure 4.46).

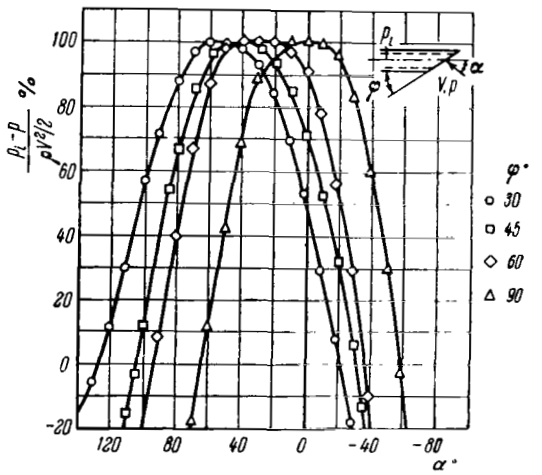

FIGURE 4.46. Variation with angle α of the difference between the pressure in the tube and the static pressure in the flow for plot tubes faced off at various angles φ.

The second group includes devices based on measuring the pressure difference between two points on the surface of a streamlined symmetrical body (sphere, cylinder, wedge, or cone). When the axis (or the plane of symmetry) of the body coincides with the direction of flow, the pressure at symmetrically located points is equal.

The orifices are situated on the body (or the direction of the tubes is chosen) in such a way that small changes in flow direction cause large pressure differences between the orifices which are connected to a differential manometer.

The sensitivity p_i of the tube is determined by the change in pressure at one of the orifices, due to a change in yaw:

$$k = \frac{d\bar{p}}{d\alpha}, \text{ where } \bar{p} = \frac{p_i - p}{\rho V^2/2}.$$

The sensitivity is thus defined as the slope of the tangent to the curve $\bar{p} = f(\alpha)$ The pressure at an orifice in a circular cylinder, whose axis is perpendicular to the flow, is most affected by the flow direction if the radius through the orifice makes an angle of 40 to 50° with the flow direction (see Figure 4.4).

A differential manometer connected to the yawmeter measures the pressure difference between two such orifices (1 and 2) so that the true sensitivity of the nozzle

$$k = \frac{d\left(\frac{p_1 - p_2}{\rho V^2/2}\right)}{d\alpha},$$

must be twice the value of $d\bar{p}/d\alpha$, obtained from the slope of the curves in Figure 4.4. The value of k varies between 0.04 and 0.08 per degree for different types of tubes.

The yawmeters are sensitive to transverse velocity gradients, which cause the pressures at two points situated symmetrically about the axis of the tube to be unequal, even when the tube axis coincides with the direction of flow. In this case the pressure difference between the orifices is zero at an angle which depends on the magnitude of the gradient, the distance between the orifices, their size, and the sensitivity of the tube [to pressure changes]. The best method to reduce the error due to transverse velocity gradients is to decrease the distance between the orifices. This, however, causes a decrease in the diameter of the orifices and of the tubes between the orifices and the manometer, which, in turn, increases the lag of the manometer indications because of the high flow impedance of the tubes. This should be taken into account when choosing the tube and manometer.

Yawmeters can be used directly or as null instruments. In the null method the yawmeter is rotated on a cradle until its axis coincides with the direction of the flow, as indicated by zero pressure difference in the differential manometer connected to the orifices. The direction of flow is then indicated by graduations on the cradle.

In the direct method the tube is held at a constant angle to the tunnel wall, and the yaw is determined in terms of the pressure drop between the orifices, measured by a differential manometer. The relationship between yaw and manometer indication is established by calibrating the tube in a wind tunnel of negligibly small transverse velocity gradients and flow

inclination. The direct measuring method requires less complicated equipment and less time than the null method, but is less accurate, especially at large angles of yaw. Because of its simplicity, and because it is possible to obtain simultaneous readings from an array of tubes, the direct method is usually employed in the calibration of wind tunnels, where normally the flow inclination is small. In the direct method the tubes can be easily adapted for measuring the velocity and direction of the flow in two planes.

The advantage of the null method of yaw measurement lies in the independence of the measurements on **M** and **Re**. It is also less important to locate the orifices very accurately on the tube in this method, since their positions merely affect the relationship between yaw and pressure drop. The null method is usually chosen for measuring flow angles in wakes, e.g., in experiments with blade cascades.

The combination of a direct and a null method is sometimes used in studying three-dimensional flow.

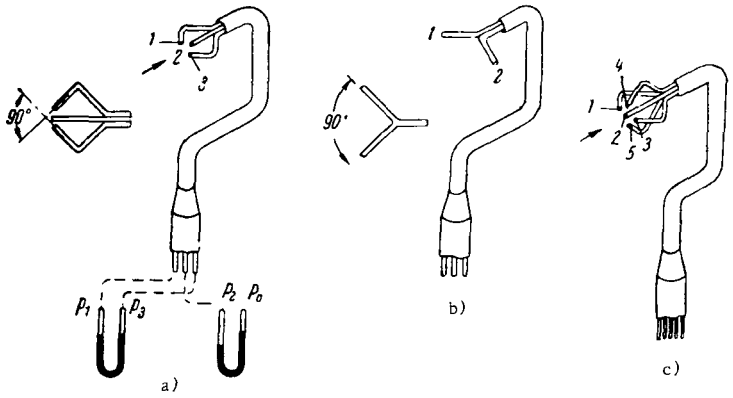

FIGURE 4.47. Tubular yawmeters cut at right angles. a and b — for two-dimensional flow; c — for three-dimensional flow.

Tubular yawmeters shown in Figure 4.47 consist of coplanar bent tubes, with ends cut at right angles, inclined to each other at an angle of 90°. The tube in Figure 4.47c is intended for three-dimensional flow. The angle of flow inclination in the xz plane can be measured by the null method (by rotating the tube about the y axis until the pressures in orifices 1 and 3 are equal), while the angle of inclination in the xy plane is found by the direct method in terms of the pressures difference between tubes 4 and 5. For measuring the flow velocity, yawmeters of this type are equipped with the additional tube 2, which senses the total pressure. The flow velocity can be determined from the pressure difference between the orifices of this tube and one of the lateral tubes, if the tube is calibrated against a reference dual-purpose tube. The drawback of these tubes is their low rigidity. Small deformations of the tubes can cause considerable errors when measuring yaw.

Recently, tubular yawmeters with beveled ends are increasingly being used for the study of blade cascades. Such tubes have external diameters of 0.5 to 2 mm. The tubes are mounted parallel to each other, so that the distance between their orifices is very small. In two-dimensional flow the influence of velocity gradients can be almost completely eliminated by locating the tube axes not in the plane of flow inclination but in a plane perpendicular to it, as shown in Figure 4.48d.

Figure 4.46 shows that in order to obtain maximum sensitivity to yaw, the tubes should be cut at an angle between 30 and 45°. Figure 4.48a gives the sensitivity characteristics of a two-tube yawmeter designed for small flow velocities. The characteristics of three-tube yawmeters for the direct method of measurement are usually expressed as a graph showing $\varkappa_\alpha$ as a function of α, where

$$\varkappa_\alpha = \frac{p_1 - p_3}{(p_2 - p_1) + (p_2 - p_3)}.$$

Figure 4.48b shows the variation of $\varkappa_\alpha$ with α for three-tube yawmeters of various bevel angles φ.

At small flow velocities (up to $M \approx 0.3$ to 0.4) a beveled-tube yawmeter can be used for the measurment of both direction and speed. The total and static pressures can be determined with a two-tube yawmeter (4.48a), for example, by the following method: the yawmeter is turned until the pressures in tubes 1 and 2 are equal ($p_1 = p_2 = p'$). The values of p_1 and p_2 are then determined after further rotation of the tube by angles of ±10°. The total and static pressures are then found with the aid of experimentally determined calibration coefficients k_1 and k_2 /13/,

$$p_0 = p' + k_1\Delta,$$
$$p = p' + k_2\Delta,$$

where

$$\Delta = \frac{1}{2}\{(p_1)_{+10^\circ} - (p_2)_{+10^\circ} - (p_1)_{-10^\circ} + (p_2)_{-10^\circ}\},$$

whence

$$\frac{\rho V^2}{2} = (k_1 - k_2)\Delta.$$

The yawmeter shown in Figure 4.48b is fitted with a central tube 2 for measuring the total pressure p_0, which can be determined by adjusting the tube so that $p_1 = p_3 = p'$. The flow velocity can be found with the aid of the coefficient ξ_V:

$$\xi_V = \frac{\frac{\rho V^2}{2}}{2(p_2 - p')} \approx \frac{p_0 - p}{2(p_2 - p')},$$

which is also determined by calibration against a reference tube.

Figure 4.48c shows the design of a four-tube yawmeter for three-dimensional flow measurements. The yawmeter consists of tubes whose outside and inside diameters are 0.8 mm and 0.5 mm respectively; the

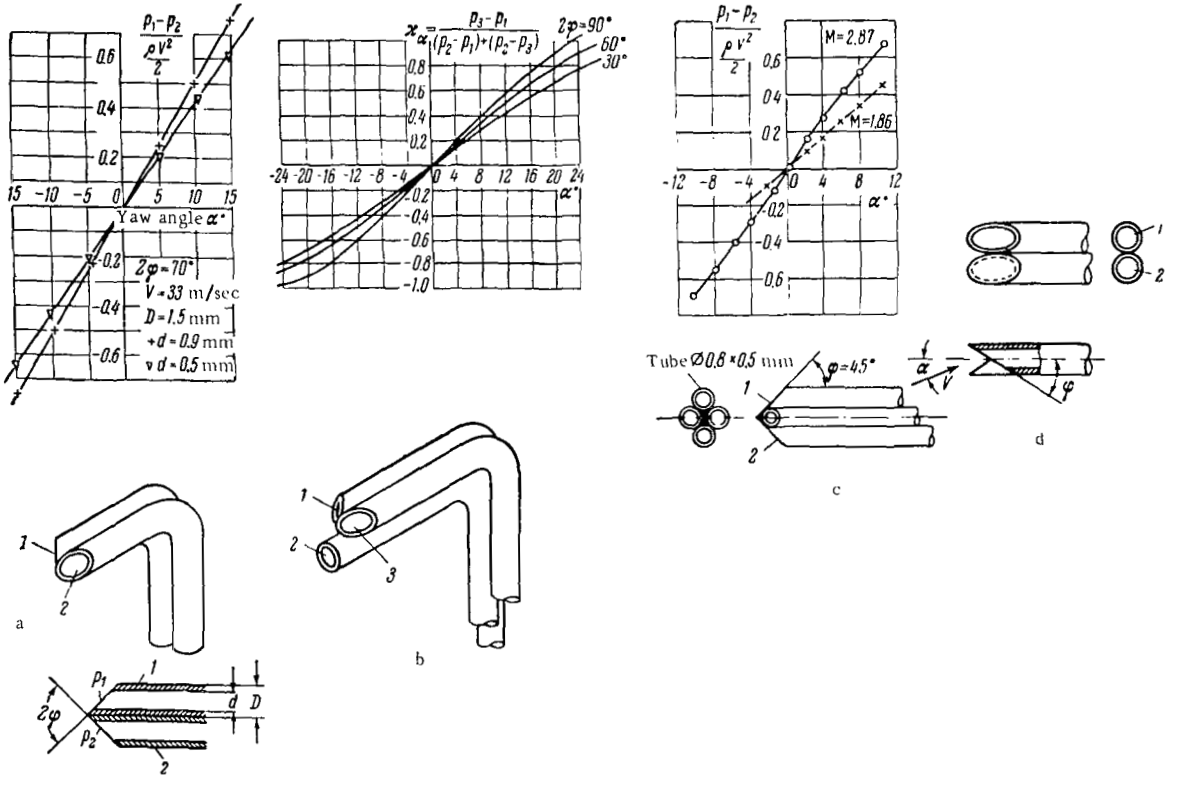

FIGURE 4.48. Tubular yawmeters with beveled ends. a—two-tube arrangement; b — three-tube arrangement; c — four-tube arrangement for three-dimensional flow; d — tube for two-dimensional flow with zero vertical distance between tube centers.

tubes are connected at the nose, and cut at 45°. The characteristics of this tube for $M = 1.86$ and 2.67 are shown in the same figure /14/. The sensitivity to yaw of such tubes is similar to that of wedges (Figure 4.53) and other types of yawmeter for supersonic velocities.

Cylindrical yawmeters

Cylindrical yawmeters (Figure 4.49) are used for determining the direction of two-dimensional flow. As can be seen from the characteristics shown in Figure 4.49b, their sensitivity is highest when the included angle 2γ between orifices (1) and (3) is between 90 and 100°. A third orifice, for measuring the total pressure, is drilled in the center between the two yawmeter orifices. Cylindrical yawmeters are generally used for the null method; the total pressure is measured when the pressures at the outer orifices are equal. The flow velocity can thus be determined from the pressure difference between the central and one of the outer orifices, provided that the velocity-calibration coefficient ξ_v is known; it is determined in the same way as for multiple-tube yawmeters. The value of ξ_v depends on the flow regime around the tube. The pressure at the front of the cylinder may differ from the theoretical value for potential flow (see Figure 4.4) because of boundary-layer separation. If boundary-layer separation takes place symmetrically on the upper and lower surfaces of the front quadrants of the cylinder, the change of pressure at the wall, due to the consequent change in Reynolds number , will not affect the yaw calibration coefficient $\varkappa_\alpha$, but there may be a considerable change in the velocity-calibration coefficient ξ_v. Figure 4.49c shows that $\varkappa_\alpha$ is virtually independent of Re, and is directly proportional to the yaw angle α for values below 15°. Nevertheless, the cylindrical yawmeter should be used with caution at $M > 0.6$, since local asymmetrical shocks may appear. The velocity coefficient ξ_v begins to be affected by compressibility at $\lambda \approx 0.3$ as can be seen from the graph of Figure 4.49d.

The advantage of the cylindrical yawmeter over other types is its small diameter, since it occupies an area, perpendicular to the flow, determined merely by the outside diameter of the tube, which can be very small. This is important, e.g., when investigating the flow between stator and rotor blades of axial turbomachines. Tubes with outside diameters up to 2.5 or 3 mm are used for blade-cascade investigations.

Spherical yawmeters

Spherical yawmeters (Figure 4.50) permit flow-direction measurements in three-dimensional flow with the aid of four orifices located in pairs in two mutually perpendicular planes. A fifth opening, at the intersection of these planes, serves for measuring the total pressure. The determination of the direction of a three-dimensional flow by the null method requires the use of a complicated cradle giving indications of the angular position in two planes. Only the angle β, in the xy plane, is therefore measured by

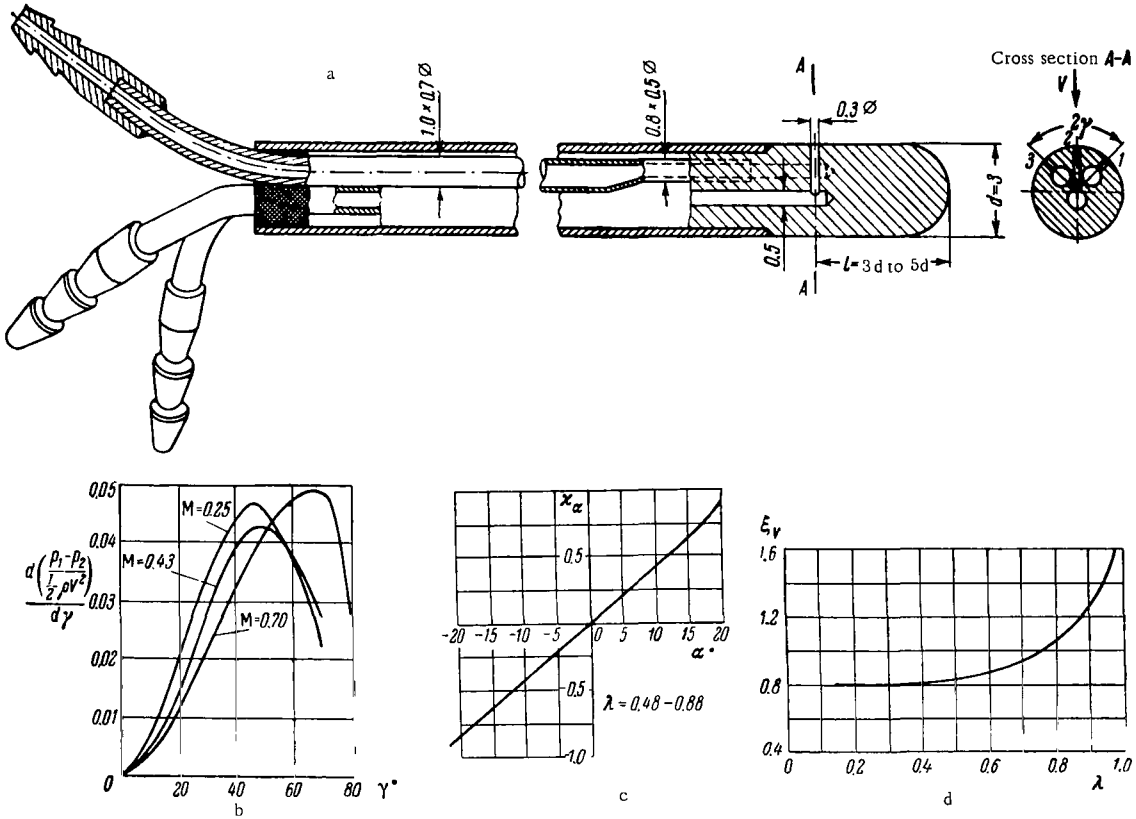

FIGURE 4.49. The cylindrical yawmeter and its characteristics.

the null method; the angle α in a plane perpendicular to the xy plane is determined by the direct method with the aid of a calibration curve obtained by two-dimensional flow tests (Figure 4.50).

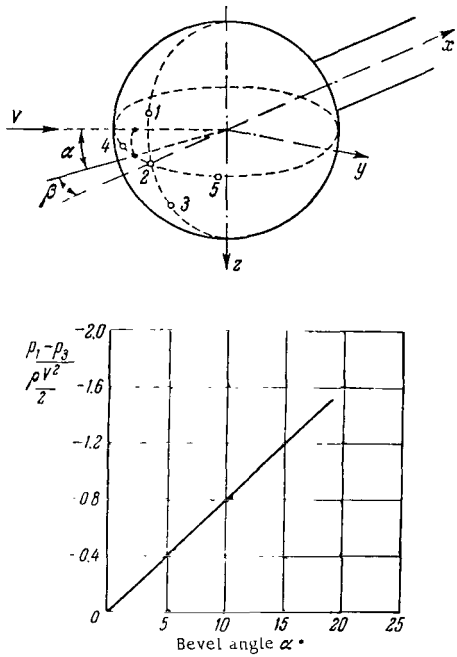

FIGURE 4.50. Spherical yawmeter and its characteristics (included angle between orifices is 90°).

When the yawmeter cannot be turned (e.g., when it is mounted on a turbine rotor) we can measure both angles directly with an accuracy of ± 1 to 2°, while simultaneously measuring the velocity and static pressure with an accuracy of the order of $\pm 3\%$ /15/.

The drawback of spherical yawmeters is the limited range of Reynolds numbers (from 4×10^3 to 1.5×10^5) within which their calibration coefficients are constant. When the laminar boundary layer becomes turbulant, the point of flow separation on the surface of the sphere becomes indeterminate; the flow around the sphere becomes asymmetrical, and this causes inaccuracies in measurement.

Hemispherical yawmeters

If we replace the rear half of the sphere by a cylinder, the flow conditions are improved and the point of boundary-layer separation is removed from the neighborhood of the orifices. Hemispherical yawmeters have the same sensitivity as spherical ones, but the influence

of the Reynolds number on their characteristics is much smaller. The sensitivity of hemispherical yawmeters decreases at large Mach numbers.

Figure 4.51 shows the TsAGI six-bore yawmeter /22/. In addition to the five openings in the hemispherical nose for measuring total pressure and flow direction, the yawmeter has an opening on its cylindrical stem for measuring the static pressure.

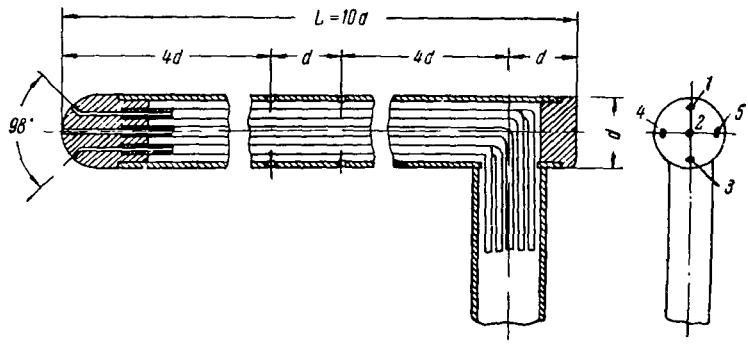

FIGURE 4.51. TsAGI six-bore yawmeter.

The TsAGI yawmeter is used for determining the magnitude and direction of the flow velocity in subsonic wind tunnels. The flow inclination in wind tunnels is generally small, so that the measurements are made by the direct method, i.e., without rotating the yawmeter. By calibrating [the yawmeter] in a wind tunnel in which the flow inclination is very small, we obtain

$$x = \frac{p_1 - p_3}{(p_1 - p_2) + (p_3 - p_2)} = f(\alpha),$$

$$\sigma = \frac{p_4 - p_5}{(p_4 - p_2) + (p_5 - p_2)} = f(\beta),$$

where p_1, p_3 and p_4, p_5 are the pressures in the orifices located in the vertical and horizontal planes respectively. At small yaw angles the yaw measurements in one plane are independent of the yaw in the other. Corrections must, however, be made when the yaw exceeds 5°, and these are determined by calibration as $\sigma = f(\alpha)$ and $x = f(\beta)$.

Wedge-type and conical yawmeters

Wedge-type yawmeters (Figure 4.52) can be used for measuring the flow inclination at velocities above those at which shocks appear on the surface of a sphere or cylinder, i.e., at $M > 0.55$ to 0.6 /16/. The advantage of these over cylindrical yawmeters is that the position of the orifices on the surface is less critical. The pressure-distribution curves

in Figure 4.52 show that with wedge-type yawmeters the pressure measurement is far less sensitive to the location of the orifices than with cylindrical yawmeters, so that manufacturing tolerances can be far wider. Either a separate orifice on the leading edge of the wedge, or a

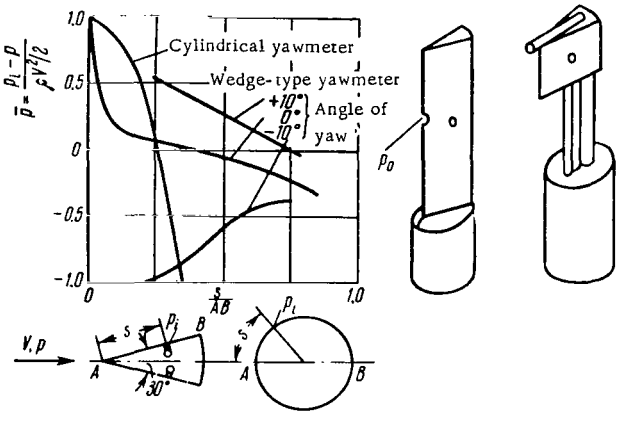

FIGURE 4.52. Wedge-type yawmeter and its characteristics (the pressure distribution on the surface of a cylindrical yawmeter is shown for comparison).

completely separate tube, can be used for measuring the total pressure. Wedge-type yawmeters can be used to measure the static pressure at higher Mach numbers than cylindrical yawmeters.

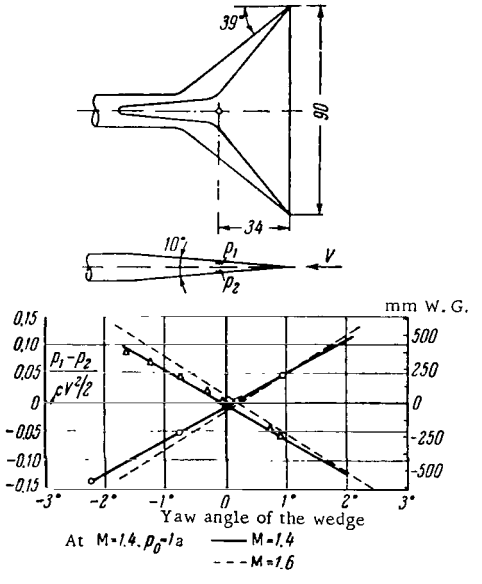

FIGURE 4.53. Wedge-type yawmeter for measuring the direction of supersonic flow.

Wedge-type and conical yawmeters with small included angles are among the most reliable instruments for investigating supersonic flow. Figure 4.53 shows the characteristic of a wedge-type yawmeter designed by the NAE Laboratory (Great Britain) for calibrating the 0.9 m×0.9 m test section of a continuous-operation supersonic wind tunnel /17/. The wedge yawmeter is installed on a spherical cradle so that it can be used for null-method measurements of the flow inclination.

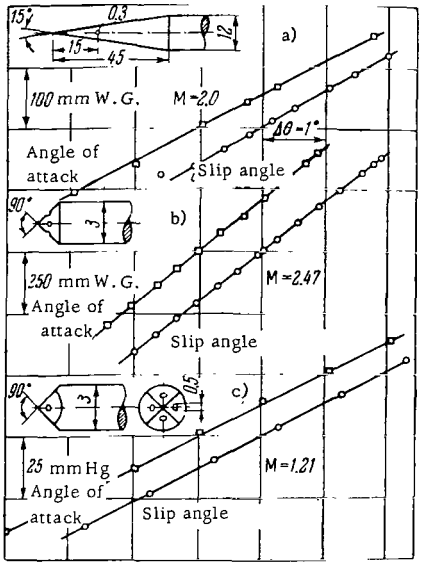

FIGURE 4.54. Characteristics of yawmeters for three-dimensional supersonic flow. a and b — conical yawmeters; c — pyramidal yawmeters.

Figure 4.54 shows the characteristics of conical and pyramidal RAE yawmeters for the direct-method measurement in three-dimensional supersonic flow. The sensitivity of conical yawmeters increases with the cone angle, but an included angle of 15° provides sufficient sensitivity, since an error of 1 mm W.G. in the measured pressure causes an error of only 0.02° in the yaw determination. Yawmeters can therefore be designed with other (e.g., production) considerations in mind. If the nose is pyramidal (Figure 4.54c) the exact location of the orifices is much less critical than for circular cones (where they must lie exactly in two mutually perpendicular planes) because flow round a pyramid is much less precisely defined. The calibration curves for these yawmeters remain linear even when the shock has become detached. All measurements in a series must, however, be carried out with the shock either attached or detached, since the calibration differs in these two cases /18/.

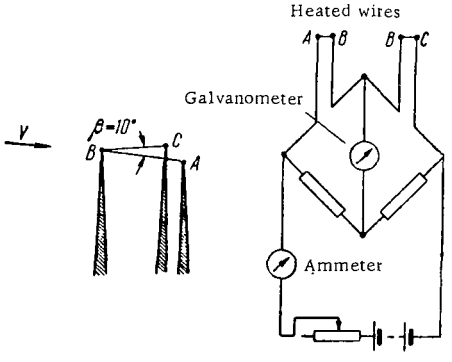

FIGURE 4.55. Hot-wire yawmeters.

Measurements of flow direction with a hot-wire yawmeter

If two identical wires are heated by the same current and placed in a uniform flow parallel to their plane, their rates of cooling will differ unless they are inclined at the same angles to the flow direction. Hot-wire yawmeters function on this principle. The wires are stretched between manganin posts A, B, and C (Figure 4.55) so as to include an angle β, and are connected to adjacent arms of a Wheatstone bridge. The instrument is rotated about an axis perpendicular both to the flow and to the plane of the wires, until both wires are at the same temperature and have the same resistance, so that the Wheatstone bridge is balanced. The flow direction is then parallel to a line bisecting the angle β. Since the dimensions and the electrical characteristics of the wires may differ, the instrument must be calibrated in a wind tunnel where the flow direction is known.

§ 14. MEASUREMENT OF TEMPERATURE IN FLOW

The measurement of the temperature of a flowing gas is important in investigations of the aerodynamic heating of the surfaces of aircraft and rockets, and in studies of the operation of gas turbines, compressors, aircraft engines, etc.

The state of a stationary perfect gas can be defined by two independent physical magnitudes, one of which may be the temperature. If the flow velocity is such that compressibility effects are important it is necessary to differentiate between the static temperature T and the stagnation (total) temperature T_0. A thermometer moving with the fluid, and emitting no thermal radiation would measure the static temperature. In practice the static temperature can be determined only indirectly, for instance by measuring the static pressure with a tube and the density optically, and then using (4.1); or by measuring the velocity of sound a and using (4.3a).

Measurements of the velocity of sound in a moving medium must be corrected for the flow velocity. Both electronic and optical methods are used for these measurements, but only a mean temperature within a certain region can be determined thus, so that this method is seldom used. It is much simpler to determine the temperature T by measuring the stagnation temperature and the Mach number. The stagnation temperature is the temperature which the gas would attain if brought to rest adiabatically, so that its entire kinetic energy is transformed without loss into heat. This temperature would be shown by a thermometer placed at the stagnation point of a body in the stream, provided no heat is lost to the surrounding medium. However, it is virtually impossible to make a thermometer which loses no heat at all. Furthermore, it would always have finite dimensions and thus cause turbulence, thus changing the local temperature. A thermometer inserted into a fast-flowing gas will therefore indicate a temperature lying between the static and the stagnation temperatures.

The difference between the stagnation temperature T_0 and the true temperature T of a moving perfect gas (in which temperature changes

are adiabatic) can be determined from

$$T_0 - T = \frac{V^2}{2gJc_p}.$$

Since shocks do not affect the enthalpy of a gas, this equation is true both for subsonic and supersonic flow.

A thermally insulated surface will be heated by a gas flowing past it to a temperature called the recovery temperature T_a. The recovery temperature depends on the local Mach number (or on the static temperature) at the outside limit of the boundary layer, on the dissipation of kinetic energy by friction in the boundary layer, and on the rate of heat exchange.

The difference between the recovery temperature and the static temperature is a fraction r of the adiabatic temperature rise:

$$T_a - T = r\frac{V^2}{2gJc_p}. \tag{4.48}$$

The coefficient r, called the coefficient of thermal recovery, is defined by

$$r = \frac{T_a - T}{T_0 - T}. \tag{4.49}$$

In general the coefficient of thermal recovery, which represents the proportion of the kinetic energy of the medium recovered as heat, depends on the shape of the body, and on M, Re, Pr and $\varkappa$. For a given gas, Pr and $\varkappa$ are constant over a wide range of the temperatures usual in subsonic and supersonic wind tunnels (for air, Pr = 0.72, $\varkappa$ = 1.4) and we can thus consider r as a function of M and Re only. The value of r may vary over the surface.

For laminar flow of an incompressible fluid around a flat plate, r depends only on the rate of heat exchange and the friction in the boundary layer on the surface of the plate. When Pr = 1, heat exchange and frictional heating compensate each other, and the adiabatic temperature on the surface is equal to the stagnation temperature T_0, i.e., $r = 1$.

Theoretically the recovery coefficient in laminar and turbulent boundary layers at a flat plate should be $r = \mathrm{Pr}^{1/2}$ and $r = \mathrm{Pr}^{1/3}$ respectively, but experimental values of 0.85 and 0.89 respectively, have been obtained.

The coefficient of thermal recovery depends on the shape of the surface. Studies in supersonic wind tunnels have shown that for poorly streamlined bodies r varies between 0.6 and 0.7, and for well streamlined bodies, between 0.8 and 0.9.

The relationship between the recovery temperature and the stagnation temperature depends on the Mach number, and can be deduced from (4.4) and (4.49):

$$\frac{T_a}{T_0} = 1 - \frac{\frac{\varkappa - 1}{2}\mathrm{M}^2}{1 + \frac{\varkappa - 1}{2}\mathrm{M}^2}(1 - r). \tag{4.50}$$

This function is plotted for $\varkappa$ = 1.4 and various values of r in Figure 4.56. In subsonic flow T_a decreases with increasing velocity. When M exceeds unity, a shock appears upstream of the body whose leading edge is therefore in a subsonic region; hence, the Mach number in (4.50) is less

than unity. With increasing supersonic free-stream velocity, the strength of the shock increases, the Mach number decreases, and therefore the value of T_a rises.

In the absence of heat transfer, a thermometer on the wall of a tube inserted into a gas stream would indicate a recovery temperature T_a dependent only on the flow characteristics in the boundary layer around the tube. When $r = 1.0, T_a = T_0$. However, an actual thermometer, in which heat exchange with the surrounding medium cannot be prevented, will indicate a temperature T_n differing from the recovery temperature T_a.

The principal characteristic of a thermometer is therefore the dimensionless quantity

$$\zeta = \frac{T_n - T}{T_0 - T}, \tag{4.51}$$

which is called the recovery coefficient of the instrument. By definition, the recovery coefficient ζ allows for the effects of heat exchange between the thermometer and the surrounding atmosphere caused by the heat conductivity of the instrument holder and by heat radiation.

The value of ζ for a given instrument can be established experimentally by calibration in a special wind tunnel. Knowing the temperature T_n, as measured by the instrument, and its recovery coefficient ζ, we can determine the stagnation temperature T_0, by substituting T_a and r for T_n and ζ in (4.50).

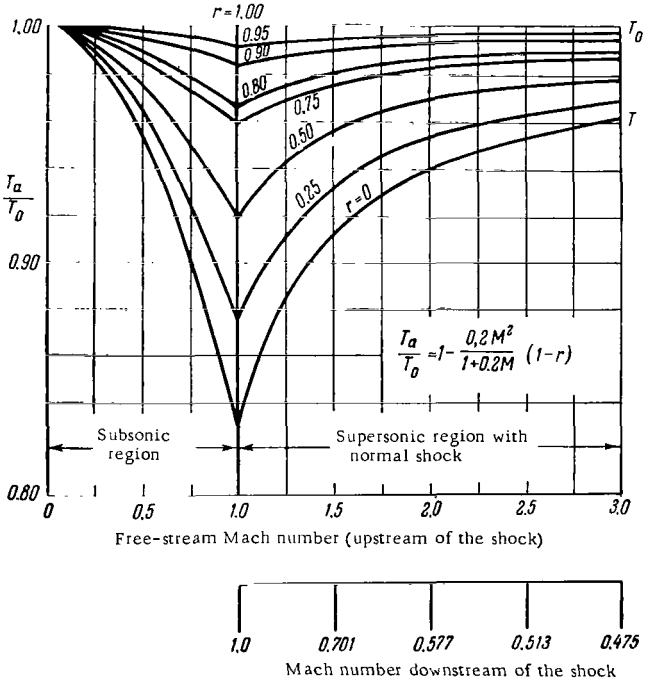

FIGURE 4.56. Ratio T_a/T_0 as a function of the Mach number for a thermometer of finite dimensions in subsonic flow, and in supersonic flow with a shock.

Sensors for measuring stagnation temperature

The design of a temperature sensor depends on the intended range of flow velocities and temperatures. The design and material of the sensor can be so chosen that it will indicate a temperature T_n which is sufficiently close to the stagnation temperature of the flow. Such a sensor can be called a stagnation-temperature sensor.

For a good stagnation-temperature sensor, the value of ζ should be close to unity. However, it is even more important that ζ should be constant, or change very little over the relevant range of velocities and temperatures.

The deviation from unity of the value of ζ depends on: 1) convectional heat exchange between sensing element and medium; 2) heat loss by conduction from the sensor through the device holding it; 3) radiant-heat exchange between sensor and the surroundings.

Since the processes by which heat exchange takes place vary with flow velocity and temperature, the design of the sensor depends on the values within the test range of all the physical parameters. Sensors can be roughly divided into three groups depending on the range of measurements: 1) sensors for low and high velocities at low temperatures; 2) sensors for high velocities, and temperatures up to 300 and 400°C; 3) sensors for low and high velocities at high temperatures (up to 1000—1200°C).

Low-temperature sensors. The effect of [heat] radiation can be neglected if the temperature of the wall on which the sensor is mounted differs very little from the temperature of the flowing medium. To determine the latter in the test section of most wind tunnels (for low or high velocities) it is sufficient to measure the stagnation temperature in the settling chamber of the tunnel. Since there is practically no input or removal of heat between the settling chamber and the test section, the stagnation temperature remains constant. The flow velocity in the settling chamber does not usually exceed some tens of m/sec and the temperature, some tens of degrees centigrade.

Mercury thermometers can be used as sensing elements in this range, but resistance thermometers and thermocouples provide faster operation and permit remote indication. The design of a resistance thermometer for measuring temperatures in the settling chamber of a wind tunnel is shown in Figure 4.57. The change in the resistance of the wire, as a function of temperature, can be measured with the aid of a ratiometer or a Wheatstone bridge. If all other parameters in a wind tunnel or on a test bench are measured and recorded automatically, it is better to use the automatic electronic bridges (currently made by Soviet industry). Standard bridges have usually a recording or indicating device actuated by a balancing motor placed inside the instrument. For automatic recording of temperature together with other parameters the balancing motor of the bridge is connected to a recorder or printer by means of a Selsyn or a digital convertor (see Chapter IX). Automatic bridges permit the temperature to be measured to an accuracy of tenths of a degree.

Sensors for high velocities and medium temperatures. When testing compressors it is necessary to measure temperatures up to 300° or 400°C at up to sonic velocities. The same range of stagnation temperature is found in supersonic wind tunnels fitted with air heating and in tunnels for heat-exchange tests. In most cases the sensors are

mounted in relatively narrow channels; in order to reduce the disturbances caused by them, the sensors should be small, for which the best sensing element is a thermocouple with wires of 0.1 to 0.2 mm diameter. For the range of temperatures considered iron-constantan or copper-constantan thermocouples are generally employed; they have sensitivities of 5 and 4 millivolts per 100°C respectively. The thermal capacity of the junction of the thermocouple is very small, so that it responds rapidly and measurement can be made at rapidly changing temperatures.

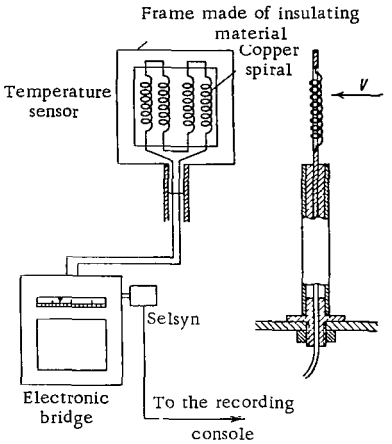

FIGURE 4. 57. Resistance thermometer for measuring the temperature in the settling-chamber of a wind tunnel.

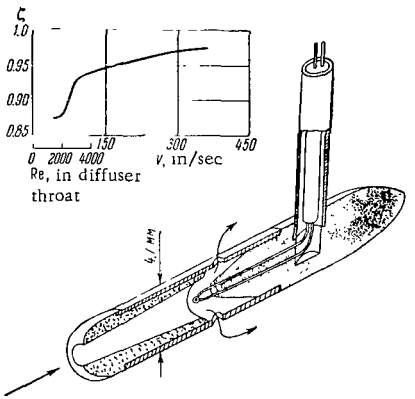

FIGURE 4. 58. Resistance thermometer for measuring the temperature in the settling-chamber of a wind tunnel.

When there is no radiant-heat exchange, a thermocouple consisting of butt-welded copper and constantan wires, inserted lengthwise into the flowing medium, will have a stable recovery coefficient ($\zeta = 0.9$) for $0.2 < M < 1.0$ and $3.8 \cdot 10^3 < Re < 14.4 \cdot 10^3$. The value of ζ is not constant for a thermocouple inserted transversely, since the recovery coefficient increases with velocity /19/. Although ζ is constant for bare wires inserted lengthwise, temperature sensors of this type are not widely used because of manufacturing difficulties.

Attempts have been made to measure the stagnation temperature with thermocouples installed at the frontal stagnation point of a streamlined sensor. It was found possible in such sensors to achieve a balance between heat exchange by convection with the medium and heat exchange by conduction with the supports. However, this type of sensor is very sensitive to slight changes in its shape, yaw, and radiant-heat exchange, and is not widely used

The most reliable design of stagnation-temperature sensors, having recovery coefficients close to unity over a wide range of velocities, relies on bringing the fluid to rest adiabatically near the thermocouple junction.

The gas upstream of the junction can be slowed down to a certain optimum velocity, where heat gained by the junction due to thermal convection in the gas is balanced by the heat lost from the junction due to the heat conduction of the supports. In low-velocity flow the temperature and velocity gradients are small, so that heat exchange and friction in the boundary layer at the junction of the thermocouple are insignificant. The medium is brought to rest adiabatically in a total-pressure tube, and the best temperature sensors so far developed are based on such tubes of modified shape. A further advantage of this design is that the tube can also be used as a radiation shield to prevent radiant-heat exchange with the surrounding medium. In order to prevent the gas from coming to rest completely, and to maintain a certain convective heat transfer to the junction in order to balance the loss through thermal conduction, the tube has outlet orifices whose area is 1/4 to 1/8 of the area of the inlet orifice. The dimensions and shape of a sensor within the stagnation zone inside a tube are less critical, and measurement reproducibility is better than if the thermometer were placed on the surface, where the recovery coefficient would depend on the flow conditions around the body. Thus, it has been possible to design sensors with recovery coefficients of the order of 0.99 for $0.2 < M < 3.0$.

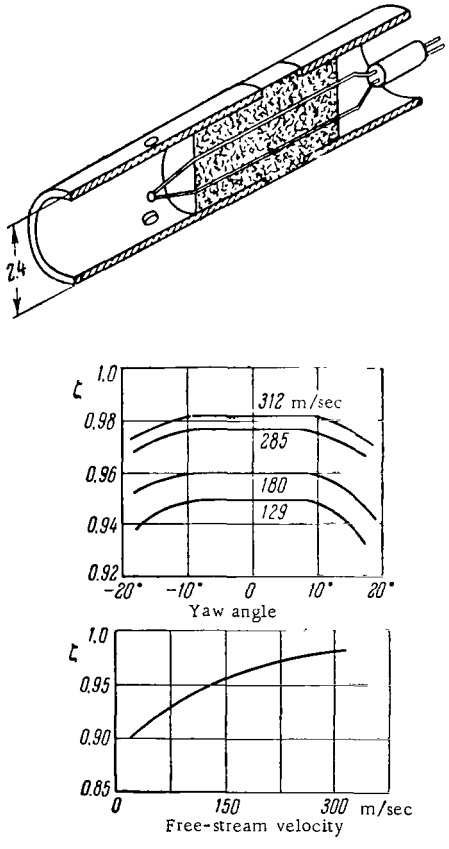

FIGURE 4. 59. Section and characteristics of the Pratt and and Whitney Pitot thermocouple .

In one of the earliest designs of shielded temperature sensors used at high velocities, the thermocouple was placed in the stagnation chamber of a round-nosed tube. Air entered into the chamber through a diffuser and small ventilating holes were drilled in the chamber walls to make up the heat losses from conduction and radiation. Figure 4.58 shows the design and characteristics of a sensor of this type, having an external diameter of 4.7 mm [20]. Such a sensor is highly sensitive to yaw; there is a large, random error in its calibration curve, caused by flow instability in the diffuser. The reason for the abrupt change in recovery coefficient at a velocity of about 90 m/sec is the transition from laminar to turbulent flow at the diffuser inlet, where Re = 2000 to 3000.

Subsequent investigations of Pitot thermocouples have shown that better reproducibility and reduced sensitivity to yaw is obtained by placing the thermocouple in a cylindrical stagnation chamber. Figure 4.59 shows the design and characteristics of such a sensor. These sensors are very widely used because of their simple design. Their recovery coefficients vary between 0.95 and 0.999.

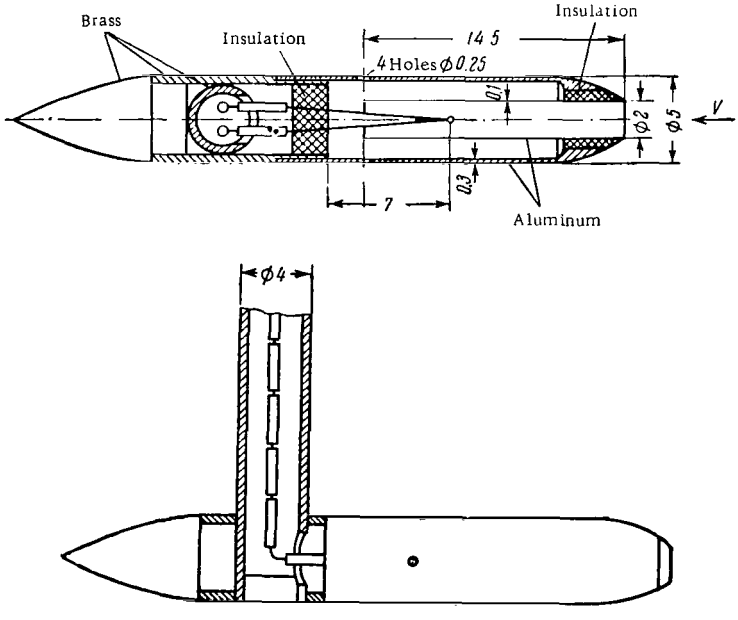

FIGURE 4.60. Double-shielded Pitot thermocouple.

Figure 4.60 shows the sensor designed at the Swedish Royal Technological Institute. It has a recovery coefficient very close to unity. The thermocouple junction, 0.15 mm in diameter and made from iron-constantan, is surrounded by two aluminum tubes, joined at the nose of the sensor by means of heat-insulating material. At zero yaw the recovery coefficients of round- and conical-nosed instruments of this type are 0.998 and 0.996

respectively. Yaws of 5 to 10° have practically no effect on the recovery coefficients, which have also been found to remain practically constant at temperatures of up to 250°C /21/.

Sensors for measuring the stagnation temperatures between the stages of turbocompressors and gas turbines must be as small as possible both in diameter and length. The designs of two such instruments are shown in Figures 4.61 and 4.62.

Boundary-layer temperature measurements are made with miniature instruments, similar to that shown in Figure 4.59. Medical hypodermic needles, whose diameters are fractions of millimeters, are used for the external tubes.

The value of ζ tends to decrease at low velocities, at which heat input by convection to the thermocouple no longer balances losses by conduction through the supports.

High-temperature sensors

For high temperatures (above 300° or 400°C), at which the temperature difference between the sensor and the surrounding medium is of the order of 50°C or more, radiant-heat losses become the principal source of error. Exact measurements of stagnation temperatures are very difficult in this range, where even slight changes in ambient temperature lead to considerable changes in the temperature of the sensor.

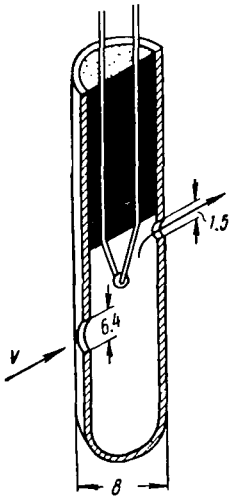

FIGURE 4.61. Cylindrical temperature sensor (M = 1, ζ = 0.98).

The amount of heat lost by radiation is proportional to the surface area of the sensor, so that for high-temperature duty, sensors should be as small as is consistent with strength requirements. The radiation capacity of the surface of the body on which the sensor is mounted should also be very low: this can be achieved, for instance, by polishing the surface. It is difficult, however, to avoid gradual oxidation of the surface of a sensor immersed in hot gases. The best method of reducing radiation is to improve the shielding of the sensor. The thermocouple of the sensor is mounted in a diffuser surrounded by several concentric tubular screens (Figure 4.63). The external screens are heated by the gas flowing through the annular gaps. The thermocouple junction may be either mounted in the middle of the central tube or welded to it. In the first case the recovery coefficient of the sensor is similar to that of a poorly streamlined body ($\zeta \approx 0.65$). In the second case, the value of the recovery coefficient approaches that of a flat plate ($\zeta \approx 0.9$). Good results have been obtained at temperatures up to 900 to 1000°C with chromel-alumel thermocouples mounted in enclosures of the above described type. The inner screen may be made of porcelain, and the three outer screens of heat-resistant steel.

Radiation losses in high-temperature sensors can be reduced by heating the shield to a temperature close to the ambient temperature of the medium.

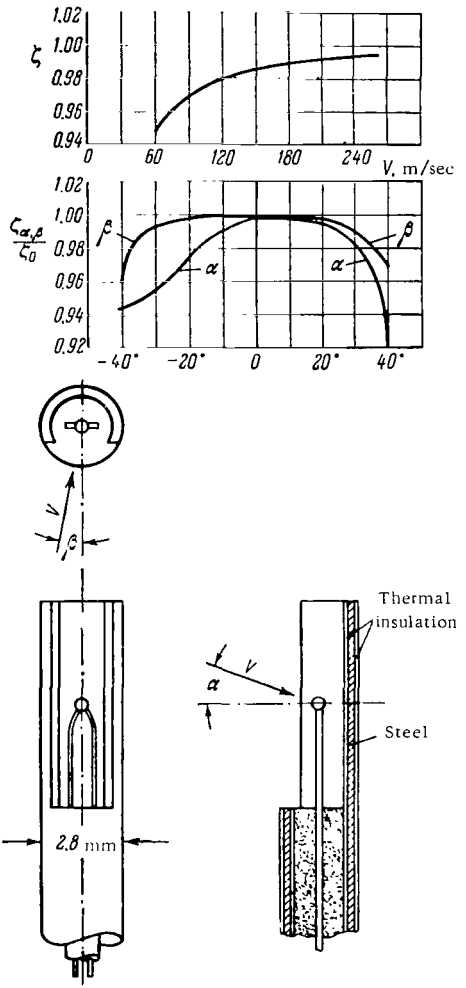

FIGURE 4.62. Cylindrical temperature sensor with open inlet.

Figure 4.64 shows the design of a miniature stagnation-temperature sensor developed by the California Institute of Technology /23/. In this sensor, an electrically heated wire on the shield reduces direct radiation losses and losses by heat conduction from the shield. To compensate for heat losses by conduction through the leads from the thermocouple and its holder, the latter is heated by a separate nichrome resistor heater. The temperatures of the shield T_s and of the holder T_h are measured by separate thermocouples, and controlled to be as nearly as possible equal to the

temperature T_n of the main thermocouple. Figure 4.65 shows the values of the recovery coefficients ζ_s, ζ_h, and ζ obtained by inserting the corresponding

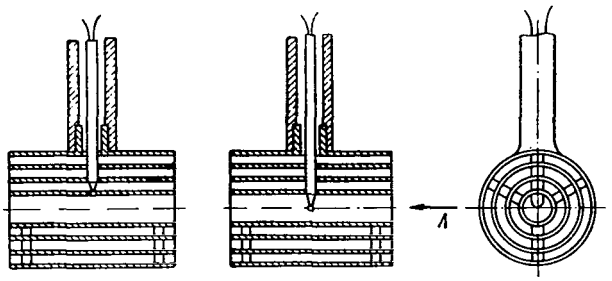

FIGURE 4.63. Shielded sensor for high temperatures.

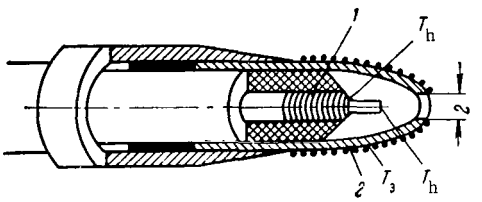

FIGURE 4.64. Temperature sensor with heated shield.
1—main thermocouple mounting and heating element;
2—radiation shield and heating element.

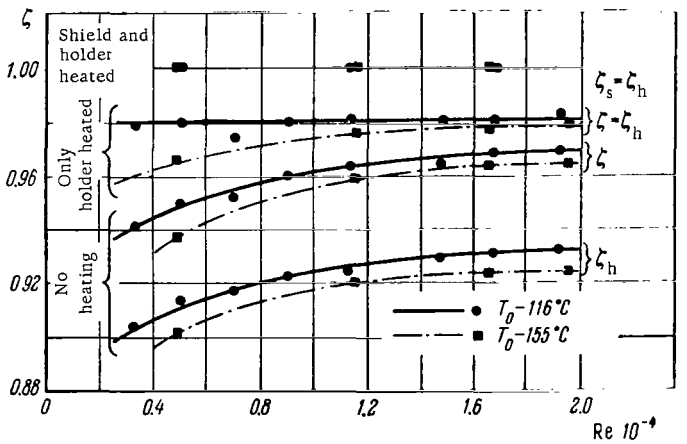

FIGURE 4.65. Characteristics of a temperature sensor with heated shield and holder (M = 5.75).

values of T_s, T_h and T_n into (4.51). In the absence of heating, ζ_h and ζ depend on both the Reynolds number and the stagnation temperature T_0.

If we heat the thermocouple holder in such a way that $T_h = T_n$, i.e., if we eliminate the heat losses due to conduction, then the recovery coefficient $\zeta_n = \zeta_h$ will be higher. If both the holder and the shield are heated, so that $T_h = T_s = T_n$, there will be no temperature gradients and the temperature of the main thermocouple will be exactly equal to the stagnation temperature ($\zeta = 1$).

Calibration of temperature sensors

Figure 4.66 shows a wind-tunnel layout for the calibration of temperature sensors. The air from the compressor is cleaned in oil-filled air filters, and after suitable cooling is led into a vertical chamber, whose upper part is a smoothly tapering cone with a small cylindrical port through which the air is ejected to the atmosphere. The chamber is placed vertically in order to avoid flow asymmetry due to convection.

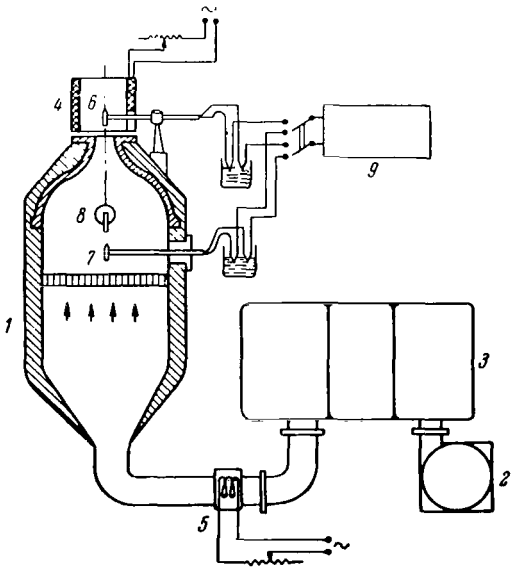

FIGURE 4.66. Installation for calibrating temperature sensors. 1 — wind tunnel; 2 — compressor; 3 — receiver, cooler and filter; 4 — radiation shield and heater; 5 — air heater; 6 — sensor being calibrated; 7 — stagnation-temperature sensor; 8 — total-pressure tube; 9 — potentiometer.

The stagnation-temperature sensor (6) to be calibrated is mounted above the outlet port. Another stagnation-temperature sensor (7) and a total-pressure tube (8) are installed at the center of the chamber, where the flow velocity is small. Assuming that there are no energy losses by friction and heat transfer, the stagnation temperature and the total pressure must have

equal values at the outlet and in the centre of the chamber. The walls of the port are lagged in order to reduce heat exchange through them.

Radiation effects are studied using an electrically heated radiation shield (4). A further electrical heater (5) is provided at the wind-tunnel inlet, for studying the performance of the sensor at high temperatures.

The cold junctions of the thermocouples are brought out to ice-water baths placed close to the lead-through of each sensor. The thermal emf of the sensors is measured with a high-accuracy potentiometer connected to a center-zero galvanometer. Temperatures can be measured with an accuracy of 0.05°C at a galvanometer sensitivity of 10^{-9} amps.

The proportionality constants k_1 and k_2 of emf versus temperature for the thermocouples in the reference sensor and the sensor being calibrated are determined beforehand by static calibration against a standard thermometer.

Before each test, the sensor to be calibrated is mounted in the chamber next to the reference sensor in steady flow conditions. The difference between the indications (thermal emfs of the sensors, in this case at the same temperature t_0) is due only to the difference ΔU between their calibration coefficients. This difference

$$\Delta U = U_1 - U_2 = \frac{t_0}{k_1} - \frac{t_0}{k_2},$$

is measured by the differential method. The sensor being calibrated is then placed at the outlet port. The indication of the reference sensor remains unchanged, being $U_1 = \frac{t_0}{k_1}$. The indication of the sensor being calibrated will have the new value $U_2' = \frac{t_n}{k_2}$ where t_n is the corresponding temperature, which depends on the recovery coefficient ζ. The difference between the indications of the two sensors, measured by the differential method, is

$$\Delta U' = U_1 - U_2' = \frac{t_0}{k_1} - \frac{t_n}{k_1}.$$

We can thus determine the true temperature difference between the two sensors:

$$\Delta U_1' - \Delta U = U_2 - U_2' = \frac{t_0 - t_n}{k_2},$$
$$t_0 - t_n = k_2(U_2 - U_2').$$

This method has the advantage of measuring the small differences ΔU and $\Delta U'$ so that the calibration errors are much smaller than if the thermal emf of each thermocouple were measured separately.

The recovery coefficient can be found from

$$T_0 - T_n = t_0 - t_n = (1 - \zeta)\frac{V^2}{2gJc_p},$$

where the flow velocity is determined by measuring the total stagnation temperature in the settling chamber.

§ 15. MEASUREMENT OF DENSITY: HUMIDITY CORRECTIONS

The density of a perfect gas can be determined from the equation of state (4.1). For air at S.T.P. ($t = 15°C$, $p = 10{,}331$ kg/m^2 or $B_{15} = 760$ mm Hg, $g = 9.81$ m/sec^2, $R = 29.27$ m/degree) we have

$$\rho_{15} = 0.125 \frac{\text{kg} \cdot \text{sec}^2}{\text{m}^4}.$$

To calculate the density of air for other conditions we use the concept of relative density

$$\Delta = \frac{\rho}{\rho_{15}}.$$

Inserting into this the value for the density determined from the equation of state, we obtain

$$\Delta = \frac{p}{T} \frac{T_{15}}{p_{15}} = \frac{B(273+15)}{760(273+t^\circ)}, \qquad \text{(A)}$$

where B is the barometric pressure in mm Hg. This value of Δ is used for determining the flow velocity in wind tunnels having open test sections, by inserting into (4.30) the value of $\rho = \rho_{15}\Delta$.

Clapeyron's equation of state no longer applies exactly to vapors near the condensation point, and we must use more complicated equations, such as that of van der Waals:

$$p = \frac{c(1-\alpha T)}{v-b} - \frac{a}{v},$$

where α is the volumetric coefficient of thermal expansion of the vapor at constant pressure, c is a constant whose magnitude depends on the molecular weight of the gas, and $v = \frac{1}{\rho}$ is the specific volume.

The constants a and b in van der Waals' equation are very small, so that for the densities usually encountered in aerodynamic experiments, van der Waals' equation reduces to that of Clapeyron.

In low-velocity wind tunnels the density can be determined from formula (A). At high velocites, the density of the gas can be found by (4.6) from the stagnation density ρ_0 :

$$\frac{\rho_0}{\rho} = \left(1 + \frac{\varkappa - 1}{2} M^2\right)^{\frac{1}{\varkappa - 1}}.$$

The value of ρ_0 is usually determined from measurements in the settling chamber of the wind tunnel, where the flow velocity is small and we can use formula (A) for Δ. In this case t° is equal to the stagnation temperature measured by a sensor in the settling chamber.

In high-velocity wind tunnels the temperature of the flowing medium is appreciably lower than the temperature at the nozzle inlet; therefore, the relative humidity rises sharply in the nozzle throat and in the supersonic region downstream. Under certain conditions saturation occurs,

and the water vapor in the air condenses. The onset of condensation may be sharply defined. Condensation shocks are similar to ordinary shocks, and cause sudden changes in the flow parameters in the test section. For these reasons condensation shocks should be eliminated, either by drying the air or by increasing the initial stagnation temperature (see Chapter II). In the absence of condensation the presence of moisture does not affect the flow, but alters the density ρ.

In determining the density of moist air, we must take into account changes in the gas constant. The value R_{mix} of the gas constant for a mixture of air and water vapor can be found by measuring the partial vapor pressure p', which is related to the saturation vapor pressure p'_s by

$$p' = \varphi p'_s,$$

where φ is the relative humidity.

Knowing the value of p', the value of R_{mix} can be found from the following equation based on Dalton's law, which states that the pressure of a mixture is equal to the sum of the partial pressures of its components

$$R_{mix} = \frac{R_a}{1 - \frac{p'}{p}\left(1 - \frac{R_a}{R_s}\right)}.$$

Substituting into this expression the values of the gas constant for air ($R_a = 29.27$ m/degree) and superheated steam ($R_s = 47.1$ m/degree) we obtain

$$R_{mix} = \frac{29.27}{1 - 0.378\frac{p'}{p}},$$

whence the density of the mixture is

$$\rho_{mix} = \frac{p}{gR_{mix}T} = \frac{p}{gR_aT}\lambda = \rho_a\lambda,$$

where ρ_a is the density of dry air at the temperature and pressure of the mixture, while $\lambda = 1 - 0.378\ p'/p$ is the correction coefficient for the moisture constant of the air. The correction coefficient for moisture content can be significant, especially at low pressures. Thus, e.g., for $\varphi = 0.8$, $p = 0.1$ ata, and $T = 303°$, the density is 13% less than for dry air.

Thus, the effect of moisture must be taken into account by determining the partial vapor pressure p' at the given temperature. Partial pressures are measured with various types of psychrometers. Figure 4.67 shows a psychrometer consisting of two thermometers placed in tubes through which passes the air whose humidity is to be measured. The top of one thermometer is covered by a moist cloth. When thermal equilibrium is reached, the quantity of heat lost by the wet-bulb thermometer will be equal to the heat gained by it from the surrounding medium. The lower the relative humidity of the air surrounding the wet-bulb thermometer, the higher will be the rate of moisture evaporation. The condition of thermal equilibrium is defined by

$$(t - t') = \frac{1}{ap_a}(p'_s - p'),$$

where p'_s is the saturation water-vapor pressure at the temperature t' measured by the wet-bulb thermometer, p_a is the air pressure at which the measurement was made, t is the temperature measured by the dry-bulb thermometer, and a is a calibration constant whose magnitude depends on the design of the psychrometer. The saturation water-vapor

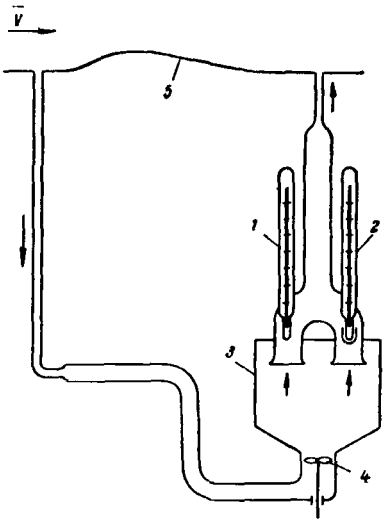

FIGURE 4. 67. Measuring the relative humidity in a wind tunnel. 1 — dry-bulb thermometer; 2 — wet-bulb thermometer; 3 — small container; 4 — fan; 5 — wind tunnel.

pressure p'_s depends only on temperature; its values are given in Table 8, which can be used in conjunction with the values of t and t' determined by the psychrometer and the wind-tunnel pressure p'_a, in order to determine p' from the formula above.

TABLE 8. Saturation vapor pressures of water

t, °C	p'_s, kg/m^2	t, °C	p'_s, kg/m^2	t, °C	p'_s, kg/m^2	t, °C	p'_s, kg/m^2
0	62	16	185	31	458	46	1029
1	67	17	198	32	485	47	1082
2	72	18	210	33	513	48	1138
3	77	19	224	34	542	49	1197
4	83	20	238	35	573	50	1258
5	89	21	254	36	606	51	1322
6	95	22	270	37	640	52	1388
7	102	23	286	38	676	53	1458
8	109	24	304	39	713	54	1530
9	117	25	323	40	752	55	1605
10	125	26	343	41	793	56	1683
11	134	27	364	42	836	57	1765
12	143	28	385	43	881	58	1850
13	153	29	408	44	928	59	1939
14	163	30	433	45	977	60	2031
15	174						

For measuring the relative humidity of air in a wind tunnel, the psychrometer is placed in a small container, through which a fan circulates air drawn from the tunnel. The circulation must be sufficient to prevent the moisture, evaporated from the wet cloth, from affecting the humidity of the air in the container. In order to avoid moisture condensation in the container, the temperature in it must not be less than the tunnel temperature The readings of the psychrometer must be corrected for temperature and pressure differences between the air in the wind tunnel and that in the container. In the absence of moisture condensation in the container, the gas constant of the air in it and in the tunnel are equal, and we may write

$$\frac{p}{p_1} = \frac{\rho T}{\rho_1 T_1},$$

where p, ρ, and T are the pressure, density, and temperature of the air in the tunnel, while p_1, ρ_1, and T_1 are the respective values for the air in the container.

From the definition of partial pressure, $p_1'/p' = \rho_1 T_1/\rho T$, where p' and p_1' are the partial pressures in the tunnel and in the container respectively, we obtain

$$p' = p_1' \frac{p}{p_1},$$

i.e., the partial pressure varies in direct proportion to the pressure of the moist air.

Another method of measuring the relative humidity of the air in wind tunnels is based on dew-point determination. We observe, either visually, or with a photoelectric device, the instant at which dew forms on the surface of a metal mirror when its temperature is lowered. Knowing the temperature t of the mirror surface and the air pressure p_a we can find the relative humidity and partial vapor pressure from available tables.

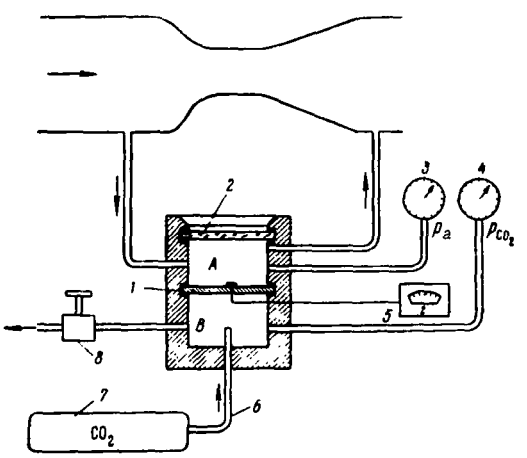

FIGURE 4.68. Determining relative humidity by measurement of dew-point temperature.

Figure 4.68 shows an instrument of this type, which is used in an RAE supersonic wind tunnel. The air from the settling chamber is led into a hermetically sealed chamber (A) containing a copper disk (1) whose polished surface can be viewed through a glass window (2). The air pressure p_a in the chamber is measured by a pressure gage (3). Through tube (6), whose internal diameter is 0.5 mm, CO_2 is fed from the bottle (7) into a second sealed chamber (B) on the opposite side of the disk. As the gas flows from the tube into chamber (B) it expands, thus cooling the disk.

A precise relationship exists between the pressure and the temperature of the expanding CO_2, so that by controlling the gas flow rate with a needle valve (8), connecting (B) to atmosphere, we can change the temperature of the disk (1); this temperature can be determined from the pressure measured by a gage (4). The exact temperature of the disk is determined with the millivoltmeter (5), which measures the emf of a copper-constantan thermocouple welded to the disk (1).

Dew-point instruments measure relative humidity accurately to 0.05% and determine the water-vapor pressure to ±1%.

§ 16. BOUNDARY-LAYER MEASUREMENTS

Measurements of the flow parameters in the boundary layer around streamlined bodies are necessary mainly in studies of drag. The parameters depend almost entirely on skin friction. The skin friction of a body can be determined by subtracting from the total drag (determined, for instance, by wake traverse) the value of the form drag, obtained by measuring the pressure distribution over the surface (Chapter VII). Since both quantities, especially the form drag, are very difficult to measure accurately, skin friction, in practice, is determined by other means. It is better to determine the distribution over the surface of the body of the frictional shearing stress

$$\tau_0 = \mu \left(\frac{\partial u}{\partial y} \right)_{y=0},$$

where u is the velocity component parallel to the wall in the boundary layer at a distance y from the wall, and μ is the viscosity coefficient of the fluid at the wall temperature.

Boundary-layer investigations involve the determination of certain arbitrarily defined characteristics, namely, the boundary-layer thickness δ, the displacement thickness δ^*, and the momentum thickness δ^{**}. The boundary layer thickness is understood as the distance from the wall at which the velocity is 0.99 of the undisturbed flow. The magnitudes of the displacement and momentum thicknesses are defined as

$$\delta^* = \int_0^\delta \left(1 - \frac{\rho u}{\rho_\infty V_\infty} \right) dy,$$

$$\delta^{**} = \int_0^\delta \frac{\rho u}{\rho_\infty V_\infty} \left(1 - \frac{u}{V} \right) dy,$$

where ρ_∞ and v_∞ are the density and flow velocity at the outer limit of the boundary layer. Boundary-layer studies demand more precise methods of measurement and more sensitive equipment than is usual in experimental aerodynamics. The boundary layer has a small thickness and large transverse velocity gradients, so that elaborate miniature instruments are needed.

Velocity-profile determinations in the boundary layer

In a thin boundary layer the static pressure, measured perpendicular to a wall of small curvature, is constant, while the transverse velocity gradients are very large. Velocity distributions can therefore be determined by measuring the total pressure at different points along the normal to the surface, and the static pressure at the wall.

At high flow velocities it is also necessary to know the temperature of the medium, which can be determined, for instance, by measuring the density in the boundary layer with an interferometer and using the equation of state (4.1). In the absence of heat exchange between the medium and the wall, the stagnation temperature in the boundary layer will differ very little from the free-stream stagnation temperature and the velocity in the boundary layer can then be determined from (4.44).

The insertion of a tube into the boundary layer may seriously modify the flow conditions in it. Disturbances so caused are propagated upstream and affect the flow conditions at the wall ahead of the tube. The measured pressure will not then correspond to the pressure in the undisturbed boundary layer. The magnitude of the disturbances introduced by the tube depends on its thickness in relation to the local thickness of the boundary layer. The effect of introducing the tube is therefore determined by measuring the velocity distribution in the boundary layer with tubes of different diameters. A second difficulty, related to the first, is that the tube will function in a large transverse velocity gradient, so that a correction for the displacement of its effective center must be introduced (see § 11).

These difficulties can be reduced by using microprobes, i.e., total-pressure tubes with internal diameters of 0.05 to 0.3 mm (such as the tubing used for manufacturing hypodermic [medical] needles). However, pressures measured with tubes of these very small diameters are subject to considerable transmission lags in the readings of the associated pressure gage. This is often reduced by using tubes with flattened noses (Figure 4.69a), which provide a sufficiently large cross section, while the part inserted into the boundary layer is thin. The transmission lag may nevertheless still be many tenths of seconds, so that measurements in the boundary layer are very complicated and time-consuming.

The tube dimensions are very important in the study of boundary layers in supersonic flow. Thus, for instance, for flow around a cone at $M = 2$, the thickness of the laminar boundary layer at a distance of 250 mm from the apex may be less than 0.8 mm. The distortion of the velocity profile in this layer, due to the comparatively large thickness of the tube, is shown

schematically in Figure 4.70 /24/. This distortion results in the displacement of the whole of the boundary-layer profile (sometimes accompanied by changes in the velocity gradient), in changes of the shape of the velocity profile near the wall, and in the appearance of a peak on the velocity profile close to the outer limit of the boundary layer. This displacement of the whole profile is caused by the displacement of the "effective center" of the tube. In supersonic flow this displacement may be toward lower velocities, i.e., in the direction which is opposite to the displacement in noncompressible flow (see § 11). Close to the wall the

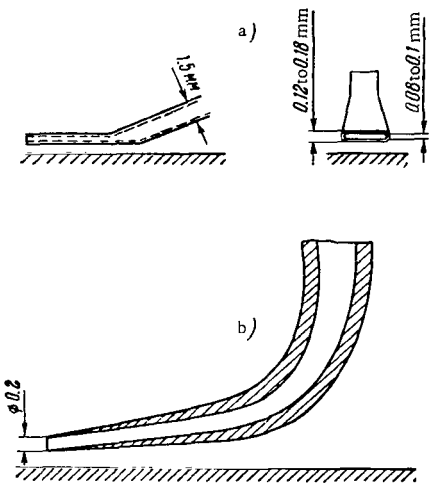

FIGURE 4.69. Miniature total-pressure tube. a — flattened metal tube; b — quartz tube.

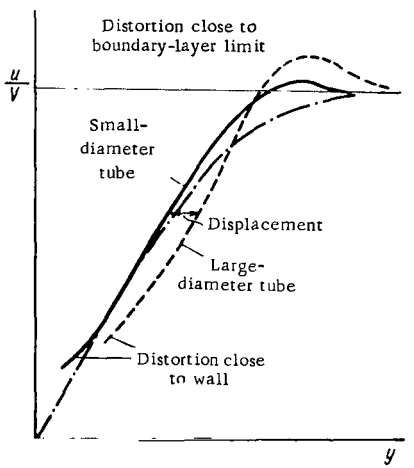

FIGURE 4.70. Effect of total-pressure tube dimensions on the velocity distribution in the boundary layer.

error is due also to the influence of the Reynolds number, since at $Re < 200$, indications of total-pressure tubes are excessive. At supersonic velocities this error can be considerable, since the gas densities are small.

The appearance of a peak on the velocity profile close to the outer limit of the boundary layer can affect the determination of the displacement and momentum thicknesses. In supersonic flow, the actual values of these quantities can be determined by multiplying with a correction coefficient, due to Davis, the respective values determined from velocity-profile measurements /24/,

$$\delta^*_{ac} = \delta^*_{me}\left(1 - \frac{d}{\delta}\right)^{0.18}; \quad \delta^{**}_{ac} = \delta^{**}_{me}\left(1 - \frac{d}{\delta}\right)^{0.18},$$

where d denotes the outside diameter of the total-pressure tube.

In addition to flattened tubes, conical quartz tubes with a circular orifice of 0.1 mm diameter are used for measurements in a supersonic boundary layer. In spite of the smaller orifice, the quartz tube has a smaller

transmission lag than the flattened metal tube, because of the smoothness of its walls and thin conical shape (Figure 4.69b). Further,

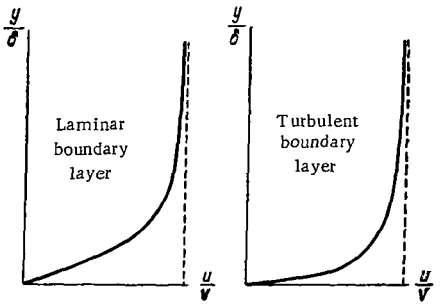

FIGURE 4.71. Velocity profiles in the boundary layer.

any condensed moisture in the orifice or dust which may have entered it, are more easily observed in a transparent tube.

For investigating the velocity distributions in boundary layers, special traversing cradles are used, having micrometer screws which permit the distance of the tube from the wall to be measured accurately to 0.02 mm. Contact by the tube nose with the surface of the body is detected electrically. To prevent arcing which might otherwise occur at very small clearances, the applied voltage is sometimes reduced by inserting the contacts into the grid circuit of an electron tube.

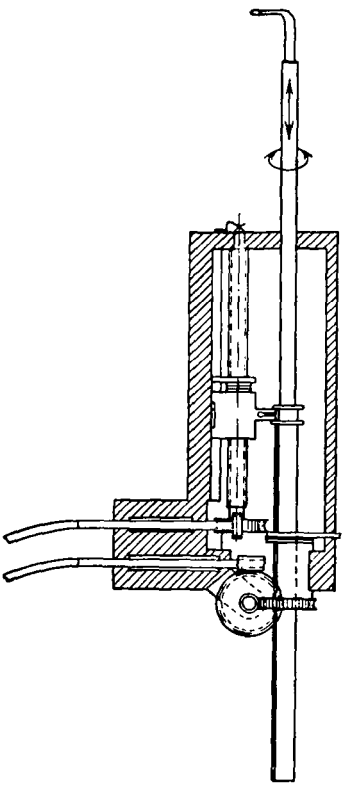

FIGURE 4.72. Microtraversing cradle.

When the surface of the model has a large curvature, the static pressure along a normal to the wall is not constant; it is then necessary to use static-pressure microprobes. The static- and total-pressure tubes are then fixed on a common traversing cradle and are moved simultaneously.

The results of measurements of the velocity distribution in the boundary layer are presented in the form of curves $u/V = f(y/\delta)$ (Figure 4.71) or in the form of velocity isolines. These are families of curves, each of which joins the points at which the ratio of local to free-stream velocity is the same.

Lately, low-speed wind tunnels have been used for intensive research on the flow around sweptback and delta wings. For a detailed study of three-dimensional boundary layers, we require exact and simultaneous measurements of the

magnitude and direction of the velocity in a traverse of a given cross section of the boundary layer. Figure 4.72 shows a microtraversing cradle which permits such measurements to be made with the aid of double or triple tubes (Figure 4.48). Difficulties in the use of pneumometric microprobes (due to clogging of the orifices, or the necessity to correct for the displacement of the effective center) have encouraged use of miniature hot-wire anemometers for velocity measurement in the boundary-layer. However, because of the fragility of such instruments, and the complication of using it, most experimental studies of boundary-layer conditions are still made with pneumometric probes.

Determination of the local coefficient of surface friction

For plane-parallel flow, the frictional drag of a cylindrical body, whose generatrix is perpendicular to the undisturbed flow, can be expressed as

$$Q_{\text{тр}} = \int_0^l c_f \frac{\rho_\infty V_\infty^2}{2} b\, dx,$$

where l is the chord length, and b the width of the body; c_f is the local coefficient of skin friction:

$$c_f = \frac{\tau_0}{\rho_\infty V_\infty^2/2},$$

and x denotes distance along the chord.

Below, several experimental methods are described for determining τ_0 and c_f.

Direct method. The frictional force acting on an element of the surface of a body can be measured directly. Such measurements usually are made on a flat wall. A rectangular or circular surface element is separated from the remainder by an annular gap, 0.1 to 0.15 mm wide, and is placed on a balance. The surfaces are polished and adjusted together to ensure that the plane of the element coincides exactly with that of the wall; this is checked with a micrometer or an optical interferometer. It is especially important that the disk should not project from the surface of the wall, though it may be recessed to the extent of 0.01 mm without adverse effect. A balance for measuring the friction on a 50 mm diameter disk is shown in Figure 4.73. The disk is mounted on a pair of leaf springs in an annular gap. Since changes in the width of this gap during the measurement are undesirable, the force is measured by a null method. The force acting on the disk causes it to be displaced by an amount indicated by the displacement transducer. The force is then balanced with the aid of an electromagnet which returns the disk to its initial position in the gap. The current through the electromagnet is a measure of the restoring force, and thus of the friction. To avoid the adverse effects of a non-uniform pressure distribution in the gap, this pressure is measured at a series of orifices arranged uniformly around the disk. Since the frictional force on the disk is only 10 to 20 gram, a high-sensitivity balance is necessary.

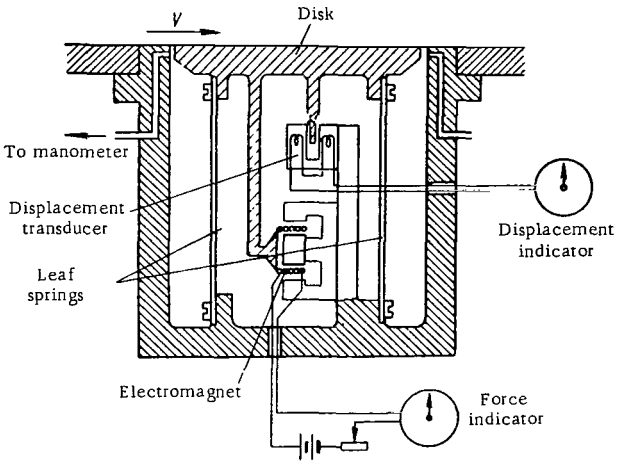

FIGURE 4. 73. Friction balance.

Surface-tube method. In this method the velocity at a point very close to the surface, and just inside the boundary layer, is measured with a so-called surface tube. In estimating the skin friction by this method it

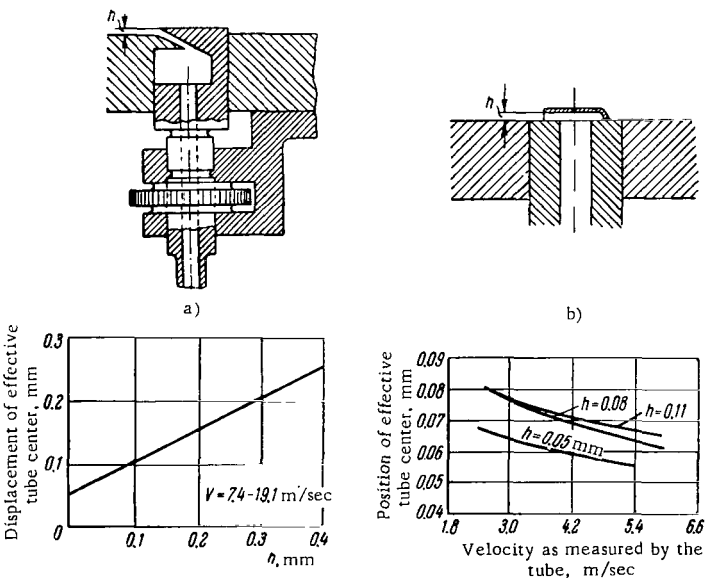

FIGURE 4. 74. Surface tube for total-pressure measurement. a—Stanton tube; b—Fage and Faulkner tube.

is assumed that the velocity increases linearly from zero at the wall to a value corresponding to the pressure indicated by the surface tube,

i.e., $\tau_0 = \mu u/y$, where y is the distance of the "effective center" of the tube from the wall.

Figure 4.74 illustrates two types of surface tubes used by Stanton and Fage for determining τ_0. The Stanton tube is rectangular, its inner surface being formed by the wall. The Fage tube consists of a thin rectangular plate, three edges of which are bent over and soldered to a circular rod let into the surface. The inlet orifice of the tube is formed by the straight leading edge of the plate and the butt end of the rod. The graphs show the distance of the "effective center" from the wall as a function of the width of the inlet port; this dimension can be adjusted with a micrometer screw. The relationship is determined from calibrations of the instrument in a laminar-flow boundary layer of known profile, but may also be used when interpreting measurements in turbulent boundary layers.

It is very difficult to prepare surface tubes so short that the inlet port (Figure 4.74) is entirely within the viscous sublayer, and τ_0 is more simply estimated from measurements in the turbulent layer, as suggested by Preston. In this method τ_0 is measured with the aid of circular total-pressure tubes held against the wall /25/. The method is based on the observation, that there is a region close to the wall in which

$$\frac{u}{u_\tau} = f\left(\frac{yu_\tau}{\nu}\right),$$

where $u_\tau = \sqrt{\tau_0/\rho}$ is called friction velocity (dynamic velocity). This region is much thicker than the viscous sublayer, so that a tube of comparatively large section can be placed in it. In the viscous sublayer the above equation becomes $u/u_\tau = yu_\tau/\nu$, and the use of the Fage and Stanton surface tubes is based on this. The above equation can be rewritten

$$\frac{p_0 - p}{4\rho\nu^2} = F\left(\frac{\tau_0 d^2}{4\rho\nu}\right)^2,$$

where p_0 is the total pressure as indicated by a tube held against the wall, p is the static pressure at the wall, and d is the diameter of the total-pressure tube. All the test results from four tubes of different diameters, and internal to external diameter ratio $d/D = 0.6$, lay with small scatter on a curve, which, for $\lg(p_0 - p)d^2/4\rho\nu^2 > 5.0$ can be expressed in the form

$$\lg \frac{\tau_0 d^2}{4\rho\nu^2} = \bar{2}.604 + \frac{7}{8} \lg \frac{(p_0 - p)d^2}{4\rho\nu^2}.$$

The value of τ_0 can be derived from this relationship.

Projecting-plate method. This method consists in measuring the difference in pressures on the wall upstream and downstream of a plate projecting from the surface of the body by some hundredths of a millimeter. Assuming that beyond the projection the velocity increases linearly with distance from the wall, this pressure difference is proportional to τ_0:

$$\Delta p = 2.90 \frac{\mu u}{h} = 2.90\tau_0,$$

where u is the flow velocity at the level of the upper edge of the projection where $y = h$. This equation is of the form $\Delta p = k\tau_0$ in which the value of the coefficient k depends only on the height of the projection /26/.

Methods based on measuring velocity profiles. The frictional stress τ_0 on the wall of a body can be found in principle by determining the value of $\partial u/\partial y$ at the wall from the velocity distribution in the boundary layer as determined with a miniature total-pressure tube and an orifice in the wall. Since the minimum distance of the "effective center" of the tube from the wall is limited by the tube dimensions, the curve $u = f(u)V_\infty$ must be extrapolated to $y = 0$; values of τ_0 found by this manner are not sufficiently accurate.

However, if the velocity profile is known, a more accurate value of τ_0 can be found from calculating the change of momentum in the boundary layer. The relevant equation for the momentum is /1/

$$\frac{d\delta^{**}}{dx} + \frac{dV}{dx}\frac{1}{V}(2\delta^{**} + \delta^{*}) = \frac{\tau_0}{\rho V^2},$$

where the x coordinate is taken along the surface of the body. To determine τ_0 from this equation it is thus necessary to find the variables for several values of x. The mean value of τ_0 over a certain region of the surface can be found simply by measuring the parameters at the boundaries x_1 and x_2 of the region and integrating the momentum equation between the limits x_1 and x_2.

In the case of infinite flow around a flat plate, the momentum equation takes the form (when the velocity V does not depend on x) of

$$\tau_0 = \frac{d}{dx}\int_0^{\delta} \rho(V - u)\,u\,dy.$$

All of the above methods of measuring the coefficient of friction give good results for incompressible fluids. For the turbulent boundary layer in supersonic flow, balance measurements of τ_0 give the most accurate results.

Determining the transition point from laminar to turbulent flow in the boundary layer

The accurate determination of frictional drag on a body depends upon knowledge of the transition point from laminar to turbulent flow in the boundary layer, and of the point of flow separation from the surface of the body. Relevant experimental studies provide auxiliary qualitative criteria for comparative evaluation of the aerodynamic characteristics of models and for checking theoretical predictions of these characteristics.

With the increasing velocity of modern aircraft it becomes necessary to design for lower drag, more uniform moments and increased flight stability. This requires extended maintenance of laminar flow in the boundary layer, and delayed separation.

For the study of transition phenomena in the boundary layer the tunnel should have a low free-stream turbulence, and the surface of the model should be well finished. Special low-turbulence wind tunnels are therefore used for boundary-layer studies.

Boundary-layer transition is accompanied by a more rapid increase of velocity with distance from the surface and by faster thickening of the boundary layer. These phenomena form the basis of several experimental methods for transition-point determination. The principal methods are:

1. **Method based on measuring the velocity profiles.** The velocity profile is determined in several sections along a chord. The transition point (or more exactly the transition zone) is established from the change in shape of the velocity profile, which has a very steep slope in the turbulent region (Figure 4.71).

2. **Method based on detection of turbulent velocity fluctuations.** The transition from laminar to turbulent flow is accompanied by velocity fluctuations, whose onset indicates the position of the transition point. Velocity fluctuations are detected most easily with a hot-wire anemometer or a total-pressure tube connected by a short pipe to a low-inertia pressure transducer (Chapter V). The tube or the hot-wire anemometer is moved in a traversing cradle along the surface. The oscillogram of the pulses received at various distances from the stagnation point indicates the transition position (or zone) clearly by the sharp increase in pulsation amplitude associated with it.

3. **Method of total measurement.** A miniature total-pressure tube is moved along the wall in contact with the surface of the body parallel to the flow direction. In the transition zone there is a marked increase in total pressure, since at a given distance from the wall the velocity is higher in a turbulent boundary layer than in a laminar boundary layer. However, if the tube is moved at a constant distance from the surface which is slightly greater than the boundary-layer thickness upstream of the transition point, then the rapid growth of the layer behind the transition point will give rise to a sudden decrease of the total pressure indicated by the tube, as it enters the thicker turbulent boundary layer.

4. **Visualization methods at velocities up to 30 m/sec.** Wing-profile boundary layers are observed by injecting smoke filaments into the flow through openings drilled 5 to 10% of the chord length from the leading edge. In laminar flow the smoke has a well-defined stratified appearance and the point of flow separation is easy found since at it the smoke filaments leave the surface. In the turbulent boundary layer the smoke filaments merge.

Chemical methods are used nowadays for higher velocities. In one of these the body is coated with a thin layer of material which reacts chemically with an active gas added to the wind-tunnel air or injected directly into the boundary layer. The rate of mixing, and the rate at which visible reaction products appear in the turbulent region is higher than in the laminar region, so that the transition between the two is readily observed.

Other chemical methods (the sublimation method, Kaolin method, and fluid-film method) do not require the use of an active gas and are therefore more widely used in wind tunnels. These methods make use of the increased diffusion rate in the turbulent boundary layer, which causes more rapid evaporation or sublimation of the active material from the surface of the body in that region /27/.

§ 17. INSTRUMENTS FOR MAPPING DISTRIBUTIONS

For investigating the distributions of velocity, pressure, and temperature within fluids, traversing devices and combs or rakes of probes are commonly used. Traversing cradles are instruments for moving a measuring tube and accurately indicating its position in terms of the coordinates of the tunnel. Probe combs are devices for measuring the flow parameters simultaneously at a large number of points; some probe combs can also be traversed. When using combs, calibration coefficients for each of the tubes must be separately taken into account, and the mutual interaction of tubes may not be overlooked. The advantage of traversing cradles with single tubes is the simplicity of processing and the high accuracy of the results, since the systematic errors introduced by the tube are the same throughout the field. However, investigation of a field with a traversed tube requires more time than with a comb of tubes. Equipment for this purpose should therefore be selected in accordance with the required accuracy and rapidity of measurement. In intermittent-operation supersonic wind tunnels, it is better to make measurements simultaneously by several tubes which are installed on a comb. In low-speed tunnels the velocity distribution is usually mapped with a single tube installed on a traversing cradle. In installations for investigating blade cascades both traversing cradles and combs are used.

Traversing cradles. When investigating the flow in wind tunnels having open test sections, the tube is installed on a streamlined support which is moved along guides, parallel to the x-axis of the flow system of coordinates (Figure 4.75). Pitot-Prandtl tubes are generally used. Dual-purpose TsAGI-type tubes are used when small angles of yaw have to be determined. (Figure 4.51).

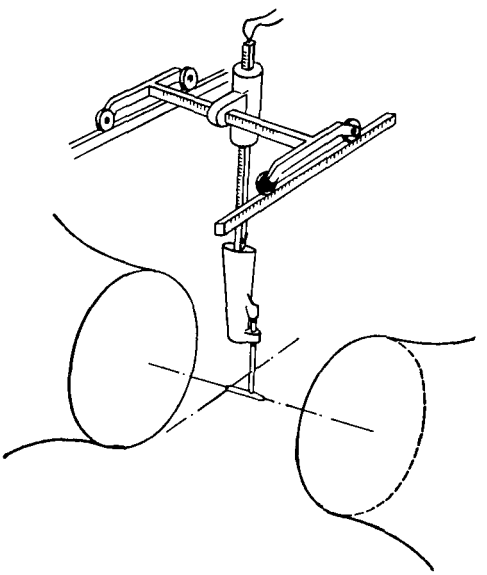

FIGURE 4.75. Traversing cradle for a wind tunnel with open test section.

In strongly inclined flow this indirect method of yaw measurement is often insufficiently accurate; in such cases the traversing cradle is fitted with a goniometer, so that yaw can be measured by the null method.

In small, low-speed wind tunnels the traversing cradle is adjusted manually, and the coordinates are shown on a scale attached to it.

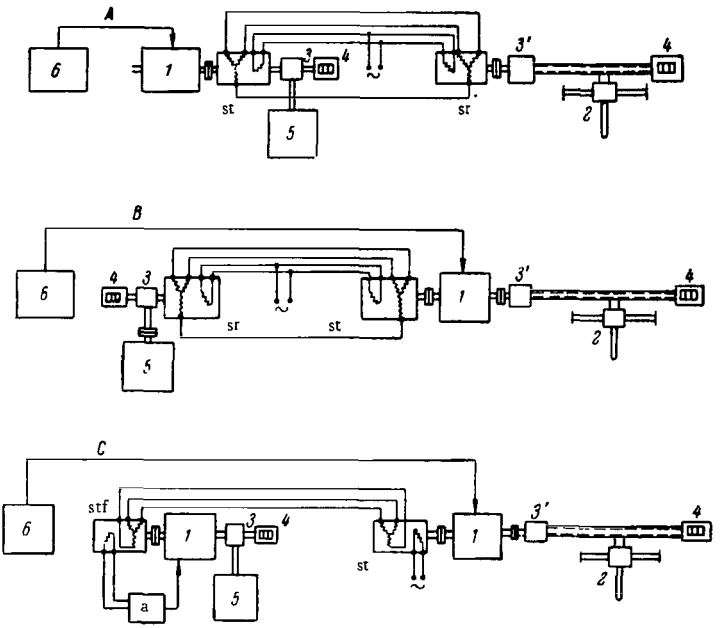

FIGURE 4.76. Remote control of a traversing cradle. 1 — main motor; 2 — traversing cradle; 3 and 3' — reduction gear boxes with equal transmission ratios; 4 — displacement register; 5 — recording or integrating device; 6 — control panel; st — selsyn transmitter; sr — selsyn receiver a — amplifier; stf — selsyn-transformer.

The high noise-levels associated with the operation of high-speed wind tunnels can be very tiring to the operator, so that the accuracy of the experiment suffers. Further, it is hazardous to approach too closely bench-test rigs of rotating equipment, e.g., turbine disks. Modern wind tunnels are therefore equipped with remotely controlled traversing cradles and automatic data-handling and recoring equipment.

Among other methods, selsyns are often used for electrical control of the position and altitude of the remotely controlled equipment.

Three possible systems for selsyn remote-control of the position of a probe are shown in Figure 4.76. The selsyn developes only a small torque, so that the direct drive (system A) can be used only when the resistance to rotation of the remotely controlled shaft is small. The main motor is installed in the control cabin and is directly connected to the selsyn transmitter and to the counting and recording devices; the remotely controlled shaft of the traversing cradle is driven by the selsyn receiver

through a reduction gear box. System *B* is used if large torques are needed to drive the control shaft of the traversing cradle. The motor (which may be of any power) is connected through a reduction gear box directly to the traversing cradle, and the selsyns drive the register and the recording instruments. System *C* is used when considerable power is needed for driving both the traversing cradle and the recording gear. It is a servo system in which the selsyn receiver operates as a transformer to produce a noncoincidence signal which is amplified and controls the servo drive.

An example of the design of a remotely-controlled traversing cradle, used in a high-speed tunnel for testing blade cascades /28/, is shown in Figure 4.77. The carriage (*A*), carrying a goniometer and tube *X*, is moved with the aid of a screw (*C*) along two cylindrical guides (*B*). The guides are installed parallel to the axis of the cascade. The screw can be turned either through a reduction gear by the selsyn receiver (*L*), or by handwheel (*R*). The tube is fixed to a special holder, mounted on a worm wheel, whose worm is driven by another selsyn receiver (*N*) or handwheel (*M*). Springs to take up backlash are inserted between the lead screw and the nut, which is fixed to the carriage, and also between the worm wheel and the worm. A nut (*V*) is turned in order to move the tube in planes perpendicular to the blade edges; this causes the tube to slide along a key inside the worm gear. Limit switches (*U*) cut the power to the servomotors when the carriage reaches its extreme positions.

Yawmeters. Flow investigations are performed either by moving the traversing cradle to a series of chosen points or by continuous movement. In the first case the tube can be directed manually (by turning a handwheel on the rotating mechanism or by remote servocontrol). The attitude of the tube is adjusted by equalizing the heights of the columns in the legs of a U-tube manometer and the angles of the goniometer, read directly from scales on the head, are used in the subsequent calculations.

For continuous displacement of the tube carried, the equipment should include recording or integrating instruments, to determine the average value of the quantities measured by the tube (see Chapter VII). In this case servo systems are needed for aligning the yawmeter in the flow direction. Figure 4.78 is a simplified diagram of an automatic yawmeter fitted with a diaphragm-type differential-pressure transducer. The diaphragm is made of phosphorus-bronze; its diameter is 125 mm, its thickness is 0.06 mm, and it is fixed between two hermetically sealed disks. The pressures from the yawmeter tube are transmitted to the two sides of the diaphragm to which platinum contacts are soldered. Each chamber contains a fixed insulated contact. When the attitude of the tube differs from the flow direction, the diaphragm bends, closing one of the contacts; an intermediate relay then switches on a servomotor which rotates the yawmeter until the pressure is equalized and the diaphragm returns to its central position. Push buttons and signal lamps are fitted for overriding manual control. The tendency of the system to hunt is reduced by small air-chambers in the differential-pressure transducer and short air pipes to the tube. At a separation of 0.025 mm between the diaphragm and each of the contacts, the transducer is actuated by a pressure difference of about 1.25 mm W.G.

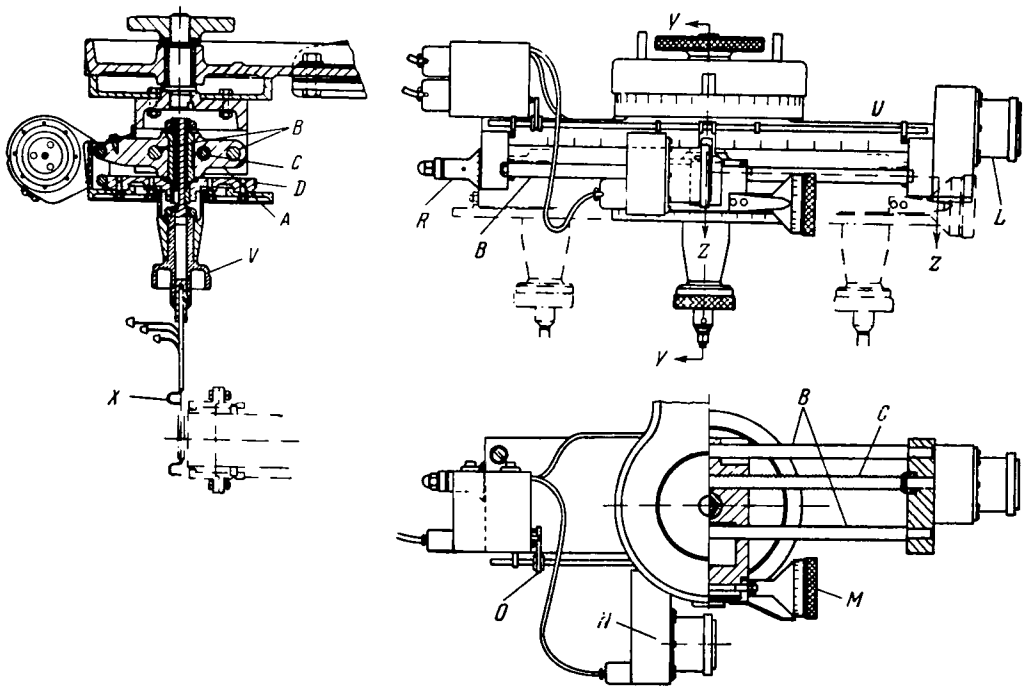

FIGURE 4.77. A remotely controlled traversing cradle. A — carriage; B — guides; C — lead screw; L — selsyn-receiver for tube translation; R — handwheel for turning the lead screw; N — selsyn-receiver rotating tube; M — handwheel for rotating tube; V — nut for raising the tube; U — limit switches; X — tube.

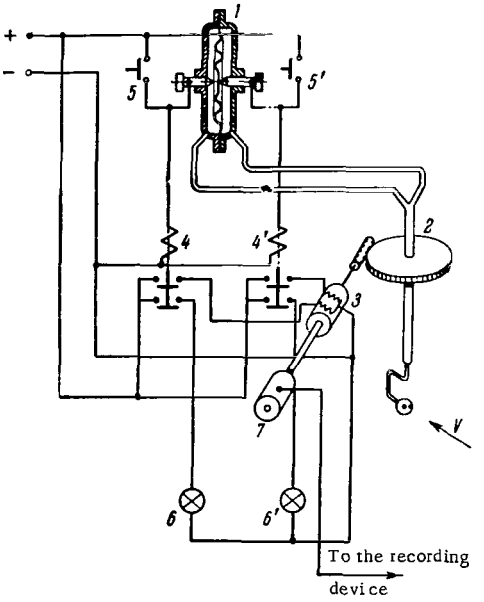

FIGURE 4.78. Automatic device for continuous measurement of flow direction by null method. 1 — diaphragm transducer of pressure difference in tube orifices; 2 — rotating head; 3 — servomotor; 4 and 4' — relays; 5 and 5' — push buttons; 6 and 6' — signal lamps; 7 — selsyn-transmitter.

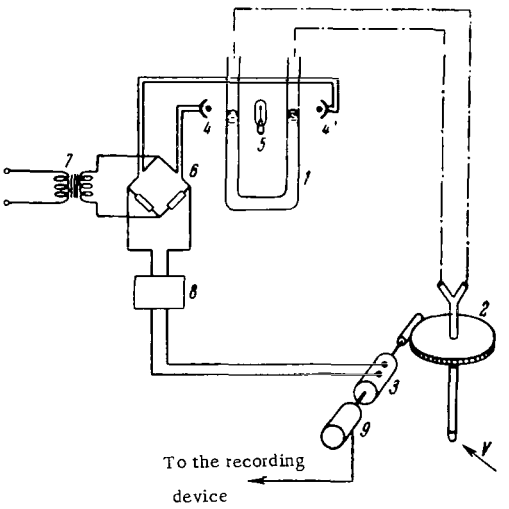

FIGURE 4.79. Automatic yawmeter with photoelectric transducer. 1 — U-tube manometer; 2 — rotating head; 3 — servomotor; 4 and 4' — photoelectric cells; 5 — lamp; 6 — Wheatstone bridge; 7 — transformer; 8 — amplifier; 9 — selsyn-transmitter.

Figure 4.79 shows an automatic yawmeter using a photoelectric servo system. The light source consists of an incandescent wire, placed between the two glass legs of a U-tube water manometer. Two photoelectric cells are installed on the other sides of the tubes. Any liquid in one of the legs acts as cylindrical lens and concentrates the light onto the corresponding photoelectric cell. In the empty tube the light is dispersed. Thus, the photoelectric cell adjacent to the leg at lower pressure will be illuminated more strongly than the other. A corresponding electrical imbalance signal is fed to the amplifier in the supply circuit of the goniometer servomotor, which turns the yawmeter tube into the flow direction. This restores the liquid in the manometer to the null position.

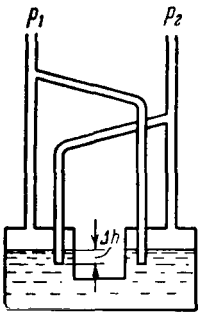

FIGURE 4.80 Safety device to prevent loss of water from a U-tube manometer.

This photoelectric system reacts to a change in water level of 2 mm, which at M = 0.2 and 0.6 corresponds to changes in yaw by 0.2° and 0.02° respectively when a cylindrical yawmeter tube is used. It may happen that when the wind tunnel is started up, the yawmeter is not installed in the flow direction, so that a large pressure difference will act on the manometer before the automatic attitude-adjustment system becomes operative. A safety device, such as that shown in Figure 4.80, is installed to prevent loss of water from the U-tube manometer in this eventuality. At pressure differences above a predetermined value Δh the legs of the U-tube are automatically interconnected.

For simultaneous measurement of the flow parameters at several points Pitot combs are used; they consist of streamlined supports carrying arrays of measuring tubes. The combs are suitable for measuring total pressure, static pressure, and temperature over the height of blade cascades. In addition to the total- and static-pressure combs, combined combs, fitted alternatingly with total- and static-pressure tubes, are employed. Figure 4.81 shows a comb for measuring the total pressure over the pitch of annular and flat blade cascades /4/. To reduce the measuring error caused by the downwash behind the cascade, the total-pressure tubes are mounted as nearly as possible in the theoretical flow direction. The tubes are sometimes spaced nonuniformly on the comb in order to increase the measuring accuracy in regions of large pressure gradients.

To avoid interference between the tubes of a static-pressure comb, the distance between individual tubes should not be too small. Interference is especially pronounced at high subsonic velocities, at which the distance between the tube centers should not be less than 15 to 20 tube diameters. Total-pressure tubes are considerably less sensitive, and can even be installed in contact with each other.

Combs of total- and static-pressure tubes are also used for calibrating the test section in supersonic wind tunnels. Thus, Figure 4.82 shows a cross-shaped comb for pressure measurements along two perpendicular axes of the test section. The comb can be moved along the axis of the test section.

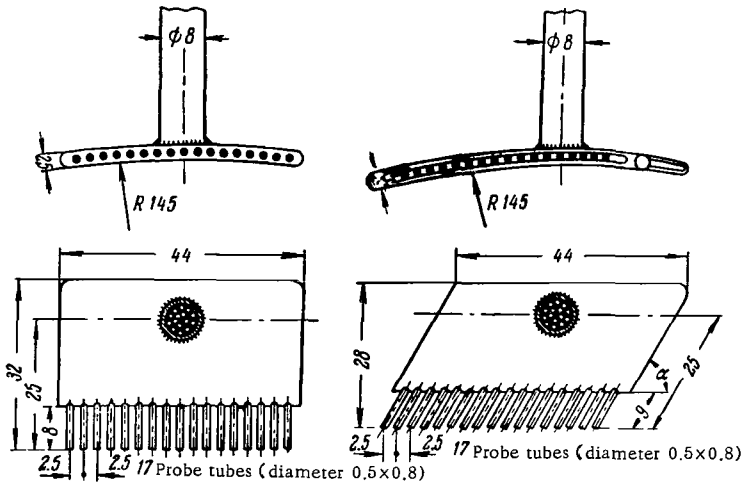

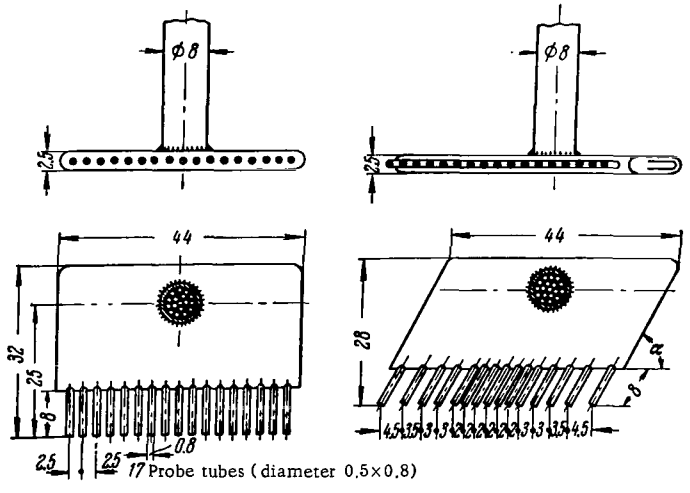

FIGURE 4.81. Plane and arc-formed combs of total- pressure tubes.

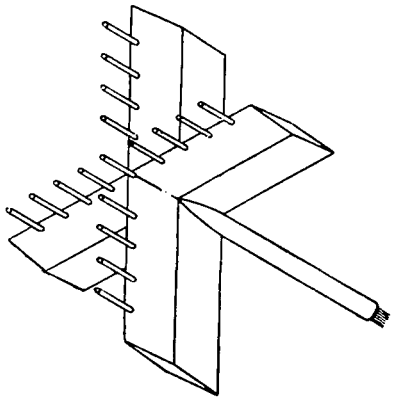

FIGURE 4.82. Cross-shaped comb for supersonic wind tunnels.

§18. VISUAL AND OPTICAL METHODS OF FLOW INVESTIGATIONS

When discussing methods for the visualization of fluid flow, one must consider the difference between streamlines, particle paths, and filament lines of tracer particles. The tangent to the streamline coincides with the velocity vector at that point and instant. The streamlines give an instantaneous picture of the flow directions. At different instants the streamline at each point are determined by the directions of motion of the different particles of the fluid.

A particle path is the path traversed by an individual particle of the fluid during a definite period of time.

A filament line is the line drawn at a given instant through the positions of all tracer particles which have passed through a given point.

In steady flow the streamlines, particle paths, and filament lines coincide. In this case their positions can be established from long-exposure photographs of a stream into which particles have been injected. If, however, we photograph a nonsteady flow, the lines on the picture will indicate the motion of the separate particles, i.e., they will be the particle paths. If we photograph the nonsteady flow at a short exposure time Δt, the picture will show a number of separate lines of length $V_i \Delta t$, where V_i is the velocity of each separate particle. The envelopes of these lines will be the streamlines at the instant of exposure. Thus, by injecting into the stream at some point tracer particles, differing in optical density or color from the fluid, or by coloring parts of the flowing medium (e.g., fuchsin in water), we can determine the filament line by instantaneous photography.

In addition, it should be remembered that an observer at rest with respect to the model will observe a different flow pattern than an observer at rest with respect to the undisturbed flow.

Methods of visual flow investigation. Direct observation and photography of details of fluid flow is impossible, because the uniformity of the medium does not provide any contrast between the various

particles. Flow visualization involves giving different physical qualities to the tested region, to enable details of the flow to the discerned either directly, or with an instrument which amplifies the discriminating power of the naked eye.

The most widely used method of visualization is that of injecting solid liquid or gas particles into the stream, and viewing them in reflected or dispersed light. It is implicitly assumed that the particles have a very low inertia and acquire the local direction of motion of the fluid, and that they are of sufficiently small weight to obviate any disturbances due to gravity. Visualization techniques include smoke filaments, the observation of very small particles which occur naturally in the stream and can be seen with the aid of a microscope and an intense light source, and the observation of fixed tufts, used widely for investigations near the surface of a body.

Smoke method. This method is widely applied at low flow velocities (up to 40 or 50 m/sec) and consists in injecting smoke filaments into a transparent gas stream through nozzles or openings in the model. The smoke is produced in special generators either by burning organic substances (rotten wood, tobacco), or by combining or evaporating different chemicals, such as, titanium and stannic tetrachloride, mineral oil, etc.

The tuft method consists in fixing light silk threads to thin wires inside the stream. The threads remain in a definite position in steady flow, but vibrate at points where the flow is nonsteady or turbulent. It is thus possible to establish the flow direction and regime at the surface of a model; quiescence of the tufts indicates a laminar boundary layer. Behind the point of boundary-layer separation the vibrations of the threads become very intense. The tuft method is widely used in qualitative analyses of flow around models, since the motion and location of the tufts can be easily observed and photographed (Figure 7.13).

Optical methods of flow investigation

Optical investigation methods have found wide application in high-velocity flow, where compressibility effects are important. At hypersonic velocities these are powerful methods for determining the flow pattern; they make possible tests which cannot be performed by other means. The main advantage of the optical methods is the complete absence of transmission lag and of the need to insert mechanical devices into the stream. Using spark illumination, we can photograph processes completed in a millionth part of a second. Spark sources are used to obtain sequences of flow photographs, separated by very small intervals, showing the development of processes in nonsteady flow. Even better results can be obtained in the study of nonsteady processes by combining several of the instruments described below with an ultrahigh-speed movie camera, (for instance, model SFR, which has speeds of up to 2 1/2 million frames per second).

Optical methods of flow investigation are based on the dependence of the index of refraction on the density of a gas, which is given by the

[Gladstone-Dale] equation

$$\frac{n-1}{\rho} = \frac{n_0-1}{\rho_0} = \text{const.}$$

Here n and n_0 are the respective indices of refraction at densities ρ and ρ_0, and $n = \frac{c}{v}$, where c is the velocity of light in vacuo, and v is the velocity of light in the medium at density ρ.

For air of density $\rho_0 = 0.125\ \text{kg} \cdot \text{sec}^2 \cdot \text{m}^{-4}$; $n_0 = 1.000294$, whence $n = 1 + 0.00235\,\rho$.

For optical study of flow around a model in a wind tunnel, optically-parallel glass ports are installed in the walls of the tunnel. A light beam is projected through the ports across the tunnel perpendicularly to the direction of undisturbed flow, and fall on a screen at P_1 (Figure 4.83).

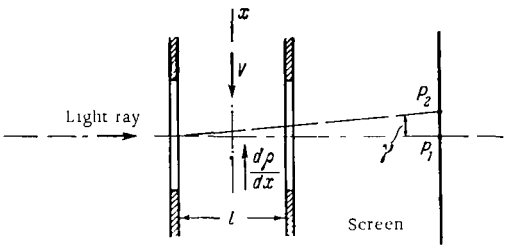

FIGURE 4.83. Deflection of a light ray in a gas of varying density.

In the neighborhood of the model the change in gas density causes a change in the index of refraction, so that the light beam is refracted through an angle γ and falls on the screen at P_2. The refraction due to passage through a gas layer of thickness l is

$$\gamma = \frac{1}{n}\frac{dn}{dx}\,l,$$

where $\frac{dn}{dx}$ is the gradient of the index of refraction in a direction perpendicular to the direction of incidence of the light. For air, using the above relationship between n and ρ, we have

$$\gamma = l\,\frac{0.00235}{1 + 0.00235\,\rho}\,\frac{d\rho}{dx}.$$

The refraction angles γ are usually very small. For example, if $l = 1$ m, $\rho = 0.125$, and the density doubles along a light path of 1 m length, then $\gamma = 0.015°$. The refraction of the light beam can be detected by the shadow method or by schlieren photography.

The shadow method. The shadow method is less sensitive than other optical methods and it is therefore used only for detecting large density gradients, for instance in shock waves in supersonic flow. It has the advantage of simplicity. A shadowgraph of the flow around a model can be obtained with the aid of a powerful point source of light (Figure 4.84).

The diverging beam from the source is projected onto the screen. In each region of optical inhomogeneity, the rays will be refracted, causing corresponding shadows on the screen where the different areas will be illuminated at different intensities.

The ratio of the brightness of the direct beam (solid lines) to that of the refracted beam (broken lines) is expressed by

$$\frac{\Delta x}{\Delta x + l\Delta\gamma} \approx \frac{1}{1 + l\frac{d\gamma}{dx}}.$$

The above relationship between γ and ρ shows that the brightness ratio depends on the second derivative with respect to x of the density and we must integrate twice to find ρ. It is very difficult to interpret the brightness changes of shadowgraphs quantitatively, and this method is used in practice

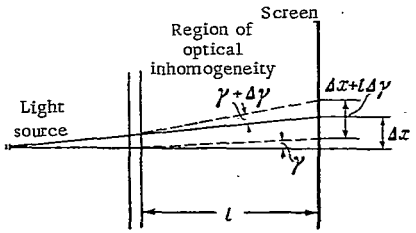

FIGURE 4.84. Shadowgraph method for studying the flow around a model.

only for qualitative investigation. An example of the shadowgraph of flow around a blade cascade is shown in Figure 4.85. The photographs were taken with the aid of a spark light source of about 10^{-6} sec duration.

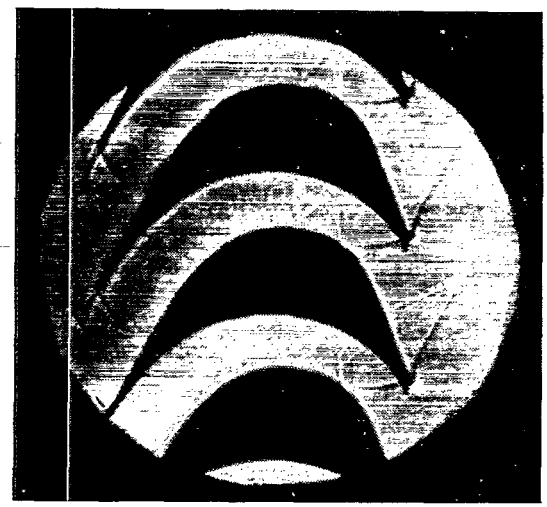

FIGURE 4.85. Shadowgraph of the flow around a blade cascade.

The photograph shows shocks of different configurations in the local supersonic regions, and the boundary-layer separations on the convex surfaces of the blades.

The schlieren method. The schlieren method, due to Töpler, is more sensitive to small density changes than the shadow method and permits study of the flow around models at subsonic velocities. The schlieren method is widely used at present in every aerodynamic laboratory.

This method is based on the measurement of the angle of refraction of light rays (γ in the figure), which, as was shown above, is proportional to the density gradient (Figure 4.86). Light from a point source S (or a line-source between 0.01 and 0.1 mm wide), placed at the focus of the lens O_1, passes in a parallel beam to the plane-parallel glass ports in the walls of the tunnel through which the gas flows, and is condensed at the focus of the lens O_2. If the beam passes through a region in which the density

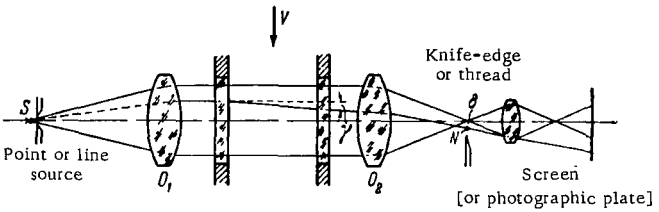

FIGURE 4.86. Schlieren system.

varies in the flow direction it is refracted through an angle γ and crosses the focal plane of the lens O_2 at a distance δ from the optical axis (point N), where $\delta = f\gamma$, f being the focal length of the lens O_2.

A thin thread (of about 0.1 mm diameter), passing parallel to the line source through point N, will cast a shadow on the ground-glass screen of a camera, focused on the center line of the tunnel. This shadow indicates the regions in which the density variations cause the beam to be refracted through an angle γ.

Micrometer adjustment, parallel to itself of the shadow thread [or knife edge] to another position δ_1 in the focal plane, will cause it to stop all rays refracted by an angle γ_1, and so on. Each shaded area (stripe) on the screen will correspond to a region in which a definite density gradient exists.

Knowing the value of δ for each position of the thread we can integrate the expression

$$\delta(x) = f\gamma = fl\,\frac{0.00235}{1+0.00235\rho}\,\frac{d\rho}{dx},$$

to obtain $\rho(x)$, which is approximately

$$\rho(x) = \rho(x_0) + \frac{1}{0.00235fl}\int_{x_0}^{x}\delta(x)\,dx.$$

Thus, knowing the density at a certain point x_0, we can determine ρ at every point by a single integration.

Instead of a single thread it is possible to use a grid, consisting of many threads, so that an instantaneous photographic record is obtained of the family shadow stripes corresponding to the different density gradients.

If a knife edge is placed in the focal plane instead of the thread, it will stop all rays deflected by amounts larger than the distance of the knife edge from the optical axis. The screen of the camera will be shaded for all regions in which the density gradient exceeds the corresponding value (Figure 4.87), and the qualitative flow pattern (compression and condensation shocks, flow separation, etc.) will appear on the schlieren photograph.

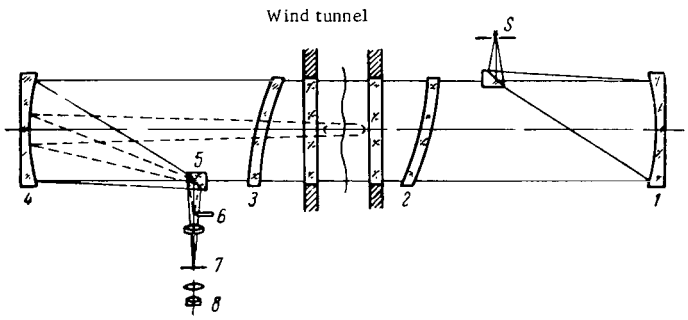

FIGURE 4.87. [Modified] schlieren instrument (according to D. D. Maksutov).

Getting sharp (high-definition) images by the schlieren method requires not only great experimental skill and careful adjustment of the instrument, but also the use of very good telephotographic lenses of the type used in astronomy. The preparation of such lenses, or of the large parabolic mirrors sometimes used instead, is very difficult so that it is difficult to construct good schlieren instruments with field diameters larger than 200mm. D. D. Maksutov suggested an improved optical design, providing, at comparative ease, an instrument of high quality and large field of view. In this system (Figure 4.87) the light beam from a line source is reflected from a spherical mirror (1), and passes as a parallel beam first through a meniscus lens (2), then through the glass port of the wind tunnel and across the inhomogeneous stream. After emerging from the second port, the light passes through the second meniscus lens (3), and is reflected by a second spherical mirror (4) first onto a flat diagonal mirror (5) and then through the diaphragm (6) (situated at the focus of the second spherical mirror). onto a screen (7) or onto the eyepiece of a magnifying glass (8). The preparation of spherical mirrors and meniscus lenses is relatively simple, and by assembling them so as to compensate for their mutual aberration, high-quality optical systems can be obtained with considerable field diameters (up to between 300 and 500mm).

Figure 4.88 shows the IAB-451 [Soviet Union] schlieren instrument, designed according to Maksutov's principle. The instrument has two main parts: a collimator I, designed to project a parallel light beam of 230 mm diameter through the field investigated, and an observation tube II, designed for visual observation and photography of the schlieren picture.

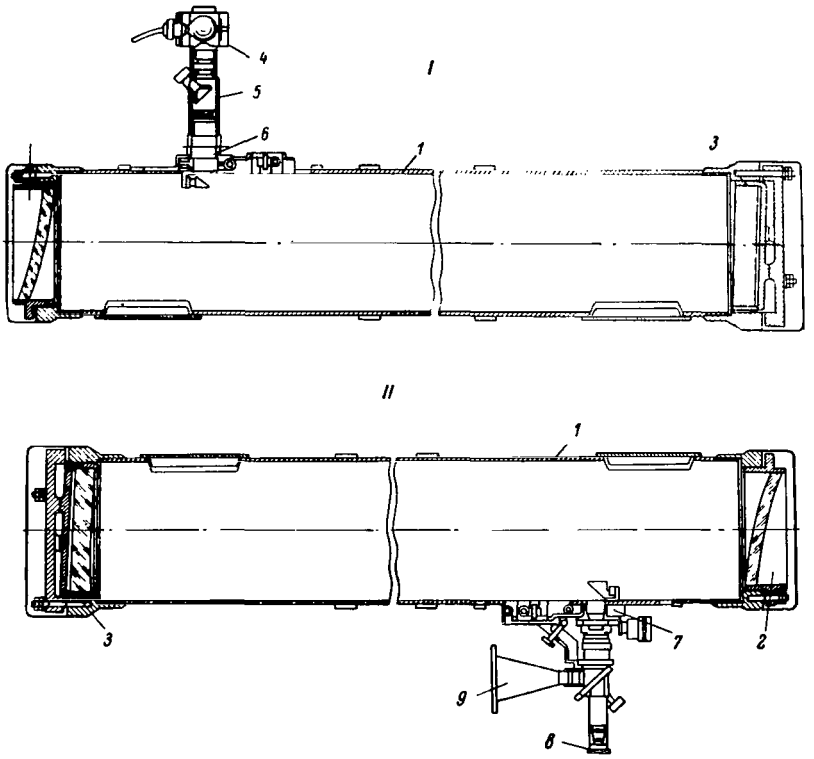

FIGURE 4.88. IAB-451 type schlieren instrument.

Meniscus lenses (2) and mirrors (3) are fixed in holders in both collimator and observation tube. The tubes (1) are mounted on brackets on opposite sides of the test section of the wind tunnel so that the optical axes of the mirrors and lenses coincide.

The collimator is fitted with a light source (4), condenser lens (5), and slit carriage (6), so that the collimator slit can slide along (for adjustment at the focus of the optical system) and be rotated about the collimator axis. The sharpest definition is obtained when the slit is perpendicular to the direction of the largest density gradient. The slot is formed by parallel knife edges with micrometer adjustment of their separation, so that the slot width can be read off with an accuracy of 0.01 mm.

The observation tube is fitted with a carriage (7) for the knife edge and for either interchangeable lenses (8), or a camera adaptor (9). The carriage (7) serves for focusing the knife edge and for rotating it about an axis parallel to the slot. In addition, the carriage has a micrometer slide for adjusting the knife edge in a plane perpendicular to the axis, for the purpose of stopping the rays from the lens. The position of the knife edge is indicated on the scale to an accuracy of 0.01 mm.

A drawback of schlieren instruments with large fields of view is that they extend over a considerable distance outside the wind-tunnel perpendicular to its axis. In the design of modern schlieren instruments with 500-mm field diameters the collimator and observation tube are shortened by up to 1.5 m by repeatedly bending the optical axis with the aid of spherical mirrors and inclined lenses.

The interferometric method. The interferometric method of flow investigation is based on the difference in the velocity of light in media of different densities. The phenomenon of interference of light can be understood by considering a light beam as a train of waves. Whenever two light beams intersect, they reinforce each other at points where the wave peaks of one train coincide with those of the other, but cancel each other at points where the peaks of one train coincide with the troughs of the other. If two coherent light beams (i. e., beams from two sources which oscillate in phase or at constant phase difference) converge at a point on a screen after traveling by different paths, their relative phase will be determined by the difference between their optical path lengths. Depending on this difference, they will reinforce or weaken one another. [Two coherent parallel line sources] will thus project onto a screen a sequence of dark and light fringes. If both light beams have *passed through a medium of the same density, the interference fringes* will be parallel to each other. If the density of the medium is different over part of the path of one beam, the light-propagation velocity (which depends on density) in this beam will change, and the interference pattern will be disturbed. Density gradients in the medium will also distort the fringes. The magnitude of the displacement and change of shape of the fringes provide a measure of the density changes within the field of view. The optical interferometer can thus be used for quantitative and qualitative investigations of the density and for determining the flow pattern around a model.

The Mach-Zehnder interferometer is used for aerodynamic research. The schematic diagram of this instrument is shown in Figure 4.89. An image of the light source (1) is focused on the slot (2) of the collimator (I), situated at the focus of the lens (3). The parallel light beam from the lens (3) falls on the interferometer (II), of which the principal components are the two half-silvered plates (4) and (5) and the two mirrors (6) and (7). The plate (4) divides the light into two beams a_1 and a_2. The beam a_1 passes through the glasses (10) and (11) on either side of the test section of the wind tunnel, and is reflected by the mirror (6) and the half-silvered plate (5) onto observation tube (III). The beam a_2 is reflected by mirror (7) through the half-silvered plate (5) onto the observation tube. In this way plate (4) divides the beam from the collimator (I) into two parts, which are reunited by plate (5) and focused by lens (8) onto the plane of the photographic plate or the screen.

Depending on the transit time from the common light source to the camera or screen, the waves in beams a_1 and a_2 will arrive either in phase or with a finite phase difference. The superimposed beams produce an interference pattern on the screen, which can be observed visually or can be photographed.

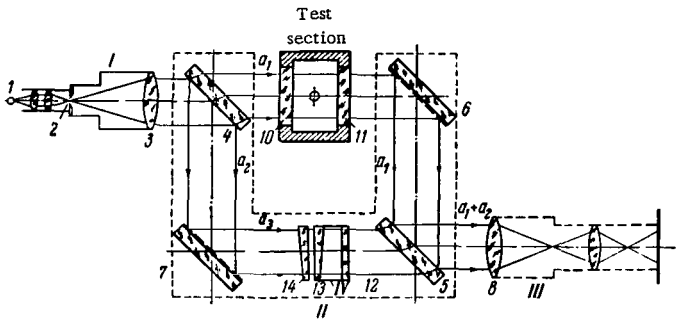

FIGURE 4.89. The Mach-Zehnder interferometer. I — collimator with light source; II — interferometer mirror system; III — observation tube; IV — compensator.

The velocity of light in air increases with decreasing density, so that the transit time along a given air path will decrease with decreasing density. The interference pattern will be affected by changes in density along the paths of the beams a_1 and a_2 and in particular, by changes in density in the test section of the wind tunnel, through which beam a_1 has passed.

The interferometer can be arranged to obtain fringes of either infinite or finite* width. These two methods yield different interference patterns.

For infinite-width fringes, the plates and mirrors of the interferometer are installed parallel to each other at an angle of 45° to the flow direction. When both beams a_1 and a_2 pass through media of the same density, their optical paths will be equal; they will arrive in phase on the screen, and the screen will be uinformly illuminated. When the density of the medium changes uniformly in the test section, the transit time of beam a_1 will differ from that of beam a_2, so that the light waves in the two beams (which are coherent since they originate in the same light source) will arrive out of phase at the screen. A gradual change in density throughout the test section will cause a corresponding gradual change in the brightness of the screen, which will be maximum for phase differences corresponding to 1, 2, 3, etc., wavelengths and minimum for phase differences corresponding to $\frac{1}{2}$, $1\frac{1}{2}$, $2\frac{1}{2}$, $3\frac{1}{2}$, etc., wavelengths. When the wind tunnel is first started up the density changes around the model will produce a complicated interference pattern on the screen, each line being a contour of equal density. The distance between adjacent lines corresponds to one wave length, or, as will be shown below, to a change in air density of 4.68×10^{-4} kg·sec^2/m^4 for a test-section width of 500 mm. Setting up the

* [Also called fringe-displacement method.]

interferometer for fringes of infinite width does not give high accuracy, since the number of interference fringes is small, and this method is used only for qualitative analysis.

To obtain data from a large number of points in the field the plate (5) of the interferometer is rotated so that light beams a_1 and a_2 emerge from it at a small angle α to each other. With undisturbed flow in the test section, the different path lengths of the beams give rise to an interference pattern consisting of alternately dark and light straight fringes, whose width (the distance between the centers of adjacent dark and light regions) is $B = \frac{\lambda}{\alpha}$; their direction is perpendicular to the plane containing the axes of the beams a_1, a_2. The width and direction of the fringes can be changed by adjusting the mirrors of the interferometer. When the density of the air in the test section changes gradually and uniformly, the whole system of straight interference fringes becomes displaced parallel to itself. A density change causing a phase shift equivalent to one wavelength λ (for the green spectrum line generally used, λ can be taken as 5.5×10^{-4} mm), will cause the pattern to move by one fringe width. If different rays of the beam a_1 cross the test section of the wind tunnel in regions of different density, (i.e., of different index of refraction n), there will be a corresponding shift of parts of the interference pattern and deformation of the fringes. We can measure these shifts, and calculate the difference of the indices of refraction $\Delta n = n_2 - n_1$ in the corresponding sections of the tunnel to determine the density changes $\Delta\rho = \rho_2 - \rho_1$ in these sections, assuming that the density along each light path across the test section is constant, i.e., that the flow is two-dimensional.

In order to calculate $\Delta\rho$ for two-dimensional air flow we can use the above relationship between the index of refraction and the density. Differentiating, we obtain

$$dn = 0.00235\, d\rho.$$

The magnitude of the shift of an interference line at a given point in the xy plane, which is perpendicular to the optical axis, is determined by two photographs, one under static conditions, and the other with full flow in the test section. This shift is expressed by the number $N(x, y)$ which is equal to the ratio of the interference-fringe shift at the point (x, y) to the width of this fringe. Knowing $N(x, y)$ we can calculate the corresponding difference in transit time with and without flow

$$t_2 - t_1 = \frac{N(x, y)}{f},$$

where subscript 1 denotes static conditions and subscript 2, full flow in the test section, and f is the frequency of light, which is a constant for a given color and depends on the filter used.

The difference between the transit times of the beams can be expressed in terms of the change in the speed of light in the test section

$$t_2 - t_1 = l\left(\frac{1}{v_2(x, y)} - \frac{1}{v_1(x, y)}\right),$$

where l is the path length of the beam in the test section. Equating the last two expressions, we obtain

$$\frac{N(x, y)}{f} = l\left(\frac{1}{v_2(x, y)} - \frac{1}{v_1(x, y)}\right).$$

By definition the index of refraction is the ratio of the velocity of light in vacuo v_{vac} to its velocity v in the given medium:

$$n = \frac{v_{vac}}{v},$$

so that

$$\frac{N(x, y)}{f} v_{vac} = l[n_2(x, y) - n_1(x, y)] = l\,\Delta n(x, y);$$

since the length of a light wave in vacuo is

$$\lambda_{vac} = \frac{v_{vac}}{f},$$

then

$$N(x, y)\lambda_{vac} = l\,\Delta n(x, y) = l \cdot 0.00235\,\Delta\rho(x, y),$$

and

$$\Delta\rho(x, y) = \frac{\lambda_{vac} N(x, y)}{0.00235 l}.$$

If the density ρ_1 at zero flow in the tunnel is known, the density of the flowing medium at a given point can be found from

$$\rho_2(x, y) = \rho_1 + \Delta\rho(x, y).$$

If a monochromatic light source with a green filter is used in the interferometer, we can take $\lambda_{vac} = 5.5 \times 10^{-4}$. In a wind tunnel with a test-section width of 500 mm, the density change corresponding to a pattern shift of one fringe width is

$$\Delta\rho = \frac{5.5 \cdot 10^{-4}}{0.00235 \cdot 500} = 4.68 \cdot 10^{-4}\ \text{kg} \cdot \text{sec}^2/\text{m}^4.$$

The displacement or distortion of the interference fringes can be measured to an accuracy of 0.1 or 0.2 fringe widths, which correspond to

$$\Delta\rho \approx 5 \cdot 10^{-5} \text{ to } 10^{-4}\ \text{kg} \cdot \text{sec}^2/\text{m}^4.$$

The processing of interferograms in density determinations is shown schematically in Figure 4.90. The interference fringes corresponding to zero flow are indicated by broken lines; those obtained during tunnel operation, by full lines. We denote by ΔA and ΔB the changes in [horizontal] distance from an arbitrary point M at the edge of the field to points A and B. In the figure, ΔA is 0.7 of a fringe width and ΔB is 0.9 of a fringe width. Taking the fringe width as as $4.68 \times 10^{-4} \cdot \text{kg} \cdot \text{sec}^2/\text{m}^4$, we obtain the absolute values of the density differences:

$$\Delta\rho_A = \rho_A - \rho_M = 0.7 \cdot 4.68 \cdot 10^4 = 3.38 \cdot 10^{-4}\ \text{kg} \cdot \text{sec}^2/\text{m}^4,$$

$$\Delta\rho_B = \rho_B - \rho_M = 0.9 \cdot 4.68 \cdot 10^4 = 4.21 \cdot 10^{-4}\ \text{kg} \cdot \text{sec}^2/\text{m}^4.$$

By this method we can measure the difference in densities at points situated on a vertical line in the field of view. To measure the difference in densities in the horizontal direction the fringes are obtained horizontally.

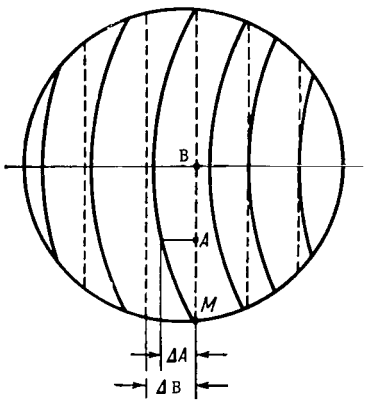

FIGURE 4.90. Quantitative interpretation of interferograms.

The relative error of measuring the density by the interferometer increases with Mach number, because of the decrease in absolute density.

It is simpler to determine the shift of the fringes if they are first aligned perpendicularly to the chord of the model or to the wall. Thus, for instance, Figure 4.91 shows the interferogram of flow past a flat plate with a laminar boundary layer for which $M = 2.04$. In this case the density gradient is normal to the direction of the fringes at zero flow and each fringe on the photograph is a line of [constant] density difference (with density as the abscissa).

Knowing the density distribution, we can find the pressure distribution, for instance, on the surface of a wing. In this respect the advantage of the interference method over the manometric method is that it provides pressure data for a larger number of points and does not require the preparation of a complicated model with many orifices.

Pressure can be determined as follows: at any point on the wall of the test section, a measured pressure p_r will correspond to a density ρ_r. These are related to the flow parameters at any other point by the expression

$$\frac{\rho(x, y)}{\rho_0} = \frac{\rho_r}{\rho_0} + \frac{\lambda_{vac} V(x, y)}{0.00235 l \rho_0},$$

or, since $\rho_0 = p_0/gRT_0$,

$$\frac{\rho(x, y)}{\rho_0} = \frac{\rho_r}{\rho_0} + k \frac{T_0}{p_0} N(x, y),$$

where

$$k = \frac{\lambda_{vac} Rg}{0.00235 l}.$$

If the flow is isentropic up to the point where the pressure is known, then $p_r/p_0 = (\rho_r/\rho_0)^\varkappa$, whence

$$\frac{\rho(x, y)}{\rho_0} = \left(\frac{p_r}{p_0}\right)^{\frac{1}{\varkappa}} + k \frac{T_0}{p_0} N(x, y);$$

if the flow is also isentropic up to the point (x, y) where the pressure is to be determined, then

$$\frac{p(x, y)}{p_0} = \left\{\left(\frac{p_r}{p_0}\right)^{\frac{1}{\varkappa}} + k \frac{T_0}{p_0} N(x, y)\right\}^\varkappa.$$

Thus, in order to determine the pressure at any point (x, y), it is necessary to measure the stagnation temperature T_0, the total pressure p_0, the pressure p_r, and the relative fringe displacement $N(x, y)$. The pressures determined in this way are in good agreement with the results of manometric measurements.

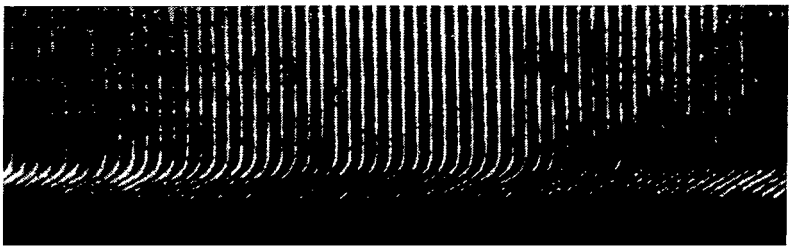

FIGURE 4. 91. Interferogram of a laminar boundary layer on a flat plate (M = 2.04; Re = 200,000).

For accurate quantitative analyses with an interferometer the light source must be as perfectly monochromatic as possible. The mercury lamps mostly used for this purpose are fitted with interference filters which isolate the green mercury line ($\lambda = 5.46 \times 10^{-4}$ mm). Since clear interferance pictures demand very short exposures, spark-light sources having durations of a few microseconds are also used.

In some modern instruments the interferometer is combined with a schlieren apparatus, using a separate observation tube mounted coaxially with the collimator.

The error in measuring the distortion or shift of the fringes of the interference pattern is about 0.2 fringe width in visual observation and 0.1 fringe width when using photographs. This accuracy is achieved by the use of a wedge compensator (IV) (Figure 4. 89) inserted into one branch of the interferometer. The compensator consists of a hermetically sealed air chamber, one wall of which is formed by a plane-parallel glass plate (12), and the other by a pair of wedge-shaped glass plates (13) and (14). Plate (14) can slide over plate (13), thus forming a plane-parallel plate, whose thickness can be adjusted to compensate for the effect of the beam a_1 having to pass through the glass windows of the wind tunnel. The magnitude of the adjustment also indicates the effects on light-transit time of changes of air density in the wind tunnel. The displacement is measured by a micrometer. The compensating air chamber serves to compensate for changes in the initial density of the air in the wind tunnel. By changing the pressure inside the chamber, we can change its equivalent optical thickness.

The interferometric method provides more accurate quantitative results. than the schlieren method. The principal difficulties in both methods are due to the fact that all inhomogeneities encountered along the light path in the wind tunnel are superimposed.

In two-dimensional flow, where the density is constant along any light path, quantitative measurements present no difficulty to an experienced

worker. It is much more difficult to determine the density changes, when the axis of flow symmetry is perpendicular to the direction of the light beams. Quantitative optical investigations are therefore largely restricted to two-dimensional problems.

When comparing the use, in qualitative studies, of the interferometer, shadowgraph, and schlieren instrument, the following should be noted. The shift of the interference fringes is proportional to the changes in density of the flowing medium, whereas the results obtained by schlieren and shadow methods depend to a first approximation respectively on the first and second derivatives of the density with respect to distance.

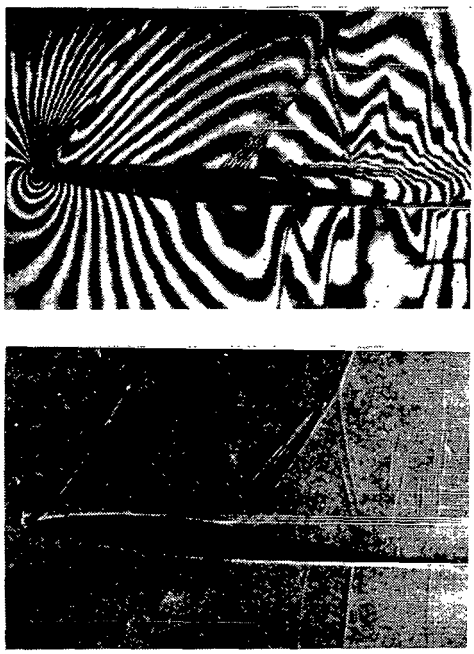

FIGURE 4. 92. Interference (a) and shadow photographs (b) of flow around airfoil ($M = 0.95$; $\alpha = 6°$).

Interference photographs therefore show clearly changes in density for which other methods are not sufficiently sensitive. Thus, for instance, Figure 4. 92 shows interference and shadow photographs for a flow around an airfoil at $M = 0.95$. The outer zones of expansion of the gas at the leading edge, and the density change behind the compression shock and along the lower surface of the wing can be clearly seen on the interference photograph. On the other hand, the interferometer is less sensitive to small sudden changes in density, which are more readily seen on the shadow picture. This insensitivity to small but sudden changes is useful because flaws in the windows, or dust on them, reduce the clarity of the schlieren photographs.

Bibliography

1. Loitsyanskii, L.G. Mekhanika zhidkosti i gaza (Mechanics of Liquids and Gases). — GTTI, Moskva. 1957.
2. Shaw, R. Influence of Hole Dimensions on Static Pressure Measurements. — J. Fluid Mech., Vol. 7, pt. 4. 1960.
3. Dean, R.C. Aerodynamic Measurements. — Mass. Inst. of Technology. 1953.
4. Petunin, A.N. Priemniki dlya izmereniya davleniya i skorosti v gazovykh potokakh (Probes for Measuring Pressure and Velocity in Gas Flows). — TsAGI. Collection of articles "Promyshlennaya Aerodinamiko" Issue No. 19. Oborongiz. 1960.
5. Holder, D.W. Experiments with Static Tubes in Supersonic Airstream. — ARC Rep. Mem., No. 2782. 1953.
6. Fizicheskie izmereniya v gazovoi dinamike i pri gorenii (Physical Measurement in Gas Dynamics and Combustion). — Moskva IL. 1957.
7. Winternitz, F.A.I. Simple Shielded Total Pressure Probes. — Aircraft Engng., Vol. 30, No. 356. 1958.
8. Markowski, S.J. and E.M. Moffat. Instrumentation for Development of Aircraft Powerplant Components Involving Fluid Flow. — SAE Quarterly Trans., Vol. 2, No. 1. 1948.
9. Young, A.D. and J.N. Maas. The Behavior of a Pitot-Tube in a Transverse Total-Pressure Gradient. — ARC Rep. and Mem., No. 1770. 1937.
10. Barry, F.W. Determination of Mach Number from Pressure Measurements. — Trans. ASME, Vol. 78, No. 3. 1956.
11. Malikov, M.F. Osnovy metrologii (Fundamentals of Metrology). — Moskva. 1949.
12. Ower, E. The Measurement of Air Streams [Russian Translation]. — Moskva - Leningrad. 1935.
13. Bryer, D.W. Pressure Probes Selected for Three-Dimensional Flow Measurements. — ARC Rep. and Mem., No. 3037. 1958.
14. Fusfeld, K.D. A Probe for Measurements of Flow Inclination in a Supersonic Air Stream. — J. Aero. Sci., Vol. 18, No. 5. 1951.
15. Lee, J.C. and J.E. Ash. A Three-Dimensional Spherical Pitot Probe. — Trans. ASME, Vol. 78, No. 5. 1956.
16. Keast, F.H. High Speed Cascade Testing Technique. — Trans. ASME, Vol. 74, No. 5. 1952.
17. Morris, D.E. Calibration of the Flow in the Working Section of the 3 ft × 3 ft Tunnel NAE. — ARC C.P., No. 261. 1956.
18. Raney, D.J. Flow Direction Measurements in Supersonic Wind Tunnels. — ARC C.P., No. 262. 1956.
19. Gukhman, A.A. and others. Eksperimental'noe issledovanie prodol'no obtekaemoi termopary pri techenii gaza s bol'shoi skorost'ya (Experimental Study of High-Speed Hot Gas Flowing Lengthwise around a Thermocouple). — Sbornik Trudy TsKTI, No. 21. 1951.
20. Hottel, H.C. and A. Kalitinsky. Temperature Measurements in High-Velocity Air Streams. — J. Appl. Mechanics, Vol. 12, No. 1. 1945.

21. Malmquist, L. Temperature Measurements in High - Velocity Gas Streams. — Kungl. Tekniska Högskolans Handlinger. Trans. of the Royal Inst. of Techn. Stockholm, Sweden, No. 15. 1948.
22. Martinov, A.K. Eksperimental'naya Aerodinamika (Experimental Aerodynamics). — Oborongiz. 1958.
23. Wood, R.D. A Heated Hypersonic Stagnation Temperature Probe. — J. of the Aero - Space Sci., Vol. 27, No. 7. 1960.
24. Monaghan, R.J. The Use of Pitot - Tubes in the Measurements of Laminar Boundary Layers in Supersonic Flow. — ARC Rep. and Mem., No. 3056. 1957.
25. Preston, I. Determination of Turbulent Surface Friction with the Aid of Pitot Tubes. [Russian Translation] In: Sbornik Perevodov i obzorov inostrannoi literatury "Mekhanika", No. 6. 1955.
26. Konstantinov, N.I. and G.L. Dragnysh. K voprosu ob izmerenii poverkhnostnogo treniya (The Problem of Measuring *Skin Friction*). — *Trudy Leningradskogo Politekhnicheskogo* Instituta, No. 176. 1955.
27. Preston, J.H. Visualisation of Boundary Layer Flow. — ARC Rep. and Mem., No. 2267. 1946.
28. Carter, A.D.S. Some Fluid Dynamic Research Techniques. — The Institution of Mechanical Engineers Proceedings, Vol. 163 (W.E.P. No. 60). 1950.

Chapter V

INSTRUMENTS AND APPARATUS FOR PRESSURE MEASUREMENT

The pressure measurement is the most important measurement in the experimental study of the motion of a liquid or a gas. It is sufficient to note that measuring the pressure is the simplest way to find the magnitude and direction of the flow velocity; by measuring the distribution of the pressures on the surface of a model or in the wake behind it, we can determine the aerodynamic forces and moments which act on the model and its separate parts.

The methods of measuring the pressure in a moving liquid or gas are the subjects of much theoretical and experimental research. Instruments for measuring pressures are continuously being improved. However, despite the large number of available designs for measuring instruments, the researcher sometimes needs a special instrument which will satisfy in the best way possible the requirements of certain problems, since very often standard equipment cannot be used for this purpose.

The pressure of a liquid or gas is determined by the force acting normally on unit surface. In aerodynamic calculations, the unit of pressure very often used is that of the technical m·kg·s system, (meter, kilogram force, sec) which is equal to 1 kg/m^2. A pressure of 1 kg per cm^2 is called one technical atmosphere or simply one atmosphere. Units of pressure ordinarily used are the mm of water column (mm H_2O) and the mm of mercury column (mm Hg), i. e., the pressure exerted on its base by a 1 mm-high column of the given liquid. The height of the column corresponds to the normal gravitational acceleration (980.665 cm/sec^2) and to different temperatures (4°C for water and 0°C for mercury). When measuring pressures by U-tube manometers, liquids other than water or mercury are ordinarily used, but the heights of the columns of these liquids are referred to the heights of the corresponding column of water or mercury.

The use as unit of measurement of 1 kg/m^2 is very convenient in experimental aerodynamics. The pressure of 1 kg/m^2 corresponds to a 1 mm-high water column. This simplifies calculations according to the data provided by U-tube manometers. When measuring pressures the researcher has to take into account the absolute pressure p, the gage pressure p_g, and the pressure difference Δp. The absolute pressure is the pressure referred to perfect vacuum. The gage pressure is the difference between the absolute pressure and the atmospheric (barometric) pressure B

$$p_g = p - B.$$

A negative gage pressure is called rarefaction. The pressure difference is the difference between any two absolute pressures p_1 and p_2

$$\Delta p = p_1 - p_2.$$

In most cases a manometer is an instrument which measures the gage pressure. An instrument for measuring the pressure difference is usually called a differential manometer. This term is to a certain degree arbitrary, since the gage pressure also represents the difference between the pressure, which is of interest to the researcher, and the atmospheric pressure.

In many aerodynamic experiments the most important magnitudes measured are the pressure differences from which the flow velocity, the mass flow, and the coefficients of pressure are determined. In other experiments the absolute pressures are most important. Thus, for instance, absolute pressure enters in many formulas of gas dynamics. Most often the absolute pressure is determined as the algebraic sum of the readings of a barometer and of a manometer showing the gage pressure. A barometer is an instrument which measures the atmospheric pressure referred to perfect vacuum, and is an essential part of the equipment of an aerodynamic laboratory.

In addition to manometers which measure pressure differences, aerodynamic laboratories also use manometers which measure directly the absolute pressure. The use of "absolute" manometers of special design for aerodynamic research prevents additional errors due to the barometers, thus reducing the time needed for calculations.

The main characteristics of manometers are pressure range, accuracy, sensitivity, linearity, and speed of response.

The range of pressures which can be measured in aerodynamic tests extends from almost perfect vacuum (for instance in wind tunnels for free molecular flow) up to several hundreds of atmospheres in supersonic installations. In shock and pulse tunnels, steady and nonsteady pressures attaining 3000 to 5000 atm have to be measured. For any given wind tunnel the pressure range is narrower, but still cannot always be covered by a single type of manometer.

The accuracy of a manometer can be improved by increasing its sensitivity. However, an increase in sensitivity is usually concomitant with a smaller pressure range, since the smaller the permissible relative error, the more complicated, expensive, and difficult to operate becomes the manometer. The pressure range can be reduced, for instance, by choosing a comparison pressure close to the measured pressure. Excessive sensitivity is undesirable in manometers, since a sensitive manometer, reacting to small disturbances causes an increase in the time needed for, and sometimes a reduced accuracy of, the measurements.

Maximum accuracy is required in measuring static and total pressures in wind tunnels for continuous and intermittent operation, since the velocity, the Mach number of the flow, and all aerodynamic coefficients are determined from these magnitudes. U-tube manometers are used for these measurements, providing measuring accuracies from 0.02 to 0.1% of the maximum measured value.

The accuracy requirements are lower for multiple manometers by which the pressure distributions on surfaces are determined, since with a large number of experimental points, the pressure distribution curve can be drawn sufficiently accurately even if it does not pass through all points. It is difficult to provide a high measuring accuracy in each separate tube of a multiple manometer because the absolute pressure at different points of the body can differ considerably (at hypersonic velocities by several orders of magnitude).

Linearity is also related to accuracy, because, when the instrument scale is nonlinear, we have to use approximate functional relationships in order to simplify the calculations. Therefore, we always try to ensure proportionality between the measured pressure and the readings of the manometer, even if this leads to more complicated instruments.

The instruments used for measuring pressures in aerodynamic research can be divided into the following groups:

1) liquid-column manometers,
2) pressure gages with elastic sensing elements,
3) pressure transducers,
4) manometers for measuring low absolute pressures.

The operating principle of manometers of the last group is based on the change of several physical properties of rarified gases when their pressure varies. A description of these manometers, used for measuring pressures below 1 mm Hg in special wind tunnels, can be found in the literature on vacuum techniques /1/.

§ 19. LIQUID-COLUMN MANOMETERS

According to their operating principle, liquid-column manometers can be divided into two groups: manometers for direct reading, and manometers of the null type. Manometers for direct reading are used for measuring the difference in height between the two levels of a liquid in communicating vessels. Each height is determined in relation to the stationary instrument frame. In manometers of the null type the frame is displaced, this displacement being measured after the displacement of the liquid in relation to the frame is reduced to zero.

Manometric liquids

The medium used in liquid-column manometers is most often alcohol, water, or mercury; the properties of these and other manometric fluids, which are complicated organic compounds /2/, are shown in Table 9.

The main requirements for manometric fluids are: high chemical stability, low viscosity, low capillary constant, low coefficient of thermal expansion, low volatility, low tendency to be contaminated, and low tendency to absorb moisture from the air. All these requirements are aimed at increasing the measuring accuracy. Thus, a high chemical stability and low volatility are important for maintaining a constant specific

gravity of the manometric fluid, on which the manometric constant depends. A high viscosity causes an increased transmission lag of the instrument.

Properties of manometric fluids at t = 20°C

TABLE 9

Fluid	Specific gravity g/cm³	Boiling point °C at a pressure of 760 mm Hg	Surface tension dyn/cm	Viscosity centipoise	Coefficient of volumetric expansion X 10^5	Remarks	Physiological effects
Methyl alcohol CH_3OH	0.792	64.7	22.6	0.59	-	-	Narcotic. Strong poison
Ethyl alcohol C_2H_5OH	0.789	78.4	22.0	1.9	110	Optimum fluid. When water is added, the specific gravity increases.	
Distilled water	0.999 (1.0 at 4°C)	100	72.8	1.000	15.0		
Tetrabromoethane $C_2H_3Br_4$	3.42	189.5	76.8	-	-	Reacts strongly with metals	Narcotic. Poison
Carbon tetrachloride CCl_4	1 594	76.8	26.8	0.97	-	Corrodes rubber	Narcotic. Poison
Ethylene bromide	2.18	132	38	-	-	Reacts strongly with rubber	Poison
Mercury	13.55 (13.59 at 0°C)	356.9	465	1.55	18.0	Reacts strongly with aluminum, copper, and soldering alloys; weakly with iron and steel the meniscus should be covered with an oil film.	Very toxic vapors
Ethyl bromide	1.43	38.4	-	0.40	-		Narcotic. Poison
Toluene	0.866	110.8	28.4	-	-		

Thermal expansion of the liquid, causing changes in its specific gravity, also causes changes in the zero reading and the instrument constant. Capillarity affects the level of the fluid in the tube, which depends on the surface tension of the liquid σ and on its wetting properties. For wetting liquids the meniscus inside the tube is concave upward and the liquid in the tube rises under the action of capillary forces above the level of the liquid in a wide vessel (Figure 5.1a). For nonwetting liquids the meniscus is convex upward and the level of the liquid in the tube is lower than in a wide vessel (Figure 5.1b).

The rise and fall of a liquid (the capillary depression) is

$$\Delta h = \frac{4\sigma \cos \theta}{\gamma d}, \qquad (5.1)$$

where γ is the specific gravity of the liquid, d is the internal diameter of the tube, θ is the wetting angle. For a given fluid the coefficient of surface tension σ varies inversely with temperature. Tentatively, we can write for water: $\Delta h = \frac{30}{d}$; for alcohol: $\Delta h = \frac{8}{d}$; for mercury: $\Delta h = -\frac{8}{d}$.

When measuring low pressures, an important parameter of the liquid is its vapor pressure, since at a pressure equal to the vapor pressure of the liquid at a given temperature, the liquid evaporates.

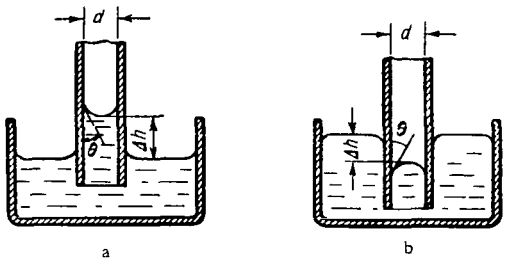

FIGURE 5.1. Capillary change in level of liquid in a tube.
a — wetting liquid; b — nonwetting liquid.

When the internal diameter of the manometric tube is constant along its length, the capillary change in level of the liquid can be ignored, since it will be equal for both tube legs. In noncalibrated tubes the capillary depression may vary along the height of the tube. In addition, the capillary depression depends on the state of the internal tube surface and on the purity of the liquid. For these reasons low values of the capillary depression should be aimed at. This is achieved by using tubes having large internal diameters (8 to 12 mm) and by choosing a liquid having a low surface tension. Alcohol is used in manometers having tubes of small diameter (2 to 5 mm). It should be remembered, however, that alcohol has a higher coefficient of thermal expansion than water or mercury, so that alcohol manometers require accurate temperature verification. Impurities in mercury greatly influence the value of its surface tension, so tha that mercury has to be cleaned frequently. Dirt on the tube walls not only prevents accurate reading, but also increases random changes in shape of the meniscus and in the capillary forces when the mercury rises or falls in the tube. Contamination of the mercury can be reduced by a thin film of oil or alcohol on its surface.

U-tube manometers

The U-tube manometer consists of two communicating vertical glass tubes (legs) (Figure 5.2). The pressure difference to be measured is related to the level difference h in the tubes (legs) of the manometer by the equation

$$p_1 - p_2 = \gamma h^* , \qquad (5.2)$$

* More exactly from $p_1 - p_2 = \gamma h (1 - \gamma_1/\gamma)$, where γ_1 is the specific gravity of the liquid in the left-hand leg. The value of γ_1/γ is usually neglected.

where γ is the specific gravity of the manometric liquid.

This equation shows that the range of the measured pressure differences can be altered by changing the specific gravity of the liquid and the height of the tube.

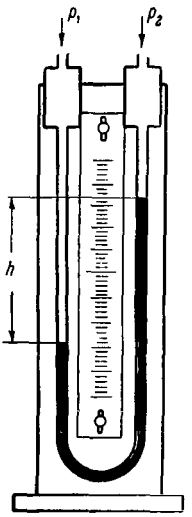

FIGURE 5.2. A U-tube manometer.

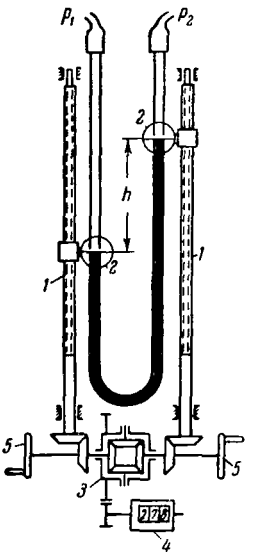

FIGURE 5.3. U-tube manometer with totaling device. 1 — lead screws; 2 — optical sighting devices; 3—differential gear; 4 — counter; 5 — handle for turning screws.

The sensitivity $dh/d(p_1 - p_2)$, varies inversely with the specific gravity of the liquid. The maximum practical tube height is about 3 m (i.e., the height of the laboratory room); hence, the range of pressures which can be measured by mercury manometers is limited to about 4 atm. The same height for tubes filled with alcohol corresponds to a pressure range of about 0.24 atm. It may happen that mercury manometers are not sensitive enough, while alcohol or water manometers cannot provide the required measuring range. In such cases recourse is had to heavy liquids, such as tetrabromoethane, carbon tetrachloride, and Thoulet solution (a solution of mercuric iodide in potassium iodide).

When the manometer is filled with water, the reading of the height differences in mm gives the numerical value of the pressure difference in kg/m^2.

Since the diameters of the glass tubes are in general not uniform along their length, the level difference h must be calculated from the change in height of the columns of liquid in both legs. An exception to this rule is

a specially calibrated tube. Usually U-tube manometers are equipped with sliding scales; before the experiment the zero graduation is adjusted to the level of the liquid in both legs.

If the height of the column of liquid is read by the naked eye, the absolute error in height may be about 0.5 mm. Since two readings are required for determining the height difference, the error may attain 1 to 2 mm. When higher accuracy is required, the manometers are equipped with optical reading devices.

Figure 5.3 shows a U-tube manometer with a device permitting the difference in height in both legs to be determined without intermediate calculations. For this purpose the sighting devices (2) are located at the level of the meniscuses with the aid of lead screws (1) which are connected to the differential gear (3). The latter is connected to counter (4), on which the height difference h is read off.

If the above precautions are taken to reduce the influence of surface tension in the U-tube manometer, it can be used as a primary instrument which requires no calibration by another [reference] instrument. The only correction necessary is for the influence of temperature. The true difference in the levels of the liquid, expressed through the specific gravity of the liquid at temperature t_0, is

$$h_{tr} = h_t \frac{\gamma_t}{\gamma_{t_0}}, \tag{5.3}$$

where h_t and γ_t correspond to the temperature t at which the measurement is made, or

$$h_{tr} = h_t \frac{1}{1+\beta(t-t_0)}, \tag{5.4}$$

where β is the coefficient of volumetric expansion of the liquid.

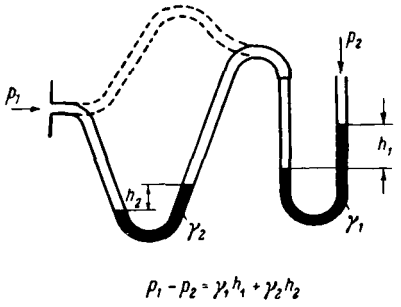

FIGURE 5.4. Effect of liquid, present in the connecting tube on the manometer readings.

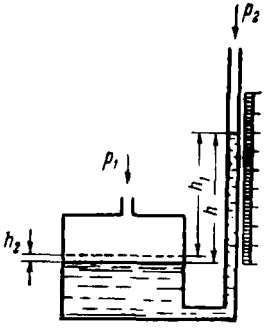

FIGURE 5.5. Well-type manometer.

For accurate pressure measurements, it is sometimes necessary to make a correction for temperature distortions of the scale. In order to reduce the reading to the temperature t_0' at which the scale was etched, we use the equation

$$h_0 = h_{tr}\,[1 + \alpha(t - t_0')]. \tag{5.5}$$

where α is the coefficient of linear expansion of the material from which the scale is made.

In order to prevent loss of liquid from the manometer when the pressure varies abruptly, traps in the form of wells or widenings in the upper parts of the tubes are provided. When liquid is present in the inclined connecting tube (due to overflowing or condensation), the actual pressure difference will exceed by $\gamma_2 h_2$ the readings of the manometer (Figure 5.4). In order to prevent the collection of liquid in the tube bends they are best arranged in the manner shown in Figure 5.4 by broken lines.

Well-type manometers

The drawback of U-tube manometers is the necessity to read the indications of two tubes. This is avoided in the well-type manometer. (Figure 5.5) which is a U-tube manometer one of whose legs has a larger cross section than the other. The higher pressure acts on the leg having the larger cross section (well). Under the action of the pressure difference, the liquid rises in the glass tube to a height h_1, and falls in the well by an amount h_2. The height of the column which balances the pressure difference is

$$h = h_1 + h_2.$$

Since the volume of the liquid displaced from the well, whose cross-sectional area is F_2, is equal to the volume of the liquid which enters the measuring tube, whose cross-sectional area is F_1, the measured pressure difference is

$$p_1 - p_2 = h_1\gamma\left(1 + \frac{F_1}{F_2}\right). \qquad (5.6)$$

The ratio F_1/F_2 allows for the change in level of the manometric fluid in the well. To avoid additional calculations, the cross-sectional area ratio should be very small ($< 1/500$); it is either ignored, or special scales are made.

Figure 5.6. shows schematically an electrical device for automatically measuring the level of the liquid in the tube of a well-type mercury manometer /3/. It consists of a servo system, whose sensing element is a photo-electric cell mounted on a movable carriage together with a lamp throwing a light beam through the liquid onto the photo-electric cell. When the meniscus moves in relation to the light beam, the Wheatstone bridge into one arm of which the photoelectric cell in inserted (semiconductor resistance), becomes unbalanced, and an amplified imbalance signal is fed to a servomotor which with the aid of a micrometer screw returns the carriage to a position fixed in relation to the meniscus. The displacement of the carriage is measured by a counter connected to the micrometer screw. The range of the measured pressures is only limited by the length of the micrometer screw, while the accuracy of the device depends on the

accuracy of the alignment of the carriage with the meniscus (0.15 to 0.25 mm). Such a servo device simplifies the task of the

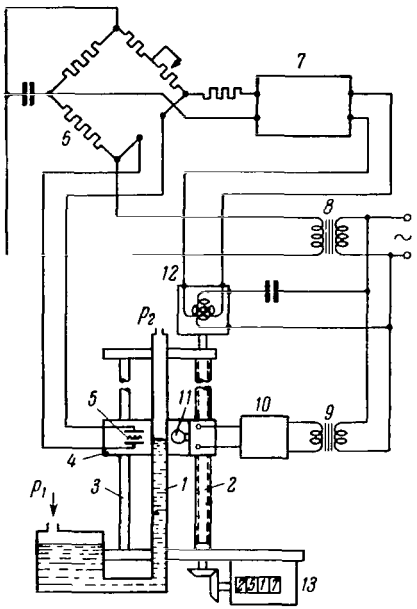

FIGURE 5.6. Device for automatically measuring the height of a mercury column. 1 — tube filled with mercury; 2 — micrometric screw ; 3 — guide column; 4 — carriage; 5 — photoelectric cell; 6 — Wheatstone bridge; 7 — a. c. amplifier; 8 — bridge-supply transformer; 9 — lamp-supply transformer; 10 — rectifier; 11 — lamp; 12 — servomotor; 13 — counter.

experimenter, freeing him from the work of visually aligning the sighting device with the meniscus in the tube.

Liquid-column micromanometers

These are sensitive manometers designed for indicating pressure differences from a few up to 500 mm W.G. at errors between a few tenths and a few thousandths of a millimeter. The lower limit of the pressure range mentioned is found, for instance, in boundary-layer velocity investigations. Thus, the velocity head of air at atmospheric pressure, flowing at 10 and 1 m/sec, is 6 and 0.06 mm W.G. respectively; for measuring these velocities with an accuracy of 1%, the micromanometer error must not exceed 0.12 and 0.0012 mm W.G. respectively.

The sensitivity of liquid-column manometers is raised by increasing the displacement per unit pressure difference, of the meniscus in relation to

the stationary tube walls and by increasing the accuracy in measuring this displacement with the aid of optical devices.

Two-fluid micromanometers. If the legs of a U-tube manometer are enlarged at the top to form two wide vessels and are filled with two immiscible liquids whose specific gravities are γ_1 and γ_2 (Figure 5.7), we can observe the displacement of the interface separating the two liquids.

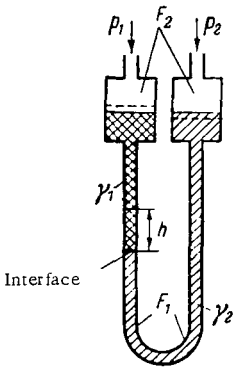

FIGURE 5.7. Two-fluid micromanometer.

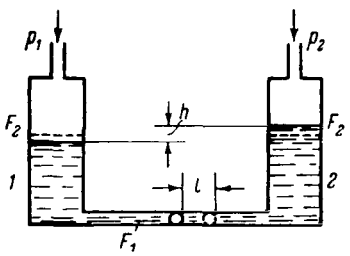

FIGURE 5.8. Increase of meniscus displacement in a narrow connecting tube.

We then have

$$p_1 - p_2 = h\left[(\gamma_2 - \gamma_1) + \frac{F_1}{F_2}(\gamma_2 + \gamma_1)\right], \tag{5.7}$$

where h is the displacement of the interface under the action of a pressure difference $p_1 - p_2 = \Delta p$, and F_1 and F_2 are respectively the cross-sectional areas of the tube and the well, which for simplicity are assumed to be the same for both legs. When F_1/F_2 is very small, the displacement is approximately

$$h = \frac{\Delta p}{\gamma_2 - \gamma_1}. \tag{5.8}$$

The immiscible liquids may be, for instance, ethyl alcohol and kerosene. For measuring small pressure differences in rarefied gases it is suggested /14/ to use liquid organosilicon polymers whose vapor pressures vary between 10^{-4} and 10^{-5} mm Hg (the vapor pressures of mercury and water are 1.2×10^{-3} and 17.5 mm Hg respectively). The value of $\gamma_2 - \gamma_1$ varies between 0.07 and 0.2 g/cm^3. The use of liquids whose specific gravities differ less reduces the response of the manometer and causes large temperature errors.

Bubble micromanometers. A widely used method of increasing the displacement of the meniscus is illustrated in Figure 5.8. The displacement l of an air bubble or an oil drop in the tube connecting the wide vessels (1) and (2), can be found for a two-fluid manometer from (5.7), if we put $\gamma_1 = \gamma_2 = \gamma$. In this case the sensitivity of the instrument is

$$\frac{h}{\Delta p} = \frac{1}{2}\frac{F_2}{F_1}\frac{1}{\gamma}. \tag{5.9}$$

The designs of many sensitive micromanometers intended for measuring very small pressure differences are based on this principle, e.g., the Chattock gage, which is widely used in Great Britain and the U.S.A. /5/.

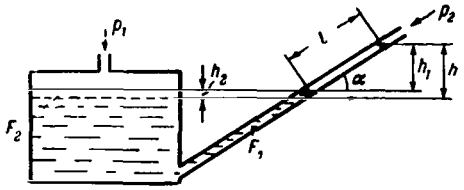

FIGURE 5.9. Inclined micromanometer.

A peculiarity of this micromanometer is that small pressure differences are measured by returning the bubble to its initial position in relation to the instrument frame, which is tilted with the aid of a micrometric screw connected to the scale which is graduated in units of pressure.

Direct-reading inclined-tube micromanometers. A simple method of increasing the displacement of a meniscus in relation to the tube walls consists in inclining the tube at an acute angle to the horizontal (Figure 5.9). This is one of the most widely used instruments for measuring flow velocities in low-speed tunnels. The relationship between the displacement of the liquid along the tube axis and the measured pressure difference is

$$p_1 - p_2 = \gamma l \left(\sin\alpha + \frac{F_1}{F_2}\right). \qquad (5.10)$$

The sensitivity of the micromanometer can thus be increased by reducing the specific gravity of the liquid, the angle of inclination of the tube α, or the area ratio F_1/F_2. Alcohol is ordinarily used in inclined-tube micromanometers. In order to reduce capillarity effects, calibrated tubes having internal diameters of 1.5 to 3 mm are used.

Soviet wind tunnels are largely equipped with TsAGI micromanometers (Figure 5.10). This instrument has a cylindrical well rigidly connected to a glass tube enclosed in a metal casing. The tube is provided with a manometric scale graduated to 200 mm. By rotating the well about its horizontal axis, the tube can be inclined so that $\sin\alpha = 0.125$; 0.25; 0.5; and 1.0. The ratio between the cross-sectional areas of the tube and the well is 1/700.

Inclined-tube micromanometers are equipped with levels which permit adjustments of the horizontal position of the stand. These micromanometers have to be calibrated, since slight bends in the tubes or small changes in capillary depression, due to small variations of the internal tube diameter, may cause considerable errors.

The errors due to capillarity in inclined-tube manometers are the same as in vertical manometers. There exists therefore a minimum

angle α, below which no increase in sensitivity is obtained because of the capillarity error. In practice $\alpha = 6°$.

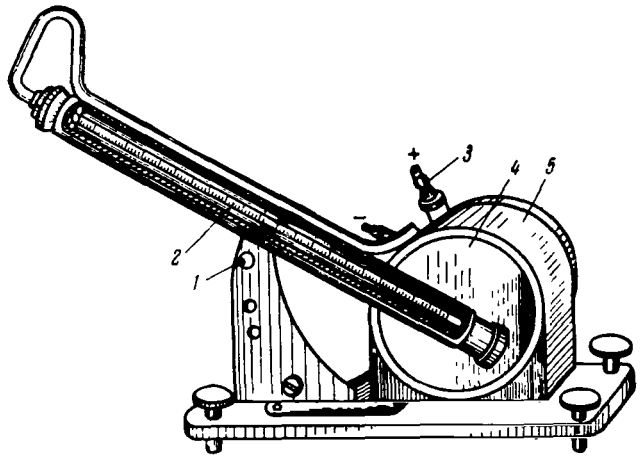

FIGURE 5.10. TsAGI micromanometer. 1—clamping device ; 2 — glass tube; 3 — spigot; 4—rotating well; 5 — casing.

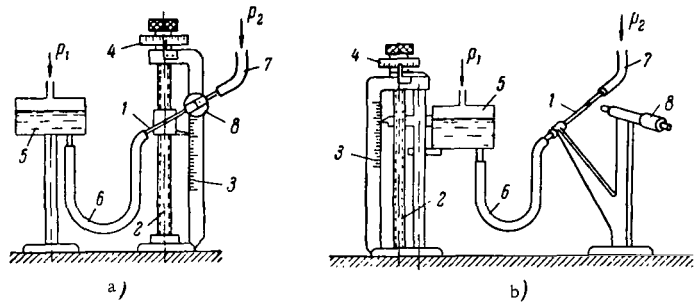

FIGURE 5.11 Null-type liquid-column micromanometer. a — with movable inclined tube; b — with movable well; 1 — inclined tube; 2 — micrometric screw; 3 — scale for reading number of screw turns; 4 — scale for reading angle of rotation of screw; 5 — well; 6, 7 — flexible tubes; 8 — sighting device.

Inclined null micromanometers. The capillarity error can be reduced considerably by using manometers in which the level of the liquid is held in a constant null position in relation to the walls of the capillary tube.

In the null micromanometer shown in Figure 5.11a, the inclined capillary tube is movable and has a null line on it. The position in which the meniscus is aligned with this line is called the zero position of the

instrument. When the pressure difference changes, the inclined tube is moved until the meniscus is again aligned with the null. This is done with the aid of a micrometric screw. The meniscus is observed with the aid of a sighting device which moves together with the inclined tube.

The second type of null micromanometer (5.11b) differs from the former in that the inclined tube is stationary; in order to return the meniscus to the null position the well has to be moved. Because of this, the meniscus can be observed with the aid of a stationary microscope, while the eye of the observer is always at constant level. Such a device permits the measured pressure difference to be increased up to 500 or 600 mm W.G. The reading accuracy of the column of liquid depends mainly on the manufacturing accuracy of the micrometric screw, and attains 0.03 to 0.05 mm.

In experiments requiring accurate measurements of pressure, attention must be paid to reducing the transmission lag of manometers. For instance, when determining the velocity profile in a boundary layer by a tube having an internal diameter of 0.2 to 0.4 mm, the transmission lag of the manometer amounts to tens of seconds and sometimes to minutes. The errors caused by the lag are not only due to the fact that readings are made before the pressure in the tube orifice is in equilibrium with the pressure in the well, but because during the time required for the complete series of measurements, the temperature of the surroundings can change (for instance, due to heat transfer through the walls of the wind tunnel). The volume of liquid in both legs of a liquid-column null micromanometer at the instance of reading remains the same, irrespective of the measured pressure difference. The lag, due to the flow of liquid from one leg to the other, therefore depends only on the skill of the experimenter (or on the response of the automatic device used) in realigning the meniscus with the null line.

Increasing the sensitivity of a null micromanometer by increasing the inclination of the capillary tube increases the lag (the volume of displaced liquid increases for a given pressure difference).

A temperature change of the liquid in a well-type micromanometer causes a change in the zero reading; for this there are two reasons:

1) the change in volume of the liquid due to thermal expansion;

2) the change of the surface tension of the liquid in the capillary tube.

These factors act in opposition, and thus may compensate mutually.

The relationship between the geometrical parameters of the manometer, necessary for the compensation of temperature changes, is when the well is made of steel and is filled with alcohol /6/:

$$\frac{vd}{F_2} = 0.29 \text{ cm}^2,$$

where v is the volume of the liquid-column micromanometer; d is the internal diameter of the tube; F_2 is the area of the well cross section.

This compensation enables the temperature error of the micromanometer to be reduced to less than 0.01 mm/1°C /7/.

Float-type micromanometers. Determining the position of a meniscus by accurate measurements requires much effort. In float-type micromanometers, the position of a solid body floating on the surface of the liquid is determined instead of the position of the meniscus.

Figure 5.12 shows a float-type micromanometer which enables differences up to 200 mm W.G. to be measured. The difference in level of the liquid between the annular well (2) and the cylinder (1) is measured with the aid of scale (3) which is attached to a body floating on the surface of the liquid in the cylinder. The scale can be observed and the difference in level read off through window (4) and microscope (5). The micrometric device (6) serves for aligning the sighting line of the microscope with the null line of the scale.

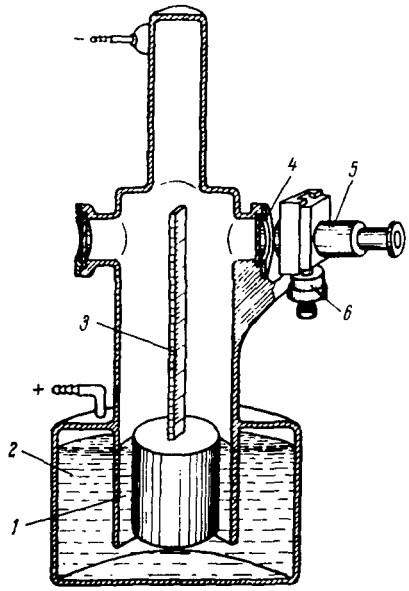

FIGURE 5.12 Float-type micromanometer with optical reading. 1 — cylinder ; 2 — annular well; 3 — scale; 4 — window; 5 — microscope; 6 — aligning device.

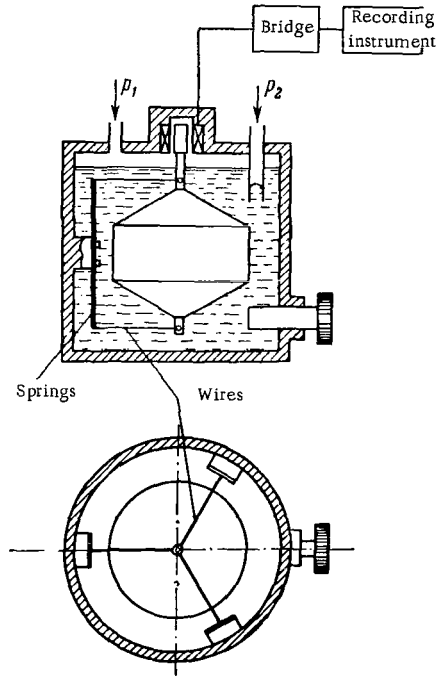

FIGURE 5.13. Float-type micromanometer with remote indication.

In another float-type micromanometer /8/, intended for measuring pressure differences up to 25 mm W.G., the position of the float in relation to the walls of the vessel is recorded with the aid of an induction-type displacement transducer connected to an electronic bridge. The float is secured to the walls of the vessel with the aid of six 0.075 mm thick wires, which are tensioned in pairs by 3 flat springs located at angles of 120° around the axis of the float (Figure 5.13). This instrument is calibrated by displacing the liquid with the aid of a piston moved by a micrometric screw. The accuracy of the instrument depends on the sensitivity of the transducer and the measuring system connected to it.

An error of less than 0.5% of the measurement range is difficult to obtain, but by reducing the measurement range to 1 mm W.G., the absolute error can be reduced to about 0.005 mm.

Balance-type micromanometers. Very high sensitivity and accuracy can be obtained with micromanometers in which measuring the height of a column of liquid is replaced by measuring forces with the aid of balances.

In the instrument shown in Figure 5.14 the pressures p_1 and p_2 act via elastic metal tubes on the liquid in communicating vessels mounted on the arms of a balance. If the right-hand vessel is at a higher pressure, some liquid will flow from it into the left-hand vessel. Equilibrium is restored either manually or automatically by moving a counterweight. The sensitivity of this instrument is independent of the specific gravity of the manometric liquid. For vessels of given height, a change in the liquid is only reflected in the range of measured pressure differences.

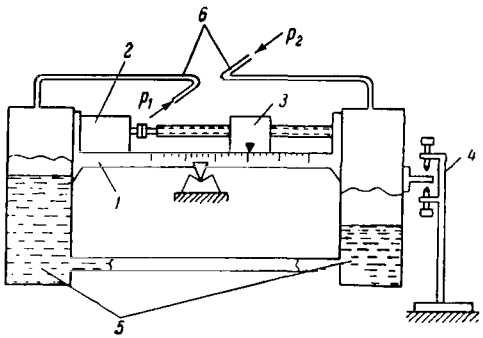

FIGURE 5.14. Compensated manometer. 1 — lever; 2 — servomotor for lead screw; 3 — movable counterweight; 4 — contact system for switching on the servomotor when the lever is not in null position; 5 — communicating vessels; 6 — elastic tubes.

Figure 5.15 shows a bell-type manometer for direct reading. Pressures p_1 and p_2 act on the inside of communicating vessels (bells) (1) and (2),

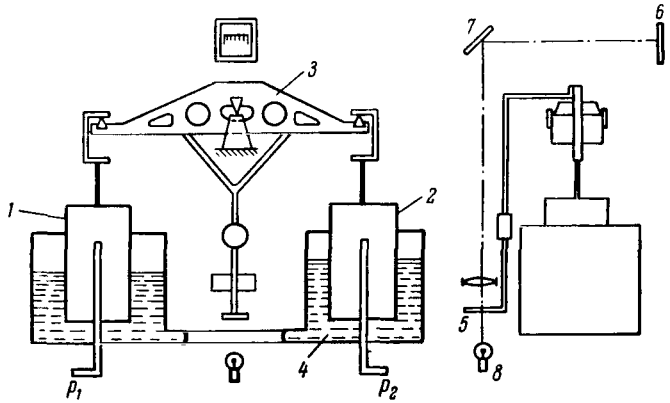

FIGURE 5.15. Bell-type manometer. 1 and 2 — bells; 3 — balance lever; 4 — communicating vessels; 5 — transparent scale; 6— screen; 7 — mirror; 8 — light source.

which are suspended from a balance lever (3). The open ends of the bells are immersed in the liquid contained in vessels (4). Under the action of the pressure difference some liquid is forced out from one bell into the other, and the lever tilts by a small angle which is proportional to the pressure difference and depends on the sensitivity of the balance. This angle can be measured by different methods, for instance, with the aid of an optical system which projects an enlarged image of the transparent scale (5) onto the screen (6).

In compensated bell-type manometers (Figure 5.14) the lever is returned to the null position with the aid of a movable counterweight, whose travel is proportional to the measured pressure difference.

Damping the pulsations of the columns of liquid in manometers

The pressures measured in different aerodynamic test installations are very seldom steady. Usually the pressure fluctuates about a certain mean value. The amplitude and wave form of these pulsations depend on the design and type of the installation. The oscillations of the columns of liquid in manometric tubes, caused by the pressure pulsations, reduce the measuring accuracy. In order to prevent build-up of oscillations, forced damping sometimes becomes necessary.

There exist three ways of damping in manometers: inertial, volumetric, and resistance damping. Volumetric damping is applied to manometers in which large changes in volume are required for measuring small pressure differences, as for instance, in manometers where the cross-sectional areas of the tubes are large. Inertial damping is used when the liquid has a large mass. The inertia of the mass prevents motion caused by sudden pressure pulses of short duration. Inertial damping is not always sufficient for damping oscillations of the level of the liquid. Resistance damping is caused by resistance of the system, which limits the flow velocity of the liquid during sudden pressure pulsations. This type of damping is very effective, and is easily obtained in existing manometers by inserting a damping resistance. In order that the manometer readings correspond to a mean value, the resistance must be linear, i.e., proportional to the flow velocity of the liquid. Nonlinear damping may occur if a throttle is inserted into the pneumatic or hydraulic line of the instrument. Linear ("viscous") damping is obtained simply by inserting a capillary tube into the pneumatic line of the instrument. The tube length is chosen by experiment, taking into account that an excessive length may cause considerable transmission lag in the manometer. Another method of resistance damping of the liquid-column oscillations in a manometer is to insert small felt or cotton-wool pads into the pneumatic line of the instrument.

§ 20. MECHANICAL MANOMETERS

Manometers with elastic sensing elements and small moving masses have a quicker response than liquid-column manometers. The transmission

lag in such manometers is determined mainly by the time required for the equalization of the pressure in the chamber of the elastic element with the pressure to be measured, whereas in liquid-column manometers an additional lag is caused by the displacement of the liquid. Using elastic elements, and keeping the volume of the pressure chamber small, we can reduce the dimensions of the manometer and install it near the place where the pressure is being measured. When the volume of the chamber and the length of the connecting tube are reduced, the transmission lag of the manometer decreases.

Due to their high natural frequency, elastic elements can be used for measuring not only steady but also fluctuating pressures. Pressures are measured by means of elastic elements by determining either the deformation of an elastic element or the force required to prevent the deformation (force-compensation method).

The deformation of the elastic elements is measured with the aid of kinematic, optical, or electric systems. Kinematic pointer-type or recording instruments and optical devices are used mainly in spring-type manometers, while electric systems are found in pressure transducers.

In comparison with the method of determining the pressure from the deformation of elastic elements, the force-compensation method is more exact since it enables the effects of elastic hysteresis to be reduced. However, the force-compensation method requires more time. When measuring rapidly fluctuating pressures, only the first method is therefore used. The force-compensation method is used for measuring steady or slowly varying pressures when the error must not exceed 0.1 to 0.5% of the upper limit of the measured value.

Types of elastic elements

The following three types of elastic sensing elements are most widely used: Bourdon tubes, bellows, and diaphragms (flat or corrugated).

The operating principle of a Bourdon-tube manometer is well-known. Under the action of the pressure, a tube of oval or elliptic cross section, bent in a circular arc (Figure 5.16a), tends to straighten itself. The displacement of the tube end is measured with the aid of a kinematic device.

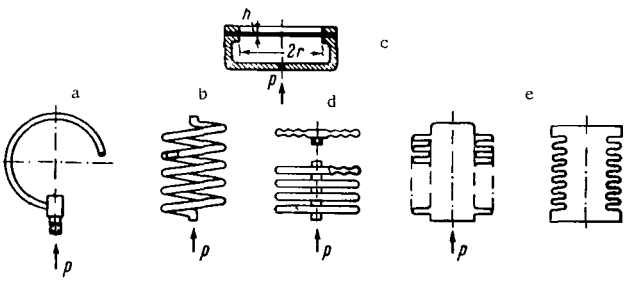

FIGURE 5.16 Elastic elements for measuring pressures. a — Bourdon tube; b — spiral tube; c — flat diaphragm; d — corrugated diaphragm and set of aneroid boxes; e — bellows.

The action of a spiral tube (Figure 5.16b) is based on the same principle. Flat diaphragms (Figure 5.16c), which have higher natural frequencies than Bourdon tubes, can be used for measuring high-frequency pressure pulsations. Flat diaphragms can be installed flush with the surface of a body. The pressure to be measured acts directly on the diaphragm, hence there is no transmission lag due to the resistance of the connecting tubes and the volume of air in the system.

The sensitivity of a flat diaphragm, which can be considered as a plate fixed along a circular contour, can be defined as the ratio of the deformation δ at the center of the diaphragm to the pressure p

$$k = \frac{\delta}{p} = \frac{3(1-\mu^2)}{16E} \frac{r^4}{h^3}.$$

The natural frequency of the diaphragm, which should be 3 to 4 times higher than the frequency of the pressure pulsations, is

$$\omega = 10.2 \left[\frac{E}{12\rho(1-\mu^2)} \right]^{1/2} \frac{h}{r^2},$$

where r and h are respectively the radius and the thickness of the diaphragm, while E, μ, and ρ are respectively the modulus of elasticity, Poisson's ratio, and the density of the diaphragm material. Thus, the sensitivity and the natural frequency are related by the equation

$$k = \frac{1.63}{\omega^2 h \rho}.$$

The sensitivity of a diaphragm is inversely proportional to the square of its natural frequency and to its thickness. The sensitivity of a diaphragm can therefore be increased by lowering its natural frequency. The sensitivity of a diaphragm-type manometer depends not only on the value of k but also on the method used for measuring the deformation of the diaphragm.

The range of pressure differences which can be measured with a single diaphragm depends on its thickness and diameter, and varies from hundredths of a mm Hg to thousands of atmospheres. Since the absolute deformations of a flat diaphragm are very small, they are measured by optical or electrical methods. Mechanical methods change the natural frequency of the system because of the masses connected to the instrument. Electrical methods are simpler and do not lead to large dimensions, as do optical methods. For a given sensitivity of the diaphragm, the sensitivity of the manometric system can be increased only by amplifying the output signal which corresponds to a given deflection of the diaphragm.

Corrugated diaphragms permit considerably larger deflections than flat diaphragms. For even larger deflections, corrugated diaphragms are made in the form of boxes which can be assembled into sets (Figure 5.16d).

Bellows are most widely used in the design of manometers employed for measuring steady pressures in wind tunnels. A bellows (Figure 16e) is a cylindrical thin-walled tube with uniform folds. The presence of a large number of folds makes possible large deformations of the moving bottom of the bellows under the action of pressure differences.

The gage pressure acts inside the bellows or the vessel which surrounds it. The movable bottom of the bellows, which is connected with the measuring mechanism of the manometer, can be considered as a piston moving without friction in a cylinder under the action of the pressure forces, and loaded by a spring which, in this case, is formed by the folds of the bellows.

The bellows is made of brass, phosphorus-bronze, beryllium-bronze, or stainless steel. Brass bellows are most widely used, but their hysteresis is high (up to 3% of the full travel). The hysteresis of bellows made of beryllium-bronze or phosphorus-bronze is lower.

The characteristics of a bellows as a measuring element depend on two factors: the rigidity c, and the effective area F_{ef}. The rigidity is the ratio of the force acting on the moving bottom of the bellows to its travel δ. The effective area of the bellows is the ratio of the force N to the gage pressure p required to restore the bottom of the bellows to its original position:

$$F_{ef} = \frac{N}{p}.$$

The maximum permissible travel of the bottom of the bellows is about 5 to 10% of the bellows length, if residual deformations are to be avoided. Proportionality between the travel and the force acting on the bottom is best maintained if the bellows is subjected to compression.

The ratio of the length to the outside diameter of the bellows should be less than unity. When the bellows is longer, there is a danger of longitudinal instability caused by bending and transverse deformation of the bellows. In order to prevent this the movable bottom of the bellows is usually connected to a guiding device which ensures axial travel of the bottom.

Spring-type manometers

Standard manometers with spring-type sensing elements in the form of Bourdon tubes have errors of 1 to 3% of the scale range, which are inacceptible for aerodynamic measurements. For certain types of multi-point measurements (for instance, in testing engines or compressors), Bourdon-tube reference manometers made by the Soviet industry are suitable; they are from high-quality material and have low hysteresis. The scale of a reference manometer has 300 one-degree graduations on a convex scale. Reference manometers are available for measuring negative pressures down to 760 mm Hg vacuum, and positive pressures up to 1.5, 5, 10, 25, and 50 kg/cm^2 or more. According to the existing specifications for manometers, the permissible measurement errors are as follows: for vacuum meters and manometers for pressures up to 2 kg/cm,^{2} $\pm$0.35% of the scale limit; for manometers for pressures above 2 kg/cm^2, $\pm$0.2% of the scale limit.

The accuracy of spring-type manometers can be increased by reducing or eliminating friction in the transmission mechanism. When friction is eliminated, the accuracy of the manometer is mainly determined by the hysteresis of the elastic element.

An example of a frictionless spring-type manometer is the manometer in which the deflection of the Bourdon tube is measured with the aid of an accurate micrometric mechanism or a dial indicator (5) (Figure 5.17). The micrometric mechanism is isolated from the tube (1), to which the flexible contact plate (2) is soldered. A second flexible plate (3) is soldered to the micrometer screw. Electric contact between the plates is sensed by a so-called "magic eye" electronic tube normally used in radio receivers. The wiring diagram is shown in Figure 5.17. To measure the pressure, contact between the screw and tube is first broken. Plate (3) is then slowly brought back into contact with plate (2); this is sensed by the "magic eye." Such a device permits the error to be reduced to 1/2 or 1/3 of the error of a reference manometer with pointer, but this is accompanied by an increase in time required.

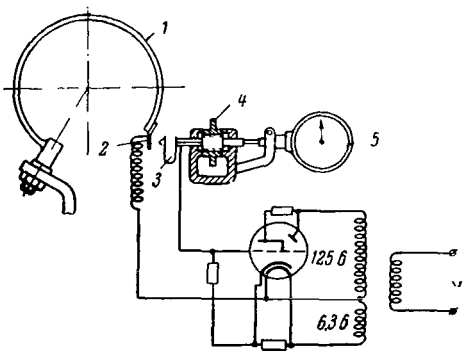

FIGURE 5.17. Spring-type manometer with contacts. 1—Bourdon tube; 2 and 3 — contact plates; 4 — micrometric device; 5 — dial indicator.

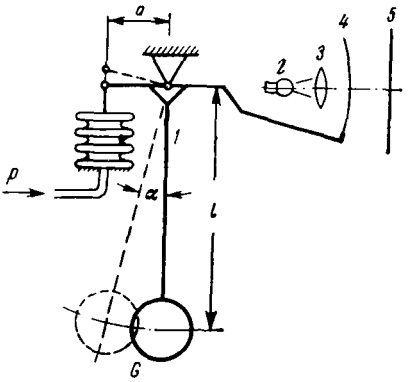

FIGURE 5.18. Pendulum-type manometer. 1 — pendulum; 2 — lamp; 3 — lens; 4 — transparent scale; 5 — screen.

When using bellows made of tompac or semitompac for spring-type manometers, the influence of hysteresis of the bellows is reduced by an additional spring of high-quality steel or beryllium-bronze. In this case the elastic force of the bellows is small in comparison with the elastic force of the spring which has a low hysteresis, and therefore, the error due to hysteresis of the bellows decreases proportionally with the ratio of the rigidities of bellows and spring. The reduction in sensitivity of the elastic element, caused by the additional spring, is compensated for by the higher transmission ratio to the pointer.

Bellows manometers have measurement errors of the order of 1%. The error can be reduced to 0.2 to 0.5% when the bellows are of beryllium-bronze or phosphorous-bronze. Bellows manometers can be used to measure pressures between perfect vacuum and 10 to 20 atm.

In the bellows-type pendulum manometer, shown schematically in Figure 5.18, the elastic force of the additional spring is replaced by the restoring moment of the pendulum (1), which eliminates the influence of the hysteresis of the bellows. For angles of pendulum inclination below $\alpha = 6°$, the relationship between the pressure and the angle is linear,

being expressed as follows with an accuracy better than 3%:

$$\alpha = \frac{F_{ef}a}{Gl + ca^2} p .$$

Here, G is the weight of the pendulum counterpoise, p is the gage pressure acting inside the bellows, a is the distance between the pendulum support and the center line of the bellows. By altering the weight of the counterpoise or the length l of the pendulum, we can vary the range of the measured pressures. The influence of hysteresis of the bellows can be almost eliminated by selecting the ratio of the static moment of the pendulum to the rigidity of the bellows so that $Gl \gg ca^2$. Accurate measurement of the angular displacement of the pendulum is ensured by an optical system consisting of lamp (2) which projects, with the aid of lens (3), a large image of scale (4) on screen (5).

Force-compensation manometers

Manometers in which the deflections of elastic elements are measured have errors caused by hysteresis and the influence of temperature on the rigidity of these elements. Such errors can almost completely be avoided if the pressure force acting on the elastic element is equilibrated by a force which returns the elastic element to its initial position.

The equilibrating force can be caused by mechanical or electric mechanisms. The former include devices which use counterweights or springs; the latter include devices based on the interaction of magnetic or electrostatic fields. Compensation is effected automatically in certain instruments.

One of the best designs of force-compensation manometers for wind tunnels is a combination of bellows or sets of aneroid boxes with automatic beam-type balances. Such a bellows-type manometer is shown in Figure 5.19. Bellows (1) and (2) are connected to balance lever (3) on either

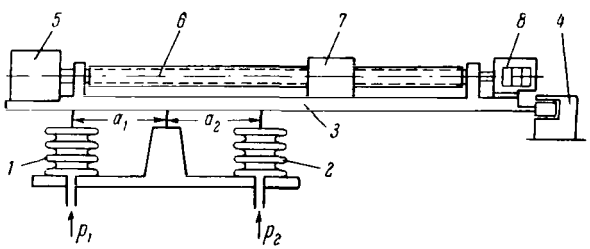

FIGURE 5.19. Automatic force-compensation beam-type manometer. 1 and 2 — bellows; 3 — balance lever; 4 — transducer controling the servomotor, 5 — servomotor; 6 — lead screw; 7 — counterweight; 8 — counter.

side of the knife edge. The pressures p_1 and p_2, whose difference has to be measured, act inside the bellows. When the pressure difference changes,

the equilibrium is disturbed and transducer (4) reacts to the displacement of the beam end by switching on servomotor (5), which turns lead screw (6) to move counterweight (7), creating a moment which restores the lever to its initial position. The travel of the counterweight is measured by counter (8). The wiring diagrams of automatic servomotor controls for lever-type balances are described in Chapter VI.

Let the beam be in the initial position when $p_1 = p_2$. When the pressures are varied, the equation of equilibrium becomes

$$a_2 p_2 F_{ef_2} - a_1 p_1 F_{ef_1} = Gx,$$

where a_1 and a_2 are the arms of the pressure forces acting respectively on bellows 1 and 2; F_{ef_1} and F_{ef_2} are the effective areas of these bellows. G is the weight of the counterweight; x is the displacement of the counterweight from its initial equilibrium position (for $p_1 = p_2$).

In order that the displacment of the counterweight be proportional to the pressure difference $p_1 - p_2$, it is necessary that

$$a_1 F_{ef_1} = a_2 F_{ef_2} = aF.$$

In this case the equilibrium conditions for the lever is

$$\Delta p = p_2 - p_1 = An,$$

where n is the number of turns of the lead screw, corresponding to the displacement x, recorded by counter (8) (the screw has a pitch t).

$$A = \frac{Gt}{aF}.$$

If the bellows (1) is acted upon by atmospheric pressure ($p_1 = B$), then $p_2 - B = An$, and the instrument will measure gage pressure. If bellows (1) is evacuated ($p_1 = 0$) and soldered, the manometer will show the absolute pressure $p_2 = An$. In the latter case we must take into account that when bellows (2) is connected to atmosphere, a force BF_{ef_1} will act on bellows (1), which must be balanced with the aid of an additional counterweight.

In practice it is difficult to obtain a pair of bellows which have equal effective areas. In accurate bellows-type manometers, one of the arms a_1 or a_2 is therefore adjustable.

Figure 5.20 shows a set, consisting of two automatic lever-type balance elements, which serve to measure pressure differences and the static gage pressure in the Moskva University wind tunnel. The lever-type balances are installed one on top of the other, while the bellows are located on a bracket fixed to the instrument base, and linked to the levers by rods and cross beams. The static pressure acts on the bellows at the extreme right, which is linked by a rod to the lever of the upper balance.

The accuracy of such manometers depends largely on the design of the connections between the bellows and the crossbeams, which must ensure perfectly axial displacement of the bellows. For this purpose elastic hinged sleeves are provided (shown in the lower part of the picture),

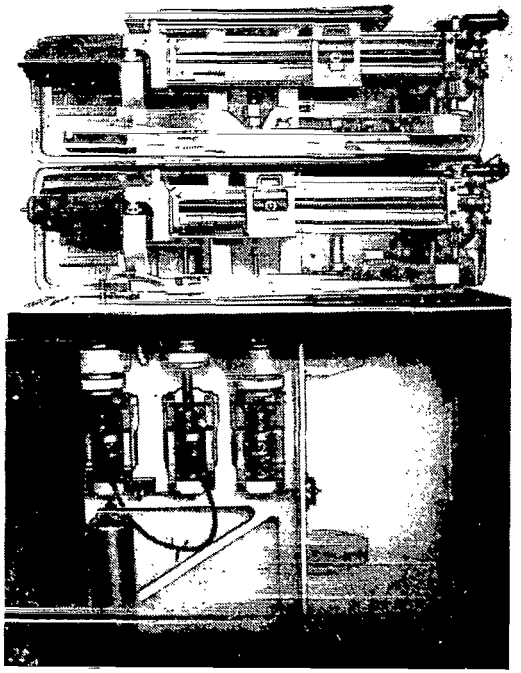

FIGURE 5.20. Set of lever-type balances for measuring Δp and p.

which prevent displacement of the rods in the direction perpendicular to the center line of the bellows. In order that the forces acting on the knife edges at the contact points between the rods and the levers be of constant sign, irrespective of the pressures in the bellows, the cross beams are provided with counterweights, so that the total weight acting on each knife edge exceeds the product of maximum negative pressure and effective area of the bellows.

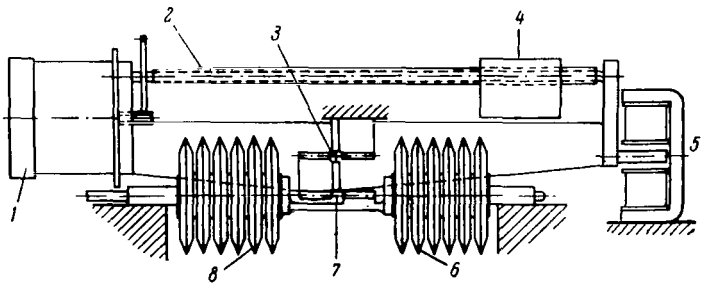

FIGURE 5.21 RAE automatic self-balancing capsule manometer 1 — servomotor; 2 — lead screw; 3 — elastic cross-shaped hinge; 4 — counterweight; 5 — inductive transducer; 6 — set of evacuated aneroid boxes; 7 — connecting element; 8 — set of aneroid boxes under pressure.

Figure 5.21 shows the connections between the aneroid boxes and the levers in the automatic self-balancing capsule manometer of the RAE laboratory /9/. The lever is mounted on a cross-shaped hinge and linked to the aneroid boxes, which are rigidly interconnected, by a flexible strip. The drawback of this design is the requirement that the aneroid boxes have exactly equal effective areas.

The accuracy of such a manometer is mainly determined by two factors: the insensitivity of transducers to displacements and the rigidity of the bellows. If the insensitivity range of the transducer corresponds to a bellows displacement $\pm\delta$, the random error of pressure measurement, due to the unbalanced residual electric force, will not exceed

$$\sigma_{\Delta p} = \pm \frac{c}{F_{ef}} \delta.$$

For most industrial bellows the ratio of the rigidity c to the effective area F_{ef} varies between 0.1 and 1 kg/cm^3. In order that the value of $\sigma_{\Delta p}$ should not exceed 1 mm Hg, the value of δ must be less than from 0.013 to 0.13 mm.

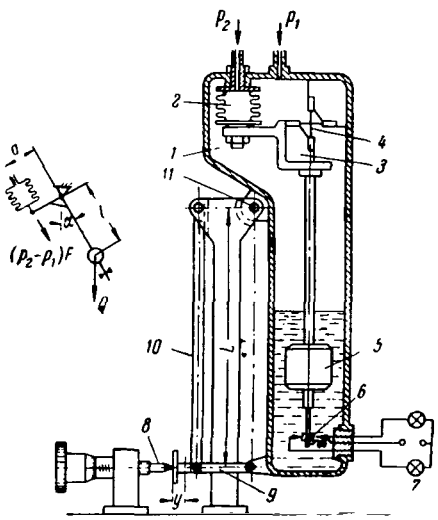

FIGURE 5.22. Pendulum-type compensation manometer. 1 — hermetically sealed chamber; 2 — bellows; 3 — lever; 4 — elastic cross-shaped hinge; 5 — counterweight; 6 — contacts; 7 — signal lamps; 8 — micrometric screw; 9 and 10 — links for scale linearizing; 11 — hinge.

The contact and inductive transducers at the end of the lever, whose displacement is many times larger than the deflection of the bellows, permit measurement of δ with an error of 10^{-2} to 10^{-3} mm. With a good-quality lead screw, which moves the counterweight, and when pressure differences up to 3000 to 4000 mm Hg are being measured, the errors of compensation-type manometers may be a few hundredths of a percent of the maximum measured value. With bellows of low rigidity and large effective area, such manometers permit measurements of absolute pressures between 10 and 20 mm Hg with an error not exceeding 0.1 mm Hg. In order to reduce the influence of rigidity of the bellows, the sensitivity of the lever system of the manometer is increased with the aid of compensating devices described in Chapter VI.

Since remote indication of the angle of turn of the lead screw is possible, lever-type bellows manometers are widely used for measuring total pressure, static pressure, and the pressure drop in the test section of subsonic and continuously or intermittently operating supersonic wind tunnels.

Another manometer design in which a bellows is also used as elastic element and a counterweight as a compensating element is shown in Figure 5.22. Pressures, whose difference has to be measured, act inside the hermetically sealed chamber (1) and the bellows (2), which

is connected to lever (3) fixed to an elastic hinge (4). A rod with counterweight (5) is fixed to the lever. In order to return to its initial relative position the lever (3), which is deflected by the action of the difference of pressure on the movable bottom of the bellows, the chamber is turned about hinge (11) by an angle α. This is controlled with the aid of contacts (6) and signal lamps (7) which go out when the initial position is reached. The value of the angle α is related to the measured pressure difference as follows:

$$(p_2 - p_1) F_{ef} a = Ql \sin \alpha,$$

where F_{ef} is the effective area of the bellows, a is the distance from the point of support of the lever to the center line of the bellows, l is the distance from the point of support to the center of gravity of the pendulum, Q is the weight of the pendulum together with the counterweight. It is assumed that when $p_2 - p_1 = 0$ then $\alpha = 0$, i.e., the center of gravity of the pendulum and part of the bellows lies on the vertical through the point of support.

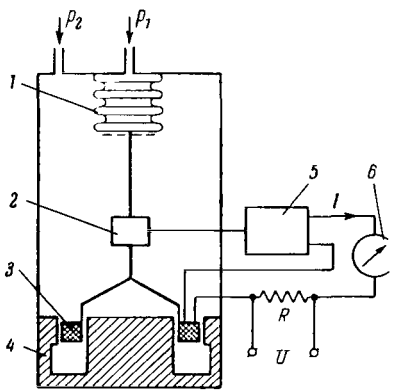

FIGURE 5.23. Electromagnetic compensation-type manometer. 1 – bellows; 2 – displacement transducer; 3 – coil; 4 – permanent magnet; 5 – amplifier; 6 – milliammeter.

To provide a linear scale, the micrometric screw (8) moves the chamber with the aid of an intermediate link (9) hinged to chamber (1) and link (10) of length L. The relationship between the pressure difference and the travel y of the screw is given by $p_2 - p_1 = my$, where $m = Ql/F_{ef}aL$ is the instrument constant.

Figure 5.23 shows a manometer with electromagnetic force compensation /10/, which can be used for measuring pressures fluctuating at frequencies of up to 10 kc. The pressure acting on bellows (1) displaces the moving system with fixed coil (3) which is placed in the field of permanent magnet (4). The displacement transducer (2) sends a signal to amplifier (5). The output current of the amplifier passes through coil (3), its intensity and direction being such that the interaction force between the

coil and the magnet balances the pressure force. The pressure is determined from the current intensity I, indicated by milliammeter (6), or from the voltage U across an output resistance R. When the voltage is measured, this circuit provides for a sufficiently strong signal, and the measurements can be automatically recorded. Thus, at a maximum current intensity $I = 30$ ma and with a resistance $R = 2500$ ohm the voltage $U = 75$ v. The error of such an electromagnetic manometer is only 0.1%; for measuring pressure differences from several millimeters to several hundreds of millimeters Hg, it can compete with liquid-column manometers.

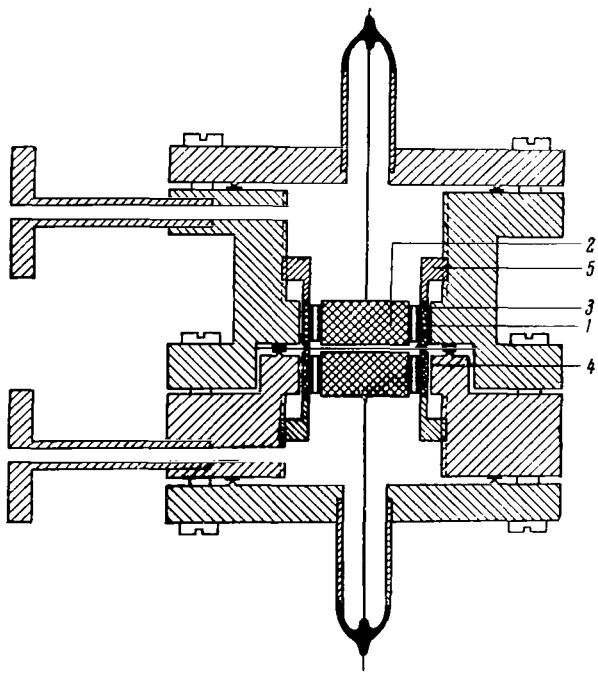

FIGURE 5.24. Capacitive compensation-type manometer. 1—diaphragm; 2 — metal electrodes; 3 — annular inserts; 4 — ceramic insulators; 5 — nuts.

For measuring very small pressure differences (up to 1 mm Hg) the manometer shown in Figure 5.24 can be used. It is a compensation-type manometer in which the force of the pressure acting on the diaphragm is balanced by an electrostatic force /11/. The 0.02 mm-thick stainless-steel diaphragm (1) is held between annular inserts (3). Metal electrodes (2) are rigidly connected to the inserts (3) by means of ceramic insulators (4). The tension of the diaphragm can be adjusted by nuts (5).

The capacitor formed by the diaphragm and the electrodes is connected to the arms of a capacitive bridge fed from a 500 kc signal generator according to the circuit shown in Figure 5.25. The displacement of the diaphragm, due to the difference in pressures on either side, is compensated

by an electrostatic force, adjusted with the aid of a calibrated potentiometer R_1. At a constant supply voltage V_0, the scale of the micromanometer is linear. By varying V_0, we change the sensitivity of the instrument. The series-connected inductances and capacitances L_1C_1, L_2C_2, L_3C_3 and L_4C_4 are tuned to the signal-generator frequency. The signal at the bridge output, caused by the deflection of the diaphragm, is amplified, and then measured by a microammeter. Observing the latter, the reading is reduced to zero by means of the calibrated potentiometer. At zero reading, the diaphragm returns to its initial position, and the position of the potentiometer R_2 gives the pressure difference. The potentiometer R_1 serves for the initial balancing of the bridge. In the pressure range from 10^{-2} to 10^{-1} mm Hg, the instrument error is only 0.1%. The design of the manometer permits pressure differences up to one atmosphere; therefore, if we connect one side of the diaphragm to vacuum (obtained, for instance, with the aid of a diffusion pump) the instrument will indicate absolute pressures in the above-mentioned range.

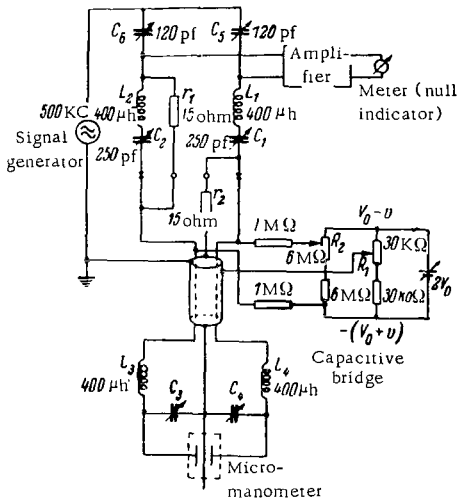

FIGURE 5.25 Wiring diagram of a capacitive compensation-type manometer

§ 21. ELECTRICAL PRESSURE TRANSDUCERS AND MICROMANOMETERS

Pressure transducers are instruments which convert the deformation of an elastic pressure-sensitive element into an electric signal.

In connection with experimental research on high-speed aircraft, methods for measuring variable pressures have been developed in recent years. These measurements are necessary when investigating dynamic loads due to vibrations, and also for studying problems of dynamic stability of aircraft components. Thus, for instance, when considering wing

flutter, we sometimes determine transient aerodynamic forces by investigating the pressure distribution on a vibrating wing. The measurements are made by special miniature pressure transducers, (of 5 to 6 mm diameter),, which are placed directly on the surface of the model or inside its body, close to the orifices. The nature of the investigated problems does not demand a high measuring accuracy. Good transducers permit the error in measuring the amplitude of pressure pulsations to be reduced to between 1 and 2%, but often transducers are acceptable which permit the pressure to be measured with an accuracy of from 5 to 10% of the maximum amplitude.

Quite different requirements apply to high-sensitivity transducers, used for measuring steady or slowly-varying pressures. Such transducers are used in intermittently-operated supersonic wind tunnels where measurement by liquid-column manometers is not always possible because of high lag. Such transducers can have comparatively low natural frequencies, but must have much smaller errors than transducers for measuring dynamic processes. High sensitivity is usually obtained with transducers of relatively large dimensions.

If the transducer is connected by a tube to an orifice in the wall, then, with high-frequency pulsations the pressure close to the elastic pressure-sensing element of the transducer may differ in phase and amplitude from the pressure on the wall. To reduce dynamic distortions, the lowest

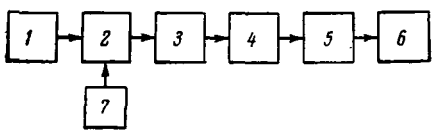

FIGURE 5.26. Schematic layout for recording pressure pulsations. 1—carrier-frequency oscillator; 2—measuring bridge; 3—amplifier; 4—rectifier; 5—filter; 6—oscillograph; 7—transducer.

resonance frequency of the pressure-measuring system must be higher than the highest frequency of the measured pressure pulsations. The lowest acoustic-resonance frequency of a closed pipe of length L is

$$\omega = \frac{a}{4L},$$

where a is the velocity of sound. The amplitude distortions caused by the elastic pressure-sensing element can be reduced by increasing its natural frequency. In order that the error should not exceed 6 to 7%, this natural frequency must be 4 to 5 times higher than that of the measured pressure pulsations. Best results are obtained by sensing elements shaped like flat diaphragms.

Pressure transducers whose operating principle is based on measuring changes in inductive, capacitive, or ohmic resistances, caused by the deformation of an elastic element, are mainly used in aerodynamic experiments. Bridge systems are most widely used for these measurements.

Although there exist many different schemes for measuring varying pressures, the above-mentioned types of transducers are usually employed as shown schematically in Figure 5.26. The measuring bridge, one, two, or all four arms of which are formed by transducers, is fed from a carrier-frequency oscillator. The amplifier, connected to the measuring diagonal of the bridge, amplifies the imbalance signals caused by the changes in transducer resistance due to the pressure variations. The amplified signals are transmitted through a phase-sensitive detector and a filter, which discriminates the carrier frequency, and are then measured by a galvanometer or loop oscillograph. The carrier frequency must be 6 to 10 times higher than the frequency of the investigated process.

Inductive transducers

The design principle of inductive transducers is based on the changes in the inductance of a coil, caused by changes in the magnetic permeability of a circuit consisting of a core, a magnetic circuit, and a ferromagnetic elastic element. The latter is usually a flat steel diaphragm, which, when deformed, alters the air gap between it and the core of the coil which is

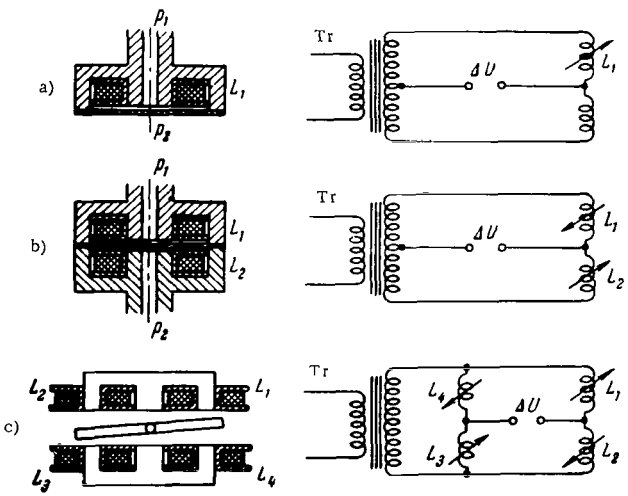

FIGURE 5.27. Circuits for inductive pressure transducers.

connected to an a.c. circuit. The reactance of the coil depends on the air gap, and when the coil is inserted into a measuring bridge-circuit, the change in air gap, due to the variation of the pressure acting on the diaphragm, causes a proportional imbalance signal.

Figure 5.27 shows three arrangements for connecting inductive transducers in a measuring bridge fed from a transformer T_r. In Figure 5.27a, three arms of the bridge are fixed inductors. The fourth arm L_1 is a variable inductor. One of the pressures whose difference is being measured acts directly on the outer surface of the diaphragm, while the other pressure acts upon the internal area of the transducer. A differential circuit (Figure 5.27b) is ordinarily used for increased sensitivity. The diaphragm is placed between two inductive coils L_1 and L_2.

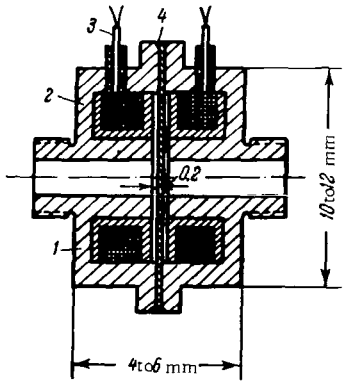

FIGURE 5.28. Miniature inductive transducer. 1 — body; 2 — coils; 3 — coil leads; 4 — diaphragm soldered to body.

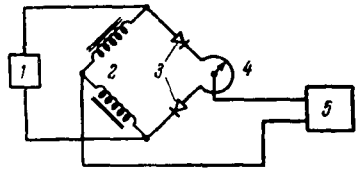

FIGURE 5.29 Circuit diagram of an inductive transducer with rectifiers. 1 — supply voltage; 2 — differential inductive transducer; 3 — rectifiers; 4 — zero adjustment; 5 — oscillograph.

The movement of the diaphragm causes an increase in the inductance of one coil and a decrease in the inductance of the other coil; the amplitude of the signal is twice that obtained in the circuit shown in Figure 5.27a.

The circuit in Figure 5.27c has an even higher sensitivity. A pivoted armature connected to the elastic element of the manometer changes the inductance of all four arms of the bridge.

Figure 5.28 shows a typical miniature inductive transducer for measuring pulsating pressures. The thickness of the diaphragm can vary from 0.025 mm (for measuring pressure differences of the order of 25 mm Hg) to 0.25 mm for measuring pressure difference of the order of 7 atm. When the amplitude of pressure pulsations, small in comparison with the mean pressure, has to be measured, the diaphragm has a hole whose diameter is between 0.05 and 0.1 mm. To reduce temperature effects, the transducer coil is made of manganin wire. The accuracy of measuring the amplitudes of pressure pulsations with these transducers depend on the type of equipment used, and may vary from 2 to 10% of the maximum measured value.

Since the frequencies used in inductive transducers do not exceed a few kc, the indications are usually recorded by loop oscillographs. When two or four arms of the bridge have variable inductors, a sufficiently strong signal can be obtained without an amplifier. This simplifies the use of inductive transducers for simultaneous pressure measurements at several

points. A simple and sensitive bridge circuit in which one half of the bridge is formed by semiconductor rectifiers is shown in Figure 5.29. To record low-frequency pressure pulsations (up to 4 to 5 cycles), balanced measuring circuits with fast-acting electronic bridges can be used (Figure 5.30).

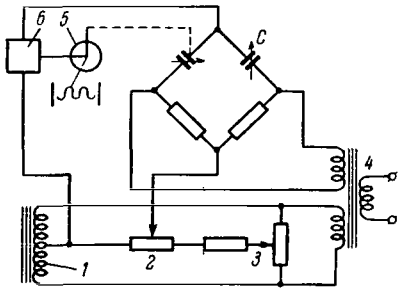

FIGURE 5.30. Circuit diagram of a balanced bridge for measuring the signal from an inductive transducer. 1 — inductive tranducer; 2 — sensitivity adjustment; 3 — zero adjustment; 4 — transformer; 5 — servomotor; 6 — amplifier.

An example of an inductive pressure transducer, whose sensitivity is comparable to that of liquid-column manometers, is the NPL inductive micromanometer /12/ shown in Figure 5.31. This instrument is intended for remote measurement of pressure differences of up to 100 mm W.G., and

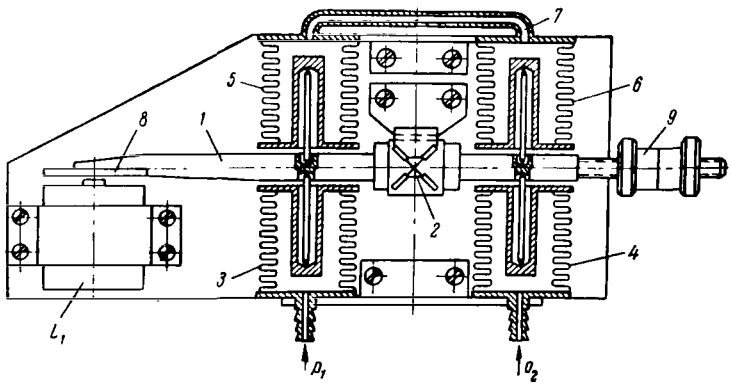

FIGURE 5.31. NPL inductive micromanometer. 1 — lever; 2 — elastic hinge; 3 and 4 — bellows acted upon by pressures to be measured; 5 and 6 — bellows serving for damping vibrations; 7 — connecting channel; 8 — soft-iron plate; 9 — counterweight; L_1 — primary induction coil.

consists of four bellows connected to lever (1) which is supported on an elastic cross-shaped hinge (2). Bellows (3) and (4) are acted upon by the pressures whose difference has to be measured; the other two bellows (5) and (6), interconnected by channel (7), are filled with oil and serve as dampers. One end of lever (1) carries a soft-iron plate (8), balanced by counterweight (9) on the other end of the lever. When the lever is displaced due to the pressure difference $p_1 - p_2$ in bellows (3) and (4), the air gap between plate (8) and the induction coil L_1 changes. This causes an imbalance in the inductive bridge (Figure 5.32). The rectified imbalance current causes the pointer of galvanometer (6) to be deflected.

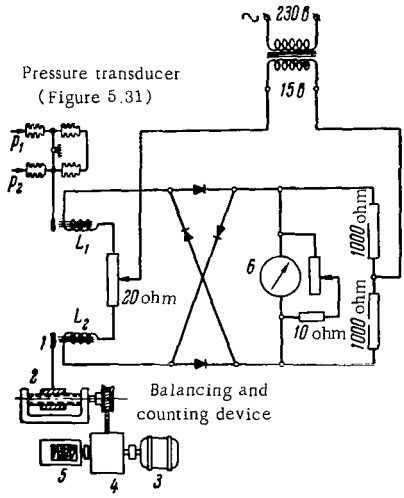

FIGURE 5.32 Circuit diagram of an inductive micromanometer. 1 — iron plate; 2 — micrometric screw; 3 — reversible electric motor; 4 — reduction gear; 5 — counter; 6 — galvanometer; L_1 — primary induction coil; L_2 — secondary induction coil.

The bridge is balanced by adjusting the air gap in the secondary induction coil L_2 with the aid of iron plate (1) which is moved in the magnetic field of coil L_2 by micrometric screw (2). The screw is rotated by a low-power electric motor (3) through a reduction gear (4) having a large transmission ratio. The displacement of plate (1) in relation to coil L_2, required to restore the balance of the bridge, is proportional to the difference between the pressures in the bellows, and is measured by counter (5) connected to the reduction gear. Very small pressure differences can be measured directly with the galvanometer by the unbalanced-bridge method.

Capacitive transducers

A capacitive transducer for measuring the deflection of an elastic diaphragm uses a capacitor one of whose plates is the diaphragm itself, the other plate

being fixed. The capacitor is connected into a suitable electric circuit which produces a signal which depends on the capacitance.

Maximum sensitivity to pressure changes is ensured in a capacitive manometer by a very small air gap. However, a linear relationship between the change in capacitance and the change in pressure requires the distance between the plates to be large in comparison with the mean deflection of the diaphragm. Thus, the increased sensitivity of a capacitive manometer reduces the linearity, and vice versa. In practice, a compromise has to be accepted. Sometimes, a thick diaphragm is used. Its deflections are small, but the air gap can be reduced. However, it should be taken into account that when the air gap is reduced, temperature effects increase; temperature changes can cause harmful deformations of the diaphragm.

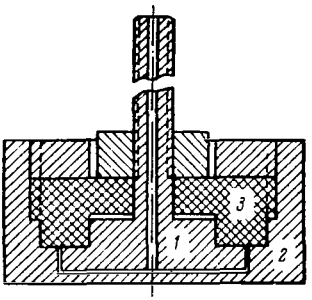

FIGURE 5.33. Capacitive pressure transducer. 1 — diaphragm; 2 — indeformable electrode; 3 — high-frequency insulator

Figure 5.33 shows a small capacitive pressure transducer in which the diaphragm is integral with the body. The insulation of the fixed plate is made of ceramic material offering a large impedance to high frequencies. To remove internal stresses in the transducer diaphragm, which are liable to increase temperature effects, the diaphragm is heat-treated before and after being machined.

A diaphragm integral with the body has a lower hysteresis than one clamped at the edges. However, the range of measured pressures is easier to change in clamped diaphragms. With diaphragms of different thicknesses and diameters we can make capacitive manometers and transducers for pressures ranging from fractions of a mm Hg to thousands of atmospheres. In the lower part of this range, corrugated diaphragms having thicknesses of up to 0.025 mm and diameters from 50 to 100 mm are used; they are made of silver or bronze. When low absolute pressures have to be measured, one side of the diaphragm is subjected to a pressure close to perfect vacuum.

In addition to ordinary capacitive transducers, wide use is made of differential capacitive transducers. Such a transducer consists of two series-connected capacitors, with a common plate in the middle serving as the diaphragm. When the differential transducer is connected to the

measuring circuit, the sensitivity is doubled in comparison with an ordinary transducer; a linear relationship between the deflection of the diaphragm and the output voltage of the circuit is obtained.

The RAE miniature differential capacitive transducer intended for investigating wing flutter /13/, is shown in Figure 5.34. The diaphragm is located between two fixed electrodes, while the air gaps on both sides of the diaphragm are connected to the upper and lower wing surfaces. Several tens of these transducers, which permit the force normal to the wing section to be measured, are fixed to the wing.

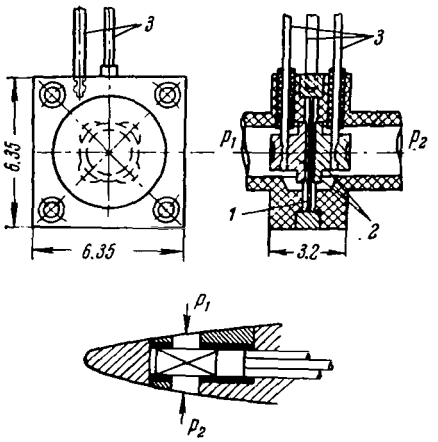

FIGURE 5.34. Differential capacitive pressure transducer. 1 — diaphragm ; 2 — electrodes; 3 — electric leads.

When the diaphragm is deflected due to a difference in pressure across it, the capacitance of the condenser formed by the diaphragm and one of the fixed electrodes increases, while the capacitance of the condenser formed by the diaphragm and the other electrode decreases.

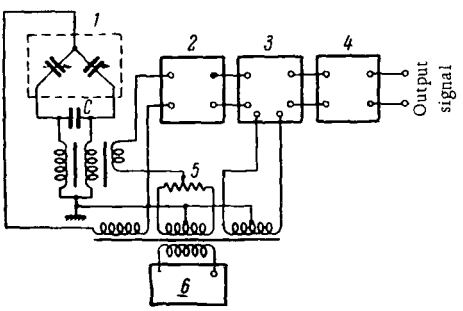

FIGURE 5.35. Circuit diagram of a differential capacitive pressure transducer. 1 — transducer; 2 — carrier-frequency amplifier; 3 — demodulator; 4 — filter; 5 — zero adjustment; 6 — carrier-frequency oscillator.

The capacitors are connected to adjacent arms of an a.c. bridge whose other two arms are formed by mutually coupled induction coils (Figure 5.35). The coils are wound in opposite directions; when the bridge is balanced equal currents pass through them, and the resulting field equals zero. The output signal of the bridge is taken from a third winding inductively coupled to the first two. The capacitor C serves for noise suppression. The bridge is fed from a 20 kc carrier-frequency oscillator, which permits frequencies up to about 3000 cycles to be recorded. The output voltage of the bridge, which is about 100 mV at a maximum pressure difference of 0.3 kg/cm^2, is fed via an amplifier to an oscillograph.

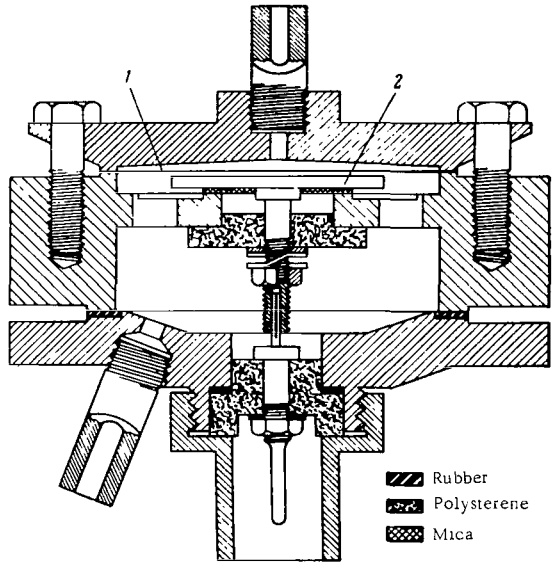

FIGURE 5.36. Differential capacitive manometer. 1 — diaphragm; 2 — fixed disc.

The combined errors of these transducers and the measuring circuits are about ±3% of full scale. The transducers are not sensitive to accelerations normal to the plane of the diaphragm; this is very important when measuring pressures acting on a vibrating wing. When the bridge is fed at a carrier frequency of 400 kc, it is possible to measure transient processes (for instance, in shock tubes). At an input-tube length of 3 mm, the transducers permit pulsation frequencies of up to 15,000 cycles to be measured; they can be used for turbulence investigations.

A capacitive micromanometer, designed for measuring pressure differences from zero to 10 mm W.G. at low frequencies, is shown in Figure 5.36.

A steel diaphragm (1), having a thickness of 0.05 mm and a diameter of 46 mm, is clamped between steel flanges. A 30 mm-diameter disc (2) is fixed at a distance of 0.01 mm from diaphragm (1). The capacitance of the condenser is about 80 pF, its sensitivity being 0.23 pF per mm W.G.

A peculiarity of this manometer is the low temperature dependence of the capacitance, which at room temperature is about 0.1% per 1°C /14/.

To measure the frequency signals of capacitive transducers, resonance circuits are used in addition to bridge systems. A simple resonance circuit of an electronic amplifier, used in measuring very low steady pressures, is shown in Figure 5.37 /15/. The circuit contains only one electronic tube, which operates as an oscillator. The frequency of oscillations is determined by the capacitance of the condenser C_1, which changes when the pressure acting on the diaphragm varies.

The resonant circuit used for measuring this frequency consists of inductance L_2 and capacitor C_5. The shaft of the latter is connected to an indicating pointer and to a handle, with the aid of which the capacitor is tuned into resonance with the second harmonic frequency of the oscillator. The point of resonance is determined approximately when minimum plate current, measured by milliammeter M_1, flows through the tube. Final tuning of the capacitor C_5 is carried out using the fine-adjustment galvanometer M_2.

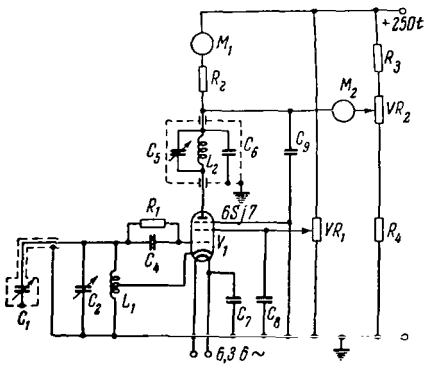

FIGURE 5.37. Resonance measuring circuit; C_1 - capacitive manometer; C_2 - 20 pF maximum; C_{41} = 100 pF; C_5 = 15 pF maximum; C_6 - 0.01 μF; C_7 = 0.1 μF; C_8, C_9 = 0.01 μF; R_1 = 150 K ohm; R_2, R_3 = 85 K ohm; R_4 - 60 K ohm, VR_1, VR_2 = 50 K ohm; L_1, L_2 = 15 turns, M_1 = milliammeter for 5 ma; M_2 - galvanometer for 540 ohm.

Capacitive manometers of this type are used for measuring pressures from 0.001 to 0.1 mm Hg. The corrugated diaphragm, made of silver, copper, or bronze, has a thickness of 0.025 mm and an external diameter of 76 mm; the diameter of the flat central part is 18 mm. The same electronic circuit is suitable for other pressure ranges and diaphragm dimensions.

The drawback of this measurement method is the effect of parasitic capacitances, mainly in the connecting wires. To reduce errors caused by parasitic capacitances the transducers are connected to the measuring circuit by screened cables.

Strain-gage transducers

Strain gages, whose operating principle is described in Chapter VI, provide simple miniature transducers for measuring variable pressures acting on the surface of a model. Both glued wire and foil strain gages are used for pressure transducers, as are nonglued tension wires.

In small transducers, wire strain gages having 2.5 to 5 mm bases are glued directly to diaphragms which are integral with the body or soldered to it (Figure 5.38). Such transducers are used by NACA for installation in airfoils, and are employed in investigating pressure pulsations ranging from 0.07 to 1.4 kg/cm^2 /16/. Temperature compensation in transducers of this type whose diameters are between 6 and 12 mm is effected with the aid of a second strain gage glued to the body. When the mean pressure need not be measured, temperature compensation is not necessary. In ONERA transducers, intended for this purpose, (Figure 5.39) the deflection of the corrugated diaphragm is measured with the aid of wire strain gages glued to both sides of the diaphragm for temperature compensation. The diaphragm is located inside a cylindrical body having a diameter of 10 mm and a height of 3 mm /17/. The strain gages, whose dimensions are 6×2.5 mm and whose resistance is 120 ohm, are inserted into the arms of a half-bridge. At the maximum deflection of the diaphragm, which corresponds to a pressure difference of 0.15 kg/cm^2, the relative imbalance of the bridge is $0.5 \cdot 10^{-3}$.

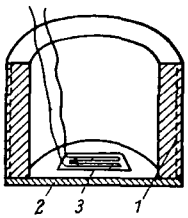

FIGURE 5.38. Strain-gage pressure transducer. 1 — body; 2 — diaphragm; 3 — resistance strain gage.

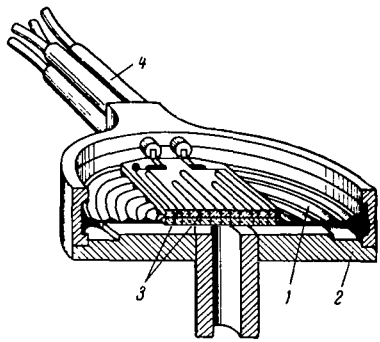

FIGURE 5.39. Strain-gage pressure transducer with corrugated diaphragm. 1 — diaphragm; 2 — body; 3 — strain gage; 4 — leads.

Glued strain gages with small bases, used in the pressure transducers described, have low resistances, and consequently, to limit the current, a low supply voltage is required. At large currents the heat dissolves the glue. A low supply voltage necessitates a higher

signal amplification. Nonglued resistance strain gages are used to obtain stronger signals. They disperse heat better and therefore permit higher supply voltages, and hence stronger output signals.

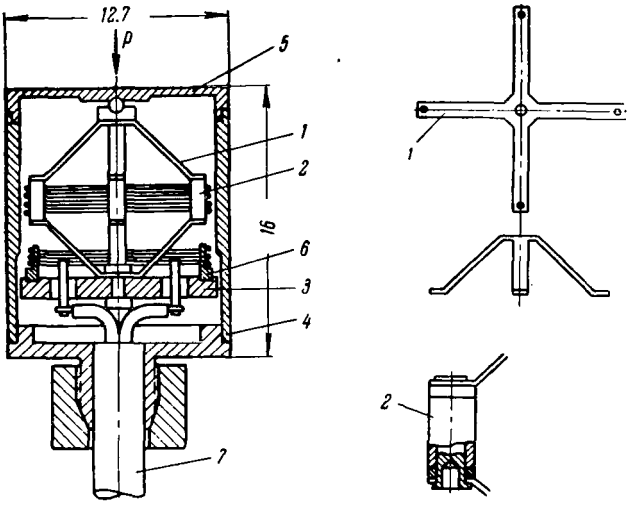

FIGURE 5.40. *Pressure transducer with a nonglued strain gage.* 1 — cross-shaped spring; 2 — rod; 3 — disc; 4 — body; 5 — diaphragm; 6 — support of insulating material; 7 — leads.

In the transducer shown in Figure 5.40 /18/, the deflection of the diaphragm is transmitted to an elastic element consisting of two cross-shaped springs (1) interconnected by four rods (2). The spring is fixed to a disc (3) whose position can be adjusted along the center line of body (4) which is covered by diaphragm (5). When the diaphragm is deflected, an axial force acts on the elastic element, bending springs (1) and causing rods (2), to move outward. The strain gage, which is wound around rods (2), is inserted into two opposite arms of a Wheatstone bridge. The other two arms, which serve for temperature compensation of the bridge, are formed by a wire wound around the undeformed supports (6) which are fixed to disc (3). Since all four bridge arms are located in the same way inside one housing, temperature equilibrium is attained very quickly. When fitting the springs into body (4), the position of disc (3) is adjusted in such a way that the strain-gage wire is slightly prestressed. A variable resistance is inserted between adjacent bridge arms in order to balance the bridge after this adjustment. When the supply is 10 V d.c. the transducers can be connected to sensitive galvanometers or oscillographs without amplification.

In transducers intended for measuring steady pressures, the wire strain-gages are very often placed on auxiliary elastic elements (for instance, on cantilever beams) connected to the sensing elements (diaphragms, aneroid boxes, or bellows) on which the pressures act (Figure 5.41). A bellows is best, since for equal diameters of the elastic elements and at equal rigidities of the auxiliary elements it permits the

highest load to be taken up. For bellows and for diaphragms these loads are respectively

$$N_c = \Delta p \pi r_c^2 \frac{1}{1+\frac{c_c}{c_b}}, \text{ and } N_м = \Delta p \pi r_м^2 \frac{1}{1+\frac{c_м}{c_b}},$$

where c_c and $c_м$ are respectively the rigidities of the bellows and the diaphragm when acted upon by a concentrated load, c_b is the rigidity of the beam, r_c is the effective radius of the bellows and $r_м$ is the radius at which the diaphragm is fixed. When $r_c = r_м$ $c_м$ is much larger than c_c at the same pressures, hence $N_c > N_м$, i.e., considerably higher loads can be transmitted to the beam by means of a diaphragm.

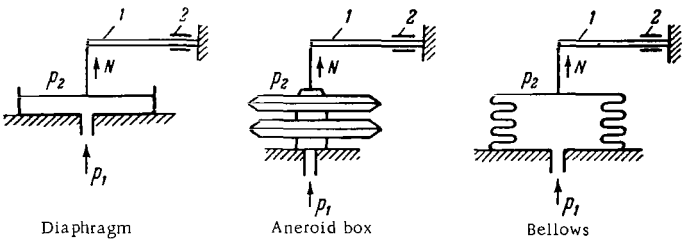

FIGURE 5.41. Strain-gage pressure transducers with auxiliary beams. 1 — elastic beam; 2 — strain gage.

Figure 5.42 shows designs of transducers for measuring absolute pressures. Bellows (1) is evacuated and soldered. The measured pressure acts either on bellows (2) (Figure 5.42a), or inside a hermetically sealed casing (5.42b).

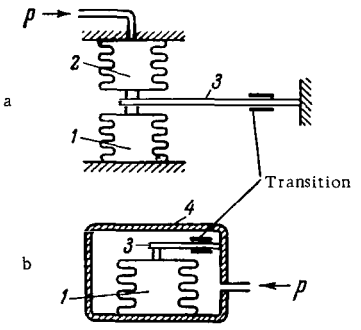

FIGURE 5.42. Transducers for measuring absolute pressures. 1 and 2 — bellows; 3 — elastic element; 4 — hermetically sealed casing.

In addition to diaphragms and bellows, pressure transducers are also used in which the axial and tangential stresses are determined on the walls of a tube whose inside is under the pressure to be measured. When metal tubes are used, such transducers have high natural frequencies, but due to the difficulties in making thin-walled tubes they can be used only for high pressures (tens and hundreds of atmospheres). If rubber or plastic tubes instead of metal tubes are employed, such transducers can be used for much lower pressures.

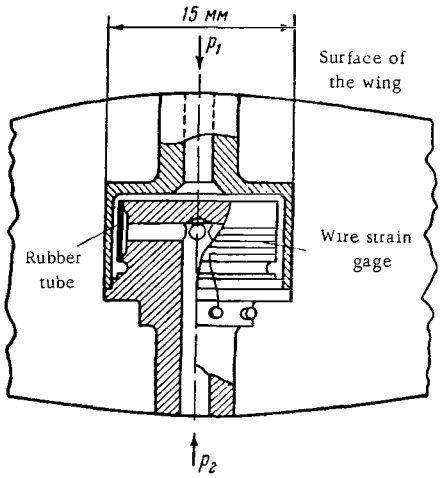

FIGURE 5.43. Pressure transducers in a vibrating wing.

An RAE tube-type strain-gage transducer for measuring pressures on airfoils oscillating at frequencies of up to twenty cycles in a low-speed wind tunnel /19/ is shown in Figure 5.43. The main element of the transducer is a cylindrical rubber tube to which a wire strain gage forming two arms of a Wheatstone bridge is glued. The tube itself is glued to a plastic beam, which has openings for leading in the pressure acting on one of the measuring points on the wing. The outside wall of the rubber tube is under the pressure acting on a point on the opposite surface of the wing; the transducer thus records the difference of the pressures on both surfaces. The resistance of each bridge arm is 250 ohm. The signals of the transducer, which is suitable for pressure differences up to 300 mm mercury, can be measured without amplifier with the aid of a sensitive recording galvanometer.

§ 22. EQUIPMENT FOR MEASURING PRESSURE DISTRIBUTION. MULTIPLE MANOMETERS

The most widely used instrument for measuring pressure distributions is a liquid-column multiple manometer. Such manometers very often

function according to the principle of well-type manometers. U-tube manometers are used only when the measured pressure differences may have different signs.

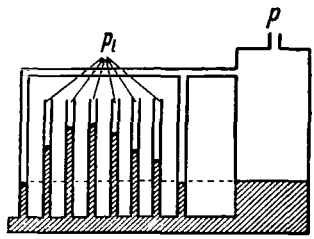

FIGURE 5.44. Schematic view of a well-type multiple manometer.

A well-type multiple manometer is shown in Figure 5.44. The well and the outermost tubes are under the pressure p with which the other pressures p_i are to be compared. The outermost tubes serve for controlling the level of the liquid in the well.

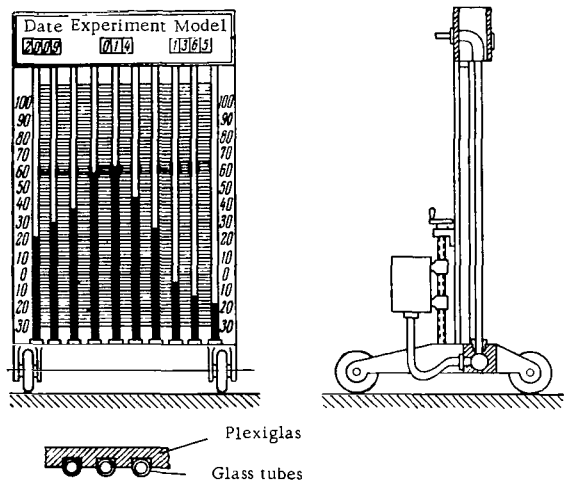

FIGURE 5.45. Well-type multiple manometer.

A typical well-type multiple manometer designed for measuring pressures corresponding to relatively high columns of liquid (up to 2 or 3 m) is shown in Figure 5.45. To prevent bending of the glass tubes they are located in slots milled into Plexiglas shields. Marks, spaced 5 or 10 mm, into which black paint is rubbed, are etched on the Plexiglas. Numbers which correspond to the column height in centimeters are written on both sides of these lines. The use of Plexiglas permits

the scale and the tubes to be illuminated from the rear for photographing. The upper part of the instrument contains a numerator, which enables the number of the experiment, the number of the model, and the date of the experiment to be photographed.

The lower ends of the glass tubes are connected through gaskets or rubber tubes to a common auxiliary tube which passes along the width of the manometer frame and is connected at the center to a well by means of a rubber tube. The height of the well can be adjusted to align the lower mark on the scale to zero level. The upper parts of the glass tubes are connected to rubber tubes with metal nipples, to which tubes from the tested object are connected.

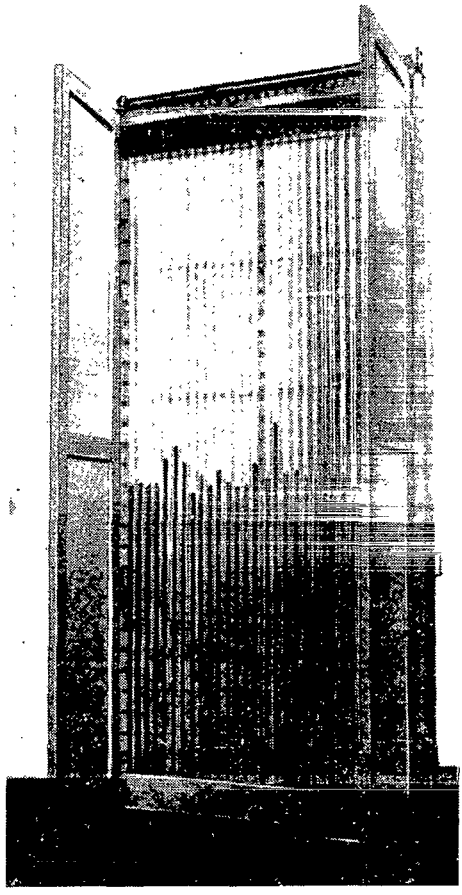

FIGURE 5.46. Multiple U-tube manometer.

In some multiple manometers the glass tubes are replaced by channels drilled into plates of Plexiglas.

When the number of tubes is large, it is practically impossible to take into consideration the meniscus-level changes caused by capillary effect, and the change in level of the liquid in the well. Multiple manometers therefore have tubes of sufficiently large internal diameters and wells with large cross-sectional areas. Nevertheless, when the multiple manometers contain twenty to thirty tubes of diameters between 8 and 10 mm, and the heights of the columns exceed 100 cm, a change of 2 to 3 mm in the level of the liquid in the well is acceptable. Such an error is permissible, since with long scales, analysis of the photographs with an accuracy exceeding 3 to 5 mm is difficult.

For high-density transonic wind tunnels, 2 or 3 mm high well-type multiple manometers are used which are filled with mercury or tetrabromoethane.

Long glass tubes are difficult to bend and to fill with liquid; in U-tube multiple manometers (Figure 5.46) the lower ends of each pair of glass tubes are therefore interconnected by rubber, PVC, or polyethylene tubes. The design of connections permitting drainage of contaminated liquid is shown in Figure 5.47. In order to prevent loss of liquid from the glass tubes during sudden pressure variations a protective device should be used.

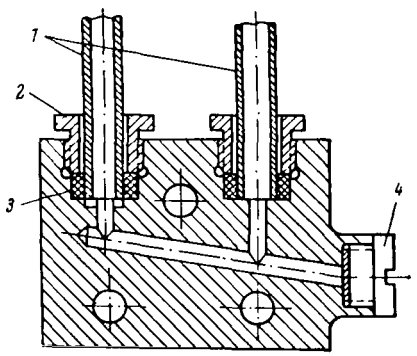

FIGURE 5.47. Device for the drainage of liquid from a U-tube manometer. 1 – glass tubes; 2 – nut for gasket tightening; 3 – gasket; 4 – drain plug.

Traps in the form of wells or widenings in the upper parts of the tubes are not suitable for multiple manometers due to their large size and the increase in air space which causes additional transmission lags. A good protective device is the nonreturn valve shown in Figure 5.48. A wooden or plastic ball in the lower part of the nipple permits the entry of air into the glass tube. When liquid is suddenly ejected from the glass tube, the ball is forced upward and closes an opening in the upper part of the nipple, thus preventing further loss of liquid.

The vapors of mercury, tetrabromoethane and some other liquids used in manometers are very toxic; recharging and adjustment of manometers filled with these liquids is carried out in special rooms.

Multiple manometers designed for wide measuring ranges, which are very heavy, are mounted on carriages which facilitate removal from the room where the experiments are made.

The manometer indications can be recorded by any photographic camera, but for ease of analysis of the negatives, wide-film cameras should be used.

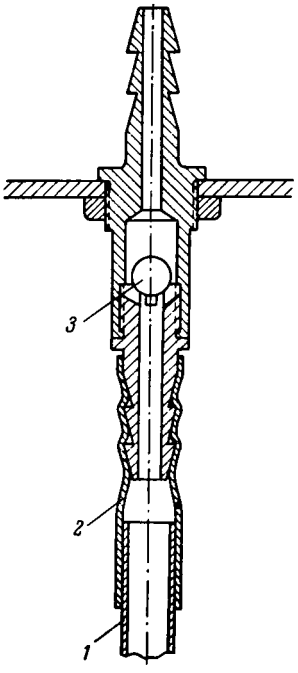

FIGURE 5.48. Nonreturn valve to prevent loss of liquid from the manometer. 1 — upper end of glass tube; 2 — rubber tube; 3 — ball.

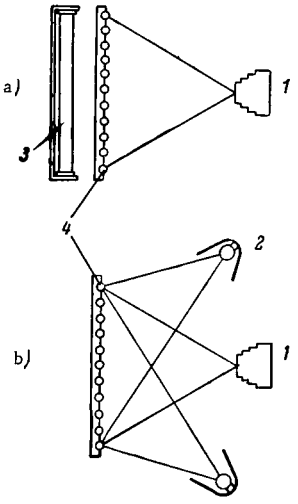

FIGURE 5.49. Illumination when photographing manometer scales. a — transillumination; b — illumination from the front. 1 — camera; 2 — reflectors; 3 — fluorescent lamp; 4 — manometer tubes.

When the pressure distribution is measured simultaneously with other magnitudes (for instance, with the forces acting on wind-tunnel balances), remotely controlled cameras are used. By pressing a button on the control panel, the experimenter obtains simultaneously all magnitudes of interest.

Clarity of the pictures is ensured by intensive and uniform illumination of tubes and scale. Stationary multiple manometers with Plexiglas panels are illuminated from behind (Figure 5.49a). In order to reduce glare the Plexiglas should be frosted on one side. Uniform lighting is more easily provided by a large number of low-power, then by a small number of high-power lamps. Good uniform lighting is obtained by fluorescent lamps.

Portable manometers can also be illuminated from the front (Figure 5.49b) with the aid of high-power lamps having reflectors or projectors, but transillumination gives better defined pictures.

In order to increase the reading accuracy, inclined multiple manometers with 600 to 700 mm long tubes are sometimes used in low-speed wind tunnels (Figure 5.50). The manometric liquid is usually alcohol. Glass tubes and the connecting metal tube are mounted on a common table which can be pivoted together with the camera about a horizontal axis. A multiple

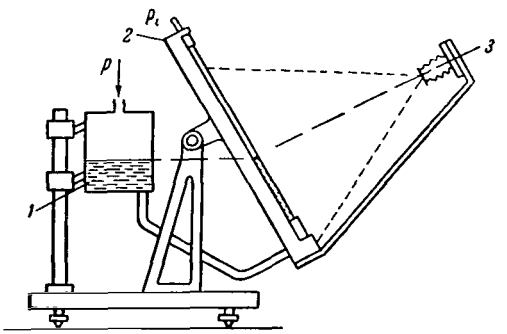

FIGURE 5.50. Inclined multiple manometer. 1 — well; 2 — inclined table with tubes; 3 — camera.

manometer can be read visually with an accuracy of up to 1 mm by fixing the manometer indications with the aid of a valve. While the indications are being recorded the conditions in the wind tunnel change; the pressure in the connecting tubes has time to become partially or fully equalized with the measured pressure.

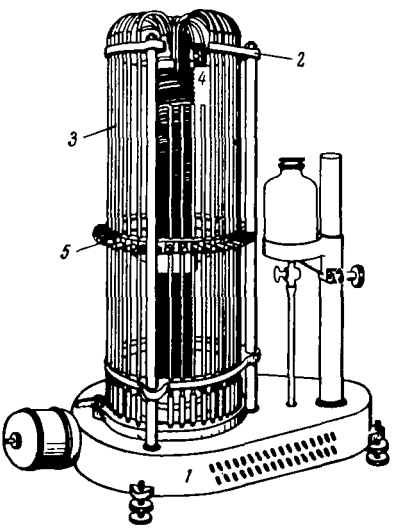

FIGURE 5.51. Multiple manometer with photoelectrical counter. 1 — base with nipples for connecting the pressure tubes; 2 — upper frame with bearing for spindle; 3 — glass tubes; 4 — spindle; 5 — carriage with photoelectric elements.

Figure 5.51 shows a Göttingen Aerodynamic Institute multiple manometer with automatic recording of the indications in numerical form /20/. Vertical tubes, whose lower ends are connected to a common vessel, are placed in a ring. The heights of the columns of liquid in the tubes are read with the aid of photoelectric cells, which are moved on a common annular carriage by a lead screw (Figure 5.52). Counting mechanisms for each tube are switched on when the carriage passes through a zero level while moving upward.

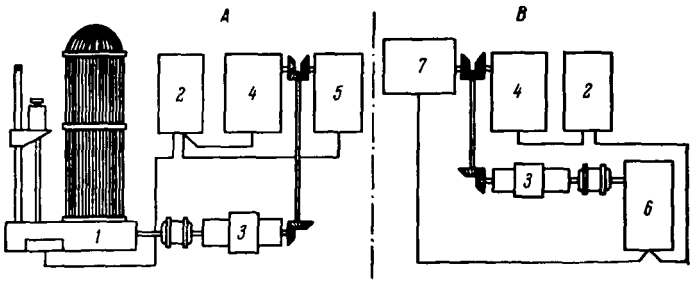

FIGURE 5.52. Recording the indications of a photoelectric multiple manometer. 1 — multiple manometer; 2 — relay installation; 3 — converter; 4 — electromechanical counter; 5 — punch-card system; 6 — punch-card reader; 7 — curve plotter.

At the instant when the light beam from a lamp (also installed on the carriage) falls on the meniscus in a tube, the counter sends a pulse to a relay installation which records the height of the meniscus. After a series of measurements has been taken the values recorded by the relay installation are fed to punch-cards. The punch cards are sent to a computing office, where the recorded values are automatically decoded and fed to a plotter which records on paper the coordinates of the points through which the pressure distribution curve can be drawn.

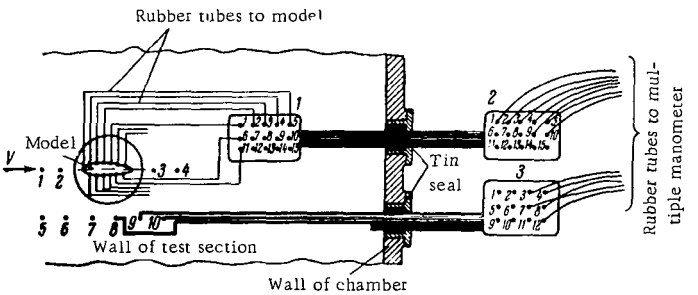

FIGURE 5.53. Wiring diagram for a multiple manometer with measuring orifices in the model and on the wind-tunnel walls.

Rubber tubes are used to connect the manometer to the measured pressure, as are tubes from various plastics, which are more stable than rubber tubes and resist chemicals better. If the pressure in the tubes is

above atmospheric, the tubes are secured to the nipples by soft iron or copper wire. When the pressure in the tubes is below atmospheric, special thick-walled rubber tubes are used, since thin-walled tubes may be forced in under the action of the external pressure.

In supersonic tunnels it is not always possible to connect the multiple manometer directly by flexible tubes to the metal tubes in the model. A good outlet from the variable-pressure chamber is shown in Figure 5.53. Two similar metal panels (1) and (2) are installed respectively in the chamber and close to the multiple manometer. The shields are rigidly fixed together by copper tubes. The tubes are led out through the chamber wall by means of a copper bushing to which all tubes are soldered. The coupling elements of panel (1) are connected before the experiment by rubber tubes to the metal tubes in the model, while the coupling elements of panel (2) are connected to the multiple manometer.

The orifices in the walls of the wind tunnel are permanently connected by metal tubes to panel (3) which is located outside the chamber.

Mechanical multipoint manometers

With all their simplicity, liquid-column multiple manometers have several serious drawbacks. They are unwieldy and take up much space. Thus, a multiple manometer designed for measuring pressures up to 4 at at 100 points takes up an area of about 20 m^2 (in the vertical plane). The danger of leakages of liquid increases in proportion to the number of separate tubes in the multiple manometer. Photographing the indications of multiple manometers, analyzing the pictures, and subsequent processing of the measurements, requires much work and causes delays in obtaining the final results of the experiment.

Sometimes groups of standard spring-type manometers are used for multipoint measurements, their indications being recorded by photography. However, analyzing the photographs of dials of standard manometers is even more difficult than analyzing the photographs of the scales of liquid-column manometers.

The best way of satisfying the requirements of aerodynamic experiments is by special multipoint manometers with elastic sensing elements and automatic recording of their indications. The small dimensions of multipoint manometers permit their siting in close proximity to the points of measurement; the reduction in length of the connecting tubes also causes a reduction in transmission lag of the manometers and in the total duration of the experiment.

Automatic recording of the indications of multipoint manometers can be simultaneous or consecutive. With consecutive recording all readings are made during a certain period of time. Consecutive recording is employed mainly in continuous-operation wind tunnels, where the pressures during a measurement cycle remain constant. In intermittent-operation wind tunnels it is preferable to record all indications simultaneously, but when the cycle lasts only a few seconds, consecutive recording with the aid of electronic circuits is also possible.

Simultaneous recording of pressures. Lever-type manometers with moving counterweights can be used for simultaneous multipoint pressure measurements. The main difficulty in using such manometers is their size and complexity. The reduction of the dimensions of RAE manometers (Figure 5.21) is achieved by connecting the bellows to the vertical lever arm. In a supersonic RAE wind tunnel a group of fifty such manometers is used for measuring the distribution of pressures varying from zero to 1800 mm Hg /9/. The indications of the manometers are printed on a diagram in the console of the observation cabin of the tunnel. For visual observation of the pressure distribution on the surface of the model and for discovering faults in the manometers, a vertical panel is provided on which the servo systems of the manometers move colored ribbons. Externally, such a panel looks like a liquid-column multiple manometer.

Lever-type manometers of simpler design are those in which the forces due to the pressure on the bellows bottom are not balanced by a counterweight but by a spring [spring-opposed bellows], one end of which is connected to the lever, and the other to a tensioning device. The tensioning device is located on a fixed base; hence, the dimensions of spring-type balances are considerably less than those of balances with movable counterweights. In GRM group manometers produced by the Soviet industry (Figure 5.54), twenty lever-type manometers are equilibrated with the aid of one motor. When any one of the levers is moved out of its equilibrium position, the circuit of a corresponding electromagnetic reversing clutch, whose drive shaft is continuously rotated by the motor, is closed. The clutch connects the shaft to a micrometric screw, which changes the tension of the spring and restores the lever to its equilibrium position. The pressures are determined from the turning angles of the micrometric screws each of which is connected to a digital printing counter. When a button is pressed, the indications of all twenty counters are printed on a paper tape with the aid of an electromagnetic mechanism. Vertical scales for visual observation are provided on the front wall of the instrument. The pointers on the scales are kinematically linked with the micrometric screws. The maximum error of the GRM manometer is about 0.5% of the maximum pressure measured.

Consecutive (cyclic) recording of pressures. Figure 5.55 shows a multipoint recording manometer, based on the consecutive measurement of the deformation of ten or more Bourdon tubes grouped together /21/. Carriage (1) has flexible contacts (3) and the Bourdon tubes (7) have flat contacts (5). Carriage (1) is periodically moved by a lead screw toward the Bourdon tubes in such a way that contacts (3) are consecutively closed with all contacts (5). Synchronously with carriage (1), but at a speed a hundred times higher, travels carriage (2), which has sharp-tipped metal electrodes (4) moving above a paper tape. When contacts (3) and (5) touch the circuit of sparking device (8) is closed which causes a spark to be discharged from electrodes (4) through the paper to ground. This forms a pinhole in the paper. When carriage (1) moves farther, contacts (3'), also on it, close with fixed rigid contacts (6) in positions corresponding to the zero position of the springs. This causes a second hole on the tape. Thus, the deformation of each Bourdon tube, which is

proportional to the measured pressure, is determined by the distance between two pinholes on the tape.

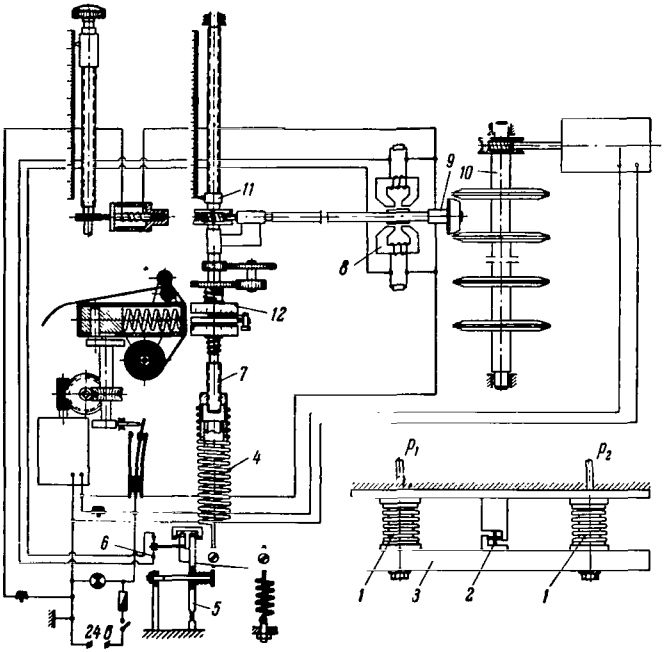

FIGURE 5.54. GRM-2 recording group manometer. 1 — bellows; 2 — elastic hinge; 3 — lever; 4 — balancing spring; 5 — destabilizing device for increasing the sensitivity; 6 — contact for switching on the electromagnet of the reversing clutch of the tensioning device; 7 — tensioning device; 8 — electromagnets; 9 — driven shaft of reversing clutch (20 nos.); 10 — driving shaft of reversing clutch, continuously rotated by electric motor; 11 — visual pressure indicator; 12 — printing device for recording serial number of reading.

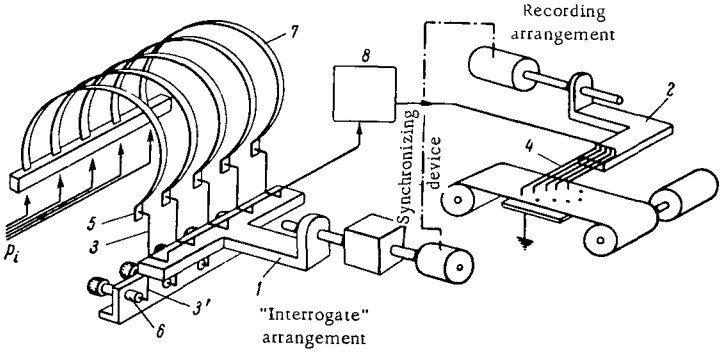

FIGURE 5.55. Multipoint Bourdon manometer. 1 — carriage with contacts; 2 — carriage with electrodes; 3 — 3' contacts; 4 — electrodes; 5 — flat contacts on Bourdon tubes; 6 — fixed contacts; 7 — Bourdon tubes; 8 — sparking device.

The strain-gage manometers and pressure transducers described in § 20 can be used for multipoint measurements if they are combined with automatic compensation (for instance by means of an automatic bridge). With the aid of a commutation arrangement, the transducers are consecutively connected in a given order to a single automatic compensator.

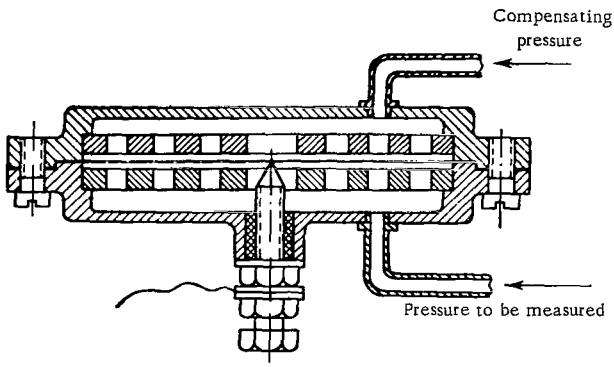

FIGURE 5.56. Diaphragm contact-type pressure transducer.

The commutator can be driven from a telephone uniselector or by a small electric motor. The commutation period must be longer than the time taken by the compensator to process the maximum signal. Modern automatic bridges permit the consecutive recording during one to two minutes of indications from 50 to 100 transducers with a maximum error of ± 0.5%. Such circuits usually contain auxiliary devices, which permit the recording, simultaneously with the measured value, of the serial number of the transducer. Certain designs permit the recording in digital form of the strain-gage indications.

Dynamic-compensation method. Aerodynamic laboratories in the U.S.A. widely use a method of consecutive pressure measurement in which the pressures to be measured are compared with a variable compensating pressure with the aid of diaphragm contact-type transducers (dynamic-compensation method) (Figure 5.56). A 0.05 to 0.075 mm thick diaphragm made from beryllium bronze and clamped at its rim between two plastic flanges, divides the transducer body into two chambers; one chamber is acted upon by the measured pressure while the other is acted upon by the compensating pressure which is the same for all transducers. Under the action of the pressure difference, the center of the diaphragm is displaced a small distance, closing or opening an electric circuit at the instant the measured and compensating pressures are equal. The magnitude of the compensating pressure at this instant is measured by an accurate manometer. To prevent residual deformation or rupture of the diaphragm when the pressure difference is large, the deflection of the diaphragm is limited by plastic discs located at small distances on either side. Multipoint instruments functioning on this principle, in which the compensating pressure is measured by electronic digital devices /24/, are described in Chapter IX.

The electromagnetic manometer shown in Figure 5.23 can also be used for multipoint measurements by the dynamic-compensation method. The wiring diagram of a multipoint electromagnetic manometer is shown in Figure 5.57. The movable coils (3) of all manometers are fed from a common generator (5), whose current varies linearly from zero to maximum (or vice versa). The coils convert the current into compensating forces simultaneously at all measuring points. A highly accurate linear relationship exists between the current and the force. Knowing the instantaneous current intensity at which the elastic element (bellows or diaphragm) connected to the coil returns to its zero position, we can determine the compensating force, and thus the magnitude of the measured

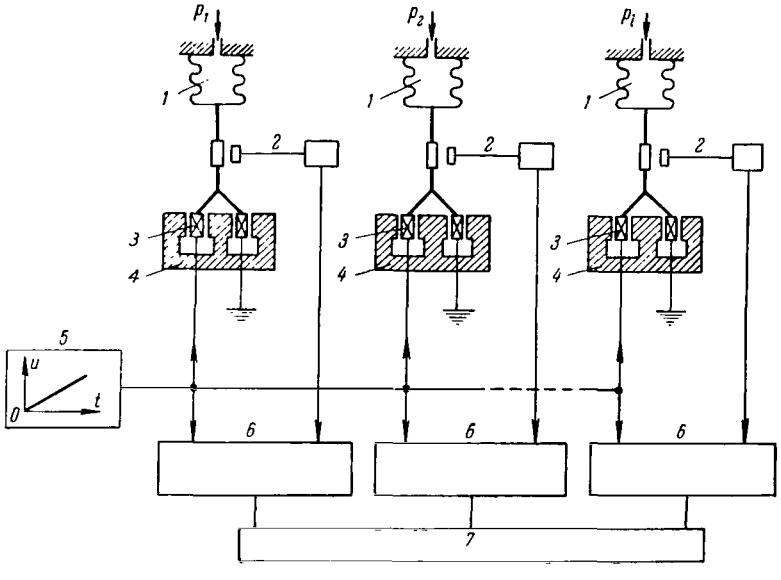

FIGURE 5.57. Multipoint electromagnetic manometer. 1 — bellows; 2 — zero-position transducers. 3 — movable coils; 4 — permanent magnets, 5 — generator of linearly varying current; 6 — counters; 7 — recording device.

pressure. Before the measurement cycle is begun, all elastic elements (1) are displaced under the action of the measured pressures. When the generator, which has a saw-tooth characteristic, is started, the electromagnetic interaction forces between the coils and the permanent magnets deform the elastic elements. At the instant when the electromagnetic force balances the pressure force acting on a given elastic element, the latter returns to its zero position and a transducer emits a signal. This signal is received by the current recorder; the latter measures the instantaneous current intensity which is proportional to the measured pressure, memorizes it for the duration of the cycle, and records it.

In the multipoint manometer shown in Figure 5.58, the compensating pressure serves at the same time to measure the pressure /22/. The manometer consists of a number of contact transducers (1), a recording device (2), a compensating-pressure regulator (3), and air pumps (4)

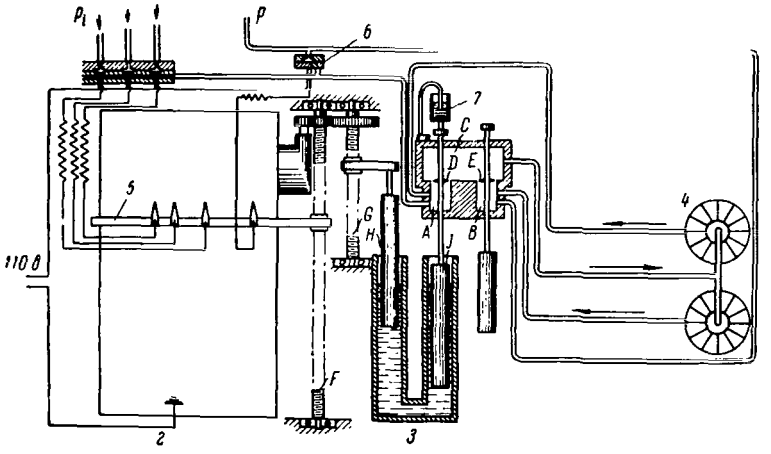

FIGURE 5.58. Multipoint manometer with contact-type pressure transducers. 1 — contact transducers; 2 — recording device; 3 — compensating-pressure regulator; 4 — air pumps; 5 — lath with pens; 6 — zero-reading transducers; 7 — damper.

which continuously supply air to the cylindrical chambers *A* and *B* of the compensating-pressure regulator. A fine micrometric screw *F*, rotated by a small motor, moves along the paper tape lath (5) with pens (electrodes), each of which is inserted into the circuit of a contact transducer. The paper is covered with a thin conductive layer, which becomes black where it touches a pen when a current flows through it. A second lead screw *G*, which is connected by gears to the screw *F*, moves an iron piston *H* inside a U-tube containing mercury. The mercury level in both legs of the U-tube will change in proportion to the travel of the lath with the pens; this alters the effective weight of the second iron piston *J* which floats on the mercury. The variation of this weight causes a proportional change of the pressure in chamber *A*. When this pressure is less than the measured pressure, the diaphragm of the transducer keeps open the electric circuit into which the corresponding pen is inserted. At the instant when the compensating pressure becomes equal to the measured pressure, the electric circuit is closed. Since the electrode draws a line on the paper only when the electric circuit is closed, the length of this line is proportional to the pressure acting on the given diaphragm of the transducer. All pressures must be compared with the static pressure in the wind tunnel; hence, one of the transducers is acted upon by the static pressure, and the contacts of this transducer are connected to two recording pens located on either side of the paper tape. The horizontal line which can be drawn by pencil on the paper in prolongation of the short line, marked by these pens, is the zero line. The instrument, intended for

relatively small pressure ranges (from 650 to 900 mm W.G.), permits in one minute thirty pressures to be recorded with a maximum error of 0.4% of the maximum measured value.

Selector valves

Due to the small cross-sectional area of the supports of the model in the test section of the wind tunnel, it is not always possible to lead out of the model a sufficiently large number of tubes. Sometimes the number of tubes will be less than the number of measuring points. The ends of the tubes are connected inside the model to the measuring points by flexible rubber tubes. Between two experiments, the tubes are disconnected from one group of measuring points and connected to another group. The complete pressure-distribution pattern is obtained after several experiments.

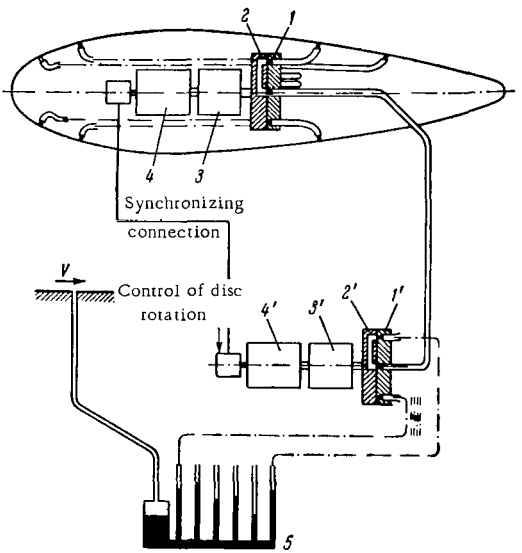

FIGURE 5.59. Selector valve with transmission of pressure through one tube. 1 — 1' - stationary discs; 2 — 2' - rotating discs; 3 — 3' - reduction gears; 4 — 4' - synchronized electric motors; 5 — multiple manometer.

When testing models of airplanes, rockets, etc., whose central part is axisymmetric, re-installation of the tubes can be avoided by means of the selector valve shown in Figure 5.59. The device requires only one outlet tube and one electric connection. It permits investigation of the pressure distribution together with the measurement of the aerodynamic forces acting on the model, which is suspended from wind-tunnel balances by

wires or a rigid support. There are two synchronized selector valves one of which, consisting of a stationary disc (1) and a rotating disc (2), is located inside the model. The other valve, which consists of a stationary disc (1') and a rotating disc (2'), is located in the observation cabin of the tunnel. The openings on the periphery of the stationary discs (1) and (1') are connected respectively to the orifices on the surface of the model and to the tubes of the multiple manometer. The central openings in the discs (1) and (1') are interconnected by the outlet tube. When the discs (2) and (2') are rotated by the synchronized electric motors (4) and (4') through reduction gears (3) and (3'), the channels in these discs successively connect each orifice with a corresponding tube of the multiple manometer.

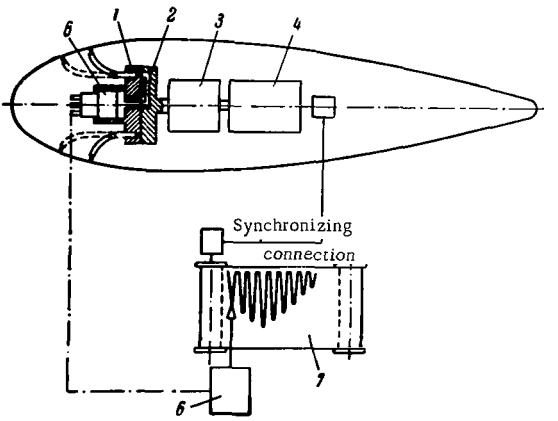

FIGURE 5.60. Selector valve with electric transmission of signals. 1 — stationary disc; 2 — rotating disc; 3 — reduction gear; 4 — miniature motor; 5 — pressure transducer; 6 — electronic bridge or oscillograph; 7 — recording tape.

In order that the pressure in the manometer tubes can become equalized with the measured pressure, discs (2) and (2') are automatically stopped when the channels coincide with the peripheral openings of discs (1) and (1'). After a certain interval the motors are switched on again and turn the discs (2) and (2') by an angle which corresponds to the distance between neighboring openings in the discs (1) and (1'). When one of the openings is connected to the corresponding tube of the manometer, all other manometric tubes are sealed off. Thus, when the discs (2) and (2') have completed a full turn, the heights of the columns in the tubes of the multiple manometer correspond to the pressure distribution on the surface of the model. Similar devices are used when testing relatively large models in subsonic wind tunnels, if the transmission lag of the manometer is small due to large tube cross sections and small pressure changes.

Figure 5.60 shows a selector valve which can be located in a body of revolution having a maximum diameter of 40 mm, and is therefore suitable for supersonic wind tunnels /23/. The device permits the pressures at twenty to thirty points to be measured with the aid of one

strain-gage transducer which is installed inside the model. The transducer (5) is directly connected to the central opening of stationary disc (1). Due to the short connecting tube and small volume of the transducer chamber, the device permits pressures to be recorded at the rate of up to three points per second. A quick-acting electronic bridge or oscillograph (6) serves for recording. The movement of the recording tape (7) is synchronized by a servo system with miniature motor (4) which rotates disc (2) through reduction gear (3). The pressure distribution is recorded as a series of equidistant peaks whose heights are proportional to the pressures at the corresponding points of the model. The obvious advantage of locating the selector valve inside the model is the complete absence of outlet tubes, which in conventional designs pass through the supports of the model.

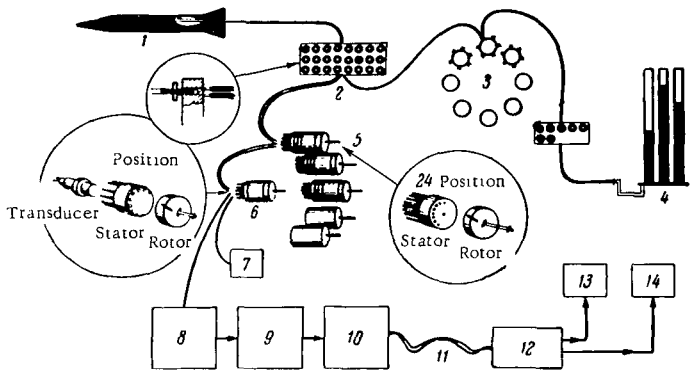

FIGURE 5.61. Layout for measuring pressures at 192 points. 1 — model; 2 — panel with tubes; 3 — shut-off valves; 4 — visual-observation multiple manometer; 5 — selector valves; 6 — main selector valve; 7 — vacuum pump; 8 — digital converter; 9 — memory device; 10 — puncher; 11 — punched tape; 12 — read-off device; 13 — print-out device; 14 — chart recorder.

Figure 5.61 shows a layout for measuring pressure at 192 points with the aid of selector valves, used at the Jet Propulsion Laboratory of the California Institute of Technology /25/. The tubes from model (1) are led to panel (2). The 192 points are divided into 8 groups of 24 points each, each group being served by a selector valve (5). The central openings of the discs of all eight valves (5) are connected to eight peripheral openings of the stationary disc of the main selector valve (6) which is so designed that before each reading the air space between the valves (5) and (6) can be connected to vacuum. This permits rapid pressure equalization in the strain-gage transducer connected to the central opening of valve (6). Shut-off valves (3) serve for visual pressure observation with the aid of multiple manometer (4). The use of one transducer for measuring all pressures makes possible a measuring accuracy of 0.2% of the full scale.

With the aid of an automatic electronic bridge and a digital converter (8) (see Chapter IX), the signal of the transducer is converted to a four-digit decimal number, which is stored in the memory device (9) and then punched

by puncher (10) on tape (11). Data recorded on the tape can be read off at any time with the aid of read-off device (12) which is connected to the print-out device (13) and the chart recorder (14).

Such selector devices are widely used outside the USSR. For instance, the ARA Aerodynamic Laboratory uses a system of six 48-channel "Scanivalve" valves, each of which is connected to a nonglued strain gage having a flat 12.7 mm-diameter diaphragm (as in Figure 5.40). The accuracy of these transducers amounts to 0.1% of the measurement range (0.15 to 1 atm). The small air space in the transducers (0.08 cm^3) permits all 288 pressures to be recorded within about one minute. Together with the pressures, the punched tape also records the moments and forces, measured on a wind-tunnel balance /26/.

§ 23. TRANSMISSION LAG IN MANOMETRIC SYSTEMS

When the pressure changes near the orifice or probe which is connected by a tube to the manometer, equilibrium in the manometer is established not immediately, but after a certain time. If the manometer is read off earlier, this can cause gross errors affecting the final results of the experiment. Small transmission lags are necessary not only for high reliablility but also in order to reduce the duration of the experiments. Thus, the performance of intermittent-operation wind tunnels depends on the transmission lag of the manometric systems. When starting such wind tunnels the pressure in the test section changes suddenly, after which a constant pressure is established at each orifice of the model. Equilibrium will be established in those manometers, which are connected to points where the pressure changes most sharply, later than in other manometers. Therefore, for determining the pressure distribution, the intervals must be not less than the longest transmission lag. Unsuitable selection of the manometric system may sometimes cause the duration of steady tunnel operation to be less than the transmission lag.

The transmission lag is mainly caused by the resistance of the tubes, the change in air density, and the inertia of the moving masses. The transmission lag increases with the volume of air in the manometric

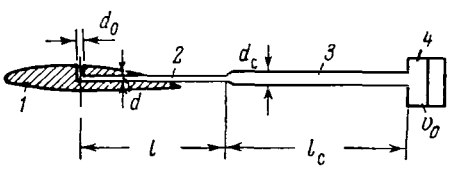

FIGURE 5.62. Pneumatic circuit. 1 — model; 2 — capillary tube; 3 — connecting tube; 4 — air space of sensing element of manometer.

system and with the resistance of the connecting tubes. When measuring pressures by microprobes in the boundary layer, the transmission lag attains several minutes. Airfoil models tested in supersonic wind tunnels have usually small cross sections; the pneumatic connections in them are

made by tubes having internal diameters less than 1 to 1.5 mm, and the orifices on the surface of the model have diameters of 0.2 to 0.5 mm. To reduce the transmission lag, optimum dimensions of the connecting tubing must be selected. Usually, the pneumatic system for measuring the pressure on the surface of the model consists of a metal tube fixed to the model, a flexible connecting tube, and a manometer (Figure 5.62).

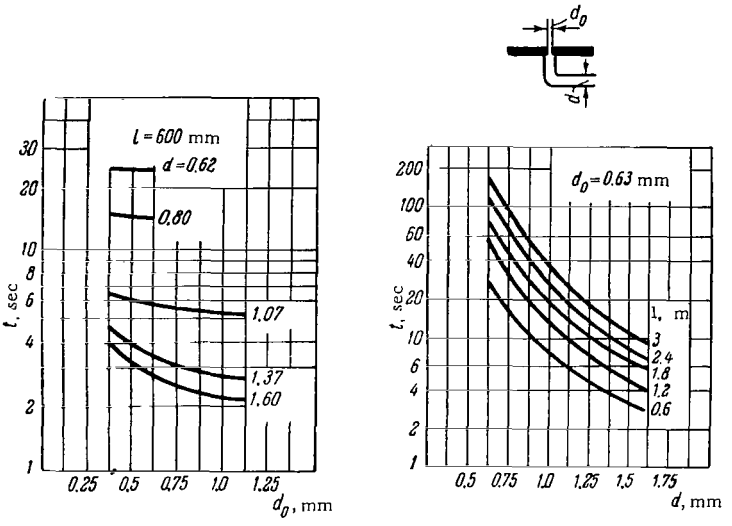

FIGURE 5.63. Transmission lag t as function of orifice diameter d_0, and capillary-tube length l and diameter d; $v_0 = 1.74$ cm^3; $l_c = 1500$ mm; $d_c = 1.7$ mm.

In manometers having elastic sensing elements, the change in volume of the sensing element, caused by the pressure variation, is usually so small that it can be ignored. The main factors influencing the transmission lag are the orifice diameter d_0, the internal diameters d of the capillary tube and d_c of the connecting tube, and their respective lengths l and l_c.

Figure 5.63 shows the relationships between the transmission lag and d_0, d, and l for $v_0 = 1.74$ cm^3 (Figure 5.62), $d_c = 1.7$ mm, and $l_c = 1500$ mm /27/. Initially this system was under atmospheric pressure; the pressure at the orifice was then suddenly reduced to 20 mm Hg. These conditions approximate those of manometers in intermittent-operation supersonic wind tunnels.

The orifice diameter is of small influence when $d/d_0 < 2.5$. When $d/d_0 > 2.5$ the transmission lag increases sharply. The orifice diameter should therefore not be less than half the diameter of the capillary tube. An increase in orifice diameter up to the diameter of the capillary tube has little effect on the transmission lag.

The influence of the diameter of the capillary tube is very strong. A reduction of this diameter has as its main effect an increase in the resistance to the flow of gas. A length increase of the capillary tube has a greater

effect when its diameter is small. Capillary tubes should therefore have diameters as large as possible and be as short as possible.

The influence of the connecting tube is twofold. Firstly, the connecting tube has the largest volume in the system, and secondly, it offers resistance to the gas flow. When d_c is small, the transmission lag is, as in a capillary tube, increased due to this resistance. When d_c is large, the lag increases due to the volume increase. The connecting tubes should therefore be as short as possible. The optimum diameter is between $1.25d$ and $1.50d$.

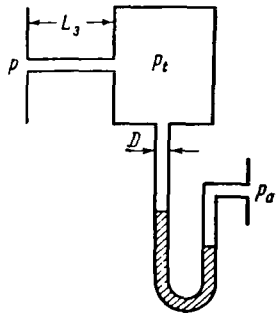

FIGURE 5.64. Determination of manometer transmission lag.

At very low pressures, for instance, in wind tunnels with free molecular flow, where the mean free-path length of the molecules is large in comparison with the cross section of the orifice for the tube leading to the manometer, the transmission lag can be considerable. For $d = d_c$ the lag can be determined according to the following approximate formula /31/:

$$t = \left(\frac{8vl}{d^3} + \frac{32v}{3d_0^2} + \frac{8\pi d^2 l}{\pi d_0^2} + \frac{8l^2}{\pi d}\right)\frac{3}{4}\frac{1}{\sqrt{2\pi RT}},$$

where v is the volume of the manometer chamber. As in the case considered above, an optimum value exists for the internal diameter of the tube.

Liquid-column manometers have in most cases larger transmission lags than manometers provided with elastic sensing elements. This is due to the large volumes of the air, the large moving masses, the viscosity of the liquid, and the additional volume change when the liquid flows from one leg to the other. In well-type manometers the lag depends on the method of connection. The air volume above the capillary tube in a well-type manometer is many times less than the volume of the air in the well. Whenever possible, the well should be at that pressure which varies less during the process (for instance, the total pressure).

For the manometric system shown schematically in Figure 5.64, the transmission lag is /28/:

$$t = k \ln \frac{p_{fin} - p_{init}}{p_{fin} - p_t},$$

where

$$k = \frac{128\mu L_{eq}}{\pi d_1^4 \bar{p}}\left[\frac{F_{eq}}{\gamma}\frac{p_{fin} - p_{init}}{2} + v_\infty\right]$$

is the time constant of the system, i.e., the time during which the pressure p_t in the manometer changes by 63.2% of the total pressure difference ($p_{fin} - p_{init}$) at the orifice; v_∞ is the volume of the air after the final pressure equalization.

These formulas take into account the compressibility of the air in the manometer but ignore the inertia and viscosity of the liquid.

In the second formula, L_{eq} is the "equivalent length" of the capillary tube which, when there are several connecting tubes of different diameters, is

$$L_{eq} = L_1 + L_2\left(\frac{d_1}{d_2}\right)^4 + \ldots + L_n\left(\frac{d_1}{d_n}\right)^4,$$

where L_1 is the length of the tube whose diameter is d_1.

The time-averaged pressure $\bar{p}$ in the manometer is

$$\bar{p} = \frac{\int_0^t p_t\, dt}{t}.$$

Instead of this value, we can substitute in this formula the approximate value of $\bar{p}$ up to the instant t when the pressure change in the manometer amounts to 98% of the total pressure difference:

$$\bar{p} = p_{\text{fin}} - \frac{(p_{\text{fin}} - p_{\text{init}})}{4}.$$

The equivalent area F_{eq}, which depends on the geometry of the manometric system, can be determined from Figure 5.65.

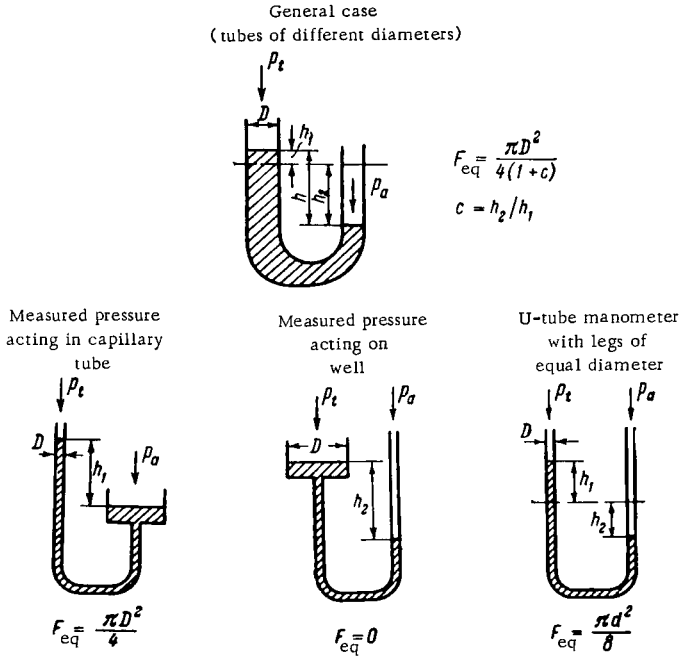

FIGURE 5.65. Determination of equivalent area of a manometer.

Thus, when the pressure changes abruptly, we can assume that the transmission lag is inversely proportional to the fourth power of the diameter of the capilllary tube, directly proportional to the length of the tube, and depends also on the volume of the air in the instrument and the geometry of the system.

§ 24. MANOMETRIC INSTRUMENTS FOR DETERMINING DIMENSIONLESS CHARACTERISTICS

Many dimensionless coefficients and parameters of experimental aerodynamics are determined as the ratios between dimensional magnitudes. For instance, all aerodynamic coefficients (Chapter I) are proportional to the ratios of the forces and moments to the velocity head of the undisturbed flow, while the Mach number is a function of the ratio between two pressures (Chapter IV). When each magnitude entering into the nominator and denominator of the ratio is measured independently, it is assumed that these magnitudes refer to the same flow conditions. However, if these magnitudes are not read off at the same instant, then, due to the fluctuations in flow velocity or pressure in the wind tunnel, this assumption leads to not accurately determinable errors in the calculated ratios. In most cases these errors can be reduced by obtaining more steady flow conditions in the wind tunnel or using quick-acting measuring instruments with simultaneous automatic recording of their indications. However, in some cases a better accuracy can be achieved by measuring not each magnitude separately but their ratio directly. Such a "coefficient meter", which is mainly a simplified computing device, was first used by K. A. Ushakov in 1924 for determining the aerodynamic coefficients of airfoils in the TsAGI wind tunnel /29/.

Nowadays, aerodynamic experimental techniques are so developed that in many large wind tunnels the coefficients are automatically calculated on digital computers. The simple devices described in this section permit automation of these calculations in those small wind tunnels and installations where the use of computers and complicated devices for measurements and data input is not justified.

Instruments for measuring force and pressure coefficients

At low flow velocities, any of the aerodynamic coefficients c_x, c_y, c_z, m_x, m_y, m_z are proportional to the ratio of the force or moment to the difference between total and static pressure, e. g.,

$$c_y = \text{const}\frac{Y}{\rho V^2/2} = \text{const}\frac{Y}{\Delta p}.$$

The principle of measuring the coefficient of lift in a wind tunnel is schematically shown in Figure 5.66. The aerodynamic force Y, which acts on the model installed on the wind-tunnel balance, is transmitted by rod (1) to beam (2), at whose end contact (3) is located between two stationary contacts (4). Beam (2) is connected with lath (6) by means of link (5), which can be moved along the beam and the lath by lead screw (7) which is turned by servomotor (8). The force, which acts on the lever-type manometer consisting of bellows (11) and lever (9), is transmitted to lath (6) by means of two levers (10) which have the same arm ratio. When beam (2) becomes unbalanced, one of the contacts (4) is closed, servomotor (8) is switched on, and lead screw (7) moves link (5) to the position at which the moment acting on the beam, due to force Y, is balanced in its absolute value

by the moment due to pressure on the bellows, which is proportional to Δp. It is easy to see that the distance x from the fulcrum of beam (2) to link (5), at the instant when equilibrium is attained, is

$$x = k\frac{Y}{\Delta p},$$

where k depends on the transmission ratio of the levers and on the area of the bellows. The weight of levers (9) and (10), link (5), the connecting rods, and lath (6) is balanced by counterweight (13), while the weight of beam (2) and the parts connected to it is balanced by counterweight (12). The value of x, which is proportional to c_y, can be read off from a counter connected to the lead screw.

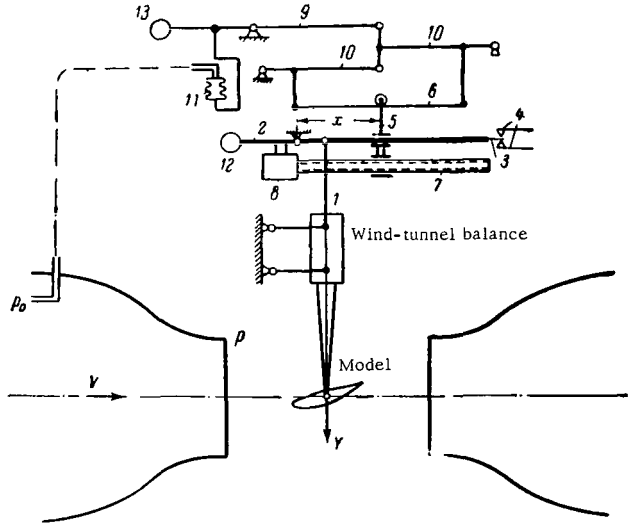

FIGURE 5.66. Direct measurement of coefficient of lift. 1 — rod; 2—beam; 3 — contact at end of beam (2); 4 — stationary contacts; 5 — link; 6 — lath parallel to beam (2); 7 — lead screw; 8 — servomotor; 9 — lever; 10—levers with equal arm ratios; 11 — bellows acted upon by pressure difference Δp; 12 and 13—counterweights.

Figure 5.67 illustrates how the dimensionless total-pressure coefficient $\overline{H}$ of a fan is determined. Here,

$$\overline{H} = \frac{H}{\rho u^2},$$

where u is the peripheral velocity of the impeller tip. The pressure p_e, which is proportional to ρu^2, is created by a so-called unit fan, rotating at the same speed as the tested fan and operating in air of the same density /30/.

The pressure H, created by the tested fan, and the pressure p_e act respectively on bellows (5) and bell (4), whose effective areas are F_1 and F_2. The force on the bellows acts on the left-hand arm of lever (1).

Bell (4) is mounted on a carriage moving along guides (3); the force $p_e F_2$, acting on the bell, is transmitted to the other arm of the lever by means of a roller. Lever (1) is balanced with the aid of lead screw (2), rotated in either direction by means of a servo system consisting of a continuously rotating friction wheel (6) and electromagnets (7), switched in by contacts (8). The total-pressure coefficient $\overline{H}$ is proportional to the distance x between the roller and the fulcrum of lever (1), which can be read off from a scale or counter.

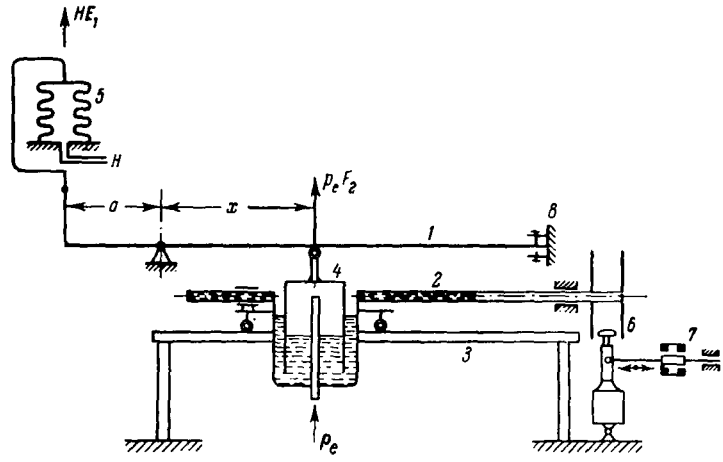

FIGURE 5.67. Determination of the total-pressure coefficient of a fan. 1 — lever; 2 — lead screw; 3 — guides; 4 — bell; 5 — bellows; 6 — friction wheel; 7 — electromagnets; 8 — contacts.

When the beam is in equilibrium, $HF_1a = p_e F_2 x$, whence

$$\frac{H}{p_e} = \frac{F_2 x}{F_1 a}.$$

Since the pressure p_e is proportional to ρu^2, the value of x is proportional to the total-pressure coefficient of the tested fan:

$$x = \text{const}\, H.$$

Similar instruments can be used for measuring pressure coefficients when investigating the pressure distributions on bodies.

Instruments for measuring the Mach number of the flow

Since in high-speed tunnels the flow characteristics depend to a large degree on the Mach number, its free-stream value must be controlled

during the experiment. The use of a Machmeter (as instruments for measuring the Mach number are called) simplifies experiments at high subsonic velocities, where models are very often tested by varying the flow velocity at constant angle of attack. This instrument is also suitable for modern supersonic wind tunnels with adjustable nozzles. The Mach number in the test section of such a tunnel is changed gradually by adjusting the shape of the nozzle, and the direct measurement of **M** permits control of the flow conditions in the tunnel.

The Mach number is a function of the ratio of two selected pressures p_1 and p_2 in the gas (see Chapter IV). Therefore, any instrument which measures the ratio of p_1 and p_2 can be used as Machmeter. The scale of such an instrument need not be linear, since the functional relationship $\mathbf{M} = f(p_1/p_2)$ is not linear. The Mach number can be determined from the ratio of the total pressure p_0 (or the pressure difference $\Delta p = p_0 - p$) to the static pressure p in the undisturbed flow.

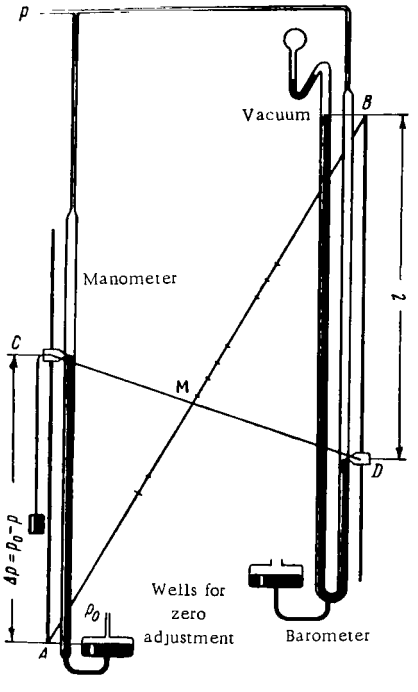

FIGURE 5.68. Liquid-column Machmeter.

The simplest device for measuring the Mach number is shown in Figure 5.68. It consists of a well-type manometer with measures Δp, and a manometer which measures the absolute static pressure p. The zero markings of the scales of both instruments are interconnected by a diagonal line AB. A string is stretched between the moving verniers C and D. When the verniers are aligned with the meniscuses in the manometric tubes, the intersection of lines AB and CD divides the former into two parts whose ratio is $\Delta p/p$. Thus, the divisions marked on line AB correspond to values of the Mach number, which is read off with the aid of string CD.

Figure 5.69 shows another device, which permits control of the Mach number when the pressures are measured with the aid of two pendulum-type manometers. When the pressure p_1 changes, the angle of inclination of pendulum (1), to which a curved mirror (3) is fixed, also changes. A light beam falls on mirror (3) from light source (4) and is reflected onto plane mirror (5). The latter is turned around a vertical axis OO when pendulum (2) is inclined by the action of pressure p_2. The beam is reflected from mirror (5) onto screen (6). The vertical displacement of the beam is proportional to p_1 and its horizontal displacement to $p_2 - p_1$. The Mach number is determined from the lines $\mathbf{M} = \text{const}$, drawn on the screen.

Automatic instruments for measuring **M** can be divided into two groups. The first group includes instruments which are simple electrical

analog computers, while the second group includes instruments which are based on force-balancing principles. In instruments of the first group, the

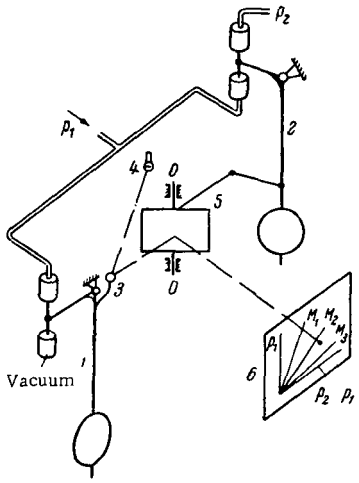

FIGURE 5.69. Optical Machmeter with pendulum-type manometers. 1 and 2 — pendulum type manometers; 3 — curved mirror; 4 — light source; 5 — plane mirror; 6 — screen.

input into the computer is formed by magnitudes proportional to the pressures p_1 and p_2 which are measured by separate manometers. Automatic self-balancing manometers, whose output is an angular displacement of the

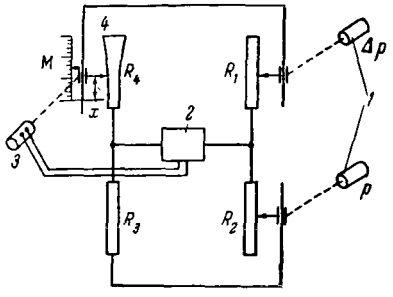

FIGURE 5.70. Determining the Mach number with the aid of a balanced bridge. 1 — servomotors or selsyn receivers connected to self-balancing manometers; 2 — amplifier (zero indicator); 3 — balancing servomotor; 4 — resistor with scale for **M**.

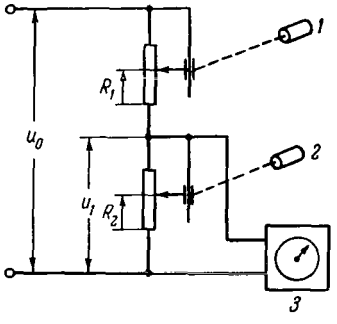

FIGURE 5.71. Potentiometric determination of Mach number. 1 and 2 — selsyn receivers connected to manometers measuring p and Δp; 3 — automatic potentiometer.

servomotor shaft, are most suitable for this purpose. Figure 5.70 shows a wiring diagram used in the automatic computation of **M** with the aid of a

balanced bridge, in which the resistances of two arms are changed in proportion to the indications p and Δp of the manometers. The other two bridge arms are formed by a constant resistance R_3 and a variable resistance R_4. The bridge is balanced by varying the resistance R_4 with the aid of a balancing servomotor which moves the contact of the resistor into the position which corresponds to the balancing of the bridge, so that

$$\frac{R_1}{R_2} = \frac{R_4}{R_3},$$

whence

$$R_4 = k\frac{\Delta p}{p} = k\left[\left(1 + \frac{\varkappa - 1}{2}\mathrm{M}^2\right)^{\frac{\varkappa}{\varkappa - 1}} - 1\right].$$

If the resistance R_4 varies in proportion to the displacement x of the contact of the resistor and the counter connected to it, then x is linearly related to the pressure ratio and nonlinearly to the Mach number. The scale from which M is determined is thus nonlinear. For x to be proportional to M, it is necessary that the following relationship exist between the resistance and the displacement of the contact:

$$R_4 = k\left[\left(1 + \frac{\varkappa - 1}{2}k_1 x\right)^{\frac{\varkappa}{\varkappa - 1}} - 1\right]$$

where k and k_1, are constants.

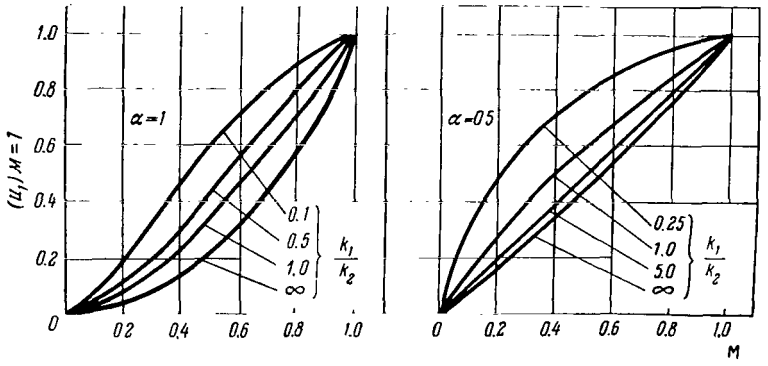

FIGURE 5.72. Output voltage of potentiometric system as function of Mach number.

Figure 5.71 shows the wiring diagram of a computing device based on the principle of the potentiometer. A constant voltage u_0 forms the input of the potentiometer which consists of two variable resistances R_1 and R_2. The output voltage u_1 is a function of the ratio of the resistances R_1 and R_2. If the resistances R_1 and R_2 vary in such a way that $R_1 = k_1 p$ and $R_2 = k_2 \Delta p$, then $[u_1 = u_0/(1 + k_1 p/k_2 \Delta p)]$ and u_1 will therefore depend only on the Mach number. The output voltage can be measured with high accuracy by the null method, for instance, by an automatic electronic potentiometer. By changing the raio k_1/k_2 the function $u_1 = f(\mathrm{M})$ can be varied considerably. Thus, for instance, for $k_1/k_2 = 0.5$, the output voltage changes almost linearly with the Mach number in the range $0.3 < \mathrm{M} < 1$. The linearity can be improved if the

resistance R_1 and R_2 change with the pressure in such a way that

$$R_1 = k_1 p^{\alpha} \quad \text{and} \quad R_2 = k_2 \Delta p^{\alpha}.$$

In this case the functional relationship between u_1 and the pressure ratio is

$$u_1 = \frac{u_0}{1 + \frac{k_1}{k_2}\left(\frac{p}{\Delta p}\right)^{\alpha}}.$$

By varying α, we obtain different functional relationships, so that in different parts of the Mach-number range linearity will be maintained as closely as possible. Figure 5.72 shows that for $k_1/k_2 = 5$ and $\alpha = 0.5$ we obtain a relatively high linearity in the entire range $0 < M < 1$ /32/.

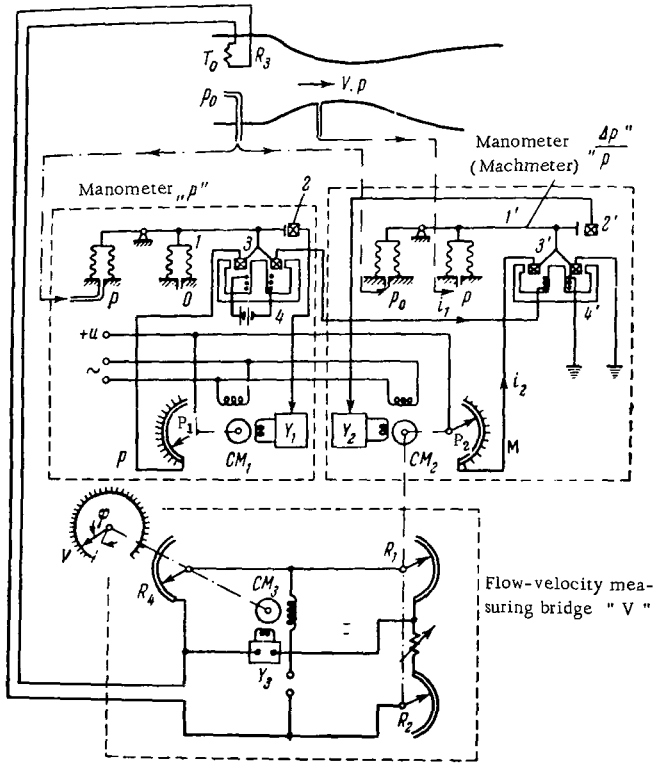

FIGURE 5.73. Determination of the Mach number with the aid of electromagnetic manometers and of the flow velocity with the aid of a resistance bridge. 1 — 1' - lever-type manometers; 2 — 2' - transducers; 3 — 3' - coils; 4 — 4' - permanent magnets; CM_1, CM_2, CM_3 - servomotors; Y_1, Y_2 и Y_3 — amplifiers.

Figure 5.73 shows the wiring diagram of a manometric system which permits the Mach number and the actual flow velocity to be measured

simultaneously. The system consists of two electromagnetic lever-type manometers and a computing device in the form of an automatic measuring bridge. One manometer serves for measuring the absolute static pressure p. When p changes, the equilibrium of lever (1) is disturbed, and transducer (2), through amplifier Y_1, switches on servomotor CM_1 which, with the aid of variable rheostat P_1, changes the current intensity i_1 in coil (3). The latter is fixed to the lever, and the variation in current intensity causes the force of interaction between the magnetic fields of the coil and the permanent magnet (4) to change in such a way that lever (1) returns to its equilibrium position. The current, which is proportional to p, can be measured by the position of the shaft of the servomotor CM_1 or of the slider of the rheostat P_1.

A second manometer differs from the first only in that its balancing coil (3'), connected to lever (1'), is acted upon by electromagnet (4'), whose winding is connected in series with coil (3). Hence, the force of interaction between coil (3') and electromagnet (4') is proportional to the product of the current intensities i_1 and i_2. Lever (1') is acted upon by a moment which is proportional to the pressure difference Δp. When Δp changes, transducer (2'), through amplifier (Y_2), switches on servomotor CM_2, which moves the slider of the variable rheostat P_2. This alters the current intensity i_2 in the circuit of coil (3'), and restores lever (1') to its equilibrium position. Since i_1 is proportional to p, the current intensity i_2 at the instant when lever (1) returns to its equilibrium position depends only on the pressure ratio:

$$i_2 = \text{const}\,\frac{\Delta p}{p} = f(\mathbf{M});$$

the second manometer is therefore a Machmeter.

The device for computing V is a four-arm bridge, two of whose arms are formed by resistances R_1 and R_2. The magnitudes of the latter are changed by servomotor CM_2 simultaneously with that of rheostat P_2. The third arm of the bridge consists of a resistance thermometer in the settling chamber of the wind tunnel. The magnitude of this resistance is

$$r_{t0} = r_0[1 + \alpha(T_0 - 273)],$$

where r_0 is the resistance of the thermometer at 0°C, α is the temperature coefficient of the resistance, and T_0 is the stagnation temperature of the gas. The resistance r_{t0} is connected in series with a constant resistance which has a negligibly small temperature coefficient, and is equal to $R_3 = r_0(1 - 273\alpha)$. Hence, the total resistance of the arm will be

$$R_3 = \alpha r_0 T_0.$$

When the supply voltage u of the coils is constant, the rotation angle of the shaft of servomotor CM_2 and the displacements of the sliders of rheostats R_1 and R_2 are proportional to $\Delta p/p$. The resistances R_1 and R_2, which vary with the displacements of the sliders, can be chosen in such a way that they are proportional respectively to

$$\mathbf{M}^2 \text{ and } 1 + \frac{\varkappa - 1}{2}\mathbf{M}^2.$$

The bridge is balanced by servomotor CM_3 which is fed from amplifier (null indicator) Y_3. When the bridge is balanced,

$$\frac{R_1}{R_2} = \frac{R_4}{R_3} = \frac{\mathrm{M}^2}{1 + \frac{\varkappa - 1}{2}\mathrm{M}^2},$$

whence

$$R_4 = \frac{ar_0T_0\mathrm{M}^2}{1 + \frac{\varkappa - 1}{2}\mathrm{M}^2}.$$

The actual flow velocity is expressed through the Mach number and the stagnation temperature:

$$V^2 = \frac{\varkappa gRT_0\mathrm{M}^2}{1 + \frac{\varkappa - 1}{2}\mathrm{M}^2}.$$

Since for a given gas $\varkappa$ and R are constant, R_4 is proportional to V^2. If R_4 varies like the square of the slider displacement, the rotation angle of the shaft of servomotor CM_3 will be directly proportional to the actual flow velocity.

In all these instruments one or both pressures entering into the functional relationship $\mathrm{M} = f(p_1/p_2)$ are measured independently, so that the Mach number is determined indirectly.

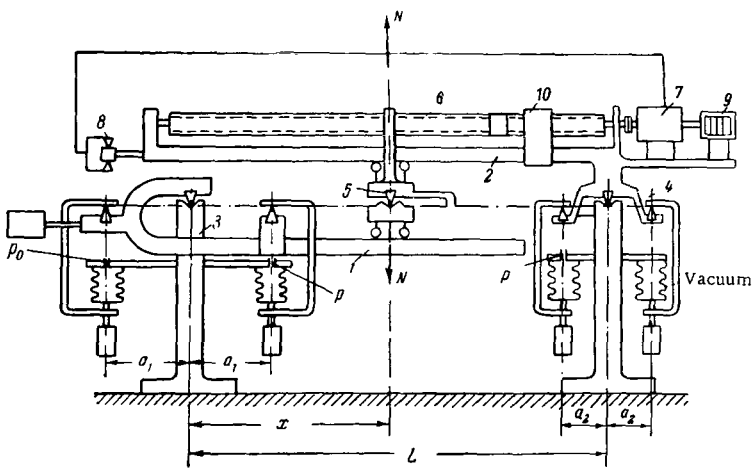

FIGURE 5.74. *Electromechanical Machmeter.* 1 and 2 — levers; 3 and 4 — fixed knife edges; 5 — movable knife edge; 6 — lead screw; 7 — servomotor; 8 — transducer; 9 — counter; 10 — counterweight.

Figure 5.74 shows an electromechanical device which directly measures the ratio of two pressures, i.e., permits the Mach number to be found directly. The advantage of such devices is that there is no need to balance each pressure separately. The device consists of two levers (1) and (2), resting on fixed knife edges (3) and (4). Each lever is connected to a pair

of bellows, acted upon by the total pressure, static pressure, and vacuum in such a way that the moments of the pressure forces, about the fulcrums of levers (1) and (2) are proportional to Δp and p respectively. These moments are balanced by the moment of the reaction N of movable knife edge (5), which connects levers (1) and (2). The position of knife edge (5) can be changed with the aid of lead screw (6), which is rotated by servomotor (7). The change in the moment about the fulcrum of lever (2), of the weight of knife edge (5) when the latter is displaced, is compensated by moving counterweight (10), in the opposite direction.

For this purpose part of lead screw (6) has a left-hand thread. When the equilibrium of the levers is disturbed by a pressure variation, the servomotor is switched on by transducer (8) and moves knife edge (5) into a new position at which the equilibrium of the levers is restored. The equilibrium condition is given by

$$Nx = \Delta p F_1 a_1 = \frac{px}{L-x} F_2 a_2,$$

where L is the distance between knife edges (3) and (4), while F and a with corresponding subscripts are the effective areas of the bellows and the distances between their center lines and knife edges (3) and (4), respectively. When the static pressure is equal to the total pressure, i.e., when the flow velocity is zero, lever (1) exerts no force on lever (2), because in this case the reaction N passes through the fulcrum of lever (1). The initial position of knife edge (5) is in line with knife edge (3), its displacement from this initial position being

$$x = L \frac{\Delta p/p}{k + \Delta p/p},$$

where $k = \frac{F_2 a_2}{F_1 a_1}$ is constant.

Thus x is a function of the Mach number which can be determined with high accuracy from the indications of counter (9), which is connected to lead screw (6).

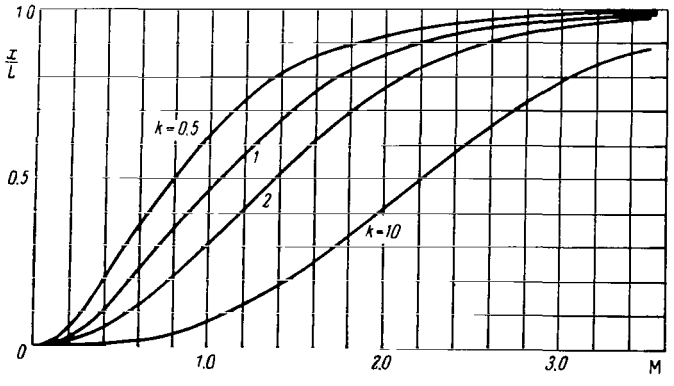

FIGURE 5.75. Dependence of relative knife-edge displacement on Mach number.

Figure 5.75 shows the dependence of the relative displacement x/L on the Mach number. By selecting different values of k, we can obtain maximum sensitivity of the instrument dx/dM for different sections of the Mach-number range. In practice, use of the instrument is limited to the range $0.5 < M < 3$, since for $M > 3$ the static pressure p drops very sharply and the accuracy of the instrument is reduced due to the small displacements of knife edge (5), required to restore the system to its equilibrium position.

Bibliography

1. Deshman, S. Nauchnye osnovy vakuumnoi tekhniki (Scientific Basis of Vacuum Technology). [Russian translation. 1950.]
2. Spravochnik khimika (Chemical Handbook). — Goskhimizdat. 1951.
3. Farquharson, J. and H.A. Kernikle. Precise Automatic Manometer Reader. — Rev. Sci. Instr., Vol. 28, No. 5. 1957.
4. Zhukova, L.A., N.A. Kolokolova, and V.A. Sukhnev. Izmerenie malykh perepadov davleniya v razrezhennykh gazak (Measurement of Small Pressure Drops in Rarified Gases). — Izvestiya AN SSSR, OTN, Mekhanika i Mashinostroenie, No. 6. 1961.
5. Falkner, V.M. A Modified Chattock Gauge of High Sensitivity. — ARC Rep. and Mem. 1589. 1934.
6. MacMillan, F.A. Liquid Micromanometers with High Sensitivity and Small Time Lag. — J. Sci. Instr., Vol. 31, No. 1. 1954.
7. Smith, A. and J.S. Murphy. *Micromanometer for Measuring* Boundary Layer Profiles. — Rev. Sci. Instr. Vol. 26, No. 8. 1955.
8. Hart, H.R. Electric Micromanometer. — J. Sci. Instr., Vol. 38, No. 7. 1961.
9. Midwood, G.F. and R.W. Hayward. An Automatic Self-Balancing Capsule Manometer. — ARC Cur. Pap., No. 231. 1956.
10. Kinkel, J.F. A Precision Pressure Balance. — Proc. Instr. Soc. Am., Vol. 7. 1952.
11. Opstelten, J.J. and N. Warmoltz. A Double-Sided Micromanometer. — Appl. Sci. Res., B 4, No. 5. 1955.
12. Halliday, A.S. and H. Deacon. A Distant Reading Manometer for Particular Application to the Measurement of Small Pressures. — ARC Rep. and Mem., No. 2744. 1952.
13. Neubert, N.K.P., W.R. Macdonald, and P.W. Cole. Sub-Miniature Pressure and Acceleration Transducers. — Control, Vol. 4, No. 37. 1961.
14. Pressey, D.C. Temperature-Stable Capacitance Pressure Gauges. — J. Sci. Instr., Vol. 30, No. 1. 1953.
15. Cook, D.B. and C.J. Danby. A Simple Diaphragm Manometer. — J. Sci. Instr., Vol. 30, No. 7. 1953.
16. Wrathall, T. Miniature Pressure Cells. — Proc. Instr. Soc. Am., Vol. 7. 1952.
17. Bassiere, M. Une manomètre differential miniature. — Technique et science aéronautique, No. 3. 1956.

18. Delmonte, J. A Versatile Miniature Flush-Diaphragm Pressure Transducer. — Proc. Instr. Soc. Am., Vol. 7. 1952.
19. Molyneux, W. Measurement of the Aerodynamical Forces on Oscillating Aerofoils. — Aircraft Engg. 28, 232. 1956.
20. Wuest, W. Vielfach-Registrier-Manometer für langsamveränderliche Drücke in der Strömungsmesstechnik. — ATM, Lief. 271. Aug., 1958.
21. Taudler, W. S. Automatic Instument for Reading Bourdon Gages. — Rev. Sci. Instr., Vol. 27, No. 2. 1956.
22. Campbell, P. J. A Multiple Recording Manometer. — J. Aero. Sci., Vol. 10, No. 8. 1943.
23. Parker, W. E. and J. C. Pemperton. Scanning Valve Speeds Up Pressure Plots. — Aviation Age, Vol. 26, No. 4. 1956.
24. Sharp, E. M. A Digital Automatic Multipoint Pressure-Recording System. — Proc. Instr. Soc. Am., Vol. 7. 1952.
25. Bain, M. and M. Seamons. Economical On-Line Data-Reduction System for Wind-Tunnel Force and Pressure Tests. — IRE Transact. on Instrumentation, Vol. 1 - 7, No. 2. 1958.
26. Wood, M. B. and J. N. W. Baldwin. Digital Recording in Multipoint Pressure Surveys. — Control, Vol. 3, No. 21. 1960.
27. Dyukov, A. Inertsiya izmeritelei davleniya v sverkhzvukovykh aerodinamicheskikh trubakh (Transmission Lag of Pressure Meters in Supersonic Wind Tunnels). — "Mekhanika" No. 1, IL. 1955.
28. Benedict, R. P. The Response of a Pressure-Sensing System. — Trans. ASME, J. of Basic Engng., Vol. 82, No. 2. 1960.
29. Ushakov, K. A. Novyi metod izmereniya sil pri aerodinamicheskikh ispytaniyakh (New Method for Measuring Forces during Aerodynamic Tests). — Trudy TsAGI, No. 5. 1924.
30. Ushakov, K. A. Metod neposredstvennogo polucheniya bezrazmernykh kharakteristik ventilyatorov (Method of Directly Determining Nondimensional Characteristics of Fans). — In: Sbornik "Promyshlennaya aerodinamika", No. 17, Oborongiz. 1960.
31. Schaaf, S. A. and R. R. Cyr. Time Constants for Vacuum Gage Systems. — J. Appl. Phys., Vol. 20, No. 9. 1949.
32. Manaldi, I. F. Mach Number Measurement. — ISA Journal, Vol. 2, No. 4. 1955.

Chapter VI

WIND-TUNNEL BALANCES

The aerodynamic forces and moments acting on models tested in wind tunnels can be determined indirectly by measuring the pressures at many points of the model surface. A more accurate and reliable method is the direct measurement of the forces and moments with the aid of wind-tunnel balances.

In contrast to ordinary scales, which serve to measure forces acting in a known direction, wind-tunnel balances must measure not only aerodynamic forces, the direction of whose resultant is unknown, but also the moments about certain axes, due to this resultant and to couples. In the most general case, wind-tunnel balances must measure the components of this resultant (called total aerodynamic force), along three mutually perpendicular axes passing through an arbitrary point, and the three components of the total moment about these axes (Figure 6.1). The peculiarity of an aerodynamic experiment is that in the process the magnitude and direction of the total force and the moment can change; in the design of wind-tunnel balances this has to be taken into account.

Having determined the projections of the total aerodynamic force and the moment in the coordinate system of the given wind-tunnel balance, we can transform them into another coordinate system, whose origin can be placed at any desired point, for instance, at the center of gravity of the airplane or rocket.

The main characteristic of wind-tunnel balances is the number of measured components. Depending on the problem considered, this number can vary from 1 to 6. The design of the balances must provide the possibility of measuring and altering the angle of attack, and in many cases also of the slip angle of the model. When solving a two-dimensional problem, for instance, for a symmetrical model of an airplane at zero slip angle, three-component balances are used, which measure the lift, the drag, and the pitching moment. In this case the balance must have a mechanism permitting only the angle of attack to be changed. When problems connected with lateral control of flying missiles are investigated, four-component balances are used which permit also the angle of heel to be measured. In certain partial problems single- and two-component balances are used, most often for measuring drag and lift or one component of the moment.

Depending on their location, wind-tunnel balances can be divided into two types: balances located outside the model and the test-section of the wind tunnel, and balances located inside the model or its supports. In the

balances of the first type, the total aerodynamic force and moment are resolved into components with the aid of various mechanisms. These balances will be called mechanical balances. The model is installed in the test section of the tunnel with the aid of supports connected to these mechanisms. The supports are also acted upon by aerodynamic forces and moments whose values have to be taken into account when determining the true aerodynamic forces and moments acting on the model. In addition, it is necessary to take into account the interaction (interference) between the supports and the model, caused by flow perturbation near the model due to the presence of the supports. Methods of determining the influence of the supports are described in Chapter VII.

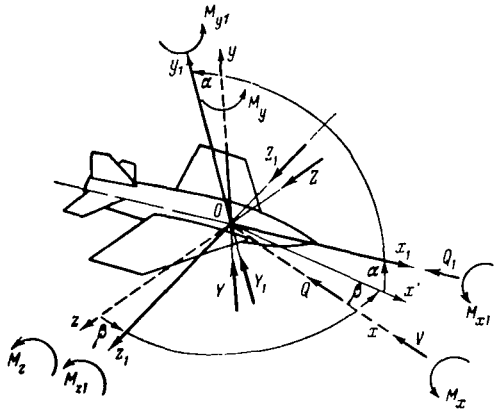

FIGURE 6.1. Coordinate axes and projections of aerodynamic loads acting on the model. The broken lines represent the flow system of coordinates xyz. The full lines represent a coordinate system fixed to the model. The x'-axis belongs to the semifixed coordinate system .

In many cases, especially at large flow velocities, the drag of the supports can be considerable and lead to large systematic errors. Hence, reducing the drag of the supports is very important, and the design of the wind-tunnel balances depends greatly on the type of support.

In "external" (mechanical) wind-tunnel balances the components of forces and moments are usually determined in a system of "balance" axes parallel to the flow axes of coordinates. Some low-speed tunnels have revolving frames which serve to alter the slip angle of the model; the indications of such balances refer to semifixed coordinate axes.

The drawback of mechanical wind-tunnel balances is the comparatively high weight of their elements; due to the inertia of the measuring system such balances cannot be used in tunnels having short operating durations.

Wind-tunnel balances located inside the model enable the influence of the supports to be excluded almost completely at supersonic flow velocities. The small dimensions of the models tested in supersonic wind tunnels do not permit mechanical balances to be placed inside the models. Practical

designs of "internal" wind-tunnel balances became possible only with the development of strain-gage measurement methods during the past two decades.

Methods of measuring forces by strain gages are based on the use of elastic systems whose deformations (which are proportional to the mechanical loads, and therefore to the forces and moments) are determined with the aid of small strain gages. The latter emit electric signals whose values are simple functions of the forces and moments. Using different electric diagrams, we can convert these functions so as to obtain signals which are proportional to the components of the aerodynamic forces and moments.

At present, balances placed inside the models are widely used in high-speed wind tunnels. Another advantage of wind-tunnel balances based on strain-gage principles is their rapid response, which permits measurements of forces in tunnels in which steady flow lasts only tenths of second.

§ 25. WIND-TUNNEL BALANCES LOCATED OUTSIDE THE MODEL

In spite of the many different designs of mechanical wind-tunnel balances, there are several elements which are common to most types. These elements are: the supports for the model; the floating frame for holding the supports and for taking up the forces acting on the model; the mechanical system for resolving into components the forces taken up by the floating frame, and balance elements or dynamometers connected to the output links of this system; and mechanisms for changing the angle of attack and the slip angle of the model.

According to the design of the devices supporting the model, we distinguish between balances with rigid and with flexible model supports. In balances with rigid supports the model is secured to the floating frame with the aid of rigid supports or struts. In balances with flexible supports the model is secured with the aid of wires, strings, or tapes tensioned with the aid of auxiliary weights or springs. In several designs the separate links of the flexible or rigid supports form the elements of the mechanical system for resolving the aerodynamic force into components. In this case no floating frame is required as a separate element.

The tested model is very often installed in a reverse position in the test section of the wind tunnel so that the positive lift is added to the weight of the model and the floating frame. In this case the balance is placed above the test section. The weight of the floating frame is chosen in such a way that at the maximum negative value of the lift, the hinges and links of the mechanism will be subjected to a certain load, so as to maintain them in contact.

Models in the true ("flying") position are installed in large wind tunnels. In such tunnels the weight of the tested models is large and it is good practice to increase the accuracy of measurements by partly unloading the floating frame of the lift acting upward. In addition, placing the balance above the test section when the latter is large complicates the design of the supporting devices for the balance .

The aerodynamic forces and moments taken up by the model and transmitted to the floating frame (or to elements replacing it), are measured by determining the reactions necessary to prevent translational and rotary displacement of the model. This is done by force-measuring instruments (balance elements or dynamometers) in the links of the system for resolving the force into components, which usually consists of a multi-link articulated mechanism. The links must be designed so as to reduce to a minimum the work done by friction during the displacments. A number of non-Soviet wind tunnels are provided with hydraulic and pneumatic mechanisms for resolving the forces into components; they consist of kinematic pairs with very low friction.

For better utilization of the wind tunnel and to speed up the tests, it is desirable that the forces be measured on the balance as quickly as possible. This is made possible in modern wind tunnels by using special balance elements with automatic equilibration and recording of the indications.

In order to determine the dimensionless aerodynamic coefficients, it is necessary to measure, simultaneously with the forces acting on the model, the parameters from which the velocity head can be determined (see Chapter IV).

The simultaneous measurement of all force and moment components is very important for the accuracy of the experiment. In several old designs of balances, which today have only historical interest, each component was measured separately. The accuracy of determining dimensionless coefficients by measuring forces at different instants is reduced, for instance, because of possible variations of the velocity head between readings. The dynamical characteristics of all balance elements should be uniform and close to those of the instruments used for measuring the flow parameters.

One of the most cumbersome operations when preparing the experiment is the mounting of the model and its supports. In a modern wind tunnel this takes far more time than the measurements. The tendency in designing the supports is to provide maximum ease of model installation and interchangeability of parts and sub-assemblies. In several industrial wind tunnels, two or three sets of balances are provided to speed up replacement of the model. While one set is used for the experiment, different models are mounted on the other sets. In supersonic tunnels, each set of balances is installed in a separate test section provided with wheels and carried on rails. Replacing the test section requires less work than exchanging the model.

Mechanism for resolving the forces into components

Depending on the method of resolving the forces into components, wind-tunnel balances can be divided into two groups:

1. Balances in which the loads taken by one or several elements depend on two or more components.
2. Balances in which each element takes up a load which is proportional to only one component.

Balances of the first group have a simpler system for resolving the forces into components than those belonging to the second group. In balances of the first group the loads taken up by the elements are functions of the sums or differences of two or more components. Some calculations are required to determine the separate components; this makes observation of the experiment difficult. In some earlier designs of such balances, several magnitudes were measured separately, while after each measurement certain manipulations with the balance mechanism were necessary. Such were, for instance, the balances based on the three-moment principle, used in N. E. Joukowski's laboratory at the University of Moscow and in the Eiffel Laboratory in France. In these balances, the moments about three points of the floating frame to which the tested model is secured are measured successively. Solving equatations of statics, the drag Q, the lift Y, and the pitching moment M_z are then determined.

In balances of the second group, each element is intended for measuring a separate component. These balances require more complicated mechanisms for resolving the forces into components, but their advantage is the simplicity of processing the results of measurements and the possibility of directly controlling the experiment. This is most important in modern high-power wind tunnels, in which maximum reliability of experimental results is aimed at.

To simplify the control of the experiment when using balances of the first group, primary automatic processing of the measurements is sometimes employed. This processing consists of algebraically summimg up indications of separate elements, resulting in "net" values of the components.

For all designs of mechanical wind-tunnel balances it is possible to deduce general conditions necessary for the independent measurement of each component by one balance element. These conditions are that the work done by the component of the total aerodynamic force or moment over the corresponding displacement of the model must be equal to the work done by the force acting on the balance element over the measuring distance of the latter. In the absence of friction in all kinematic pairs, and of deformation of the links in the mechanism which resolves the forces into components, we obtain

$$N_Q\Delta_Q - Q\delta_x = 0, \qquad N_{M_x}\Delta_{M_x} - M_x\delta_\gamma = 0,$$
$$N_Y\Delta_Y - Y\delta_y = 0, \qquad N_{M_y}\Delta_{M_y} - M_y\delta_\beta = 0,$$
$$N_Z\Delta_Z - Z\delta_z = 0, \qquad N_{M_z}\Delta_{M_z} - M_z\delta_\alpha = 0.$$

Here δ_x, δ_y, δ_z are the possible translational displacements of the model parallel to the coordinate x, y, and z-axes, δ_γ, δ_β δ_α, are the possible rotations of the model about these axes, Δ_Q, ... Δ_{M_z}, are the displacements of the input links of the balance elements, and N_Q, ..., N_{M_z}, are the loads acting on the latter.

Kinematically these conditions mean that for a small translational displacement of the model parallel to any axis, there must be a motion, parallel to its axis, only of that link which connects the balance system with the element intended to measure the force component acting in the direction of the axis considered. For a small rotation of the model about any axis, only that link must move parallel to its axis, which connects the system with the element intended to measure the moment about said axis.

If we disconnect the balance elements from the mechanism resolving the forces into components, the model will have a number of degrees of freedom, equal to the number of the measured components. Each element is connected to such a point of the mechanism that when the latter is fixed the model is deprived of only one degree of freedom. Thus, if all the scale elements were absolutely rigid and fixed (i.e., the link taking up the force did not move under the action of the force), the system for resolving the forces into components would become a statically determined system.

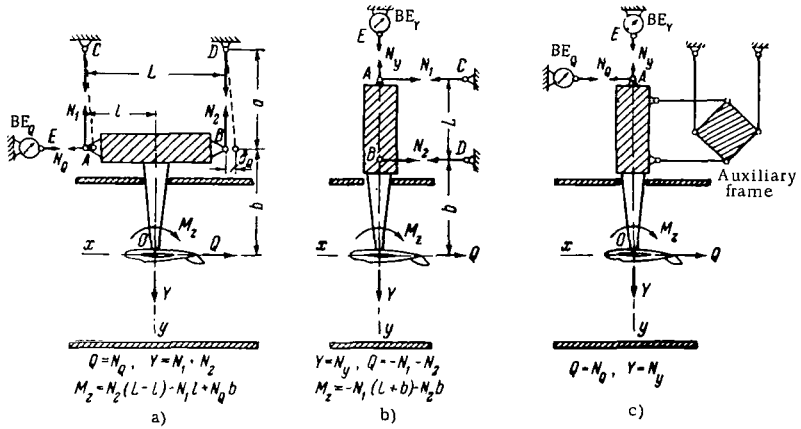

FIGURE 6.2. Parallelogram mechanisms for measuring forces. a — measurement of Q; b — measurement of Y; c — measurement of Q and Y.

Thus, the components can be measured independently by using mechanisms which permit free translational displacements of the model, parallel to the coordinate axes, for measuring forces, and free rotational displacements about the coordinate axes, for measuring moments. The number of degrees of freedom of the mechanism must be equal to the number of the measured components. Such systems can be formed from a number of elementary mechanisms: mechanisms for translational displacements, mechanisms for rotational displacements, and combined mechanisms.

Mechanisms for translational displacements. The simplest mechanism for measuring forces, which is widely used in wind-tunnel balances, is a hinged four-link mechanism forming a parallelogram. Figure 6.2 shows balances for measuring the drag Q and the lift Y with the aid of parallelogram mechanisms. The floating frame is connected to rods AC and BD, whose direction is perpendicular to that of the measured force and which are hinged at C and D respectively. By means of the rod AE, which is parallel to the direction of the measured force, the floating frame is connected directly (or through a lever transmission which is not shown) with the corresponding balance element (BE_Q, BE_Y).

At a small displacement of the hinge E along AE, the frame AB together with the model moves parallel to the direction of the drag Q (Figure 6.2a)

or the lift Y (Figure 6.2b). In these displacements, work is done only by the force components Q and Y respectively; they are thus measured independently of each other and of the pitching moment. If we measure the forces N_1 and N_2 acting in the rods AC and BD by separate elements, the indications of these elements enable us to determine the moment M_z about any axis perpendicular to the xy plane. However, if the hinges C and D are displaced in the direction of the rods AC and BD, work is done (by the forces Y and Q in Figure 6.2a or the force Q in Figure 6.2b, and the moment M_z); the balance elements connected with these rods would thus measure forces N_1 and N_2 depending both on the components of the total force and on the moment. In this case the values of Y (or Q) and M_z can be determined from the indications of two or three balance elements by solving the corresponding equations given in the figure.

By combining two parallelogram mechanisms, we obtain a mechanism which permits independent measurement of two orthogonal forces (Figure 6.2c). This system employs, in addition to the main floating frame to which the model is secured, a rigid auxiliary floating frame to which the rods are hinged.

When measuring the horizontal forces with the aid of parallelogram mechanisms, a small ratio of the horizontal force ΔQ to the horizontal displacement δ_Q of the floating frame, caused by it, is important; (δ_Q is reckoned from the zero position at which the rods AC and BD are vertical and perpendicular to AB (Figure 6.2a). The force ΔQ represents the horizontal components of the forces N_1 and N_2 induced by the weight of the floating frame in rods which are inclined at an angle of δ_Q/a. If the weight of the floating frame is G while the length of the rods AC and BD is a, then when δ_Q is small,

$$\Delta Q = (N_1 + N_2)\frac{\delta_Q}{a} \approx G\frac{\delta_Q}{a},$$

whence

$$\frac{\Delta Q}{\delta_Q} = \frac{G}{a}.$$

It follows from this that the sensitivity of the system measuring the force Q can be increased by lengthening the rods or reducing the weight of the floating frame.

When the floating frame is heavy, high sensitivity of the parallelogram mechanism can be achieved only through long rods which require a high room for installing the wind-tunnel balances. The "antiparallelogram" support of a floating frame (Figure 6.3a) increases the sensitivity when short rods are used. The translational displacement of the frame is obtained by hinging it at O_1 and O_2 to the equal-arm levers P_1 and P_2 linked to vertical rods (1), (2) and (1') and (2'). The sensitivity is increased by the forces in rods (1) and (2) (and also in (1') and (2')) having different signs; when the floating frame is displaced, the horizontal projections of the forces in the inclined rods act pairwise in opposite directions. For the antiparallelogram support we have

$$\frac{\Delta Q}{\delta_Q} = G\frac{a_2 - a_1}{a_1 a_2},$$

where a_1 and a_2 are respectively the length of rods (1) and (2) (or (1') and (2')). If rods (1) and (2) are of equal length the sensitivity is infinitely large.

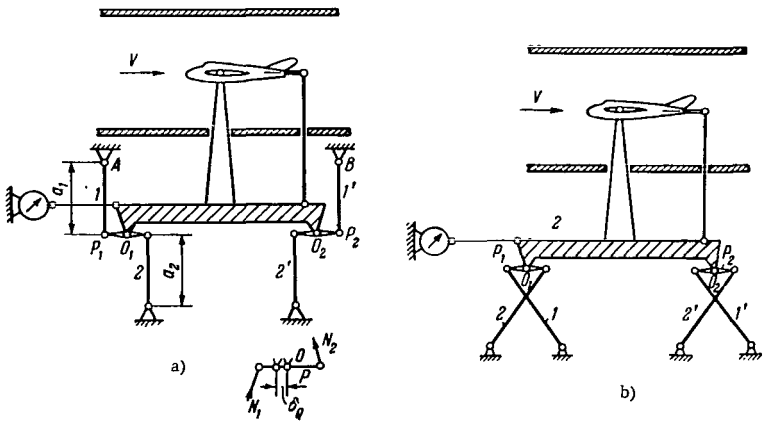

FIGURE 6.3. Measurement of drag Q. a — with the aid of antiparallelograms; b — with the aid of Chebishev mechanisms.

In a parallelogram support this is possible only with infinitely long rods.

Figure 6.3b shows a system which provides translational displacement of the floating frame with the aid of Chebishev mechanisms, in which the equal-arm levers P_1 and P_2 are carried by inclined crossed rods. The advantage of this mechanism is in that the lift on the model and the weight of the floating frame act on rods (1) and (2) (or (1') and (2')) in the same direction. This facilitates the design of the hinges.

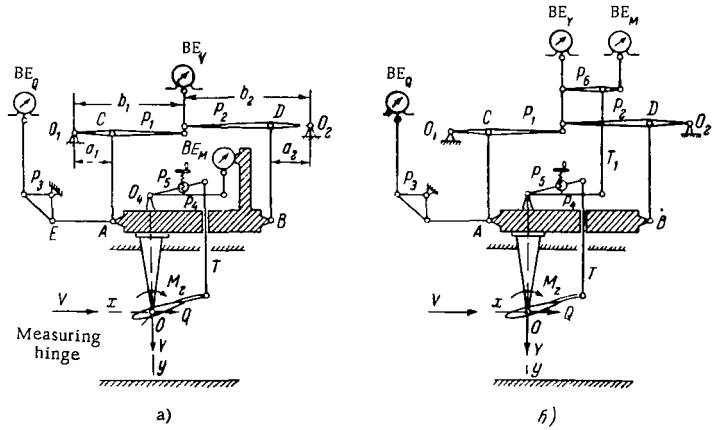

FIGURE 6.4. Three-component wind-tunnel balance with lever adding system. a — balancing elements for measuring M_Z, on a floating frame; b — balancing element for measuring M_Z, on "ground".

For measuring the lift, a lever adding system is mostly used, which permits translational displacement of the floating frame parallel to the vertical y-axis. Figure 6.4 shows a three-component wind-tunnel balance, in which the lift is measured with the aid of levers P_1 and P_2, at whose fulcrums C and D the floating frame is suspended by rods AC and BD. The levers are hinged to fixed supports at O_1 and O_2 and connected at their free ends by a pull rod to the balance element BE_Y. The forces which are proportional to the forces acting in rods AC and BD are added in the pull rod. The levers P_1 and P_2 have the same arm ratio $i = a_1/b_1 = a_2/b_2$; hence, the load taken up by the pull rod and the balance element BE_Y is equal to iY, irrespective of the point where the force Y is applied, i.e., of the pitching moment M_z.

The drag Q is measured with the aid of a hinged parallelogram, which consists of a floating frame, rods AC and BD, and crank lever P_3 through which the force acting in rod EA, which is equal to Q, is transmitted to the balance element BE_Q. Crank levers are used whenever the balance elements can take up only vertical loads.

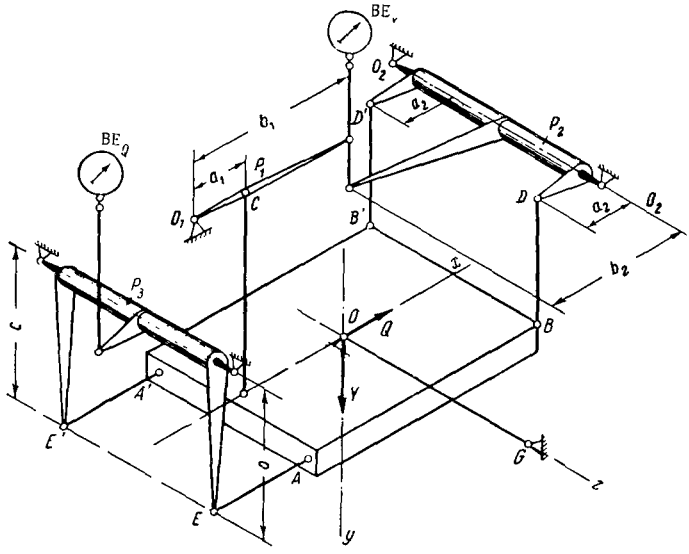

FIGURE 6.5. Method of removing excessive degrees of freedom of a floating frame

Figure 6.5 shows a method for removing excessive degrees of freedom, in the directions of the components not measured, of a floating three-component frame. For this purpose, the adding lever P_2 has two equal horizontal arms of length a_2, which are connected to each other and to the central arm (of length b_2) by a rigid transverse element. The lever P_2 can rotate about axis O_2O_2, at the same time preventing the floating frame from rotating about any axis parallel to Ox. The crank lever P_3 which has two equal arms of length C, also interconnected by a rigid transverse element, adds the forces acting on the rods AE and $A'E'$ which are parallel to the x-axis, and transmits the load, which is proportional to the drag Q, to the balance element BE_Q. This lever prevents

the frame from rotating about any axis parallel to Oy. Translational displacement of the frame in the direction parallel to the z-axis is prevented by a hinged rod OG which connects the frame to a fixed support.

Mechanisms for measuring moments. The transverse axis Oz of wind-tunnel balances is usually the axis about which the model rotates when its angle of attack is altered. Hence, at all angles of attack, the origin of the balance coordinate system remains fixed in relation to the model. When the model is sufficiently large it can be hinged along the z-axis to the fixed part of the support. The tail section of the model has hinged to it a movable streamlined strut by means of which the angle of attack is altered.

Mechanisms for measuring moments can be divided into two groups: mechanisms with measuring hinges on the model and mechanisms without measuring hinges. Measuring hinges are bearings on the supports with whose aid the angle of attack of the model can be altered, while at the same time a slight rotation of the model, at low friction, enables a force to be transmitted through the tail strut to a balance element which measures the pitching moment M_z. An example of a three-component balance with a measuring hinge on the model is shown in Figure 6.4a. The pitching moment M_z is measured with the aid of lever P_4 and balance element BE_M supported on the floating frame AB.

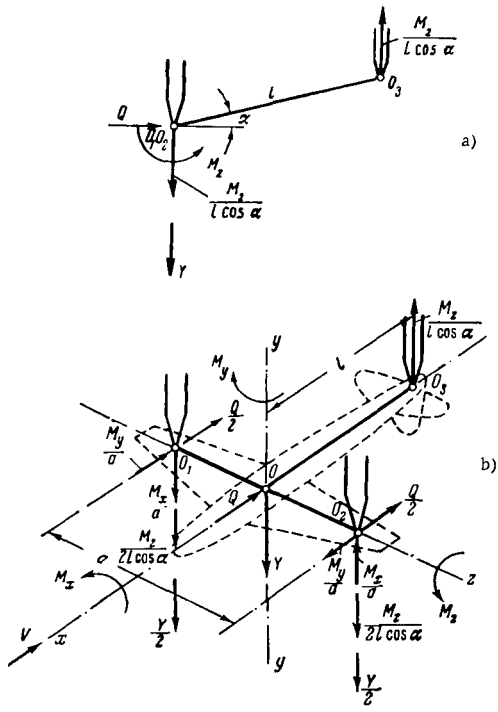

FIGURE 6.6. Load distribution on hinges of model supports.

The pitching moment is transmitted to lever P_4 by strut T, hinged to the tail section of the model and to an intermediate lever P_5. Rotation of the latter about support O_4 of lever P_4 causes the angle of attack of the model to be altered.

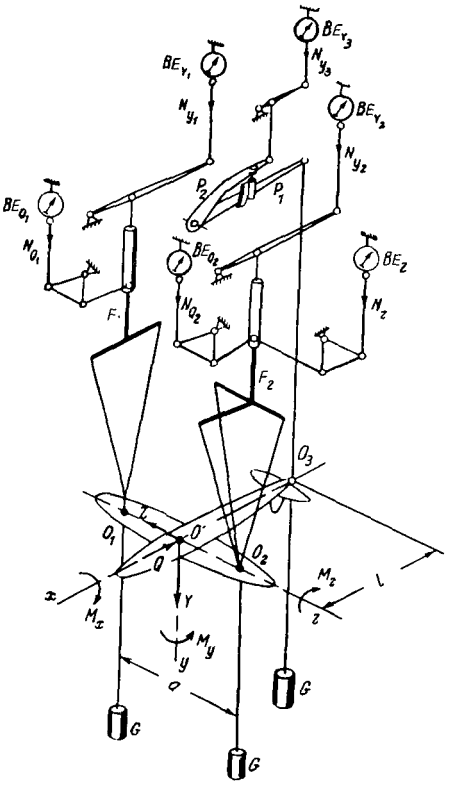

FIGURE 6.7. Six-component balance with measuring hinges on the model.

If, in addition to the pitching moment M_z, the components M_x and M_y have to be determined, the measuring hinges have two or three steps. The model, which is fixed to the supports at three points, can in this case be considered as a three-dimensional statically determined beam supported at three points (Figure 6.6). The components of the total aerodynamic moment cause reactions at the hinge supports O_1 and O_2, which can be geometrically added to the reactions at these supports, caused by the components of the total force.

A six-component balance /2/ with measuring hinges on the model is shown in Figure 6.7. The model is supported at points O_1 and O_2, which are located at a distance a from each other (transverse base) in the wings of the model, by means of wires or tapes connected to two separate floating frames F_1 and F_2. The tail hinge O_3, located at a distance l (longitudinal base) from

the line O_1O_2 (the z-axis), is connected by a wire or tape to the lever P_1 whose rotation in relation to a lever P_2 indicates the angle of attack of the model. Levers P_1 and P_2 are connected by means of a worm gear. Lever P_2 transmits the load due to the pitching moment M_z, to the balance element BE_{y_3}.

All vertical components acting at O_1, O_2 and O_3 are transmitted to balance elements BE_{Y_1}, BE_{Y_2} and BE_{Y_3} respectively through levers having equal transmission ratios i_y. The horizontal components acting at O_1 and O_2, which are parallel to the x-axis, are transmitted to balance elements BE_{Q_1} and BE_{Q_2} through crank levers whose transmission ratio is i_Q, while the side force Z is transmitted to balance element BE_z through a crank lever having a transmission ratio i_z. If we denote the loads taken up by the balance elements by N with the corresponding subscript, the different components of forces and moments are:

$$
\begin{aligned}
Q &= i_Q(N_{Q_1} + N_{Q_2}),\\
Y &= i_y(N_{y_1} + N_{y_2} + N_{y_3}),\\
Z &= i_z N_z,\\
M_x &= i_y \frac{a}{2}(N_{y_2} - N_{y_1}),\\
M_y &= i_Q \frac{a}{2}(N_{Q_2} - N_{Q_1}),\\
M_z &= i_y l N_{y_3}.
\end{aligned}
$$

In order to permit negative values of M_x, M_z and Y to be measured, the balance elements BE_{Y_1}, BE_{Y_2} and BE_{Y_3} are preloaded by weights G.

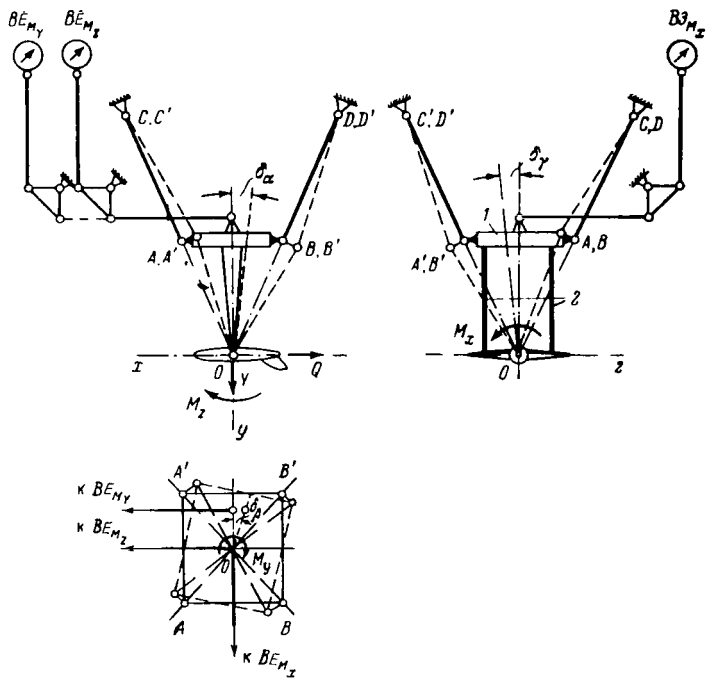

FIGURE 6.8. "Pyramidal" support for floating frame.

The design of this balance does not permit independent measurements of the components. The above formulas show that only Z and M_z are determined as the indications of a single balance element. The other force components are determined as sums, and the other moment components, as differences of the indications of balance elements.

Measuring hinges are comparatively easily installed on models of wings tested in subsonic wind tunnels. When models are tested at high flow velocities, it is extremely difficult to install the measuring hinges, because of the small dimensions of the model and the large loads . Transonic and supersonic wind tunnels often have, therefore, balances in which the instantaneous axes of rotation of the model coincide with the coordinate axes of the balances without measuring hinges being provided on the model.

Differing in design from balances with measuring hinges, where displacements of the balance elements measuring the moments are caused by displacements of the model in relation to its supports, in balances without measuring hinges, displacements of the balance elements are caused by displacements of the model together with its supports. An example of such a design, the so-called "pyramidal" support (Figure 6.8), is used in several types of wind-tunnel balances in the U. S. A. and Britain /3/, /4/.

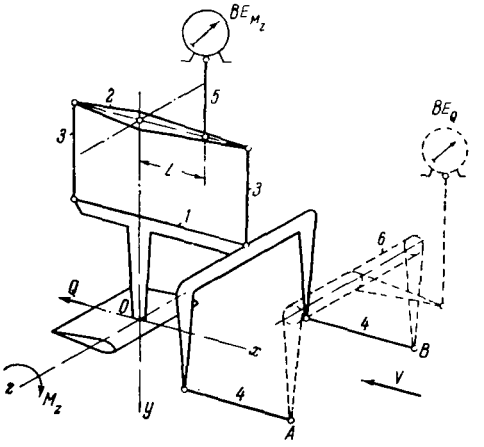

FIGURE 6.9. System whose instantaneous axis of rotation coincides with Oz.

Frame (1), which rigidly supports the model with the aid of streamlined struts (2), is suspended on three-step hinges from four rods AC, $A'C'$, BD, and $B'D'$, whose prolongations intersect at O. This point is the intersection of the three instantaneous axes of rotation, which coincide with the x-, y-, and z-axes, about which the frame with the model can turn through small angles δ_α, δ_β and δ_γ. These angles are transmitted as measurement displacements to the balance elements BE_{M_z}, BE_{M_y} and BE_{M_x}, connected to the frame by three rods.

A simple two-dimensional system with instantaneous center of rotation in the model and with mutually perpendicular links is shown in Figure 6.9. The floating frame (1) is hinged by parallel rods (3) to beam (2). In the direction parallel to the x-axis, the frame is connected to the fixed points A and B by two rods (4), located at either side of the test section of the wind tunnel in the xz plane.

Beam (2) is connected by rod (5) to a balance element BE_{M_z} located at distance l from the axis of rotation of the beam. The instantaneous axis of rotation Oz of the model coincides with the intersection of the vertical plane passing through the axis of rotation of beam (2), with the horizontal plane containing rods (4). The pitching moment M_z acting on the model is taken up by beam (2) and transmitted to the balance element as load $N_{M_z} = M_z/l$.

If points A and B are not fixed, but form the ends of a crank lever (6), as shown by broken lines, the frame with the model has an additional degree of freedom in translational motion along the x-axis, permitted by rods (3) of the parallelogram. When lever (6) is connected to balance element BE_Q, we obtain a system with two degrees of freedom, which permits us to measure simultaneously and independently the moment about the z-axis and the drag Q.

Combined moment-force mechanisms. Among the designs of wind-tunnel balances there exists a group of mechanisms which are intended for simultaneous and independent measurements of coplanar forces and couples. These mechanisms do not require measuring hinges on the model.

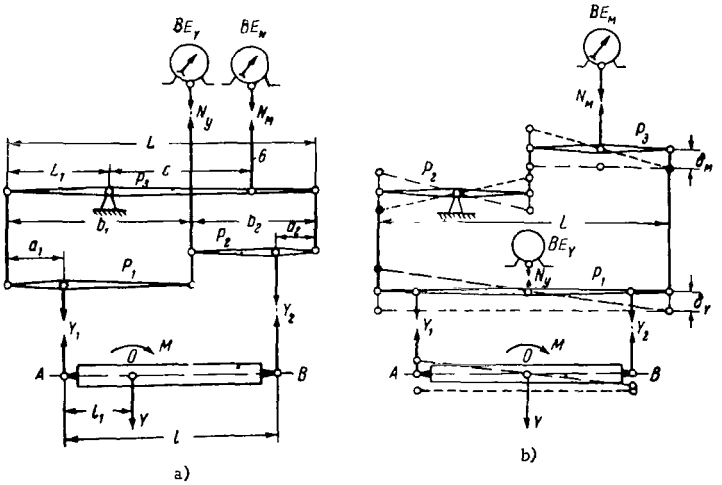

FIGURE 6.10. Lever systems for measuring forces and moments.

Figure 6.10 shows lever systems with two degrees of freedom, developed by the author from original designs of wind-tunnel balances by G. M. Musinyants.

The system shown in Figure 6.10a consists of a beam P_3 supported on a fixed hinge, and two adding levers P_1 and P_2, whose outer ends are suspended by rods from beam P_3, their inner ends being connected by a rod to balance element BE_Y. Beam P_3 is connected to scale element BE_M. The lengths of these members are shown in the figure.

Let the link AB, connected by vertical rods to levers P_1 and P_2, be acted upon by a vertical force Y passing through O and a couple M. The loads acting on the levers are then respectively

$$Y_1 = Y\frac{l-l_1}{l} - \frac{M}{l}; \quad Y_2 = Y\frac{l_1}{l} + \frac{M}{l}.$$

The loads acting on balance elements BE_Y and BE_M are

$$N_y = (Y_1 + Y_2)i = Yi, \tag{a}$$

$$N_M = Y\frac{1-i}{c}\left(L\frac{l_1}{l} - L_1\right) + M\frac{1-i}{lc}L, \tag{b}$$

where $i = a_1/b_1 = a_2/b_2$ is the transmission ratio of levers P_1 and P_2.

In order that the load N_M on balance element BE_M be independent of the force Y, it is necessary and sufficient to place the origin of the balance coordinate system at a point 0 between A and B so that the condition:

$$\frac{L}{L_1} = \frac{l}{l_1}$$

is satisfied.

In this case, when link AB rotates about 0, the inner ends of levers P_1 and P_2, which are connected to balance element BE_Y, remain stationary and

$$N_M = M\frac{1-i}{c}\frac{L}{l}.$$

The link AB is usually the floating frame of the balance.

An example of the use of the combined system in three-component balances is shown in Figure 6.11. To increase the sensitivity of drag measurements, the floating frame is supported on two antiparallelograms. The upper rods of the antiparallelograms are connected to levers P_1 and P_2 of the combined system. This permits Y and M_z to be measured independently by balance elements BE_Y and BE_{M_z}. In order to eliminate the effect of drag on the pitching moment, a compensating lever P_4 is used (see p. 344).

In the second lever system of G. M. Musinyants (Figure 6.10b) the link AB is connected by rods to an equal-arm lever P_1 whose fulcrum is suspended by a rod from balance element BE_Y. Two further equal-arm levers are provided: lever P_2 with a fixed fulcrum and lever P_3 whose fulcrum is suspended by a rod from balance element BE_M. Under the action of the force Y the link AB undergoes a translational displacement δ_Y as shown by broken lines in Figure 6.10b. Levers P_2 and P_3 turn about their fulcrums and transmit only the force $N_Y = Y$ to balance element BE_Y. Under the action of the moment M, the link AB rotates about O, levers P_1 and P_2 turn about their fulcrums, and lever P_3 is displaced parallel to itself over a distance δ_M, transmitting a force $N_M = 2M/L$ to balance element BE_M

Figure 6.12 shows a six-component wind-tunnel balance consisting of three-dimensional levers with two-step hinges /6/. The three-dimensional element (Figure 6.12a), like the two-dimensional mechanisms described above, makes possible measurements of the vertical force passing through a given point and the moment about this point. It consists of two plane levers: the equal-arm front lever P_1 and the one-arm back lever P_2, both rigidly interconnected. The axis of rotation of the three-dimensional lever passes through the fixed support O_2 and the hinge O_1 which is connected by rod T_1 to balance element BE_Y. Rod T_1 lies in the vertical plane of rods AC and BD through which the force Y and the couple M are transmitted to lever P_1.

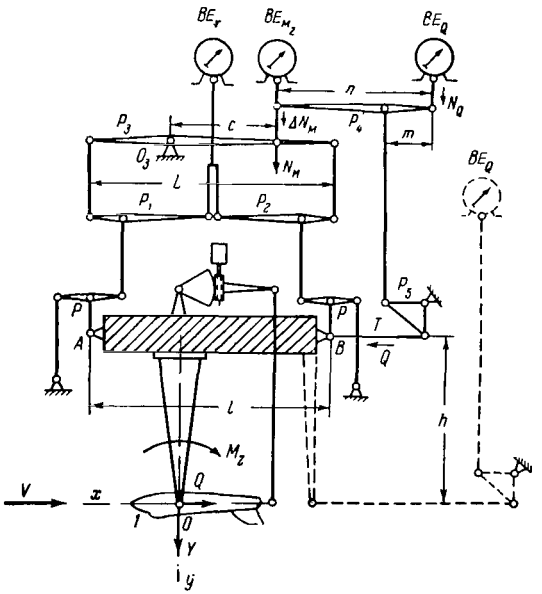

FIGURE 6.11. Three-component wind-tunnel balance using combined moment-force mechanism.

The vertical plane containing rod T_1 and support O_2 is perpendicular to the plane $ACDB$. The force Y is taken up by rod T_1 and transmitted to balance element BE_Y. The moment is taken up by rod T_2 which is connected to balance element BE_M. In this way the balance elements are acted upon by the forces $N_y = Y$ and $N_M = M/a$, so that the mechanism permits the force and the moment to be measured independently.

Mechanisms with "hydrostatic" pairs. Outside the USSR, wind-tunnel balances are widely used in which the forces are resolved into components with the aid of kinematic pairs based on hydrostatic principles. The weight of the moving element and the load applied to it are taken up by the pressure of oil or air. Pressurized air or oil is circulated between the surfaces of the moving and the stationary links of the pair; dry friction

between two solid surfaces is thus replaced by friction between a liquid and a solid surface. Surfaces of suitable shape can provide

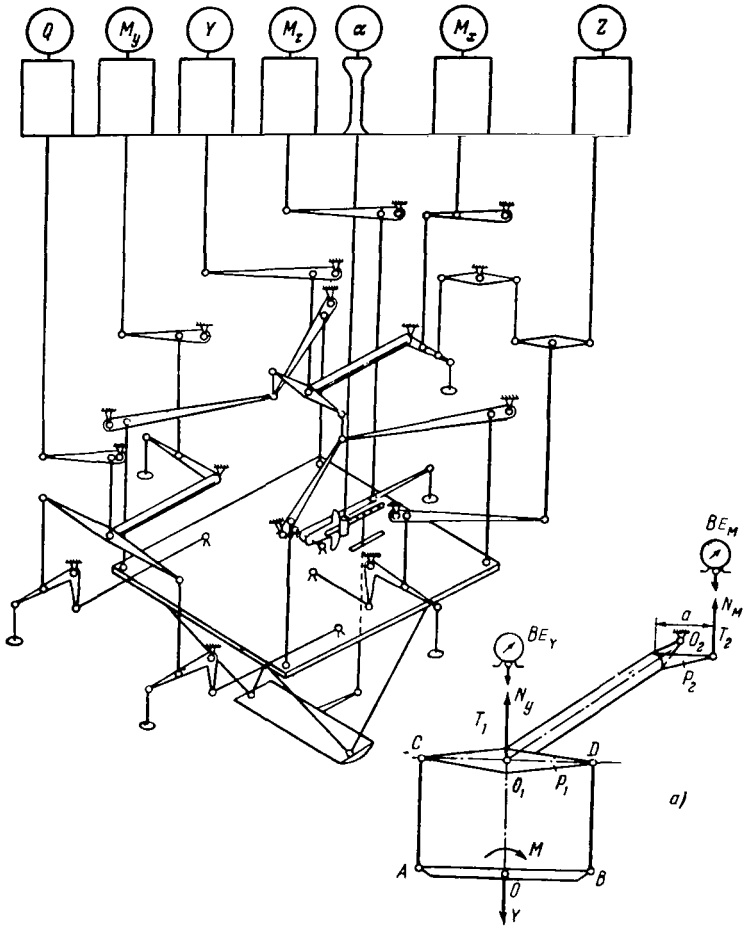

FIGURE 6.12. Six-component wind-tunnel balance with three-dimensional mechanisms.

those degrees of freedom of the moving link which correspond to the directions of the measured components of the force and the moment. By connecting in these directions the link to balance elements, we can measure the components. Since the frictional force between a solid body and a liquid is proportional to the velocity of the body, while the balance element measures the force at the instant when the body is stationary, friction in the "hydrostatic" pair is very small.

Figure 6.13 shows kinematic pairs providing two degrees of freedom (translation along, and rotation about an axis perpendicular to the plane of the paper), and three degrees of freedom (rotation about three coordinate axes passing through O). In the pair shown in Figure 6.13a only translational displacement is normally used for measuring the force component parallel to the cylinder axis.

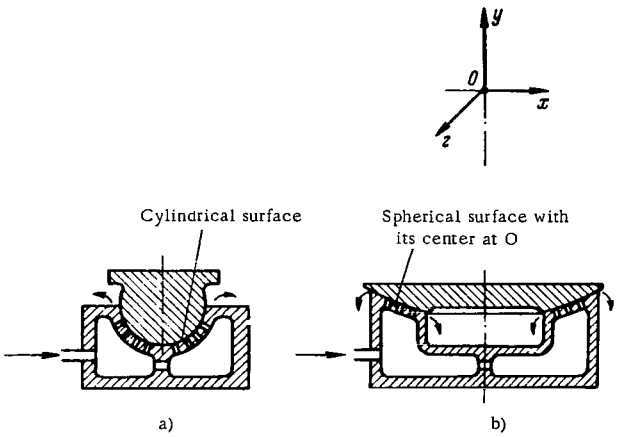

FIGURE 6.13. "Hydrostatic" pairs. a — with two degrees of freedom ; b — with three degrees of freedom.

Compensating mechanisms. In order to prevent the moment from affecting the measurement of forces, the balance element BE_M in many designs of wind-tunnel balances is placed on a floating frame as shown in Figure 6.4a. When the balance elements are located on a stationary base instead, maintenance, and in some cases also the design of the balance , can be simplified. However, when the balance elements are located on "ground", it becomes necessary to compensate the additional force acting on the floating frame in the direction of the link rod of the balance element BE_M

For instance, if in the system shown in Figure 6.4a we transfer the balance element to "ground", as shown in Figure 6.4b, rod T_1, which connects lever P_4 to the balance element BE_{M_z} will also take up part of the vertical load, unloading rods AC and BD. In order to direct this part of the load to balance element BE_Y, a compensating lever P_6, having the same transmission ratio as levers P_1 and P_2, is provided.

Figure 6.14 shows a three-component wind-tunnel balance /3/. For measuring drag and lift, the floating frame F_1 has two degrees of freedom in translation, provided respectively by the parallelogram mechanism $ACDB$ and the adding mechanism consisting of levers P_1 and P_2. For measuring the moement M_z, a second floating frame F_2 is connected to F_1 by a pyramidal support whose instantaneous center of rotation lies on the z-axis. Since the balance element which measures the moment is

installed on the "ground", the external forces acting on floating frame F_1 consist, in addition to the aerodynamic forces, also of the force M_z/l in the horizontal rod EF connecting the "moment" frame F_2 to balance element BE_{M_z}.

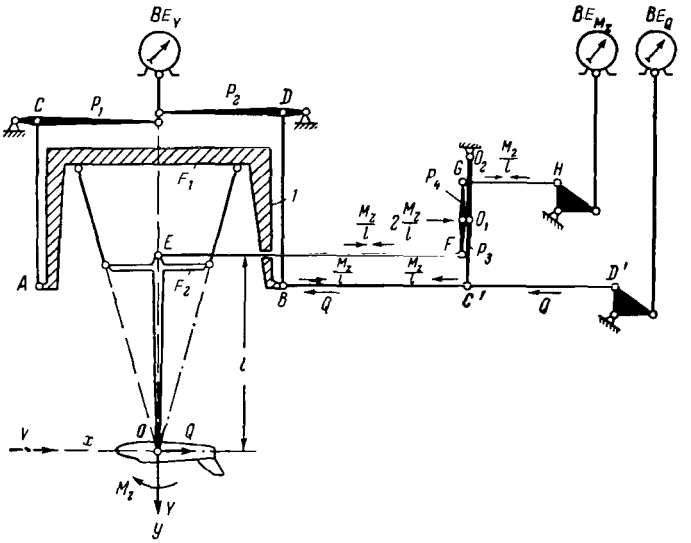

FIGURE 6.14. Removing the reaction moment from the balance element BE_{M_z}.

Part BC' of the horizontal rod BD', connecting frame F_1 to the system for measuring the force Q, is acted upon by a load $-Q + M_z/l$. The compensating device used in this system differs from the previous one (Figure 6.4b) in that the compensating lever P_3 has a fixed fulcrum. An equal-arm lever P_4 is hinged at the center O_1 of lever P_3. One end of lever P_4 is connected to rod EF, and the other end to balance element BE_{M_z} (through an intermediate crank lever). A force $2M_z/l$ acts on lever P_4 at O_1. The moment due to this force, about the fixed support O_2 of lever P_3, is balanced by the moment due to the force acting in part BC' of rod BD'. Thus when only a couple acts on the model, the force in CD' is zero and balance element BE_Q does not take up any load.

In wind-tunnel balances without measuring hinges on the model, where the measured moments are transmitted to the balance elements through a floating frame, the latter is in addition to the components of the aerodynamic moment, also acted upon by the moments due to the reactions in the hinges of the links connecting the frame with the balance elements. The effect of the reaction moments on the balance indications can also be elmininated by compensating devices.

Thus, for instance, in three-component wind-tunnel balances (Figure 6.11) the drag is taken up by the horizontal rod T, connecting the floating frame to the balance elements through crank lever P_5. Rod T

is connected to the floating frame at a distance h from the x-axis. Hence, in addition to the moment M_z the frame is also acted upon by a counter-clockwise moment due to the couple Qh. The lower hinge of the rod connecting lever P_3 to balance element BE_{M_z} is loaded by the force

$$N_M = (M_z - Qh)\frac{1-i}{c}\frac{L}{l}.$$

To balance the moment Qh, crank lever P_5 is connected by a rod to the fulcrum of a compensating lever P_4 whose ends are hinged to rods connected to balance elements BE_{M_z} and BE_Q. If the arms of lever P_5 are equal, lever P_4 transmits to balance element BE_{M_z} an additional load

$$\Delta N_M = Q\frac{m}{n}.$$

The total load acting on balance element BE_{M_z} is

$$N'_M = N_M + \Delta N_M = (M_z - Qh)\frac{1-i}{c}\frac{L}{l} + Q\frac{m}{n}.$$

Thus, when the compensating lever P_4 has a transmission ratio $m/n = (1-i)Lh/cl$, the effect of the drag Q on the measurement of M_z can be eliminated. The loads on the balance elements will then be

$$N'_M = \frac{1-i}{c}\frac{L}{l}M_z,$$
$$N_Q = \left(1 - \frac{m}{n}\right)Q.$$

If the direction of rod T coincides with the x-axis, as shown in Figure 6.11 by the broken line, then $h = 0$, $m/n = 0$, and no compensating lever is necessary.

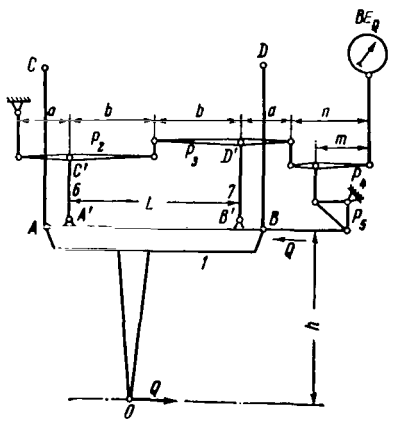

FIGURE 6.15. Compensating the reaction moment by applying to the floating frame an opposing moment.

In the system shown in Figure 6.11, the influence of the reaction moment Qh is eliminated by adding a load to balance element BE_{M_2}. An alternative method is to apply to the floating frame a moment opposed to the reaction moment (Figure 6.15). The floating frame is suspended at A and B from a lever system (not shown) which measures the vertical load and the moment while at A' and B' it is connected by rods to levers P_2 and P_3 which have the same arm ratio a/b. Lever P_3 takes up part of the load due to the force Q, which is transmitted by means of lever P_4, having a transmission ratio m/n, and equal-arm crank lever P_5. This load, equal to Qm/n, causes equal and opposite forces in rods $A'C'$ and $B'D'$ which cause a moment $Qm(a+b)L/bn$ to act on the floating frame. This moment is opposed to the reaction moment Qh. Hence, if the transmission ratios of levers P_2, P_3, and P_4 are such that

$$\frac{m}{n}\,\frac{(a+b)}{b}\,L = h,$$

the reaction moment will be fully compensated.

Elements of wind-tunnel balances

The main elements in the described mechanisms of wind-tunnel balances are levers, hinges, and rods. Sensitivity and accuracy of the balances depend on the design of these elements, which are very similar to those used in ordinary balances. The main design requirements are:

1) small friction during measurement displacements;

2) high sensitivity;

3) high accuracy of the transmission ratios of the levers in the adding and "moment" systems;

4) rigidity of all levers, rods and frames; this is necessary for minimum distortion of the system under the action of aerodynamic loads;

5) adjustability of the fixed supports, to permit elimination of systematic errors due to initial incorrect installation of the system.

The first two requirements are best met by lever systems employing knife edges and elastic hinges. Ball bearings should be avoided, but are sometimes used in highly loaded supports of crank levers. In this case the effects of friction are reduced by using large lever arms; this decreases the work done by friction when the levers undergo angular displacements.

Knife edges. Figure 6.16 shows two types of knife edges which are very often used in wind-tunnel balances. A double knife edge (Figure 6.16a) ensures high stability of lever (1) in relation to its longitudinal axis, and is generally used as fixed or main support of a lever. The second design (Figure 6.16b) is employed for connecting a lever with a rod. In both types of hinges, the working edges of the knives are obtained by milling surfaces forming angles of 50 to 60° in cylindrical rods (2). Pads (3) are self-adjustable along pins (4) which are perpendicular to the knife edges.

The other degrees of freedom of the pads, necessary for aligning the knife edges with the notch in the pad in case of manufacturing errors,

are provided by radial and transverse clearances e_1 and e_2 of 0.2 to 0.3 mm. To prevent lateral friction between knife edge and pad, the lateral surfaces of the latter have conical protrusions whose peaks press against the knife edge, while the end surfaces of the latter are milled at right angles to the edge (Figure 6.16a). Alternatively the lateral surfaces of the pad are flat while those of the knife edge are formed by two planes each, whose intersections are coplanar with the edge and inclined to it at angles of 60 to 75° (Figure 6.16b).

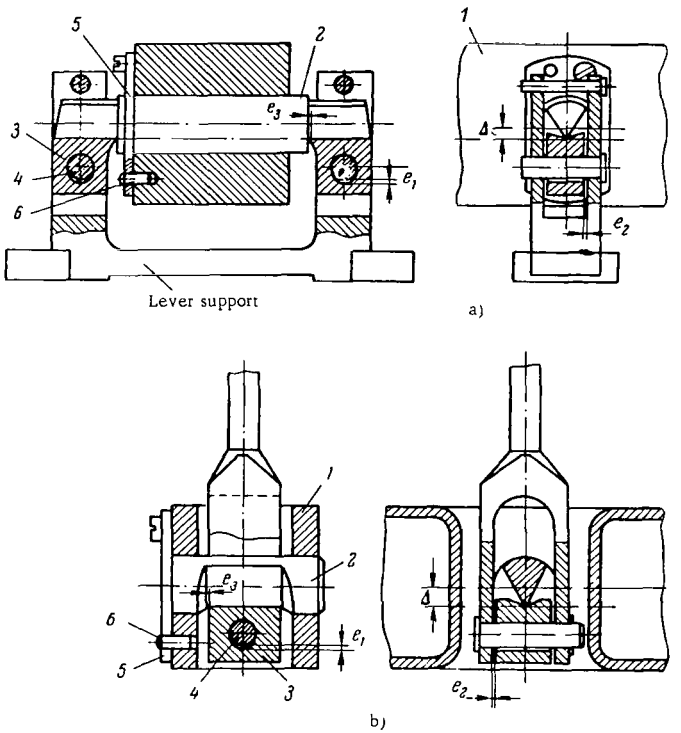

FIGURE 6.16. Knife edges. a — for main support of lever; b — for connecting lever and rod.

In order to prevent the knife edge from sticking between the pads, an axial clearance e_3 of 0.2 to 0.3 mm is provided. The knife edge is fixed to the lever with the aid of integral flange (5). This design permits adjustment of the lever-arm lengths by turning the knife edge about the axis of its cylindrical part, which is at a distance Δ from the edge. After adjustment the knife edge is fixed in the lever with the aid of pin (6).

Figure 6.17 shows another design of a knife edge used in fixed lever supports. The triangular knife edge (1), which is pressed into lever (2), is supported on a split pad consisting of two parts (3) and (4), interconnected by rings (5) located on projections of said parts. The opening between parts (3) and (4) contains, perpendicular to the knife edge,

a roller (6) on which pad (3) can turn. Rotation of the pad about an axis, perpendicular to the axis of knife edge (1) and roller (6), is made possible by the cylindrical tail of part (4) being inserted into a hole in support (7). Axial displacement of the knife edge beyond the permitted clearance e_3 is prevented by plate (8), fixed by screws to pad (3).

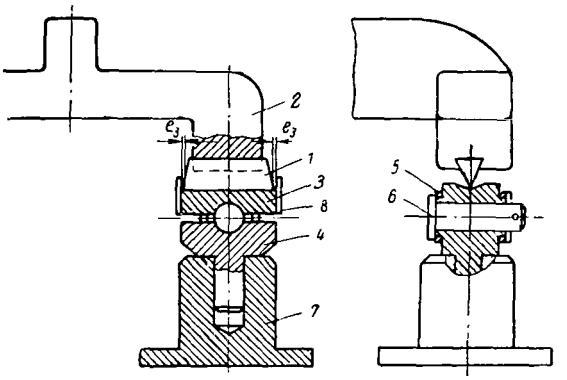

FIGURE 6.17. Knife-edge support.

The knife edge and pad are made from case-hardened alloy steels which are heat-treated. The pads have a Rockwell hardness of 63 to 65.

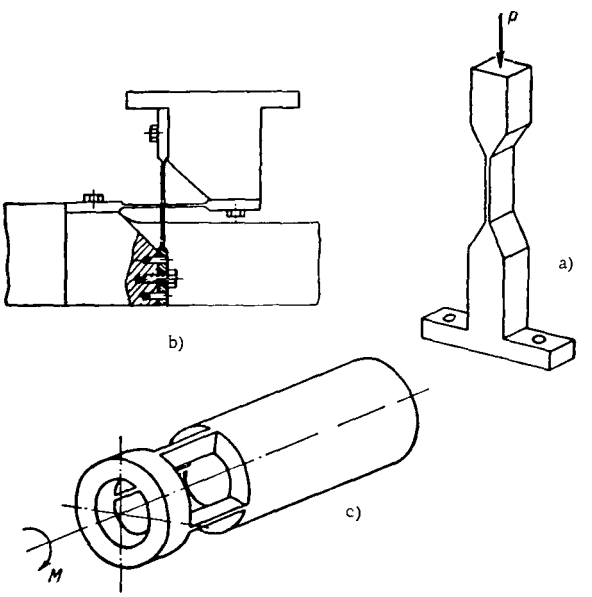

FIGURE 6.18. Single-stage elastic hinges: a — without fixed center; b, c — with fixed center.

To prevent the knife edges from leaving marks on the pad surfaces, the hardness of the former is 2 to 4 degrees less than that of the pads. The case-hardened layer has a thickness of 0.8 to 1 mm. Pads and knife edges can also be made from noncarburized steel and have equal hardness. The load acting on hardened knife edges is usually 200 to 400 kgs per cm of edge length.

The drawback of knife edges is that they can take up only positive loads which force the edge onto the pad. When negative loads have also to be measured, the balances are preloaded by counterweights. These counterweights are calculated in such a way that at the maximum possible negative aerodynamic forces the loads on all hinges will still be positive. Transverse loads on the knife edges are permitted only within small limits (of the order of a few % of the normal load).

Elastic hinges. Elastic hinges are plates which have low bending rigidity in one plane but a considerable rigidity in a plane perpendicular to the first.

The advantages of elastic hinges over knife edges are: 1) simplicity of manufacture, 2) high reliability in operation and ease of obtaining hinges with two degrees of freedom, required for three-dimensional measurement systems, 3) complete absence of friction, 4) capability of taking up loads of different signs.

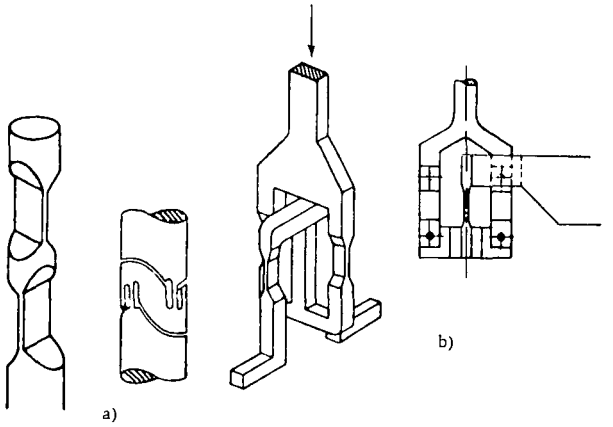

FIGURE 6.19. Two-step elastic hinges.

There are two types of elastic hinges: hinges without fixed centers and hinges with fixed centers. In an elastic hinge without fixed center (Figure 6.18a) the position of the instantaneous center of rotation depends on the deformation of the hinge; such hinges are therefore used for fixing rods to levers and floating frames only when the displacements of the latter are very small. Hinges without fixed centers cannot take up transverse loads.

Hinges with fixed centers consist of two or more plates intersecting at right angles (Figure 6.18b and c). The hinge shown in Figure 6.18c is made by milling side openings into a hollow cylinder. Under the action of the moment applied to it, the frontal part of the cylinder turns, in relation to the rear part, by a small angle about the axis of the cylinder. Hinges with fixed centers are used as principal supports of levers and can take up considerable transverse loads.

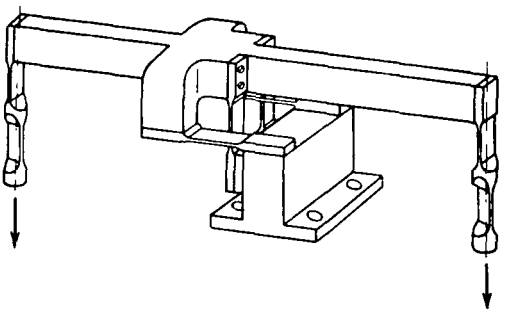

FIGURE 6.20. Lever on elastic hinges.

The design of elastic two-step hinges is shown in Figure 6.19. A two-step hinge can be made by machining mutually perpendicular planes into a rod (Figure 6.19a). In this widely used design the instantaneous axes

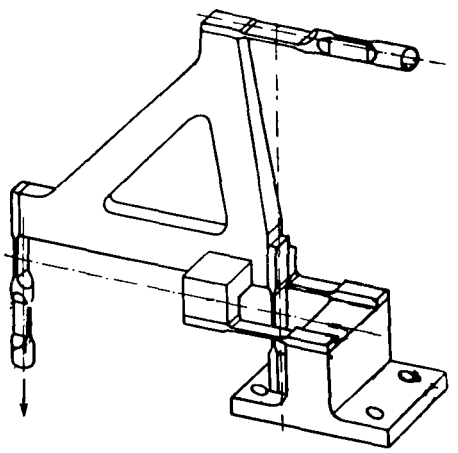

FIGURE 6.21. Crank lever on elastic hinges.

of rotation in the two planes do not coincide, but this is usually not important. Rods with such two-step hinges at both ends are suitable for interconnecting

levers with nonparallel axes of rotation, or with parallel axes of rotation when, due to manufacturing errors, the rods are slightly inclined to the planes of rotation of the levers.

Figures 6.20 and 6.21 show levers on elastic hinges. The principal hinges, which ensure the required transmission ratios (for instance, in lever adding systems), are very often knife edges, while elastic hinges are used for those links of the system which need not have accurate transmission ratios, since they are adjusted with other links or parts of the system.

Elastic hinges are milled from high-alloy steel rolled sections. Machining is carried out after heat treatment designed to provide a yield stress of about 80 kg/mm^2. After this heat treatment steel can still be machined. In order to avoid stress concentrations, transitions from thin to thick sections must have fillet radii not smaller than the plate thickness. The maximum permissible load must not exceed 0.3 to 0.4 times the yield stress. Elastic hinges made from flat spring steel are simpler to manufacture but less reliable, since it is difficult to fit them without clearances. Reliable fixing is the main requirement for elastic hinges. Experimenters sometimes waste much time finding out why the accuracy in wind-tunnel balances is reduced, while the only reason is small clearances in some of the connections of the elastic hinges.

The main characteristic of the elastic hinge is its rigidity or stability. When the hinge is turned the bending stresses in the material cause a restoring moment proportional to the angle of rotation. When this angle is very small, the restoring moment is much higher than the frictional moment of an equivalent knife edge. Hence, these hinges are best used in those elements of lever systems of wind-tunnel balances, which take up the highest loads, and thus have the smallest displacements. If necessary, elastic hinges can be used when the angles of rotation are large (up to several degrees of an arc); their extreme rigidity is then compensated by inserting into the system unstable links, for instance, of the type shown in Figure 6.43.

Hermetically sealed openings for rods. In several designs of supersonic wind tunnels the floating frame of the balance is inside a hermetically sealed chamber surrounding the test section, while the lever system of the balance is outside the chamber. In order to lead out the force-transmitting rods from the chamber, packings are used which prevent entry of air into the chamber from the atmosphere. A reliable packing, which frees the rod from the action of the difference of pressure in the chamber and the surrounding atmosphere, is shown in Figure 6.22. Packings are made from multi-ribbed metal membranes (bellows) which have a relatively small rigidity. Similar packings are sometimes used to lead out parts of the model support from the test section of the wind tunnel.

Model supports. According to the method of connecting the model to the balance system we distinguish between flexible supports (wires or tapes) and rigid supports (stands or struts). Wire supports, first used by Prandtl in wind-tunnel balances of his design, are still used in some low-speed wind tunnels. Many wind-tunnel balances with wire supports have no floating frames, since the wires (or tapes) themselves, when tensioned by counterweights, can serve as links of the mechanism for resolving the forces into components.

The principle of measuring forces, used when the model is flexibly supported, is illustrated in Figure 6.23. The vertical force Y is directly

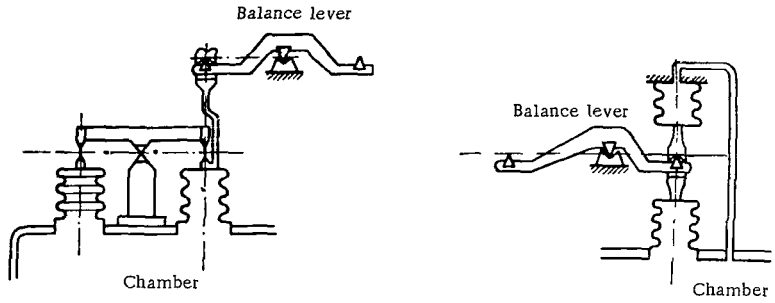

FIGURE 6.22. Hermetically sealed rod outlets.

taken up by wires (1) and (2), pre-tensioned by counterweights G_1 and G_2. When wires (4) and (5) are inclined at angles of 45°, the tension in wires (2) and (3), due to the counterweight G_2, is $G_2\sqrt{2}/2$. The change in tension in wire (3), which is measured by balance element BE_Q, is equal to the drag Q of the model.

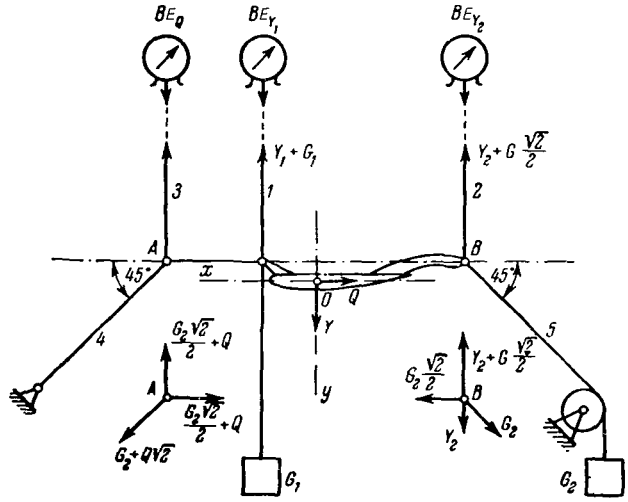

FIGURE 6.23. Resolving a force into components with the aid of wire supports.

The three-strut support (Figure 6.24) is most widely used for fixing the model to the floating frame of the balance in a subsonic tunnel. The parts adjacent to the model have the shape of symmetrical airfoils. In order to reduce the drag of the struts and increase the measurement accuracy, those parts which are farthest away from the model are covered with shrouds secured to the wind-tunnel walls. The shroud of the trailing

support, which moves in the flow direction when the angle of attack of the model is altered, has a large clearance in relation to the strut or is moved with the aid of a servo mechanism along the tunnel wall in such a way that the clearance between the support and the shroud remains constant.

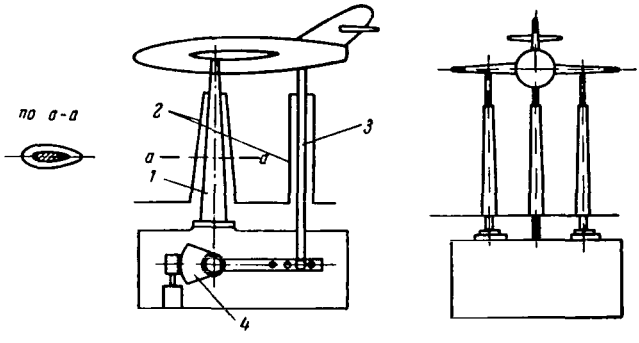

FIGURE 6.24. Three-strut support devices. 1 — leading strut; 2 — shrouds; 3 — trailing strut; 4 — mechanism for altering angle of attack.

At large flow velocities, interference between the supports and the model increases, but its influence is difficult to determine. At transonic velocities the additional blockage of the tunnel by struts and shrouds is very serious, and may lead to premature choking of the tunnel. Shocks at the unshrouded parts of the struts cause additional drag whose magnitude varies considerably even with small changes in flow velocity.

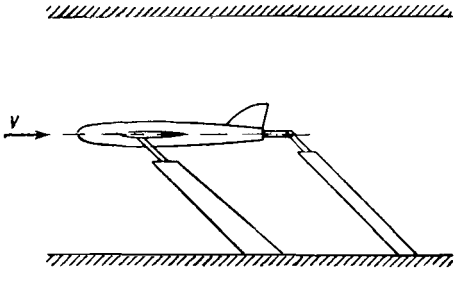

FIGURE 6.25. Arrow-type struts.

The degree of tunnel blockage, the additional drag, and the effect of the struts on the flow around the model can be reduced by the use of arrow-type struts (Figure 6.25) or arrow-type tape supports.

It is also possible to fix models of rockets or airplanes with short wings on single rigid arrow-type struts. The angle of attack of the model is in this case altered with the aid of a rod inside the streamlined strut (Figure 6.26).

A serious drawback of wind-tunnel balances with strut supports is the reduced accuracy of measuring side forces and heeling moments.

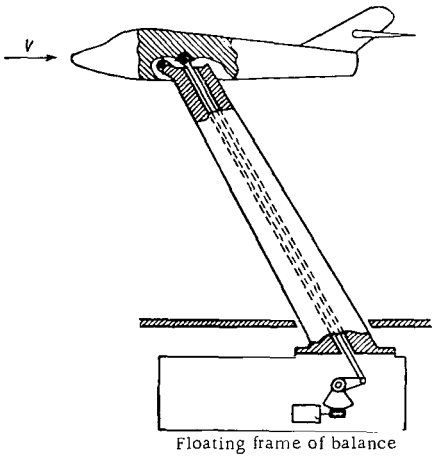

FIGURE 6.26. Model fixed to single arrow-type strut

A small asymmetry of the supports, a small flow inclination, or non-symmetrical shocks cause a transverse force to act on the strut.

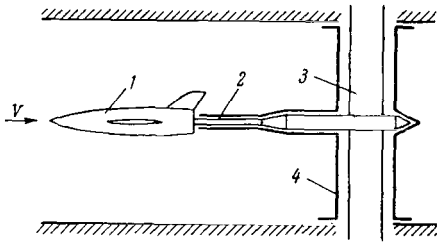

FIGURE 6 27. Cantilever support. 1 — model; 2 — cantilever support; 3 — strut; 4 — shroud.

This force, taken up by the balance element measuring the side force, also causes a moment about the x-axis of the balance, which is taken up by the balance element measuring the heeling moment M_x on the model. It is not always possible to eliminate completely the additional loads taken up by the supports at large flow velocities.

The perturbations caused by the struts at the sides of the model distort the flow pattern near the model at supersonic velocities in a way that cannot practically be taken into account. Hence, in a supersonic wind tunnel the model is installed with the aid of a cantilever tail support (Figure 6. 27). Downstream, the support is rigidly fixed to a strut mounted at the rear of the test section, where its presence does not affect

the flow in the test-section where the model is installed. This installation is particularly suitable for models of modern rockets and airplanes having blunt tails. In mechanical wind-tunnel balances, which are placed outside the test section, supports and struts must be shrouded.

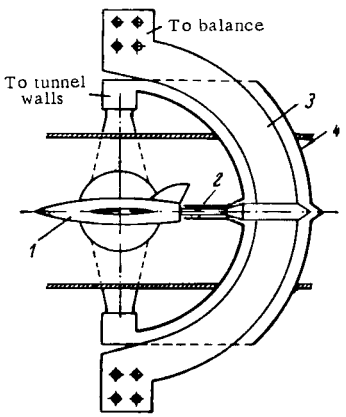

FIGURE 6.28. Semicircular strut. 1 — model; 2 — cantilever support; 3 — semicircular strut; 4 — shroud.

A good system of supports in a supersonic wind tunnel is shown in Figure 6.28.

Model (1) is fixed at its tail to cylindrical cantilever support (2), which is installed in the central part of strut (3). The latter is shaped like an arc of a circle whose center is at the origin of coordinates of the balance . The tail support and the strut are covered by shroud (4), which turns together with the strut when the angle of attack of the model is altered. A servo device, which synchronizes the rotation of strut and shroud, permits a constant small clearance to be maintained between the strut, which is connected to the balance , and the shroud, which is connected to the tunnel walls. This design permits the cross section of the shroud to be reduced to a minimum.

The minimum sections of strut and tail support are determined from their deformations. Under no circumstances must the deflected support touch the shroud since otherwise part of the aerodynamic forces would be taken up by the shroud and the balance would give false indications. In order to increase the range of angles of attack, supports curved in the $x\,y$-plane are sometimes used. Curved supports serve also in model tests at different slip angles. In this case the plane of bending is perpendicular to the plane in which the angle of attack changes.

Figure 6.29 represents a simplified diagram of the balance for the 18"×20" cross-section supersonic wind tunnel of the Jet-Propulsion Laboratory of the California Institute of Technology. The floating "moment" frame of the balance , to which an arc-shaped strut is fixed, rests on a pyramidal rod system. The instantaneous axis of rotation of the floating frame coincides with the axis of the strut, about which the latter can turn on the floating frame, and with the z-axis of the balance /7/.

For load tests of airfoils in supersonic wind tunnels the model is inserted with a small clearance through the tunnel walls which can be rotated in order to maintain the clearance constant at different angles of attack. When optical observations of the flow around the model are undertaken simultaneously with the force measurements, the rotating walls are made from optical glass (Figure 6.30). Such designs are used also for measuring forces acting on half-models, i.e., three-dimensional models of wings or finned bodies which are installed on the tunnel wall in such a way that the plane of symmetry of the model coincides with the plane of the wall (Figure 6.31).

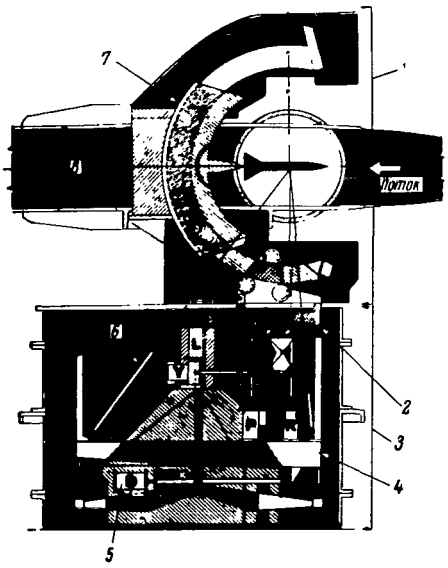

FIGURE 6.29. Six-component wind-tunnel balance with curved strut, of the California Institute of Technology. 1 — support; 2 — moment table; 3 — balance ; 4 — force table; 5 — balance element ; D — drag; S — side force; P — pitching moment; R — heeling moment; Y — yawing moment; L — lift; 6 — struts of pyramidal floating-frame suspension; 7 — shroud; 8 — wind tunnel.

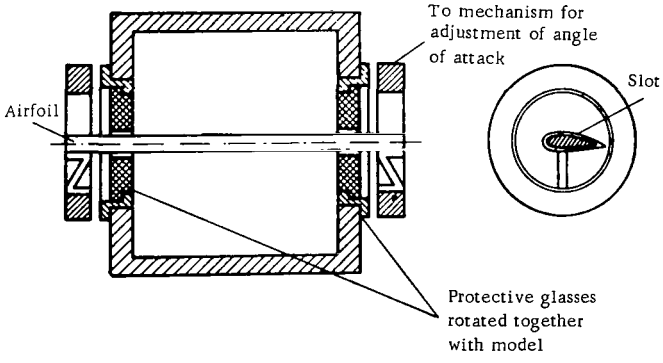

FIGURE 6.30. Airfoil mounted in a supersonic wind tunnel.

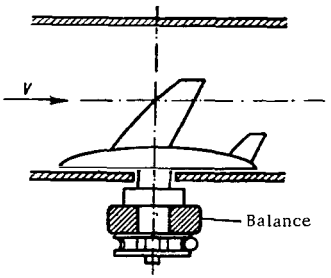

FIGURE 6.31. Half-model mounted in a supersonic wind tunnel.

§ 26. DESIGN EXAMPLES OF WIND-TUNNEL BALANCES

Wind-tunnel balances for low-speed tunnels. Figure 6.33 is a simplified diagram of a six-component wind-tunnel balance with a

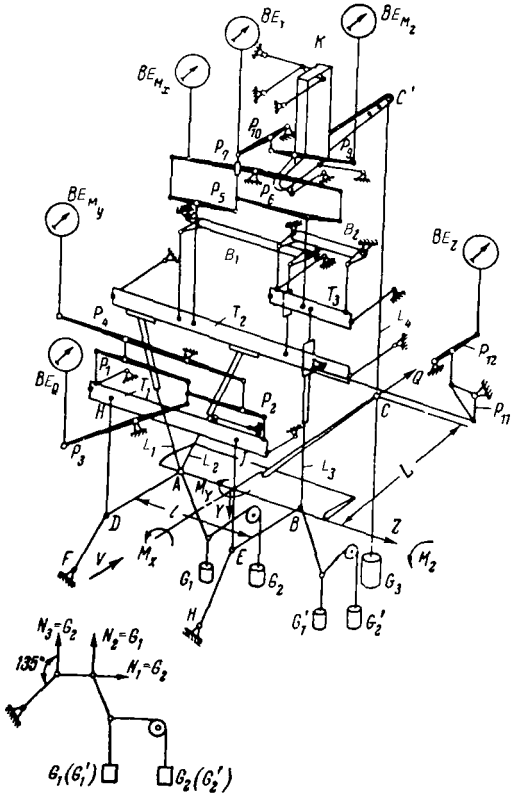

FIGURE 6.32. Six-component wind-tunnel balance with flexible model supports.

flexible tape suspension. Balances of this type are intended for tunnels with open test sections, as are installed in the subsonic tunnel of the Moscow State University. The balance is mounted on a platform supported by columns on a carriage located outside the flow. The carriage with the balance and the suspended model (Figure 6.33) is rolled onto a rotating table in the test-section floor; by turning this table about a vertical axis, the angle of yaw β of the model can be altered.

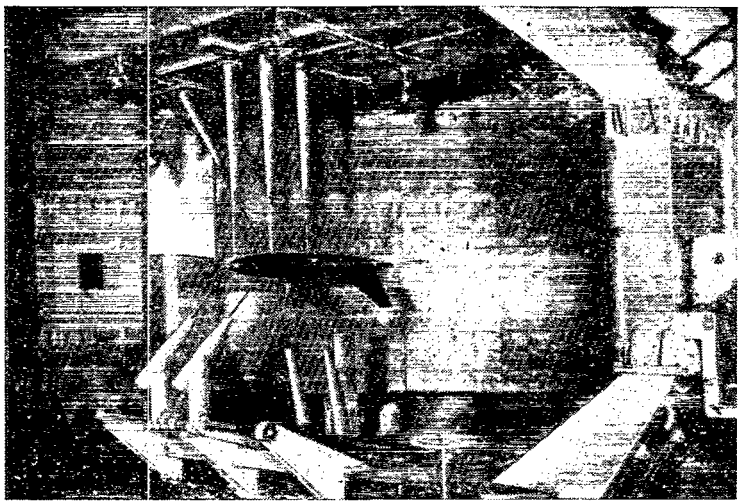

FIGURE 6.33. Carriage with wind-tunnel balance (see diagram in Figure 6.32).

The tested model is suspended from the balance at points A, B and C (Figure 6.32) in inverted position by means of a combined suspension which consists partly of rigid shrouded rods and partly of tapes of streamlined section. The origin of coordinates of the measuring system is at the midpoint of $\overline{A\ B}$ in the vertical plane of symmetry of the model. The same plane contains the tail support point C of the model. At A and B, two horizontal rods are secured which are connected at D and E to inclined tension wires, fixed at F and H, and to vertical tapes connected to the horizontal beam T_1. Counterweights G_1, G_1', G_2, G_2' and G_3 serve to pretension all tapes, as shown at the bottom of Figure 6.32. The tensions in rods AD and BE, caused by the aerodynamic forces acting on the model, are respectively $\frac{Q}{2}+\frac{M_y}{l}$ and $\frac{Q}{2}-\frac{M_y}{l}$ where l is the distance between A and B.

Since the inclined tension wires form angles of 135° with the horizontals and verticals, the total vertical force acting on beam T_1 is equal to the sum of the forces acting on rods AD and BE. The drag Q is measured by balance element BE_Q with the aid of levers P_1, P_2, and P_3. The moment, due to the

vertical forces acting on beam T_1, is equal to the moment M_y measured by balance element BE_{M_y} with the aid of lever P_4. The lift is taken up by tapes L_1, L_2, L_3 and L_4; the directions of tapes L_1, L_2 and L_3 lie in the same vertical plane. Beam T_2 takes up that part of the lift which acts at A. Since tapes L_1 and L_2 are inclined to the vertical, beam T_2 takes up also the total side force Z.

In order to transmit these forces to the balance elements BE_y and BE_z, beam T_2 is suspended from rocking lever B_1. This permits translational motion of beam T_2 in the yz plane. Rocking lever B_1 takes up all moments acting in the vertical plane on beam T_2 and prevents its rotation. Tape L_3 is fixed to beam T_3 which is suspended from rocking lever B_2 similarly as beam T_2 is suspended from rocking lever B_1.

By rearranging the points at which the tapes are fixed to beams T_1 and T_3, we can vary the length l without affecting the equilibrium conditions of the system. Beams T_2 and T_3 are connected by rods to levers P_5, P_6 and P_7 intended for measuring the lift Y and the heeling moment M_x. The vertical force acting on tape L_4 is proportional to the pitching moment M_z. At C' this tape is fixed to a rotating lever of the mechanism for altering the angle of attack (column K). The length L can be varied by fixing hinge C' to different holes in the lever. The mechanism for altering the angle of attack is suspended from lever P_9, one end of which is connected to balance element BE_{M_z}. The other end is connected to lever P_{10} of the system for measuring the lift Y.

The load transmitted to lever P_9 is equal to the vertical force in tape CC', since five horizontal rods, connecting column K to fixed points, prevent its movement except for vertical translation. Heeling moments are measured with the aid of lever P_7 which is connected by a rod to balance element BE_{M_x}. The side force Z is taken up by beam T_2 and transmitted to balance element BE_z with the aid of crank lever P_{11} and intermediate lever P_{12}.

The loads on the balance elements are

$$
\begin{aligned}
N_Q &= (Q + G_2 + G_2')\, i_x, \\
N_Y &= (Y + G_1 + G_1' + G_3)\, i_y, \\
N_Z &= Z i_z, \\
N_{M_x} &= \left(\frac{M_x}{l} + G_1 - G_1'\right) i_{M_x}, \\
N_{M_y} &= \left(\frac{M_y}{l} + G_2 - G_2'\right) i_{M_y}, \\
N_{M_z} &= \left(\frac{M_z}{L\cos\alpha} + G_3\right) i_{M_z},
\end{aligned}
$$

where $(i_x, \ldots, i_{M_z})$ are the transmission ratios of the lever systems and α is the angle of attack of the model.

Knowing the calibration coefficients $(k_x, \ldots, k_{M_z})$ the components of the aerodynamic forces acting on the model are

$$
\begin{aligned}
Q &= k_x (n_x - n_{x_0}) - Q_S, & M_x &= k_{M_x} (n_{M_x} - n_{M_{x_0}}) - M_{xS}, \\
Y &= k_y (n_y - n_{y_0}) - Y_S, & M_y &= k_{My} (n_{My} - n_{My_0}) - M_{yS}, \\
Z &= k_z (n_z - n_{z_0}) - Z_S, & M_z &= k_{Mz} (n_{Mz} - n_{Mz_0}) - M_{zS}.
\end{aligned}
$$

Here Q_s, Y_s, Z_s, M_{xs}, M_{ys}, M_{zs} are the additional components of the aerodynamic forces due to the supports, which are determined by operating the tunnel without the model, while n with the corresponding subscript is the indication of the balance element. The additional subscript 0 corresponds to the zero readings of the balance elements before the experiment, when no aerodynamic forces act on the model.

The counterweights are selected not only for tightening the suspension system but also for pre-tensioning certain balance elements to enable them to measure negative loads. For this the following inequalities must hold:

$$G_1 + G_1' + G_3 > |-Y_{\max}|,$$
$$(G_1 - G_1')\, l > |-M_{x\,\max}|,$$
$$(G_2 - G_2')\, l > |-M_{y\,\max}|,$$
$$G_3 L \cos\alpha > |-M_{z\,\max}|.$$

An example of a balance with rigid supports is the six-component wind-tunnel balance of the University of Washington (Figure 6.34). This balance,

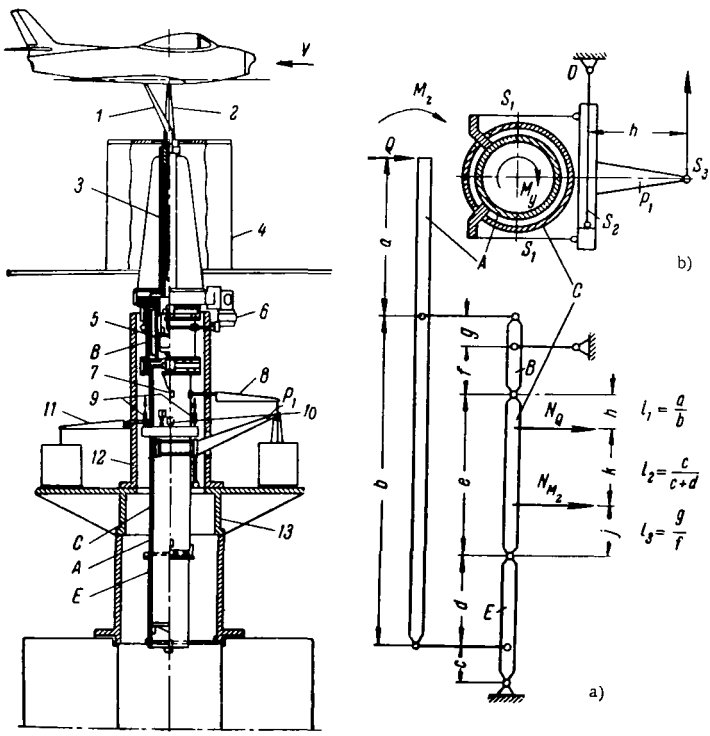

FIGURE 6.34. Six-component wind-tunnel balance of the University of Washington. 1 — movable strut; 2 — fixed strut; 3 — motor-driven lead screw for moving strut; 4 — shroud; 5 — motor for adjusting angle of attack α; 6 — motor for adjusting angle of yaw β; 7 — rod for transmission of force; 8 — crank lever to take up drag; 9 — rods to take up lift; 10 — rods to take up reaction due to heeling moment; 11 — crank lever to take up pitching moment; 12 — pedestal; 13 — electromagnetic balance element.

intended for measuring forces in a low-speed tunnel having a closed test section measuring 3.6 m×2.4 m, has electromagnetic balance elements and vertically disposed links of the lever system. The basic lever system consists of tubes A, B, C and E supported on universal elastic hinges. The inner tube A contains the support for the model and transmits the aerodynamic forces acting on the latter to the outer tubes (levers) B and E.

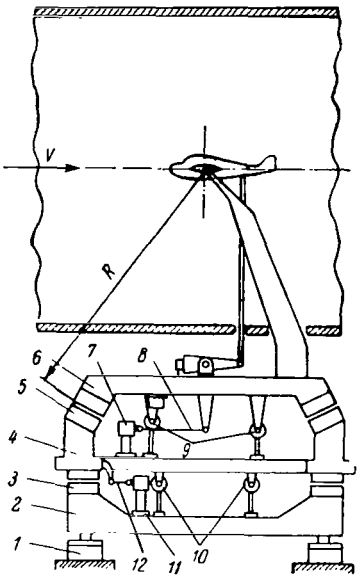

FIGURE 6.35. Six-component wind-tunnel balance on hydrostatic pairs. 1—support (dynamometer for measuring Y); 2—main floating frame; 3—flat pad; 4—intermediate floating frame; 5—spherical pad; 6—moment frame; 7 — dynamometer for measuring M_z; 8—rod; 9—dynamometers for measuring M_x and M_y; 10—dynamometers for measuring z; 11 — dynamometer for measuring Q; 12—rod.

The outer tube C is a compensating lever which permits independent measurement of Q and M_z, or Z and M_x, as illustrated in Figure 6.34a which shows the connections of the levers for measuring the components Q and M_z. Similar connections of levers in the plane passing through the vertical axis and perpendicular to the plane of the paper, enable Z and M_x to be measured. For independent measuring of all four elements it is necessary that the following relationships obtain between the transmission ratios of the levers:

$$\frac{n}{k} = i_1\left(1 + \frac{i_2}{i_3}\right),$$
$$\frac{j}{k} = i_1\left(1 + \frac{i_3}{i_2}\right) + \frac{i_3}{i_2}.$$

The magnitudes entering into the above formulas are indicated in Figure 6.34a. When these conditions are satisfied, the forces in the rods connecting the levers with the balance elements BE_Q and BE_{M_z} are respectively

$$N_Q = [(1 + i_1)\, i_3 + i_1 i_2]\, Q,$$
$$N_{M_z} = (i_2 + i_3)\frac{M_z}{b}.$$

The same conditions are necessary for the independent measurement of Z and M_x. The lift is transmitted to the balance element BE_y with the aid of rod (9).

Figure 6.34b shows the system for measuring M_y. The main lever A is connected by hinges through rods S_1 to floating lever P_1. Rod S_2, which is perpendicular to S_1, connects the lever to the fixed hinge O. A couple thus counteracts the moment M_y. One constituent force acts along rod S_2 and the other along rod S_3 which is connected to balance element BE_{M_y}.

The model support consists of fixed strut (2), mounted on tube A, and movable strut (1), which serves for altering the angle of attack by means of a motor-driven lead screw. For changing the angle of yaw, the entire support can be turned by another motor /26/.

Wind tunnel balances with hydrostatic pairs. Balances with hydrostatic pairs are used mainly in large transonic wind tunnels where the aerodynamic forces acting on the model amount to hundreds or thousands of kilograms.

The designs of the six-component balances for the wind tunnels in Modane (France) and Pasadena (U.S.A.) are based on the same principle (Figure 6.35).

The main floating frame (2) rests on three supports (dynamometers) (1). Three hydraulic dynamometers are inserted between the supports and the frame in order to measure the lift. Three flat pads (3), resting on the upper surface of the main frame, carry an intermediate floating frame (4). The surfaces of the pads and the support plates of frame (4) are polished. During measurements oil (or air) is constantly circulated between the pads and the intermediate frame, which is supported on a layer of liquid and can slide over pads (3) with negligible friction. The intermediate frame is restrained in the longitudal direction by rod (12) which connects the frame to dynamometer (11) which is fixed to the main frame and takes up the drag Q of the model. Frame (4) is restrained in the transverse direction by two horizontal rods connecting it to frame (2) via two dynamometers (10). The sum of the loads on these dynamometers is equal to the side force Z.

The upper part of the intermediate frame carries three pads (5) with spherical surfaces whose center lies on the wind-tunnel axis and is the origin of the balance coordinate system. The spherical pads carry on oil films the moment frame (6), which takes up all moments and forces acting on the model. The forces are transmitted through the intermediate frame to dynamometers (1), (10), and (11).

The moments tend to rotate frame (6) which can slide with negligible friction on pads (5). Rotation of the frame in the vertical plane passing through the tunnel axis is prevented by rod (8) which connects the moment frame to frame (4) via the dynamometer (7) which serves to measure the pitching moment M_z. Rotation of the frame in a transverse vertical plane is prevented by two horizontal rods which connect frames (4) and (6) via two dynamometers (9). The sum of the forces acting on these dynamometers is proportional to the heeling moment M_x, while their difference is proportional to the yawing moment M_y. Adding and subtracting is done outside of the balance with the aid of hydraulic measuring instruments (Figure 6.42).

In wind-tunnel balances of this type the total weight of the floating frame can reach tens of tons, but the friction in the system is so small that with this high weight the system for drag measurement is sensitive to forces of a few hundreds of grams.

The model is usually installed in the normal position and positive lift unloads the dynamometers.

§ 27. BALANCE ELEMENTS OF WIND-TUNNEL BALANCES

The main characteristics of balance elements are their load capacities, accuracy, and rapidity of response.

The transmission ratios of the levers used for measuring the separate components of the aerodynamic forces and moments are chosen in such a way that the maximum possible loads on all balance elements are approximately equal. In very small wind tunnels or in tunnels with very low gas pressures the aerodynamic forces acting on the model may amount to tens or single grams. At such small loads the transmission ratios of the levers are sometimes less than unity. In large wind tunnels, where

the forces acting on the model may reach 10 to 20 tons, the transmission ratios of the levers are very high (100 to 200).

Rapidity of response is very important in high-power wind tunnels. Rapid-action balance elements permit the test program of wind tunnels to be increased and the obtaining of experimental data to be speeded up.

The loads taken up by the balance elements can be equilibrated by counterweights, pressure of a liquid or air, elastic forces, electromagnetic or electrostatic forces. Irrespective of the nature of the equilibrating force, the balance-element indications can be either direct or by compensation, returning a movable link to its null position. Elements of the compensating type are most widely used in wind-tunnel balances because they permit higher measurement accuracy. In addition, outside energy sources are used in compensating instruments, which can be easily used for operating remote-recording devices.

The required accuracy of the balance elements is determined by the range of measured values. This range can be very wide, since the same balance may be used for testing well-streamlined bodies of revolution, having small drag and lift, and transport craft having large drag and lift at large angles of attack. At the same time wind-tunnel balances must enable us to determine relatively small advantages of one model over another.

Experience shows that these requirements are best satisfied by balances of the mechanical type, which under conditions of static calibration have limiting errors of between 1/400 and 1/2000 of the maximum load. Highest accuracy is only required when measuring drag and lift. Since the system for resolving forces into components introduces by itself an error into the measurement, mechanical wind-tunnel balances have balance elements with limiting errors from 1/500 to 1/5000 of the maximum load.

Balance elements equilibrated by counterweights

Balance elements based on the gravitational principle can be divided into lever balances and pointer balances. Equilibrium in lever balances is usually attained by compensation, the magnitude of the counterweight being changed at constant lever arm, or by moving a counterweight of constant magnitude (rider) in relation to the fulcrum of the lever. The measurement is made at the instant when the lever is in equilibrium in a given position.

Directly-indicating pointer balances equilibrate the load with the aid of one or several pendulums whose displacements are indicated by a pointer on a scale. The drawback of these balances is the large motion of the link which takes up the load. In some cases this may alter the attitude of the model, and this has to be taken into account. In addition, pointer balances are less accurate than lever balances. The limiting error in the better designs of pointer balances is about 1/1000 of the maximum load, while good lever balances can have a limiting error of less than 1/5000. Pointer balances are ordinarily used when measuring very large loads, for instance in full-scale wind tunnels where the size of the balance is unimportant. In order to reduce the displacement of the model, pointer balances sometimes have compensating devices (Figure 6.36).

Lever elements, equilibrated manually by weights or riders, were widely used in old designs of wind-tunnel balances. Simultaneous measurement of all components on a six-component balance requires many operators who communicate by sound or sight. Flow fluctuations in the tunnel always cause certain variations in the forces acting on the model; hence, manual equilibration is characterized by large subjective errors and requires much time. At the same time, lever balances belong to the most accurate measuring instruments. Automatic lever balances were therefore developed to provide rapid operation with a high accuracy. In addition, these balance elements permit transmission of the indications to remote recording devices in a simple and readily available form.

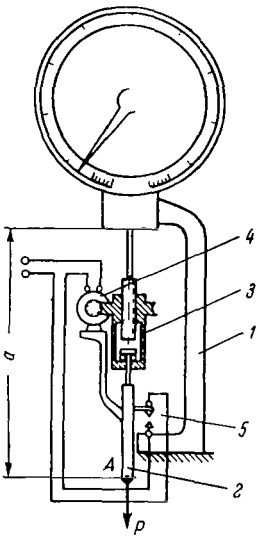

FIGURE 6.36. Displacement compensation in pointer balances. 1 — balance base; 2 — rod; 3 — screw mechanisms for adjusting rod length a; 4 — servomotor; 5 — contacts for automatic switching-in of servomotor when rod is pulled down.

The automatic balance element (Figure 6.37) consists of a lever (balance beam) (1), supported by a knife edge on stand (2). The measured force P is taken up by the knife edge on the left-hand arm of the lever. The right-hand arm has an accurate lead screw (6), by which counterweight (7) can be moved. The lead screw is connected to a reversible servomotor (5). The rotation of the servomotor is controlled by transducer (10), which reacts to displacements of the right-hand end of the lever. When the load is increased, the right-hand lever end moves upwards, transducer (10) switches in the servomotor, and the lead screw moves counterweight (7) to the right, restoring the equilibrium of the lever. At the instant of equilibrium the signal of the transducer becomes zero and the servomotor is stopped. When the load is reduced, the right end of the lever moves downward, the transducer switches in the servomotor in the reverse direction, and load (7) moves to the left until equilibrium is attained again.

At a measured load P, the number of revolutions of the lead screw, required to restore lever equilibrium, is

$$n = \frac{Pa}{Gt},$$

where t is the pitch of the lead screw, G is the weight of the counterweight, and a is the length of the left-hand lever arm. The value of n is shown by decimal counter (9), in which the digit on the extreme right usually corresponds to one tenth of a revolution of the lead screw.

The measurement accuracy is increased by using a screw with micrometric thread and by taking up clearances with the aid of springs. Oscillations of the lever are reduced by hydraulic shock absorber (8). The electric supply to the motor on the lever is through flexible wires coiled like spirals. Due to the small displacements of the points where the wires are fixed to the panel, installed near the fulcrum of the lever, the influence

of the rigidity of the wires on the sensitivity of the lever is usually negligible.

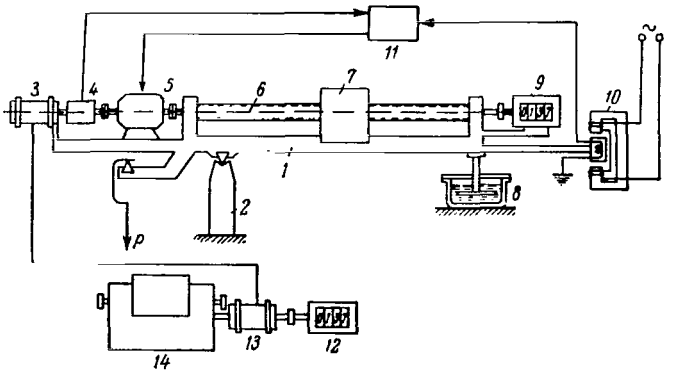

FIGURE 6.37 Automatic lever-balance element with inductive transducer. 1 — lever, 2 — stand; 3 — selsyn transmitter; 4 — feedback tacho-generator; 5 — servomotor; 6 — lead screw; 7 — traveling counterweight; 8 — hydraulic shock absorber, 9 — counter, 10 — inductive transducer; 11 — amplifier; 12 — counter; 13 — receiver selsyn; 14 — printing device.

In modern wind tunnels where the measurement data are transmitted to control cabins, selsyn servo systems are often used. Such systems consist of a selsyn transducer and a selsyn receiver, instruments which resemble miniature electric motors. The rotor of selsyn transmission (3), which has a three-phase winding, is connected to the servomotor shaft of the balance element. Under the action of a variable magnetic field, created by the single-phase a.c. in the stator of the selsyn transmitter, the rotor of the latter generates an a.c. voltage which is uniquely determined by the angular position of the rotor in relation to the stator. Under the action of this voltage, the rotor of selsyn receiver (13) in the control cabin turns to the same angular position in relation to its stator. The rotor of the selsyn receiver is connected with counter (12) and printing device (14). which records the indications of the counters of several balance elements in numerical form (see Chapter IX).

The displacement transducer forms together with the servomotor a closed-loop automatic-control system in which the control parameter is the angular position of the lever, the controlling member being the lead screw with the counterweight. There are several designs of transducers. The most widely used are inductive (transformer) and contact transducers.

The system shown in Figure 6.37 employs an inductive transducer consisting of a moving coil fixed to the end of lever (1), and located between two excitation coils wound on stationary iron cores /9/, /10/. The coil is excited from one phase of a three-phase supply. Since the coils are wound in opposite directions, they create opposed magnetic fields, which induce in the moving coil an a.c. voltage whose amplitude and phase depend on the position of the moving coil in the air gap between the stationary coils. The voltage is amplified by amplifier (11), and is fed to the rotor of

servomotor (5) which is excited by another phase of the a.c. supply. If the lever is in equilibrium and the moving coil is in a central position between the stationary coils, the voltage in the moving coil is equal to zero and the servomotor is at rest. When the equilibrium is disturbed, the moving coil is brought nearer to one of the stationary coils, and a voltage is induced. The servomotor begins to rotate, and the lead screw moves the counterweight in the direction required for restoring the equilbrium of the lever.

The automatic mechanism for controlling the servomotor and the counterweight must follow the changes in load caused by variations in flow velocity or in the angle of attack of the model. In order to reduce oscillations of lever and lead screw, the control system is equipped with flexible feedback consisting of an inductive tacho-generator mounted on the servomotor shaft.

In contrast to inductive transducers, which provide continuous speed regulation of the servomotor from zero to maximum, contact transducers cause the servomotor to attain instantaneously a finite speed. The simplest contact transducer consists of a flexible moving contact located at the end of the lever in a small gap between two stationary contacts. When the equilibrium is disturbed, the moving contact closes a circuit with one of the stationary contacts and the servomotor is switched in; the latter moves a counterweight on the beam so as to restore the equilibrium.

The drawback of balance elements with contact transducers is their tendency to cause free oscillations of the entire automatic balancing system when the sensitivity is increased. These oscillations are due to the inertia of lever, servomotor, and rotating parts, and cause the position of the counterweight on the lever to vary in relation to its static-equilibrium position. If the amplitude of the load variations is less than the permissible measurement error, these self-induced oscillations do not affect the measurements and cause only burning of contacts.

The counterweight displacements during self-induced oscillations increase with angular velocity of the servomotor but decrease with increasing resistance torque acting on the servomotor shaft after breaking contact. In addition, they depend on the degree of oscillation damping. In order not to reduce the speed of operation of the balance elements (the rapidity of equilibrating at a given load) a two-speed system is used for controlling the servomotor (Figure 6.38), which provides for a sharp reduction of the rotational speed of the servomotor immediately before the counterweight attains a position corresponding to static equilibrium of the lever, and powerful braking of the servomotor after it is switched off.

For this purpose the shaft of servomotor (5) and selsyn transmitter (8) carries an electromagnetic brake (6), consisting of an iron rotor rotating in the magnetic field of a d.c.-excited stator. When the rotor revolves (eddy) currents are induced in it. This causes a torque proportional to the rotational speed to act on the shaft. The lever has, in addition to the system of "fine" contacts (1) and (2) also a second system of "coarse" contacts (3) and (4). The gap between moving contact (3) and stationary contact (4) is slightly larger than the gap between moving contact (1) and stationary contact (2). The stator of the brake is supplied with current when contacts (3) and (4) are open. At a small imbalance of the lever, contacts (1) and (2)

are closed and the servomotor rotates slowly. At a large imbalance, the flexible plate containing contact (1) is bent and contacts (3) and (4) are closed. The winding of the brake stator is short-circuited, and the servomotor begins to rotate rapidly.

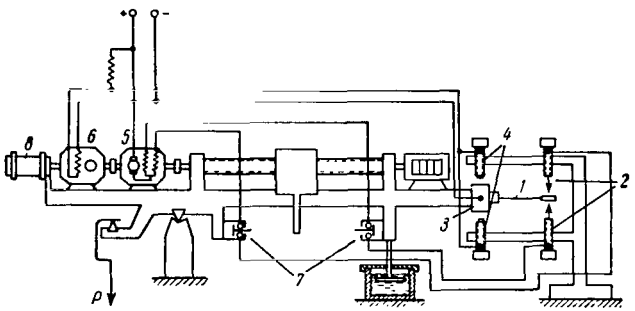

FIGURE 6.38. Automatic balance element with contact transducer. 1— moving "fine" contact; 2 — stationary "fine" contact, 3 — moving "coarse" contact; 4 — stationary "coarse" contact; 5 — servomotor; 6 — electromagnetic brake; 7 — limit switches; 8 — selsyn transmitter

Balance elements with contactless transducers can operate under conditions of vibrations and fluctuations of the measured forces, when balance elements with contact transducers lose their sensitivity due to burning of contacts. Automatic balance elements contain limit switches (7) (Figure 6.38), which open the circuit of servomotor (5) when the measured force exceeds predetermined limits.

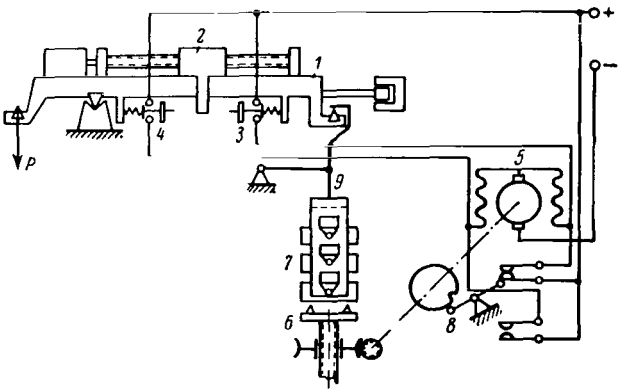

FIGURE 6.39. Automatic-loading mechanism. 1 — lever; 2 — counter-weight; 3, 4 — limit switches; 5 — servomotor for loading; 6 — moving platform; 7 — weights; 8 — change-over switch; 9— link for load suspension.

The accuracy of measuring forces on wind-tunnel balances with lever elements depends greatly on the degree of damping of the lever oscillations caused by nonsteady loads on the model. Excessive damping causes delayed opening of the "fine" contacts, especially if the contact plate is not very rigid. This causes hunting of the counterweight and leads to self-induced oscillations. When damping is very weak after the "fine" contacts open, the kinetic energy of the lever cannot be absorbed, and self-induced oscillations can occur at very small inertial overtravel of the counterweight. Hence, the damping should be chosen in such a way that after contact (1) and one of contacts (2) are opened, the kinetic energy of the lever is absorbed before it is able to close the opposite contact.

The amplitudes and frequencies of the force pulsations, caused by oscillations of the tested model and by flow fluctuations, vary with the flow velocity, the angle of attack of the model, the rigidity of the suspension device and lever system, etc. Hence the capacity of hydraulic shock absorbers of automatic balance elements is sometimes varied with the aid of electric motors during the experiment, or an electromagnetic damper is used which is switched in only when the "fine" contacts are open; this reduces the delay in contact breaking.

In order to increase the load capacity of the balance elements, the latter are equipped with auxiliary mechanisms for automatic addition of weights. A single weight balances a load corresponding to the full travel of the counterweight between the limit switches. A simplified diagram of the mechanism for weight addition is shown in Figure 6.39. When the load P on lever (1) exceeds a predetermined value, counterweight (2) moves to the right and closes limit switch (3). Servomotor (5) is switched on and lowers platform (6) with weight (7) to a predetermined height, after which the current to the servomotor is cut off by change-over switch (8), which interrupts the circuit of limit switch (3). When the platform is lowered one of weights (7) becomes suspended on link (9). When the load is reduced below a predetermined value counterweight (2) closes limit switch (4); this causes the platform to rise and take off a weight from link (9).

Pneumatic and hydraulic balance elements

Pneumatic and hydraulic balance elements usually consist of two separate instruments: a primary instrument taking up the load (dynamometer), and a secondary measuring instrument (manometer). The manometers are connected with the primary instruments by metal tubes up to 20 or 30 m long. One of the principal advantages of pneumatic and hydraulic balance elements is the simplicity of their design, which makes possible remote measurement. The simplest pneumatic measuring device is shown in Figure 6.40. The measured force P is transmitted to bell (1), which is immersed in vessel (2), filled with mercury or some other liquid. The pressure in the air space under the bell is thus raised; this increase is transmitted by a tube to U-tube manometer (3). If we neglect the wall thickness of the bell, the differences in heights of the columns of liquid

in the bell and in the manometer are respectively

$$h_1 = \frac{P}{\gamma_1 F} \text{ and } h_2 = \frac{P}{\gamma_2 F},$$

where F is the cross section of the bell, γ_1 and γ_2 are the specific gravities of the liquids in the bell and in the manometer respectively. The errors of such pneumatic dynamometers are caused mainly by irreproducibility

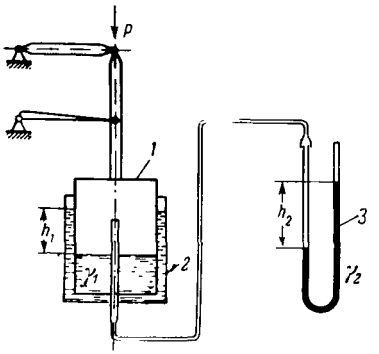

FIGURE 6.40. Pneumatic balance element. 1 – bell; 2 – vessel with mercury; 3 – manometer

of indications due to variations in the surface tension of mercury when it becomes oxidized and contaminated, and by the temperature variation of γ_1 and γ_2. The range of the measured forces is determined by the permissible height variation of the column of liquid in vessel (2), and by the permissible travel of the bell, which is related to the displacement of the model in the wind tunnel.

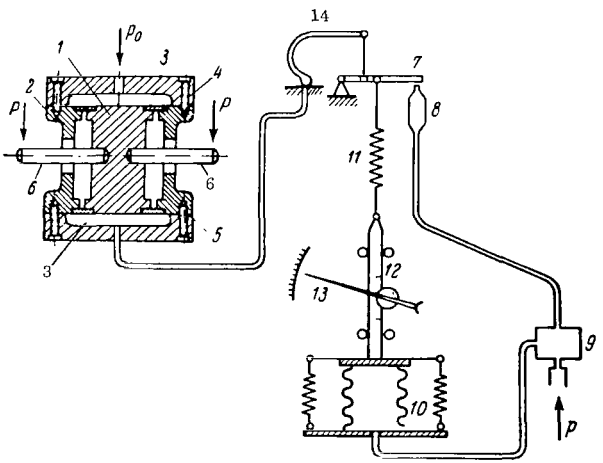

FIGURE 6.41. Hydraulic dynamometer. 1 – piston, 2 – cylinder; 3 – diaphragms; 4, 5– plates; 6 – rods taking up measured load; 7 – baffle plate; 8 – nozzle; 9 – air chamber; 10 – bellows; 11 – spring; 12 – rod with rack; 13 – pointer; 14 – Bourdon tube.

Figure 6.41 shows a system of measuring forces with the aid of a hydraulic dynamometer with a manometric spring device /11/. In contrast to other force-measuring devices, hydraulic dynamometers permit loads of several tons to be measured without intermediate lever systems of balance elements. Such hydraulic dynamometers are used in U.S. balances, in which the forces are resolved into components by means of hydrostatic pairs. In balances of this type the vertical load, which includes the total weight of the floating frame, is usually taken up by three dynamometers which carry the frame. The dynamometer consists of piston (1), inserted with a small clearance in cylinder (2). The flat ends of the piston carry diaphragms (3), which seal the oil spaces in the upper and lower plates (4) and (5). The full travel of the piston is about 0.05 mm. The lower oil space is connected by a metal tube to a measuring device, while the upper oil space is under a constant pressure p_0.

This design permits measurement not only of positive but also of negative loads acting on the piston through rods (6). The pressure in the oil space connected with the measuring system depends only on this load and on the pressure p_0. The pressure in the wind tunnel acts on both sides of the piston and is therefore not transmitted to the measuring device. The dynamometer is equipped with volumetric temperature compensation whose operating principle is the same as in the system shown in Figure 6.44. When the pressure changes in the lower oil space, the Bourdon tube (14) of the measuring device tends to bend and thus alter the gap between baffle plate (7) and nozzle (8), through which air is discharged continuously from a throttle opening in chamber (9). The change in the gap also causes the pressure to vary in bellows (10), which is connected with the chamber. When this happens, the upper surface of the bellows moves, thus altering the tension of spring (11) in such a way that the position of the Bourdon tube remains fixed at small displacements of the baffle plate. The tension of spring (11) and thus, of rod (12) and pointer (13) connected to it, is proportional to the oil pressure and therefore to the force P.

The spring is made of Elinvar which contains 35% nickel and 8% chromium. The material has a stress-strain relationship which is linear with an accuracy of 0.05%, and its properties vary very little with temperature. In certain U.S. wind tunnels, where the balances are equipped with such measuring devices, the angular motion of the pointer is converted into electrical pulses which are fed to a system for processing the measurement data.

Preliminary simplified processing of the data, in order to obtain net values of the force and moment components, is carried out according to the system shown in Figure 6.42, which makes possible wind-tunnel balances without lever systems for resolving the forces into components.

Figure 6.43 shows a hydraulic system which is a combination of an automatic lever-balance element with a certain type of hydraulic lever. Such a system is advantageous when, due to space limitations or for other reasons, the balance elements have to be at a certain distance from the wind tunnel. The primary instrument consists of bellows (1), connected with bellows (2) by a brass tube of 2 to 4 mm diameter. Bellows and tube are filled with oil or distilled water. The pressure, caused by the load P_1 on bellows (1),

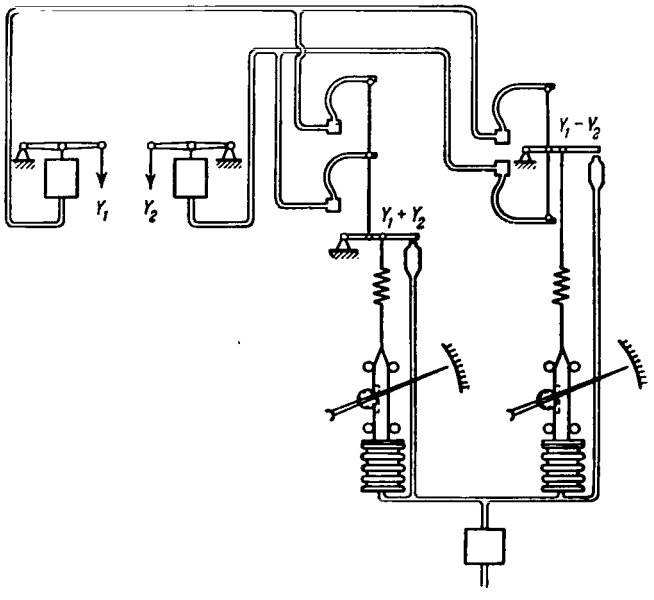

FIGURE 6.42. Adding and subtracting forces with the aid of a hydraulic force-measuring device.

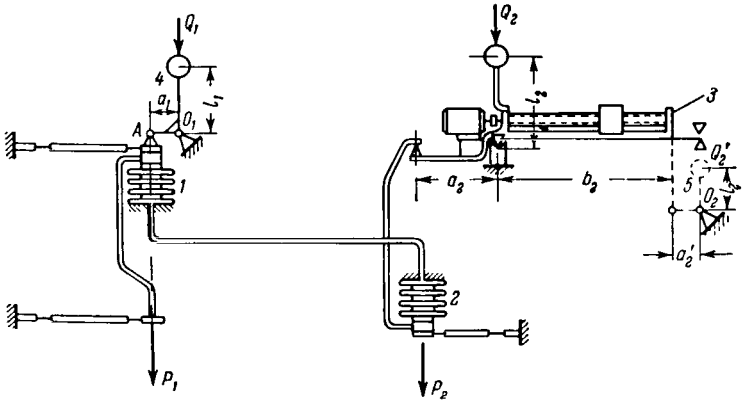

FIGURE 6.43. Hydraulic transmission of forces 1 — bellows to take up load; 2 — bellows connected with balance element, 3 — balance lever; 4 — crank lever to compensate for rigidity of bellows (1); 5 — crank lever to compensate for rigidity of bellows (2).

is transmitted through the tube to the bottom of bellows (2) which is connected with lever (3) of the automatic balance element. The left-hand arm of the lever is thus acted upon by a force P_2 which is equilibrated by a counterweight.

The displacement of the bottom of bellows (2) depends on the distance between the contacts of the automatic balance element and usually does not exceed a few hundredths or even thousandths of a millimeter; when the system is properly filled with liquid the displacement of the bottom of bellows (1) is also very small. Hence, hysteresis effects on the bellows do not influence the measurement of the force P_1. The transmission ratio of the hydraulic system is determined by calibration. It can be assumed that $P_2/P_1 = F_2/F_1$ where F_1 and F_2 are respectively the effective areas of bellows (1) and (2). When air bubbles are present in the system, the initial part of the dependence curve can be nonlinear; to avoid this, the system is filled under vacuum after all connections have been soldered, or the bellows are preloaded.

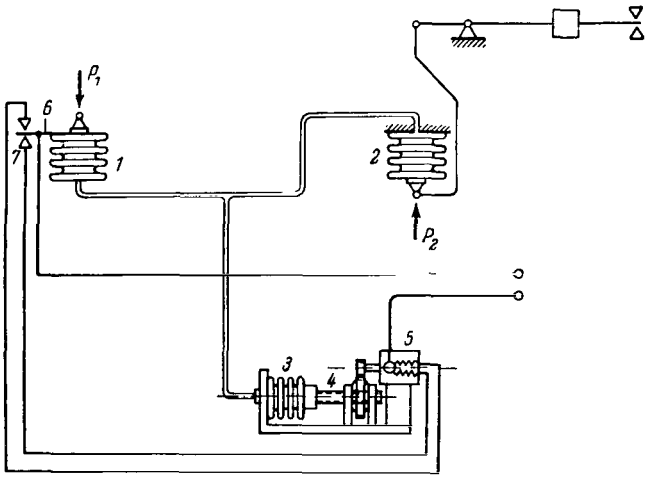

FIGURE 6 44. Volumetric temperature compensation for a hydraulic system
1 — bellows to take up load; 2 — bellows connected to balance element; 3 — compensating bellows, 4 — lead screw and reduction gear, 5 — servomotor, 6 — contact connected to movable part of bellows; 7 — stationary contact

In such closed hydraulic systems a change in the temperature of the surroundings causes a change in the volume of the liquid and can be the cause of systematic errors. If bellows (2) is connected with a null instrument (as in the case considered), the difference Δv_t between the thermal dilatations of the liquid and of the bellows material causes a displacement $\delta_t = \Delta v_t / F_1$ This gives rise to an elastic restoring force $\Delta P_t = c_1 \delta_t$ acting on the bottom and opposing its motion. Here c_1 is the spring rate of bellows (1) and the links connected to it. The magnitude ΔP_t is a systematic error of measuring the force P_1 and is very difficult to take into account.

The temperature error ΔP_t can be avoided by means of force or volumetric compensation. Force compensation consists of applying to the bottom of bellows (1) a force which is equal and opposite to the elastic restoring force ΔP_t. Figure 6.43 shows a force-compensation system which consists of crank lever (4), whose horizontal arm is hinged at A to bellows (1) and whose vertical arm carries a weight Q_1. When the bottom of bellows (1) moves a distance δ_t, the force acting on it changes by

$$\Delta P_t = \left(c_1 - \frac{Q_1 l_1}{a_1^2}\right)\delta_t.$$

Full compensation ($\Delta P_t = 0$) is obtained when $Q_1 l_1 = c_1 a_1^2$; this is easily achieved by adjusting the value of l_1.

In order to compensate fully the reduction in sensitivity caused by lever (3) being connected to bellows (2), it is sufficient to raise the center of gravity of the lever by fixing to it a weight Q_2 at a height l_2 above the fulcrum of the lever. Similarly to the above, full compensation of the elastic restoring force acting on bellows (2) is obtained when $Q_2 l_2 = c_2 a_2^2$. When a_2 is large, the weight Q_2 becomes heavy; in this case, in its place, the right-hand end of the lever is connected to an additional crank lever (5), shown by broken lines in Figure 6.43, carrying a weight Q_2'. For full compensation of the rigidity of the bellows, the static moment of this weight about O_2 must be

$$Q_2' l_2' = \left(\frac{a_2'}{b_2}\right)^2 c_2 a_2^2.$$

The ratio a_2'/b_2 is taken as 1/10 to 1/20, so that Q_2' is some hundreds of times less than Q_2.

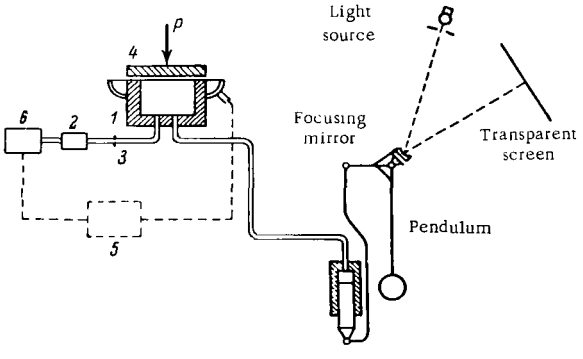

FIGURE 6.45. Through-flow dynamometer. 1 — vessel; 2 — pressure regulator; 3 — throttle; 4 — disc; 5 — filter; 6 — pump.

Volumetric compensation for a closed hydraulic system is illustrated in Figure 6.44. The system includes an additional compensating bellows (3), whose volume can be changed with the aid of lead screw (4), turned by servomotor (5).

There is no necessity for temperature compensation in through-flow hydraulic dynamometers. Such a system is shown in Figure 6.45. Oil is forced by pump (6) into a cylindrical vessel (1), open at the top, after passing through pressure regulator (2) and throttle (3). On the vessel there is a disc (4), which takes up the force P whigh has to be determined. Under the action of the oil pressure, an annular slot is formed between vessel (1) and disc (4), through which the oil is continuously discharged into a drain. The disc thus floats on an oil film. After being cleaned in filter (5), the oil is returned to pump (6). When the disc floats up the force P is fully equilibrated by the force of the oil pressure on the disc. The oil pressure in vessel (1), which is proportional to the force P, can be measured by any type of manometer.

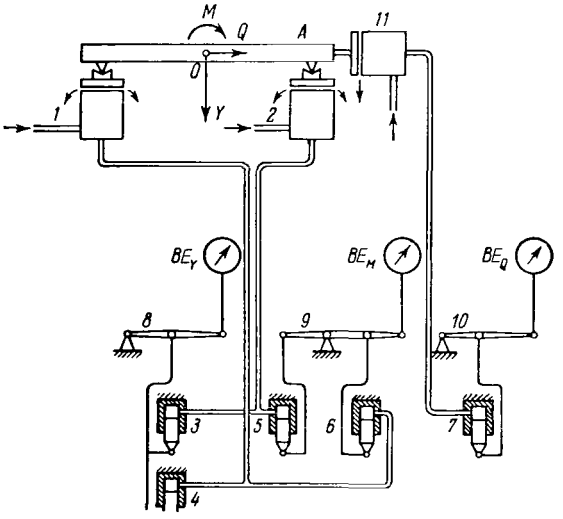

FIGURE 6.46. Operating principle of wind-tunnel balances resting on through-flow dynamometers. 1, 2, 11 — through-flow dynamometers, 3, 4, 5, 6, 7 — piston-type manometers; 8 — adding lever for measuring Y; 9 — subtracting lever for measuring M_z; 10 — lever for measuring Q.

Figure 6.45 shows a system for measuring the pressure by a pendulum piston-type manometer with optical read-out. In order to reduce friction between the piston and the cylinder the latter is kept vibrating continuously by the action of an electromagnet.

Intended for measuring forces perpendicular to the disc surface, the through-flow dynamometer permits free motion of the disc in its plane at negligible friction, the disc floating on an oil film. These characteristics of through-flow dynamometers are used for measuring mutually perpendicular forces. This is illustrated in Figure 6.46 which is a simplified layout of a wind-tunnel balance. The floating frame A of the balance rests on two through-flow dynamometers (1) and (2), having equal effective areas. Dynamometer (1) is connected by tubes to manometers (4) and (6), and dynamometer (2) to manometers (3) and (5). The pistons of manometers (3) and (4) are connected by rods to lever (8), which adds the forces acting

on these pistons; the indication of balance elements BE_Y, which is connected to lever (8), is thus proportional to the vertical force Y. The pistons of manometers (5) and (6) are connected to equal-arm lever (9), which serves for measuring, by means of balance element BE_M, the moment about point O which is centrally located between dynamometers (1) and (2). Dynamometer (11) takes up the horizontal component of the force, which is measured with the aid of balance element BE_Q, connected by lever (10) to the piston of manometer (7), on which the pressure in dynamometer (11) acts.

Spring and strain-gage balance elements

The accuracy of a spring balance element is mainly determined by the accuracy of measuring the deformation of an elastic link and the physical characteristics of its material. The error in measuring the deformations can be easily reduced to a negligible value if we use an elastic link with a large absolute deformation, for instance, a spiral spring.

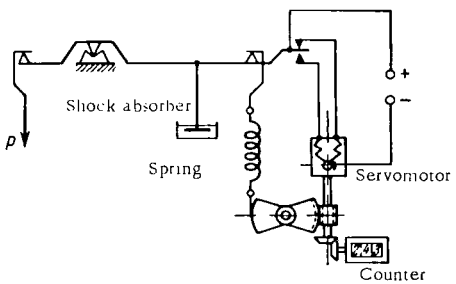

FIGURE 6.47 Spring balance element.

Due to hysteresis effects and residual stresses, the error in measuring forces with the aid of elastic links made from different types of steel is about 0.2 to 0.5% of the maximum measured force. Better physical properties are provided by special alloys like beryllium bronze and Elinvar whose stress—strain relationships are linear with an accuracy of 0.02 to 0.05%.

When spiral springs are used, the effect of their deformation on the attitude of the model in the test section is eliminated with the aid of a null method of measurement. The spring is deformed manually or automatically (Figure 6.47) so that the lever, which takes up the load from the wind-tunnel balance, maintains its initial position. A visual indicator is read off when the lever is in equilibrium.

Elastic force links in the form of beams subjected to bending have usually such small deformations that the displacements of the model caused by them can be ignored. Small deformations are measured with the aid of different types of electric transducers which convert the magnitude of the

deformation into a change of inductance, capacitance, or resistance, which is then measured by an appropriate electrical instrument.

Wide use is made of methods for measuring deformations of elastic elements with the aid of glued resistance strain gages, which are described in detail in the next section. A dynamometer with glued wire transducers is shown in Figure 6.64. Due to their small dimensions in comparison with other types of balance elements, such dynamometers are used in electric strain-gage balances located inside the model.

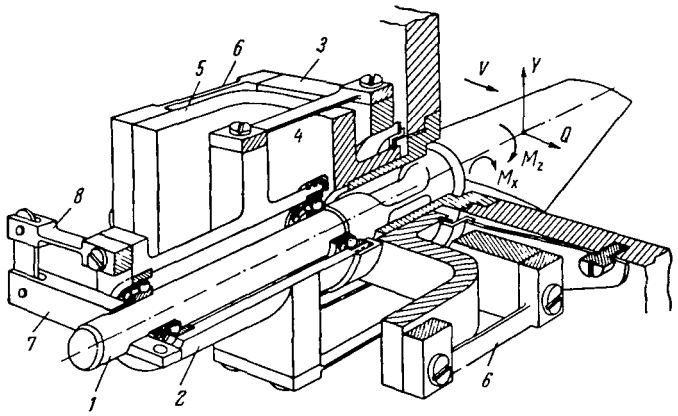

FIGURE 6.48. Four-component balance for testing wings. 1 — spindle; 2 — spindle support; 3 — intermediate frame; 4, 6, 8 — elastic beams with strain-gage transducers; 5 — stationary support; 7 - moment lever.

In balances located outside the test sections, strain-gage transducers are used very often for measuring aerodynamic loads on half-models, i.e., models whose plane of symmetry coincides with the test-section wall. Figure 6.48 shows a four-component balance for testing models of wings /12/. A wing model is mounted on spindle (1), by means of which it can be turned and the angle of attack altered. Spindle support (2) is carried by a parallelogram suspension on intermediate frame (3).

The lift Y is taken up by elastic beam (4), which connects spindle support (2) with frame (3), and is measured by transducers glued to the beam. Intermediate frame (3) is supported with the aid of beam (6) on stationary support (5) which permits movement of support (2) and frame (3) parallel to the flow direction. Transducers, which measure the drag Q, are glued to beam (6). The pitching moment is measured with the aid of lever (7), rigidly connected to the shaft, and beam (8) to which transducers for measuring M_z are glued. The heeling moment M_x is measured by transducers glued to spindle (1) where its cross section is reduced.

The balance shown in Figure 6.49 employs a support consisting of curved strut (1) surrounded by shroud (2). The measuring elements A, B, and C, which have the form of elastic parallelograms, are installed in such a way that element A takes up only the lift Y_1 while the loads on elements B and C depend on the drag Q_1 and the pitching moment M_{z_1}.

The connections of the strain-gage transducers, which are glued to elastic elements B and C and arranged in bridge systems as shown at the bottom of the drawing, permit Q_1 and M_{z_1} to be measured independently. The stationary parts of the elastic parallelograms are fixed to the shroud. In order to alter the angle of attack of the model, the shroud is turned about the origin of coordinates O of the balance together with the strut, the elastic elements, and the model.

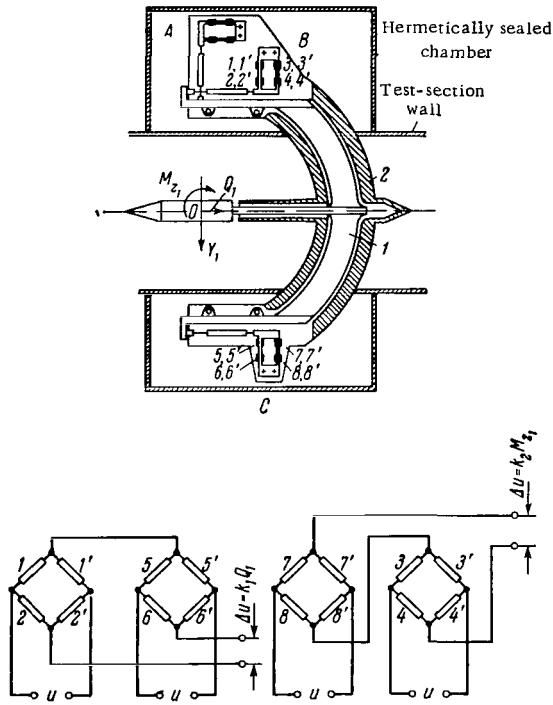

FIGURE 6.49 Three-component strain-gage balance. 1 — curved strut; 2 — shroud, A, B, C, — strain gages.

Mechanical wind-tunnel balances may also be provided with balance elements with nonglued wire resistance transducers. The characteristics of these transducers are more constant in time than those of glued transducers whose accuracy is affected by the nonstable properties of the glue. In the balance element shown schematically in Figure 6.50, thin constantan wires are connected to an insulated plate at the end of a lever mounted on an elastic support, and to two other insulated plates fixed to the base of the balance element.

The tension in the wires is changed under the influence of the load to be measured. The change in resistance thus caused is measured by a Wheatstone bridge, in all four arms of which the wires are inserted.

The instrumentation used for this is described in the next section.

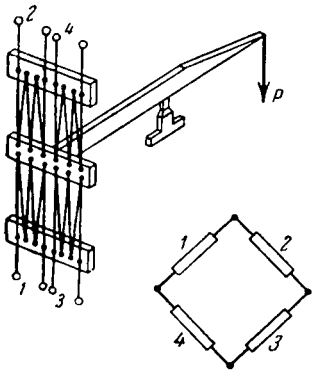

FIGURE 6.50. Balance element with nonglued wire resistance transducers.

Electromagnetic balance elements

Figure 6.51 shows two circuit diagrams of balance elements, based on the interaction between the field of a permanent magnet and the field of a d.c.-excited coil. Coil (4) is connected to the arm of lever (1), whose other arm is acted upon by the force P. The force F of the interaction between permanent magnet (5) and coil (4) is

$$F = 2\pi r I n H,$$

where r is the mean radius of the coil, n is the number of turns, H is the field strength of the permanent magnet, I is the current intensity in the coil.

When the equilibrium of the lever is disturbed, lever-motion transducer (2) sends a signal to amplifier (3). In the circuit shown in Figure 6.51a, the lever is returned to equilibrium with the aid of servomotor (7), which moves the slider of variable rheostat (6). This changes the current intensity in the coil. The force P is determined from the current intensity which is read off from milliammeter (8), or from the position of the slider of the variable rheostat (at a stable supply voltage), when the lever is in equilibrium.

The circuit shown in Figure 6.51b permits faster operation than that shown in Figure 6.51a, and can serve for measuring loads changing at frequencies up to 10 to 20 cycles /13/, /15/. The electric signal from transducer (2) (photoelectric element, capacitive or inductive transducer) is amplified by amplifier (3) feeding coil (4). The current intensity is measured either directly or by the voltage drop across resistance R. In this circuit the magnetic system, which consists of coil (4) and magnet (5), is similar to a spring, since the force F is proportional to the displacement

of lever (1). The amplification coefficient of amplifier (3) can be so chosen that at the maximum load the coil moves less than 0.01 mm. Hence, the rigidity of the electrical spring, on which the operating speed of the system depends, can be very high. Thus, for instance, the electromagnetic wind-tunnel balance element of the University of Washington has a spring rate of about 2000 kg/cm and a natural frequency

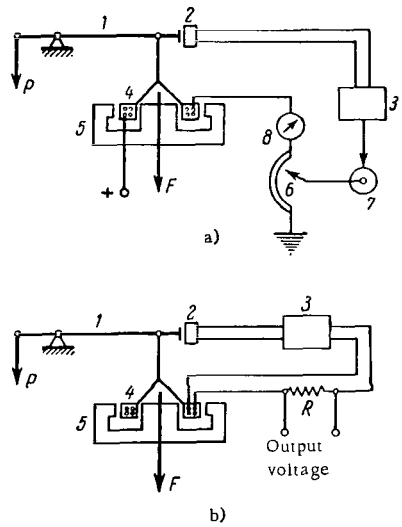

FIGURE 6 51. Electromagnetic balance elements. a — equilibration by means of servomotor; b — static equilibration; 1 — lever; 2 — lever-motion transducer; 3 — amplifier, 4 — coil; 5 — permanent magnet, 6 rheostat; 7 — servomotor; 8 — milliammeter

of 200 cycles /14/. The maximum current in the coil of such a balance element is between 30 and 50 ma at a maximum load of 3 to 5 kg. Using an appropriate circuit, an accuracy and linearity of the order of 0.1% can be obtained. Balance elements of this type can be used in special wind-tunnel balances serving, for instance, for measuring loads acting on vibrating wings.

§ 28. WIND-TUNNEL BALANCES LOCATED INSIDE THE MODEL

As was already stated in the introduction to this chapter, wind-tunnel balances located inside the models were developed due to the need to exclude forces acting on the supports. At supersonic velocities, flow around the model is least affected by supports in the form of cantilever

supports. "Internal" wind-tunnel balances are installed at the joints between the models and such supports or in the supports themselves (Figure 6.52).

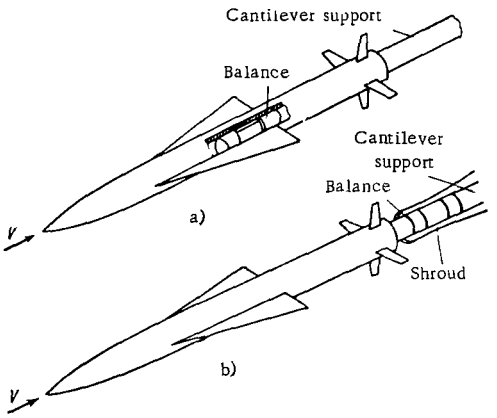

FIGURE 6.52. Installation of strain-gage balances. a — inside model; b — inside support.

When the balance is installed inside the model, the forces acting on the support are not measured and the support only causes certain perturbations in the flow at the tail of the model. When the balance is installed in the support, the latter is protected from the flow by a cylindrical or conical shroud. The "ground" pressure acting on the rear of the model is measured with the aid of orifices through which the region behind the model is connected to a manometer.

The possibility of installing the wind-tunnel balance inside the model is so attractive, that in recent years balances of this type, called strain-gage balances, have found very wide use in spite of the fact that their accuracy and the reproducibility of their indications are still less than those of ordinary mechanical balances. A measuring error of the separate components, equal to ±1% (under conditions of static calibration), is considered satisfactory, while ordinary balances have under the same conditions errors of about 0.1%. The latter are very reliable instruments which maintain constant their characteristics for months. Internal balances have to be calibrated and checked very often, sometimes before and after each experiment. Particular care should be taken to eliminate or take into account temperature errors.

A strain-gage balance forms an elastic system the deformations of whose elements are proportional to the components or the algebraic sums of the components of the total aerodynamic force and moment acting on the model. These deformations are measured as electrical magnitudes with the aid of electrical converters. Wind-tunnel balances employ almost exclusively strain-gage resistance transducers which are based on the conversion of the deformation of an elastic element into a change of the electrical resistance, which can be measured by a instrument connected to a corresponding measuring circuit.

Strain-gage resistance transducers

Strain-gage resistance transducers may be of different designs. Wire and foil strain-gage transducers are most widely used. Wind-tunnel balances have mostly wire strain-gage transducers (Figure 6.53) which consist

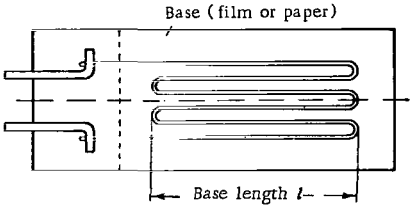

FIGURE 6.53. Wire strain-gage-transducer

of several turns (grids) of wire of very small diameter (0.025 to 0.03 mm), made from an alloy having a high electrical resistance, and glued between two layers of paper or film. If the strain-gage transducer is glued to the surface of an elastic element, the transducer is deformed together with this surface. The length l of the wire grid is called the base length of the transducer. The characteristics of strain-gage transducers are described in detail in /16/, /17/.

The advantages of strain-gage transducers, which make them particularly suitable for measuring aerodynamic forces, are:

1) small dimensions and weight;

2) possibility of measuring very small relative deformations of elastic elements (less than 10^{-3}); this permits the use of very rigid elastic elements having high natural frequencies;

3) small inertia, which permits not only static but also dynamic loads to be measured;

4) possibility of remote measurements.

The main characteristic of resistance strain-gage transducers is the coefficient of strain sensitivity, which is determined as the ratio of the relative change in electrical resistance of the wire to its relative linear deformation

$$s = \frac{\Delta R}{R} \Big/ \frac{\Delta l}{l},$$

where R is the [initial] resistance of the wire, and l is its length.

Thus, if we determine the value of $\Delta R/R$, we can, knowing the coefficient of strain sensitivity, find the relative elongation of the wire and, therefore, of the elastic element to which the strain-gage transducer is glued:

$$\varepsilon = \frac{\Delta l}{l} = \frac{1}{s} \frac{\Delta R}{R}.$$

For a monoaxial state of stress, the relationship between the strain ε and the stress σ is, within the proportionality limits of the material, given by $\varepsilon = \sigma/E$, where E is the modulus of elasticity of the material.

The stress at any point of an elastic element depends on the forces and moments acting on this element. Hence, the relative change in the resistance of the transducer, mounted on the elastic element, is proportional to the components of the resultant force and moment, causing the deformation of the element. The coefficient of proportionality depends on the strain sensitivity of the transduer wire, on the elastic characteristics of the material, and on the shape and size of the elastic element.

In the general case, the state of stress on the surface of an elastic element, to which a strain gage is glued, can vary from point to point. Hence, the change in the resistance of the transducer is proportional to a certain mean stress over the base of the transducer. In order that the transducer measure the stress at a point (this is particularly important due to the small dimensions of the elastic elements used in multi-component balances located inside models), its dimensions have to be small. Wind-tunnel balances employ transducers having bases of 5 to 20 mm and resistances of 100 to 200 ohm. It is possible to obtain transducers having even smaller bases (down to 2 mm), but a small base causes the resistance of the strain-gage transducer to decrease; this complicates the measurements.

The most commonly used material for wire transducers is constantan, whose coefficient of strain sensitivity is $s = 1.9$ to 2.1. For approximative calculations we assume $s = 2$.

Bridge measuring circuits. The resistance of a strain-gage transducer mounted on an elastic element changes very little when the latter is deformed. Thus, at 0.1% strain (which, for steel, corresponds to a stress of about 2000 kg/cm^2), and at an [initial] transducer resistance of 100 ohm, the change in the resistance is

$$\Delta R = Rs\varepsilon = 100 \cdot 2 \cdot 10^{-3} = 0.2 \text{ ohm}$$

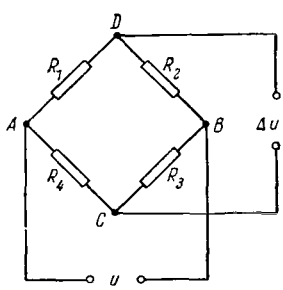

FIGURE 6.54. Measuring bridge.

If the measuring accuracy required corresponds to 0.1% of the maximum stress (i.e., 2.0 kg/cm^2), the resistance must be measured with an accuracy of 0.0002 ohm, which corresponds to a relative accuracy of 2×10^{-6}. Such an accuracy can be obtained only with a compensation method of measurement, for instance, by means of a Wheatstone bridge.

The simplest measuring bridge consists of four ohmic resistances (arms) R_1, R_2, R_3, and R_4 (Figure 6.54). Points A and B (the supply diagonal) are at a voltage difference u (from an a.c. or d.c. source), while points C and D (measuring diagonal) are connected to the measuring instrument. In ordinary systems, the strain-gage transducers are usually inserted into one or two arms of the bridge, while the other arms are formed by constant resistances. In wind-tunnel balances, however, the strain-gage

transducers are inserted into all four arms of the bridge; this increases the sensitivity and exploits the bridge characteristics to compensate the different errors.

If the ratios of the resistances of adjacent bridge arms are equal, i. e.,

$$\frac{R_1}{R_2} = \frac{R_4}{R_3},$$

then the potential difference across the measuring diagonal is zero. The bridge is then balanced.

When the resistance of one arm of an initially balanced bridge changes, a potential difference Δu appears between points C and D of the measuring diagonal. This is the imbalance voltage of the bridge. At small relative resistance changes the imbalance voltage depends linearly on the sum or difference of these changes.

The imbalance voltage Δu across the measuring diagonal is measured by an indicating or recording instrument (millivoltmeter or oscillograph galvanometer). Recording instruments of the oscillograph type permit dynamic processes to be investigated.

In order to obtain high accuracy, Δu is measured by a compensating method with the aid of a separate compensator. In this case the measuring instrument (zero indicator) serves only as an imbalance indicator for the compensator circuit, while the measured value is read off from the compensator scale at the instant of balancing. The indication is usually in the form of a linear or angular magnitude, related to the imbalance voltage by the expression $n = m\Delta u$, where n is the number of divisions of the scale, and m is a constant for the given compensator.

Most wind-tunnel balances employ balanced systems which are far more accurate than imbalance systems. Balanced systems are used for measuring static or slowly varying magnitudes. In order to speed up the measurements, the bridge is usually balanced automatically.

A measuring bridge is most sensitive when all arms are equal ($R_1 = R_2 = R_3 = R_4 = R$). Such bridges are normally used in wind-tunnel balances. The measuring diagonal is usually connected to a tube amplifier for the imbalance voltage, whose input resistance is large in comparison to that of the strain-gage transducer. When the resistance of one arm of the equal-arm bridge changes by ΔR, an imbalance voltage

$$\Delta u = \frac{u}{4}\frac{\Delta R}{R} = \frac{us\varepsilon}{4}$$

will appear across the measuring diagonal.

Hence, to increase the imbalance voltage Δu it is best to increase the supply voltage u. However, at a given resistance R of the transducer, an increase in u will cause an increased current to flow through the wire of the transducer, which becomes heated. This changes the resistance of the strain-gage transducer, introducing considerable measuring errors. It is therefore better to increase the transducer resistance, while simultaneously increasing the supply voltage, but to limit the current to a certain value determined by the heating of the wire. Experience shows that in constantan wires of about 0 25 mm diameter, currents of about 30 ma are permissible; strain gages whose resistance is of the order of 200 ohms have limiting supply voltages of about 6 v.

The relationship between the imbalance voltage of the bridge and the strain in the transducer. Measuring circuits of multi-component wind-tunnel balances employ bridges consisting of 2, 4, 8, and sometimes 12 transducers. In addition to the increased sensitivity, bridges with large numbers of transducers permit independent measurement of the separate components of the forces. It is particularly important that the output signal of a bridge circuit have a linear relationship to the measured magnitude. If the measuring diagonal of the bridge constitutes a high input impedance for a tube amplifier, then, in the case of an equal-arm bridge, changes in the resistance of the arms, amounting to $\Delta R_1, \ldots, \Delta R_4$, cause an imbalance voltage at the extremities of the measuring diagonal, which, for small values of ΔR, can be assumed to be

$$\Delta u = \frac{u}{4}\left(\frac{\Delta R_1}{R} - \frac{\Delta R_2}{R} + \frac{\Delta R_3}{R} - \frac{\Delta R_4}{R}\right).$$

If all transducers have the same coefficient of strain sensitivity, the imbalance voltage is

$$\Delta u = \frac{uS}{4}(\varepsilon_1 - \varepsilon_2 + \varepsilon_3 - \varepsilon_4).$$

The total imbalance voltage can be considered as the sum of the imbalance voltages of two half-bridges separated by the supply diagonal. If the transducers of the lower half-bridge are shunted by equal resistances R_{sh} (Figure 6.55), then

$$\Delta u = \frac{uS}{4}[\varepsilon_1 - \varepsilon_2 + c(\varepsilon_3 - \varepsilon_4)],$$

where $c = R_{sh}/(R_{sh} + R)$ determines the attenuation of the signal of the lower half-bridge. This method of attenuating the signal of one half-bridge in strain-gage balances is used for eliminating the mutual influences of the components.

Factors which influence the measuring accuracy

The errors which occur in force-measuring devices using strain-gage transducers are caused by hysteresis effects, temperature influences, and the electrical characteristics of strain-gage transducers and measuring circuits. A special feature of wind-tunnel balances using strain-gage transducers is the influence of asymmetry of the elastic elements and the strain-gage transducers themselves (i.e., nonuniform mounting, different resistance and coefficients of strain sensitivity, etc.).

The influence of asymmetry is reduced by inserting the strain-gage transducers into the measuring bridges in such a way that the electrically and mechanically induced errors are mutually compensated.

The hysteresis effects depend on the mechanical properties of the material of the elastic elements, of the wires of the strain-gage transducers,

of the bases of the transducers, and of the glue used to fix the transducers to the elastic elements.

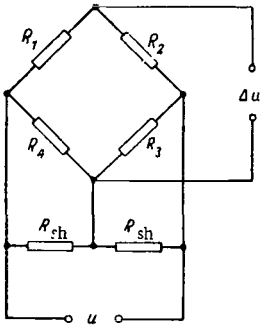

FIGURE 6.55. Shunting of transducers in a half-bridge by constant resistances.

For the same material of the elastic element, hysteresis varies directly with the maximum strain of the material.

The material of the transducer wires is, in addition to hysteresis, also characterized by variable absolute resistance and temperature coefficient of resistance. To stabilize these values, the wire is subjected to aging by means of repeated heating and cooling.

Errors caused by the instability of the glue and the base of the strain-gage transducer are most important. They are caused by creep of the strain-gage transducers, and sliding of the wires on the base. Transducers on a film base are best; when polymerized, a good bond with the metal of the elastic element is obtained. In order to improve the bond it is best to use strain-gage transducers with as large base lengths as the dimensions of the elastic element permit.

Electrically induced errors are caused by temperature effects and by the characteristics of the electric circuits used for measuring the signals of the transducers.

Temperature effects and their compensation. The overall relative change in resistance of a strain-gage transducer with temperature is

$$\frac{\Delta R_t}{R} = [\alpha + s(\beta_1 - \beta_2)]\,\theta,$$

where α is the temperature coefficient of the resistance of the transducer wire, β_1 and β_2 are respectively the coefficients of temperature expansion of the elastic element to which the transducer is glued, and of the wire, while θ is the change in temperature which causes the zero shift in the measurement diagonal of the bridge. Denoting the overall temperature coefficient of the transducer by α_d, we obtain

$$\frac{\Delta R_t}{R} = \alpha_d \theta.$$

The value of α_d for constantan strain-gage transducers glued to steel is about 10^{-5}. The strain which causes the same relative change in resistance of the transducer is

$$\varepsilon_t = \frac{\Delta R_t}{R}\frac{1}{s} = \frac{\alpha_d \theta}{s}.$$

Thus, the apparent strain per 1°C of a constantan transducer is about

$$\varepsilon_t \approx 0.5 \cdot 10^{-5}.$$

Since the maximum strain usually does not exceed 0.5×10^{-3} to 1.0×10^{-3}, the error per 1°C may attain 0.5 to 1% of the maximum value. This large temperature error makes its compensation very important.

When transducers are inserted into all arms of the bridge, the imbalance voltage due to the change in temperature of the transducers is

$$\Delta u_t = \frac{u}{4}(\alpha_{d_1}\theta_1 - \alpha_{d_2}\theta_2 + \alpha_{d_3}\theta_3 - \alpha_{d_4}\theta_4).$$

If all the transducers had the same temperature coefficient and were at the same temperature, the imbalance voltage would be zero. The same would happen if two half-bridges were at different temperatures, while the transducers of each half bridge were at the same temperature. However, under actual conditions, the temperature coefficients of individual transducers may differ, while separate transducers (even when belonging to the same half-bridge) may be at different temperatures.

The total imbalance voltage Δu_t, caused by the change in temperature, is thus composed of two parts /18/:

$$\Delta u_t = \frac{u}{4}(\Delta\alpha_d\theta + \alpha_d\Delta\theta),$$

where $\Delta\alpha_d = \alpha_{d_1} - \alpha_{d_2} + \alpha_{d_3} - \alpha_{d_4}$ is the total change of the temperature coefficients α_d for the entire bridge, while

$$\Delta\theta = \theta_1 - \theta_2 + \theta_3 - \theta_4$$

is the sum of the temperature differences between the transducers of each half-bridge.

The value of $\Delta\alpha_d$ can be reduced by choosing strain-gage transducers whose overall temperature coefficients are as nearly equal as possible, or pairs of strain-gage transducers having overall temperature coefficients nearly equal but differing in sign.

In order to determine their temperature sensitivity, strain-gage transducers are tested at different temperatures. One method of testing consists of transferring the strain-gage transducers from one medium (for instance, paraffin) to another medium whose temperature is 20 to 30°C higher. The change in overall resistance of the strain-gage transducer is determined by comparison with a reference [resistance] a few seconds after transfer to the hot bath. Small changes in resistance occurring after an hour or more are thus neglected. In order to prevent bending, the strain-gage transducers are sometimes held between copper plates during heating.

The first part of the temperature error, which depends on $\Delta\alpha_d$, is compensated by superimposing on the potential in the measuring diagonal an additional potential proportional but opposite in sign to Δu_t. This can be done, for instance, with the aid of a resistance thermometer, which is a small piece of copper wire connected in series with one of the strain-gage transducers of the half-bridge and having the same temperature.

The second part of the temperature error, which depends on $\Delta\theta$, is compensated by locating more closely together the transducers in the half-bridges. If the measuring bridge must respond to tensile or compressive strains of the elastic element, ordinary measuring circuits employ compensating transducers mounted on nondeformed elements which are at the same temperatures as the deformed elements. These transducers are inserted into the arms in series with the active transducers of the bridge. In order to increase the sensitivity of the bridge in wind-tunnel balances all strain-gage transducers are active, and temperature effects are reduced by symmetric disposition of the elastic elements. If the measuring bridge must respond to bending strains the strain-gage transducers of one half-bridge are mounted on either side at equal distances from the neutral axis of the element. In this case the compensating strain-gage transducer is also active.

Measuring equipment

The range of voltages measured with strain gages is determined by the maximum strains of the elastic elements. When the bridge supply voltage is $u = 6$ v and the maximum strain is $\varepsilon = 10^{-3}$ the maximum voltage signal of a four-arm bridge is $\Delta u = us\varepsilon = 6 \times 2 \times 10^{-3} = 12$ mv. In order to reduce hysteresis of the elastic elements, the maximum strain should not exceed 0.25×10^{-3} to 0.5×10^{-3} and therefore the instrument scale must be suitable for a maximum value of Δu between 3 and 6 mv.

Experience shows that in order to determine the components of the aerodynamic loads with an accuracy of the order of 1%, the measuring equipment must have a sensitivity of about 0.1% of the measured range. Thus, the scale of the measuring or recording instrument must have at least 1000 divisions, and must provide several ranges within the above-mentioned limits.

The number of channels in equipment used in wind-tunnel balances must be equal to the number of measured magnitudes. Usually, the apparatus is equipped with additional channels which also permit the pressures to be measured simultaneously. All channels should be interchangeable and capable of being calibrated independently on the wind-tunnel balances.

The apparatus used for measurements with the aid of strain-gage transducers is mainly selected according to the type of supply to the measuring bridges (d. c. or a. c.) and the operating conditions of the measuring circuit (balanced or unbalanced). Since in aerodynamic measurements the output signal has to be amplified, selection of the amplifier also depends on the type of supply. D.c. amplifiers have the

advantage that they do not require rectification when they feed electromagnetic instruments.

However, a considerable drawback of d.c. amplifiers is the instability of their characteristics. In addition, a drawback of d.c. supply is the potential difference caused by the welded joints between the copper and the constantan wires forming the thermocouples. In fact, at a bridge supply voltage of 6 v, a strain $\varepsilon = 10^{-6}$ in one of the transducers causes a voltage imbalance of 3×10^{-6} v in the measuring diagonal. On the other hand, a temperature difference of 1°C in the joints between the copper and the constantan creates an emf of 40×10^{-6} which corresponds to a strain of 13×10^{-6} The values of the thermoelectric emf can be easily found by switching off the supply source. However, taking into account temperature changes during the experiment is rather difficult.

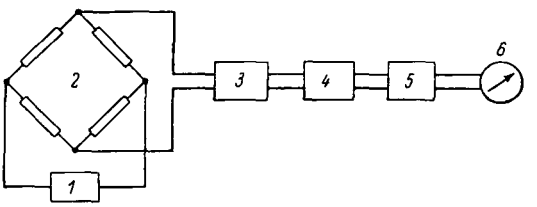

FIGURE 6.56. Carrier-frequency measuring circuit. 1 — generator for bridge; 2 — measuring bridge; 3 — amplifier; 4 — demodulator; 5 — filter; 6 — measuring instrument.

The thermocouple effect is eliminated when the bridge is supplied by a.c. In this case, the constant component caused by the thermoelectric emf is transmitted through the amplifier.

Imbalance method of measurement. Rapidly-varying loads are most often measured by the imbalance method in which the bridge is supplied with a.c. at a frequency which is called the carrier frequency (Figure 6.56). Carrier-frequency amplifiers permit measurements of static processes as well as of dynamic processes when the modulating frequency does not exceed 10 to 15% of the carrier frequency.

A carrier-frequency circuit is simple and stable, but when used in the imbalance method with loop-oscillograph recording, the error is not less than ±3% of the maximum. In strain-gage balances this accuracy is not always sufficient, hence, imbalance circuits are used for measuring the dynamic components of the aerodynamic forces, and also for measurements in shock wind tunnels of very short operating durations. Measurements of mean or quasisteady aerodynamic forces by strain-gage balances are performed with the aid of balanced circuits, whose advantage over imbalance circuits is in that the indications are independent of the supply voltage and of the amplification coefficient of the amplifier.

Balance method of measurements. Balanced circuits provide considerably higher measuring accuracies than the imbalance circuits, and do not require accurate measuring instruments with wide scales. Sensitive null-type measuring instruments are used instead, which show the imbalance of the circuit. The voltage imbalance of the

bridge is measured in this case by a compensating method, while the compensator scale is read off at the instant when the signal of the null instrument is zero.

Wind-tunnel balances employ exclusively automatic bridges and compensators in which the null instrument is replaced by an a.c. or d.c. amplifier.

The circuit of an automatic bridge with a.c. amplifier is shown in Figure 6.57. The bridge is supplied from a transformer T. A change in the resistance of the transducers causes a disturbance of the bridge balance, causing an a.c. voltage, whose amplitude is proportional to the measured strain, to appear across the measuring diagonal. The voltage is amplified and fed to the field winding of a miniature asynchronous reversible motor which restores the bridge balance by moving the contact of rheostat P. Many automatic bridges produced by Soviet industry work on this principle. However, direct use of standard bridges in automatic balances is difficult. In standard instruments the moving contact of the rheostat is connected to a pen writing on a tape driven by a clockwork mechanism. In wind-tunnel balances several magnitudes have to be recorded simultaneously, while standard multipoint instruments record the indications at fixed time intervals. Standard bridges can be used for automatic measurements if the tapes are moved by the mechanism which alters the angle of attack of the model. Wind-tunnel balances employ special multi-channel automatic bridges permitting simultaneous recording of several magnitudes in digital form, which is more suitable for subsequent

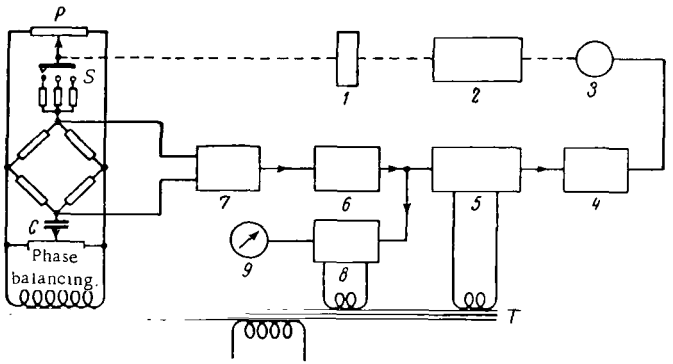

FIGURE 6.57 Automatic a.c. bridge. 1 — digital converter; 2 — reduction gear, 3 — servomotor, 4 — power amplifier, 5 — phase discriminator; 6 — band filter; 7 — amplifier; 8 — phase-sensitive rectifier; 9 — reactive-balance indicator, S — sensitivity switch.

decoding and processing (see Chapter IX). Because the digital device is connected directly to the rotor of the servomotor, the accuracy of such compensators attains 0.1% of the scale maximum, while tape-type recording instruments have an accuracy of only 0.5%.

Modern rapid-action automatic bridges with electronic amplifiers enable values corresponding to the scale maximum to be measured during 0.1 to 0.5 seconds. Automatic bridges are suitable for measuring not only static but also slowly varying loads, for instance, when the angle of attack of the model is continuously altered.

Another a.c. compensator is the automatic measuring compensator with decade resistances /19/, /20/. In this circuit the imbalance voltage of one or several bridges with strain-gage transducers is balanced by the imbalance voltage of bridges with known resistances. Each bridge of the circuit is fed from a separate winding of transformer T (Figure 6.58). The rheostat in this system is replaced by a resistance box, the resistors of which are switched over by a balancing motor M. The box has decades of ten ($n/10$), hundred ($n/100$), and thousand ($n/1000$) divisions, assembled from stable resistors. The decades are connected to the corners of two bridges. The decades of

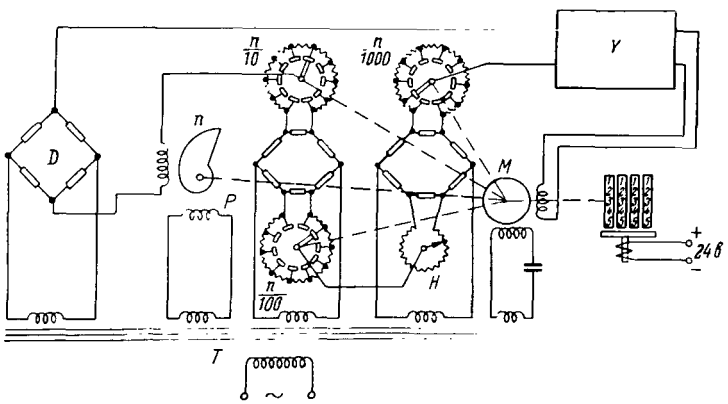

FIGURE 6.58 Automatic compensator with box of decade resistors. H — zero set; M — balancing motor; C — printing counter; Y — amplifier; D — transducer bridge; P — contactless inductive converter.

units (n) have a round contactless inductive converter P, whose imbalance voltage depends linearly on the angle of rotation of the core and is in phase with the transducer-bridge supply. The brushes for switching over the decade resistors are connected with the decade drums of the digital counter, whose unit shaft is directly connected with the balancing motor. The indications of the counter, which correspond to the signal of the transducer bridge, are printed on a tape.

An example of a balancing system with d.c. bridge is a circuit developed by ONERA, based on the Speedomax potentiometer /18/. The bridge is balanced by rheostat Rh_1 (Figure 6.59). The imbalance voltage across the diagonal AB is amplified and fed to reversible motor M which moves the slider of rheostat Rh_1 in the direction required for balancing the bridge. In order to eliminate the influence of the thermoelectric emf, the latter is balanced by an equal voltage taken from an auxiliary source E_k and adjusted by potentiometer Rh_2.

For this, the supply to the transducer bridge is periodically cut off by switch S, and motor *M* connected to potentiometer Rh_2 instead of Rh_1. Since the bridge then creates no potential difference induced by its imbalance, the amplifier is fed only with the voltage of the thermoelectric emf. The motor drives the slider of Rh_2 until the sum of the thermoelectric emf and the voltage of the compensating circuit is equal to zero.

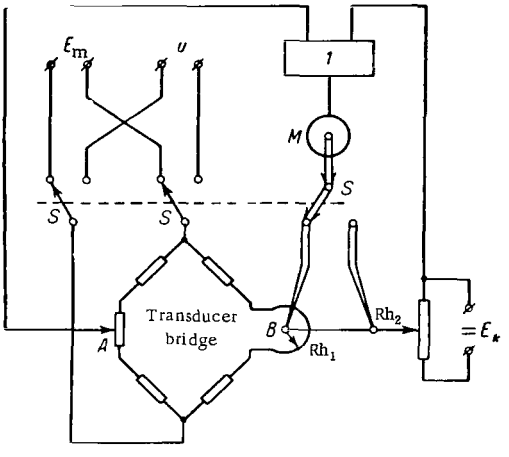

FIGURE 6.59. Circuit of automatic d.c. bridge. 1 — amplifier; E_m — source of d.c. voltage for feeding transducer bridge; E_k — source of d.c. voltage for compensation of thermoelectric emf; U — source of a.c. voltage for heating transducers of measuring bridge during compensation of thermoelectric emf; S — switches "measuring — compensation of thermoelectric emf".

After the motor is again connected with potentiometer Rh_1, the adjustment which was made when it was connected with Rh_2 is still in force and compensates the thermoelectric emf during the measurements. The duration of switch-over for compensation is about 1 second in every 6 seconds. In order to prevent cooling of the strain-gage transducers during compensation of the thermoelectric emf, switch S simultaneously connects the bridge to an a.c. supply.

A.c. and d.c. supply circuits for transducer bridges have advantages and disadvantages. A.c. systems are mostly used in the USSR; their advantage lies in the absence of complicated devices for compensating the thermoelectric emf. Their disadvantage is the necessity for balancing not only the active (ohmic), but also the reactive (capacitive) component of the impedance of the strain-gage transducers and the connecting wires.

Circuits for bridge balancing. For accurate measurements of the aerodynamic forces by strain-gage balances, a correct choice of the measuring system is very important. Account must be taken of the operating characteristics of strain-gage transducers, and the possibility of compensating the errors introduced must be provided. Manual initial

regulation (zero regulation) is provided in the measuring system in addition to the principal automatic bridge balancing. It is intended for compensating the bridge asymmetry caused by the resistance spread of the separate strain-gage transducers, the weight of the model, the influence of the resistance of the connecting wires, the initial temperature distribution in the elastic elements, etc.

The rheostat of the automatic compensator is inserted into the bridge circuit in different ways, providing a linear relationship between the variation of the measured magnitude and the displacement of the sliding contact of the rheostat. The rheostat of the automatic compensator can be connected either in series with the arms of a transducer half-bridge (Figure 6.60a) or parallel to them (Figure 6.60b). The latter is possible

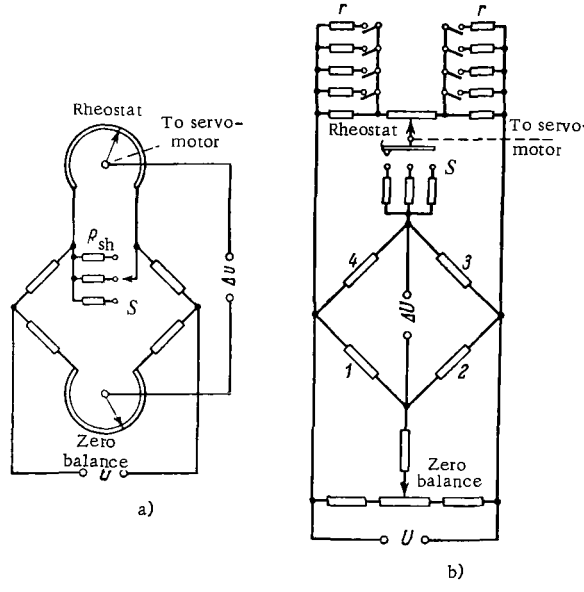

FIGURE 6.60. Connections of rheostat and potentiometer for zero regulation a — in series, b — in parallel, Δu — initial imbalance voltage which is reduced to zero by the rheostat

only with a high-resistance rheostat, since with a low-resistance rheostat the relationship between the displacement of the sliding contact of the rheostat and the variation of the measured magnitude is nonlinear. Either a low- or a high-resistance rheostat shunted by a low resistance can be connected in series with the arms of the half-bridge.

When a high-resistance rheostat is inserted between the arms of a bridge (Figure 6.60a) we can, by changing the shunting resistor R_{sh} with the aid of switch S, change the range of measured values corresponding to the full travel of the rheostat contact. When the rheostat is in parallel with the supply diagonal (Figure 6.60b), the range is changed with the aid of switch S, which inserts different resistors between the corners of the bridge and the sliding contact of the rheostat. In addition, the measuring range can be changed by expanding the scale.

When during strain measurements the rheostat contact reaches either of the limits of its travel, this switches in the shunting resistor r and the bridge is balanced at the strain attained by the transducers. This corresponds to a displacement of the strain readings over the whole travel of the sliding contact. Using a number of resistors r which are switched in automatically, we can expand the measuring range.

The initial balancing of the bridge is most often carried out with the aid of a rheostat connected in parallel to the supply diagonal (Figure 6.60b). Bridge arms (1) and (2) are shunted in such a way that the ratios of their equivalent resistances is equal to the ratio of the equivalent resistances of the other pair of arms when the slider of the rheostat is in a position which corresponds to zero strain. The shunting resistances are not mounted on the elastic element; thus, when the strain of the latter lis ε, the relative change of the equivalent resistance of the shunted arm is

$$\frac{\Delta R_{eq}}{R_{eq}} = s\varepsilon \frac{R_{sh}}{R_{sh}+R},$$

where R_{sh} is the shunting resistance of the strain gage whose resistance is R. The value $R_{sh}/(R_{sh}+R) = c$ determines the attenuation of the signal of the shunted arm.

If the resistances of strain gages (1) and (2) differ from their nominal values by $+aR$ and $-aR$ respectively, where a is small, while strain-gage transducers (3) and (4) actually have the nominal resistance R, the balancing shunting resistance for strain-gage transducer (1), is determined from

$$R(1-a) = \frac{R(1+a)R_{sh}}{R_{sh}+R(1+a)},$$

whence $R_{sh} \approx R/2a$ and $c \approx 1/(1+2a)$.

If strain-gages (1) and (2) are subjected to equal and opposite strains ε, the imbalance signal of the bridge is

$$\Delta u = \frac{us\varepsilon}{4}(c+1) \approx \frac{us\varepsilon}{2}(1-a).$$

Thus, if the resistance of transducers (1) and (2) differs from the nominal value by 1% ($a = 0.01$), the sensitivity of the half-bridge also changes by 1%. This should be taken into account when designing the measuring circuit. If the elastic element is deformed only by the force to be measured, the error introduced by the balancing shunt causes a difference between the measured and the true strain of the element. If other forces act (e.g., forces normal to that to be measured), these cause additional strains of the elastic element. When their compensation is provided in the bridge circuit, the error introduced by the shunt appears as a shift of the zero position of the automatic compensator, which depends on the magnitudes of these forces /7/, /21/.

When the bridge is fed by a.c., balancing of the reactive impedance component is provided with the aid of a capacitor (C in Figure 6.57) in addition to balancing of the active component.

The principles of strain-gage balances

Wind-tunnel balances of the strain-gage type measure the forces of interaction between the model and the cantilever support, caused by the aerodynamic loads on the model. Since the angle of attack of the model is adjusted by moving it together with its support, the components of the total aerodymamic force and moment are measured in the fixed coordinate system $x_1y_1z_1$. When analyzing the forces acting on a wind-tunnel balance located inside the model of an airplane or rocket representing an elongated body with an axis or plane of symmetry, the components are best considered in pairs: lift and pitching moment (Y_1 and M_{z_1}); side force and yawing moment (Z_1 and M_{y_1}). These components cause bending of the balance represented in Figure 6.61 as a cylindrical cantilever beam, while the drag Q_1 and the heeling moment M_{x_1} cause respectively axial compression and torsion of the beam.

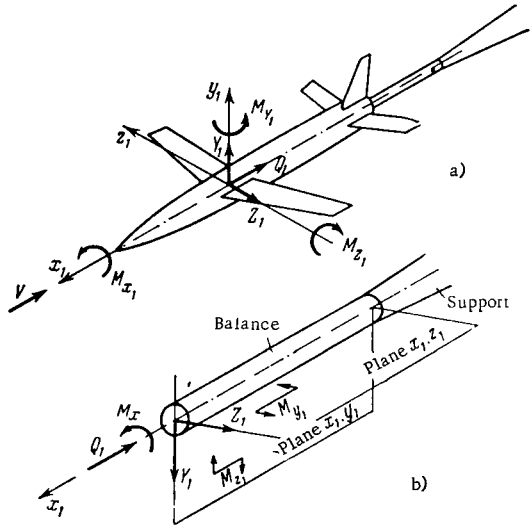

FIGURE 6.61. Strain-gage balance as beam bent in two planes.

Multi-component wind-tunnel balances located inside the model can be classified by the following design characteristics:

1) balances entirely inside the cantilever supports of the models;
2) balances with floating frames.

The arrangement of a balance of the cantilever type is based on the characteristics of the measuring bridge, which permit its use as a simple computing device. The various components of the aerodynamic load can be determined by measuring the strains at different points of the surface of the cantilever beam. By suitably connecting the strain-gage transducers mounted at these points to measuring bridges, the output signal of each bridge can be made to depend mainly on one component of the aerodynamic load. Examples of such wind-tunnel balances are the "beam" balances

which are widely used in aerodynamic laboratories in the U.S.A., U.K., and France /22/, /23/.

Balances in the form of simple cantilever beams make it possible to measure at a sufficiently high accuracy, forces and moments causing bending strains in the beam (Y_1, M_{z_1}, Z_1, M_{y_1}). The drag Q_1 and the heeling moment M_{x_1} usually cause in the beam only very small compressive and torsional strains whose accurate measurement is practically impossible. To permit measurement of these components and also to increase the accuracy of measuring other components when the model is only slightly loaded, the cantilever beam is machined in a complicated manner so as to form a number of elastic elements. These elastic elements permit the influence of any single component of the aerodynamic load to be separated partially or entirely from those of the other components.

In a wind-tunnel balance located outside the model, the aerodynamic load is resolved into components with the aid of kinematic mechanisms consisting of links which are considered undeformable. Such kinematic mechanisms cannot in practice be placed inside a small model whose breadth varies between 2 and 20 cm, as in most supersonic wind tunnels. However, if we replace the usual kinematic hinges by elastic hinges, the model is converted into a kind of floating frame connected to the cantilever support by a statically determined system of links. By measuring the reactions in these links with the aid of elastic measuring elements, we can determine the components of the aerodynamic load as functions of the strain of one or several elastic elements.

Direct resolution of the aerodynamic load into components can be carried out in a dynamometric cantilever with the aid of either elastic kinematic or elastic measuring elements. Elastic kinematic elements are used to permit translational or rotational motion (kinematic isolation) of any rigid element of the balance , while elastic measuring elements are intended to prevent such motion. The reaction between two elastic elements, of the first and the second type respectively, is proportional to the measured component. The higher the ratio of the rigidity of the elastic measuring element to the rigidity of the elastic kinematic element, the more exact is this proportionality. Strain-gage transducers mounted on the elastic measuring element permit this reaction to be measured by calibrating the balances, the reactions are compared with the measured components. Thus, Figure 6.62 shows an elastic element consisting of two parallel plates (1), interconnected by rigid elements (an elastic parallelogram) and serving for the kinematic isolation of the force P; the elastic hinge (2) is intended to isolate the moment M. The elastic measuring elements (3) and (4) measure respectively P and M.

By suitably mounting the strain-gage transducers, the kinematic element can at the same time act as measuring element. In this case the entire measured force (or moment) is equilibrated by the elastic restoring force, while the strain-gage transducers are located at the points of maximum strain. The strains at these points are affected also by the components which are not being measured.

By suitably selecting the shape of the elastic element the strain caused by the component to be measured can be made to exceed that caused by any other component. This can in particular be achieved when the component to be measured induces bending strains in the element, while the

other components cause compression or tension. The residual interference varies directly with the absolute deformation (displacement) of the elastic

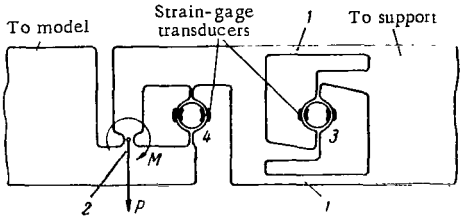

FIGURE 6.62. Direct measurement of force and moment.

element, and can be reduced or entirely eliminated with the aid of compensating systems based on the properties of the measuring bridges into which the strain-gage transducers are inserted.

Elastic elements for measuring forces

The simplest elastic element for measuring forces is a beam (Figure 6.63).

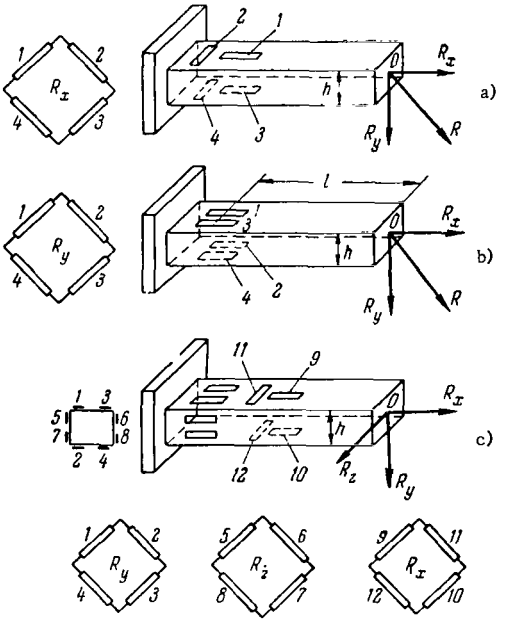

FIGURE 6.63. Systems for measuring the components of a force resultant. a — axial component R_X; b — vertical component R_Y; c — all three components R_X, R_Y, and R_Z.

For measuring the component R_x along the beam axis (Figure 6.63a), the active transducers (1) and (3) are mounted on opposite surfaces of the beam in such a way that their bases are parallel to the direction of the longitudinal strains. Transducers (2) and (4), which serve for temperature compensation, are mounted perpendicular to the longitudinal direction. If the neutral surface of the rod lies in the middle between the wire grids of transducers (1) and (3), the strains of the latter, caused by the bending of the beam, are equal and opposite ($\varepsilon_{1b} = -\varepsilon_b$). Hence, when transducers (1) and (3) are inserted into opposite arms of the bridge, the vertical component R_y does not cause an imbalance, and the latter is determined only by the axial component of the force.

For measuring the vertical component R_y (Figure 6.63b), the transducers are glued to opposite sides of the beam and inserted into adjacent arms of the bridge. The active transducers serve at the same time for compensation; this increases the sensitivity of the bridge. In contrast to the arrangement in Figure 6.63a, which permits the axial component R_x to be determined irrespective of its point of application, the arrangement in Figure 6.63b permits the component R_y to be determined only if its point of application O is known and if the axial component R_x does not cause bending of the beam, i.e., causes no moment about the origin of coordinates O on the neutral axis of the beam at a distance l from the midpoints of the transducers.

If the point of application of the resultant force is known and lies on the intersection of the neutral planes of the beam, we can, with the aid of three separate measuring bridges, measure independently each of the components R_x, R_y, and R_z, by suitably mounting transducers on the surface of the beam (Figure 6.63c). The accuracy of measuring the components depends on the ratios of their magnitudes, the accurate mounting of the transducers, their individual strain sensitivities, the uniform stress distribution at the points where the transducers are mounted, and several other factors.

When a cantilever beam of height h is bent by a transverse force, the maximum signal voltage at a distance l from the point of force application is $6l/h$ times higher than when a rod of equal cross section is tensioned or compressed by an equal force. Hence, axially stressed rods are used mainly for measuring large loads. However, for equal strains, the displacement of the point of load application is larger in bending than in axial loading.

Large displacements in multi-component strain-gage balances should be prevented, since they cause interaction between the components and displacements of the points where the forces are applied. A compromise design is therefore usually adopted, in which both sensitivity and displacements are restricted. Sensitivity is frequently more important, so that strain-gage balances are mostly provided with elastic dynamometric elements subjected to bending. Only when the loads to be measured are large or when the natural frequency of the balance has to be increased, is recourse had to elastic elements subjected to compression or tension. This is necessary, for instance, in hypersonic wind tunnels with very short operating durations.

Elastic elements in the form of eccentrically loaded rods (Figure 6.64a) have the disadvantage that during bending the arm of the force changes;

this causes nonlinearity of the force-strain relationship. This drawback is eliminated in symmetrical elastic elements (Figure 6.64b).

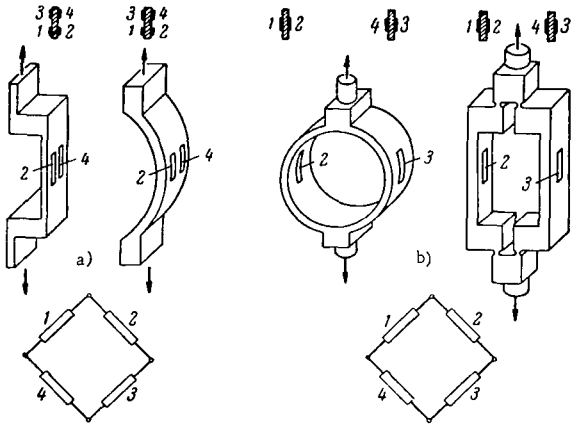

FIGURE 6.64. Elastic elements for measuring forces.

If the point of force application is unknown, the force is measured by elastic elements permitting displacement, in the direction of the force, of the balance link taking up this force. For instance, an elastic parallelogram (Figure 6.65) permits measurement of the force component perpendicular to two thin plates connecting two rigid links. This component (R_y) causes S-shaped bending of the plates, so that the rigid links are translated one with respect to the other. The strains on both surfaces of each plate are determined by two straight lines intersecting in the center of the plate. At the ends of the plates the strains are equal and opposite; their absolute value is $R_y l/4WE$, where l is the length and W is the modulus of section of the plate.

When transducers mounted on both sides of one or both plates are inserted into the measuring bridge according to diagram *a* or *b* in Figure 6.65 the bridge must respond only to the vertical component R_y. The component R_x, parallel to the plate, and the moment M cause compression or tension in the plates, which influence the bridge indications only when the plates are deflected (f). This influence can be reduced, if a third, thick plate is inserted between the two outermost plates (Figure 6.66a), which takes up the greater part of the vertical component. The bending moment is almost completely taken up by tension or compression of the outermost plates. The elastic parallelogram is thus mainly a purely kinematic element while the center plate is the elastic measuring (dynamometric) element, and carries strain-gage transducers which respond to transverse deformation. The dynamometric element for measuring the axial force Q_1 is usually a plate which is sufficiently thin to provide the necessary signal voltage due to tension or compression (Figure 6.66b). If an elastic parallelogram is used as kinematic element the thickness of the plates is small in relation to their length, and the greater

part of the force to be measured is taken up by the measuring element. If the elastic parallelogram is at the same time also the measuring element, the plates are thicker in order to reduce their deflections.

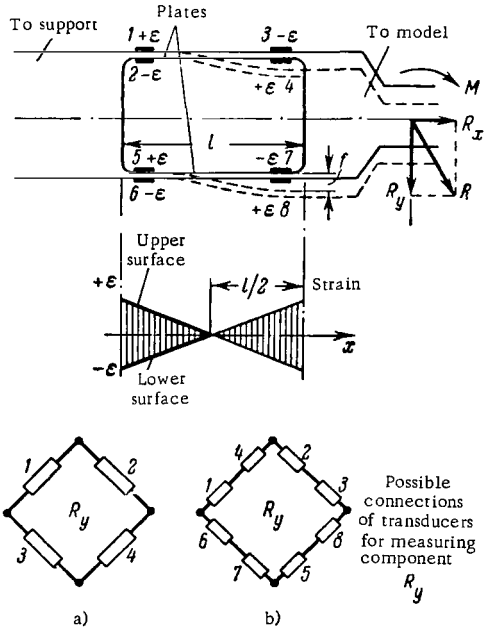

FIGURE 6.65. Force measurement with the aid of an elastic parallelogram.

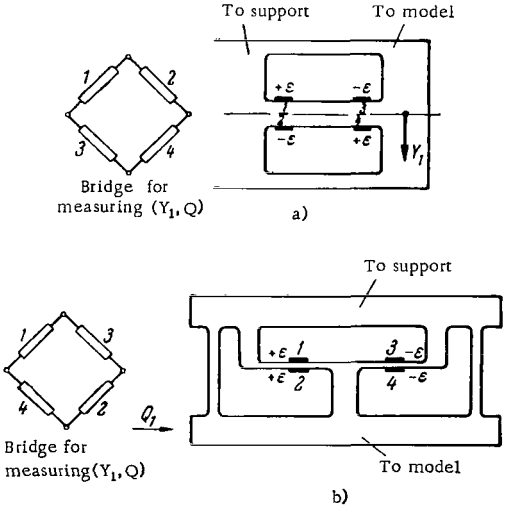

FIGURE 6.66. Elastic parallelogram used as kinematic element.

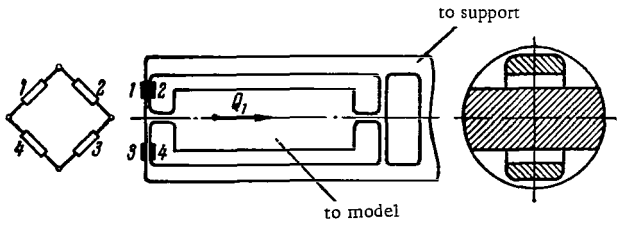

FIGURE 6.67. Double elastic parallelogram for drag measurements.

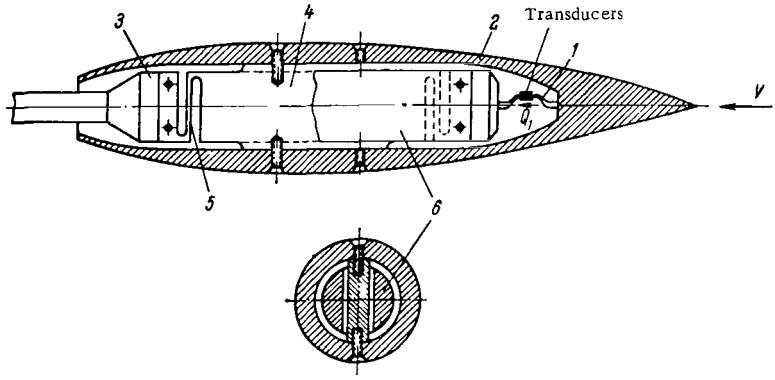

FIGURE 6.68. Single-component balance for drag measurements . 1 — measuring element; 2 — model; 3 — support; 4 — moving link of parallelogram; 5 — elastic plates of parallelogram; 6 — rigid connecting walls.

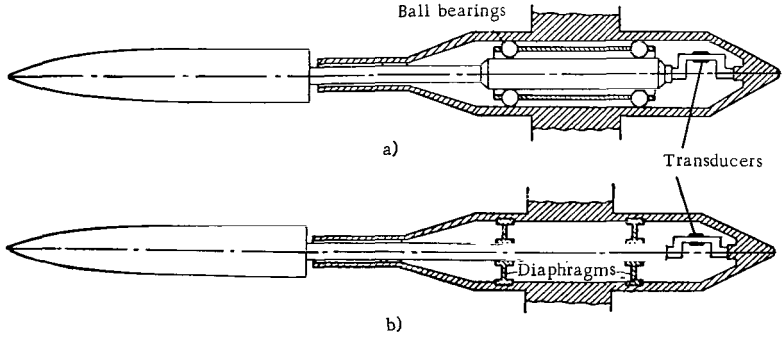

FIGURE 6.69. Measuring drag with the aid of supports mounted on ball bearings (a) and on diaphragms (b).

Figure 6.67 shows a slightly modified design of an elastic parallelogram intended for measuring drag. The model is fixed to the rigid center link of the elastic element, whose outermost links are rigidly connected to the support. The center link is the common moving link of the two elastic parallelograms. This design permits the influence of transverse forces to be reduced, since the bending moments caused by them are mutually compensated.

In the single-component balance for drag measurements (Figure 6.68), the measuring element (1) is an eccentrically loaded bent rod, inserted between model (2) and support (3). Moving link (4) of the parallelogram is rigidly connected with the model and elastically with the support, whose front and back are connected by rigid walls (6).

The use of kinematic elements for measuring the drag reduces the influence of the components Y_1 and M_{z_1}. Hence, the drag can also be measured with the aid of other devices which permit axial translation of the model, such as ball-bearing guides or elastic diaphragms of small rigidity in the axial direction (Figure 6.69).

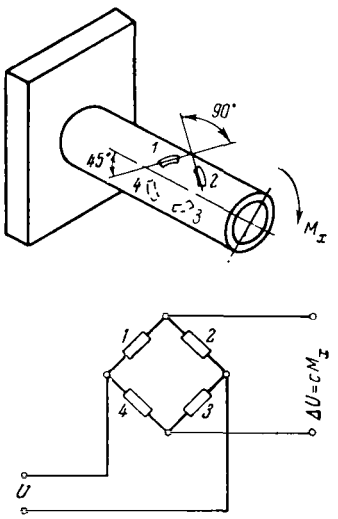

FIGURE 6.70. Torque measurements.

Elastic elements for measuring moments

Since the heeling moment M_{x_1} causes twisting of the cantilever support (Figure 6.61), M_{x_1} can be determined by measuring the strains on the surface of a circular rod or a tube. In a twisted circular rod the principal stresses are equal and opposite in directions inclined at 45° to the rod axis. Transducers glued to the rod and connected to the measuring bridge

as shown in Figure 6.70 undergo strains equivalent to a state of pure shear

$$\varepsilon_1 = \varepsilon_3 = \frac{M(1+\mu)}{W_p E}; \qquad \varepsilon_2 = \varepsilon_4 = -\frac{M(1+\mu)}{W_p E};$$

here μ and E are respectively Poisson's ratio and the modulus of elasticity of the rod material, and W_p is the polar moment of resistance of the rod cross section where the transducers are mounted.

Thus, the imbalance voltage of the measuring bridge is

$$\Delta u = \frac{us}{4}(\varepsilon_1 - \varepsilon_2 + \varepsilon_3 - \varepsilon_4) = \frac{us}{W_p E}(1+\mu)M.$$

In bending of the rod the strains of the transducers connected to the adjacent arms of the bridge are equal in sign and magnitude. The same

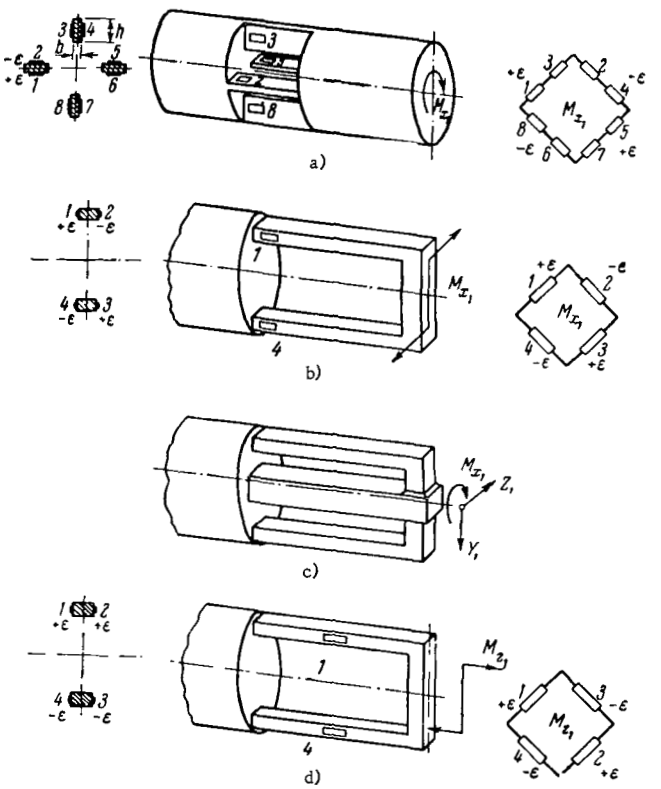

FIGURE 6.71. Elastic elements for measuring moments. a and b — measurement of M_{x_1}; c — elastic element for taking up the shearing forces; d — measurement of M_{z_1} (or M_{y_1}).

applies to compression and tension. Hence, the bridge is theoretically not sensitive to any component other than M_{x_1}. Nevertheless, in order to

reduce the influence of the components causing bending of the rod, due to nonsymmetrical mounting of the transducers, the latter are mounted as close as possible to the front of the rod. When the separate transducers are at the same temperature, the bridge is fully compensated.

A higher sensitivity to the moment M_x than in a twisted rod can be provided with the aid of elastic elements in which the torque causes bending of one or more pairs of beams or plates (Figure 6.71). The design of the elastic element (Figure 6.71a) is similar to that of an elastic hinge with fixed center (Figure 6.18). The moment M_{x_1} causes S-shaped bending of the plates. Strain-gage transducers for measuring M_{x_1} are mounted on both sides of the plate roots. The influence of the forces Y_1 and Z_1 and the moments M_{y_1} and M_{z_1}, which cause bending of the plates in the radial directions, is very small when the ratio of the plate height h to the thickness b is large. The influences of the forces Y_1 and Z_1 can be still further reduced if the axis of the elastic element is formed by a central rod taking up the greater part of these forces (Figure 6.71c). An elastic element (Figure 6.71b) which externally is similar to an elastic parallelogram, can, when $h \approx b$, be used for measuring not only M_{x_1} but also moments acting in longitudinal planes (M_{y_1} and M_{z_1}). The transducers are then mounted and inserted into the measuring bridge in such a way that the bridge responds to tension and compression of the rods (Figure 6.71d).

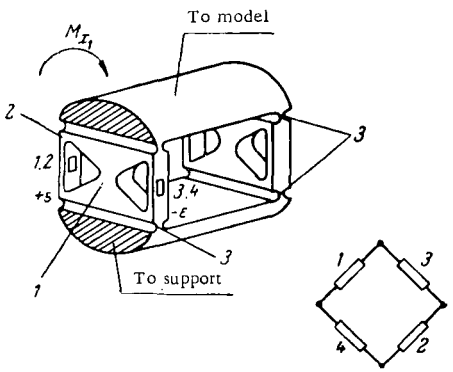

FIGURE 6.72. Measurement of M_{x_1} by an elastic element subjected to compression and tension.

In the elastic element shown in Figure 6.72, the central part of element (1) is an elastic hinge which takes up only a small part of the moment M_{x_1}. The greater part of the moment is taken up by lateral plates (2) carrying strain-gage transducers connected to the measuring bridge, which responds to tensile and compressive strains of the plates. The rigid top and bottom of the elastic element are fixed respectively to the model and to the support. Necks (3) reduce the rigidity of the elastic parallelogram, one of whose links forms the elastic element when the drag is being measured.

Figure 6.73 shows the measurement of the moment M_{x_1} by a kinematic method. The support is mounted on ball bearings inside a shroud and is connected to an elastic plate fixed at its other end to a stationary strut.

The moment M_{x_1} causes bending of the plate in a plane perpendicular to the axis of the support.

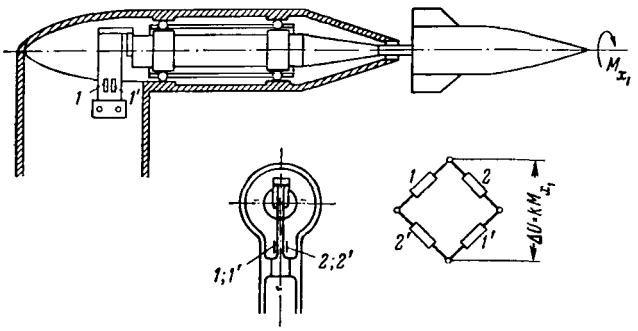

FIGURE 6.73. Measuring the moment M_{x_1} with the aid of a kinematic device.

If the origin of coordinates of the balance is placed in the beam section which passes through the center of the transducer base, the bending moment in this section will be equal to the aerodynamic moment in the plane of bending of the beam; hence, the unbalance of the bridge consisting of these transducers will be proportional to M_{z_1} (or M_{y_1}). The origin of coordinates can be transferred to any point on the axis of the support by inserting into the circuit auxiliary transducers whose strains are proportional to a force. Thus, for instance, in the circuit shown in Figure 6.74,

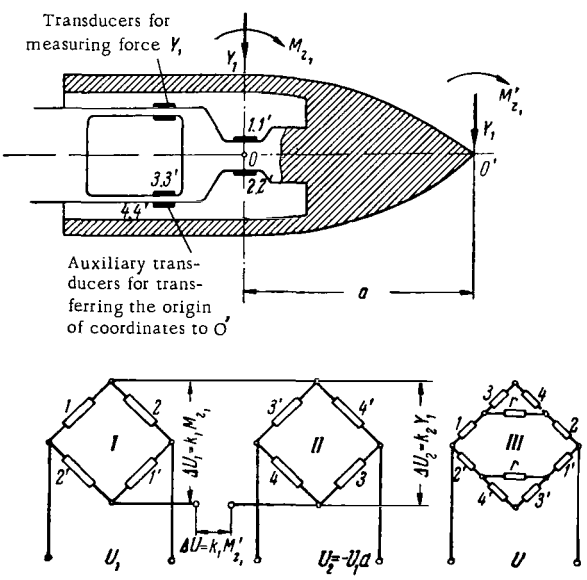

FIGURE 6.74. Circuit for transferring the origin of coordinates.

the moment M_{z_1} about the origin of coordinates O can be measured by bridge I, which consists of transducers (1), (1'), (2), and (2'). In order to transfer the origin of coordinates to O', where the bending moment is $M'_{z_1} = M_{z_1} - aY$, a bridge II is connected in series with bridge I, whose arms consist of the auxiliary transducers (3), (3'), (4), and (4'), glued to the members of an elastic parallelogram. Since these members are only strained by the transverse force Y_1, the imbalance signal of bridge II is proportional to this force. The proportionality coefficient depends on the supply voltage of the bridge. Hence, the total signal of bridges I and II is

$$\Delta u = k_1 M_{z_1} + k_2 Y_1,$$

where k_1 and k_2 are constants which characterize the sensitivities of bridges I and II. The supply voltage of bridge II can be chosen in such a way that $k_2 = -k_1 a$, so that

$$\Delta u = k_1 (M_{z_1} + aY_1) = k_1 M'_{z_1},$$

i. e., the total signal is proportional to the moment about O'.

The same problem can be solved in a simpler way with the aid of a single bridge III in which the force-sensitive strain-gage transducers are shunted by equal resistances r.

Independent measurement of forces and couples

The circuit shown in Figure 6.74 corresponds to two-component balances which permit independent measurement of a force and a moment about a given point with the aid of two separate elastic elements. This problem can also be solved with the aid of two elastic elements which are so placed that they are kinematic elements in relation to one another. Thus, for instance, in the elastic element shown in Figure 6.75, the central rod (1)

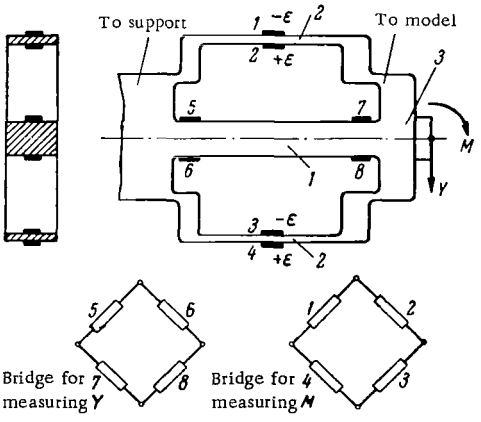

FIGURE 6.75. Elastic element for measuring force and moment. 1 — rod taking up transverse force; 2 — rods taking up bending moment; 3 — rigid link.

is subjected to bending, as in an elastic parallelogram (Figure 6.66a), taking up the greater part of the force Y. The outer rods (2) form the links of an elastic parallelogram permitting translation of link (3) under the action of this force. Strain-gage transducers mounted on central rod (1) are inserted into a measuring bridge, which permits the force Y to be measured independently of the couple. The couple, whose moment is M, is taken up almost entirely by the outer rods. These rods are eccentrically loaded by axial forces of opposite signs, which cause bending. The central beam forms an elastic hinge (i.e., a kinematic element), about which link (3) rotates. If we insert the strain-gage transducers mounted on the outer rods into a measuring bridge which responds to the algebraic sums of their bending strains, the bridge will measure the moment M about a point lying on the axis of symmetry of the elastic element.

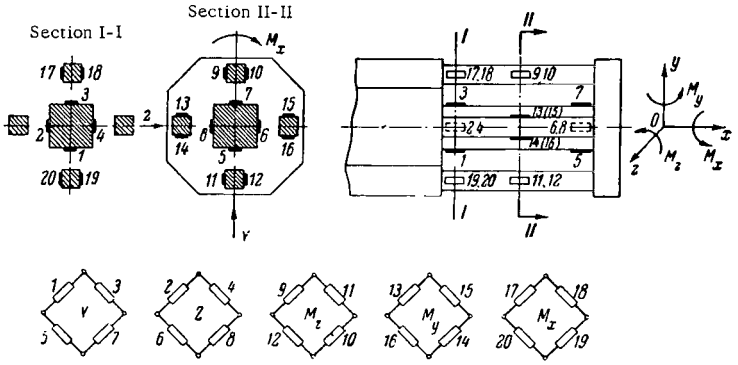

FIGURE 6.76. Five-component elastic element.

Similarly, to measure a force together with a moment we can use the central rod in the elastic element shown in Figure 6.71c. A combination of two such elastic elements with a common central rod (Figure 6.76) permits simultaneous measurement of two forces and two moments in mutually perpendicular planes, i.e., Y_1, M_{z_1}, and Z_1, M_{y_1}.

The forces are determined with the aid of measuring bridges responding to strains caused by bending of the central rod in two planes, while the moments are determined with the aid of bridges responding to tensile and compressive strains of the outer rods. The same complex elastic element can be used for measuring a fifth component (M'_{x_1}) with the aid of strain-gage transducers mounted at the roots of the rods and inserted into a measuring bridge responding to S-shaped bending of the rods (Figure 6.71a). The strain-gage transducers which are connected to bridges measuring M_{y_1} and M_{z_1} are mounted at the center of the rods, where the deformation is closest to pure tension or compression.

A basically different method of measuring forces and moments (Y_1 and M_{z_1} or Z_1 and M_{y_1}) consists in determining by two separate elastic measuring elements, the reactions R_1 and R_2 between the model and the support at two points lying on the x-axis (Figure 6.77). A couple and a force can be

determined as in a mechanical wind-tunnel balance, since the rigid balance link, which is connected to the model, serves as a floating frame.

If the resultant of the forces passes through O, which is equidistant from the measuring elements, the force is determined as the sum of the measured reactions, while the moment is proportional to their difference. This corresponds to determining the forces and moments from the indications of balance elements of mechanical wind-tunnel balances in which the forces are not resolved into components. However, the characteristics of the bridge make possible adding and subtracting operations similar to those performed in moment- and- force lever mechanisms (Figure 6.10).

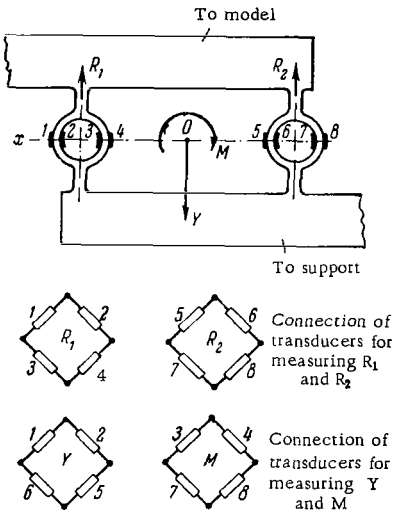

FIGURE 6.77. Installation of internal balances with floating frames.

In fact, these lever systems are actually mechanical computing devices which add and subtract the forces acting in the rods connected to the floating frame. Measuring bridges perform the same operations on the values of the strains which depend linearly on the forces and moments. An example of such a connection of strain-gage transducers to measuring bridges for the independent measurement of forces and moments is shown in Figure 6.77. An example of a strain-gage balance with floating frame is shown in Figure 6.88.

A force and a couple can also be determined from the bending moments in two cross sections of the cantilever support of the model. The solution of the problem is obtained from the fact that a bending moment due to a transverse force (Y_1 or Z_1) is proportional to the distance between the point of application of the force and the considered cross section of the rod, while the bending moment due to a couple is constant over the length of the rod. By measuring the strains in two different cross sections of the rod we obtain two independent equations whose solution yields the unknown force

and couple. The design of beam-type strain-gage balances (Figure 6.78) is based on this principle.

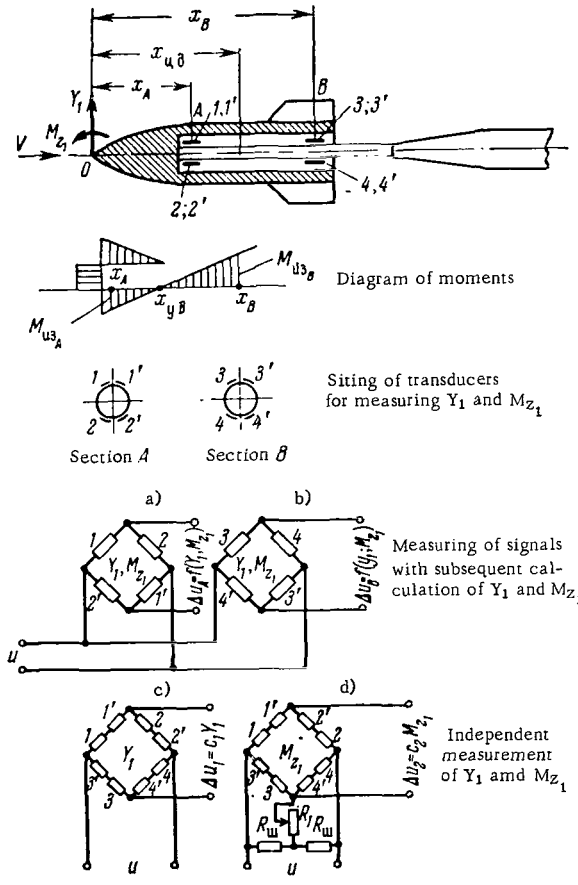

FIGURE 6.78. Beam-type strain-gage balance.

A prismatic or circular beam carries at A and B strain-gage transducers which respond to strains caused by bending moments acting in the plane of the paper.

If the origin of coordinates is at O, the bending moments in sections A and B are respectively

$$M_A = M_{z_1} - Y_1 x_A; \quad M_B = M_{z_1} - Y_1 x_B.$$

When the cross sections A and B are equal, the strains of the sensitive grids of the transducers are:

for transducers (1) and (1') $\varepsilon_1 = \frac{M_A}{WE}$,

for transducers (2) and (2') $\varepsilon_2 = -\frac{M_A}{WE}$,

for transducers (3) and (3') $\varepsilon_3 = \frac{M_B}{WE}$,

for transducers (4) and (4') $\varepsilon_4 = -\frac{M_B}{WE}$,

where E is the modulus of elasticity of the beam material and W is the modulus of section of the beam.

If we insert the strain-gage transducers in sections A and B into separate measuring bridges a) and b), the output voltages of the bridges will be

$$\Delta u_A = \frac{us}{4}(2\varepsilon_1 - 2\varepsilon_2) = \frac{us}{WE} M_A,$$

$$\Delta u_B = \frac{us}{4}(2\varepsilon_3 - 2\varepsilon_4) = \frac{us}{WE} M_B.$$

Substituting in the expressions for the bending moments the measured values of Δu_A and Δu_B, we obtain two equations with two unknowns; solving for the required components we find,

$$Y_1 = k\frac{\Delta u_A - \Delta u_B}{x_B - x_A},$$

$$M_{z_1} = k\frac{\Delta u_A x_B - \Delta u_B x_A}{x_B - x_A},$$

where $k = WE/us$.

The constants entering into these formulas, which depend on the elastic properties of the beam, the characteristics of the transducers, and their siting, are determined by calibration. If the origin of coordinates lies in the section passing through the center of the transducer base at A, then $x_A = 0$ and the indications of bridge a) in Figure 6.78 will depend only on M_{z_1}.

In order to increase the measuring accuracy, strain-gage transducers can be mounted in more than two sections /22/. The number of equations then exceeds the number of unknowns; and the moment and force are determined by the method of least squares. The unknowns Y_1 and M_{z1} are found from the following equations:

$$Y_1 = k\frac{n\Sigma x_i \Delta u_i - \Sigma x_i \Sigma \Delta u_i}{n\Sigma x_i^2 - (\Sigma x_i)^2},$$

$$M_{z_1} = k\frac{\Sigma x_i^2 \Sigma \Delta u_i - \Sigma x_i \Sigma x_i \Delta u_i}{n\Sigma x_i^2 - (\Sigma x_i)^2}.$$

In these equations n is the number of sections where strain-gage transducers are mounted, while x_i are the coordinates of these sections, and Δu_i are the output signals of the measuring bridges, which are proportional to the bending moments in the corresponding sections.

The last equations can be transformed into a simpler form which permits the unknowns to be found by multiplying the known values of Δu_i by the constants of the system:

$$Y_1 = k(a_{11}\Delta u_1 + a_{12}\Delta u_2 + a_{13}\Delta u_3 + \ldots),$$
$$M_{z_1} = k(a_{21}\Delta u_1 + a_{22}\Delta u_2 + a_{33}\Delta u_3 + \ldots),$$

where

$$a_{1q} = \frac{nx_q - \Sigma x_l}{n\Sigma x_l^2 - (\Sigma x_l)^2},$$

$$a_{2q} = \frac{\Sigma x_l^2 - x_q \Sigma x_l}{n\Sigma x_l^2 - (\Sigma x_l)^2}.$$

For independent measurements of the force and the moment we can use the measuring bridge as a simple computing device. Thus, if all strain-gage transducers in sections A and B are inserted respectively into the upper and lower half-bridge in such a way that the signal of one half-bridge is subtracted from that of the other, the imbalance voltage at the output of bridge c) (Figure 6.78) will be proportional to the difference of the bending moments acting in sections A and B:

$$\Delta u_1 = \frac{us}{4}(\varepsilon_1 - \varepsilon_2 + \varepsilon_4 - \varepsilon_3) = \frac{1}{2k}(M_A - M_B) = \frac{x_B - x_A}{2k} Y_1.$$

The imbalance voltage of bridge c) is thus proportional to the force Y_1 and does not depend on the pitching moment M_{z_1}. In order to measure M_{z_1}, the strain-gage transducers of the lower half-bridge are shunted by equal resistances R_{sh}. This reduces the imbalance signal caused by a change in the resistance of the transducers of this half-bridge to m times its former value ($m < 1$). The total imbalance signal of bridge d) is then

$$\Delta u_2 = \frac{us}{4}[\varepsilon_1 - \varepsilon_2 + m(\varepsilon_4 - \varepsilon_3)] = \frac{1}{2k}[M_{z_1}(1 - m) - Y_1(x_A - x_B m)].$$

If we choose the resistance of the shunt in such a way that ($m = x_A/x_B$), the coefficient of Y_1 vanishes so that the imbalance voltage of bridge d) is proportional to the moment:

$$\Delta u_2 = \frac{x_B - x_A}{2kx_B} M_{z_1}.$$

By adjusting the resistance of the shunt, the origin of coordinates can be transferred to different points on the x-axis.

In order to measure the side force Z_1 and the yawing moment M_{y_1}, transducers are mounted on the beam in planes parallel to the plane of the paper, and are inserted into measuring bridges in a manner similar to the above.

The disadvantage of beam-type balances is their comparatively low sensitivity, since, in order to avoid large displacements of the model caused by bending of the beam, the signal strains have to be limited. In order to increase the signal strength, the cross section of the beam is locally reduced at the points where the strain-gage transducers are mounted (Figure 6.79). The total rigidity of the rod is thus only insignificantly reduced.

When the cross section of the model is sufficiently large, the sensitivity can be increased at a smaller loss of rigidity, if the beam has internal cutouts as shown in Figure 6.79a. The total number of strain-gage transducers can then be increased by mounting them on both sides of the thin outer plates.

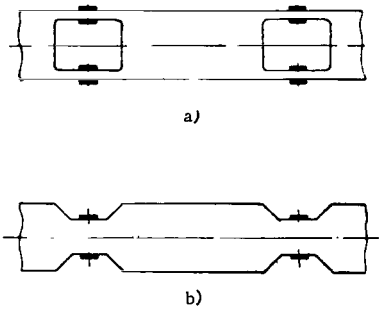

FIGURE 6.79. Local reductions of beam cross section in order to increase output signal.

Design requirements of strain-gage balances

The design of an internal wind-tunnel balance is determined firstly by the components to be measured and their limit values, and secondly, by the dimensions of the tested models. By combining in different ways the elastic elements described above, we obtain multi-component balances. The main requirements of elastic elements are large signal strains at an adequate safety factor, linearity, absence of hysteresis, and reproducibility of the measurements.

In order to increase the electrical signal for a given signal strain, the elastic element is usually provided with a large number of strain-gage transducers connected in such a way that each arm of the measuring bridge contains two, three, and sometimes four strain-gage transducers.

The maximum strains that can be measured in different types of balances vary between 0.03 and 0.1%. In order that the greatest part of the components to be measured be taken up by the measuring elements, the kinematic elements must have a low rigidity in the direction of this component and the highest possible rigidity in the directions of the components not measured.

Both linearity and reproducibility can be increased by giving to most or all elastic elements in the balances the form of integral cantilevers. If for some reason this is impossible, all connections of the elastic elements must be such that no relative displacements occur (except those caused by elastic deformations). This refers also to the connections between model and balance.

In order to reduce hysteresis, the elastic elements must be made of high-strength alloy steel having good elastic properties, small warping when heat-treated, and a high fatigue strength. One of the Soviet materials which satisfies these requirements is heat-treated grade 30 KhGSA steel which has a yield strength of 80 to 90 kg/mm^2. The best material for elastic elements is beryllium bronze.

A small interaction of the components and a small temperature sensitivity are also important requirements for balances.

The effects on the results of other components should amount to less than 1% of the limiting value of the component to be measured. If this is

not achieved, corrections are introduced whose sum must not exceed 3 to 5% of the limiting value mentioned. Interaction decreases with decreasing displacements of the model caused by deformation of the elastic elements and the cantilever support. A high rigidity of the balance should therefore be aimed at, primarily in those elements which do not take part in the measurements.

When the rigidity of the cantilever support is reduced, the amplitude of the vibrations of the model, due to load variations caused by nonuniform flow around the model, shock fluctuations, etc., increases. Vibrations of the support may introduce considerable dynamical errors into the measurements. The measuring instrument should record the mean value of the measured parameter. However, if the variations of the parameter are large, the imbalance-signal amplifier operates under saturation condition and will emit a signal even when the constant component is zero. Sometimes it is necessary to reduce sensitivity in order to increase rigidity.

Interaction depends to a large degree on the geometrical accuracy and symmetrical disposition of the elastic elements and on the correct mounting of the strain-gage transducers on them. This is done in such a way that the errors introduced by the symmetrically located elements are mutually compensated. In addition, the design of the balance must ensure accurate coincidence of the axes of model and balance. Local deformations at the joints between elastic elements must be avoided on surfaces on which strain-gage transducers are mounted.

Temperature effects are due to dynamic and static temperature gradients between individual strain-gage transducers and elastic elements. These effects can be reduced if a change in temperature does not affect the symmetry of the elastic elements or cause changes in their shape. Temperature effects in wind tunnels with high stagnation temperatures are reduced by forced cooling of the balance by water or air flowing in special channels. When the operating duration of the tunnel is short, cooling can be replaced by heat insulation.

Design examples of strain-gage balances

In wind-tunnel balances of the cantilever type, the different load components are usually measured with the aid of several elastic elements installed in series. Thus, in a three-component balance (Figure 6.80), three elastic elements are located along the x-axis, each of which is intended for measuring a separate component. The leading cross-shaped element (Figure 6.71a) is intended for measuring M_{x_1}, the thin element in the center for measuring M_{z_1}, and the elastic parallelogram (Figure 6.65), for measuring Y_1. All elastic elements are produced by milling of a cylindrical rod.

The design shown schematically in Figure 6.81 permits three components of a plane system of forces (Q_1, Y_1 and M_{z_1}) to be measured. The elastic parallelogram in the center serves for measuring the lift, and the other, for measuring the drag. In balances of this design the rigidity of the cantilever beam is lowered by reducing its cross section at the joint between the elastic element measuring drag and the model.

Bending of the beam, due to the component Y_1 and M_{z_1} or Z_1 and M_{y_1}, causes changes in the attitude of the model, displacement of the point of force application, and changes in the shapes of the elastic elements, which in turn cause additional interaction between the measured components.

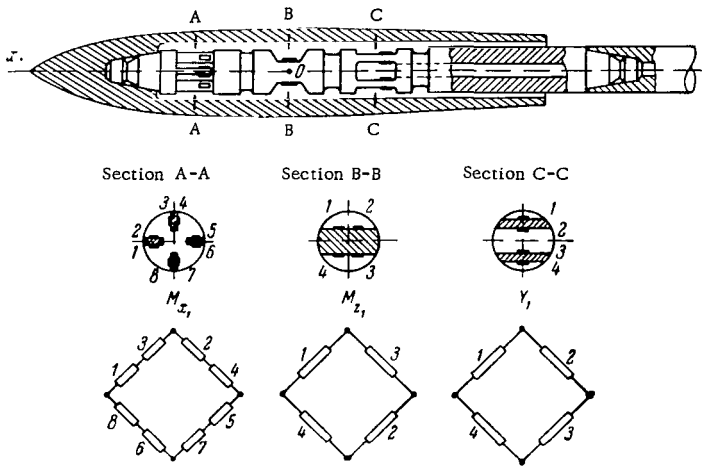

FIGURE 6.80. Three-component strain-gage balance.

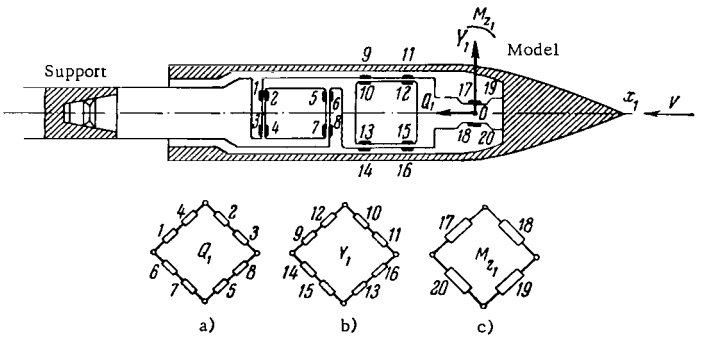

FIGURE 6.81. Three-component balance with elastic parallelograms.

Balances for drag measurement by means of an elastic parallelogram can be inserted in a model with a minimum height of 40 to 50 mm. When the height of the model is less, the plates become very short; this makes it difficult to mount strain-gage transducers on them and limits the accuracy of drag measurements.

The components Y_1 and M_{z_1} (or Z_1 and M_{y_1}) subject the plates of the elastic parallelogram to tension and compression. When the moving and stationary parts of the elastic parallelogram undergo relative

displacements, tension and compression cause eccentric bending of the plates (Figure 6.82). This causes the components Y_1 and M_{z_1} to affect the measurement of Q_1.

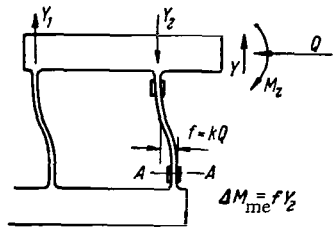

FIGURE 6.82. Interaction of load components in an elastic parallelogram.

In the six-component ARA wind-tunnel balance (Figure 6.83) this effect is reduced by using the elastic parallelogram only as kinematic element (Figure 6.66). In addition, the rigidity of the cantilever beam is increased in this balance by securing the model directly to the "moving" part of the elastic element which measures the drag /24/. The other

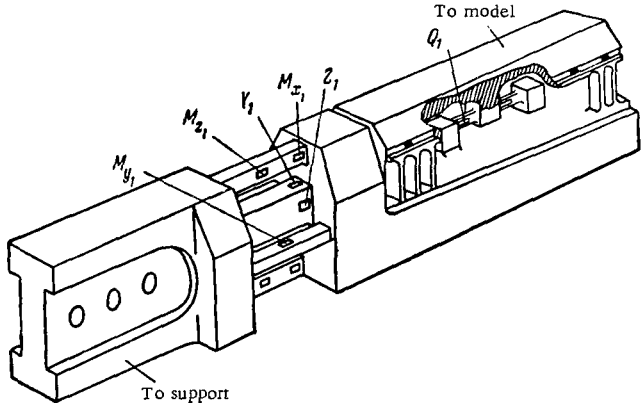

FIGURE 6.83. Six-component ARA balance.

five components are measured by an elastic element (Figure 6.76) which connects the stationary part of the elastic element measuring the drag Q_1 with the rear of the cantilever connected to the support.

In the wind-tunnel balance developed by the Royal Institute of Technology Sweden, the components Y_1, M_{z_1}, and Z_1, M_{y_1} are, in contrast, measured by elastic elements located in two sections on either side of the inner part, used for measuring Q_1 and M_{x_1}. (Figure 6.84). This internal strain-gage balance is intended for a low-speed wind tunnel (up to 100 m/sec) with an open test section measuring 4.2 m×2.7 m /25/.

The maximum loads which can be measured by the balance are: lift, 1100 kg, side force and drag, 225 kg, pitching moment, 70 kgm, heeling and yawing moments, 55 kgm. The balance consists of an inner part and two equal outer parts above and below the inner part. The components Y_1, M_{z_1}, and Z_1, M_{y_1} are measured in pairs with the aid of strain-gage transducers mounted on tension and compression plates formed by cuts in the outer parts (Figure 6.79).

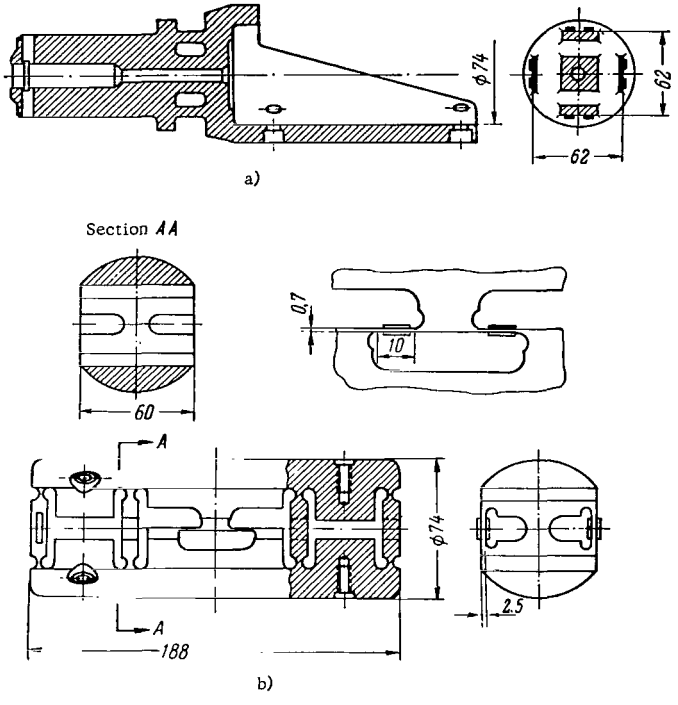

FIGURE 6.84. Elastic elements of six-component strain-gage balance for low-speed tunnels. a — outer part; b — inner part.

The heeling moment and the drag are measured by elements of the inner part formed by machining a piece of steel into two halves, connected by four vertical links and two horizontal strips. The drag causes tension in one and compression in the other strip. Two percent of the drag is taken up by the four links, in addition to the lift and the yawing moment. Of the heeling moment, 87% is taken up by two lateral links forming elastic elements (Figure 6.72) and 13% by the central links.

When the model is small the device for measuring the drag is often placed behind the model in the cylindrical part of the support strut whose cross section may exceed that of the model (Figure 6.69). The cantilever beam is covered by a shroud, which immediately behind the model forms a cylinder whose diameter is less than that of the model. At $M = 1.5$ to 3, the distance between the trailing edge of the model and the beginning of

the conical transition is between 3 and 5 diameters of the cylindrical part of the shroud. The cone angle should be as small as possible, and the cylindrical part of the strut must be located downstream of the test section where it cannot affect the flow in the latter.

An example of a six-component strain-gage balance, in which the device for measuring the drag is contained inside the strut, is the balance in the supersonic ONERA wind tunnel /12/ at Courneuve (France), whose test section measures 0.28 m × 0.28 m (Figure 6.85). The drag is measured with the aid of the kinematic suspension of support (1) on two diaphragms (2) located in the cylindrical part of strut (4). The spiral-shaped cut-outs reduce the rigidity of the diaphragms in the axial direction. The drag is taken up by elastic element (3) forming an eccentrically loaded beam. The rod in the leading part of the support has mutually perpendicular cut-outs which increase the sensitivity of the systems measuring the components Y_1, Z_1, M_{y_1}, and M_{z_1}. The sensitivity of heeling-moment measurements(M_{x_1}) is increased by the cross-shaped form of the section in which the transducers are glued. The 12 mm-diameter rod allows forces up to 5 kg and moments up to 15 kg · cm to be measured.

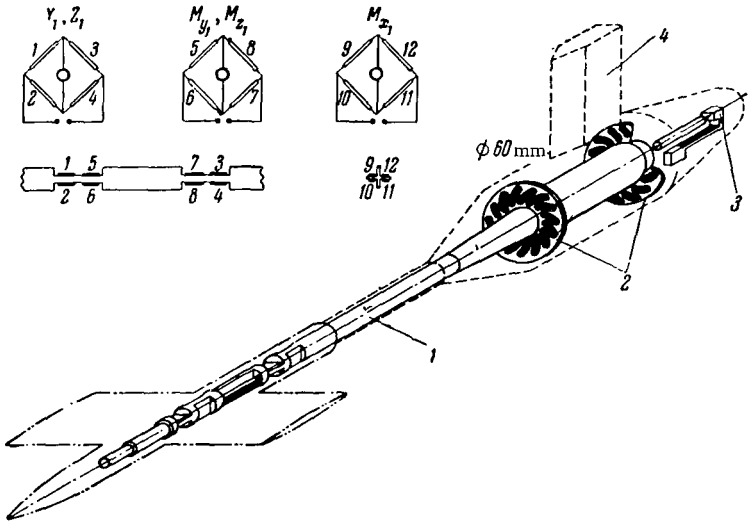

FIGURE 6.85. Six-component strain-gage balance ONERA, Courneuve. 1 — support; 2 — diaphragms; 3 — elastic element for measuring Q_1; 4 — strut.

The six-component balance of the transonic and supersonic ONERA wind tunnel (Figure 6.86) is intended for measuring the following loads: $Q_1 = 1.5$ kg; $Y_1 = Z_1 = 5$ kg; $M_{x_1} = M_{y_1} = M_{z_1} = 50$ kg · mm. The test section of the tunnel measures 0.2 m × 0.3 m. In order to increase the rigidity of the balance the components Y_1, M_z, and Z_1, M_{y_1} are measured with the aid of a cantilever beam inside the model (Figure 6.78) while the components Q_1 and M_{x_1} are measured by a kinematic method with the aid of a device in the central part of the streamlined strut. In order to reduce

the number of transducers and increase the rigidity of the support the six components are measured in two stages by switching over the electrical circuits. The lift Y_1 and the pitching moment M_{z_1} are measured by three half-bridges located in three reduced sections of the leading part of the support. One half-bridge is used in common for measuring Y_1 and M_{z_1}.

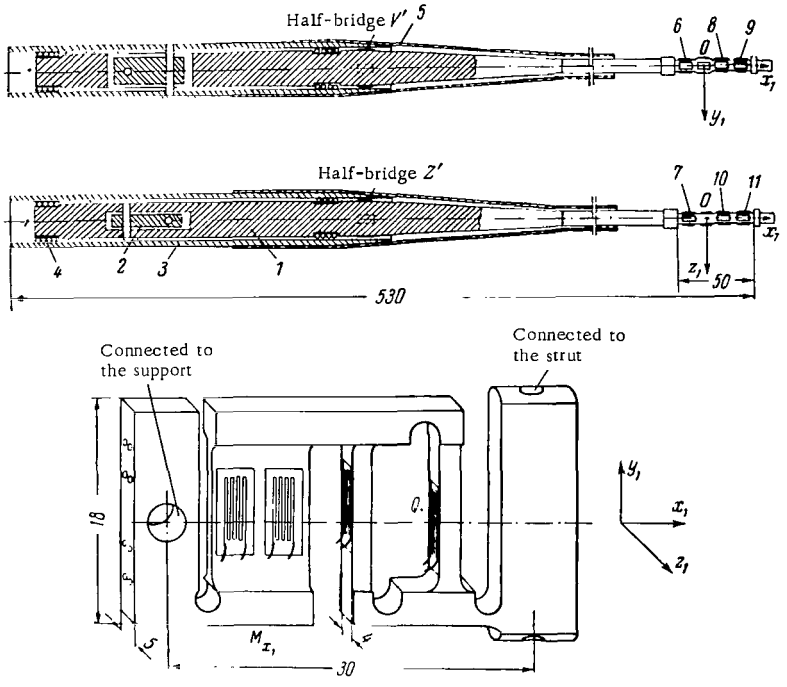

FIGURE 6.86. Six-component strain-gage balance, ONERA. 1 — support; 2 — elastic element for measuring Q_1 and M_{x_1} (shown separately below); 3 — cylindrical part of strut; 4 — ball bearing; 5 — shroud; 6 — half-bridge for measuring Y_1 and M_{z_1}; 7 — half-bridge for measuring Z_1 and M_{y_1}; 8 — half-bridge for measuring M_{z_1}; 9 — half-bridge for measuring Y_1; 10 — half-bridge for measuring M_{y_1}; 11 — half-bridge for measuring Z_1.

The transducers for measuring the side force Z_1 and the yawing moment M_{y_1} are mounted similarly. The origin of coordinates is at O. The heeling moment and the drag are measured by elastic element (2). The latter is connected by pins to the trailing part of the support and to the cylindrical part of strut (3) in which support (1) is carried on ball bearings (4) which permit rotation and axial displacement of the support. Elastic element (2), shown separately in Figure 6.86, is made integral from beryllium bronze. The drag Q_1 is measured with the aid of an elastic parallelogram whose beams are bent in the x_1y_1 plane by the action of this force. The wide plate, on which the transducers measuring M_{x_1} are glued, is bent in the y_1z_1 plane.

A simplified electrical diagram of the balance (Figure 6.86) is shown in Figure 6.87. Two half-bridges Y' and Z', which consist of transducers

mounted in front of the leading ball bearing, serve for compensating the effects of inaccurate mounting of the transducers, differences in their strain sensitivity, etc. Half-bridge Y' supplies a compensating signal to the circuit for measuring Z_1 and M_{y_1}, while half-bridge Z' supplies a compensating signal to the circuit for measuring Y_1 and M_{z_1}. The influences of Y_1 on M_{z_1} and of M_{z_1} on Y_1 are compensated by variable resistances Y_1/M_{z_1} and M_{z_1}/Y_1, whose sliders are at a potential equal to half the bridge supply voltage.

Internal wind-tunnel balances with floating frames, whose design is based on the measurement of two pairs of reactions in two mutually perpendicular planes (Figure 6.77), are more complicated than the above designs.

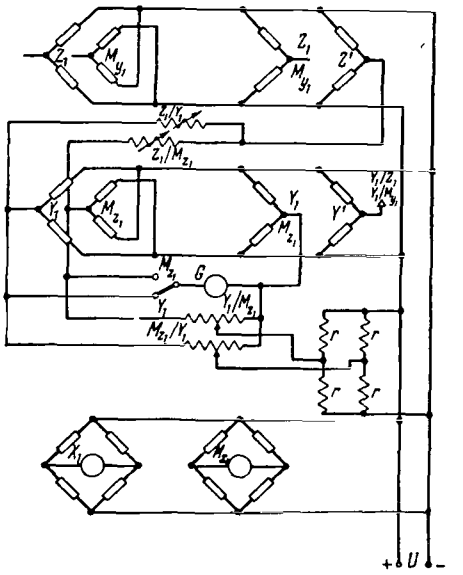

FIGURE 6.87. Simplified circuit diagram of balance shown in Figure 6.86.

The advantage of a balance with floating frame is the possibility of obtaining higher transverse rigidity, since the elastic measuring elements, which take up the transverse reactions, can be located at a considerable distance from each other. At given strains of the measuring elements, the angular displacement of the model is inversely proportional to this distance. A balance of this type (Figure 6.88) consists of a rigid support connected by the measuring elements with a tubular body carrying the model under test. The U.S. firm of Task Corporation developed a series of balances with floating frames having external diameters from 19 to 100 mm for loads (lift) from 45 to 1800 kg /7/, /25/. All reactions are determined with the aid of annular elastic elements while the heeling moment is determined by a tubular elastic element (Figure 6.70). Four

elastic elements which measure the transverse reactions (from which Y_1, Z_1, M_{y_1} and M_{z_1} are determined) participate in the strain of the elastic element measuring Q_1. These elastic elements must therefore have a small rigidity in the direction of the x-axis, since otherwise their temperature influence on the measurement of Q_1 may be large. The temperature influence can also be reduced by siting the transverse elastic elements symmetrically in relation to the elastic element measuring Q_1. The axial forces, due to temperature-induced displacements of the transverse elastic elements on either side of the elastic element measuring Q_1, are then mutually compensated.

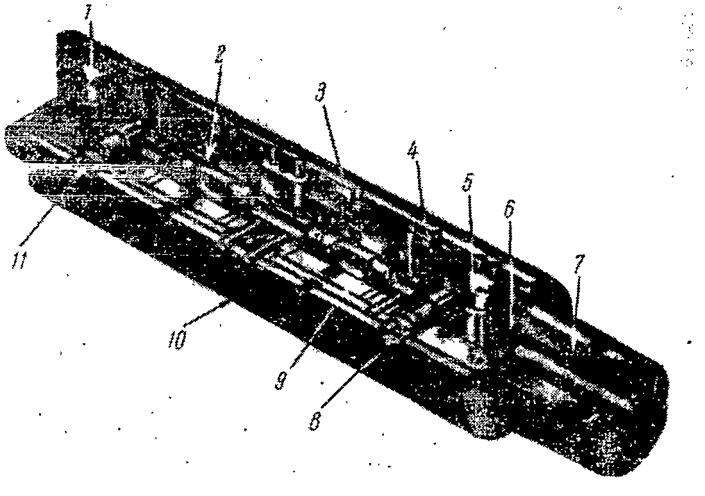

FIGURE 6.88. Six-component strain-gage balance with floating frame. 1 and 5 — elements for measuring Y_1; 8 and 11 — elements for measuring Z_1; 2 — elements for measuring M_{x_1}; 3 — hole for securing model; 4 — thermocouple; 6 — internal rod; 7 — connection to support; 9 — element for measuring Q_1; 10 — external cylinder.

The mounting of balances

An important element in the design of wind-tunnel balances of the strain-gage type is the strut which serves for holding the cantilever support and for altering the angle of attack (and sometimes the angle of yaw) of the model. The wires from the strain-gage transducers, tubes for measuring the ground pressure, and (in high-temperature tunnels) pipes for the balance coolant are brought out through this strut.

When the angle of attack is altered, the model should remain in the region of uniform flow outside the zone of reflected shocks. For this purpose a strut forming a circular arc, which permits the model to be turned in such a way that its center remains on the test-section axis, is best (Figure 6.28).

In the supersonic wind tunnel of Cornell University the mechanism for adjusting the angle of attack (Figure 6.89) consists of two arcs sliding in guide slots in the side walls of the tunnel. Between these arcs a horizontal streamlined carrying strut is fixed, whose center has a cylindrical element for securing the tail support with the balance and the model. The arcs are moved by an electric motor via a reduction gear. The joints between the mechanism for angle-of-attack adjustment and the wind-tunnel walls are sealed with rubber tubes into which air is blown after each adjustment.

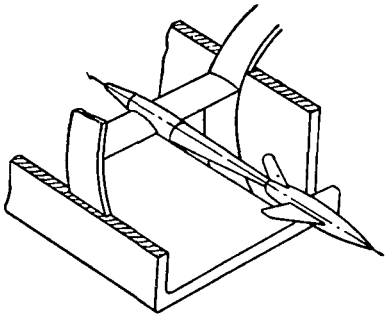

FIGURE 6.89. Mechanism for adjusting the angle of attack with two arc-shaped struts.

Figure 6.90 shows the mechanism for securing a model and adjusting its angle of attack, used in the supersonic wind tunnel of the Armstrong-Whitworth Aircraft (AWA) laboratory (U.K.). The test-section dimensions are approximately 0.5 m × 0.5 m. In this balance the angle of attack is adjusted in relation to an axis far downstream of the model; the balance is therefore equipped with a device permitting simultaneous translational motion of the model. The rear of the cantilever support is hinged inside the shrouding to two vertical struts. Each strut can be adjusted vertically with the aid of a lead screw driven by an electric motor. The movement of the struts is remotely controlled. The balance with the model is adjusted vertically in the test section by simultaneously raising and lowering the struts. The angle of attack is altered by raising one and lowering the other strut. A separate lead screw permits the model with the balance to be moved in the test section in the longitudinal direction.

Figure 6.91 shows the mechanism for mounting a six-component balance in a transonic wind tunnel of the Aircraft Research Association (ARA) laboratory (U.K.), whose test section measures 2.74 m × 2.44 m. To speed up the tests, five equal test sections, mounted on carriages, are provided. Each carriage is equipped with a balance and all necessary instruments. The cantilever support is hinged to the finely streamlined vertical strut. The lever mechanism for adjusting the angle of attack is located inside the shrouding. The angle of attack is altered by vertically moving the leading part of the strut which carries the axis of rotation of the model. The kinematics of the mechanism are such that displacement of the model in relation to the horizontal tunnel walls, caused by a change in its attitude, is compensated by translational motion together with the strut.

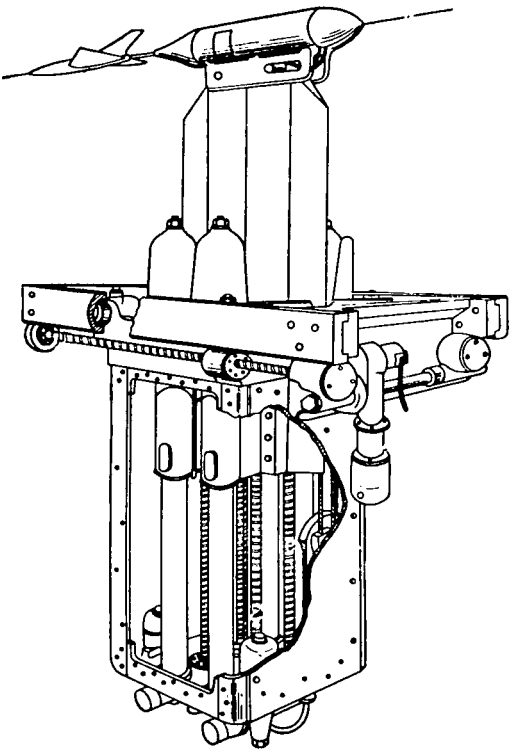

FIGURE 6.90. Mechanism for adjusting the angle of attack and moving the balance in the AWA laboratory.

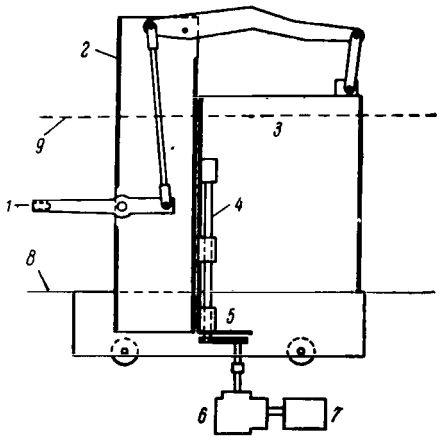

FIGURE 6.91. Mounting of model on a traveling carriage in the ARA wind tunnel. 1 — model support; 2 — sliding vertical strut; 3 — stationary vertical strut; 4 — lead screw; 5 — carriage; 6 — reduction gear; 7 — motor; 8 — and 9 — upper and lower tunnel walls.

Interaction between load components

The main causes of interaction between the load components in strain-gage balances are:

1) Differences in strain sensitivity and initial absolute resistance of the strain-gage transducers constituting the bridge;

2) Inaccurate machining of the elastic elements;

3) Inaccurate and nonsymmetrical mounting of the strain-gage transducers on the elastic elements;

4) Displacements of the elastic elements causing changes in their shape and affecting the symmetry;

5) Relative angular displacements between model and support, caused by deformation of the latter together with the balance.

In order to reduce the influence of differences in strain sensitivity, all transducers constituting a given measuring bridge must be selected from the same batch, made from wire of the same melt. In order that the resistances of the strain-gage transducers be as similar as possible, the transducers are divided into groups within which the resistance differs by not more than 0.1 ohm.

The influence of inaccurate machining of the elastic elements, or of the nonsymmetrical mounting of the strain-gage transducers on it, can be deduced from the elastic parallelogram (Figure 6.92). Let the subscript y denote bending strains of the transducers, caused by the measured force, while the subscript m denotes tensile strains caused by the moment. The imbalance signal of the bridge which serves for measuring the force Y is then

$$\Delta u = \frac{us}{4}(\Sigma\varepsilon_y - \Delta\varepsilon_m),$$

where

$$\Sigma\varepsilon_y = \varepsilon_{y_1} + \varepsilon_{y_2} + \varepsilon_{y_3} + \varepsilon_{y_4}, \qquad \Delta\varepsilon_m = \varepsilon_{m_1} - \varepsilon_{m_2} + \varepsilon_{m_3} - \varepsilon_{m_4}.$$

If at the points where the strain-gage transducers are mounted, the cross-sectional areas of the plate are not equal, or local nonsymmetrical strains exist, $\Delta\varepsilon_m \neq 0$. The bridge responds then not only to the force Y but also to the moment M.

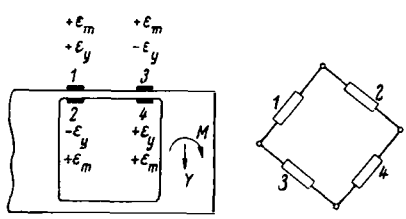

FIGURE 6.92. Influence of errors.

The same happens when the strain sensitivities of the transducers differ. If

$$|\varepsilon_{y_1}| = |\varepsilon_{y_2}| = |\varepsilon_{y_3}| = |\varepsilon_{y_4}|$$

and

$$\varepsilon_{m_1} = \varepsilon_{m_2} = \varepsilon_{m_3} = \varepsilon_{m_4},$$

then

$$\Delta u = \frac{u}{4}(\varepsilon_y \Sigma s_i - \varepsilon_m \Delta s),$$

where

$$\Sigma s = s_1 + s_2 + s_3 + s_4,$$
$$\Delta s = s_1 - s_2 + s_3 - s_4.$$

If $\Delta s = 0$, then Δu depends only on the force Y.

Inaccurate mounting of transducers in beam-type balances may also cause the base axes of the transducers measuring, e.g., Y_1 and M_{z_1}, not to lie in the x_1y_1 plane, which must be the neutral plane of bending for the force Z_1 and the moment M_{y_1} acting in the x_1z_1 plane. In this case the measuring bridges (Figure 6.78) respond not only to the components Y_1 and M_{z_1}, which tend to bend the beam in the x_1y_1 plane, but also to the components Z_1 and M_{y_1} which cause bending of the beam in the x_1z_1 plane.

When eight transducers are inserted into one measuring bridge, the transducers on the left and right of the xy-plane can be connected into a half-bridge as shown in Figure 6.93, their response being balanced in a correction circuit with the aid of a variable resistance r. We can

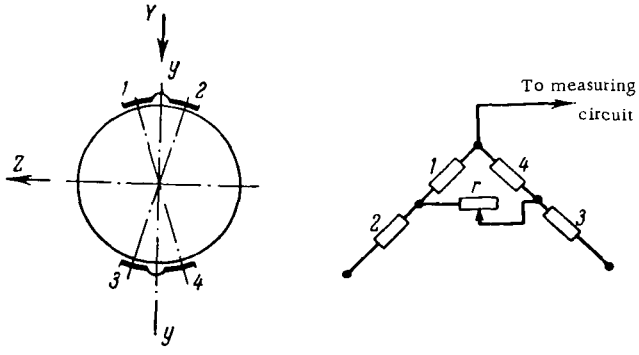

FIGURE 6.93. Compensating for incorrect mounting and different sensitivities of transducers.

experimentally choose this resistance in such a way that the force Z, which tends to bend the rod in the xz-plane, causes no response in the entire half-bridge. The circuits of the compensated bridges measuring Y_1 and M_{z_1}, which consist of transducers mounted on the beam according to Figure 6.78,

are shown in Figure 6.94. This method of eliminating interactions, used at the ONERA laboratory /23/, complicates the design of the balances, since a large number of leads are required.

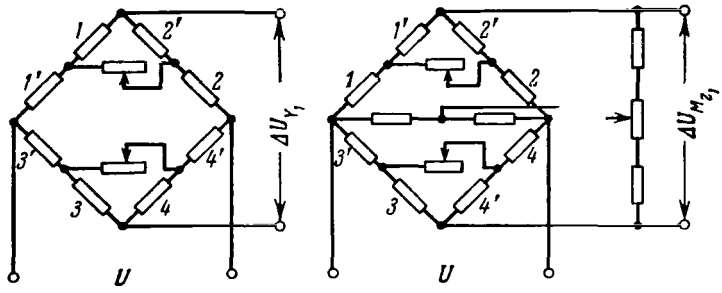

FIGURE 6.94. Circuit diagrams of compensated bridges for measuring Y_1 and M_{z_1}.

More often, the arms of a bridge measuring one component contain auxiliary transducers responding to that component which introduces an error into the measurement of the first component. The location of these auxiliary transducers and their resistance are chosen in such a way that their signal is equal and opposite to the error in the main signal. This method is applicable to all types of strain-gage balances.

Another method for reducing the interaction of components causing bending of the support in two mutually perpendicular planes consists in feeding compensating signals to the measuring bridges. Close to the point where it is secured, the support carries two half-bridges, one of which responds to the bending moment in the xy-plane (half-bridge Y' in Figure 6.95) while the other responds to the bending moment in the

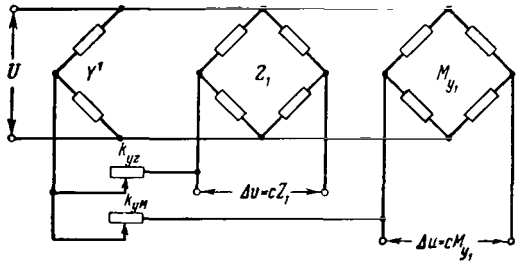

FIGURE 6.95. Circuit diagram for compensating the influence of Y_1 on Z_1 and M_{y_1}.

horizontal plane. At the point where the transducers are mounted far from where the forces are applied (the origin of coordinates of the balance), the bending moments due to couples are small in comparison with the bending moments due to the forces; we can thus assume the responses of the half-bridges to be proportional to the components Y_1 and Z_1. The influence of

the component Y_1 on the components Z_1 and M_{y_1} is compensated by connecting the ends of half-bridge Y' to the corners of bridges Z_1 and M_{y_1}. The rheostats k_{yz} and k_{yM} allow the compensating corrections to be adjusted.

Similarly, for compensating the influence of the component Z_1 on the components Y_1 and M_{z_1}, the ends of half-bridge Z' are connected to the corners of bridges Y_1 and M_{z_1} (see Figure 6.87).

Calibration of strain-gage balances

Calibration of strain-gage balances is basically similar to the calibration of mechanical wind-tunnel balances. Using a calibration device, known loads are applied in the direction of each component, and calibration curves are plotted from the indications of the instruments of each measuring channel. The calibration device is installed either instead or on the model in such a way that the directions of the loads coincide with the balance axes. The balance support is deformed under the action of the load. To maintain the model in the position corresponding to zero angle of attack irrespective of the deformation of the support, its position is corrected with the aid of a separate mechanism.

If the balance is to be operated under varying temperatures, it should be calibrated at different temperatures between 10 and 70°C in order to determine the zero drift.

Whereas in mechanical balances we can almost completely eliminate interaction between the components, this is not always possible in strain-gage balances. Special attention should therefore be paid during calibration to determine these interactions.

In three-component wind-tunnel balances, the true values of drag, lift, and pitching moment are

$$Q_1 = k_X n_X - k_{YX} n_Y - k_{MX} n_M,$$
$$Y_1 = k_Y n_Y - k_{XY} n_X - k_{MY} n_M,$$
$$M_{z_1} = k_M n_M - k_{YM} n_Y - k_{XM} n_X,$$

where n_X, n_Y and n_M are the indications of the measuring instruments, while k_X, k_Y and k_M are the calibration coefficients for the corresponding components. The coefficients accounting for the interaction between the components are k_{YX}, k_{XY}, ... k_M, where the first subscript denotes the component which affects the component denoted by the second subscript.

§ 29. THE ERRORS OF WIND-TUNNEL BALANCES. CALIBRATION

The errors of "external" aerodynamic balances are introduced by the balance elements and the system for resolving the forces into components. When the balance elements are sufficiently isolated from the effects of temperature and pressure variations, the accuracy of the balance depends mainly on random errors. The latter are found usually by calibrating the balance elements separately.

The main sources of intrinsic errors of the wind-tunnel balances are:

1) Inaccurate assembly of the system for separating the forces into components;

2) Displacements and deformations of the links due to variations in load, temperature, and pressure;

3) Inexact transmission ratios of levers;

4) Deformation of the model supports.

These are systematic errors which can be found and eliminated when calibrating the balance. In wind-tunnel balances the most characteristic systematic errors are those expressed by the interaction of the components. Random errors are caused mainly by friction in the hinges of the links and can be found by processing the calibration data by the method explained below.

For correct calibration of the wind-tunnel balances the sources of systematic errors must be known. Below, these sources are discussed in the order in which they are best discovered during calibration. For the sake of simplicity, we shall consider a two-dimensional system of forces (Q, Y and M_z).

Errors due to inaccurate assembly of the balance

The main cause of this type of errors is the nonparallelity between the directions of the coordinate axes and the directions of the links which connect the model or the floating frame with the measuring system of the balance.

Thus, for instance, if rods (1) and (2), by which floating frame (3) is suspended from the lever system which measures the lift Y and the pitching moment M_z, are inclined at an angle φ to the vertical (Figure 6.96), the

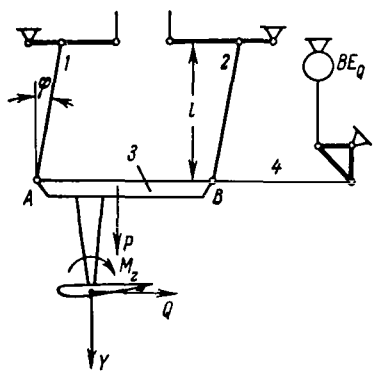

FIGURE 6.96. Effect of initial inclination of rods on drag measurement.

forces acting in these rods have horizontal components. Rod (4), which connects the floating frame to balance element BE_Q, will then take up,

in addition to the horizontal component Q, an additional load which, when φ is small, is

$$\Delta Q = (P + Y)\varphi,$$

where P is the weight of the floating frame and the model.

The value of $P\varphi$ is constant and can be easily found from the initial indication of balance element BE_Q. Inclination of the rods therefore causes an error in the measurement of Q, which is proportional to the lift and to the angle of inclination:

$$\Delta Q' = Y\varphi.$$

With a low-drag model, a small inclination of the rods can cause considerable errors when measuring Q. Thus, for instance, in order that the correction $\Delta Q'$ be less than 0.5% of Q when $Y/Q = 20$, it is necessary that

$$\frac{\Delta Q'}{Q} = 20\varphi < \frac{1}{200}.$$

The angle of inclination of the rods should therefore not exceed $\varphi = 1/4000$. When the length of the rods is l, their upper and lower hinges should lie on one vertical with an accuracy of $l/4000$. The longer the rods, the easier it is to obtain this accuracy. The adjustment must be made by a weight method. The supports of the lever carrying the upper hinges of the rods are moved horizontally to a position at which the placing of weights on the frame near hinges A and B does not affect the indications of balance element BE_Q. To prevent changes in this position during operation of the balance, the supports must rest on very rigid bases. After adjustment the supports are fixed by control pins. Adjustment is facilitated if the floating frame has additional hinges for suspending calibration weights near the hinges A and B.

The influence of displacements of the measuring links. The pendulum effect

The forces acting on the floating frame cause deformation of the balance links and displacements of the load-supporting links of the balance elements. The changes thus introduced in the geometry of the system for resolving the forces into components give rise to interactions between the latter. Horizontal displacements of the floating frame, causing the lift to affect measurement of the horizontal components, are most critical.

A system consisting of a floating frame suspended on vertical rods can be considered as a load, whose weight P is equal to the total weight of the frame and the model, suspended from a stationary hinge on a vertical rod of length l (Figure 6.97). The elasticity of the links connecting the frame with the system measuring Q can be simulated by the elasticity of spring (1) having a spring rate c_1, while the stability of the balance element can be simulated by a spring whose spring rate is c_2. If the stability

coefficient of the balance element (i. e., the ratio between the force acting on the measuring link of the balance element and the displacement of this link) is k, then $c_2 = ki^2$, where i is the transmission ratio of the lever system.

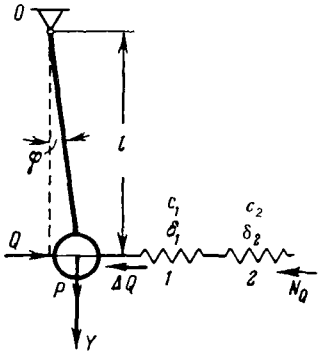

FIGURE 6.97. The pendulum effect.

The angle of inclination of the pendulum (Figure 6. 97), caused by the action of force Q, is

$$\varphi = \frac{\delta_1 + \delta_2}{l},$$

where δ_1 and δ_2 are respectively the deformations of springs (1) and (2). Setting up the equilbrium equation for the load P and considering the horizontal components, we obtain

$$\Delta Q = Q - N_Q = (P + Y)\varphi,$$

where N_Q is the force acting in link A by which the horizontal rod is connected to the balance element BE_Q. Expressing the deformations δ_1 and δ_2 through the compressive force and the spring rates, we obtain

$$\Delta Q = (P + Y)\frac{N_Q}{l}\frac{c_1 + c_2}{c_1 c_2}.$$

Since the angle φ is usually very small, we can assume $N_Q \approx Q$ and

$$\Delta Q = aQ + bYQ,$$

where a and b are constants for the given suspension and model.

Since the weight P of the floating frame is constant, the influence of the first term on the right-hand side of the last equation is expressed in the change of the transmission coefficient of the drag-measuring system. If the same suspension were always used and the weight of the model were constant, this change could easily be compensated by adjusting the arm of a lever or by changing the scale of the measuring elements. The magnitude bYQ is the absolute error in measuring the drag Q and is called

the pendulum effect. The pendulum effect, which influences also measurements of the side force Z, causes the largest systematic errors in wind-tunnel balances and must be found by calibration.

The pendulum effect varies inversely with c_1 and c_2. If the balance element used for measuring Q is based on the null method, the pendulum effect is caused only by the elasticity of the connecting links, since in this case $\delta_2 = 0$. We can thus reduce the pendulum effect by using balance elements of the compensating type and by increasing the rigidity of the connecting links in the system for measuring the horizontal component.

The above relationships for evaluating the pendulum effect are also valid for any other mechanism of translational motion of the floating frame. It is only necessary to replace the lengths l of the rods by the equivalent length l_{eq}. Thus, for the antiparallelogram mechanism (Figure 6.3a) $l_{eq} = \frac{a_1 a_2}{a_1 - a_2}$. When a_1 and a_2 are relatively small and equal $l_{eq} = \infty$. Hence, in this case there is no pendulum effect and the system is neutral with respect to the lift. Adjustment of the balance is facilitated if the floating frame on antiparallelograms has a small positive stability. For this, we take $a_1 > a_2$, so that $l_{eq} = 5$ to 10 m.

Sometimes the pendulum effect can be prevented with the aid of devices which automatically return the floating frame to its initial position by changing the length of the horizontal rod connecting the floating frame with the balance element.

Inexact transmission ratios

The effects of inexact transmission ratios of the levers can be analyzed by considering the moment-and-force lever system shown in Figure 6.10a. Let us assume that due to a manufacturing error the transmission ratios of the levers are not exact, i.e.,

$$i_1 = \frac{a_1}{b_1} \neq i_2 = \frac{a_2}{b_2} \text{ and } \frac{L_1}{l_1} \neq \frac{L}{l}.$$

We assume for the sake of simplicity that the line of action of Y passes through a point midway between hinges A and $B\left(l_1 = \frac{l}{2}\right)$. Writing

$$i = \frac{i_1 + i_2}{2}; \quad \Delta i = \frac{i_1 - i_2}{2}; \quad \Delta L = L - 2L_1,$$

where Δi and ΔL are small in comparison with i and L, we obtain

$$N_y = Yi - \frac{2M}{l}\Delta i, \tag{a'}$$

$$N_M = M\frac{1}{lc}[(1-i)L + \Delta i\,\Delta L] + \frac{Y}{2c}[(1-i)\Delta L + \Delta i L]. \tag{b'}$$

which differ only slightly from formulas (a) and (b) on page 340. The second terms on the right-hand sides of equations (a') and (b') are the errors due to the interaction between lift and pitching moment.

The influence of the pitching moment on the lift measurement is

$$\Delta Y = Y - \frac{N_y}{i} = \frac{2M}{l}\frac{\Delta i}{i},$$

and is due only to the inequality of the transmission ratios of levers P_1 and P_2. Since $\Delta i \cdot \Delta L$ is a magnitude of second order of smallness, the error in measuring the moment is

$$\Delta M = M - N_M \frac{cl}{(1-i)L} = -\frac{Yl}{2}\left(\frac{\Delta L}{L} + \frac{\Delta i}{1-i}\right).$$

Thus, the influence of the lift on the pitching-moment measurement depends on the inequality of the transmission ratios of levers P_1 and P_2, and also on the inequality of the arms of lever P_3, i.e., on ΔL.

Deformations of the supports

In the general case, deformations of the supports under the action of aerodynamic loads on the model cause translation and rotation of the model in relation to the floating frame of the balance.

During translation the vectors of the total aerodynamic force and the total aerodynamic moment move together with the model without changing in magnitude or direction. If the origin of coordinates of the balance is fixed in relation to the floating frame, displacement of the point of force application from the origin of coordinates O to point O_1 (Figure 6.98)

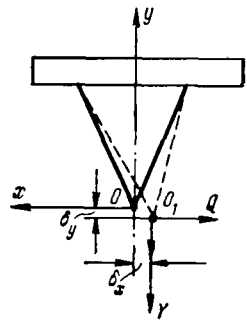

FIGURE 6.98. Effect of support deformations.

causes the pitching moment acting on the floating frame to change by $\Delta M_z = \delta_x Y - \delta_y Q$, where δ_x and δ_y are the projections of the distance $\overline{OO_1}$ on the x- and y-axes. Within the elastic limit the displacements of the suspension are proportional to the forces:

$$\delta_x = \frac{Q}{c_1} \text{ and } \delta_y = \frac{Y}{c_2},$$

where c_1 and c_2 are the "spring rates" of the model suspension in the x- and y-directions. Hence

$$-\Delta M_z = QY\frac{c_1 - c_2}{c_1 c_2}.$$

Thus, deformation of the suspension accompanied by translational motion of the model causes an error in measuring the pitching moment, which is proportional to the components of the forces. If the moment about the measuring hinge on the model is measured with the aid of a balance element located on the floating frame, translational motion of the model does not affect the measurement of M_z.

In wind-tunnel balances with flexible suspensions the wires or tapes form the links of the measuring system. The influence of changes in the directions of the vertical and inclined wires under the action of horizontal forces is completely analogical to the pendulum effect. The error in measuring the drag is again $\Delta Q = (a + bY)Q$, where a depends on the geometry of the wire suspension.

When the deformation of the suspension is accompanied by a change in attitude of the model, the correction $\Delta\alpha$ for the angle of attack has to be found. Usually, $\Delta\alpha$ depends linearly on Y and M_z and does not depend on Q. $\Delta\alpha$ is determined by special calibration of the balance together with a suspension. The calibration results are used to plot curves of the dependence $\Delta\alpha = f(M_z)$ for different values of Y. After the model has been tested, the corrections for the angle of attack are found from the measured values of Y and M_z.

The calibration of mechanical wind-tunnel balances

There are two types of calibration of wind-tunnel balances: adjustment (primary) calibrations and control calibrations. Adjustment calibration is carried out immediately after manufacture and assembly of the balance on a special test stand or in the test section of the wind tunnel. Levers and balance elements are first calibrated separately, and are then adjusted and calibrated as a complete balance. After calibration a document is prepared setting out all calibration coefficients and corrections for the interaction between the components. Control calibrations are carried out systematically for checking the condition of the balance and introducing, where necessary, corrections into the data obtained by initial calibration. The separate levers are calibrated according to the method, suggested by D. I. Mendeleev, of suspension at constant sensitivity.

Figure 6.99 shows a device permiting determination of the transmission ratio and the sensitivity (as function of the load) of lever (1) being calibrated, at a constant sensitivity of calibrating lever (2). Plate (7) carries a load which is equal to, or approximates the maximum load taken up at normal operation by the lever being calibrated. This load is balanced by a load on the plate (8), so that the pointer of lever (2) indicates zero on scale (9). Lever (1) is calibrated by removing by stages the load from plate (7) and balancing lever (2) by placing a load on plate (6). The transmission ratio of the lever is equal to the slope of the straight line passing through the

experimental points on the graph $G = f(P)$ where G is the load removed from plate (7) while P is the load placed on plate (6). The number of experimental points should be between 10 and 20. The transmission ratio is

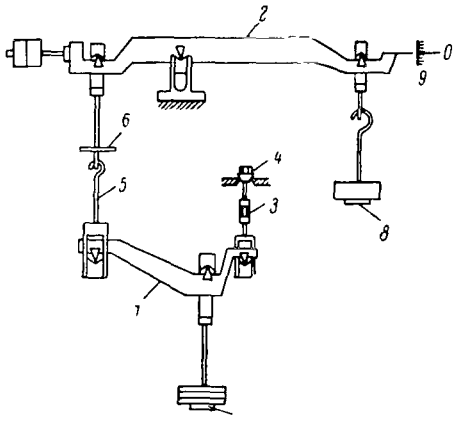

FIGURE 6.99. Device for calibrating levers.

determined by the method of least squares (see page 434) with an error not exceeding 1/10,000. Standard weights are used for calibration.

Complete wind-tunnel balances are calibrated with the aid of a calibrating device which permits known loads to be applied in directions parallel to the coordinate axes of the balance, as well as known moments about these axes.

In order to find systematic errors (interaction of components) the measuring system for each component is calibrated with different loads being applied to the systems measuring the other components. It is sufficient usually to determine the influence of the lift Y and the pitching moment M_z on the system for measuring the drag Q, and the influence of Q on Y and M_z.

The calibration device for three-component wind-tunnel balances (Figure 6.100) is a frame (1) fixed to the support in place of the model. The frame carries knife edges (2), (3), (4), and (5) to take up weights. The tip of knife edge (2) coincides with the z-axis. This permits the floating frame of the balance to be loaded by a vertical force Y by placing weights on plate (6) without applying a pitching moment M_z.

If the model is tested in its upright position, knife edge (2) is installed with its tip downward and the balance is loaded by a force directed upward. The system for measuring the drag Q is calibrated by knife edge (3), which is subjected to a horizontal force created by loading plate (7), suspended from a rope passed over roller (8). The rope must lie in the x-direction. In order that deformation of frame (1) will not cause the point of application of the horizontal force to move in the vertical direction, the tip of knife edge (3) must be as near as possible to the origin of coordinates.

Knife edges (4) and (5) serve for loading the balance by the pitching moment M_z. The distance between the knife edges is known exactly.

Plates (9) and (10), which are suspended from these knife edges, carry at first equal weights which are then partly moved from one plate to the other. The floating frame is thus subjected to a pure moment which is equal to the product of the length l and the transferred weight. The vertical load on the floating frame remains unchanged.

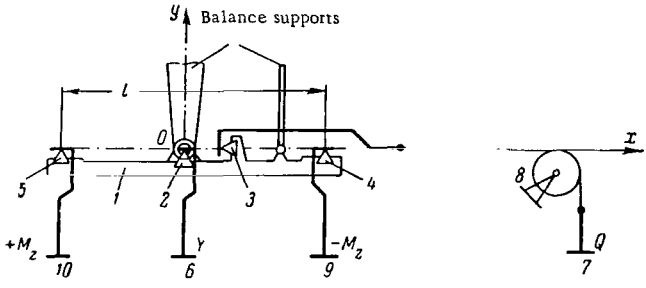

FIGURE 6.100. Calibration device for three-component wind-tunnel balances.

In order to reduce to a minimum the displacement of the calibration device in relation to the origin of coordinates of the balance, the device is fixed to the floating frame by special brackets during adjustment of the balance. These brackets are more rigid than the model support and permit the interaction between the components, caused by the suspension to be eliminated. The remaining errors, due to interaction of the components and angular displacement of the model, are determined with the aid of the calibration device which is fixed to the support on which the model is tested in the wind tunnel. If different supports are used for holding the models, the balance is calibrated for each support separately.

Processing of calibration data

The main purpose of calibrating measuring instruments is to establish the dependence between the measured value t and the indication u of the measuring instrument. The dependence is in most cases linear and for its determination it is sufficient to find the calibration constant of the instrument, i.e., $k=\frac{t}{u}$. To determine k, the measured physical magnitude is replaced by a standard. The standards in wind-tunnel balances are loads applied with the aid of weights. Other measuring instruments, such as manometers, thermometers, etc., are usually calibrated by comparing their indications with the indications of a reference instrument whose error must be at most one third of the assumed error of the instrument being calibrated.

Another purpose of calibration is to determine the accuracy characteristics of the instrument, i.e., to find the random and systematic errors of measurement. Knowing the errors of a given

instrument, we can determine their influence on the accuracy of the experiment as a whole.

The calibration constant is determined on the basis of p measurements of u_i corresponding to standard values t_i (i varies from 1 to p). The maximum value of t_i should be as close as possible to the limiting value which can be measured by the instrument. If the values of u_i and t_i are plotted (Figure 6.101), a straight line can be drawn through the experimental points, whose equation is

$$u = at + u_0, \tag{1}$$

where $a = \frac{1}{k}$, and u_0 is the null reading of the instrument.

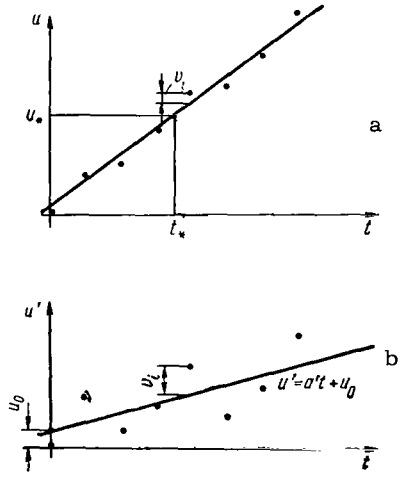

FIGURE 6.101. Calibration curves.

If u_i and t_i contain no systematic errors, the most probable values of a and u_0 can be found by the method of least squares. These values are

$$a = \frac{p\Sigma u_i t_i - \Sigma u_i \Sigma t_i}{p\Sigma t_i^2 - (\Sigma t_i)^2}, \tag{2}$$

$$u_0 = \frac{\Sigma t_i^2 \Sigma u_i - \Sigma t_i \Sigma u_i t_i}{p\Sigma t_i^2 - (\Sigma t_i)^2}. \tag{3}$$

These equations can also be written in the form

$$a = \frac{\Sigma u_i t_i - p u_* t_*}{\Sigma t_i^2 - p t_*^2}, \tag{4}$$

$$u_* = a t_* + u_0, \tag{5}$$

where u_* and t_* are the mean values of the variables u and t:

$$u_* = \frac{\Sigma u_i}{p}; \quad t_* = \frac{\Sigma t_i}{p}.$$

The equation of the most probable straight line passing through the experimental points can be presented in the form

$$u - u_* = a(t - t_*),$$

i.e., the straight line must pass through the point (u_*, t_*).

After determining the parameters a and u_0 of the most probable straight line, we can find the standard deviation of a single measurement of u, which characterizes the accuracy of the calibrated instrument. The standard deviation is

$$\sigma_u = \pm \sqrt{\frac{\Sigma v_i^2}{n-2}},$$

where $v_i = u_i - at_i - u_0$ are the random errors of measurement (Figure 6.101).

The value of σ_u is used for determining the accuracy of the values obtained for a and u_0. Suitable expressions for determining σ_a and σ_{u_0} were given by B. A. Ushakov /8/, based on the highest frequency of cumulative mean errors in the equations for a and u_{*i}:

$$\sigma_a = \pm \frac{\sigma_u}{t_p - t_1} \sqrt{\frac{12(p-1)}{p(p+1)}},$$

$$\sigma_{u_0} = \pm \sigma_u \sqrt{\frac{2(2p-1)}{p(p+1)}}.$$

When the number of experimental points is large (above 12 to 16) we can write

$$\sigma_a = \pm \frac{6\sigma_u}{t_p - t_1} \frac{1}{\sqrt{3p}},$$

$$\sigma_{u_0} = \pm \frac{2\sigma_u}{\sqrt{p}}.$$

At a given standard deviation σ_u of the calibration curve, the error in a depends on the number of experimental points and on the interval $(t_p - t_1)$. In order to increase its accuracy, the calibration should be carried out over the full range of loads, dividing the latter into a large number of intervals.

In order to simplify the calculations necessary for determining a and u_0, the values u_i in (2) and (3) or (4) and (5) are replaced by $u_i' = u_i - \bar{a}t_i$, where $\bar{a}$ is an approximate value of the coefficient a. The value of $\bar{a}$ is determined as the slope of the straight line drawn by eye through the experimental points plotted on graph paper. The value found from (2) or (4) represents a correction of the approximate value of the slope, whose exact value is

$$a = \bar{a} + a'.$$

The points corresponding to u_i' are plotted in Figure 6.101b. The deviations of these points from the straight line $u' = a't + u_0$ determine the deviations of the experimental points from the linear dependence. The missing points can then be found.

Bibliography

1. Joukowski, N. E. Polnoe sobranie sochinerii. Teoreticheskie osnovy vozdukhoplavaniya (Collection of Works. Theoretical Bases of Flight). — ONTI NKTP. SSSR. 1938.
2. Möller, E. Die mechanischen Waagen im Windkanal. p. 162. — ATM, L. 1949.
3. Leavy, L. E. and C. G. Saunders. A Modern Wind Tunnel Balance. — J. Roy. Aero. Soc., Vol. 57, No. 512. 1953.
4. Wind Tunnel Operating Equipment. — SAE Journal (Transactions), Vol. 49, No. 3. 1943.
5. Pankhurst, R. C. and D. W. Holder. Wind Tunnel Technique (an account of experimental methods in low- and high-speed wind tunnels). — Pitman, London. 1952. [Russian translation. 1955].
6. Hem, H. O. Aeroplane Testing Apparatus. — Aircraft Engineering, Vol. 17, No. 192. 1945.
7. Allen, H. J. and J. M. Spiegel. Wind Tunnel Measurements, High Speed Aerodynamics and Jet Propulsion, Vol. 8, Sect. K. — Princeton Univers. Press. 1961.
8. Ushakov, B. A. Opredelenie parametrov lineinoi zavismosti dvukh peremennykh po sposoby naimen'shikh kvadratov (Determining the Parameters of the Linear Dependence of Two Variables by the Method of Least Squares). — Trudy [Translations] No. 680. 1949.
9. Midwood, G. F. and R. W. Hayward. An Automatic Self-balancing Capsule Manometer. — ARC C. P., No. 231. 1956.
10. Barskii, B. A. Bezkontaktnye automaticheskie vesovye elementy (Contactless Automatic-Balance Elements). — Promyshlennaya aerodinamika, No. 19. Oborongiz. 1959.
11. Conard, M. Mesure des efforts aérodynamiques dans les souffleries de grandes dimensions a vitesse élevée. — Technique et Science Aéronautiques, No. 4. 1949.
12. Rebuffet, P. Quelques balances a jauges extensométriques des souffleries françaises. – Note techn. ONERA, No. 31. 1956.
13. Eastman, F. S. The Electromagnetic Balance, a High-precision Measurement and Control Device. — Instruments, Vol. 14, No. 10. 1941.
14. Bratt, J. B. Development of an Automatic Electric Balance for Research on Aerodynamic Stability. — Philosophical Magazine, Vol. 35, No. 248. 1944.
15. Kinkel, J. F. A Precision Pressure Balance. — ISA Proceedings, Vol. 7. 1952.
16. Turichin, A. M. and P. V. Novitskii. Provolochnye preobrazovateli i ikh primenenie (Strain Gages and Their Use). — Moskva-Leningrad, Gosenergoizdat. 1957.
17. Perry, C. C. and H. R. Lissner. The Strain Gage Primer. McGraw - Hill. N. Y. 1955 [Russian translation. 1960.]
18. Bassierre, M. Mesure et enregistrement des mesures sur les balances aérodynamiques à jauges à fil resistant. — Note techn. ONERA, No. 32. 1956.

19. Tsapenko, M. P. Avtomaticheskie kompensatory s dekadnym magazinami soprotivleniya (Automatic Compensators with Decade Resistance Boxes).— Priborostroenie, No. 1. 1957.
20. Tsapenko, M. P. Mnogomostovaya izmeritel'naya skhema peremennogo toka (A. C. Multi- Bridge Measuring System).— Izmeritel'naya Tekhnika, No. 6. 1956.
21. Tiffany, A. Precision Strain Gauge Techniques.— Electronic Engng., Vol. 30, No. 367. 1958.
22. Haneman, V. S. Automatic Reduction of Wind- Tunnel Data.— Aeron. Engng. Rev., Vol. 12, No. 2. 1953.
23. Devacht, M. Balances dards a 6 composants.— La Recherche Aéronautique, Vol. 52. 1956.
24. Tiffany, A. Wind Tunnel Instrumentation.— Electronic Engng., Vol. 29, No. 3. 1957.
25. Motsinger, R. N. Flexural Devices in Measurement Systems.— Strain Gage Readings, Vol. 5, No. 2. 1962.
26. Gratzer, L. B. Design of a New Balance System for the Kirsten Wind Tunnel.— Trends in Engineering in the University of Washington, July. 1952.

Chapter VII

TECHNIQUES AND METHODS OF AERODYNAMIC MEASUREMENTS

§30. ADJUSTMENT OF WIND TUNNELS

Adjustment of the flow in the tunnel. In subsonic wind-tunnels the adjustment consists of determining the positions of vanes and flaps, and the types and number of screens in the test section, in such a way that the velocity nonuniformity, flow inclination, and turbulence remain within permissible limits.

In transonic and supersonic tunnels the adjustment consists mainly in the selection of nozzles providing uniform flow velocities, in determining the position of the supersonic diffuser providing steady supersonic flow in the test section both in the presence of, and without the model, and in selecting the position of the perforated walls of the test section. Experience shows that the adjustment of the tunnel must be carried out for each new tunnel even when it was built according to the plans of a similar existing tunnel. The adjustment of wind tunnels having complicated contours is

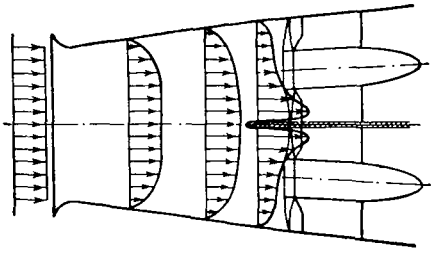

FIGURE 7.1. Velocity distribution in the diffuser of a double tunnel.

particularly difficult (*e.g.*, a tunnel with two return ducts leading into a single common duct at the nozzle inlet; Figure 2.116). In such a tunnel the diffuser is usually divided by a partition into two parts. Because the elliptical section of the diffuser passes over into two circles at the fan, the flow velocity at the outer walls is reduced, while at the return-duct inlet the velocity distribution is highly nonuniform. (Figure 7.1).

Measuring methods for determining and adjusting the velocities in subsonic tunnels

The velocities are determined with the aid of traversing cradles which permit the siting and securing of tubes measuring the magnitude and direction of the velocity at any point in the test section. The permissible inaccuracy in reading off the coordinates of the tube should not exceed 1 to 2 mm per meter length of the test section, while the angular displacements of the nozzle, caused by the deformation of the traversing cradles and the inaccuracy of the mechanism itself, should not exceed 0.05 to 0.1 degrees.

The velocity head, the static pressure, and the angles of flow inclination in the vertical and horizontal planes must be measured simultaneously. These measurements are best made with the aid of the specially designed TsAGI six-bore tube /1/ (Figure 4.51). First, by calibration with a special device, we find

$$\varkappa = \frac{p_1 - p_3}{(p_1 - p_2) + (p_3 - p_2)},$$

$$\sigma = \frac{p_4 - p_5}{(p_4 - p_2) + (p_5 - p_2)},$$

where p_1, p_2, and p_3 are the pressures in the orifices located in the vertical plane while p_4, p_5, and p_2 are the pressures in the orifices located in the horizontal plane. The calibration curve ($\alpha = f(\varkappa)$) for one of the tubes is given in Figure 7.2.

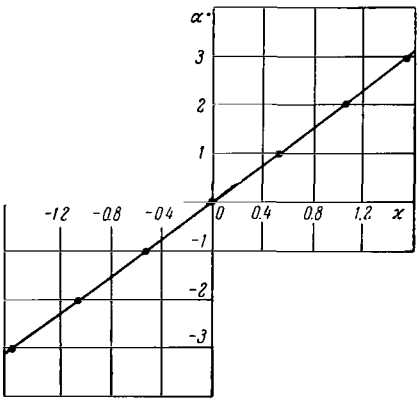

FIGURE 7.2. Calibration curve $\alpha = f(\varkappa)$ for a six-bore tube.

The pressure differences $p_1 - p_2$, $p_3 - p_2$, etc. are best measured with the aid of a five-bore tube (Figure 7.3) equipped with a blocking mechanism which permits the differences of pressure in the various orifices to be determined simultaneously. It is seen from the form of the expressions for $\varkappa$ and σ that when a five-bore tube is used, the measuring errors, due to inaccuracies of determining the inclination of the

manometer, the density of the liquid, and the temperature, are eliminated. The random error of a single measurement of the angle of flow inclination does not exceed ±0.1° in this method.

The relative velocity head in the test section is determined according to Figure 7.4 with the aid of

$$\mu = \frac{\rho \frac{V^2}{2}}{p_s - p_a} = \zeta \left[1 + \frac{p_2 - p_s}{p_s - p_a} - \frac{p_6 - p_a}{p_s - p_a} \right],$$

where p_2 and p_6 are respectively the total static and pressures measured by the tube, $(p_s - p_a)$ is the difference between the pressure in the settling chamber and in the room surrounding the tunnel, ζ is the correction coefficient of the tube. The errors in this method, which enables

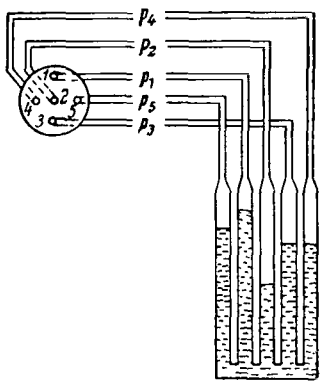

FIGURE 7.3. Connecting a six-barrelled tube to a five-barrelled manometer for calibrating the tube.

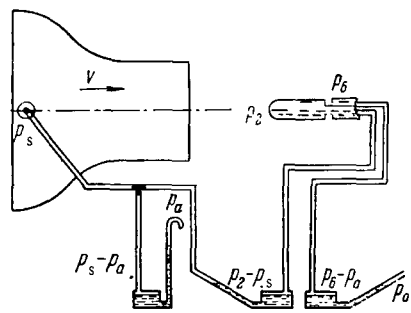

FIGURE 7.4. Connections of tubes and manometers for determining the relative velocity head in a tunnel.

small corrections to be made for $\mu \approx 1.0$, are less than when μ is found from

$$\mu = \zeta \frac{p_2 - p_6}{p_s - p_a}$$

and $(p_2 - p_6)$ is determined by a tube installed in the test section. The values of μ, obtained at different points of the tunnel, serve for evaluating the uniformity of the velocity distribution. Its values usually vary between 0.95 and 1.05. The results of processing the measurements of the angles α and β, and also the values of μ at different positions in the test section, are shown in Figures 7.5 to 7.7.

The best results after calibration are usually obtained by equalizing the velocity distribution in the return ducts behind each corner, where a nonuniformity of the velocities amounting to 10% is permitted. The angles of inclination are equalized by suitably selecting the angles at which the guide vanes are installed (especially in the fourth corner) and with the aid of baffles, which are usually placed also on the horizontal partitions of the fourth corner.

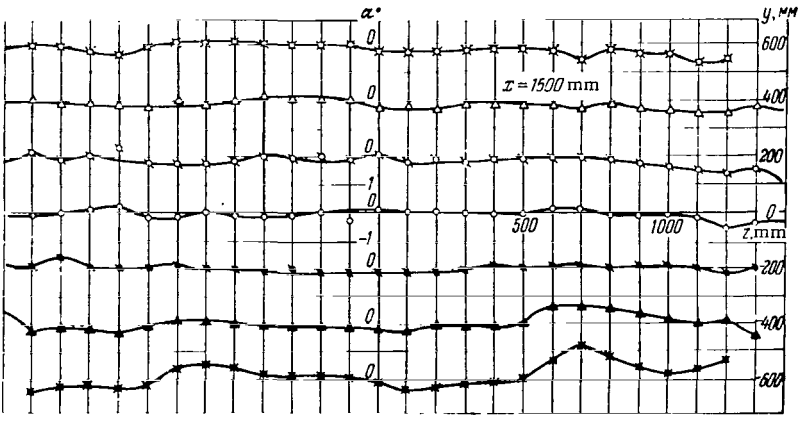

FIGURE 7.5. Distribution of angles of flow inclination in the vertical plane (distance from nozzle x = 1500 mm z = transverse coordinate, y = vertical coordinate).

Sometimes the reasons for unsatisfactory flow characteristics are the unevenness of the aerodynamic contour (large diffuser angles, small compression ratios, etc.). In these cases the velocity distribution can be equalized only by changing some of the tunnel elements. Adjustment of the

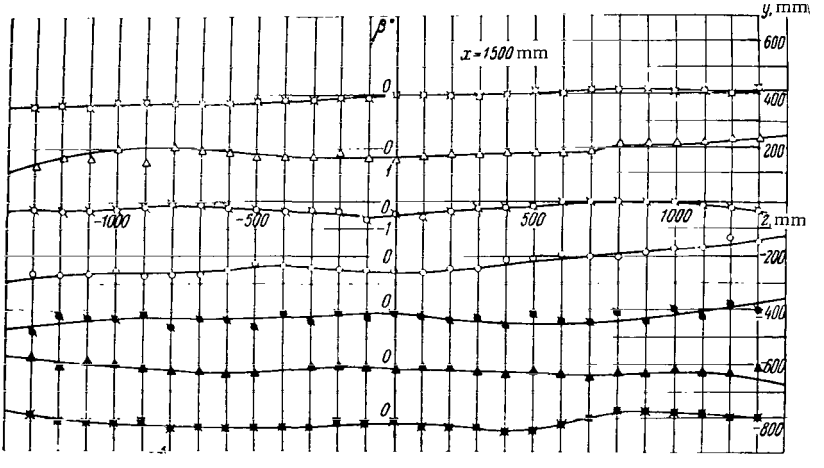

FIGURE 7.6. Distribution of angles of flow inclination in the horizontal plane.

flow in the the tunnel is very tedious, and is carried out by successive tests. The flow is more uniform in the airstream core than at the boundaries of the test section. In addition, the constant-velocity core becomes narrower in the direction from the nozzle to the diffuser (Figure 7.8). The turbulence level varies in the direction from the

core to the flow boundaries. Figure 7.9 gives the relationship

$$T_F = \frac{\mathrm{Re}_{\mathrm{cr.atm}}}{\mathrm{Re}_{\mathrm{cr.tun}}}$$

for a sphere at different positions on the horizontal axis of the tunnel section. It can be seen from Figure 7.9 that turbulence is least in the flow core.

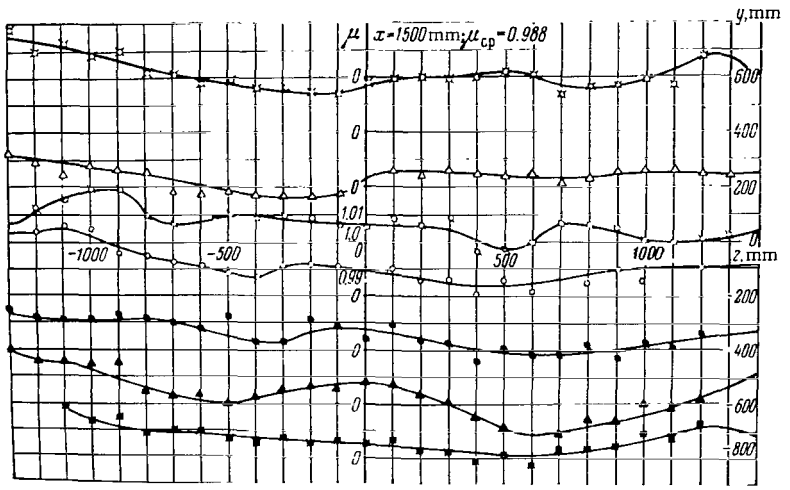

FIGURE 7.7. Distribution of relative velocity head in control section of tunnel.

The high turbulence level is mainly due to the same reasons as the velocity nonuniformity, and also to an insufficient expansion ratio in the nozzle, and can be partly reduced by the general flow adjustment in the tunnel and by installing additional smoothening screens in the settling chamber.

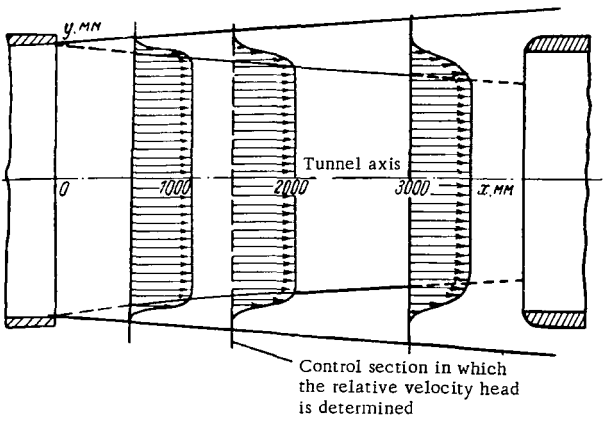

FIGURE 7.8. Airstream boundaries in an open test section.

Because the test section of a wind tunnel has restricted dimensions, no regions exist in it in which the flow is not affected by the model.

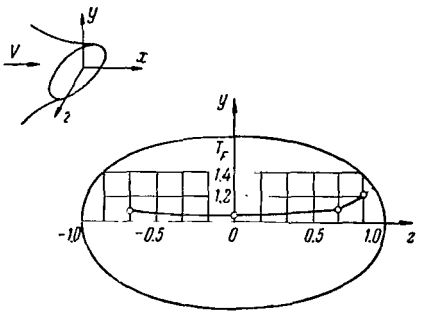

FIGURE 7.9. Turbulence distribution across the test section (x = constant).

Because of this the velocity is measured as far upstream as possible from the tested body. However, due to the velocity nonuniformity existing even in a calibrated tunnel, the mean velocity in the test section can differ from the measured flow velocity.

We obtain the mean flow velocity in the test section near the model from the measured velocity by calibrating the empty tunnel and determining μ_{av}. Multiplying by this the indications of the measuring tube, we obtain the true free-stream velocity for the tested model.

Flow inclination. In spite of the fact that the angles of flow inclination in the test section are small, their influence on the aerodynamic characteristics is considerable. This is true particularly for angles of inclination in the xOy-plane* (angles of vertical flow inclination). The corrections of the results of determining the angle of inclination consist in converting the values of the aerodynamic forces or coefficients, (c_x', c_y'), measured in the balance system of coordinates, into the corresponding values in the flow system of coordinates (c_x, c_y):

$$c_x = c_x' \cos\alpha_к + c_y' \sin\alpha_к,$$
$$c_y = c_y' \cos\alpha_к - c_x' \sin\alpha_к,$$

where $\alpha_к$ is the mean angle of vertical flow inclination, which very seldom exceeds 0.5 to 1°. Taking into account the smallness of $\alpha_к$, and also the smallness of c_x in comparison with c_y, we can write

$$c_x = c_x' + c_y\alpha_к,$$
$$c_y = c_y'.$$

The angle of attack is then

$$\alpha = \alpha' + \alpha_к.$$

* The angle of inclination in the horizontal plane (β), which usually does not exceed 0.5 to 1°, does not greatly influence the principal aerodynamic characteristics, and is usually neglected.

The angle $\alpha_к$ is considered positive if it tends to increase the angle of attack. Vertical flow inclinations can necessitate considerable corrections in the values of the drag coefficient.

The flow inclination is determined /2/ by measuring the maximum airfoil efficiency in both upright and inverse positions

$$k_{max}^{up} \text{ and } k_{max}^{in}.$$

The angle of vertical flow inclination is then

$$\alpha_к^0 = \frac{1}{2}\left(\frac{1}{k_{max}^{in}} - \frac{1}{k_{max}^{up}}\right) 57.3.$$

Another method of finding the angle of vertical flow inclination is by the difference in drag coefficients in upright and inverse position for different lift coefficients /3/:

$$c_x = c'_{x\,up} + c'_{yup}\alpha_к,$$
$$c_x = c'_{x\,in} - c'_{y\,in}\alpha_к.$$

Setting $c'_{y\,in} = c'_{y\,up} = c_y$, we obtain

$$\alpha_к = \frac{c'_{x\,in} - c'_{x\,up}}{2c_y}.$$

Knowing the polars for the upright and inverse positions, we find $\alpha_к$ for several values of c_y, and determine its mean value, which is sufficiently accurate for correcting the values of the drag coefficients of different airfoils, and also of the angles of attack.

Adjustment of transonic and supersonic wind tunnels

The flow characteristics at transonic or supersonic velocities depend mainly on the aerodynamic properties of nozzle and test section. The flow characteristics of supersonic tunnels are determined for each Mach number by measuring the pressure distribution at the test-section walls,* and by direct flow measurements in the test section by means of special probes and tubes. The variation in static pressure along the test section, which is very important in tunnels with closed test section, is determined by tubes placed along the tunnel axis and by orifices in the walls of the test section.

Direct measurement of the turbulence level in supersonic tunnels is difficult. We can indirectly establish the relative turbulence level by determining the position of the transition point in different tunnels or in the same tunnel with and without smoothening screens in the settling chamber**.

* The orifices in the test section of the tunnel are usually arranged in two sections of the vertical wall (for determining the influence of the angle of attack of the model) and in one section of the horizontal wall.

** In some tests, installation in the settling chamber of smoothening screens having a resistance coefficient $\zeta = 10$ reduces the turbulence number in the test section from 3.5% to 1% at $M = 3$ /4/.

With perforated test-section walls, introduced in recent years in transonic and supersonic tunnels, boundary-layer suction effected through the tunnel walls, and other measures, permit the flow in the test section to be uniform in magnitude and direction in the absence of a static-pressure gradient along the test section. In the best modern high-speed tunnels the velocity nonuniformity does not exceed $\pm(0.015 \text{ to } 0.02)M$, the flow inclination is less than $\pm(0.15 \text{ to } 0.2°)$, while the static pressure along the test-section axis usually varies within the limits of ± 3 to 5%.

Thus, the flow adjustment in transonic and supersonic tunnels, while maintaining the aerodynamic requirements for the subsonic part of these tunnels (settling chamber, return duct, etc.), consists in selecting the correct shapes for nozzle and test section.

§ 31. TECHNIQUES AND METHODS OF BALANCE MEASUREMENTS

Balance measurements consist in determining the aerodynamic coefficients of forces and moments acting on the model at different angles of attack and yaw.

In general such tests are carried out at varying angles of attack and yaw and constant velocity (constant values of Reynolds and Mach numbers), at different angles of attack and yaw and varying Reynolds and Mach numbers, and at different positions of the longitudinal and lateral control surfaces at varying Reynolds and Mach numbers.

Tests of elements of the airplane model (wings, fuselage, tails, engine nascelles, radomes, etc.) are intended for determining the best shapes by comparison of several alternatives. The results of these tests can only be used approximately for evaluating the specific influence of any element in the general drag or lift balance. However, in some cases we can obtain sufficiently accurate quantitative results for separate components, for instance, when determining the hinge moments of the control surfaces, when testing the isolated tails, or when determining the effectiveness of an aileron fitted to an isolated wing.

Balance tests at large flow velocities are usually accompanied by studies of the flow pattern with the aid of a Töpler instrument or interferometer.

In a number of cases there arises the necessity to investigate ground effects on the aerodynamic characteristics of an airplane. Such tests are usually made with the aid of a screen which simulates the ground. Figure 7.10 shows the model installed in the "tunnel" position and the screen. The screen is a rectangle whose horizontal dimensions correspond to the width and length of the test section. The leading edge of the screen has usually the shape of a semiellipse with an axis ratio of 1 : 2, while the trailing edge has parabolic shape.

When tests are carried out with the screen, the distance between the screen and the trailing edge of the control surface of the wing is varied by moving the screen vertically with the aid of jacks.

In some experiments the influence of the ground is simulated by a ribbon moving at the same velocity as the air. This method is more accurate (there is no boundary-layer thickening on the ribbon), and reproduces the conditions in nature where the ground is stationary, while the airplane moves in relation to it; however, because of its complexity, it is not widely used. Another method, in which the boundary layer on the screen simulating the ground is sucked off, can also be used in tests for investigating ground effects.

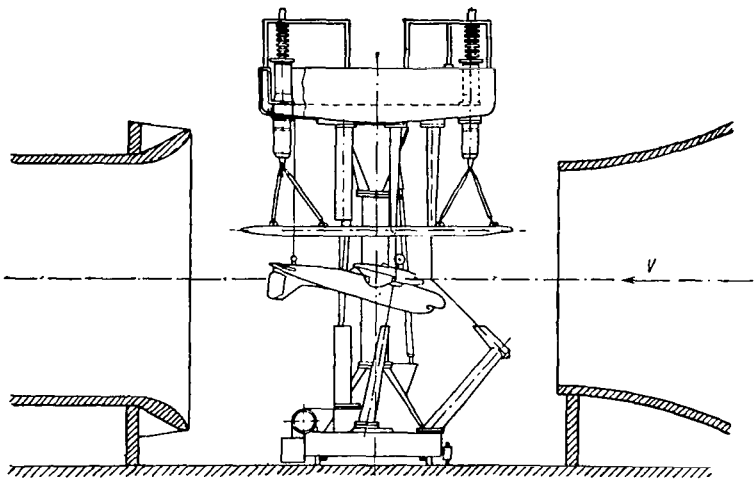

FIGURE 7.10. Installation of a model and a screen.

It is also possible to test two similar models, one in upright, the other in inverse position (wheel to wheel). In practice, despite its approximativeness, the method of investigating ground effects with the aid of a stationary screen is widely accepted.

Preparation of models and equipment for tests

The preparation of the models consists firstly in determining their dimensions by measurement on marking-off plates and in comparison with the drawings by means of templates, i.e., in establishing the full geometric similarity between model and full-scale airplane. An example of checking the dimensions of an airplane model is shown in Figure 7.11.

The condition of the model surface affects greatly the characteristics of its streamlining. In subsonic tunnels the models are made from wood and polished to a gloss corresponding to a roughness-peak height of 5μ.

In supersonic tunnels the models either have a metal core and a hard coating of special glue, resin, or plastic, or are all-metal.

The roughness-peak height is determined with the aid of special profilographs, which permit roughness peaks more than to 2μ high to be measured.

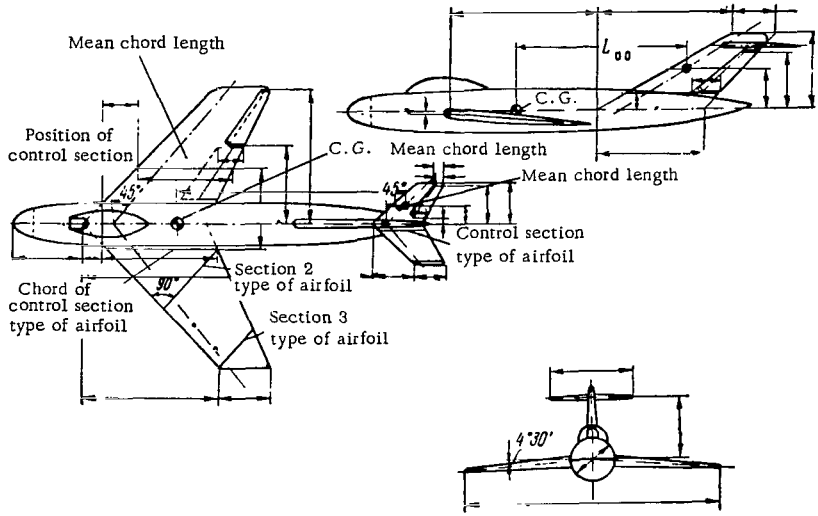

FIGURE 7.11. Checking the dimensions of an airplane model.

The equipment used in wind tunnels consists of permanently installed instruments (for instance, instruments for measuring velocities, pressures, temperatures, and humidity, wind-tunnel balances, etc.) and instruments installed especially for a particular experiment (for instance, manometer racks for determining pressure distributions, thermocouples for measuring temperatures when testing engines, tubes for measuring velocity distributions when investigating bodies in conduits, etc.). When the calibration curves of all instruments and their errors are known, we can, using the methods of the theory of probability, analyse the influence of errors of the various instruments on the measurements.

The measuring instruments used in the most common experiments should have the following standard deviations of measurement:

drag		
a) in region of $c_{x\,min}$	— ± 0.0004	
b) in region of linear variation $c_y = f(\alpha)$	— ± 0.0008	
c) $c_x = f(M)$	— ± 1.5%	
lift (at small angles of attack)	± 0.004	
pitching moment (m_z and m_{z_0})	± 0.002	at small angles of attack; for $\alpha > 10°$ the permissible error is about double
angle of zero lift (α_0)	± 0.2°	
slope of curve $c_y = f(\alpha)$	± 0.0025	
$\frac{\partial m_z}{\partial c_y}$	± 0.012	
k	± 0.2	
flow direction	± 0.25°	
propeller efficiency	± 1%	
magnitude of velocity	± 1%	
pressure coefficient $\bar{p}$	± 1%	

Technique of experimentation

An experiment consists of the simultaneous measurement of all values necessary for determining the tested phenomena. In addition to the simultaneous measurements, special procedures have been developed for each type of experiment, which permit the tests to be carried out most effectively from the viewpoint of ensuring accuracy and reliability of measurements, and also from the viewpoint of saving time.

These procedures comprise the technique of experimentation. The experimental method should permit tests to be repeated and reproducible results to be obtained.

It is absolutely necessary to maintain constant conditions of the experiment and the different phenomena occurring during it. This is particularly important when testing new elements or little-known phenomena, when the indications of the measuring equipment and the behavior of the tested object differ from normal, although an accepted experimental method is applied. The technique and methods of different dynamic tests are described below.

Tests on wind-tunnel balances. Before the experiment, a check of the balance and other measuring instruments, of the tightness of the air lines to the tubes and manometers, etc. must be made. Model tests on balances in low-speed tunnels are, as a rule, carried out at constant velocity and variable angle of attack. The angle of attack is varied from small negative values, corresponding to a small negative lift, by single degrees (sometimes by half degrees) up to angles exceeding the critical angle by several degrees. Sometimes, when the tests are made in upright and inverse positions, the steps in angle variation in the upright position are doubled. The readings in the inverse position are a check of the operation of the balance and should coincide with the readings in the upright position. Non-coincidence of the readings in these two positions indicates either considerable friction, hysteresis, or some systematic error which must be eliminated.

When the angle of attack is varied the velocity in the test section changes slightly, and should be adjusted. The instruments are read off only when, according to the indications of the control manometer, the velocity is stabilized, although the level of the spirit column in the manometer always fluctuates within ± 2 mm about a certain mean value. The art of experimenting consists in this case not only in choosing the instant of read-off, but also in the correct averaging of the control-manometer indications. This also refers to personnel recording the indications of the balance. In many modern tunnels in which the measurements are automated, the selection of the instant of read-off is less important.

In tunnels for large subsonic velocities the models are tested at varying velocities and constant angles of attack. This permits the tests to be carried out more rapidly, while the functional dependence of the force coefficients on the free-stream velocity (Mach number) can be plotted more accurately. When the tests are performed in variable-density and high-speed tunnels, the relationships $c_x, c_y, \ldots = f(\mathrm{Re})$ should first be determined, and then the relationships $c_x, c_y, \ldots = f(\mathrm{M})$. The reason for this is that in variable-velocity experiments the leading edge of the model may become slightly deformed. Tests for determining the

dependence of the aerodynamic coefficients on the Reynolds number (in variable-density tunnels) are carried out at different pressures, beginning at the maximum.

For each pressure the coefficients c_x, c_y, etc. are determined as functions of the angle of attack, as for low velocities. Silk threads are glued to the model and the flow pattern is visualized only after the balance measurements, in order to avoid damaging the surface and affecting the balance indications by the glued-on silk threads. Flow-pattern visualization consists of drawing, and more often of photographing the positions of the silk threads for each flow condition determined by the angle of attack, pressure, velocity, etc. (Figure 7.12).

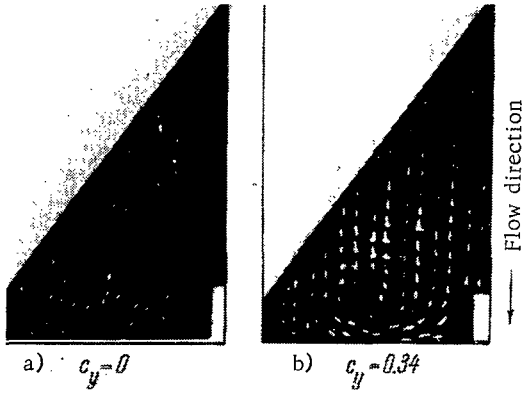

FIGURE 7.12. Flow pattern on a delta wing to which silk threads have been glued.

The pressure, temperature, and humidity of the atmospheric air are measured before and after each test. The temperature of the tunnel air is measured in low-speed tunnels before and after each test, while in high-speed and in variable-density tunnels this is done during each measurement on the balance. In addition, in variable-density tunnels the humidity of air is also measured with wet- and dry-bulb thermometers.

After each experiment on the balance of any type of tunnel, the null reading (i.e., in the absence of aerodynamic loads and flow in the tunnel) of the balance is compared with the null reading before the experiment. When the difference between the null readings exceeds the permissible value for the given balance, the experiment should be considered as unsuccessful; further tests are often possible only after establishing and eliminating the causes of the discrepancy. This refers also to other instruments, e.g., for measuring velocities, temperatures, etc.

Tests of models with different types of wings, engine nascelles, or tails, are carried out similarly as above. Special attention should be paid to the dimensional accuracy of each version (the cross-sectional area in the plane of symmetry, the area and span of wings and tail, the mean chord length, the distance between the horizontal tail and the wing, etc.). In addition, special attention should be paid in tunnels for large subsonic velocities to

interference between wings and supports. Sometimes additional tests are necessary for each combination (for instance, wing and engine nascelle) in order to determine accurately the interference between wings and model. This is particularly important with thin low-drag wings (swept-back and delta wings) which are tested at free-stream velocities at which zones of supersonic flow may occur near the model, causing a large increase in drag of the supports and interference between supports and the model.

Frequently, balance tests are accompanied by simultaneous measurement of the air flow rate and the velocity and pressure distributions (for instance, when testing models in large tunnels with the air flowing through intakes).

In order to avoid increasing the number of tests, the measuring tubes should be inserted into special shrouds, which are not connected to the balance and which insulate the tubes from the effects of the air flow.

The influence of the elasticity of the measuring tubes on the indications of the balance is taken into account by calibration. This effect is negligible when the balance is equilibrated by the null method.

Optical measurements with the aid of the Töpler instrument or an interferometer, which accompany balance tests, are usually performed either visually or by photography.

The establishment of the required flow conditions in low-speed tunnels is relatively simple, but is very difficult in supersonic tunnels. All operations with adjustable nozzles, compressors, throttling valves, supersonic-diffuser flaps, ejectors, etc. must be carried out in a strict order which is established during calibration and tunnel adjustment. This is necessary both in order to obtain the necessary flow conditions and to prevent damage to the equipment. During tests at supersonic velocities, special attention should be paid to the Reynolds number which, in practice, varies slightly due to changes in pressure and temperature in the settling chamber, test section, etc. The range of variation of the Reynolds number during and between experiments should be calculated, and its admissibility verified before the experiments. When the Reynolds number cannot be maintained constant, this should be taken into account in the analysis of the results.

The effectiveness of ailerons (the influence of their chord length and area, angle of deflection, etc.) is, as a rule, determined when the complete model is tested. The control surfaces of missiles and rockets equipped with fins, in which problems of stability and control are decisive and complex, are tested on wind-tunnel balances similarly as above. The hinge moments of the control surfaces of large models are measured on the same model on which the general aerodynamic characteristics are determined. If tunnel and model are small, the correct Reynolds number can be obtained if the hinge moments of the control surfaces are determined on a separate large model of the tail.

The measurements are carried out with the aid of the ordinary or additional balances which permit the hinge moments of the control surfaces to be determined at various angles of deflection for different angles of attack (and angles of tail slip) of the model or the fuselage, corresponding to the conditions of take-off and landing, different maneuvers, and maximum velocity. The test methods are similar to those used for models on wind-tunnel balances.

The angle of attack of the fuselage or of the tail is adjusted with the aid of the balance, while the angles of deflection of the control surfaces are adjusted manually; this requires interruption of the tunnel operation. Such tests are, therefore, performed by varying the angles of attack of model, fuselage, and tail, the position of the control surfaces being kept constant.

The optimum position of the tail on the model airplanes is best determined* beforehand, using special combs with glued-on silk threads which are installed in the tail zone.

By determining optically or visually the angle of downwash in the tail zone (with an accuracy of up to $\pm$ (0.5 to 1°)), we can find the region where the downwash downstream of the wings or body is minimum and where the effectiveness of the control surfaces is maximum, and can then proceed with the balance measurements. Sometimes the combs are replaced by nets or tightly stretched thin wires to which silk threads are fixed. Such nets permit visual observation of the three-dimensional flow pattern downstream of the wings or body, determination of the zones of turbulence, etc.

§ 32. DETERMINATION OF PRESSURE AND VELOCITY DISTRIBUTIONS

Determination of the pressure and velocity distributions is one of the most commonly performed experiments in low- and high-speed tunnels. Such tests include investigations of the pressure distributions on the surfaces of different bodies, of the velocity distributions around bodies, inside channels, etc. Before the experiments are begun, the connections between the orifices on the model or of the measuring tubes and the manometers is checked, in particular, the correspondence between the numbers of the measuring points on the model or on the tubes with the numbers on the manometer rack, and the tightness of all joints. The required degree of tightness has been obtained when the level of the spirit column drops by 1 mm per minute at a constant mean pressure in the system. The tightness of the manometers used, their rigid mounting and fixed inclination, the reliable attachment of the measuring tubes, and the availability of calibration data for the manometers and tubes are then checked.

The connecting tubes from the orifices and measuring tubes to the manometers must be free of constrictions (especially when rubber tubes are used). The absence of constriction is verified by the speed with which the level of a column of liquid drops in the manometer when the pressure at the orifice or measuring tube is reduced (usually with the aid of pumps).

The internal diameter and the length of the connecting tubes are chosen so as to obtain a minimum transmission lag. Lag reduction is particularly important in supersonic intermittent-operation tunnels, where, due to lag, the time available for measurements may be insufficient to attain stabilized conditions in all manometers.

* At small flow velocities.

Liquid-column manometers and their connection are selected so as to be suitable for the entire range of pressures assumed in the experiment, the liquid neither being ejected from the tube, nor receding into the well.

The type and design of the tubes (Pitot-Prandtl tubes, Tees, etc.) and the manner of their attachment should be selected according to their dimensions and those of the channels or the model. Steps should be taken to prevent the tubes from affecting the flow inside the channel or in the vicinity of the model, especially at large velocities.

Pressure and velocity distributions are determined by successive recording or photographing* of the manometer indications at different flow velocities and angles of attack. The pressure distributions on the surfaces of models are determined from the forces acting on them and the nature of the flow around them.

A knowledge of the pressure distribution over the body (with a sufficient number of properly chosen orifices) permits the total pressure force to be determined. However, this method is very seldom used, since in most aerodynamic problems, the total force acting on a body can be more simply, accurately, and rapidly determined by measurement on a balance. In modern practice the pressure distribution is therefore determined mainly in order to find the local distribution of the forces and the nature of the flow at the surface of the body.

Study of the pressure distribution is particularly important for determining the proper shapes of wings and fuselages intended for large flight velocities, of blades for compressors of jet engines, etc. Such investigations are also important for determining the load distributions in the strength calculations of airplanes, rockets, etc., and for determining the flow pattern around wings of finite span.

TABLE 10. Recommended positions of orifices on an airfoil (in fractions of the chord length)

Upper surface	0	0.05	0.1	0.15	0.2	0.25	0.3	0.4	0.5	0.6	0.7	0.8	0.9	0.95
Lower surface	—	0.05	0.1	—	0.2	—	0.3	0.4	0.5	0.6	0.7	0.8	0.9	—

Determination of the pressure distribution at low velocities is of primary importance when developing airfoils intended for large flight velocities. Pressure troughs near the leading edge, and the pressure distribution on the upper and lower surfaces determine not only the load-carrying properties of the airfoil, but also indicate the zones where at large flight velocities shocks may appear and greatly affect all the aerodynamic characteristics of the airfoil.

When the pressure distribution is investigated, the orifices must be arranged in such a way that all possible zones of abrupt change in pressure gradient are detected. The recommended distances of the orifices from the leading edge (in fractions of the chord length) are given for an airfoil in Table 10, while the arrangement of the orifices is shown in Figure 7.13.

In many cases it is sufficient to determine the pressure coefficient $\bar{p}_i = \frac{p_i - p_0}{q} = \bar{p}_i = f(\alpha)$ where p_i is the static pressure at the surface point

* Or recording if recording manometers are used.

considered and $q = \rho \frac{V_0^2}{2}$ is the dynamic pressure of the free-stream velocity (velocity head).

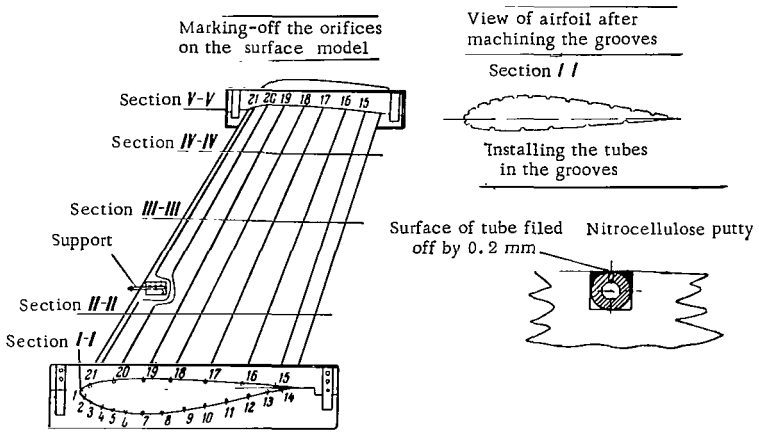

FIGURE 7.13. Orifices in an airfoil.

The velocity distribution on the surface of the body outside the boundary layer is given by

$$V_i = V_0 \sqrt{1 - \bar{p}_i}.$$

The pressure forces acting on a wing element of unit width (Figure 7.14), for which the pressure distributions on the lower and upper surfaces are known (Figure 7.15), are found (for fixed coordinate axes) from the following formulas /3/. The horizontal force acting on the given element is

$$X = q \int_{y_1}^{y_2} \bar{p}\, dy;$$

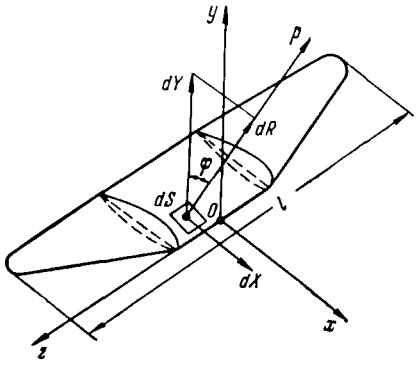

FIGURE 7.14 Forces acting on a wing element.

The horizontal pressure force acting on the entire wing is

$$X_w = q \int_{-l/2}^{+l/2} dz \int_{y_1}^{y_2} \bar{p}\, dy.$$

The horizontal-force coefficient is

$$c_t = \frac{X_w}{qS}.$$

The normal pressure force acting on the element is

$$Y = q \int_{x_1}^{x_2} \bar{p}\, dx.$$

The vertical force acting on the entire wing is

$$Y_w = q \int_{-l/2}^{+l/2} dz \int_{x_1}^{x_2} \bar{p}\, dx.$$

The vertical-force coefficient is

$$c_n = \frac{Y_w}{qS}.$$

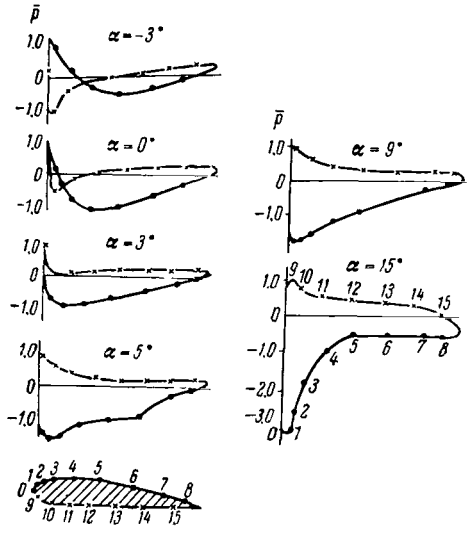

FIGURE 7.15. Pressure distribution on an airfoil at different angles of attack.

The drag and lift coefficients determined by the pressure forces are

$$c_x = c_n \sin\alpha + c_t \cos\alpha,$$
$$c_y = c_n \cos\alpha - c_t \sin\alpha,$$

where α is the angle of attack of the wing.

The moment coefficients are found similarly /3/.

The values of X and c_x are less accurately determined than those of Y and c_y. This is explained by the smallness of c_x and by the fact that in this method friction is not taken into account.

Determination of the profile drag by impulse methods

The total drag Q consists of the profile drag Q_p and the induced drag Q_i. At small angles of attack and maximum velocity, i.e.. at small lift coefficients, the induced drag is small and the profile drag is decisive. The latter consists of the form drag, caused by the normal components of the forces acting on the surface of the body (pressure forces), and of the skin friction, representing the tangential components of the forces acting on the surface of the body (friction forces).

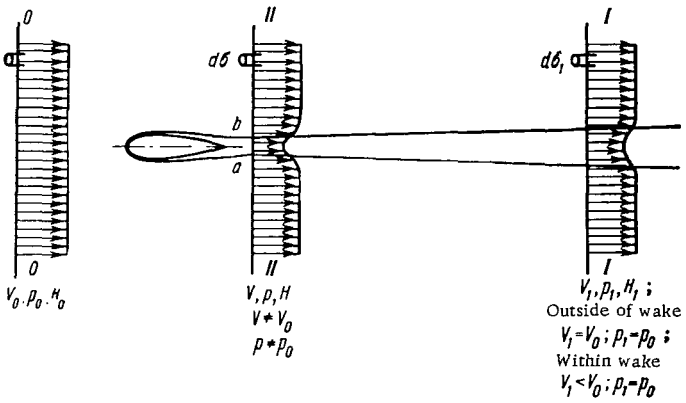

FIGURE 7.16. Velocity profiles upstream and downstream of a wing.

The profile drag is determined by methods based on the impulse theorem, according to which the change in momentum in any direction is equal to the impulse due to the force acting in the same direction. In the case of flow around a symmetrical airfoil at zero angle of attack (Figure 7. 16), the momentum change per second of the fluid passing

through the plane $O-O$ or $I-I$ in the flow direction is equal /3/ to the profile drag of the wing element:

$$dQ_p = V_0\,dm - V_1\,dm,$$

where dm is the mass of fluid which passes per second through the elemental area $d\sigma$. For an incompressible fluid

$$dm = \rho V_0\,d\sigma_0 = \rho V_1\,d\sigma_1,$$

whence

$$c_{xp} = \frac{Q_p}{\rho\frac{V_0^2}{2}S} = \frac{2}{V_0^2 S}\int\int V(V_0 - V_1)\,d\sigma.$$

In practice it is difficult to perform measurements in the plane $I-I$ which is at a large distance from the wing. For this reason, a control plane $II-II$ (Figure 7.16) is located at a distance of about 0.5 to 1 chord length downstream of the wing and the integration is performed only over the wake,

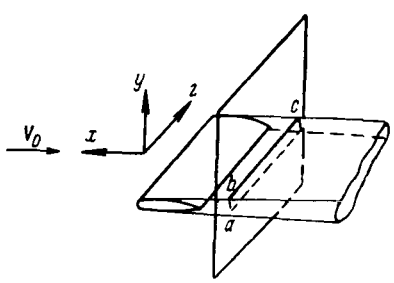

FIGURE 7.17. Intersecting the wake by a vertical plane.

i.e., from a to b and from b to c (or from $-l/2$ to $+l/2$) (Figure 7.17). After substituting

$$V_1 = \sqrt{\frac{2}{\rho}(H - p_0)},$$

$$V_0 = \sqrt{\frac{2}{\rho}(H_0 - p_0)},$$

$$V = \sqrt{\frac{2}{\rho}(H - p)},$$

$$d\sigma_1 = \frac{V}{V_1}\,d\sigma = \frac{V}{V_1}\,dy\,dz$$

we obtain /3/

$$c_{xp} = \frac{2}{S}\int_{-l/2}^{+l/2}\int_a^b \sqrt{\frac{H-p}{H_0-p_0}}\left(1 - \frac{\sqrt{H-p_0}}{\sqrt{H_0-p_0}}\right)dy\,dz.$$

It is thus necessary to determine the velocity head in the undisturbed flow ($H_0 - p_0$), the velocity head in the wake ($H - p$) and the difference between the total pressure in the wake and the static pressure in the undisturbed flow ($H - p_0$). All these measurements can be made with two Pitot-Prandtl tubes and three manometers (Figure 7.18), or by one tube and a comb (Figure 7.19).

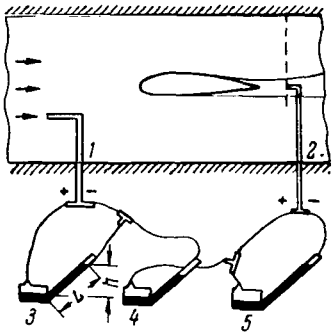

FIGURE 7.18. Connections of tubes to manometers for determining the profile drag. 1 — tube for measuring the flow velocity; 2 — microtube; 3, 4, 5 — micromanometers.

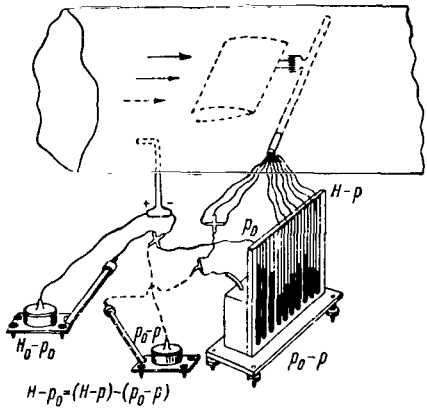

FIGURE 7.19. Connection of a comb for determining the profile drag.

The results of the measurements are processed graphically. The vertical distance between the tubes of the comb must not be less than 3 to 5 tube diameters, and the comb itself should not cause any disturbances in the flow around the tubes and downstream of the wing. The tubes should have little sensitivity to downwash when the profile drag of a body subjected to lift is determined. This method of determining the profile drag gives measurement errors of the order of ±5%, and is used mainly for comparative evaluation of the aerodynamic properties of airfoils, bodies of revolution, etc.

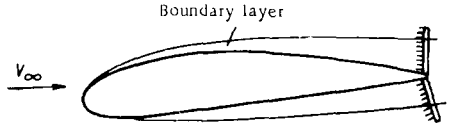

FIGURE 7.20. Comb installation for flight tests by the impulse method.

When measurements in the wake with the aid of a comb are impossible (for instance, in flight), the comb is installed on the trailing edge of the wing (Figure 7.20) or the body of revolution /5/, and the profile-drag

coefficient is determined from the Squire-Young formula

$$c_{xp} = 2\frac{\delta_к^{**}}{b}\left(\frac{U_к}{V_\infty}\right)^{3,2},$$

where $\delta_к^{**}$ is the thickness of the wake at the trailing edge of the wing, b is the wing-chord length, $U_к$ is the velocity at the outer limit of the boundary layer at the trailing edge.

The pulse method can also be applied to compressible gas, as long as no regions of supersonic flow appear on the body ($M_\infty < M_{cr}$). In this case /6/

$$Q_p = \int_{-l/2}^{+l/2} \frac{2\varkappa}{\varkappa-1} \int_a^b H\left(\frac{p}{H}\right)^{\frac{1}{\varkappa}} \sqrt{1-\left(\frac{p}{H}\right)^{\frac{\varkappa-1}{\varkappa}}} \times$$

$$\times\left(\sqrt{1-\left(\frac{p_0}{H_0}\right)^{\frac{\varkappa-1}{\varkappa}}} - \sqrt{1-\left(\frac{p_0}{H}\right)^{\frac{\varkappa-1}{\varkappa}}}\right) dy\, dz;$$

$$c_{xp} = \frac{Q_p}{\rho V^2/2 \cdot S},$$

where

$$\rho\frac{V^2}{2} = \frac{\varkappa}{\varkappa-1} p_0\left[\left(\frac{H_0}{p_0}\right)^{\frac{\varkappa-1}{\varkappa}} - 1\right].$$

It can be seen from these expressions that when compressibility effects are taken into account, the measurement system is the same as at low velocities.

§ 33. TESTING OF PROPELLERS

The installations for testing propellers. Installations for testing propellers are intended for determining the following propeller characteristics which depend on the blade angle (the propeller pitch) and the advance ratio

$$\lambda = \frac{V}{n_c D};$$

the thrust coefficient

$$\alpha = \frac{P}{\rho n_c^2 D^4},$$

the power coefficient of the propeller

$$\beta = \frac{N}{\rho n_c^3 D^5},$$

the overall propeller efficiency

$$\eta = \frac{\alpha}{\beta}\lambda,$$

where P is the thrust of the propeller, N is the shaft power, n_c is the number of revolutions per second, ρ is the density of air, D is the propeller diameter.

In installations for testing propellers the following values must therefore be measured: the thrust of the propeller, the shaft torque, and the rotational speed.

Kinematic similarity is provided during tests of geometrically similar propellers when the angles of attack of the corresponding blade elements are equal. For equal blade angles this requirement means the equality of the air outlet angles: $\beta_1 = \beta_2$; substituting for the tangents of the angles the velocity ratios (Figure 7.21) we obtain

$$\frac{V_{01}}{n_{c1}D_1} = \frac{V_{02}}{n_{c2}D_2}$$

or

$$\frac{V_0}{n_cD} = \text{const} = \lambda.$$

The dimensionless coefficient λ plays the same role in propellers as the angle of attack in airfoils.

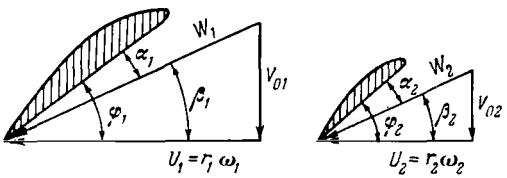

FIGURE 7.21. Velocity triangles for corresponding blade elements of geometrically similar propellers.

Dynamic similarity means that the forces acting on corresponding elements of two geometrically similar propellers are proportional, and have the same directions with respect to the blades. Dynamic similarity is provided by the equality of the dimensionless coefficients of thrust α and power β.

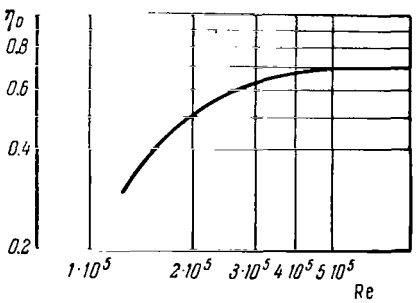

FIGURE 7.22. Dependence of propeller efficiency on Reynolds number at $\lambda = 0$.

Viscosity effects are taken into account by requiring the Reynolds numbers to be equal for model and full-scale propeller . The effect of

the Reynolds number on the propeller efficiency is shown in Figure 7.22. Equality of Reynolds numbers requires that the rotational speed of the model propeller be higher than that of the full-scale propeller. This may make attainment of equal Mach numbers impossible. It is therefore the practice to provide test Reynolds numbers of the order of $\mathrm{Re} \geqslant (4 \text{ to } 5) \times 10^5$, at which the efficiency varies very little with increasing Reynolds number.

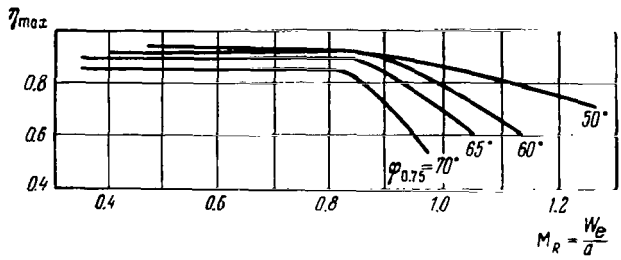

FIGURE 7.23. Dependence of η_{max} on the blade-tip Mach number and on the blade angle for a subsonic three-blade propeller.

The compressibility effect on propellers becomes noticeable at $\mathrm{M}_{cr} = \frac{W_{cr}}{a} =$ 0.7 to 0.9 and depends on λ, the aerodynamic coefficients, and the Reynolds number. At M_{cr}, the thrust coefficient decreases, the power coefficient increases, and the efficiency drops. The effect on the efficiency of the ratio between the resultant blade-tip velocity $W_R = \sqrt{V_0^2 + (\pi n_t D)^2}$ and the speed of sound is illustrated in Figure 7.23.

Determination of propeller characteristics of the aid of wind-tunnel balances

The thrust of a propeller is very often measured with wind-tunnel balances. The system for measuring the component Q must then be adapted to take up a force opposed to the usually measured drag. For this, preloading by counterweights can be arranged. When the wind-tunnel balance has a system for measuring the component M_x, the torque of the propeller can be determined from the indications of the balance element of this system. If the wind-tunnel balance is not adapted for measuring M_x, or the system measuring M_x is not sufficiently accurate, the propeller shaft torque can be determined with the aid of a separate dynamometric device or according to the power consumed by an electric motor.

Thus, for instance, in the high-speed NASA tunnel at Langley Field, which has a test-section diameter of 2.4 m, the thrust of the propeller is measured by the wind-tunnel balance as a negative drag, while the torque is measured by a separate hydraulic dynamometer (Figure 7.24). For this purpose the stator of the motor driving the propeller is mounted on

bearings. The reaction torque, which acts on the stator and is equal to the moment of resistance to rotation of the propeller, is taken up by the hydraulic dynamometer connected to a lever secured to the stator.

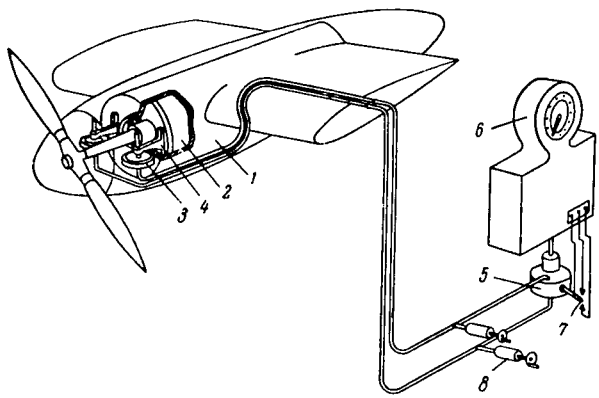

FIGURE 7.24. NASA propeller-testing installation. 1 — model of fuselage or fairing; 2 — stator of driving motor mounted inside fairing; 3 — hydraulic dynamometer taking up reaction torque; 4 — lever transmitting torque to hydraulic dynamometer; 5 — receiver connected to balance; 6 — balance; 7 — compensator for balance displacement; 8— compensator for maintaining a constant volume in the hydraulic system.

Since, in addition to the thrust of the propeller, the wind-tunnel balance also takes up the drag of the fairing, inside which the whole device is installed, the thrust P of the propeller is determined from the measured value Q according to the following expression:

$$P = Q + \Delta Q_1 + (\Delta Q_2 + \Delta Q_3 + \Delta Q_4),$$

where ΔQ_1 is the resistance of the fairing without the propeller and of the support on which the whole device is installed, ΔQ_2 is the correction for the longitudinal pressure gradient, ΔQ_3 is the correction for ΔQ_1 on account of the blocking effect of the propeller, ΔQ_4 is the increase in drag of fairing and support, due to the velocity increase in the propeller wake. Of these magnitudes ΔQ_1 is determined by direct drag measurement when the propeller is removed. The other corrections are determined as functions of the thrust coefficient of the propeller.

Propeller instruments. Special installations for measuring thrust and torque of propellers are called propeller instruments. The main operating principles of propeller instruments are in many points similar to wind-tunnel balances. The design of a propeller instrument depends considerably on the type of propeller drive used. The natural tendency is to mount the propeller directly on the shaft of the motor or of the reduction gear which is coaxial with the motor. This provides the simplest transmission design. Since in this design the motor is located inside the airstream, its diameter should be as small as possible

in order to reduce its influence on the propeller operation, and, in high-speed tunnels, to increase the critical Mach number at which blockage of the wind tunnel occurs.

The high power of electric motors installed in test sections is achieved by increased length, higher supply frequency, and special cooling methods. This permits the motor diameter to be greatly reduced. Motors of this type are suspended in the test section from special struts or braces, while the measuring element of the propeller instrument is placed inside a casing protecting the motor, or is located outside the flow boundaries.

When a large electric motor which cannot be placed in the air-stream is used, then arm-type instruments are employed. In the arm-type instrument the propeller shaft is mounted in a special body inside a casing shaped like a body of revolution and mounted on a shroud which is perpendicular to the flow direction. A shaft, which connects the propeller shaft with the electric motor, passes through the shroud. All measuring elements or transducers for the thrust and the torque are placed inside the casing and the shroud.

Propeller instruments of the suspension type. An example of such a system is shown in Figure 7.25. The body of electric

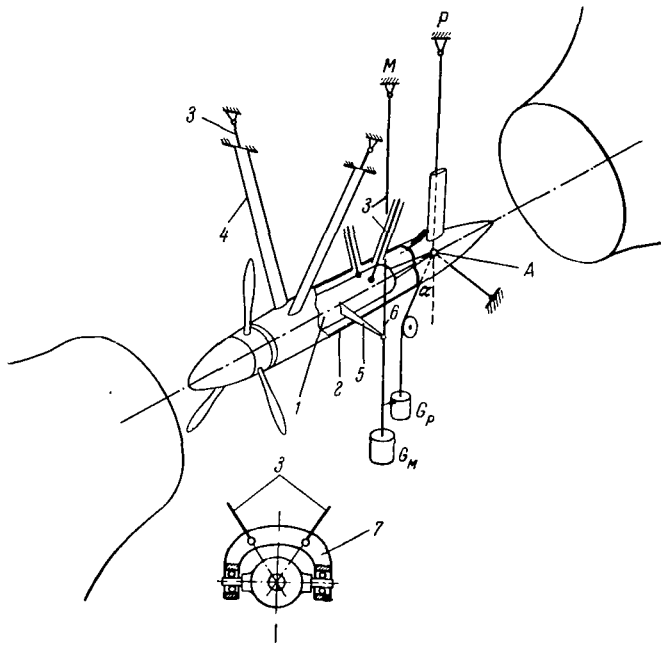

FIGURE 7.25. Suspension-type propeller instrument. 1—electric motor; 2 — casing; 3 — braces; 4 — struts; 5 — torque lever; 6 — torque rod; 7 — intermediate yoke.

motor (1), surrounded by streamlined casing (2), is suspended at fixed points from four braces (3) placed in pairs in two vertical planes. The braces are also used as electric leads for the motor. The streamlined

casing is suspended from fixed supports by means of struts (4). The reaction torque acting on the frame of the electric motor, equal to the torque on the propeller shaft, is transmitted by lever (5) and rod (6) to balance element (M) which is preloaded by counterweight G_M.

The system of securing the braces (3) to the frame of the motor is shown at the bottom of Figure 7.25. The braces are connected to the frame through intermediate yokes (7), supporting the frame by means of pins carried in ball bearings. The articulated parallelogram, formed by the braces and the frame, permits free axial movement of the frame in order to transmit the thrust P to point A where it is resolved into components. The vertical component, which at $\alpha = 45°$ equals the thrust, is measured by balance element P. The braces are connected to the yokes by means of hinges with ball bearings. The prolongations of the brace axes intersect the propeller shaft. The yokes together with the frame of the motor can therefore rotate about this shaft within the limits of the measuring displacements, in order to transmit a force to a balance element which measures the reaction torque acting on the motor frame. The influence of friction in the bearings is taken into account when calibrating the instrument with the propeller removed.

The drawbacks of a propeller instrument with brace suspension are the relatively low power, the necessity of frequent calibration due to elongation of the braces, and also the need for frequent adjustment of the clearances between the stationary parts and those connected to the balance.

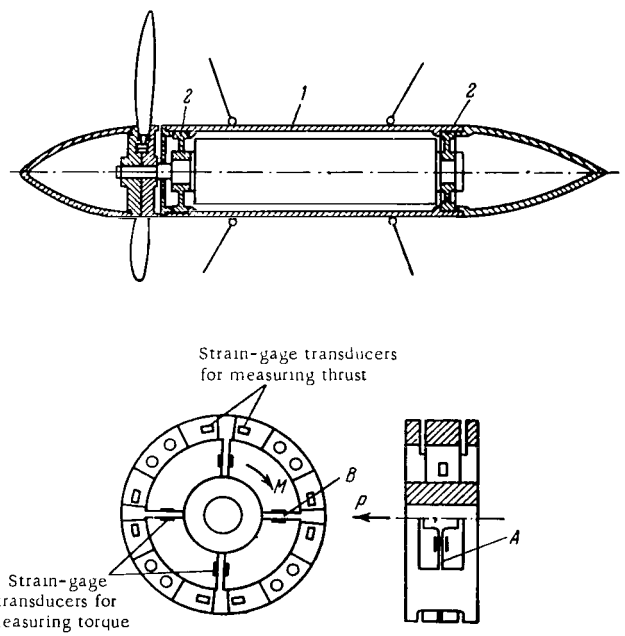

FIGURE 7.26. Suspension-type propeller instrument with strain-gage elements.

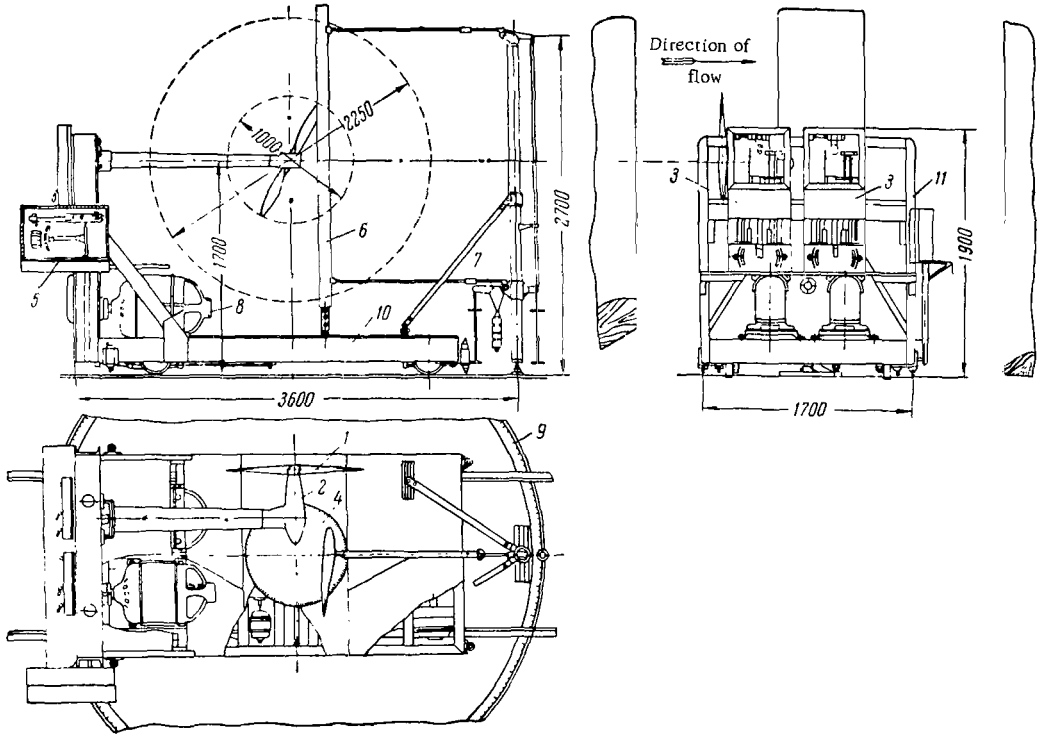

FIGURE 7.27. The B-5 instrument. 1 — propeller; 2 — head of the front propeller instrument; 3 — thrust and torque balances; 4 — platform for drag balance; 5 — drag balance; 6 — model of airfoil; 7 — lift balance; 8 — electric motor; 9 — rotating table; 10 — instrument carriage; 11 — vertical instrument frame.

The use of instruments with brace suspensions in tunnels with closed test sections (and sometimes in tunnels with open test sections) is very inconvenient because of the necessity to install and calibrate the instrument before testing the propeller and to dismantle it after the tests.

These drawbacks are mostly eliminated in instruments where the brace suspension is used only for fixing the instrument in the tunnel while the whole measuring system is placed in one casing with the electric motor. The design of such a propeller instrument, in which a strain-gage measuring system is used, is shown in Figure 7.26. Fairing (1) is rigidly fixed in the test section by tapes or wires which also serve as electric leads for the motor. The frame of the motor is mounted inside the fairing on two elastic discs (2), whose design is shown at the bottom of Figure 7.26. The discs are made of single pieces of steel. The thrust causes deformation of the elastic element *A* of the disc, which has low rigidity in the axial direction.

Wire strain-gage transducers are glued on the walls of these elements in one of the discs. The torque acting on the stator of the motor is taken up in the same way by strain-gage transducers glued on the radial elements *B* which have low rigidity in the tangential direction. The strain-gage transducers are inserted into the circuits of two automatic balancing bridges which measure separately the torque and the thrust.

Propeller instruments of the arm type. Propeller instruments of arm type make frequent reinstallation and calibration unnecessary and permit quick change-over from the propeller tests to other types of experiments. For this purpose arm-type instruments are mounted on carriages or other devices for transport from and to the test section. The typical example of such an instrument for a tunnel with open test section is the B-5 propeller instrument /7/ of the T-5 TsAGI tunnel (Figure 7.27). The layout for measuring the thrust of a propeller is shown in Figure 7.28, and that for measuring the torque in Figure 7.29.

Instruments of the arm type are used also in high-speed tunnels for testing propellers having large values of λ while maintaining equality of Mach numbers. The power required for driving the propeller can be considerably reduced by lowering the pressure in the tunnel. The resultant reduction in Reynolds number is not very important, since the influence of the latter on the propeller characteristics is insignificant at large velocities. An example of an instrument for testing propellers in tunnels with closed test sections at high subsonic and transonic free-stream velocities is shown in Figure 7.30 of the NASA tunnel at Langley Field. The power of the instrument is 2000 h.p. The diameter of the closed test section is 4.88 m, and the flow velocity, $M = 1.2$.

Propellers tested at high rotational speeds must be carefully balanced. Inadequate balancing causes vibrations of the propeller and of the instrument elements and reduces the measuring accuracy. For the sake of safety, the propellers are first tested for their strength on a special stand where they are rotated at a speed which exceeds by 10 to 15% their maximum rotational speed in the wind tunnel.

A simple device for balancing propellers is shown schematically in Figure 7.31. The device consists of a lever resting on a knife edge.

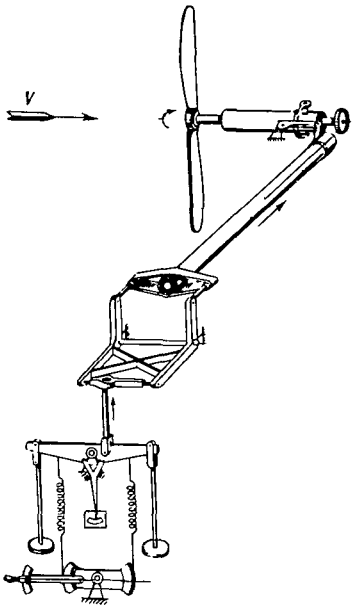

FIGURE 7.28. Measuring the thrust of a propeller on the B-5 instrument.

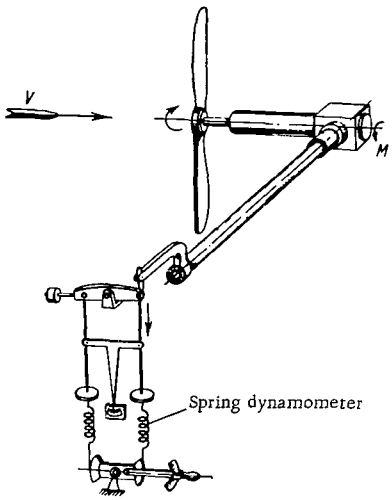

FIGURE 7.29. Measuring the propeller torque on the B-5 instrument.

The weight of the propeller, mounted on one arm of the lever, is equilibrated by weights. If the unbalanced propeller is rotated about its axis the equilibrium of the lever is disturbed. Equilibrating the lever

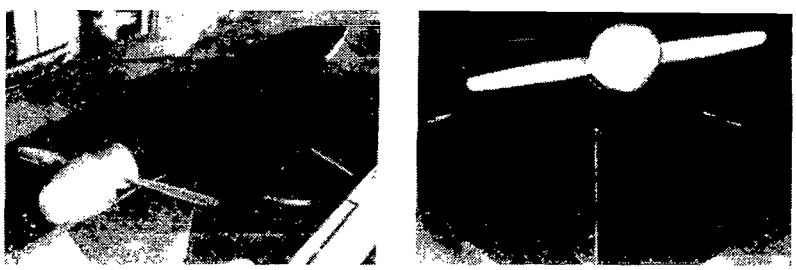

FIGURE 7.30. Propeller instrument of the high-speed NASA tunnel at Langley Field.

again by additional weight, we can determine the imbalance moment, which is then equilibrated with the aid of weights secured to the propeller hub.

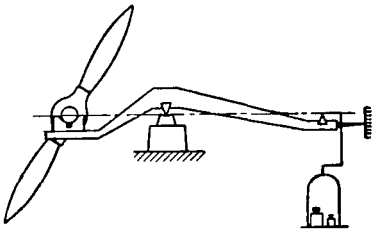

FIGURE 7.31. Device for balancing propellers.

The calibration of propeller instruments

The system for measuring the thrust of the propeller instrument is calibrated by loading the shaft with weights. A thrust plate, fixed to the end of the shaft and running on ball bearings, transmits the load. The stationary part of this thrust bearing is fixed to a rod passing through a roller to a pan with weights, The system of measuring the torque is calibrated by applying a torque to the instrument shaft by means of a pneumatic or hydraulic brake and measuring independently the torque acting on the brake.

A feature of arm instruments is that the flow perturbation caused by them in the plane of rotation of the propeller is small*. The velocity decrease, due to the instrument, in the plane of the propeller causes an increase in the thrust measured.

Measurement of the rotational speed. Errors in measuring the number of revolutions n_c affect the final accuracy of determining the dimensionless coefficients α, β and η more than errors in measuring the other magnitudes. Special attention should therefore be paid to the measuring of the rotational speed. Only special types of laboratory tachometers can be used in aerodynamic experiments.

Tests of full-scale propellers. The full-scale propellers are tested mainly in tunnels with open test sections. Experiments with full-scale propellers are performed in closed test sections only in variable density full-scale tunnels. The main purpose of such tests is to investigate the operation of the propeller- and engine-group at different altitude conditions and temperatures, created by means of compressors, vacuum pumps, and cooling installations. Reducing the pressure to below atmospheric permits high velocities (Mach numbers) to be attained, while an increase of the pressure to above atmospheric increases the Reynolds number of the experiment.

* The correction due to velocity reduction does not exceed 0.5% of the measured thrust.

The thrust is measured by a wind-tunnel balance or dynamometric installation located inside a false fuselage. The torque applied to the propeller shaft is measured by different methods depending mainly on the type of engine driving the propeller. When an electric motor is used, the power absorbed by the propeller can be measured very simply but not accurately, because it is difficult to determine the efficiency of the motor and the effects on it of temperature changes in the winding during the tests.

When an aircraft engine is used the power taken up by the propeller can be determined by calibrating the engine. This method too is less accurate than torque measurements by special dynamometric devices operating on the weighing principle. The torque applied to the propeller shaft can be determined with the aid of devices in which the angle of twist of a known length of the elastic shaft is measured with the aid of strain-gage, inductive, capacitive, or optical transducers. Determination of the power by the electric method, from the engine characteristics or from the shaft torsion, enables the torque to be found with an accuracy of ± 3 to 4%. The field of application of these methods is therefore limited mainly to comparative tests and to flight tests where the use of other types of equipment is difficult.

Methods of testing propellers

Such tests are mainly performed on propeller instruments*. The basic experiments are tests of single and coaxial propellers both as isolated units and in the presence of elements of the airplane. In the latter case the aerodynamic forces acting on the airplane elements must also be determined; this determines the interaction between propeller and airplane body.

Measurements in the range of maximum propeller efficiency η_{max} must be most accurate. This is difficult because in this range the thrust and the propeller torque are small in absolute value. Measuring accuracy can be improved by increasing the number of experimental points, and also by a high accuracy of the measuring instruments used in the load range extending from 1/5 to 1/10 of the maximum load.

Stationary tests ($V=0$; $\lambda=0$) intended to determine the aerodynamic characteristics of propellers, required for investigations of aircraft landing and engine starting on the ground (small positive and negative blade angles), can be carried out in wind tunnels with the fans nonoperative. Stationary tests intended to provide the aerodynamic characteristics of propellers required for investigations of aircraft take-off, must be performed outside the tunnel or, if possible, with the test installation at a right angle to the tunnel axis, since at large blade angles the propellers themselves create in the wind tunnel an air circulation corresponding to ($\lambda \approx 0.5$).

Determination of the thrust of the propeller is difficult in stationary tests because the blade roots operate under stalling conditions. Because knowledge of the thrust in stationary tests is important, it has to be determined by repeated measurements (3 or 4).

* The operation of individual blade sections is sometimes analyzed with the aid of measuring tubes by determining the momentum and the moment of momentum of the air upstream and downstream of the blade section considered.

Testing single propellers. Arm instruments are most suitable for testing single propellers. The tests are performed at constant blade angles (φ = constant) and different values of the coefficient λ, which is varied by changing the free-stream velocity from $V=0$ to $V = V_{max}$ at different rotational speeds. The minimum number of revolutions of the propeller is chosen in such a way that the Reynolds number does not become too small (Figure 7.22). When this condition is satisfied the number of revolutions is selected by taking into account the range of possible measurements of thrust and propeller torque, and the limiting velocity in the test section of the tunnel.

Excessive rotational speeds at a limited flow velocity in the tunnel do not permit the full characteristics of the propellers to be determined at large blade angles (large values of λ). Reducing the number of revolutions permits the propeller characteristics to be obtained for all blade angles. However, due to the smallness of the loads acting on the balance devices, the accuracy of determining the efficiency, and particularly its maximum value, is reduced. Tests of propellers of a given series (type and number of blades, propeller diameter) must therefore be preceded by an analysis of the experimental conditions and by the selection of the rotational speed of the propeller and of the flow velocity.

The velocity intervals are chosen in such a way that the intervals of the coefficient λ are equal to 0.1, and, in the neighborhood of η_{max}, to 0.05. The highest velocities should correspond to a value of λ at which the coefficients α and β assume small negative values (0.05 to 0.01). This permits the point of zero thrust to be fixed more definitely.

Tests of single propellers in the presence of the fuselage or engine nascelle with wing are performed in the same way as tests of isolated propellers, but in addition the aerodynamic forces acting on these elements are measured with and without the propeller. This permits the influence of the propeller wake to be taken into account and the effective thrust and propeller efficiency (α_e, η_e) to be determined.

In such tests the instruments must be located inside the model and attention should be paid to providing sufficient clearances between moving and stationary parts. The results of propeller tests are usually given in the form of "series" characteristics, i.e., of the characteristics of a given type of propeller for different blade angles and operating conditions ($\alpha = f(\lambda), \beta = f(\lambda)$), with lines of constant efficiency (Figure 7.32). If the free-stream velocity exceeds 70 to 80 m/sec, a correction for compressibility effects has to be introduced.

Several countries possess large wind tunnels mainly intended for testing full-size propellers. These tunnels are characterized by circular test sections, usually of the open type, having diameters of 6 to 8 m and comparatively high flow velocities (up to 100 to 150 m/sec). The installed powers of such tunnels attain from 20,000 to 30,000 kw. In such tunnels it is possible to obtain with propeller instruments characteristics like those shown in Figure 7.32. When only wind tunnel balances and devices for torque measurements or engine calibration are used, characteristics like those shown in Figure 7.33 are obtained.

It was shown by many tests that with the aid of the engine characteristics, the thrust of the propeller at take-off conditions at maximum airplane speed can be determined with an accuracy of ±10 kg, and the maximum airplane speed, with an accuracy of ±1%.

Testing of coaxial propellers

The testing of coaxial propellers, which were introduced as a result of the increased power of aircraft engines, nowadays plays an important part in propeller tests. For existing turboprop airplanes the aerodynamic characteristics of propellers must be known for blade angle $\varphi_{0.75}{}^{*} < 0°$ up to $\varphi_{0.75} = 90°$ at $0 < \lambda < \infty$, for both positive and negative thrusts and torques.

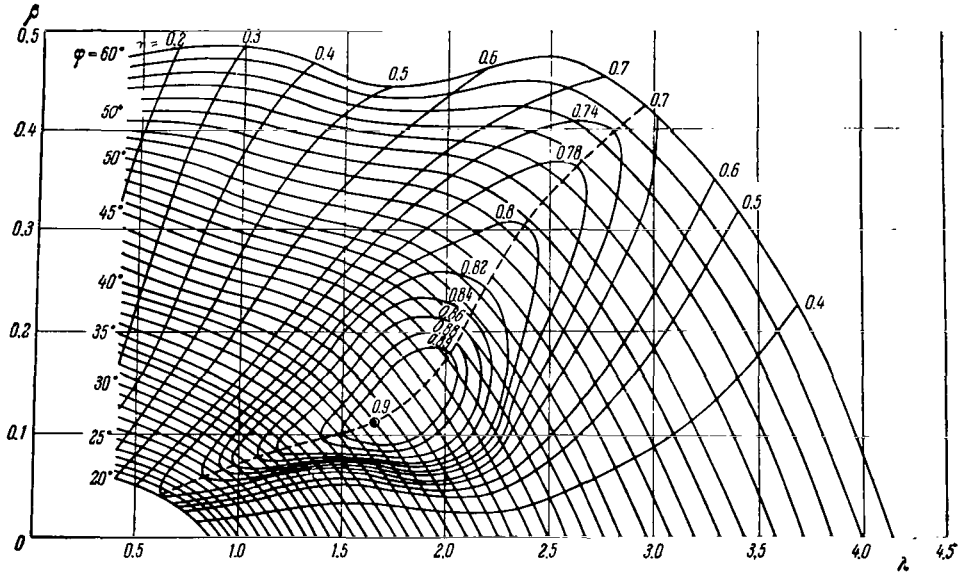

FIGURE 7.32. Characteristics of a propeller series.

Tests of propeller models over such wide parameter ranges are not feasible in high-speed tunnels. Investigations of propeller operation under take-off and landing conditions are simpler to carry out in low-speed tunnels (Figure 7.34). In high-speed tunnels such tests are difficult to perform because of the large loads acting on the balance devices which must measure even small loads accurately.

Under flight conditions the difference in the blade angles of coaxial propellers, taking up equal shares of the engine power (or installed on similar engines in tandem), is 1 to 2° at V_{max}. The reason for this is that in the region of η_{max}, at equal blade angles and equal apparent flow angles, due to the induced velocity, blade sections of the trailing propeller operate at larger angles of attack and at higher free-stream velocities than the corresponding blade sections of the leading propeller. In order that the power required to overcome the aerodynamic resistance to rotation be equal for both propellers, the blade angle of the trailing propeller must be 1 to 2° less than that of the leading propeller. For take-off conditions the difference attains 5 to 6°.

* $\varphi_{0.75}$ is the blade angle at $r = 0.75\,R$ [where R is the propeller radius.]

During tests of coaxial propellers, the following magnitudes are measured:

a) the thrust, torque, and number of revolutions of each propeller,

b) the free-stream velocity and density,

c) the pressure in the clearances between the propeller hubs and the instrument fairing (Figure 7.35).

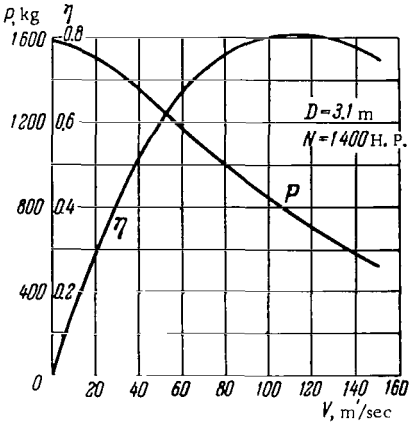

FIGURE 7.33. Velocity dependence of thrust and propeller efficiency.

In order to analyze the propeller operation at high rotational speeds (for instance, under conditions of take-off, cruising, maximum speed, landing, etc.) the results are given as variations of α, β and λ with φ (Figure 7.32).

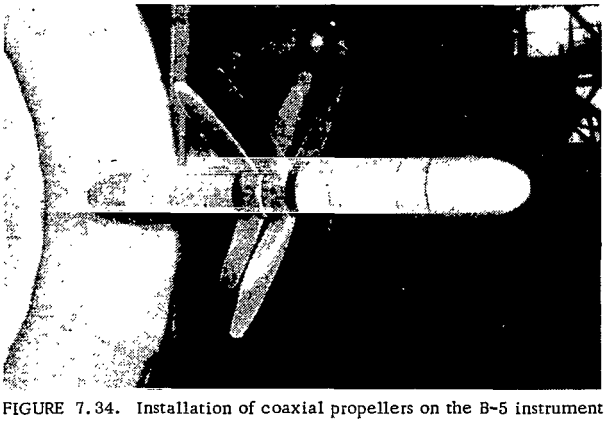

FIGURE 7.34. Installation of coaxial propellers on the B-5 instrument

In order to investigate processes connected with the reduction of the rotational speed of the propeller to values close to zero (for instance, the feathering of the propellers to reduce the drag after sudden engine shut-down in flight, or the restarting of the engine in flight), the propeller characteristics are given as coefficients c_p, c_m and $\frac{n_c D}{V} = f(\varphi, \lambda)$. These coefficients are related to the coefficients α. β and λ as follows:

$$c_p = \frac{\alpha}{\lambda^2}; \quad c_m = \frac{\beta}{2\pi\lambda^2}; \quad \frac{n_c D}{V} = \frac{1}{\lambda}.$$

If tests are carried out in the range $0 < \lambda < \infty$, one part of the experimental results (usually $0 < \lambda < 4$ or 5) is expressed by the coefficients α, β and λ, while the remainder is expressed by the coefficients c_p, c_m and $\frac{n_c D}{V}$.

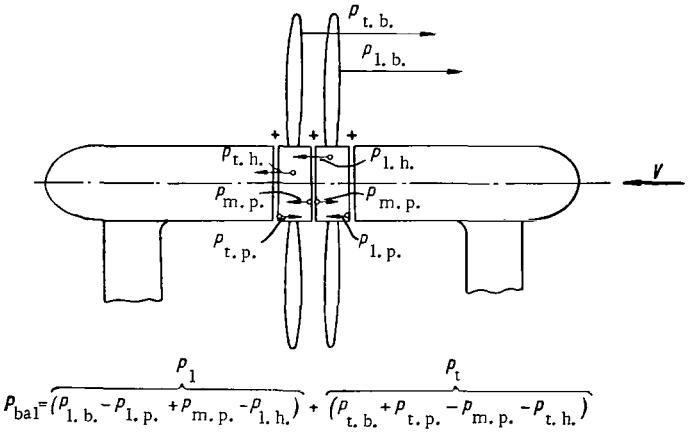

FIGURE 7.35. Forces measured by thrust balances when testing coaxial propellers.

Determining of the coefficients α and c_p. These coefficients are respectively

$$\alpha = \frac{P}{\rho n_c^2 D^4} \quad \text{and} \quad c_p = \frac{P}{\rho V^2 D^2},$$

where P is the thrust of the isolated coaxial propellers, given by

$$P = P_l + P_t - \Delta P_h - \Delta P_p \quad .$$

Here P_l and P_t are the forces measured respectively on the thrust balances of the leading and trailing arms of the instrument, ΔP_h is the drag of the hub without blades, measured on the thrust balance, ΔP_p is the total force of the pressure in the clearances transmitted to the instrument balance: $\Delta P_p = \Delta P_{l.p.} - \Delta P_{t.p.}$. The force of the pressure between the hubs does not

affect the measurement of the total thrust (Figure 7.36). The pressure forces in the leading and trailing clearances are

$$\Delta P_{\text{l. p.}} = \frac{1}{n} S_{\text{h}} \gamma \sum_{1}^{n} (h_k - h_{k_0}),$$

$$\Delta P_{\text{t. p.}} = \frac{1}{n} S_{\text{h}} \gamma \sum_{1}^{n} (h_k - h_{k_0}),$$

where S_{h} is the cross-sectional area of the hub, γ is the specific gravity of the manometric fluid, $h_k - h_{k_0}$ are the indications of the measuring tubes connected to the corresponding orifices in the end discs of the instrument fairing. The orifices are located at different radii in such a way that equal areas are served, so that integration can be replaced by summation.

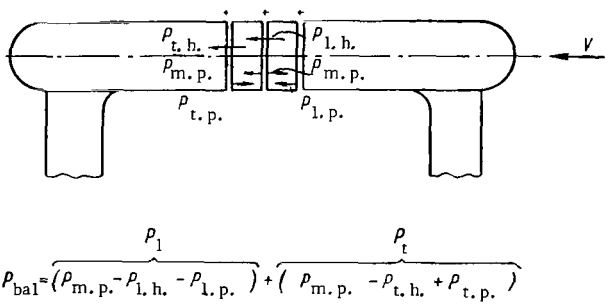

FIGURE 7.36. Forces measured by the thrust balance when the hubs are tested without blades.

We introduce the dimensionless coefficients

$$\alpha = \alpha_{\text{l}} + \alpha_{\text{t}} - \Delta\alpha_{\text{h}} - \Delta\alpha_{\text{p}}$$

$$c_p = c_{p\text{l}} + c_{p\text{t}} - \Delta c_{p\text{h}} - \Delta c_{p\text{p}},$$

where

$$\alpha_{\text{l}} = \frac{P_{\text{l}}}{\rho n_c^2 D^4}; \quad \alpha_{\text{t}} = \frac{P_{\text{t}}}{\rho n_c^2 D^4}; \quad c_{p\text{l}} = \frac{P_{\text{l}}}{\rho V^2 D^2}; \quad c_{p\text{t}} = \frac{P_{\text{t}}}{\rho V^2 D^2},$$

$$\Delta\alpha_{\text{h}} = \frac{\Delta P_{\text{h}}}{\rho n_c^2 D^4}; \quad \Delta\alpha_{\text{p}} = \frac{\Delta P_{\text{p}}}{\rho n_c^2 D^4}; \quad \Delta c_{p\text{h}} = \frac{\Delta P_{\text{h}}}{\rho V^2 D^2}; \quad \Delta c_{p\text{p}} = \frac{\Delta P_{\text{p}}}{\rho V^2 D^2}.$$

Determination of β and c_m for coaxial propellers. The total torque of coaxial propellers is

$$M = M_{\text{l}} + M_{\text{t}},$$

where M_{l} is the torque of the leading propeller and M_{t} is the torque of the trailing propeller.

We introduce dimensionless coefficients

$$\beta_{\text{l}} = \frac{2\pi M_{\text{l}}}{\rho n_c^2 D^5}, \quad \beta_{\text{t}} = \frac{2\pi M_{\text{t}}}{\rho n_c^2 D^5},$$

while $c_m = c_{m\,l} + c_{m\,t}$ where

$$c_{m\,l} = \frac{M_l}{\rho V^2 D^3}; \quad c_{m\,t} = \frac{M_t}{\rho V^2 D^3}.$$

The efficiency of coaxial propellers is

$$\eta = \frac{\alpha}{\beta}\lambda.$$

Figures 7.37 and 7.38 are typical propeller characteristics corresponding to positive thrusts. Figure 7.37 gives the coefficient β for coaxial propellers as a function of λ for different values of $\varphi_{0.75}$, together with curves of constant efficiency η.

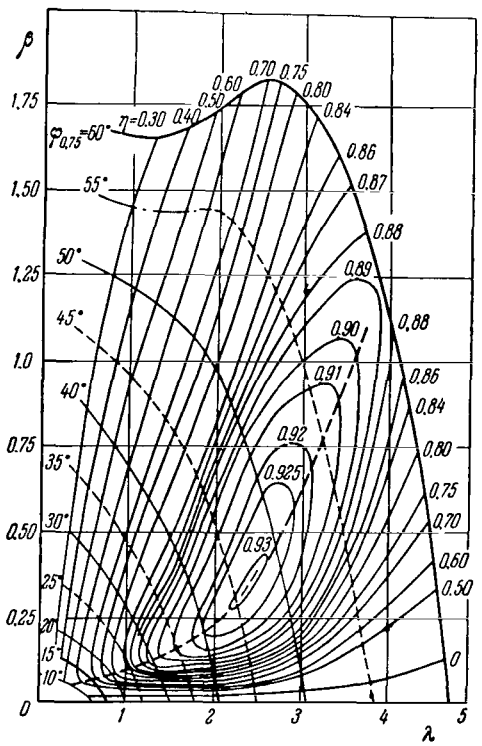

FIGURE 7.37. Characteristics of a series of coaxial propellers

Figure 7.38 gives the coefficient α for isolated coaxial propellers as a function of λ for different values of $\varphi_{0.75}$. Figures 7.39 and 7.40 give the characteristics of coaxial propellers, expressed by the coefficients c_m and c_p. Figure 7.39 gives the coefficient c_m for coaxial propellers as a function of $\frac{n_c D}{V}$ for different values of $\varphi_{0.75}$, while Figure 7.40 gives the coefficient c_p as a function of $\frac{n_c D}{V}$ for different values of $\varphi_{0.75}$.

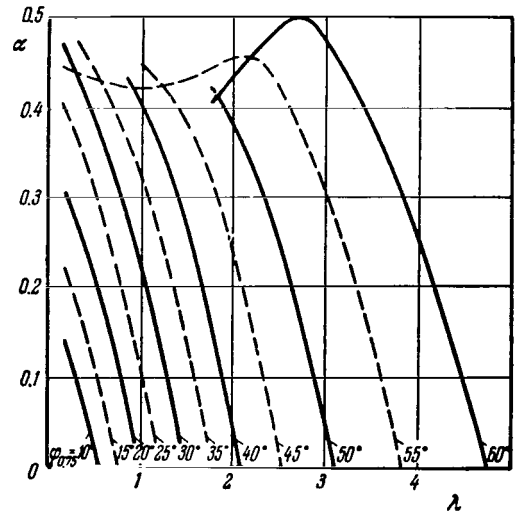

FIGURE 7.38. Thrust characteristics of coaxial propellers.

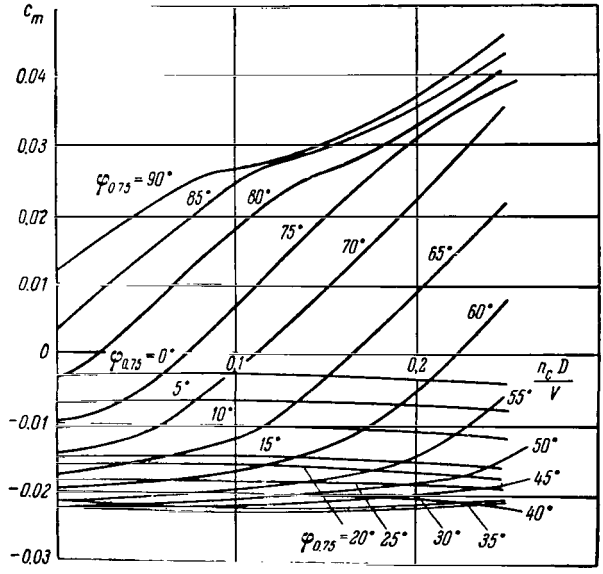

FIGURE 7.39. Total torque characteristics of coaxial propellers.

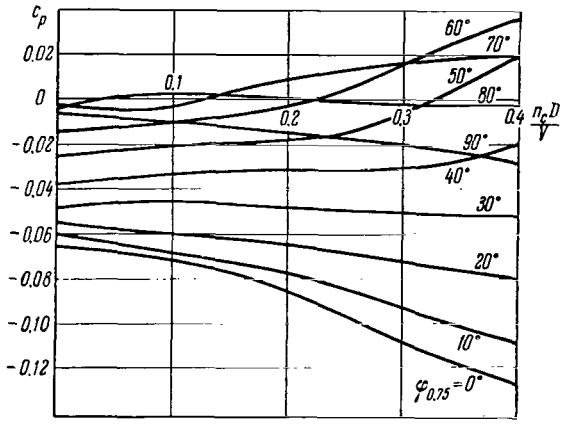

FIGURE 7.40. Coefficient c_p as function of $\frac{n_c D}{V}$.

§ 34. TESTING OF BLADE CASCADES

The main types of tests on turbomachine elements are static tests of blade cascades in special wind tunnels and stand tests of separate stages of turbines and compressors. This section deals with methods of stationary tests of blade cascades.

Determining the main aerodynamic characteristics of cascades

The efficiency of turbines, compressors, and other turbomachines is determined largely by the losses of kinetic energy in the blade cascades and impellers. If no energy is supplied to or removed from the flowing medium, the energy loss (or dissipation) in a working medium flowing in channels between blades is determined by the loss in total pressure. The principal geometrical parameters of blade cascades are indicated in Figure 7.41. The efficiency of a cascade is defined as the ratio of the energy of a given mass of the working medium at the cascade outlet to the energy of this mass at the cascade inlet.

The flow downstream of the cascade is nonuniform. In different parts of it, the velocities differ in magnitude and direction; hence, the mass flow-rate distribution is nonuniform. The amount of kinetic energy passing per second through unit cross-sectional area of the cascade outlet is

$$E_2 = \frac{QV_2^2}{2} = \frac{(\rho_2 V_2) V_2^2}{2}, \qquad (7.1)$$

where V_2 and ρ_2 are respectively the flow velocity and density at the cascade outlet, while Q is the mass flow rate per unit area. The efficiency of a cascade element is

$$\eta = \frac{\int_0^t E_2 \sin\beta_2\, dx}{V_{2\tau}^2 \int_0^t Q \sin\beta_2\, dx} = \frac{\int_0^t (\rho_2 V_2 \sin\beta_2)\, V_2^2\, dx}{V_{2\tau}^2 \int_0^t \rho_2 V_2 \sin\beta_2\, dx}, \tag{7.2}$$

where $V_{2\tau}$ is the outlet velocity at isentropic flow through the cascade, β_2 is the air outlet angle, and x is measured along the blade pitch.

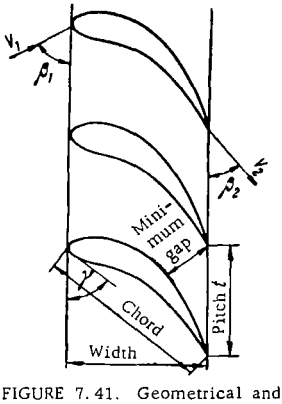

FIGURE 7.41. Geometrical and aerodynamic cascade parameters. β_1 — air inlet angle; β_2 — air outlet angle; γ — blade angle.

We can easily see that

$$\frac{\int_0^t (\rho_2 V_2 \sin\beta_2)\, V_2^2\, dx}{\int_0^t (\rho_2 V_2 \sin\beta_2)\, dx} = (V_2^2)_{av} \tag{7.3}$$

is the square of the velocity, averaged over the mass flow rate. Hence

$$\eta = \frac{(V_2^2)_{av}}{V_{2\tau}^2}. \tag{7.4}$$

The theoretical velocity $V_{2\tau}$ is determined by the total pressure p_{01} at blade inlet and by the mean static pressure p_{2av} at the blade outlet. The value of V_2 is determined by the local total pressure p_{02} and static pressure p_2 at the blade outlet.

The mean outlet velocity is determined by averaging over the mass flow rate:

$$V_{2av}=\frac{\int_0^t V_2(\rho_2 V_2 \sin\beta_2)\,dx}{\int_0^t (\rho_2 V_2 \sin\beta_2)\,dx}. \qquad (7.5)$$

The efficiency can be expressed in dimensionless form as a function of $\lambda = V/a_*$ and

$$q(\lambda)=\frac{\rho V}{\rho_* a_*}=\left(\frac{\varkappa+1}{2}\right)^{\frac{1}{\varkappa-1}}\lambda\left(1-\frac{\varkappa-1}{\varkappa+1}\lambda^2\right)^{\frac{1}{\varkappa-1}}, \qquad (7.6)$$

where ρ_* is the critical density. Noting that the value of the critical velocity does not depend on the losses in the cascade (i.e., upstream and downstream of the cascade its values are the same), we can, by dividing the numerator and denominator of the right-hand part of expression (7.2) by a_*^2, replace V_2^2 and V_{2T}^2 respectively by λ_2^2 and λ_{2T}^2.

Dividing the numerator and denominator by the unit critical mass flow rate upstream of the cascade, equal to $\rho_{*1}a_*$, and using

$$\frac{\rho_2 V_2}{\rho_{*1}a_*}=q(\lambda_2)\frac{p_{02}}{p_{01}},$$

obtained from $\frac{\rho_{*1}}{\rho_{*2}}=\frac{\rho_{01}}{\rho_{02}}=\frac{p_{01}}{p_{02}}$, we determine the cascade efficiency as a function of dimensionless magnitudes

$$\eta=\frac{\int_0^t \lambda_2^2 q(\lambda_2)\frac{p_{02}}{p_{01}}\sin\beta_2\,dx}{\lambda_{2T}^2\int_0^t q(\lambda_2)\frac{p_{02}}{p_{01}}\sin\beta_2\,dx}. \qquad (7.7)$$

The mean value of the air outlet angle is found from

$$\sin\beta_{2av}=\frac{\int_0^t q(\lambda_2)\frac{p_{02}}{p_{01}}\sin\beta_2\,dx}{\int_0^t q(\lambda_2)\frac{p_{02}}{p_{01}}\,dx}. \qquad (7.8)$$

Similarly, the mass flow coefficient is

$$\xi=\frac{(\rho_2 V_2)_{av}}{\rho_{2T}V_{2T}}=\frac{\int_0^t q(\lambda_2)\frac{p_{02}}{p_{01}}\sin\beta_2\,dx}{q(\lambda_{2T})\int_0^t \sin\beta_2\,dx}. \qquad (7.9)$$

At low velocities (incompressible fluid) ρ is constant. Assuming the static pressure at the outlet to be equal to the atmospheric pressure p_a,

we obtain

$$V_2 = \sqrt{\frac{2}{\rho_a}(\overline{p_{02} - p_a})}; \quad V_{2\tau} = \sqrt{\frac{2}{\rho_a}(\overline{p_{01} - p_a})},$$

$$\eta = \frac{\int_0^t V_2^2 V_2 \sin\beta_2\, dx}{V_{2\tau}^2 \int_0^t V_2 \sin\beta_2\, dx} = \frac{\int_0^t (p_{02} - p_a)\sqrt{(\overline{p_{02} - p_a})}\sin\beta_2\, dx}{(\overline{p_{01} - p_a})\int_0^t \sqrt{(\overline{p_{02} - p_a})}\sin\beta_2\, dx}. \tag{7.10}$$

When we can assume $\beta_2 \approx \text{const}$,

$$\eta = \frac{\int_0^t (p_{02} - p_a)\sqrt{\overline{p_{02} - p_a}}\, dx}{(\overline{p_{01} - p_a})\int_0^t \sqrt{\overline{p_{02} - p_a}}\, dx}. \tag{7.11}$$

When the efficiency is averaged over the pitch, we obtain

$$\eta_t = \frac{\int_0^t (p_{02} - p_a)\, dx}{(\overline{p_{01} - p_a})\, t}. \tag{7.12}$$

The following magnitudes have thus to be measured:

1) the total pressure p_{01} at a sufficient distance upstream of the cascade;

2) the total-pressure distribution $p'_{02} = f(x)$ over the pitch downstream of the cascade (by total-pressure tube indications);

3) the static-pressure distribution $p_2 = f(x)$ over the pitch downstream of the cascade;

4) the air-outlet angle distribution $\beta_2 = f(x)$ over the pitch downstream of the cascade.

At subsonic velocities, $p'_{02} = p_{02}$ while M_2 and λ_2 are determined as functions of p_2/p_{02}. At supersonic velocities, M_2 and λ_2 have to be determined from Reyleigh's formula (Chapter IV), since the value of p'_{02}, as measured by the total-pressure tube, is equal to the total pressure behind the normal shock formed before the tube. Usually the following differences are measured in tests:

1) $\Delta p_{01} = p_{01} - p_a$ where p_a is the atmospheric pressure,

2) $h_{p_t} = p_{01} - p'_{02}$ (loss of total pressure),

3) $\Delta p_2 = p_2 - p_a$;

4) $\Delta p_{02} = p_2 - p_a$.

As a rule, Δp_2 is very small, since cascade tests are usually carried out with discharge into atmosphere.

The layout for measuring these magnitudes with the aid of U-tube manometers is shown in Figure 7.42.

Cascade testing installations

Special wind tunnels are used to test cascades of compressor and turbine blades under static conditions. The main requirements for such

wind tunnels is the provision of operating conditions in the central part of the cascade, approaching those in an infinite cascade. The number of blades in the cascade usually varies from 7 to 14. Adjustment of the magnitude and direction of the inlet velocity must be possible. The layouts and designs of the wind tunnels differ according to the velocities obtained in them.

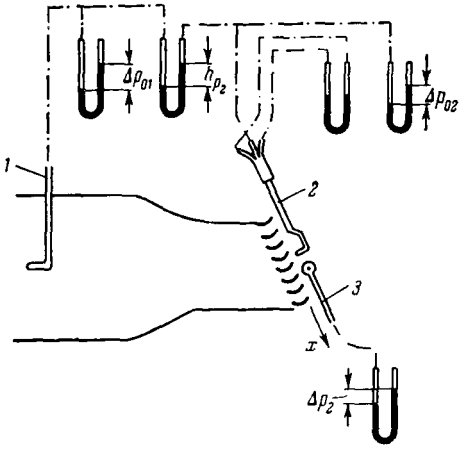

FIGURE 7.42. Measuring pressures during cascade tests. 1 — tube for measuring total pressure upstream of cascade; 2 — tube for measuring total pressure and flow direction downstream of cascade; 3 — tube for measuring static pressure downstream of cascade.

Full-scale Reynolds numbers can be obtained in low-speed tunnels by increasing the blade chord. In high-speed tunnels the blade chords are approximately equal to the mean chords of blades used in axial compressors and turbines. By varying the pressure downstream of the cascade, separate investigation of viscosity and compressibility effects can be carried out. However, such tunnels are inconvenient because of the difficult access to the tested cascade.

The simplest installation for testing cascades at small velocites has the form of an ordinary open-circuit wind tunnel. The air is aspirated from the room by a fan and discharged into the room through the cascade. To increase the flow uniformity at the cascade inlet, the air is discharged through a nozzle with large expansion ratio (from 7 to 12). Better velocity equalization is sometimes obtained by boundary-layer removal through the tunnel walls upstream of the cascade.

Tests at large flow velocities are performed in tunnels operated with air supplied by compressors. The air from the compressor is usually discharged through the cascade directly to atmosphere. An example of such an installation is the NGTE high-speed tunnel /8/, shown schematically in Figure 7.43.

If a back pressure is required in order to increase the Reynolds number, a throttling device is inserted between the tunnel outlet and the tested cascade. The air from the compressor is supplied to the tunnel through a regulating valve. This can be an ordinary valve actuated manually by a

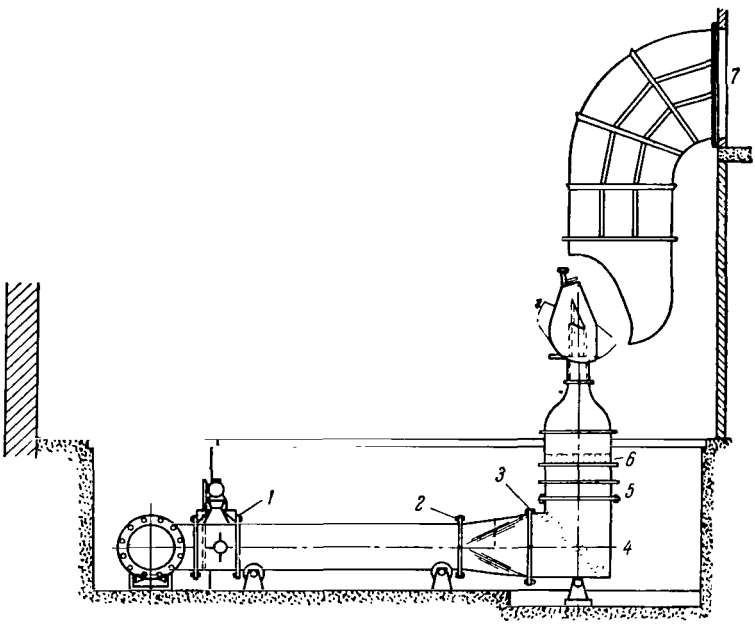

FIGURE 7.43 NGTE wind tunnel for testing cascades at large flow velocities. 1 — throttling valve for accurate inlet-pressure regulation; 2 — circular section; 3 — rectangular section; 4 — corner; 5 — cascades; 6 — honeycomb; 7 — air discharge to atmosphere through settling chamber.

motor. A special rapid-action valve permits better regulation and maintenance of pressure at the tunnel inlet. Such a valve, with hydraulic or electric drive, connected to the automatic total-inlet-pressure regulator, facilitates tunnel operation and permits increased accuracy of the experiments.

Figure 7.44 shows schematically the test section of the wind tunnel for testing cascades at the Dresden Turbine Institute (East Germany). This intermittent-operation tunnel is powered by an ejector. The air is sucked into a test section measuring 300×100 or 200×100 mm^2 in which a flow velocity corresponding to $M = 0.85$ can be attained. The Reynolds number can be varied from $1 \cdot 10^5$ to $8 \cdot 10^5$ /9/.

The same institute has a high-speed closed-circuit tunnel. The drive is by an axial 1200 kw compressor (Figure 7.45). The test section measures 300mm$\times$100 mm, and is suitable for testing blades having chords of 50mm and lengths of 100mm at $0.3 < M < 1.5$. By varying the initial pressure between 0.3 and 4 atm, the Reynolds number can be changed from 10^5 up to $2 \cdot 10^6$ /10/.

The inlet angle is adjusted either by rotating the entire test section, as shown in Figure 7.44, or by turning the cascade. In the former case,

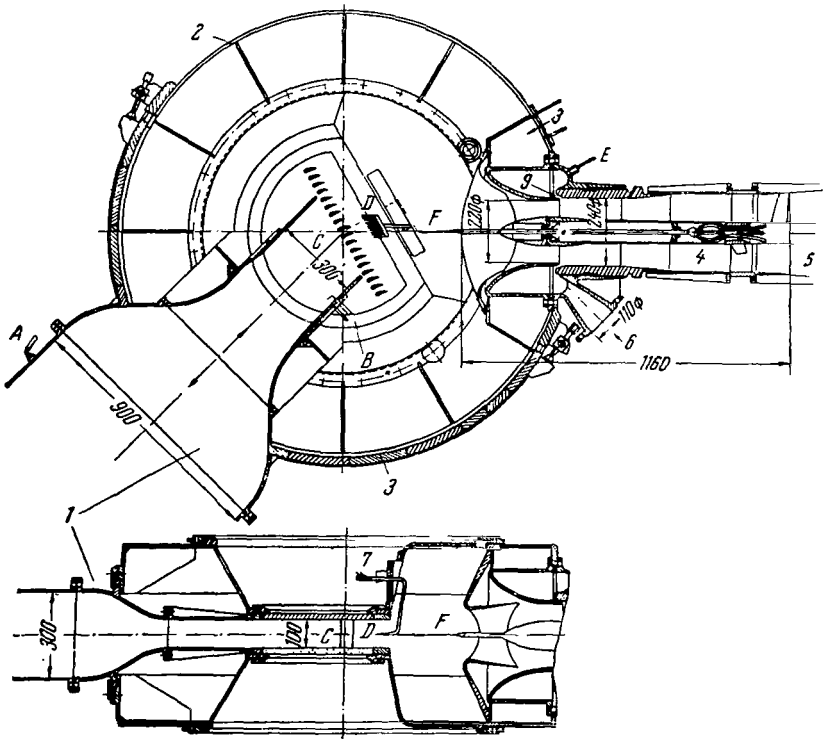

FIGURE 7.44. Ejector tunnel for cascade tests. Tunnel elements: 1 — settling chamber and nozzle; 2 — intermediate-pressure chamber; 3 — segments serving for changing the blade inlet angle; 4 — mixing chamber; 5 — diffusor; 6 — high-pressure air pipe; 7 — tubes to multiple manometer; 8 — inlet for additional aspirated air; 9 — injector throat. Orifices and tubes: A — static pressure in settling chamber; B — static and total pressures; C — static pressure at cascade inlet; D - static and total pressures downstream of cascade; E — static pressure and temperature of high-pressure air; F — tubes for measuring the flow direction downstream of the cascade.

the traversing cradle serving for flow investigations downstream of the cascade is installed on the movable tunnel wall, while in the latter case it is mounted on the device for rotating the cascade (Figure 7.46).

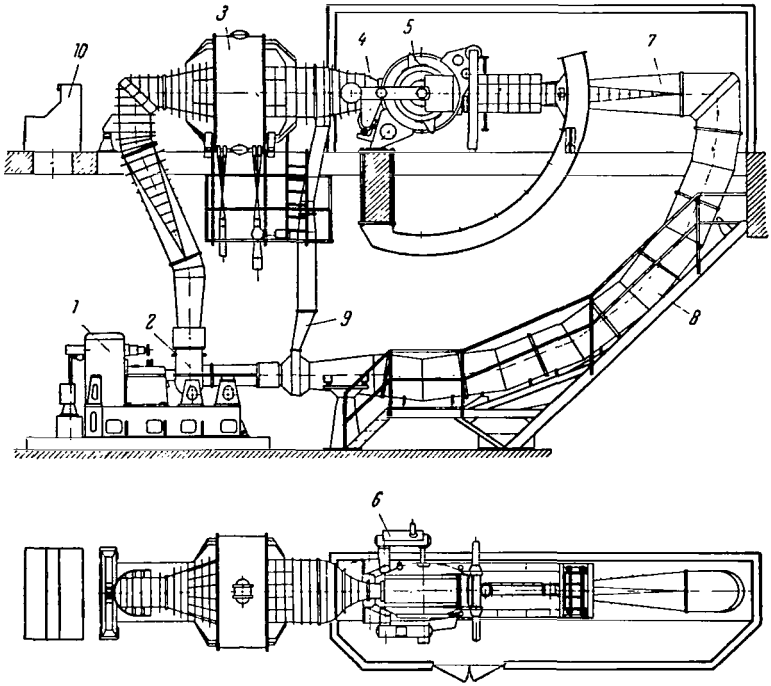

FIGURE 7.45. High-speed wind tunnel for testing cascades. 1 — steam turbine; 2 — axial compressor; 3 — cooler; 4 — nozzle; 5 — Eiffel chamber; 6 — schlieren instrument; 7 — diffusor; 8 — bend; 9 — bypass; 10 — control panel.

Measurement methods and equipment. The total pressure at the blade inlet is easily determined with the aid of stationary tubes.

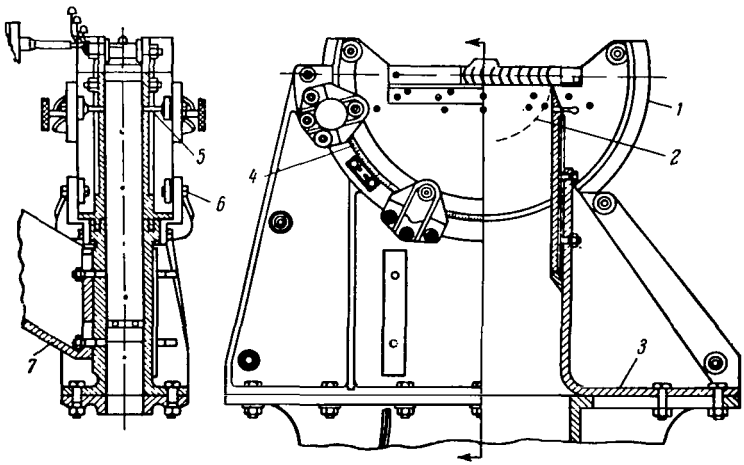

FIGURE 7.46. Test section of high-speed wind tunnel for testing cascades (see Figure 7.43). 1 — turntable for installing the cascade; 2 — vertical adjustable wall; 3 — nozzle flange for attaching the test section; 4 — scale for read-off of blade angle; 5— static-pressure tap; 6 — turntable guides; 7 — bracket for coordinating device.

The flow parameters at the blade outlet are usually determined by tubes of the type described in Chapter IV, for instance, cylindrical tubes with central orifices for measuring the total pressure and lateral orifices for measuring the flow inclination. Since the flow downstream of the cascade is nonuniform, the values of Δp_{02i} and β_{2i}, are measured at points whose coordinates are x_i with the aid of the traversing cradle. The static pressure is usually determined with a separate tube. From the measured values of Δp_{02i} and β_{2i} we obtain by numerical integration the values of η, $\sin \beta_{2av}$ and ξ.

Recording and integrating instruments. In order to determine the influence of different parameters on the characteristics of the cascade, and to compare cascade tests, a large number of tests are required, each of which consists of multiple measurements.

Visual recording of a large number of readings and the subsequent mathematical processing requires much effort and time. Large-scale cascade tests necessitate, therefore, automatic recording of the measurements, together with remote control of the tubes with the aid of automatic devices described in § 17. The advantages of automatic control and measurement systems are:

1) increased accuracy, because the parameters are recorded not at distinct points but continuously over the whole pitch;

2) speed-up of experiments and computation of final results;

3) improved work conditions due to distance from sources of noise.

Automation permits processing of the measurement results during the experiment. For this purpose special computing devices are used, which integrate and average the measured magnitudes over the pitch.

An automatic continuous-measurement system for testing cascades in low-speed wind tunnels is shown in Figure 7.47 /11/. This system permits simultaneous recording on a tape of the total-pressure loss $(p_{01} - p_{02})$ and of the angle β_2, and determination of the mean values over the pitch of these magnitudes, with the aid of mechanical integrating mechanisms. The cylindrical tube (1), which measures the total pressure and the flow direction downstream of the cascade, is installed on the head of the traversing cradle. During the experiment the head with the tube is continuously moved along the cascade by motor M_1. The maximum travel $x_2 - x_1$, which is usually a multiple of the pitch, is determined by limit switches (2) and (2'). Drum (3) of the recording device is turned in proportion to the displacement of the tube with the aid of a servo system which consists of a selsyn transmitter ST_1 and the selsyn receiver SR_1.

Tube (1) is continuously turned into the flow direction by servomotor M_2 which is controlled by an automatic angle-measuring device and by manometer A according to the system shown in Figure 4.79. Carriage (7), with pen (5), is moved in proportion to the turning angle of the tube by a lead screw which is rotated by selsyn pair ST_2 and SR_2. This pen marks off on tape (4), parallel to the drum axis, the value of angle β_2. The total-pressure loss is measured by manometer B with the aid of a servo device consisting of a photoelectric cell, amplifier Y_2, and servomotor M_3 which moves the light source and the photoelectric cell along the column of liquid (such a manometer is shown in Figure 5.6). The measured pressure difference is recorded on the tape by pen (6), secured to carriage (8), which is moved by a lead screw rotated by selsyn pair ST_3 and SR_3.

The integrating device which serves to measure the mean values of the angle β_2 and the loss in total pressure consists of discs (11) and (12), and integrating friction rollers (9) and (10). The discs are rotated by the selsyn pair ST_1 and SR_1 at a velocity $d\varphi_2/dt = k_1 dx/dt$ where k_1 is a constant.

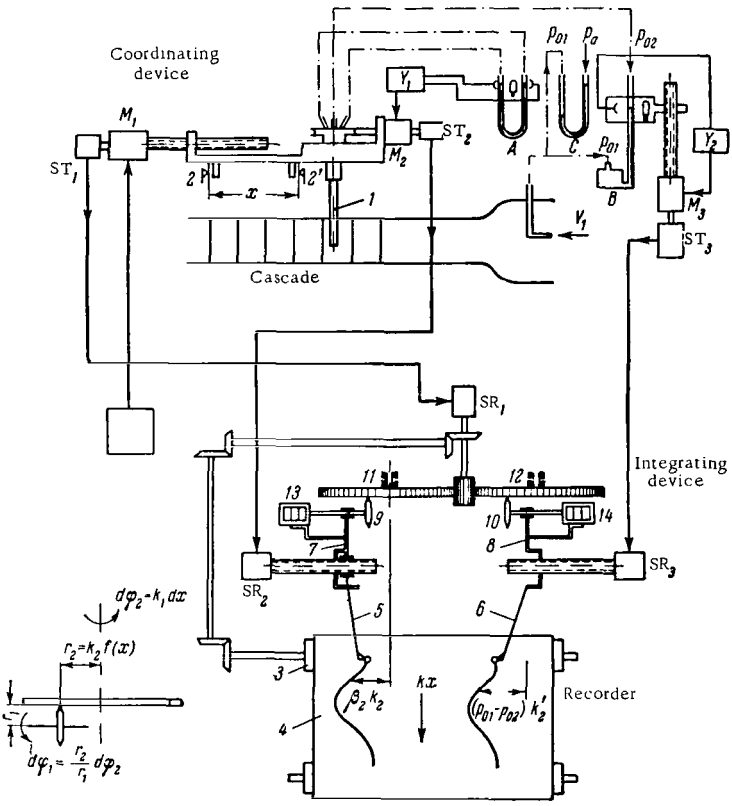

FIGURE 7.47. Automatic recording and integrating of total pressures and angles.

The rotation is transmitted by friction to rollers (9) and (10) forced against the disc edges. The rollers are mounted on carriages (7) and (8), and are moved together with pens (5) and (6). The rotation of the rollers is measured by counters (13) and (14), also mounted on the carriages.

The operating principle of the integrating device is explained by the diagram in the bottom left-hand corner of Figure 7.47. The integrating roller, whose radius is r_1, is moved by the lead screw along the radius of the disc in such a way that the distance between the axis of the disc and the point of contact with the roller is $r_2 = k_2 f(x)$ where $f(x)$ is the functional dependence of the pressure drop, angle, or other measured magnitude, on the distance along the pitch, while k_2 (like k_1) is a proportionality coefficient which depends on the transmission ratio of

the mechanism. When the disc turns through a small angle $d\varphi_2 = k_1 dx$ the angle through which the roller is rotated is

$$d\varphi_1 = \frac{r_2}{r_1} d\varphi_2 = \frac{k_2 f(x)}{r_1} k_1 dx. \tag{7.13}$$

Integrating this expression, we obtain the angle through which the integrating roller is rotated when the tube moves from x_1 to x_2:

$$\varphi_1 = \frac{k_2 k_1}{r_1} \int_{x_1}^{x_2} f(x)\, dx. \tag{7.14}$$

The magnitude $\varphi (x_2 - x_1)$ is proportional to the mean value of $f(x)$. The total number of revolutions n of the counter, which is connected to the shaft of the integrating roller, is proportional to this mean value

$$n = \frac{\varphi_1}{2\pi} = k f_{av}(x). \tag{7.15}$$

Thus the indications of counter (13) in Figure 7.47 are proportional to the mean air-outlet angle:

$$n_1 = k \frac{\int_{x_1}^{x_2} \beta_2\, dx}{x_2 - x_1} = k\beta_{2\,av}, \tag{7.16}$$

while the indications of counter (14) are proportional to the mean loss in total pressure:

$$n_2 = k \frac{\int_{x_1}^{x_2} (p_{01} - p_{02})\, dx}{x_2 - x_1} = k(p_{01} - p_{02})_{av}. \tag{7.17}$$

In (7.16) and (7.17), $k = k_1 k_2 (x_2 - x_1)/2\pi r_1$ is a constant coefficient which depends on the kinematics of each integrating mechanism and on the integration interval. Dividing the indications of counter (14) by $(p_{01} - p_a)$, measured by manometer C, we obtain the pressure-loss coefficient, averaged over the pitch:

$$\zeta = \frac{\int_{x_1}^{x_2} (p_{01} - p_{02})\, dx}{(p_{01} - p_a)(x_2 - x_1)};$$

the cascade efficiency is then

$$\eta = 1 - \zeta.$$

The efficiency can be determined directly if manometer B is connected in such a way that it measures $p_{02} - p_a$. In this case the indications of

counter (14), are proportional to the mean total gage pressure downstream of the cascade:

$$n_2 = k \frac{\int_{x_1}^{x_2} (p_{02} - p_a)\, dx}{(x_2 - x_1)} = k (p_{02} - p_a)_{av}$$

while by (7.12), the efficiency is

$$\eta = \frac{(p_{02} - p_a)_{av}}{p_{01} - p_a} = \frac{n_2}{k (p_{01} - p_a)}.$$

The first method of determining the efficiency from the pressure-loss coefficient is more accurate for two reasons: 1) the differences $p_{01} - p_{02}$ are smaller than the differences $p_{02} - p_a$, and can therefore be measured by a more sensitive manometer; 2) the fluctuations of the total inlet pressure p_{01} affect very little the values of $p_{01} - p_{02}$, but considerably the values of $p_{02} - p_a$.

When carrying out experiments with the aid of the described automatic instruments, the value of p_{01} should remain unchanged when the traversing device is moved for periods lasting one or several minutes. For this purpose the wind tunnel must be equipped with an automatic pressure regulator at the cascade inlet. A change of p_{01} affects the theoretical velocity V_{2T} and λ_T, and the processing of the experimental results then becomes difficult.

Instruments for investigations of the flow downstream of guide vanes, rotating compressor impellers, and turbine discs do not differ in principle from the instruments used in static cascade tests. Due to energy supply and removal, the stagnation temperature varies in the different flow sections of these machines. Hence, when compressors and turbines are tested, the temperature distribution is also investigated. Figure 7.48 shows a system for automatic plotting and integrating of pressures, temperatures, and angles, designed by Pratt and Whitney /12/.

The casing of the tested turbine or compressor carries a traversing device consisting of a carriage which is moved along the disc periphery by electric motor G, controlled from panel M. On the carriage a combined tube is installed for measuring three variables: total pressure, stagnation temperature, and flow direction. The tube can be moved either in the direction of the blade pitch together with the carriage by motor G, or along the blade radius by motor J. The tube is turned into the flow direction by motor H. Several similar mechanisms can be installed on the stand downstream of the individual blade discs. All movements of the tubes are transmitted to the recording and integrating instruments by servo systems consisting of selsyns whose error signals act on a follower motor through amplifiers. The servo systems permit movements to be measured with an accuracy of 0.05 mm, and angles with an accuracy of 0.1°.

In contrast to the other systems, the "Plottomac" integrating and computing device is based not on a kinematic but on an electrical principle. The schematic diagram of the system is shown in Figure 7.49. The drawings cover the recording and integrating of one variable, i.e., total pressure. The other variables — temperature and angle — are recorded and integrated similarly.

Connections between the separate units in the system are provided by selsyn pairs each consisting of a transducer and a receiver which operate as control transformers (Figure 4.76).

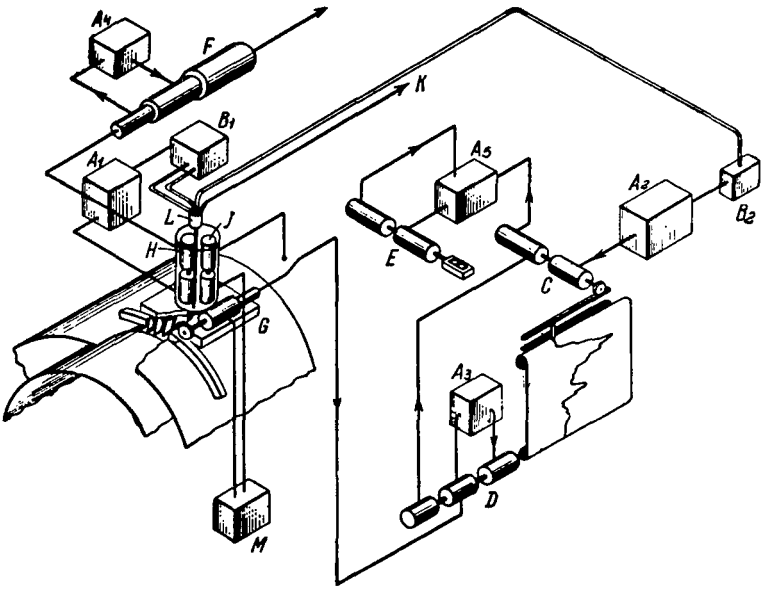

FIGURE 7.48. "Plottomac" automatic traversing device. A_1-A_5 — amplifiers; B_1 — differential-pressure transducer of angle-measuring tube; B_2 — total-pressure transducer; C — servomotor for automatic potentiometer and recording instrument; D — servomotor for moving tape in synchronization with tube and generator of a signal proportional to tube velocity; E — integrating motor, counter, and feedback generator; F — servo system for tube angle; G — motor and selsyn transmitter for motion of tube along disc periphery; H — motor and selsyn transmitter for tube rotation; motor starts upon receipt of voltage signal from transducer B_1; J — motor and selsyn transmitter for radial motion of tube; L — combined tube for measuring angle, total pressure, and stagnation temperature; M — control panel.

When the tube is moved by the traversing device, the angle through which the motor G has rotated is repeated with the aid of selsyns in the excitation unit whose duty is to transmit to the integrating device a signal which is proportional to the tube velocity. The shaft of servomotor D carries a small d.c. signal generator (1), cam disc (2) of a stroboscopic contact device for calibration of the integrating instrument, and a selsyn transmitter. The corresponding selsyn receiver is carried on the shaft of a second servomotor D_1, which rotates the drum of the recording instrument.

Generator (1) in the excitation unit creates a voltage which is proportional to the tube velocity dx/dt and to the excitation voltage u:

$$e_1 = k_1 u \frac{dx}{dt}.$$

The slider of potentiometer P_1 of the recording device, which is fed by the voltage e_1, is connected with a pen and with the slider of potentiometer P_3 of the measuring device, which are both moved by servomotor C. The

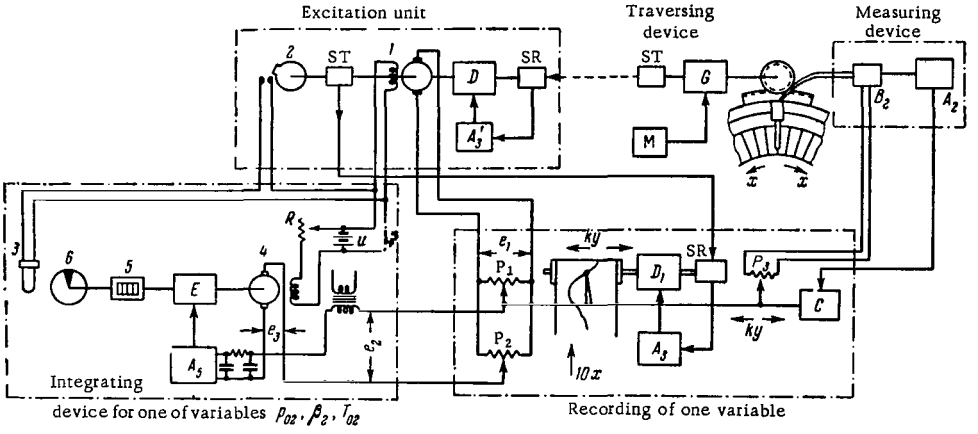

FIGURE 7.49. Schematic diagram of the "Plottomac" traversing device. The designations A to M coincide with those in Figure 7.48. 1 — d.c. signal generator ($e_1 = k_1 u\, dx/dt$); 2—cam disc for closing contacts of stroboscopic lamp; 3 — pulse light source; 4 — feedback generator; 5 — integrating counter; 6 — stroboscopic disc; ST — selsyn transmitter; SR — selsyn receiver; P_1 — potentiometer of product $f(x)\, dx/dt$; P_2 — zero-adjustment potentiometer; P_3 — potentiometer of measuring device.

displacements of pen and sliders from their respective zero positions are therefore proportional to the measured value $f(x)$ (which may be the total pressure, the air outlet angle, or the stagnation temperature).

The position of the slider of potentiometer P_2, which is fed by the voltage e_1 in parallel with potentiometer P_1, is adjusted in such a way that the voltage e_2 between the sliders of these potentiometers becomes zero when the measured variable $f(x)$ is equal to zero. The voltage e_2 is thus proportional to the product of the measured variable and the tube velocity:

$$e_2 = k_2 k_1 u \frac{dx}{dt} f(x).$$

The difference between the voltage e_2 and the voltage of feedback generator (4) is fed through amplifier A_5 to motor E driving the shaft of generator (4) and counter (5) of the integrating device. The d.c. voltage created by the feedback generator is

$$e_3 = k_3 u \frac{d\theta}{dt},$$

where θ is the angle of rotation of the shaft common to motor E, generator (4), and counter (5).

Since amplifier A_5 has a very high amplification coefficient and requires only a voltage of a few microvolts to drive the motor at full speed, e_3 can

be taken to be equal to e_2, and therefore

$$k_3 u \frac{d\theta}{dt} = k_2 k_1 u \frac{dx}{dt} f(x),$$

$$d\theta = \frac{k_2 k_1}{k_3} f(x)\, dx.$$

Thus, the angle through which the shaft of counter (5) rotates when the tube moves a distance $x_2 - x_1$ is

$$\theta = \frac{k_2 k_1}{k_3} \int_{x_1}^{x_2} f(x)\, dx.$$

The mean value of the variable is

$$[f(x)]_{av} \sim \frac{\theta}{x_2 - x_1}.$$

The constants k_1, k_2, and k_3 determine the number of revolutions of the counter which are equivalent to unit area under the curve drawn by the recording pen. The value of k_3 can be adjusted by means of variable rheostat R in order to change the scale. The scale is adjusted with the aid of a stroboscopic device consisting of stroboscopic disc (6) and pulse light source (7), which is switched on by cam disc (2), rotated at a speed proportional to the tube velocity. The transmission ratios of the reduction gears in the traversing device and in the excitation unit are such that light source is switched on 3750 times while the tube moves one inch (25.4 mm).

The rotational speed of the motor shaft of the integrating device is adjusted by the rheostat R in such a way that the shaft turns once between two light flashes at the maximum value of the measured variable $f(x)$. Counter (5) of the integrating device records two units for each revolution of the motor of the integrating device; thus, every inch of tube travel corresponds to 7500 units on the counter at the maximum value of $f(x)$. Since the chart of the recording mechanism moves ten times faster than the tube, while for $f(x) = [f(x)]_{max}$ the full travel of the pen amounts to 10 inches, one square inch on the chart corresponds to 75 units on the counter of the integrating device.

§ 35. TESTING OF FANS

The purpose of testing a fan is to determine its main characteristics as a machine creating the pressure drop necessary to induce gas flow, i.e., to determine the total head H created by the fan, the delivery Q, and the power required.

For fan tests the law of energy conservation, as expressed by Bernoulli's equation for an incompressible fluid, is applied. The flow upstream and downstream of the fan is assumed to be steady and uniform /13/.

Applying Bernoulli's equation to sections *I* and *II* upstream of the fan (Figure 7.50), sections *II* and *III* on either side of the fan, and

sections *III* and *IV* downstream of the fan, we obtain

$$p_a = p_2 + \rho\frac{V_2^2}{2} + \zeta_{suc} \text{ (for sections } I-II),$$

$$p_2 + \rho\frac{V_2^2}{2} = p_3 + \rho\frac{V_3^2}{2} - H_t \text{ (for sections } II-III),$$

$$p_3 + \rho\frac{V_3^2}{2} = p_4 + \rho\frac{V_{out}^2}{2} + \zeta_{dis} \text{ (for sections } III-IV),$$

where p_2, p_3, p_4, V_2, V_3, and V_{out} are respectively the static pressure and velocity in the corresponding sections, ζ_{suc} and ζ_{dis} are the pressure losses caused by the resistances of the suction and discharge ducts respectively, and H_t is the total head created by the fan. After adding these equations we obtain an expression for the total head created by the fan:

$$H_t = \zeta_{suc} + \zeta_{dis} + \rho\frac{V_{out}^2}{2}$$

[when $p_4 = p_a$].

The total head created by the fan is thus used to overcome the resistances in the suction and discharge ducts and for creating a velocity head at the duct outlet. From the viewpoint of the results obtained, the ratio between the losses ζ_{suc} and ζ_{dis} is immaterial, but their sum is important. During experiments it is better to insert a resistance only in the suction duct, assuming the discharge section of the fan to be the discharge section of the duct.

The fundamental equation then becomes

$$H_t = \zeta_{suc} + \rho\frac{V_{out}^2}{2}$$

or

$$H_t = H_{st} + H_d,$$

where $H_{st} = \zeta_{suc}$ is the static head created by the fan, $H_d = \rho\frac{V_{out}^2}{2}$ is the velocity head created by the fan.

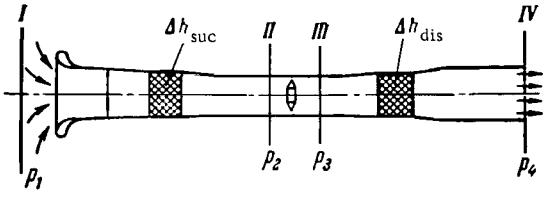

FIGURE 7.50. Operation of a fan in a duct.

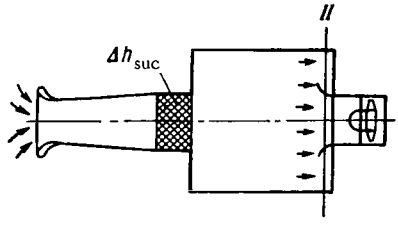

FIGURE 7.51. Operation of a fan installed downstream of an expansion chamber.

Upstream of the fan the pressure is below atmospheric because of the resistance of the suction duct and the flow velocity in it. This negative

pressure can be found from Bernoulli's equation for sections *I* and *II*

$$p_2 - p_a = -\left(\zeta_{suc} + \rho\frac{V_2^2}{2}\right).$$

If upstream of the fan there is a large expansion chamber (Figure 7.51) in which the flow velocity is negligible, we obtain

$$p_2 - p_a = -\zeta_{suc} = -H_{st},$$

i.e., the negative pressure measured in this chamber (for instance by a differential manometer) is equal in magnitude to the static head created by the fan. For this reason, in fan tests, expansion chambers are preferable to ducts in which the flow velocity fluctuates considerably.

The output of the fan is expressed through the total head, the duct cross section, and the velocity at the outlet:

$$N = H_t F_{out} V_{out} = H_t Q,$$

where Q is the delivery in m^3/sec. The ratio of the fan output ($H_t Q$) to the power required by the fan (N_{mot}) is the fan efficiency

$$\eta = \frac{H_t Q_{hr}}{3600 \cdot 75 N_{mot}} = \frac{H_t Q_{sec}}{75 \cdot N_{mot}}.$$

The complete characteristic of the fan is thus obtained by determining

$$H_t = H_{st} + H_d;\ Q;\ N_{mot}.$$

If, as is generally the case, an expansion chamber is used, H_{st} is determined by measuring the negative pressure in the chamber upstream of the fan, i.e., the static gage pressure, taking into account its sign. These measurements are made with the aid of orifices in the chamber walls.

The delivery Q can be determined from the velocity in and area of any section upstream of the tested fan. The section should be the same for all measurements. The delivery is found by averaging the velocity over the whole section. H_d is found from the velocity which is obtained by dividing the delivery Q by the flow area of the outlet section.

The shaft power of the fan drive is determined with the aid of a balance stand consisting of an electric motor whose stator can turn in bearings and is connected by a lever to a balance beam. For determining the power required by the fan, friction should be taken into account through calibration.

A typical fan characteristic at constant rotational speed is shown in Figure 7.52 /14/. To obtain the characteristics of a fan, the delivery and duct resistance must be adjustable, or it must be possible to throttle the flow. This is done with the aid of exchangeable orifice plates, screens, or other types of resistances.

The need to test fans over wide delivery and resistance ranges, including zero resistance, and also in parallel and series connections led to the use of pressure chambers as principal installations for testing fans.

Such a chamber is shown in Figure 7.53, in which the measuring points are indicated. Atmospheric air enters the chamber through a cylindrical measuring pipe with a smooth input collector. A screen* before the collector prevents objects near the collector from affecting the velocity distribution in the pipe and eliminates any turbulence in the airstream. The cylindrical pipe is connected to a diffuser at whose end there is a butterfly valve, by means of which the resistance to flow is altered. Behind the butterfly valve, which also serves as guide vane, there is a centrifugal blower intended to overcome partially or fully the resistance of the duct.

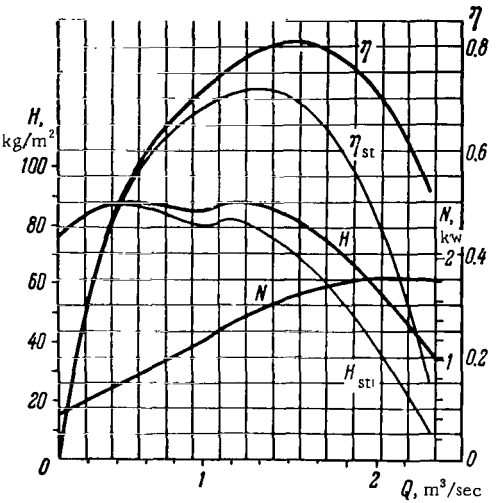

FIGURE 7.52. Characteristics of TsAGI model TS 4-70 centrifugal fan. D = 0.5 m, n = 1,450 rpm and ρ = 0.122 kg·sec²/m⁴.

From the blower the air flows to a diffuser where its velocity is greatly reduced (down to 1 or 2 m/sec). Screens and honeycombs behind the diffuser smoothen out the velocity and pressure distributions at the inlet to the cylindrical chamber.

A panel on which the tested fan is mounted is installed at the outlet section of the chamber. Special attention should be paid to the air-tightness of the chamber, since entry of air into it can reduce considerably the accuracy of the experiments. The mean velocity over the inlet-pipe section determines the delivery through the duct. The velocities are found from the expression

$$V = \sqrt{k_к \frac{2}{\rho}(p_a - p_к)},$$

* A screen is necessary when the dimensions of the room are restricted.

where $k_к$ is the calibration coefficient, whose value is usually between 0.96 and 0.98, which characterizes the uniformity of the velocity distribution in the pipe, p_a is the atmospheric pressure, and $p_к$ is the static

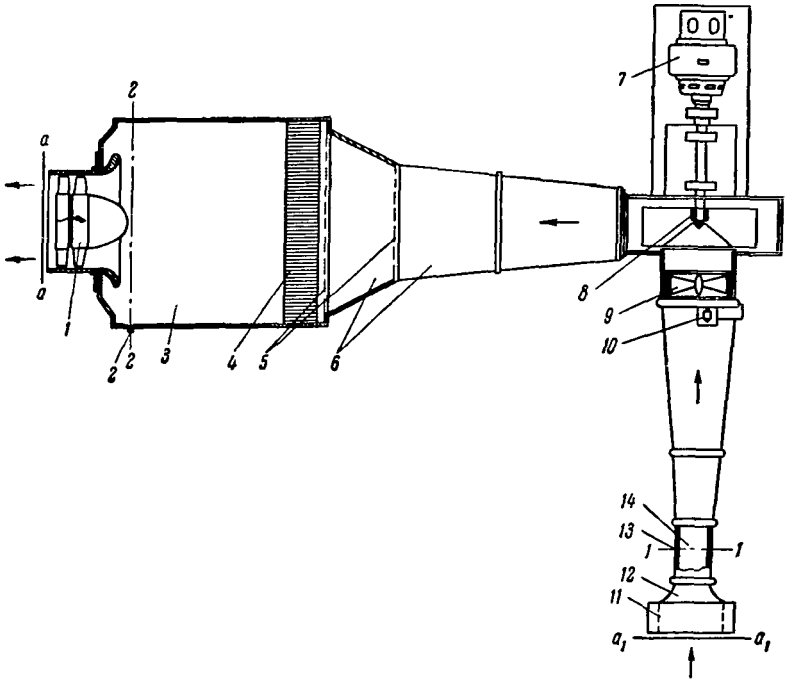

FIGURE 7.53. Pressure chamber. 1 — tested fan; 2 — static-pressure measurement; 3 — chamber; 4 — honeycomb; 5 — screens; 6 — diffuser; 7 — blower drive; 8 — blower; 9 — butterfly valve; 10 — drive for butterfly valve; 11 — drum; 12 — collector; 13 — delivery measurement; 14 — cylindrical measuring pipe.

pressure in the pipe. In order to reduce measuring errors the flow velocity in the collector should not be less than 8 to 10 m/sec.

Further calculations are performed in the dimensioned magnitudes Q, H, N, or in the dimensionless magnitudes*

$$\bar{Q} = \frac{Q}{Fu_R},$$

$$\bar{H} = \frac{H}{\rho u_R^2},$$

$$\bar{N} = \frac{N}{\rho F u_R^3},$$

where ρ is the air density under experimental conditions, F is a characteristic area, u_R is the circumferential velocity of the blade tips.

* Some installations are equipped with instruments which permit the dimensionless coefficients to be determined directly during tests. These instruments /15/ are based on the same principles as those for Mach-number determination (see § 24).

Expressing the test results in dimensionless form is very convenient, since geometrically similar fans have the same dimensionless characteristics irrespective of rotational speed, diameter, and air density*.

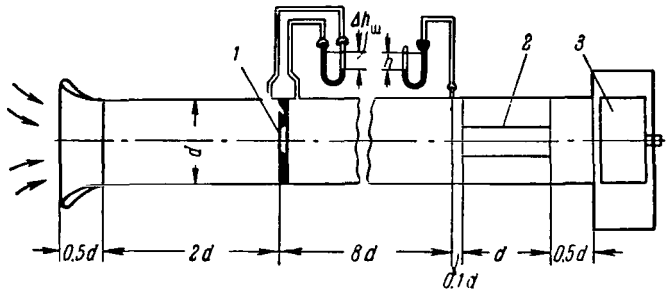

FIGURE 7.54. Testing a fan in a duct. 1 — orifice plate; 2 — straightening screen; 3 — fan.

When the fan is tested in a duct (Figure 7.54), the delivery can be measured with the aid of orifice plates. The static pressure can be measured with the aid of either orifices in the duct walls or tubes installed on the duct axis. In either case the measurement must be made at a distance not less than 8 diameters from the orifice plate, but upstream of the protective net placed directly in front of the fan. In the former method, several orifices located in a plane perpendicular to the duct axis are connected by a common tube to a manometer. The manometer thus indicates the static pressure, to which the velocity head in the section of said plane has to be added in order to obtain the total head created by the fan.

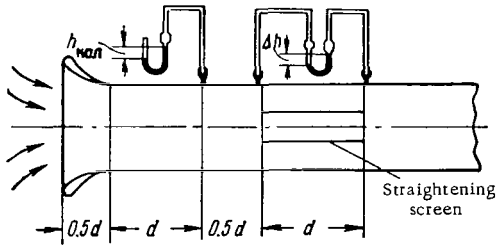

FIGURE 7.55. Measuring the resistance of screens.

When a straightening screen is installed between the measurement section and the fan, the resistance of the screen has to be added to the

* When $u_R > 80$—100 m/sec a correction for compressibility effects has to be introduced.

static head. This resistance is measured in the same duct in which the fan is tested (Figure 7.55). The relationship between screen resistance and delivery is parabolic. The static-pressure head is corrected accordingly for each delivery.

§ 36. EXPERIMENTAL DETERMINATION OF LOCAL RESISTANCES

In many practical problems it is necessary to determine the energy losses in a flowing gas or liquid. These losses result from the irreversible transfer of mechanical energy into heat. They depend on the molecular and turbulent viscosity of the moving medium and are called hydraulic losses or resistances.

It was shown in Chapter III that two types of hydraulic losses (resistances) can be distinguished:

1) Frictional losses ΔH_{fr}.

2) Local losses (resistances) ΔH_l.

Frictional losses are caused in real gases and liquids by momentum exchange between molecules (in laminar flow) and also between separate particles (in turbulent flow) of adjacent layers of the medium, moving at different velocities. These losses take place along the whole length of the flow path (e.g., pipeline), and are in practice taken into account only over considerable lengths (branches, diffusers with small divergence angles, etc.), or when they are commensurable with the local losses.

Local losses are caused by local perturbations of the flow, its separation from the wall, vortex formation, or where obstructions are encountered, (pipe inlets, widening, narrowing, turns, passage through measuring devices, air reservoirs, screens, throttling devices etc.) Losses occurring at the outlet from a pipe into a large volume (for instance, to atmosphere) are also considered as local losses. Except for exhaust losses, all local pressure losses occur over a flow path of finite length, and are therefore indistinguishable from frictional losses. For simplicity of calculation, they are considered to be concentrated in one section and are not included in the frictional losses. Summation of the losses is according to the principle of superposition.

$$\Delta H_{sum} = \Delta H_{fr} + \Delta H_l \left[\frac{kg}{m^2}\right].$$

However, when experimental values of the local losses are used, it should be remembered that in certain cases they also include frictional losses, which should not be taken again into account.

The local resistance is determined by causing a gas or liquid to flow through the tested element*, which is connected to a line. The difference in total pressure at the inlet and outlet of the element, and also the velocity in a certain section (usually the inlet) are measured. The coefficient of local

* Data on frictional resistance, its dependence on Reynolds number and degree of roughness for straight pipes and channels are given in /16/.

resistance ζ_1 is defined as the ratio of the total-pressure loss ΔH_1 to the velocity head $\frac{\gamma_p V_p^2}{2g}$ in the section considered:

$$\zeta_1 = \frac{\Delta H}{\gamma_p V_p^2/2g},$$

where V_p is the mean flow velocity in m/sec in the section considered under the conditions of the experiment, $V_p = \frac{Q_p}{F}$, Δh_d is the volumetric discharge under the conditions of the experiment, F is the flow area of the measuring section.

When the test conditions differ from standard (0°C, 760 mm Hg, dry gas) the specific gravity of the gas is determined by introducing corrections for temperature, pressure, and humidity /16/.

Determining the resistance coefficient of a diffuser

The resistance coefficient of a diffuser is defined as the ratio of the pressure loss Δh_d to the velocity head $\rho \frac{V_1^2}{2}$ at the diffuser inlet. In an ideal diffuser the increase in static pressure is, by Bernoulli's law, equal to the difference of the velocity heads at the inlet and exit

$$(p_2 - p_1)_{id} = \frac{\rho}{2}(V_1^2 - V_2^2).$$

In reality, the static-pressure increase is reduced by the loss Δh_d,

$$(p_2 - p_1)_{eff} = \frac{\rho}{2}(V_1^2 - V_2^2) - \Delta h_d,$$

whence

$$\zeta_d = \frac{\Delta h_d}{\rho \frac{V_1^2}{2}} = 1 - \left(\frac{V_2}{V_1}\right)^2 - \frac{p_2 - p_1}{\rho \frac{V_1^2}{2}} = 1 - n^2 - \frac{p_2 - p_1}{\rho \frac{V_1^2}{2}},$$

where n is the area ratio of the diffuser $\left(n = \frac{F_2}{F_1}\right)$. This expression is used when the coefficient ζ_d is determined experimentally, proceeding from the assumption of one-dimensional flow in the diffuser.

Test layout for determining ζ_d is shown in Figure 7.56 /17/. A smooth collector with a short cylindrical part is installed in front of the diffuser. The resistance is measured with the aid of orifices in the walls by the difference in pressure $\Delta H = p_1 - p_2$ in front of and behind the diffuser. The pressure p_1 is measured at the wall of the cylindrical part of the collector, and the pressure p_2 at the wall of the straight discharge duct at a distance of 5 or 6 diameters behind the diffuser exit, where the pressure and velocity distributions are sufficiently uniform over the cross section.

The velocity distribution in the exit section is usually determined by means of a total-pressure tube in conjunction with static-pressure

measurements at the wall, or with the aid of a Pitot-Prandtl tube. The mean velocity at the diffuser inlet is determined from the velocity head $H_к = p_a - p_1$ behind the collector.

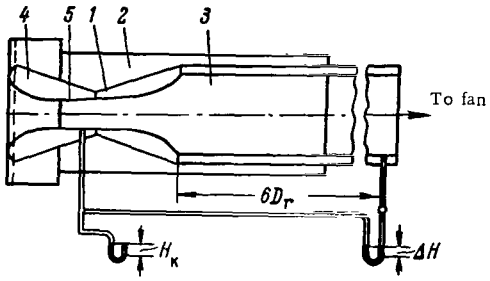

FIGURE 7.56. Test layout for determining the resistance of a diffuser. 1 — walls forming diffuser contour; 2 — plane sides of diffuser; 3 — duct; 4 — collector; 5 — cylindrical part of collector.

At large subsonic velocities the resistance coefficient of the diffuser (Figure 7.57) is

$$\zeta_d = \frac{2}{\varkappa M_1}\left(\delta - \frac{1}{2}\delta^2\right),$$

where

$$\delta = \frac{p_0 - p_0'}{p_0}.$$

Thus, to determine ζ_d in this case we have to measure the total pressure p_0 and the Mach number at the diffuser inlet and the total pressure p_0' at the

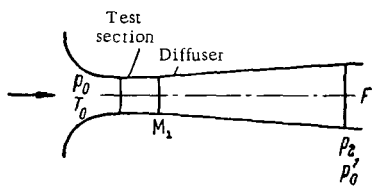

FIGURE 7.57. Diffuser.

diffuser exit. However, at the diffuser exit the nonuniformity of total pressure and velocity is considerable. This is taken into account by averaging δ over the exit section F

$$\delta = \frac{1}{F}\int_F \frac{p_0 - p_0'}{p_0}\,dF.$$

Sometimes it is advisable to average over the mass flow instead of over the area. The measuring results are usually given in the form of dependences of the resistance coefficients ζ_d on the Reynolds and Mach numbers and on the geometrical parameters (area ratio, etc.).

Determining the resistance coefficients of wind-tunnel elements

The resistance of certain wind-tunnel elements (Figure 7.58), in particular of the nozzle, is best determined with the aid of a pressure chamber (see above). Applying Bernoulli's equation to sections $I-I$ and $a-a$, and neglecting the small velocity in section $I-I$, we obtain

$$p_1 = p_a + \rho \frac{V^2}{2} + \Delta H,$$

where V is the flow velocity in section $a-a$, and ΔH is the pressure loss in the wind-tunnel element. Remembering that $p_1 - p_a = H_{st}$ is the static

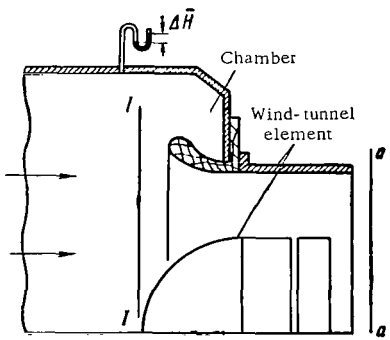

FIGURE 7.58. Test layout for determining the resistance of a wind-tunnel element in a pressure chamber.

gage pressure in the chamber, and substituting $\rho V^2/2 = H_d$, we obtain $\Delta H = H_{st} - H_d$ from which the resistance coefficient of the element is found to be

$$\zeta = \frac{\Delta H}{\rho V^2/2} = \frac{\Delta H}{H_d} = \frac{H_{st}}{H_d} - 1.$$

The results are usually given in the form of the functional relationship $\zeta = f(c_a)$ where c_a is the mean axial velocity in the exit section. The resistance of the nozzle can be determined under "in-site" conditions from the expression

$$\zeta_{noz} = 1 + \frac{p_1 - p_2}{\rho V_1^2/2} - n^2,$$

where p_1 and p_2 are respectively the static pressures at the nozzle inlet and exit, V_1 is the velocity at the nozzle inlet, and n is the nozzle area ratio $\left(n = \frac{F_1}{F_2}\right)$. It is assumed that the flow in the nozzle is one-dimensional. The pressure difference $p_1 - p_2$ is usually measured with the aid of a micromanometer and orifices in the wall at the nozzle inlet and exit, while the velocity V_1 is determined by one of the methods described above. By the same method we can determine the resistance of the fan installation, of screens installed across the flow, and of other elements, Thus, the resistance of the screens can be determined in the duct in which a fan is tested (Figure 7.55). The screen is usually installed at a distance of 1.5 to 2 diameters from the collector and 3 to 4 diameters upstream of the fan.

By measuring $h_к$ to determine the velocity upstream of the screen, and the difference Δh in static pressure upstream and downstream of the screen, we obtain the resistance coefficient of the screen

$$\zeta = \frac{\Delta h}{\rho \frac{V_к^2}{2}} = \frac{\Delta h}{k_к \Delta h_к},$$

where $k_к$ is the calibration coefficient of the collector, which characterizes the uniformity of the velocity distribution upstream of the screen ($k_к \approx 0.96$ to 0.98).

The results are given as relationships between ζ and the screen parameters (hole dimensions, wire gage, flow area, Reynolds number, mass flow rate, etc.). At large subsonic velocities the influence of the Mach number has to be taken into account /16/.

The total-pressure losses in supersonic tunnels are usually caused by friction. The total pressure loss in the nozzle can be defined as /18/

$$\sigma_c = \frac{p_a}{p_{0c}} = \left[\frac{1 - \frac{\varkappa - 1}{\varkappa + 1}\lambda_{id}^2}{1 - \frac{\varkappa - 1}{\varkappa + 1}\lambda_{id}^2 \varphi^2}\right]^{\frac{\varkappa}{\varkappa - 1}},$$

where λ_{id} defines the nozzle exit velocity in the absence of losses, p_a is the total pressure at the nozzle inlet, $\varphi = \frac{\lambda_{act}}{\lambda_{id}}$ is a coefficient by which the exit-velocity decrease due to losses is taken into account ($\varphi = 0.97$ to 0.99). Knowing λ_{id} and measuring the true exit velocity (see Chapter IV), we can determine the total pressure loss in the nozzle. This becomes considerable at large Mach numbers even when φ is small (Figure 7.59).

In order to calculate the mass flow rate through the nozzle, taking into account the losses, we replace in the relevant formulas p_{0c} by $p_{0c}\sigma_c$. For air ($\varkappa = 1.4$) we obtain

$$G = 0.4 \frac{F_{cr}}{\sqrt{T_0}} p_{cc}\sigma_c.$$

Determining the resistance of a railcar ventilating hood. The layout of an installation for determining the resistance of a ventilating hood is shown in Figure 7.60 /19/. The resistance coefficient is

defined as

$$\zeta = \frac{\Delta H_d}{\rho V_d^2/2},$$

where ΔH_d is the pressure drop between receiver and atmosphere (measured by micromanometer No. 2), V_d is the air velocity in the suction orifice

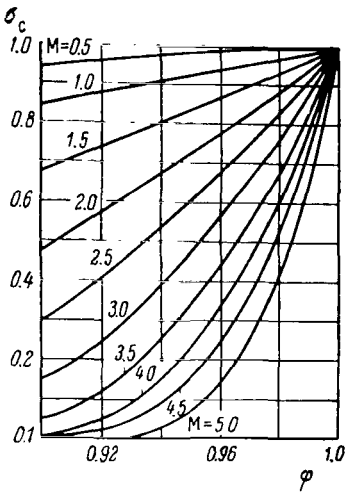

FIGURE 7.59. Dependence of total-pressure ratio on coefficient φ.

of the ventilating hood, and is determined from the mass flow rate through the ventilating hood and the area of its suction orifice $\left(\pi\frac{d^2}{4}\right)$. The mass flow rate is found from the cross section of the pipe behind the inlet collector and from the velocity in it, determined by the pressure drop $\Delta H_к$ measured by micromanometer No. 1.

Determining pressure losses in pipes

When a gas (liquid) flows in a pipe, the pressure loss ΔH is usually determined from Darcy's formula

$$\Delta H = \lambda \frac{l}{d} \rho \frac{V^2}{2}$$

or

$$\lambda = \frac{\Delta H}{\rho \cdot V^2/2 \cdot l/d},$$

where λ is the friction coefficient which has different values for laminar and turbulent flow. In order to determine λ, ΔH has to be measured by a

differential manometer connected to two points at a distance l from each other on the pipe wall, and the mean velocity V has to be found.

For steady laminar flow in a pipe, the velocity distribution is parabolic and the mean velocity is

$$V = \frac{1}{2} V_0,$$

where V_0 is the flow velocity in the center of the pipe and can be measured by a Pitot-Prandtl tube. In this case the experimental value of λ must correspond to the theoretical value

$$\lambda = \frac{64}{\mathrm{Re}} \qquad \left(\mathrm{Re} = \frac{Vd}{\nu}\right)$$

for $\mathrm{Re} \leqslant 2000$.

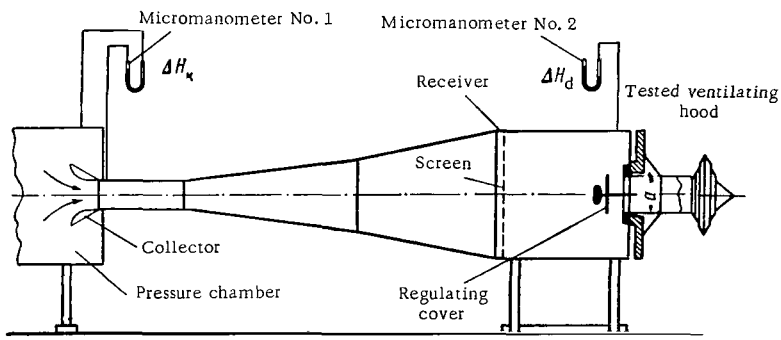

FIGURE 7.60. Installation for determining the resistance of ventilating hoods.

For steady turbulent flow the experimental value of λ must be compared with the empirical data depending on the Reynolds number. Thus, for $\mathrm{Re} \leqslant 50{,}000$.

$$\lambda = \frac{0.3164}{\sqrt[4]{\mathrm{Re}}}$$

etc.

Determining the coefficient of local resistance of bends. The coefficient of local resistance is

$$\zeta = \frac{\Delta H}{\rho \frac{V_{\mathrm{in}}^2}{2}},$$

where ΔH is the difference in pressure at the inlet and exit from the bend, V_{in} is the mean velocity at the inlet to the bend.

Determining the coefficients of local resistances in pipelines. For orifice plates, cocks, or similar elements, the coefficient of local resistance is

$$\zeta = \frac{\Delta H}{\rho \frac{V^2}{2}},$$

where V is the mean velocity in the pipe and ΔH is the pressure loss which can be determined from the indications of a differential manometer connected to the pipeline on either side as close as possible to the element considered (Figure 7.61).

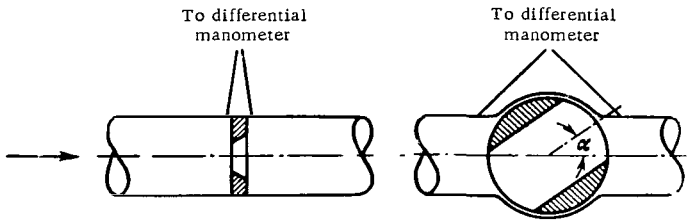

FIGURE 7.61. Determining the resistance of elements in pipelines.

§ 37. TESTING OF WIND TURBINES

Wind turbines convert the energy of an airstream into mechanical energy. In all modern wind turbines the rotational speed and output is automatically limited by changing their aerodynamic characteristics. Hence, laboratory investigations of wind turbines are mainly connected with determining the coefficient of wind-energy utilization and the coefficients of the aerodynamic forces and moments acting on the wind-turbine wheel.

Generally, the force acting on the wind-turbine wheel, whose axis of rotation forms an angle γ with the wind direction in the xz-plane, can be reduced to the total aerodynamic force and moment. The vector of the total aerodynamic force lies in the xz-plane and can be separated into a component P, normal to the plane of rotation of the wheel, and a tangential component T. The vector of the moment has components along the three axes: the torque M_x, the blade-turning moment M_y, and the overturning moment M_z.

Figure 7.62 shows the coordinate axes, the aerodynamic forces, and the moments.

The coefficients obtained from tests have the following form:

Coefficient of wind-energy utilization

$$\xi = \frac{2N}{\rho V^3 \pi R^2} = \bar{M}_x Z,$$

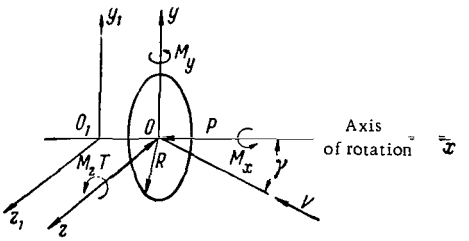

FIGURE 7.62. Coordinate axes and aerodynamic forces and moments acting on a wind turbine.

torque coefficient

$$\bar{M}_x = \frac{2M_x}{\rho V^2 \pi R^3},$$

coefficient of blade-turning moment

$$\bar{M}_y = \frac{2M_y}{\rho V^2 \pi R^3},$$

coefficient of overturning moment

$$\bar{M}_z = \frac{2M_z}{\rho V^2 \pi R^3},$$

pressure coefficient

$$B = \frac{2P}{\rho V^2 \pi R^2},$$

coefficient of tangential force

$$\tau = \frac{2T}{\rho V^2 \pi R^2}.$$

At a given blade geometry and fixed blade angles, all these coefficients are functions of the advance ratio

$$Z = \frac{\omega R}{V}.$$

In these expressions N is the shaft power of the turbine $\left(\frac{\text{kgm}}{\text{sec}}\right)$, ω is the angular velocity $\left(\frac{1}{\text{sec}}\right)$, R is the radius of the turbine wheel (m).

Figure 7.63 shows schematically the three-component 3KTsP-M instrument intended for testing wind-turbine wheels in the TsAGI wind tunnel*. This instrument permits determination by direct measurement of M_x, M_y, P, and the rotational speed of the model. Simultaneously, the moment M_y,

* The 3KTsP-M instrument and the method of its use were developed by G.I. Sholomovich from the 3KTsP instrument designed by I.D. Mogilnitskii /20/.

(about the y_1-axis) is measured, whence

$$T = \frac{M_{y_1} - M_y}{x_1}$$

or in dimensionless form

$$\tau = \frac{\overline{M}_{y_1} - \overline{M}_y}{\overline{x}_1}.$$

can be found.

In order to reduce errors arising from the determination of the difference between two almost equal magnitudes, the value of $\overline{x}_1 = \frac{x_1}{R}$ in the 3KTsP-M instrument is larger than in full-scale wind turbines. Experiments show that the measured values of $\overline{M}_y$ and $\overline{M}_{y_1}$ depend considerably on the instrument support. In a full-scale wind turbine the supporting structure (mast, tower, etc.) has relatively smaller dimensions than the instrument support. Hence,

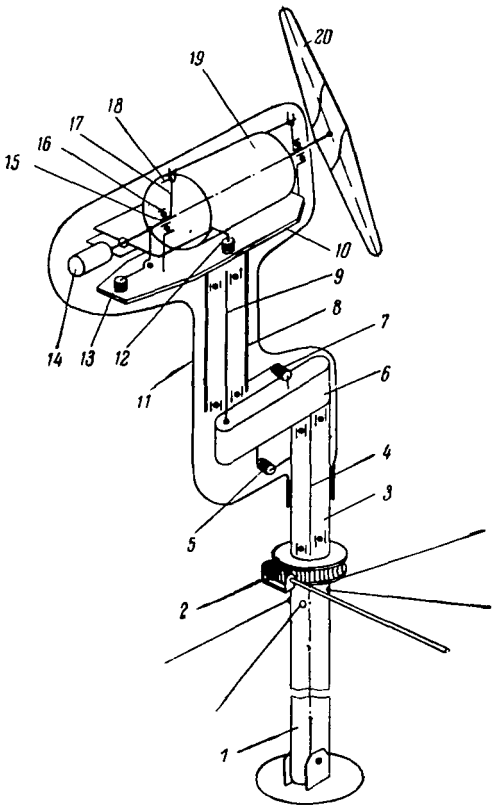

FIGURE 7.63. Instrument for testing wind turbines. 1 — column; 2 — worm gear; 3 — tubular stand; 4 — rod; 5 — bellows; 6 — intermediate plate; 7 — bellows; 8 — tubular stand; 9 — rod; 10 — upper plate; 11 — fairing; 12 and 13 — bellows; 14 — electric tachometer; 15 — plain bearings; 16 — ball bearings; 17 — followers; 18 — pins; 19 — generator; 20 — model of wind-turbine wheel.

corrections for the interference of the supports are necessary, particularly in wind turbines causing considerable deflections of the flow.

The base of the instrument is column (1), secured by stays to the test-section floor or to a platform (in a tunnel with open test-section). The top of the instrument can, with the aid of worm gear (2), be turned about the column in order to change the angle of flow inclination. Upper plate (10), fixed to tubular stand (8), can turn on ball bearings about rod (9), rigidly fixed to intermediate plate (6). The latter can turn on ball bearings about the lower tubular stand (3).

The instrument is designed in such a way that the axis of rod (4) lies in the plane of rotation of the model. The moment M_y, which tends to turn the upper plate in relation to the intermediate plate, and M_{y_1}, which tends to turn the latter about stand (3), are taken up by bellows (7) and (5), the pressures in which are usually measured by standard manometers (not shown). The upper plate of the instrument carries generator (19) on whose shaft model (20) is mounted. The generator is supported on plain bearings (15) which permit axial displacement of the generator shaft. These bearings are connected to the generator body by means of followers (17) and pins (18).

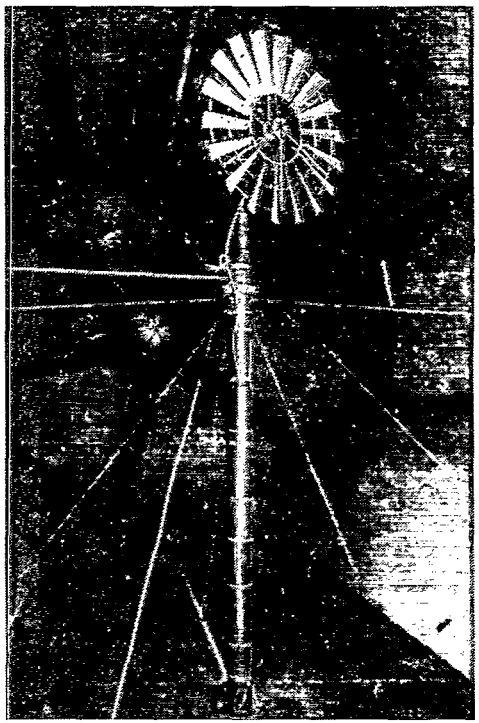

FIGURE 7. 64. Testing a wind-turbine wheel in a wind tunnel.

This design permits the torque acting on the wind turbine to be transmitted almost completely to the generator frame except for the inconsiderable losses in ball bearings (16). P and M_x are measured with

the aid of bellows (13) and (12), the pressures in which are measured as in bellows (5) and (7).

All force-measuring systems of the instrument are filled with water. The presence of even small air bubbles can cause considerable deformations of the bellows, and thus alter the position of the model during the experiment. The rotational speed of the model is measured either by electric tachometer (14), or by determining the time elapsing between pulses emitted after every 100 revolutions of the model by a special contact device installed instead of the tachometer. In order to include all moments, the tachometer or contact device is fixed to the generator body.

The entire instrument top is covered by fairing (11), fixed to stand (3) in order to avoid transmission of aerodynamic forces, caused by the flow around the instrument, to the force-measuring systems. An external view of the instrument installed in a tunnel is shown in Figure 7.64. Figure 7.65 is an experimental characteristic of a wind-turbine wheel for a flow inclination angle $\gamma = 45°$.

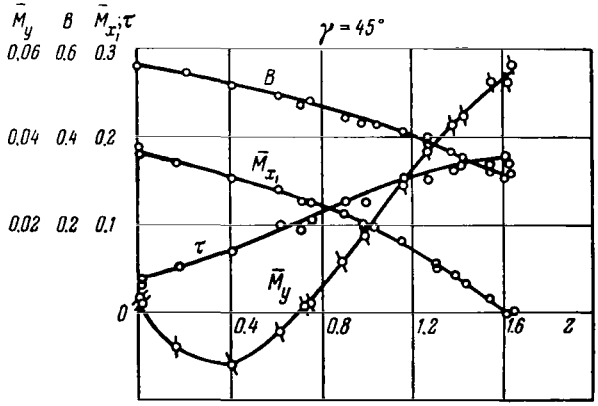

FIGURE 7.65. Experimental characteristic of a wind-turbine wheel.

Since all coefficients are referred to the flow velocity in the tunnel, this velocity must be determined reliably, in order to apply the results of tests on models to full-scale wind turbines operating in the free atmosphere. Particularly important are the relative dimensions of the test section and of the wind turbine. In a tunnel with closed test section, the head induced by the wind turbine can considerably distort the flow: hence, the ratio of the diameter of the model to the diameter of the test section should not exceed 0.2 to 0.3. In tunnels with open test sections, this ratio can be slightly increased to 0.4 or 0.5. In wind-turbine tests, attention should be paid to the correct selection of the flow velocity in the tunnel in order to obtain the appropriate Reynolds numbers, referred to the blade chord at 70% blade radius. Wind-turbine tests usually consist of simultaneous measurement of all parameters (M_x, M_y, P, etc.) as functions of the variable load on the model shaft at a given position of the wheel and at constant flow velocity. The load is adjusted by changing the resistance in the circuit of the generator driven by the wheel.

§38. TESTING OF EJECTORS

Gas ejectors are aeromechanical devices for increasing the total-pressure of a gas stream by means of a second high-pressure gas stream, and are widely used.

Ejectors are used in reservoir-operated wind tunnels to increase the operating duration. In this case, the ejector plays the role of the blower,

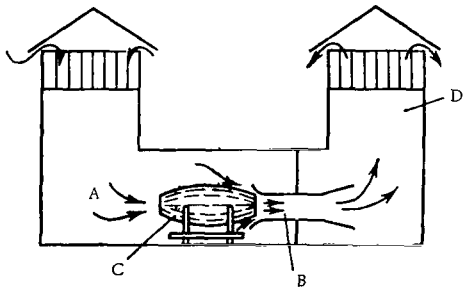

FIGURE 7.66. Ejecting air through a test stand for jet engines. A — suction shaft; B — ejector; C — engine on test stand; D — exhaust shaft.

supplying a large quantity of low-pressure gas at the expense of the energy contained in a small quantity of high-pressure gas.

The ejector can be used as an exhauster to create a low pressure downstream of the test section of the wind tunnel, or in a closed space. Very often an ejector is used to maintain air flow in a channel or room.

Figure 7.66 shows schematically a test stand for jet engines. A stream of exhaust gases sucks air into ejector *B* through shaft *A* thus providing ventilation of the room and cooling of the engine.

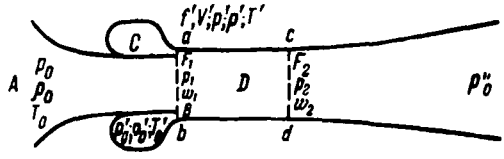

FIGURE 7.67. Ejector.

The constructional forms of ejectors differ, but they always include the following principal elements: a nozzle for high-pressure gas, a nozzle or chamber for the low-pressure gas, a mixing chamber, and a diffuser.

The disposition of the nozzles, their number, and their shape may vary, but this does not greatly affect the operation and characteristics of the ejector.

Consider a simple ejector with a cylindrical mixing chamber, whose inlet coincides with the plane exit of a high-pressure nozzle (Figure 7.67).

The operating principle of an ejector is as follows: Low-pressure (ejected) gas is sucked into mixing chamber D from reservoir A in which the pressure is p_0, the density, ρ_0, and the temperature, T_0. High-pressure (ejecting) gas flows from annular chamber C through slot B also into mixing chamber D. The pressure in the annular chamber is p_0', the density, ρ_0', and the temperature, T_0'. In order to increase the compression efficiency, a diffuser with a small divergence angle (6 to 8°) is usually placed downstream of the mixing chamber. The pressure at the diffuser exit is p_0''.

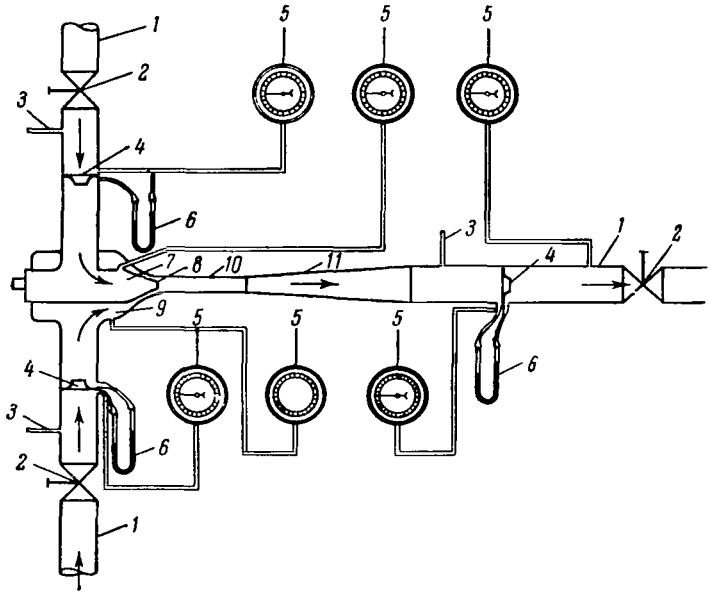

FIGURE 7.68. Installation for testing ejectors. 1 — pipe; 2 — valves; 3 — thermometers; 4 — measuring nozzles; 5 — standard manometers; 6 — differential manometers; 7 — chamber for high-pressure gas; 8 — central nozzle; 9 — chamber for low-pressure gas; 10 — mixing chamber; 11 — diffuser.

At steady operating conditions the pressure at the mixing-chamber inlet is always lower than the total pressure of the low-pressure (ejected) gas. The pressure difference causes the low-pressure gas to flow into the mixing chamber.

For supersonic flow to occur at the mixing-chamber inlet, a Laval nozzle has to be inserted between reservoir A and mixing chamber D. When the flow at the end of the mixing chamber is supersonic the diffuser must have the shape of an inverse Laval nozzle.

The main assumption made in the analysis of ejector operation is that the mixing chamber is so long that the velocity distribution at its end (section $c-d$) is uniform.

It is also frequently assumed that in section $a-b$ at the inlet to the mixing chamber the velocities are distributed uniformly across the suction pipe and the nozzle.

The theory of ejectors (cf. e.g., /18/) shows that from the experimental viewpoint, determination of the ejector characteristics is reduced to finding the pressures p_0, p_0', and p_0'', the loss coefficient μ of the suction system, and the pressure-restoration coefficient ξ of the diffuser. The coefficients μ and ξ are in practice also determined by pressure measurements. Figure 7.68 shows schematically an installation for investigating the characteristics of ejectors. The installation consists of an ejector (or its model) whose walls have orifices connected to manometers. If necessary, the velocities in different sections of the ejector can be measured with the aid of Pitot-Prandtl tubes when the dimensions of the sections are suitable The mixing process of two streams (determination of the velocity distributions over the length of the mixing chamber, of the boundaries of the ejecting stream, etc.) is studied at subsonic velocities with ordinary tubes mounted on a traversing device, or (particularly at supersonic velocities) by optical methods with the aid of a Töpler instrument or an interferometer.

§ 39. DETERMINING ROTATIONAL DERIVATIVES

The fact that various flying apparatus and objects (rockets, airplanes, missiles, torpedoes, etc.) undergo, during certain periods of their motion, large accelerations and considerable vibrations, while the trajectories of their centers of mass are curved, necessitates special experimental methods. The difficulties which arise are both technical and of principle. Technically it is very difficult to measure instantaneous values of forces and moments when the model vibrates; in principle it is almost impossible to reproduce in the experiments the surroundings and the conditions corresponding to the real flight or motion. This requires great caution in the application of experimental results.

The flow pattern around an aerodynamic surface (the shape of the wake, its position in relation to the body, the shape, number, and disposition of shocks at large velocities, etc.) and thus its aerodynamic properties depend considerably on the Reynolds number, the Strouhal number, and the Mach number. In addition, the aerodynamic properties of a body in a nonsteady flow also depend on the motion of the body during the period preceding the instant at which the kinetic parameters were measured, i.e., on the motion as a whole.

Modern methods* permit the aerodynamic properties of bodies in nonsteady motion to be determined experimentally, This is done by considering a set of parameters which determine the laws of nonsteady motion as a whole, and by expressing the coefficients of the aerodynamic forces and moments as functions of the coefficients of the rotational derivatives. The dimensionless coefficients of the rotational derivative of the first order**

* See, for instance, Belotserkovskii, S.M. Predstavlenie nestatsionarnykh aerodinamicheskikh momentov i sil pri pomoshchi koeffitsientov vrashchatel'nykh proizvoliykh (Representation of Nonsteady Aerodynamic Moments and Forces by means of the Coefficients of Rotational Derivatives). — Izvestiya AN SSSR, OTN, No. 7, 1956.

** The coefficients of linear expansions of the aerodynamic forces and moments by the dimensionless kinetic parameters of motion and their derivatives. For instance, the coefficient of lift is

$$c_y = c_{y_0} + c_y^{\alpha}\alpha + c_y^{\dot{\alpha}}\dot{\alpha} + c_y^{\omega_z}\omega_z + c_y^{\dot{\omega}_z}\dot{\omega}_z.$$

take into account, with an accuracy sufficient in practice, the main factors caused by the nonsteady flow around the tested body.

When considering the nonsteady motion of an aerodynamic surface, it is assumed that:

a) The mean translational velocity has a finite value, while the other kinetic parameters (e.g., the angular velocity of the body) have relatively small values.

b) The body moves in an infinite space which is at rest in infinity in front of the body; there are no sources of disturbance except the body and its wake.

Under these assumptions, the action of the medium on a body moving in it is completely determined by the motion of the body in relation to the stationary coordinate system *xyz* (Figure 7.69). We introduce a coordinate

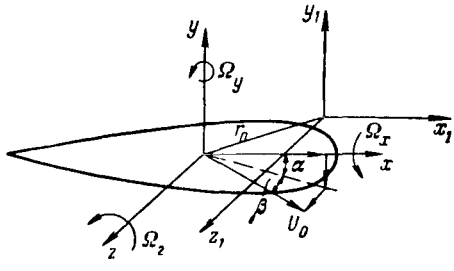

FIGURE 7.69. Coordinate systems.

system $O_1x_1y_1z_1$ moving with the body and project on its axes the vector characteristics of motion, referred to the stationary coordinate system (absolute translational velocity $\mathbf{U}_0$ and absolute angular velocity Ω_0). We denote the projections of Ω_0 in the moving system by Ω_x, Ω_y, Ω_z, and write $U_0(t) = U + \Delta U(t)$, where the mean velocity U does not depend on the time t. We also introduce the dimensionless magnitudes:

$$u = \frac{\Delta U}{U}; \qquad \alpha = \alpha(t); \qquad \beta = \beta(t);$$
$$\omega_x = \frac{\Omega_x b}{U}; \qquad \omega_y = \frac{\Omega_y b}{U}; \qquad \omega_z = \frac{\Omega_z b}{U},$$

where b is a characteristic linear dimension of the body, α is the angle of attack, and β is the angle of slip*.

The aerodynamic forces and moments acting on the body in nonsteady motion depends on the instantaneous values of these parameters, their time

* When investigating the laws of deformation, e.g., when studying flutter, additional parameters have to be introduced in order to take into account the time variation of the shape, i.e., the instantaneous values of that part of the local angle of attack which depends on the deformation of the aerodynamic surface. In particular, in airplanes and rockets with fins, these parameters are the rudder- and aileron-deflection angles.

derivatives*, and also on the whole system of factors which characterize steady motion (compressibility, viscosity, density, translational velocity etc.).

The dimensionless force and moment coefficients can be expressed through the so-called rotational derivatives which determine the change in the force or moment, due to the time variation of any parameter. By introducing these derivatives, we can eliminate the time t, since the motion of a body having six degrees of freedom is completely determined by the parameters given above and their time derivatives. In the most important cases the problem is simplified, since several parameters and their derivatives vanish.

The rotational derivatives are mostly determined experimentally by investigating the moments and forces acting on the aerodynamic surface when the rudders, ailerons, and similar devices, which affect the shape of the surface, are fixed. The coefficients of u and $\dot{u}$ are determined by measuring the forces and moments acting on the aerodynamic surface or body at $U = \text{const}$ during translational oscillations of the body in the direction of the corresponding axis. The coefficients of ω_x and $\dot{\omega}_x$, ω_y and $\dot{\omega}_y$, ω_z and $\dot{\omega}_z$ can be found by measuring the forces and moments acting during rotational oscillations of the body about the x-, y-, z-axes respectively. The effects of changes in β and α during rotation about the y- and z-axes are determined from the results obtained in investigations of the translational oscillations of the body.

It is sometimes necessary to determine the coefficients of the rotational derivatives of the forces and moments acting on the aerodynamic surface, or the coefficients which express the hinge moments, which arise during deflection of the control surfaces. This requires measuring the forces and moments appearing on the entire surface when the deflections of the control surfaces are given, or determining the hinge moments from the aerodynamic forces.

Existing experimental methods for determining the rotational derivatives can be grouped as follows:

1) Balance tests.
2) Use of whirling-arm machines.
3) Method of deformed models.
4) Method of small oscillations.

For nonsteady motion of the body (oscillations about the z-axis and [steady] translational motion along the x-axis **), we obtain

$$Y = \left(c_{y_0} + c_y^{\alpha}\alpha + c_y^{\dot{\alpha}}\dot{\alpha} + c_y^{\omega_z}\omega_z + c_y^{\dot{\omega}_z}\dot{\omega}_z\right)\rho\frac{U^2}{2}b^2,$$

$$M_z = \left(m_{z_0} + m_z^{\alpha}\alpha + m_z^{\dot{\alpha}}\dot{\alpha} + m_z^{\omega_z}\omega_z + m_z^{\dot{\omega}_z}\dot{\omega}_z\right)\rho\frac{U^2}{2}b^3.$$

* $\dot{U} = \frac{d\Delta u}{dt}\frac{b}{U^2}$; $\dot{\alpha} = \frac{d\alpha}{dt}\frac{b}{U}$; $\beta = \frac{d\beta}{dt}\frac{b}{U}$;
$\dot{\omega}_x = \frac{d\Omega_x}{dt}\frac{b^2}{U^2}$; $\dot{\omega}_y = \frac{d\Omega_y}{dt}\frac{b^2}{U^2}$; $\dot{\omega}_z = \frac{d\Omega_z}{dt}\frac{b^2}{U^2}$;
$\dot{\delta}_r = \frac{d\delta_r}{dt}\frac{b}{U}$; $\dot{\delta}_a = \frac{d\delta_a}{dt}\frac{b}{U}$.

** The most important case of nonsteady motion.

The dimensionless coefficients of α, $\dot{\alpha}$, ω_z and $\dot{\omega}_z$ have to be determined experimentally by the different methods discussed below.

Balance tests are usually undertaken in wind tunnels at constant velocity and different angles of attack. The coefficients c_y^α and m_z^α are determined from the slopes of the curves $c_y = f(\alpha)$, $m_z = f(\alpha)$. In addition, c_{y_0} and m_{z_0} are determined in the balance tests.

The whirling-arm machine is used for measuring the aerodynamic forces and moments acting on the model during its uniform rotation at an angular velocity ω_z and at constant angle of attack. The aerodynamic forces and moments can be expressed as follows:

$$Y = (c_{y_0} + c_y^\alpha \alpha + c_y^{\omega_z} \omega_z) \rho \frac{U^2}{2} b^2,$$

$$M_z = (m_{z_0} + m_z^\alpha \alpha + m_z^{\omega_z} \omega_z) \rho \frac{U^2}{2} b^3.$$

We can find $c_y^{\omega_z}$ and $m_z^{\omega_z}$ from the experimentally determined straight lines $Y = Y(\omega_z)$ and $M_z = M_z(\omega_z)$. This method also permits other coefficients (c_y^α, m_z^α) to be determined, but all coefficients are determined for zero Strouhal number*.

The method of deformed models also permits the coefficients c^{ω_z} and $m_z^{\omega_z}$ to be determined. It consists of ordinary testing of a deformed model in a tunnel. The local angles of attack of the deformed model must be equal to the local angles of attack of the undeformed model when it moves along a circle. Figures 7.70 and 7.71 show the vectors of the velocity at corresponding points of the undeformed and the deformed model. We can see that

$$\operatorname{tg} \alpha = \frac{x}{R} = \frac{dy}{dx},$$

whence

$$y = \frac{x^2}{2R}.$$

The model must thus be bent along the arc of a parabola. The forces and moments acting on the deformed and on the undeformed model are found from tests in the tunnel. The differences between these forces and moments enables the coefficients $m_z^{\omega_z}$ and $c_y^{\omega_z}$ to be determined.

The method of small oscillations permits, in contrast to all the above methods, all coefficients of the rotational derivatives to be determined. For instance, those entering into the expressions for Y and M_z are found by subjecting the model in a wind tunnel to small harmonic translational (along the y-axis**) or rotational (about the z-axis) oscillations, and measuring the aerodynamic force and moment, or several parameters of the motion. In the former case the method is called dynamic, in the latter, kinematic.

* At uniform rotation of the model $\alpha = \text{const}$; $\omega = \text{const}$ and $\dot{\alpha} = \dot{\omega}_z = 0$.

** For more details see Gurzhienko, G.A. Metod iskrivlenykh modelei primenenie ego k izucheniu krivolineinogo poleta vozdushnykh korablei (The Method of Deformed Models and its Use in the Study of Curved Flight of Airships). — Trudy TsAGI Issue 182. 1934.

The dynamic method of small oscillation. Let the model be subjected to forced translational oscillations along the y-axis:

$$y = y_0 \cos pt.$$

The angle of attack will then vary according to the law

$$\alpha = -\frac{\dot{y}}{U} = \frac{y_0 p}{U} \sin pt = \bar{y} p^* \sin pt,$$

where $\bar{y} = \frac{y_0}{b}$ is the dimensionless amplitude of the oscillations and $p^* = \frac{pb}{U}$ is the dimensionless circular frequency.

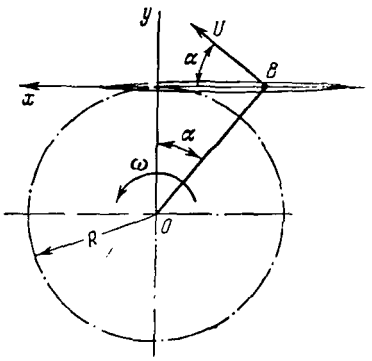

FIGURE 7.70. Velocity vector of rotating undeformed model.

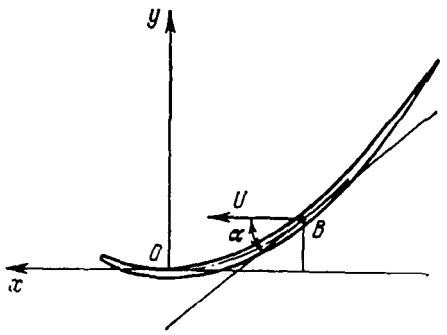

FIGURE 7.71. Velocity vector of a deformed [stationary] model.

The time derivative of the angle of attack is

$$\dot{\alpha} = \bar{y}_0 p^{*2} \cos pt.$$

When $\omega_z = \dot{\omega}_z = 0$, we obtain

$$Y = \tilde{c}_y \rho \frac{U^2}{2} b^2 \cos(pt + \varepsilon_y) = (c_{y_0} + c_y^{\alpha}\alpha + c_y^{\dot{\alpha}}\dot{\alpha}) \rho \frac{U^2}{2} b^2,$$
$$M_z = \tilde{m}_z \rho \frac{U^2}{2} b^3 \cos(pt + \varepsilon_m) = (m_{z_0} + m_z^{\alpha}\alpha + m_z^{\dot{\alpha}}\dot{\alpha}) \rho \frac{U^2}{2} b^3 *.$$

The force and the moment thus also vary harmonically, with phase shifts ε_y and ε_m in relation to the motion of the model.

The coefficients of the rotational derivatives are found by equating the coefficients of the trigonometric functions:

$$c_y^{\alpha} = -\frac{\tilde{c}_y}{\bar{y}_0 p^*} \sin \varepsilon_y, \qquad c_y^{\dot{\alpha}} = \frac{c_y}{\bar{y}_0 p^{*2}} \cos \varepsilon_y,$$
$$m_z^{\alpha} = -\frac{\tilde{m}_z}{\bar{y}_0 p^*} \sin \varepsilon_m, \qquad m_z^{\dot{\alpha}} = \frac{\tilde{m}_z}{\bar{y}_0 p^{*2}} \cos \varepsilon_m,$$

* $c_y = \tilde{c}_y \cos(pt + \varepsilon_y), \qquad m_z = \tilde{m}_z \cos(pt + \varepsilon_m).$

The coefficients of the rotational derivatives ($c_y^{\omega_z}$, $c_y^{\dot{\omega}_z}$, $m_z^{\omega_z}$, $m_z^{\dot{\omega}_z}$) can be determined by measuring the aerodynamic forces and moments during rotational oscillations of the model about the z-axis. Let the model undergo harmonic oscillations about the z-axis. The angle of attack is then

$$\alpha = \alpha_0 \cos pt$$

and therefore

$$\dot{\alpha} = \omega_z = -\frac{\alpha_0 pb}{U} \sin pt = -\alpha_0 p^* \sin pt,$$
$$\dot{\omega}_z = -\alpha_0 p^{*2} \cos pt.$$

Substituting α, $\dot{\alpha} = \omega_z$ and $\dot{\omega}_z$ in the expressions for the lift and the pitching moment, we obtain

$$Y = \tilde{c}_y \rho \frac{U^2}{2} b^2 \cos(pt + \varepsilon_y),$$
$$M_z = \tilde{m}_z \rho \frac{U^2}{2} b^3 \cos(pt + \varepsilon_m).$$

The coefficients of the rotational derivatives are in this case

$$c_y^{\dot{\alpha}} + c_y^{\omega_z} = \frac{\tilde{c}_y}{\alpha_0 p^*} \sin \varepsilon_y,$$
$$c_y^{\alpha} - p^{*2} c_y^{\dot{\omega}_z} = \frac{\tilde{c}_y}{\alpha_0} \cos \varepsilon_y,$$
$$m_z^{\dot{\alpha}} + m_z^{\omega_z} = \frac{\tilde{m}_z}{\alpha_0 p^*} \sin \varepsilon_m,$$
$$m_z^{\alpha} - p^{*2} m_z^{\dot{\omega}_z} = \frac{\tilde{m}_z}{\alpha_0} \cos \varepsilon_m.$$

Thus, by determining experimentally the coefficients c_y^{α}, $c_y^{\dot{\alpha}}$, m_z^{α} and $m_z^{\dot{\alpha}}$ during translational motion of the model, we can find the other coefficients from a rotation test. If the model oscillates about the z-axis, and only the aerodynamic moments are measured, we can determine only the combinations of the coefficients

$$m_z^{\dot{\alpha}} + m_z^{\omega_z} \text{ and } m_z^{\alpha} - p^{*2} m_z^{\omega_z}.$$

The corresponding installation is shown schematically in Figure 7.72. It consists of a centering instrument* with a dynamometric mechanism, a d.c. motor, and a system for recording the oscillations of the model, all mounted on a carriage. The aerodynamic loads are measured with the aid of strain gages, whose indications are recorded on an oscillograph together with the position of the model and the period of its oscillations.

* The centering instrument is a device which consists of a vertical shaft, carried in bearings, to whose upper end the model is fixed. The lower end of the shaft is connected to a dynamometric mechanism. The model can thus oscillate in the horizontal plane (Figure 7.72) or, when hinged, about other axes (for instance, the x-axis (Figure 7.81).

The results of the measurements are processed by equating the general expression for the moment in the form of a Taylor series with an expression for the moment in the form of a Fourier series whose coefficients are

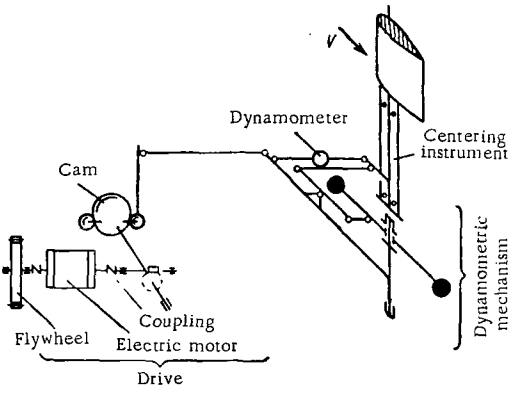

FIGURE 7.72. Layout of an installation for determining the rotational derivatives by the dynamic method.

determined by harmonic analysis. We thus obtain

$$M_z = (m_{z_0} + m_z^{\alpha}\alpha + m_z^{\dot{\alpha}}\dot{\alpha} + m_z^{\omega_z}\omega_z + m_z^{\dot{\omega}_z}\dot{\omega}_z)\,\rho\frac{U^2}{2}Sb = M_0 + M_1\cos pt + M_2\sin pt,$$

where $p=\frac{2\pi}{T}$ is the circular frequencey while T is the oscillation period when the angle of attack varies according to the law

$$\alpha = \alpha^*\sin pt\ .$$

For pure rotation

$$\dot{\alpha} = \omega_z = \alpha^* p^*\cos pt, \qquad \dot{\omega}_z = -\alpha^* p^{*2}\sin pt,$$

where α^* and p^* are respectively the dimensionless amplitude and frequency of the oscillation. Setting

$$A_0 = \frac{M_0}{qSb}, \qquad A_1 = \frac{M_1}{qSb}, \qquad B_1 = \frac{M_2}{qSb},$$

we obtain

$$m_{z_0} = A_0, \quad m_z^{\omega_z} + m_z^{\dot{\alpha}} = \frac{A_1}{\alpha^* p^*}, \quad m_z^{\alpha} - p^{*2}m_z^{\dot{\omega}_z} = \frac{B_1}{\alpha^*}$$

[where $q=\rho\frac{U^2}{2}$].

Static calibrations are performed before testing in order to determine the conversion factor from the moment, recorded on the oscillogram in mm, to the actual moment in kg · m. The instrument is also set to zero

by compensating the imbalance of the model and the inertia forces; the sensitivity of the amplifier and the recording range of the oscilloscope are then chosen. For dynamic calibration the aerodynamic load is replaced by a spring which connects the model to the stationary base. This permits conversion from the first harmonic of the recording to the first harmonic of the effect (amplitude sensitivity $\frac{\alpha_{st}}{\alpha_{dyn}}$ and time shift Δt) (Figure 7.73).

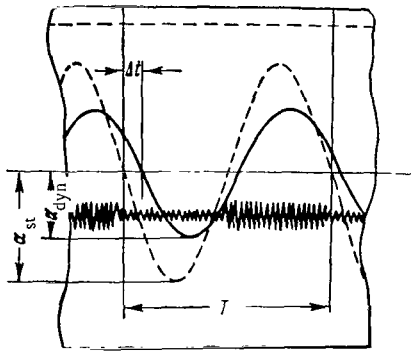

FIGURE 7.73. Dynamic-calibration oscillogram.

The oscillograms have the form shown in Figure 7.74. We can similarly determine on the same installation the aerodynamic characteristics of the model in the horizontal plane, i.e., the combinations of the derivatives $(m_y^{\omega_y} + m_y^{\dot{\beta}})$ and $(m_y^{\beta} - p^{*2} m_y^{\omega_y})$, and also the relationship $m_y = m_y(\beta_0)$ (Figure 7.75) in the absence of oscillations.

FIGURE 7.74. Oxcillations of a model. a — at zero flow; b — flow tests; c — dynamic calibration.

Results of tests on a dynamic strain-gage installation to determine the coefficients of the rotational derivatives are shown in Figures 7.76 and 7.77, which also contain the standard deviations of the measurements

for determining the rotational derivatives

$$m_z^{\omega_z} + m_z^{\alpha} \text{ and } m_z^{\alpha} - p^{*2} m_z^{\dot{\omega}_z}.$$

Use of a special harmonic analyzer instead of the oscillograph permits the accuracy of the measurements to be increased by about 50%.

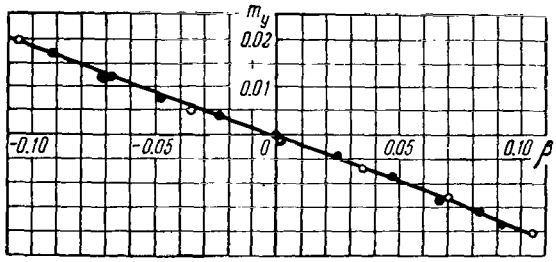

● Dynamic method
○ Wind-tunnel balance

FIGURE 7.75. Values of $m_y = f(\beta)$ obtained by dynamic method and by ordinary tests on wind-tunnel balances.

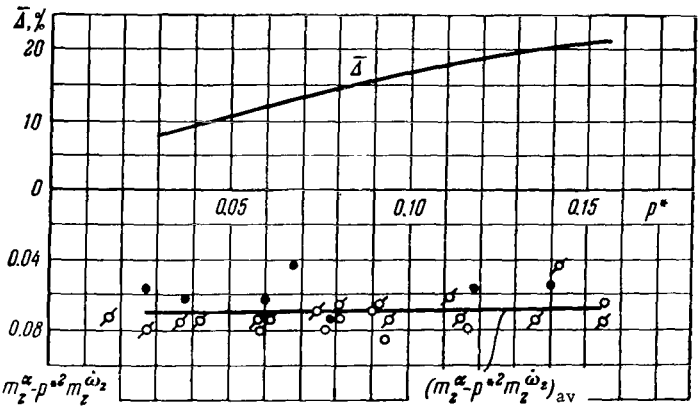

FIGURE 7.76. Values of $m_z^{\alpha} - p^{*2} m_z^{\dot{\omega}_z}$ obtained by dynamic method and standard deviation of measurements.

The kinematic method of small oscillations permits the coefficients of the rotational derivatives to be determined by measurements of several parameters of motion. This can be done by either free or forced oscillations. The installation for determining the rotational derivatives is shown schematically in Figure 7.78. It consists of a system with one degree of freedom. In the method of free oscillations, the model is first brought

out of equilibrium. It will then, under the action of springs P_1 and P_2, perform damped oscillations about the axis of the centering instrument, which are recorded on a moving chart by a pen fixed to a pendulum (Figure 7.79). This chart also contains time marks, which permit the oscillation period of the model to be determined. In the method of forced

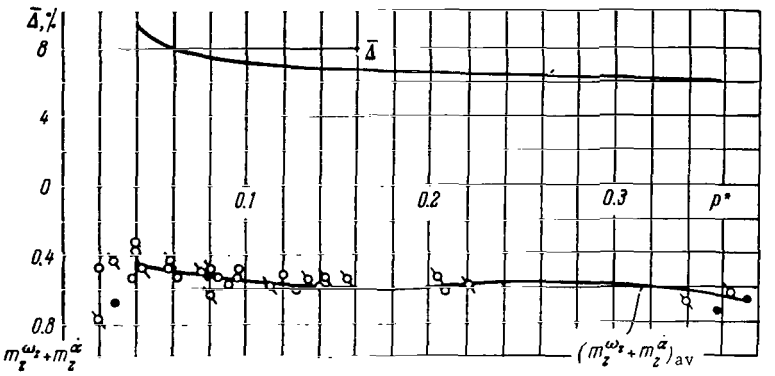

FIGURE 7.77. Values of $m_z^{\omega_z}+m_z^{\dot{\alpha}}$ obtained by dynamic method and standard deviation of measurements.

vibrations, an electric motor actuates an oscillating roller, the model being subjected to harmonic undamped oscillations. The tape on which the recording is made is fixed on a carriage driven by the electric motor

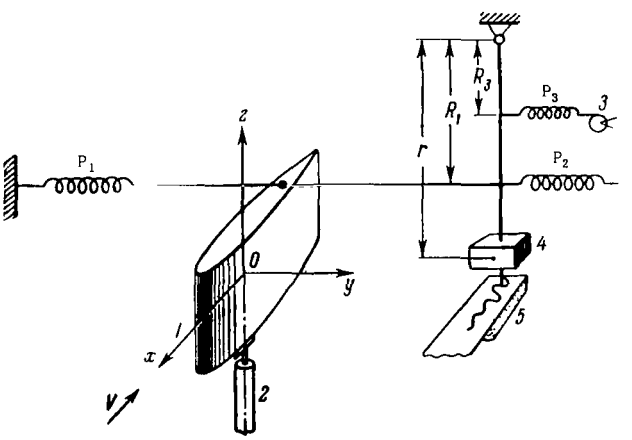

FIGURE 7.78. Installation for determining the coefficients of the rotational derivatives by the kinematic method. 1 — airfoil model; 2 — centering instrument; 3 — oscillating roller; 4 — pendulum; 5 — carriage.

in a harmonic reciprocatory motion, perpendicular to the plane of oscillation of the pendulum. By superposing the harmonic motions of the carriage and the pendulum, the pen will draw an ellipse on the tape

(Figure 7.80). The coefficients of the rotational derivatives of the moment can then be determined from the parameters and position of this ellipse.

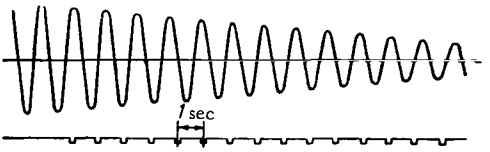

FIGURE 7.79. Recording of free oscillations.

The differential equation of motion of a model oscillating about the z-axis can be written as follows:

$$J_z \frac{d^2\alpha}{dt^2} = -M_s - k^2(\alpha_0 + \alpha) - \mu^2 \frac{d\alpha}{dt} + A \sin pt + M_z,$$

where α_0 is the angle of attack corresponding to the mean position of the model, about which the oscillations take place, α is the deviation

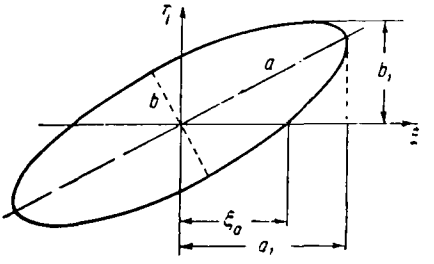

FIGURE 7.80. Recording of forced oscillations.

from α_0, $J_z \frac{d^2\alpha}{dt^2}$ is the moment [about the z-axis] of the inertia forces of the model-pendulum system, $J_z = J_{z\text{mod}} + \left(\frac{c}{R_1}\right) J_{z\text{pend}}$, M_s is the moment exerted by the springs and the weight of the pendulum, which does not depend on the angle of attack, $k^2(\alpha_0 + \alpha)$ is the moment exerted by the springs and the weight of the pendulum, which depends on the angle of attack $(\alpha + \alpha_0)$:

$$k^2 = (k_1 + k_2)c^2 + k_3\left(\frac{c}{R_1}\right)^2 R_3^2 + Qr\left(\frac{c}{R_1}\right)^2;$$

where k_1, k_2, k_3 are the rates of springs P_1, P_2, and P_3, Q is the weight of the pendulum, r and R_3 are linear dimensions (Figure 7.78), $-\mu^2 \frac{d\alpha}{dt}$ is the moment due to viscous friction in the instrument, which depends on the angular velocity $\frac{d\alpha}{dt}$, $A \sin pt$ is the moment due to the

external force causing the oscillations $\left(A = ac^2\left(\frac{R_3}{R_1}\right)^2 k_3\right)$, M_z is the aerodynamic moment on the model:

$$M_z = (m_{z_0} + m_z^{\alpha}\alpha + m_z^{\omega_z}\omega_z + m_z^{\dot{\alpha}}\dot{\alpha} + m_z^{\dot{\omega}_z}\dot{\omega}_z)\, qSb.$$

For oscillations about the z-axis, when $\omega_z = \dot{\alpha}$; $\dot{\omega}_z = \ddot{\alpha}$ we have

$$M_z = \left[m_{z_0} + m_z^{\alpha}\alpha + (m_z^{\omega_z} + m_z^{\dot{\alpha}})\frac{b}{U}\frac{d\alpha}{dt} + m_z^{\dot{\omega}_z}\frac{b^2}{U^2}\frac{d^2\alpha}{dt^2}\right] qSb.$$

Substituting this expression into the initial differential equation we obtain

$$\frac{d^2\alpha}{dt^2} + 2n\frac{d\alpha}{dt} + m^2\alpha + m_0 = A_1 \sin pt,$$

where

$$2n = \frac{\mu^2 - (m_z^{\omega_z} + m_z^{\dot{\alpha}})\frac{qSb^2}{U}}{J_z'}; \quad m^2 = \frac{k^2 - m_z^{\alpha}qSb}{J_z'}\ *,$$

$$m_0 = \frac{k^2\alpha_0 + M_s - m_{z_0}qSb}{J_z'}; \quad A_1 = \frac{A}{J_z'}; \quad J_z' = J_z - m_z^{\dot{\omega}_z}\rho S\frac{b^3}{2}.$$

When the model oscillates about the y-axis, the equation of motion is

$$\frac{d^2\beta}{dt^2} + 2n\frac{d\beta}{dt} + m^2\beta + m_0 = A_1 \sin pt$$

where

$$2n = \frac{\mu^2 - (m_y^{\omega_y} + m_y^{\dot{\beta}})\frac{qSb^2}{U}}{J_y'}; \quad m^2 = \frac{k^2 - m_y^{\beta}qSb}{J_y'},$$

$$m_0 = \frac{k^2\beta_0 + M_s - m_{y_0}qSb}{J_y'}; \quad A_1 = \frac{A}{J_y'};$$

$$J_y' = J_y - m_y^{\dot{\omega}_y}\rho\frac{Sb^3}{2},$$

β_0 is the angle of yaw which corresponds to the mean position of the model, and β is the deviation from β_0.

A similar expression can be found for oscillations of the model about the x-axis. For this motion, the model is suspended from the centering instrument by a support which permits oscillations about the x-axis (Figure 7.81). Processing of the results of the recordings permits the coefficients of the rotational derivatives of the aerodynamic moment to be determined with the aid of the above relationships. This is done by

* The coefficient m^2 must be positive, since otherwise the motion of the model will not be oscillatory. The condition that this coefficient be positive is when $m_z^{\dot{\omega}_z}\rho\frac{Sb^3}{2}$ is negligible in comparison with J_z: $k^2 - m_z^{\alpha}qSb > 0$.

determining the coefficients of the equation of motion, which for oscillations about the z-, y-, or x-axis has the same form

$$\frac{d^2\theta}{dt^2} + 2n\frac{d\theta}{dt} + m^2\theta + m_0 = A_1 \sin pt,$$

where θ is the variable part of the angle of attack, slip, or heel.

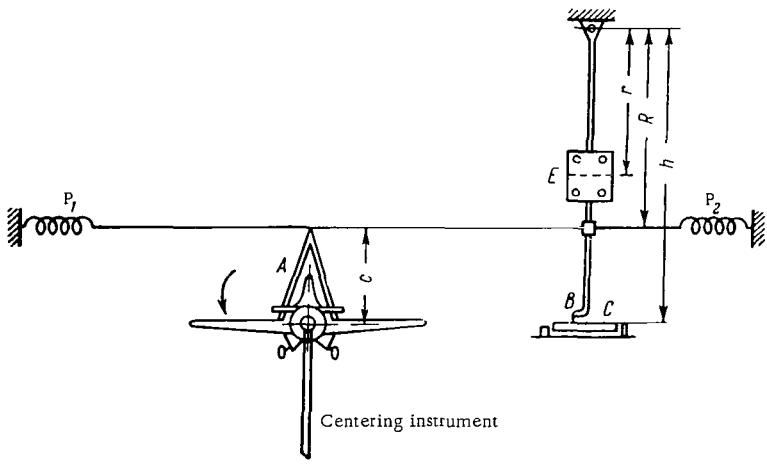

FIGURE 7.81. Suspended model oscillating about the x-axis.

The general solution of this equation is

$$\theta = \theta_0 + \theta_1 e^{-nt}\sin(\varkappa t - \varphi) + \theta_2 \sin(pt + \varepsilon),$$

where θ_0 is the angle which corresponds to the mean position of the model, $\theta_1 \sin(\varkappa t - \varphi)e^{-nt}$ is the free-oscillation term, and $\theta_2 \sin(pt + \varepsilon)$ is the forced response of the model.

For free oscillations ($A_1 = 0$) the solution is

$$\theta = \theta_0 + \theta_1 e^{-nt}\sin(\varkappa t - \varphi),$$

where θ_1 and φ are the integration constants which depend on the initial conditions, $\varkappa$ is the circular frequency of the free oscillations of the system;

$$\varkappa = \sqrt{m^2 - n^2} = \frac{2\pi}{T}.$$

Between the amplitude $\theta_1^{(0)}$ of the initial oscillation and the amplitude $\theta_1^{(i)}$ of the i-th oscillation there exists the following relationship:

$$\theta_1^{(i)} = \theta_1^{(0)} e^{-inT},$$

where T is the oscillation period.

Taking the logarithms of both sides of this equation and solving for n, we obtain

$$n = \frac{1}{iT} \ln \frac{Q_1^{(0)}}{Q_1^{(i)}}.$$

Knowing n and $\varkappa$, we can find m. Experiments yield approximately $m = \frac{2\pi}{T}$. The coefficient m_0 is determined from the equation

$$m^2\theta_0 + m_0 = 0,$$

which is obtained after substituting the solution $[\theta = \theta_0 + \theta_1 e^{-nt} \sin(\varkappa t - \varphi)]$ in the equation of motion.

For forced oscillations the solution has the form

$$\theta = \theta_0 + \theta_2 \sin(pt - \varepsilon)^*),$$

where p is the circular frequency of the excitation force, and θ_2 is the amplitude of the forced oscillations of the model,

$$\theta_2 = \frac{A_1}{\sqrt{(p^2 - m^2) + 4n^2p^2}},$$

ε is the phase shift between the excitation-force fluctuations and the forced oscillations of the model,

$$\operatorname{tg}\varepsilon = \frac{2np}{p^2 - m^2}.$$

The value of θ_2 and ε are found from the recordings of the oscillations (see Figures 7.78 and 7.80):

$$\theta_2 = \frac{K_1}{cr} b_1 \text{ and } \sin\varepsilon = \frac{\xi_0}{a_1}^{**}).$$

Knowing the values of θ_2 and ε we can find the coefficients m and n of the equation of motion:

$$n = \frac{A_1}{2p\theta_2} \sin\varepsilon; \qquad m = \sqrt{p^2 - \frac{A_1}{\theta_2}\cos\varepsilon}.$$

Henceforth, the coefficients of the rotational derivatives of the aerodynamic moment will be determined from the coefficients of the equation of motion. Thus, when the model oscillates about

* The factor e^{-nt} decreases rapidly since $n > 0$, so that after a short time the amplitude becomes constant.

** This expression is obtained by considering the parametric equation of the ellipse drawn by the pen on the moving tape $\xi = a_1 \sin pt$; $\eta = b_1 \sin(pt - \varepsilon)$, where ξ and η are respectively the displacements of the carriage and the pen from their equilibrium positions, while a_1 and b_1 are respectively the amplitudes of the oscillation of the carriage and pen.

the z-axis, we can neglect the magnitude $m_z^{\dot{\omega}_z}\rho S\frac{b^3}{2}$, which, during tests in an airstream, is small in comparison with the moment of inertia J_z. We then obtain

$$m_z^{\omega_z}+m_z^{\dot{\alpha}}=\frac{\mu^2-2J_z n}{q\frac{Sb^2}{U}}.$$

The method of determining the damping coefficient n was described above.

The moment of inertia J_z is determined from tests at $U=0$. First, the natural frequency p_0 of the system is found; a frequency p_1 is then obtained by adding to the system a weight whose moment of inertia in relation to the axis of oscillations is ΔJ_z. The moment of inertia of the system is then

$$J_z=\Delta J_z\frac{p_1^2}{p_0^2-p_1^2}.$$

The coefficient of friction in the instrument is found by replacing the model by an equivalent load and determining the damping coefficient n_1* of the system at $U=0$,

$$2n_1=\frac{\mu^2}{J_{z_1}},$$

where J_{z_1} is the moment of inertia with the equivalent load. Then

$$m_z^{\omega_z}+m_z^{\dot{\alpha}}=\frac{2U}{qSb^2}(n_1J_{z_1}-nJ_z).$$

The coefficient m_z^{α} is usually determined from balance tests of the model by graphical differentiation of the curve $m_z=f(\alpha)$. Since during oscillations the value of m_z^{α} may differ from that found in balance tests, it is better determined from tests of the oscillating model:

$$m_z^{\alpha}=\frac{J_z}{qSb}(p_0^2-p^2),$$

where p_0 and p are respectively the circular frequencies of the oscillations of the model with and without flow.

The other coefficients of the rotational derivatives of the moments m_{y_ω}, m_y^{β} and $m_y^{\omega_y}+m_y^{\dot{\beta}}$ (for oscillations about the y-axis), m_{x_ω}, m_x^{β}; $m_x^{\omega_x}-\alpha_0 m_x^{\dot{\beta}}$ (for oscillations about the x-axis), and also the rotational derivatives of the aerodynamic force and the complex rotational derivatives** are obtained similarly. In the latter case the installations and the experiments are more complicated†, but in principle the method is the same.

* $n=n_{ae}+n_1$ where n_1 is the damping coefficient of the instrument. At $U=0$, $n_{aev}=0$, $n=n_1$.

** When the vectors of the moment and of the angular velocity of the model are mutually perpendicular.

† See for instance A. L. Raikh. Teoriya i metodika opredeleniya vrashchatel'nykh proizvodnykh. (Theory and Method of Determining Rotation Derivatives). — Trudy TsAGI No. 49. 1939.

Bibliography

1. Martynov, A.K. Eksperimental'naya aerodinamika (Experimental Aerodynamics). — Moskva, Oborongiz. 1958.
2. Spravochnik aviakonstruktora t. I. "Aerodinamika samoleta" (Handbook for the Aircraft Designer, Volume 1: Aerodynamics of the Airplane). — TsAGI. 1937.
3. Zaks, N.A. Osnovy eksperimental'noi aerodinamiki (Fundamentals of Experimental Aerodynamics). — Moskva, Oborongiz. 1953.
4. Evvard, I.C., M. Tucker, and W.C. Burges. Transition-Point Fluctuations in Supersonic Flow. — JAS, No. 11. 1954.
5. Pfenninger, W. and E. Groth. Low Drag Boundary Layer Suction Experiments in Flight on a Wing Glove of an F-94A Airplane with Suction Through a Large Number of Fine Slots. Boundary Layer and Flow Control, Vol. 2. — Pergamon Press. 1961.
6. Popov, S.G. Nekotorye zadachi i metody eksperimental'noi aeromekhaniki (Certain Problems and Methods of Experimental Aeromechanics). — Gostekhizdat. 1952.
7. Gorlin, S.M. Novyi pribor dlya ispytanii vintov v trubakh s otkrytoi rabochei chast'yu (New Instrument for Testing Propellers in Tunnels with Open Test Sections). — Tekhnicheskie Zametki TsAGI, No. 114. 1935.
8. Carter, A.D.S. Some Fluid Dynamic Research Techniques.—Proc. of the Institution of Mechanical Engineers , Vol. 163 (W.E.P. No. 60). 1950.
9. Vogel, R. Ein Windkanal mit Ejektorantrieb zur Untersuchung von Einzelprofilen und Schaufelgittern. — Maschinenbautechnik, No. 9. 1959.
10. Zindner, E. Hochgeschwindigkeitskanal für Gitteruntersuchungen. — Machinenbautechnik, No. 10. 1959.
11. Todd, K.W. Apparatus for Remote Recording of Flow Conditions. — Aeronautical Quarterly, Vol. 4, pt. 4. 1954.
12. Perley, R. and B.E. Miller. Instrumentation for Automatic Plotting and Integrating of Airflow Measurements. — Proc. Instr. Soc. of America, Vol. VIII. 1952.
13. Ushakov, B.A., N.V. Brusilovskii, and A.R. Bushel'. Aerodinamika osevykh ventilyatorov i elementy ikh konstruktsii (Aerodynamics of Axial Fans and their Constructional Elements). — Moskva, Gosgortekhizdat. 1959.
14. Bychkov, A.G., I.L. Lokshin, and P.O. Mazmanyants. Novye tipy tsentrobezhnykh ventilyatorov TsAGI (New Types of TsAGI Centrifugal Fans). — Promyshlennaya Aerodinamika. In: Sbornik, No. 12. Oborongiz. 1959.
15. Ushakov, K.A. Metodika neposredstvennogo polucheniya bezrazmernykh kharateristik ventilyatorov (Methods for Obtaining Directly the Dimensionless Characteristics of Fans). — Promyshlennaya Aerodinamika. In: Sbornik, No. 15. Oborongiz. 1960.
16. Idel'chik, I.E. Spravochnik po gidravlicheskim soprotivleniyam (Handbook of Hydraulic Resistances). — Moskva, Gosenergoizdat. 1960. (IPST Cat. No. 1505).

17. Idel'chik, I.E. Aerodinamika potoka i poteri napora v diffuzorakh (The Aerodynamics of Flow and Pressure Losses in Diffusers). — Promyshlennaya Aerodinamika, In: Sbornik, No. 3. BNT TsAGI. 1947.
18. Abramovich, G.N. Prikladnaya gazovaya dinamika (Applied Gas Dynamics). — Moskva, Gostekhizdat. 1953.
19. Khanzhonkov, V.I. Ventilyatornye deflektory dlya zheleznodorozhnykh vagonov (Ventilation Hoods for Railcars). — Promyshlennaya Aerodinamika, In: Sbornik, No. 3. BNT TsAGI. 1947.
20. Sholomovich, G.I. Eksperimental'noe issledovanie modelei mnogolopastnykh vetrokoles v kosom potoke (Experimental Investigations of Models of Multiblade Wind-turbine Wheels in Inclined Airstreams). — Promyshlennaya Aerodinamika, In: Sbornik, No. 16. Oborongiz. 1960.

Chapter VIII

PROCESSING THE RESULTS OF WIND-TUNNEL TESTS

§ 40. INTERFERENCE BETWEEN TUNNEL AND MODEL

It has already been noted that in order to apply the results of the tests on models in wind tunnels to full-scale phenomena, in addition to maintaining geometrical similarity and equality of Reynolds and Mach numbers, certain corrections have to be introduced to take into account the distortion of the flow around the model, caused by the restricted cross-sectional area of the test section, and the influence of the flow boundaries, supports, etc. At small velocities, when the air can be considered as incompressible, these corrections differ from the corresponding corrections when the flow velocity in the tunnel approaches the value at which the tunnel becomes blocked. At supersonic velocities it is necessary to ensure that perturbations reflected from the walls do not reach the model, since in such cases the distortion of the flow around it cannot be taken into account by corrections.

In addition, when analyzing the experimental results it is necessary to take into account the turbulence level, which considerably affects the aerodynamic characteristics. In tests at transonic and supersonic velocities it is imperative to maintain conditions at which the behavior of the gas (air) is the same as under flight conditions. At large Mach numbers in the tunnel, the pressures and temperatures differ from those experienced in flight at the corresponding velocities, being lowered to such an extent that condensation of water vapor and sometimes, in the absence of adequate heating, liquefaction of air may occur.

In order to reduce the number and magnitude of the corrections applied to the results of tests in wind tunnels, to increase the accuracy of these tests, and to make the results correspond as closely as possible to full-scale conditions, the effects necessitating corrections should be reduced to the minimum possible. Thus, by selecting the correct cone angle of the test section, perforating the walls of the latter, and sucking off part of the air through them, we can prevent the appearance of an adverse pressure gradient along the test section and the increase of the boundary-layer thickness along the walls. We can thus also prevent the reflection of shocks from the test-section walls, and local velocity increases due to flow constriction.

We can reduce the interference between model and supports by correctly locating and properly streamlining the latter. A suitable selection of the relative dimensions of model and test section sometimes enables the

corrections for tunnel blockage by the model and its wake to be reduced to values less than 0.5 to 1% of the measured forces, so that they can be ignored altogether. However, the introduction of corrections to the results of tests in tunnels is often unavoidable, since their magnitudes become comparable with those characterizing the tested phenomena. For instance, the difference in drag of an airplane model with two different wing designs is about 10 to 20%; for a tunnel with open test section, the correction for induced drag, flow, inclination, etc., is about 15 to 20% of the drag measured by the balance.

Methods of introducing corrections

If the test-section walls were to have the shape of the streamlines for unbounded flow around the body, no wall effects would be noticed at any flow velocity in the absence of boundary layers. Since this requirement cannot be satisfied even for one wing at different angles of attack, we have to consider the real conditions of flow around the model with solid or free boundaries.

The following conditions must obtain at the flow boundaries: in tunnels with closed test sections (solid walls) the velocity component normal to the wall surface must vanish; in tunnels with open test sections (free flow) the pressure of the flowing medium must be constant, being equal to the pressure in the room surrounding the test section. Hence, due to the constancy of the mass flow rate in all cross sections of the tunnel, the velocity near a model in a closed test section is higher than the velocity upstream of it (e.g., at the nozzle exit). In tunnels with open test sections, the position is different. The static pressure in the nondisturbed flow is higher than the static pressure near the model. On the other hand, the condition of constant pressure at the flow boundary means that the latter pressure equals the static pressure in the nondisturbed flow. Hence, near the model the static pressure will increase. According to Bernoulli's equation, this leads to a velocity decrease near the model. The velocity correction for tunnels with open test sections is opposite in sign to the corresponding correction for tunnels with closed test sections.

The same effect as the blockage of the tunnel by the model is caused by the wake behind the model in a closed test section. In order that the mass flow rate along the tunnel remain constant, the reduction in velocity in the wake behind the model must be compensated by an increase in velocity outside the wake. This causes a certain velocity increase near the model. In tunnels with open test sections wake effects are practically absent.

Thus, blockage of the tunnel by the model and its wake causes changes in velocity near the model, which have to be taken into account in the test results by introducing corrections to the velocity measured in the empty tunnel or very far upstream of the model. This correction has the form

$$V_{\mathrm{tr}} = V_{\mathrm{me}}(1 + \varepsilon_{\mathrm{m}}),$$

where ε_{m} is a coefficient by which the blockage by the model is taken into account. The blockage by the wake is similarly taken into account, ε_m being replaced by ε_w . If the coefficients ε_m and ε_w are known, the corrections can be inserted directly into the values of the force and moment coefficients

determined from the measured (uncorrected) velocity head. For this, the force and moment coefficients are multiplied by the ratio of the squares of the measured and true (corrected) velocities:

$$c_{tr} = c_{me} \frac{V_{me}^2}{V_{tr}^2}.$$

Since

$$V_{tr} = V_{me}(1+\varepsilon),$$

we obtain

$$\frac{V_{me}^2}{V_{tr}^2} = \frac{1}{(1+\varepsilon)^2} \approx \frac{1}{1+2\varepsilon},$$

where

$$\varepsilon = \varepsilon_m + \varepsilon_w.$$

Hence

$$c_{tr} = \frac{c_{me}}{1+2\varepsilon_m+2\varepsilon_w}.$$

Determining the blockage coefficients of the model and its wake (ε_m and ε_w)

The wall (flow-boundary) effects and the blockage coefficients are determined by considering the flow around an airfoil in an infinite lattice system consisting of alternating upright and inverse images of the main airfoil (model). In flow around two equal airfoils placed symmetrically in relation to the line AA' which is parallel to the flow direction (Figure 8.1), the axis of symmetry AA' will be a streamline. In an ideal (nonviscous) fluid this line can be replaced by a solid boundary (wall) without affecting the flow. Inversely, the effects of the "ground" or the solid wall (AA') on the flow around the airfoil B can be determined by replacing the wall by a mirror image B' of airfoil B and considering the new problem of flow around two airfoils /1/.

The flow around airfoil B, placed between two wind-tunnel walls A_1A_1' and A_2A_2' (Figure 8.2), can be simulated to the flow around an infinite lattice system consisting of alternating upright and inverse images of the airfoil, while the wall effects on the flow around the model are reduced to the influence of the infinite number of images. An approximate solution is obtained in tunnels with open test sections by the following boundary conditions: the surface at which, in the presence of the model, the pressure is constant (no increase in axial velocity) coincides with the flow boundary before insertion of the model /2/. The blockage coefficients are found by replacing the model at its site by a system of sources and sinks (or a dipole in the case of a wing), and the boundaries of the test section by an equivalent system of mirror images of these sources and sinks (or dipoles in the case of a wing). The blockage coefficient can be determined by considering the velocities induced by these equivalent images. The images should not

induce velocities very far upstream of the model, where the measurements are performed.

This method was used by different authors to determine the blockage coefficients of the model (ε_m) and its wake (ε_{wp}) for tunnels with closed and open test sections of different cross-sectional shape . We present several

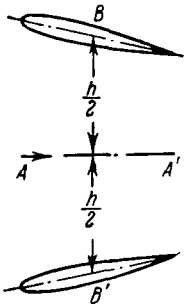

Figure 8.1. Replacing a solid wall by a mirror image of the model.

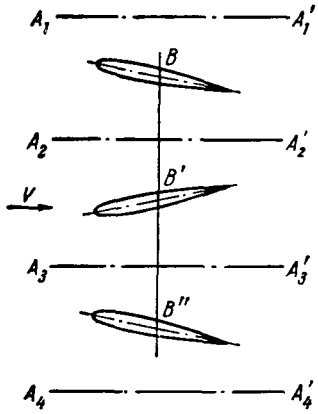

FIGURE 8.2. Two solid walls replaced by mirror images of the model.

basic formulas /1/ for determining ε_m and ε_w for subsonic tunnels.

I. Airfoils in two-dimensional flow.

1. $\varepsilon_m = \tau\lambda\left(\frac{t}{h}\right)^2$.

Here $\tau = \frac{\pi^2}{12} = 0.822$ for a closed test section, $\tau = \frac{\pi^2}{24} = 0.411$ for an open test section, t is the thickness of the airfoil, h is the height of the test section (no floor or ceiling, only side walls), λ is a coefficient which depends on the airfoil geometry for an elliptical airfoil,

$$\lambda = \frac{1}{2}\left(1 + \frac{c}{t}\right),$$

where c is the chord length /3/. The value of λ can be determined from Figure 8.3.

2. For a rectangular closed test section, Glauert /4/ suggested

$$\varepsilon_w = \eta\frac{t}{h},$$

where $\eta = f\left(\frac{c}{t}\right)$ is an empirical coefficient (Figure 8.4). The value of ε_w can also be found from the drag: /5/, /6/

$$\varepsilon_w = \frac{1}{4}\frac{c}{h}c_x,$$

where c_x is the measured drag coefficient.

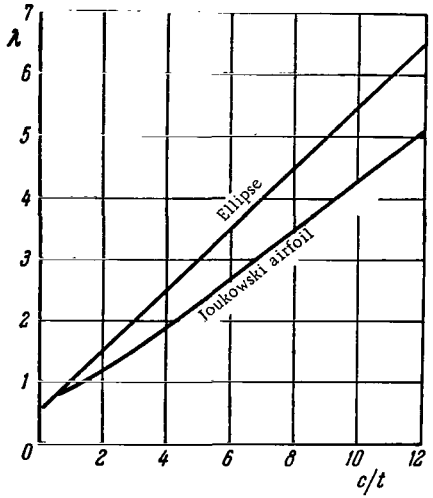

FIGURE 8.3. Coefficient λ appearing in formula for ε_m (two-dimensional flow).

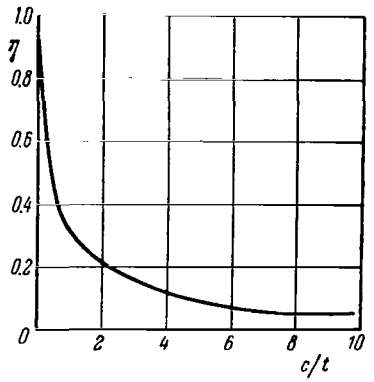

FIGURE 8.4. Coefficient η appearing in formula for ε_w (two-dimensional flow).

II. Wings of infinite span in circular closed test sections /7/.

1. $\varepsilon_m = 1.356\lambda\left(\frac{t}{d}\right)^2$, where d is the diameter of the tunnel.

2. $\varepsilon_{wp} = 0.321\,\frac{c}{d}\,c_x$.

III. Models in three-dimensional flow.

1. Body of revolution located on the tunnel axis /3/

$$\varepsilon_m = \tau\lambda\left(\frac{S_m}{F_{t.s.}}\right)^{3/2}$$

where τ is given in Table 11.

TABLE 11. Values of the coefficient τ for three-dimensional flow around a body.

Cross-sectional shape of test section	Closed test section	Open test section
Circular	0.797	−0.206
Square	0.809	−0.238
Rectangular ($b = 2h$) . .	1.03	
Rectangular ($b/h = 9/7$)	0.83	
Octangular	0.75	

The coefficient λ, which depends on the shape of the body, is found from Figure 8.5.

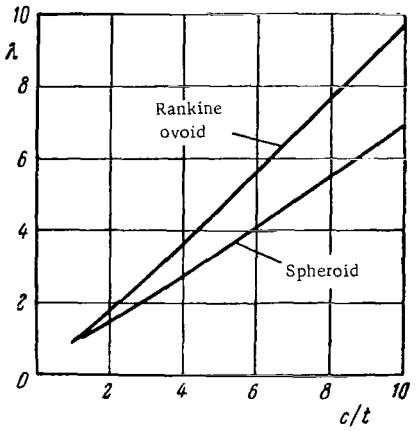

FIGURE 8.5. Coefficient λ appearing in formula for ε_m (for body of revolution).

$$\varepsilon_w = \frac{1}{4}\frac{S}{bh}c_x,$$

where S is the area to which the coefficient c_x is referred /5/.

2. Wings of finite span, including sweptback wings /1/.

$$\varepsilon_m = \left(\frac{\pi}{4}\right)^{1/2}\tau\left(1+1.2\frac{t}{c}\right)\frac{W}{F_{t.s.}^{3/2}},$$

where W is the volume of the model, $F_{t.s.}$ is the cross-sectional area of the test section, and τ is found from Table 11.

3. The blockage coefficient of an airplane model is determined by finding separately ε_m for a body of revolution and for a wing, and adding. For tunnels with closed rectangular test sections, we can use the approximate formula of Young and Squire /9/:

$$\varepsilon_m \approx 0.65\frac{W}{h^2 b},$$

where h and b are respectively the height and the width of the test section. This formula gives a correction with an accuracy of ±10%.

Taking into account the pressure gradient. The static pressure varies linearly with $\frac{d\bar{p}}{dx}$ along the test-section axis, where $\bar{p}$ is the ratio of static pressure to velocity head. The Archimedian force Q' is proportional to the volume W of the body

$$Q' = \frac{d\bar{p}}{dx}qW.$$

The correction for the pressure gradient is*

$$c_{x\ \mathrm{tr}} = c_{x\ \mathrm{me}} - \frac{d\bar{p}}{dx}\frac{W}{S},$$

where S is the area of the wing or the mid-section of the body, $W = S_{\mathrm{mid}} l \eta$ is the volume of the body, l is the length of the body, η is the coefficient of fullness. For an airplane model, $\eta \cong 0.6$; for a wing model $\eta \approx 0.8$.

The gradient $\frac{d\bar{p}}{dx}$ is assumed to be positive if the pressure decreases in the flow direction. For $\frac{d\bar{p}}{dx} \leqslant 0.001\ \mathrm{m}^{-1}$ the correction is negligibly small.

A correction for the pressure gradient must be made to the drag determined from the static-pressure distribution on the surface of the body. No correction need be made to the profile drag determined from the total-pressure distribution in the wake. Because of the smallness of the pressure gradient along the tunnel axis, no correction is ordinarily introduced in tunnels with open test sections**.

Blockage effects at large subsonic velocities

The corrections for the blockage by the model and its wake are considerable, even at velocities at which compressibility effects are still small. However, these corrections can frequently be ignored, because low-speed tunnels are intended for quantitative tests of models whose dimensions are small in relation to those of the test section. Moreover, progress in the aerodynamic design of bodies flying at hypersonic velocities has led to relatively small thicknesses of the models, and small values of c_y for the wings. This also reduces the blockage corrections when such models are tested in low-speed tunnels.

Although in principle the method of images is applicable to models of any dimensions at all subsonic velocities, the particular method of introducing corrections for boundary effects at low Mach numbers, which is based on the linear theory, is not suitable for large Mach numbers when zones of supersonic flow and shocks appear, since the equations of flow are then nonlinear. However, when the model is small in comparison with the tunnel, is not highly loaded, and the perturbations caused by it are small in comparison with the free-stream velocity, the blockage corrections obtained for small Mach numbers can also be introduced at large subsonic velocities.

According to the theory of small perturbations, the corrections obtained for small velocities must be multiplied by the factor

$$\frac{1}{\sqrt{1 - \bar{M}^2}} = \beta.$$

* We can also write /1/ $c_{x\ \mathrm{tr}} = c_{x\ \mathrm{me}} - \frac{\pi}{12}\lambda\left(\frac{t}{h}\right)^2 c_{x\ \mathrm{me}}$, where λ is found in the same way as in the determination of ε_m and ε_w.

** The correction for the pressure gradient in such tunnels is determined by highly accurate tests.

The blockage coefficients of the model and its wake are then

$$\varepsilon'_m = \varepsilon_m \frac{1}{\beta^3},$$

$$\varepsilon'_w = \varepsilon_w \frac{1}{\beta^2}.$$

The corrections for the Mach number, density, and velocity head are / 5/

$$\Delta M = \left(1 + \frac{1}{5} M^2_{me}\right) M_{me} \varepsilon',$$

$$\Delta \rho = - M^2_{me} \varepsilon' \rho_{me},$$

$$\Delta \left(\rho \frac{V^2}{2}\right) = (2 - M^2_{me}) \varepsilon' \left(\rho \frac{V^2}{2}\right)_{me},$$

where

$$\varepsilon' = \varepsilon'_m + \varepsilon'_w = \frac{\varepsilon_m}{(\sqrt{1 - M^2})^3} + \frac{\varepsilon_w}{1 - M^2}.$$

For dimensionless force and moment coefficients, the correction is

$$\Delta c = - (2 - M^2_{me}) \varepsilon' c_{me}.$$

The blockage corrections given above are applicable down to Mach numbers at which no blockage of tunnels with closed test sections occurs.

Lift effects

In contrast to blockage effects of the model, the lift effect, which causes a change in the velocity distribution in the test section, appears even when the dimensions of the model are small in comparison with those of the tunnel. This effect disappears completely only at zero lift. In order to determine the lift effect, the wing is, according to Prandtl, replaced by a system of bound vortices and vortices shed from the trailing edge of the wing. The test-section boundaries are replaced by an equivalent system of images, as explained above. The perturbations of the flow around the wing are expressed through the velocities induced by these images.

A system of images simulating the boundary conditions at the walls, with flow around a uniformly loaded wing of finite span in a tunnel with closed rectangular test section, is shown in Figure 8. 6.

It can be shown / 2/ that in the limit, when the span tends to zero, the perturbations in a tunnel with open test section are equal and opposite to the perturbations occurring in a tunnel with a closed test section of the same shape when the wing is turned by 90° about the tunnel axis. In other words, the flow perturbations in a tunnel with open test section of height h and width b are equal and opposite to the perturbations in a tunnel with a closed test section of height b and width h.

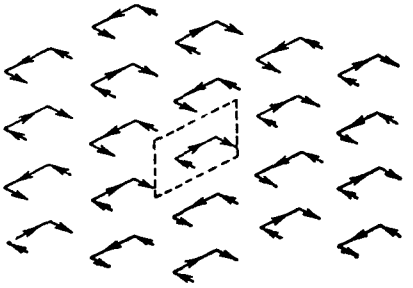

FIGURE 8.6. A system of images simulating the boundary conditions at the walls of a closed rectangular test section, with flow around a wing of finite span.

Lift effects in two-dimensional flow

In a plane tunnel with closed test section the streamlines are the same as in unbounded flow, curved in such a way (Figure 8.7) that the velocity component normal to the horizontal boundaries (floor and ceiling of the test section) vanishes. The same reasoning applies to the pressure distribution in a tunnel with open test section. A small curvature of the streamlines is equivalent in its effects to bending and alteration of the angle of attack of the airfoil. Figure 8.8 shows schematically the flow around an airfoil in a tunnel with closed test section. The vortex images lie on the line yy, which is perpendicular to the tunnel axis. The lines PP and QQ correspond qualitatively to the streamlines of the induced flow, which causes an increase in the effective curvature of the airfoil. In addition, the vertical components of the induced velocity change the angle of attack of the airfoil. The local change in the angle of attack is $\left(\frac{w}{V}\right)$ where w is the vertical component of the induced velocity at point O. In tunnels with open test sections, the streamlines are curved in the other direction, and the effective curvature and the angle of attack of the airfoil are thus reduced.

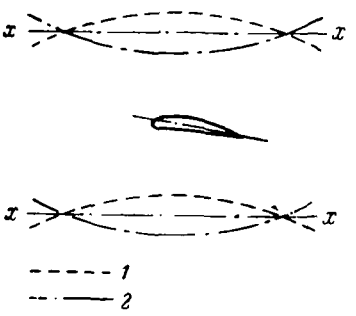

FIGURE 8.7. Curvature of streamlines induced by flow boundaries. 1 — curvature of streamlines due to lift effects in unbounded flow; 2 — curvature of streamlines induced by test-section walls; the curvature must be such that the walls are streamlines.

According to Glauert /2/, the lift effect for a thin airfoil is proportional to $(c/h)^2$; this result can be used with sufficient accuracy in most problems;

The change in curvature and angle of attack can be determined for a tunnel with closed test section from the formulas /2/

$$\Delta\gamma = +\frac{\pi}{192}\left(\frac{c}{h}\right)^2 c_{y\,me},$$

$$\Delta\alpha = +\frac{\pi}{96}\left(\frac{c}{h}\right)^2 (c_{y\,me} + 4c_{m\,me}) \text{ (in radians)};$$

for a tunnel with open test section

$$\Delta\gamma = -\frac{\pi}{96}\left(\frac{c}{h}\right)^2 c_{y\,me},$$

$$\Delta\alpha = -\frac{\pi}{48}\left(\frac{c}{h}\right)^2 (c_{y\,me} + 4c_{m\,me}) \text{ (in radians)},$$

where c_m is the coefficient of the pitching moment about the quarter-chord point (c_m is positive if the moment causes an increase in the angle of attack).

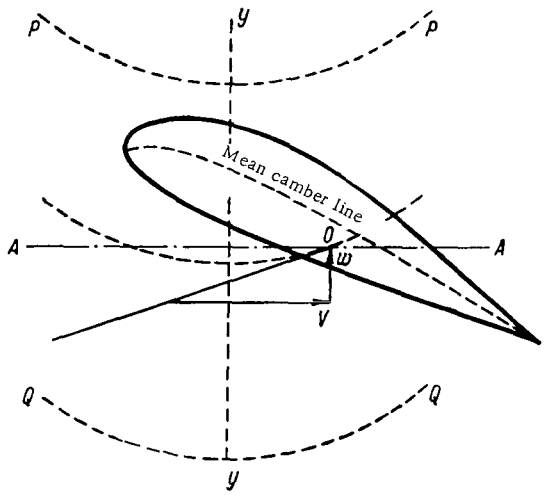

FIGURE 8.8. Flow pattern around airfoil in tunnel with closed test section.

In tunnels with open test sections the angle of attack is additionally reduced, because of the general downward inclination of the flow near the airfoil, by an amount determined by Prandtl /10/ as

$$-\frac{1}{4}\frac{c}{h}c_{y\,me}.$$

Thus, in tunnels with open test sections the total change in the angle of attack is

$$\Delta\alpha = -\frac{\pi}{48}\left(\frac{c}{h}\right)^2 (c_{y\,me} + 4c_{m\,me}) - \frac{1}{4}\frac{c}{h}c_{y\,me},$$

the second term usually predominating. The change in the effective angle of attack of the model, due to the boundary effects, necessitates correction of the force coefficients measured by the balance (c_x and c_y). The measured lift and drag are the components of the total aerodynamic force R and are respectively normal and parallel to the axis (Figure 8.9). Since the effective angle of attack is changed by $\Delta\alpha$, the measured forces must be resolved in the x_1 and y_1 directions. We obtain

$$c_{y\,cor} = c_{y\,me}\cos\Delta\alpha - c_{x\,me}\sin\Delta\alpha.$$

Since $c_{x\,\mathrm{me}}$ and $\Delta\alpha$ are small, we can write

$$c_{y\,\mathrm{cor}} \approx c_{y\,\mathrm{me}}.$$

Also,

$$c_{x\,\mathrm{cor}} = c_{x\,\mathrm{me}} \cos\Delta\alpha + c_{y\,\mathrm{me}} \sin\Delta\alpha \approx c_{x\,\mathrm{me}} + c_{y\,\mathrm{me}}\Delta\alpha.$$

The magnitude $(c_{y\,\mathrm{me}}\Delta\alpha)$ is called the induced drag coefficient.

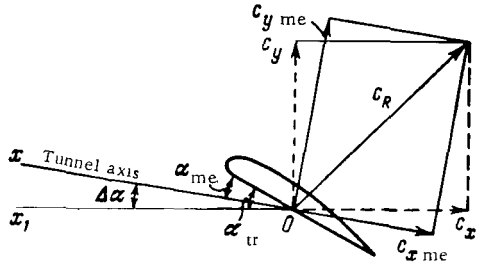

FIGURE 8.9. Components of total aerodynamic force.

We can, according to Glauert /11/, write

$$c_y = 2\pi(\alpha + 2\gamma),$$
$$c_m = -\pi\gamma.$$

where γ is the concavity of the equivalent circular arc. Assuming that

$$c_{y\,\mathrm{me}} = 2\pi[\alpha + 2(\gamma + \Delta\gamma)],$$
$$c_{y\,\mathrm{tr}} = 2\pi(\alpha + 2\gamma),$$
$$c_{m\,\mathrm{me}} = -\pi(\gamma + \Delta\gamma),$$
$$c_{m\,\mathrm{tr}} = -\pi\gamma,$$

we obtain

$$c_{y\,\mathrm{tr}} = c_{y\,\mathrm{me}} - 4\pi\Delta\gamma,$$
$$c_{m\,\mathrm{tr}} = c_{m\,\mathrm{me}} + \pi\Delta\gamma.$$

The final corrections /1/ for lift effects in two-dimensional flow are given in Table 12.

Table 12. Corrections for lift effect in two-dimensional flow

Correction	Closed test section	Open test section
Δc_y	$-\frac{\pi^2}{48}\left(\frac{c}{h}\right)^2 c_{y\,\mathrm{me}}$	$+\frac{\pi^2}{24}\left(\frac{c}{h}\right)^2 c_{y\,\mathrm{me}}$
Δc_m	$+\frac{\pi^2}{192}\left(\frac{c}{h}\right)^2 c_{y\,\mathrm{me}}$	$-\frac{\pi^2}{96}\left(\frac{c}{h}\right)^2 c_{y\,\mathrm{me}}$
$\Delta\alpha$ (in radians)	$+\frac{\pi}{96}\left(\frac{c}{h}\right)^2 (c_{y\,\mathrm{me}}+4c_{m\,\mathrm{me}})$	$-\frac{\pi}{48}\left(\frac{c}{h}\right)^2 (c_{y\,\mathrm{me}}+4c_{m\,\mathrm{me}})-\frac{1}{4}\frac{c}{h}c_{y\,\mathrm{me}}$
Δc_x	$+\Delta\alpha c_{y\,\mathrm{me}}$	$+\Delta\alpha c_{y\,\mathrm{me}}$

Lift effects on wings of finite span. In most wind-tunnel tests the chord of the wing is small in comparison with the dimensions of the test section, so that the curvature of the streamlines, caused by the tunnel boundaries, can be ignored. The lift effects can then be simulated by the flow perturbations caused by the images of vortices shed from the trailing edge (Figure 8.10). Under these conditions the corrections for wall effects become

$$\Delta\alpha = \delta\frac{S_{\mathrm{cr}}}{F_{\mathrm{t.s.}}}c_{y\,\mathrm{me}},$$

$$\Delta c_x = \Delta\alpha c_{y\,\mathrm{me}} = \delta\frac{S_{\mathrm{cr}}}{F_{\mathrm{t.s.}}}c_{y\,\mathrm{me}}^2.$$

For tunnels with closed test sections, δ is positive, since the effective angle of attack is increased; for tunnels with open test sections, δ is negative.

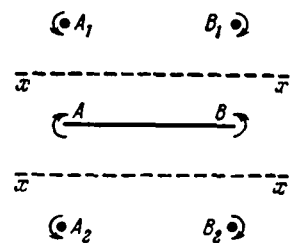

FIGURE 8.10. Wing of finite span located between solid walls, and its images.

Comparative values of δ for different types of test sections are given in Table 13 /1/.

However, experiments show that the corrections for flow-boundary effects not only differ from the theoretical values but depend on the

downwash and induced drag. This discrepancy is caused by the non-correspondence of the boundary conditions to the actual phenomena (in open test sections), and the influence of the nozzle and diffuser which are in the vicinity of the model. The difference between δ_{a_l} and $\delta_{c_{xl}}$ can be explained by the influence of the wing chord and the differences in downwash along the chord, which cause a change in the effective curvature of the wing.

TABLE 13

Values of δ

a) Circular tunnel with closed test section

Model span / Tunnel diameter	0	0.1	0.2	0.3	0.4	0.5	0.6	0.7	0.8
Elliptical load distribution over the span	0.125	0.125	0.125	0.125	0.125	0.127	0.128	0.131	0.137
Uniform load	0.125	0.125	0.125	0.126	0.126	0.127	0.130	0 136	0.148

For an open test section δ has the opposite sign

b) Octagonal tunnel with closed test section

Model span / Tunnel diameter	0	0.1	0.2	0.3	0.4	0.5	0.6	0.7	0.8
Elliptical load distribution over the span	0.126	0.126	0.126	0.127	0.127	0.128	0.130	0.133	0.139
Uniform load	0.126	0.126	0.126	0.127	0.127	0.129	0.132	0.138	0.151

c) Rectangular test section

Width / Height	0.25	0.5	0.75	1.0	1.66	2.0	4.0
Closed	0.524	0.262	0.176	0.137	0.120	0.137	0.262
Open	−0.262	−0.137	−0.120	−0.137	−0.196	−0.262	−0.524

d) Elliptical test section. Wing tips located at foci of ellipse

Width / Height	1.0	1.5	2.0	2.5	3.0
Closed	0.125	0.10	0.084	0.072	0.062
Open	−0.125	−0.15	−0.166	−0.178	−0.188

For instance, with a chord length equal to 13% of the horizontal diameter of the open test section, and $c_y \frac{S_{cr}}{F_{t.s.}} = 0.3$, the difference in induced angle of attack at the leading and trailing edges amounts to 1.5°; the lift therefore becomes smaller and the correction $\delta_{c_{xl}}$ is reduced. For these reasons it is advisable to reduce the ratio between the dimensions of the model and the test section $\left(\frac{S_{cr}}{F_{t.s.}}\right)$, while δ_{a_l}, $\delta_{c_{xl}}$ are determined for each tunnel experimentally*.

The coefficient δ_{a_l} can be determined as follows: Experimental curves $c_v = f(\alpha - \alpha_0)$ are plotted for geometrically similar models, where α_0 is the angle of zero lift. All these curves pass through the origin of coordinates.

* The tabulated data should be used if the experimental values of δ_{a_l} and $\delta_{c_{xl}}$ are not known for the tunnel in which the tests are performed.

The relationships $\alpha - \alpha_0 = f\left(\frac{S_{cr}}{F_{t.s.}}\right)$ are then plotted for fixed values of c_y ($c_y = 0.1$; $c_y = 0.2$; etc.); these are extrapolated to the intersection with the ordinate axis, i.e., to $\frac{S_{cr}}{F_{t.s.}} = 0$, which corresponds to unbounded flow. The values of $(\alpha - \alpha_0)$ for $\frac{S_{cr}}{F_{t.s.}} = 0$ are the angles of attack of the tested models at the given values of c_y in the case of unbounded flow, while the induced angle of attack is

$$\Delta\alpha_i = (\alpha - \alpha_0)_{S/F} - (\alpha - \alpha_0)_{S/F=0}.$$

Plotting the relationships

$$k_{\alpha_i} = \frac{\Delta\alpha_i}{S_{cr} F_{t.s.}} = f(c_y),$$

we can determine

$$\delta_{\alpha_i} = \frac{k_{\alpha_i}}{c_y}.$$

The procedure for determining $\delta_{c_{xi}}$ is similar. Proceeding from the experimental polars $c_x = f(c_y)$ for the model, c_y and the relationships $c_x - c_{x_0} = f\left(\frac{S_{cr}}{F_{t.s.}}\right)$ are plotted for fixed values of c_y, where c_{x_0} is the coefficient c_x at $\alpha = 0$. We then obtain by extrapolating

$$\Delta c_{xi} = (c_x - c_{x_0})_{S/F} - (c_x - c_{x_0})_{S/F=0}$$

which are corrections of c_x for flow-boundary effects at given values of $S/F_{t.s.}$ and c_y. After determining $k_{c_{xi}}$ and plotting the relationships

$$k_{c_{xi}} = \frac{\Delta c_{xi}}{S/F} = f(c_y^2),$$

we obtain $\delta_{c_{xi}} = \frac{k_{c_{xi}}}{c_y^2}$. By experiments with geometrically similar wings in tunnels with elliptical test section, it was found that $\delta_{\alpha_i} = 0.24$ and $\delta_{c_{xi}} = 0.17$.

Corrections for $c_{y\,max}$. At angles of attack approaching the critical value, the expressions

$$c_y = 2\pi(\alpha + 2\gamma),$$
$$c_m = -\pi\gamma,$$

are no longer valid because of boundary-layer separation. The value of $\frac{\partial c_y}{\partial\gamma}$ becomes less than 4π, and $\frac{\partial c_m}{\partial\gamma}$ is less than π. Hence, no correction for flow-boundary effects is introduced in $c_{y\,max}$, but in the curve $c_y = f(\alpha)$ the change in the angle of attack is taken into account. For three-dimensional flow

$$\Delta\alpha = \delta_{\alpha_i} \frac{S_{cr}}{F_{t.s.}} c_{y\,me},$$

for two-dimensional flow

$$\Delta\alpha = \frac{\pi}{96}\left(\frac{c}{h}\right)^2 (c_{y\,me} + 4c_{m\,me})$$

(in a tunnel with closed test section),

$$\Delta\alpha = -\frac{\pi}{48}\left(\frac{c}{h}\right)^2 (c_{y\,me} + 4c_{m\,me}) - \frac{1}{4}\frac{c}{h} c_{y\,me}$$

(in a tunnel with open test section).

Correction for blocking effect

In closed-circuit tunnels with either open or closed test sections the influence of lift on the free-stream velocity distribution has also to be taken into account.

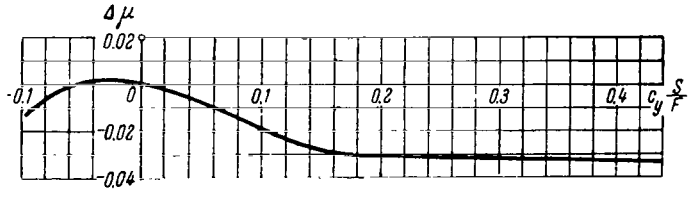

FIGURE 8.11. Blocking effect in a tunnel with open elliptical test section.

The downwash induced by lift is considerable, particularly in tunnels with open test sections, and the velocity distribution at the diffuser inlet is highly nonuniform. Despite the use of straightening devices in the tunnel and the streamline convergence in the nozzle, the flow in the test section will still be nonuniform. A tunnel containing a model subjected to lift thus has a smaller velocity coefficient than an empty tunnel (Figure 8.11).

The change in the velocity coefficient, which depends on the lift, is called blocking effect and must be taken into account when determining the aerodynamic coefficients referred to the velocity head. The correction has the form

$$c_{tr} = c_{me} \frac{\mu}{\mu + \Delta\mu},$$

where the correction for the blocking effect $\Delta\mu$ is found by averaging the results of experiments with different wings. In tunnels with closed test sections or with single return ducts the correction for the blocking effect is small and is mostly neglected. In tunnels with dual return ducts this correction is considerable.

Different methods of introducing corrections
for the lift effect

In practice, corrections for the lift effect can be introduced by two methods: all corrections can be reduced either to a change in the angle of attack at constant lift ($c_{y\ tr} = c_{y\ me}$), or to a change in the lift at constant angle of attack ($\alpha_{tr} = \alpha_{me}$).

In order to reduce all corrections to a change in the angle, the latter has to be corrected twice: firstly by $\Delta\alpha_1$, which depends on the change in flow direction, secondly by $\Delta\alpha_2$, which depends on the change in concavity of the airfoil:

$$\Delta\alpha_2 = 2(\gamma_{tr} - \gamma_{me}) = -\frac{1}{2\pi}(c_{y\ tr} - c_{y\ me}).$$

The total angle, to which the experimental value $c_{y\,me}$ should be referred, is (Figure 8.12)

$$\alpha = \alpha_{me} + \Delta\alpha_1 + \Delta\alpha_2 = \alpha_{me} + \Sigma\Delta\alpha.$$

When all corrections are reduced to an equivalent change in the lift, a certain slope, valid in the linear region, has to be assumed for curve $c_y = f(\alpha)$*. The total change in lift will then be equal to the sum of Δc_{y_i},

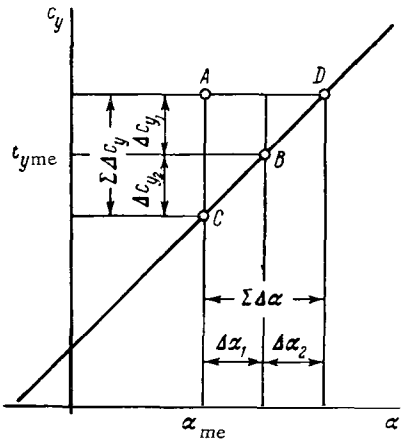

FIGURE 8.12. Different methods of correcting the curve $c_y = f(\alpha)$; A — point on uncorrected curve obtained by direct measurement in tunnel; B — correction for change in angle of attack and lift; C — all corrections reduced to change in lift ($\alpha_{tr} = \alpha_{me}$); D — all corrections reduced to change in angle of attack ($c_{y\ tr} = c_{y\ me}$).

* Strictly speaking, the slope is $\frac{\partial c_{y\,me}}{\partial\alpha}$, but the error is negligible.

due to the change in concavity ($\Delta\gamma$), and

$$\Delta c_{y_1} = \frac{\partial c_{y\,\mathrm{me}}}{\partial \alpha}\,\Delta\alpha,$$

due to downwash induced by the flow boundaries:

$$c_y = c_{y\,\mathrm{me}} - \Delta c_{y_1} - \Delta c_{y_2} = c_{y\,\mathrm{me}} - \Sigma\,\Delta c_y.$$

Similar corrections should be introduced in the experimental coefficients of drag and pitching moment, but because of the smallness of the ensuing changes, these coefficients can be left unchanged, being referred to the changed angle of attack. Similarly, for a wing of finite span, the correction for the angle of attack $\Delta\alpha = \delta\,\frac{S_{\mathrm{cr}}}{F_{\mathrm{t.s.}}}\,c_{y\,\mathrm{me}}$ can be reduced to an equivalent change in lift with the aid of the relationship

$$\Sigma\,\Delta c_y = -\,\delta\,\frac{S_{\mathrm{cr}}}{F_{\mathrm{t.s.}}}\,c_{y\,\mathrm{me}}\,\frac{\partial c_{y\,\mathrm{me}}}{\partial \alpha}.$$

The corrected curve $c_y = f(\alpha)$ is then obtained by plotting the relationship

$$(c_{y\,\mathrm{me}} + \Sigma\Delta c_y) = f(\alpha_{\mathrm{me}}).$$

Influence of lift on the flow around the horizontal tail

The induced downwash near the horizontal tail of a model in a tunnel differs from the downwash near the wing. This necessitates corrections in the measured value of the pitching-moment coefficient m_z. The difference between the pitching moments in unbounded flow and in a tunnel (at equal values of c_y) is equal to the difference in the moments due to the horizontal tail:

$$\Delta m_{z\,\mathrm{h.t.}} = m_{z_\infty} - m_{z\,\mathrm{tu}}.$$

The value of $\Delta m_{z\mathrm{h.t.}}$ can be found by testing geometrically similar models and using the methods described above for determining δ_a and

$$\Delta m_{z\,\mathrm{h.t.}} = 57.3\,\delta_{\mathrm{t}}\,\frac{S}{F_{\mathrm{t.s.}}}\,c_y\,\frac{S_{\mathrm{h.t.}}}{S}\,\frac{L_{\mathrm{h.t.}}}{b_A}\left(c^{\alpha}_{y\,\mathrm{h.t.}}\,\frac{q_{\mathrm{h.t.}}}{q}\right),$$

where $S_{\mathrm{h.t.}}$ is the area of the horizontal tail, $L_{\mathrm{h.t.}}$ is the distance from the wing to the horizontal tail (usually from the center of gravity to the hinges of the elevator), b_A is the mean aerodynamic chord, and

$$\left(c^{\alpha}_{y\,\mathrm{h.t}}\,\frac{q_{\mathrm{h.t.}}}{q}\right) \approx 0.046$$

(according to experimental data).

Experiments show that δ_t can be assumed equal to 0.08. Hence

$$\Delta m_{z\,h.t.} = 0.21 \frac{S}{F_{t.s.}} \frac{S_{h.t.}}{S} \frac{L_{h.t.}}{b_A} c_y$$

and

$$m_{z\,tr} = m_{z\,me} - \Delta m_{z\,h.t.}$$

We can also use expression

$$\Delta m_{z\,h.t.} = 0.061 \frac{S_{h.t.}}{b_A} \tau c_y,$$

where $\tau = f(L_{h.t.})$ is a coefficient which characterizes the influence of the flow boundaries on the downwash near the tail in comparison with the downwash near the wing.

$L_{h.t.}$	0.6	0.8	1.0	1.2	1.4	1.6	1.8	2.0
τ	0.16	0.27	0.395	0.535	0.685	0.83	0.98	1.12

With correctly selected dimensions of the model, $\Delta m_{z\,h.t.}$ in most tunnels is 1 to 1.5% of the mean aerodynamic chord.

Influence of lift at large subsonic velocities

The influence of the lift at large subsonic velocities is taken into account by multiplying the expressions for $\Delta\gamma$ (see page 535) by $\beta = \frac{1}{\sqrt{1-M^2}}$. We thus obtain:

$$\Delta\gamma = +\frac{\pi}{192}\left(\frac{c}{h}\right)^2 c_{y\,me} \frac{1}{\sqrt{1-M^2}} \quad \text{for a closed test section,}$$

$$\Delta\gamma = -\frac{\pi}{96}\left(\frac{c}{h}\right)^2 c_{y\,me} \frac{1}{\sqrt{1-M^2}} \quad \text{— radians for an open test section}$$

$$\Delta\alpha = +\frac{\pi}{96}\left(\frac{c}{h}\right)^2 (c_{y\,me} + 4c_{m\,me}) \frac{1}{\sqrt{1-M^2}} \quad \text{radians for a closed test section}$$

$$\Delta\alpha = -\frac{\pi}{48}\left(\frac{c}{h}\right)^2 (c_{y\,me} + 4c_{m\,me}) \frac{1}{\sqrt{1-M^2}} \quad \text{radians for an open test section.}$$

In these formulas it is assumed that

$$c_y = \frac{2\pi}{\sqrt{1-M^2}} (\alpha + 2\gamma),$$

$$c_m = -\frac{\pi}{\sqrt{1-M^2}} \gamma.$$

which is true for a thin airfoil. The additional correction to the angle of attack $\Delta\alpha = -\frac{1}{4}\frac{c}{l}c_{y\,me}$, necessitated by the general flow inclination in an open test section, should not be made; neither should there be a change in the correction for the induced drag ($\Delta c_{xi} = c_y \Delta\alpha_i$).

Applicability of corrections

In most cases the dimensions of the model are small in comparison with those of the test section $\left(\frac{S_{cr}}{F_{t.s.}} \leqslant 0.15 - 0.2\right)$ and the above corrections give sufficiently reliable results at small velocities when compressibility effects are absent.

With increasing lift, the method of introducing corrections becomes less reliable for small models, since the velocities induced by the flow-boundary effects must be determined not only on the tunnel axis but at all points of the model. Such calculations are very difficult. It is therefore better to introduce corrections based on the results of tests of geometrically similar models in the same tunnel, or of the same model in geometrically similar tunnels having different test-section dimensions.

For example, a series of similar wings, rectangular in plane, were tested in a tunnel with an open test section of elliptical shape (Figure 3.18). The wings had a relative thickness of 12% and aspect ratio $\lambda = 6$; the ratio of the span to the horizontal test-section diameter was approximately 0.75. The aerodynamic characteristics obtained were corrected for down wash, drag of supports, blocking effect, and lift effect. The same series of wings was tested in a similar tunnel whose linear dimensions were several times smaller. Practically the same correction coefficients $\delta_{\alpha_l} = 0.25$ and $\delta_{c_{xl}} = 0.17$ were obtained in both tunnels for all wing dimensions. On the basis of experiments in low-speed tunnels, it was established that for the following relative dimensions of models and test sections, it is possible to neglect blockage by the model, its wake, and the boundary layer:

ratio of span to test-section width	0.75 for models with rectangular wings, 0.6 for models with sweptback wings.

When these conditions obtain, there remain corrections for lift effect (Δc_{xi}, $\Delta\alpha_i$; $\Delta m_{z\,\mathrm{nt}}$), blocking effect, downwash effect of the supports (on drag and pitching moment), and pressure gradient.

When wings supported on the side walls of the tunnel are tested, the pressure distribution is usually determined in the mid-section. The lift effect can then be ignored, only blockage corrections being introduced in the velocity when quantitative results are required. When only comparative data on the pressure distribution are needed, the corrections can be omitted, but equality of Reynolds numbers must be maintained.

When balance measurements of a half-wing supported on the wall of a closed test section are performed (such tests enable the span of the model and the Reynolds number to be increased), it can be assumed that the flow perturbations caused by the boundaries, and thus, the relevant corrections, will be the same as when a complete model is tested in a tunnel having a test section of double the width.

The influence of the boundary layer at the tunnel wall on which a model supported can be ignored if, on both sides of the tunnel, false end sections of a wing of the same profile are placed with a clearance between the wall and the model wing. These end sections should, on each side, extend a distance a into the tunnel where $\frac{a}{c} = \text{tg}\, 10°$, c being the chord length of the wing. This is illustrated in Figure 8.13. The influence of the boundary layer on the wall is sometimes eliminated by placing, with clearances, profile plates between the model and the wall.

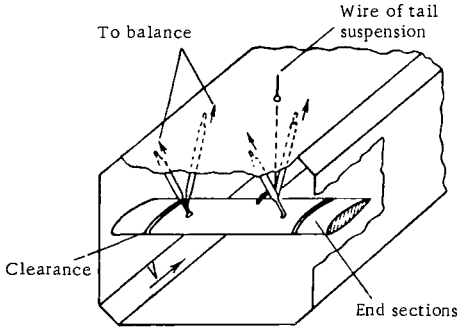

FIGURE 8.13. Installation of a wing with false end sections.

The corrections for blockage by the model and its wake can be estimated from the experimentally determined increase in velocity (or pressure) on the tunnel wall opposite the model. If ΔV_1 is the increase in velocity at the wall, due to blockage by the model and its wake, while ΔV_2 is the velocity increase far downstream of the model, then for small models /5/

$$\varepsilon_w = \frac{\Delta V_2}{2},$$

$$\varepsilon_m = \frac{1}{3}\left(\Delta V_1 - \frac{\Delta V_2}{2}\right)$$

$$\varepsilon = \varepsilon_w + \varepsilon_m = \frac{1}{3}(\Delta V_1 + \Delta V_2).$$

The blocking effect can be determined from the pressure distributions on the upper and lower tunnel walls by means of the relationship

$$\frac{\Delta V_{t.s.}}{V_{me}} = -\frac{1}{2}\frac{\Delta p_{t.s.}}{\frac{1}{2}\rho V_{me}^2}.$$

This method can be used as long as the theory of small perturbations is applicable, i.e., for velocities at which the supersonic region on the airfoil is small and shocks do not extend to the tunnel walls. At these velocities more accurate results are obtained from the expressions /12/.

$$\varepsilon_w = \Delta V_2,$$

$$\varepsilon_m = \frac{1}{2}(\Delta V_1 - \Delta V_2),$$

$$\varepsilon = \frac{1}{3}(\Delta V_1 + 2\Delta V_2).$$

These methods are also used in high-speed tunnels. Large subsonic velocities are corrected for blockage by measuring the change in pressure on the tunnel walls, and referring the results of the balance measurements to the corrected free-stream velocity.

In modern transonic tunnels it is possible to omit corrections for flow-boundary effects by perforating the test section walls, or by sucking off the boundary-layer through the walls in supersonic tunnels. Because of the aerodynamic perfection of present-day models (airplanes, rockets, etc.), corrections for flow-boundary effects can also be omitted in supersonic tunnels, if no shocks are reflected from the walls onto the model. In both cases there remain experimentally determined corrections for the influence of the model suspensions and supports.

§ 41. INTERFERENCE BETWEEN MODEL AND SUPPORTS

The tested model is mounted in the tunnel with the aid of different types of suspensions, supports, struts, etc. Their influence on the flow pattern in the tunnel and around the tested model is considerable. In the general case, these effects are expressed in changes in the velocity and pressure distributions, which are noticed:

a) as changes in the average velocity in the test section, which necessitates corrections in the velocity coefficient of the tunnel;

b) as changes in the pressure gradient, which create a horizontal Archimedian force affecting the drag, thus necessitating a correction in the pressure gradient;

c) as changes in the flow inclination in the vertical plane near the supports, which affect the distribution of the downwash over the span of the model and near the tail, and necessitate corrections in the angle of flow inclination and in the downwash near the tail;

d) as changes in the downwash along the chord of the wing (along the flow direction), which affect the lift and the pitching moment, and necessitate corrections in the induced curvature of the streamlines;

e) as changes in flow velocity near the tail, which necessitate corrections in the longitudinal-stability characteristics;

f) as different local influences affecting boundary-layer flow, vortex formation, local flow separation, etc.

Figure 8.14 shows the influence of supports of the type shown in Figure 8.15 on the static pressure and the downwash in the test section of the tunnel. Immediately behind the tail strut, the static pressure is reduced by an amount equal to 8% of the velocity head. In front of and

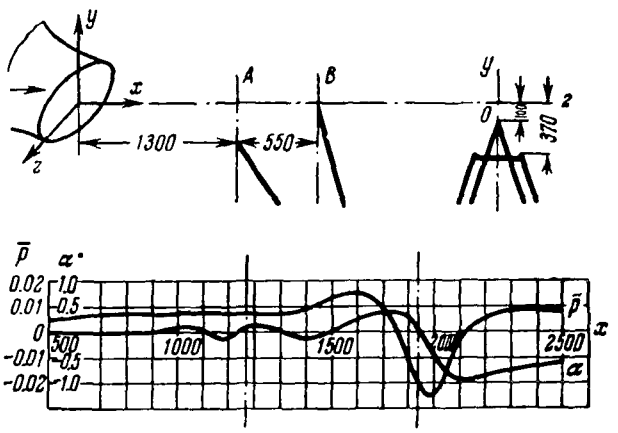

FIGURE 8.14. Influence of supports on static pressure and downwash in test section ($z=0, y = 0$).

above the tail strut a static-pressure increase of the same order is observed. Local pressure gradients of different signs are observed in various parts of the test section, where the pressure differences attain 1 to 2% of the

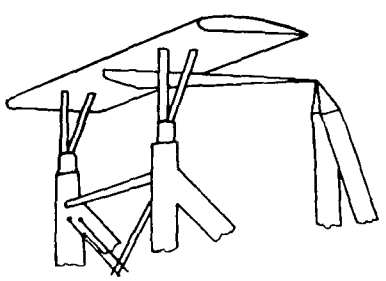

FIGURE 8.15. Wing supports in a large tunnel.

velocity head. The downwash angle changes, sometimes by up to 2.5%, near the tail strut. These effects cause the forces and moments measured by the balance to differ from those acting on the isolated model.

The system of supports shown in Figure 8.15 has a drag which is equal to about 30 to 50% of the minimum drag of a fighter-plane [model]. The same is true for the supports shown in Figure 8.16. At the same time, the drag of and the moments acting on these supports when isolated, differ

considerably from the corresponding values in the presence of the model because of its influence on the flow around the supports. Determination of the effects of interference between the model and its supports is therefore important in aerodynamic measurements, particularly in high-speed tunnels, where the supports can radically change the flow pattern around the model.

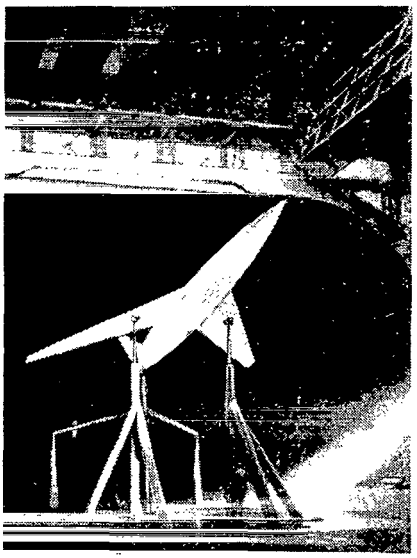

FIGURE 8.16. Model of an airplane with swept-back wings in a full-scale tunnel.

Due to the large differences in the supports used, and the complexity of the phenomena, it is difficult to perform a generalized analysis of the interference for different models tested in tunnels of various dimensions and types. In practice, in each wind tunnel this problem is solved individually by collecting experimental data on which corrections in the test results are based. The corrections are obtained by several general methods. In so-called comparative tests, at velocities at which compressibility effects can be neglected, it is sufficient to take into account the drag of the supports by testing the latter without the model. This procedure is correct when the overall change in velocity around the model, caused by the flow constriction at the supports, is negligible, as in low-speed tunnels, where wire and tape supports are used. When the changes in velocity cannot be neglected, tunnel blockage by the supports can be taken into account by the methods described above (similar to the effects of blockage by the model itself).

Thus, a sufficiently accurate correction factor is /5/

$$\varepsilon = \frac{1}{4}\frac{Sc_x}{bh},$$

where c_x is the drag coefficient of the supports, S is the area to which c_x is referred, b and h are respectively width and height of the test section. The coefficient c_x is either determined experimentally or calculated on the basis of tests of the support elements (wires, tapes, cylinders, etc.). When the aerodynamic properties of the model must be determined very accurately, interference between the model and the support must be fully taken into account. This interference is determined experimentally, mostly by the method of "doubling", by testing the supports with the model, and by the method of false supports.

The method of "doubling" consists of successive tests of the model on the main supports and additional similar supports with different positions of the model. The difference in the balance indications permits the influence of the supports to be determined. Thereafter, the forces

acting on the main supports at a given position of the model are deduced from the test results, and the forces acting on the model alone are thus found.

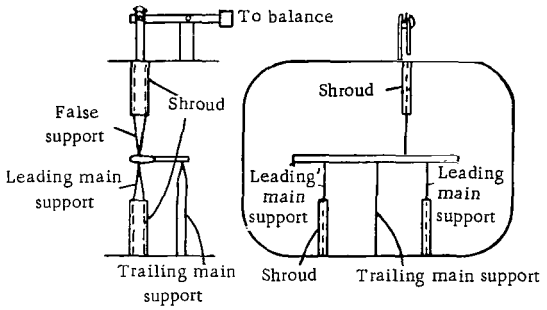

FIGURE 8.17. Interference determination by means of false supports.

Testing of supports in the presence of the model

This method consists of determining the forces acting on the supports in the presence of the model. For this the model must be mounted independently of the balance, in such a way that the position of the supports connected to the balance corresponds to their position during tests of the model (Figure 8.18). The forces acting on the supports at different angles

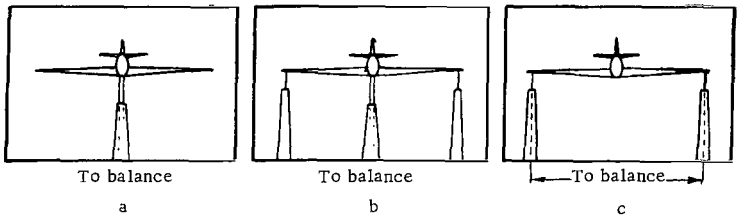

FIGURE 8.18. Determining interference between model and supports by means of calibrating support. The corrected result is "a" + "c" - "b".

of attack of the model are measured and then deducted from the corresponding values obtained at the same angles of attack in tests of the model. The forces acting on the model alone are thus found.

The method of false supports consists in testing the model in the presence of an additional false support, not connected to the balance, and located close to the model in the same manner as the main support whose influence is to be determined (Figure 8.17). If the forces acting on the false support are measured on an independent balance, the influence of the model on the support can be determined. False or additional supports must be placed at points where the interference between them and the model can be assumed

to be equal to the interference between the main supports and the model. The false supports should therefore not be located at the wing tips, close to the engine nascelles, etc.

It is possible to combine these methods, and also other methods of taking into account the interference between the model and the supports. In particular, in high-speed tunnels the influence of the supports is determined not only by means of balances but by measuring the pressures beneath the model, where it is connected to the supports. The difficulty of accurately determining the interference between the model and the supports makes it necessary to reduce its effects to minimum when the balance and the model supports are designed. This can be done by reducing the number of supports and their cross sections, and by suitably selecting the point where they are fixed to the model. These points should not be in the region of maximum wing thickness (especially on the upper surface) near the leading edge or engine nascelles, at the wing tips, etc.

Symmetrical swept back supports are used in high-speed tunnels. The angle of sweepback exceeds by 5° to 10° the angle of sweepback of the wings usually tested on these supports. Rigid shrouded tail supports are successfully used in supersonic tunnels. It is mostly possible by repeated tests, to determine accurately the interference effects of the supports selected for a given tunnel and to take them into account in the results of the aerodynamic measurements. When designing the supports, special attention must be paid to their rigidity. This is particularly important for tail supports in supersonic tunnels.

Influence of turbulence and Reynolds number

The direct influence of these factors on the aerodynamic characteristics is not taken into account during preliminary processing of the test results. However, for further analysis and comparison of the aerodynamic properties of the tested model with those of other models, the turbulence level, and the Reynolds number at which the test results were obtained, have to be taken into account. This is most important when the drag characteristics of models with laminar-flow (low-drag) wing sections ($c_{x\,min}$) and the values of the maximum lift ($c_{y\,max}$) are being determined. In order to avoid inaccuracies in determining the value of $c_{y\,max}$, the tests should be performed at the maximum possible Reynolds number or over the whole possible range of Reynolds numbers.

For the purposes of comparison the test results are sometimes converted to other Reynolds numbers. This is done on the basis of similar tests of aerodynamically related airfoils and models, performed at various Reynolds numbers. The results are not recalculated for other turbulence levels since no tests are performed for different values of ε. Only approximative corrections, based on the results of tests of similar models in low-turbulence tunnels or in free flight, are introduced.

The main criterion of the appropriateness of the corrections, as of the experimental procedure as a while, is the agreement between the results of experiments on models in the tunnel and of tests on full-scale objects*.

* Comparison of investigations in small tubes with the investigated model in larger natural tubes makes it possible to solve many problems of the reliability of using some of the corrections. Such comparisons are carried out in all possible cases.

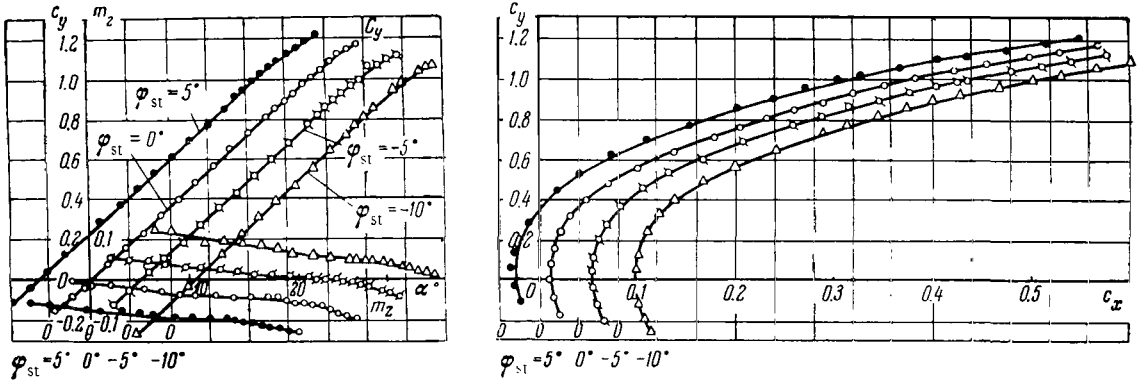

FIGURE 8.19. Typical presentation of measurement results of $c_y = f(\alpha)$, $c_y = f(c_x)$ and $m_z = f(\alpha)$.

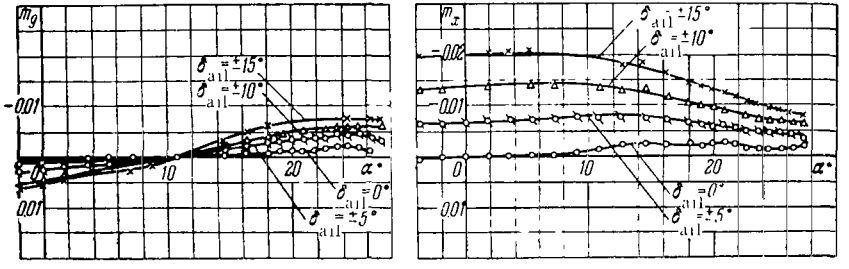

FIGURE 8.20. Typical presentation of measurement results of $m_y = f(\alpha, \delta_{ail})$ and $m_x = f(\alpha, \delta_{ail})$.

Because of the difficulties and expense involved, such comparisons cannot be made for most tests (different versions of models, etc.), but are performed systematically in all cases in which the results of full-scale tests are available. Such comparisons include also an evaluation of different methods for determining the aerodynamic characteristics. Thus, for instance, when the drag coefficients, obtained by experiment on the model in the tunnel and in flight (referred to the maximum air speed V_{max}), are compared, the accuracy with which the value of c_x is calculated for the nonsimulated airplane elements, the influence on c_x of the Reynolds number, and other factors are also considered.

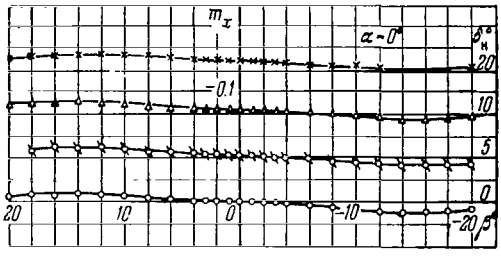

FIGURE 8.21. Typical presentation of measurement results of of $m_x = f(\beta, \delta_н)$ ($\delta_н$ = angle of rudder deflection).

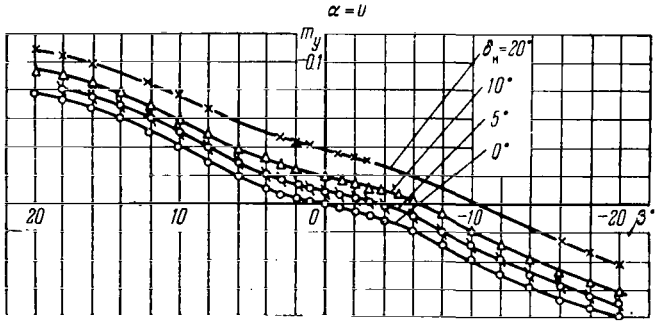

FIGURE 8.22. Typical presentation of measurement results of $m_y = f(\beta, \delta_н)$.

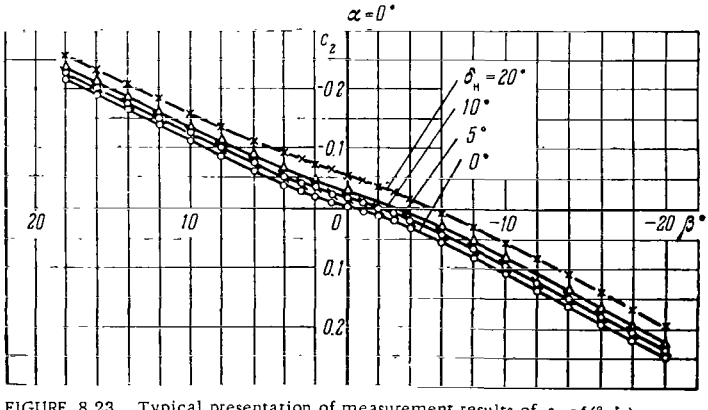

FIGURE 8.23. Typical presentation of measurement results of $c_z = f(\beta, \delta_н)$.

TABLE 14. Example of program for processing the results of tests on a six-component wind-tunnel balance in a low-speed tunnel with open test section

Number	Order of calculation	Dimensions	Remarks
1	α	degrees	Angle of attack. The angle between the projection of the velocity vector on the plane of symmetry of the model, and the model axis
2	$Y = k_y(Y_c - Y_{co})$	kg	k_y — Coefficient of counter of lift balance Y Y_c — Indications of counter of lift balance Y
3	$c_y = \frac{Y}{qS}$		S — Wing area of model q — Velocity head corrected for blocking effect $q = q_{me}b$ for $c_yS = -2$ $b = 1.022$, for $c_yS = +2$ $b = 1.032$, for $c_yS = 0$ $b = 1.0$
4	$X = k_x(X_c - X_c)$	kg	Indications of drag balance
5	$c_{x\,me} = \frac{X}{qS}$		
6	$c_x = c_{x\,me} - c_{xs}$		c_{xs} — Drag of supports
7	$\Delta c_{xi} = \delta_{c_{xi}} \frac{S}{F} c_y^2$		$\delta_{c_{xi}} = 0.17$, $F = 7.32\,m^2$ Drag correction for lift effect:
8	$c_{x\,tr} = c_x - \Delta c_{xi}$		
9	$\Delta\alpha_i = 1.88\,Sc_y$	degrees	$\Delta\alpha_i = \delta_{\alpha_i} \frac{S}{F} c_y$; $\delta_{\alpha_i} = 0.24$ Correction in angle of attack for lift effects
10	$\alpha_{tr} = \alpha - \Delta\alpha_i$	degrees	
11	$M_z = k_{m_z}(M_{zc} - M_{zc})$	kg	Indications of moment balance l_x — Longitudinal balance base
12	$l_x \cos(\alpha^0 - \alpha_1^0) \frac{1}{b_A}$		b_A — Mean aerodynamic chord α_1^0 — Angle between chord and longitudinal base
13	$A = \frac{M_z}{qS} \frac{l_x}{b_A} \cos(\alpha^0 - \alpha_1^0)$		Moment about balance axis (the axis which passes through the front links)
14	$m_z = -(A + c_xD)$		c_xD — Moment about the center of gravity due to drag
15	$m_{z\,tr} = m_z - \Delta m_{z_0}$		$\Delta m_{z_0} = 0.061 \frac{S_{h.t.}}{b_A} \tau c_y$ Moment correction for downwash at tail
16	$Z = k_z(Z_c - Z_{co})$	kg	Indications of side-force balance
17	$c_{z\,me} = \frac{Z}{qS}$		
18	$c_z = c_{z\,me} - c_{z\,s}$		$c_{z\,s} = \frac{R_{z\,s}}{S}$, $R_{z\,s}$ is the side force of the support referred to the velocity head, and depends on the angle of slip. $\beta = 26°$ $R_{z\,s} = -0.0138$, $\beta = 0$ $R_{z\,s} = 0$, $\beta = -26°$ $R_{z\,s} = +0.0138$
19	$M_x = k_{m_x}(M_{xc} - M_{xco})$		
20	$m_{x\,me} = \frac{M_x}{qS}$		

TABLE 14 (cont'd)

Number	Order of calculation	Dimensions	Remarks
21	$m_x = m_{x\,\bar{me}} \bar{r}_x c_z - m_{xs}$		$m_{xs} = \frac{R_{mxs}}{Sl}$, where R_{mxs} is the heeling moment of the supports referred to the velocity head, and depends on β^0; $\bar{r}_x c_z$ is the moment, due to the side force, about the center of gravity, l is the wing span
22	$m_y = k_{m_y}(m_{y\,c} - m_{y\,c_0})$	kg·m	
23	$m_{y\,me} = \frac{M_y}{qS}$		Yawing moment of supports referred to velocity head
24	$m_y = m_{y\,\bar{me}} \bar{r}_y c_z - m_{ys}$		$m_{ys} = \frac{R_{mys}}{Sl}$; $R_{my\,s}$ = yawing moment of supports referred to velocity head; $\bar{r}_y c_z$ = dimensionless moment, due to side force, about center of gravity

Program for processing test results. The results of tests on the balance shown in Figures 6.34 and 6.35 in a tunnel with an elliptical open test section (Figure 3.18) are processed in table 14. The results of tests in low-speed tunnels are usually presented in the form of diagrams as shown in Figures 8.19 to 8.23. The results of tests in supersonic tunnels are usually given in the form of dependences of the force and moment coefficients on the Mach number at fixed angles of attack, which can then be presented in the form of relationships $c_x = f(\alpha)$ etc. for fixed Mach numbers.

§42. ACCURACY AND REPRODUCIBILITY OF TESTS

Accuracy and reproducibility of aerodynamic experiments are considered from the following angles:

1. Accuracy of single tests of the same type.
2. Reproducibility of tests performed at different times and under different conditions.
3. Agreement between the results of tests in different tunnels.
4. Agreement between the results obtained in tunnels and by full-scale tests.

Accuracy and reproducibility of experiments. In laboratory tests both random and systematic errors are encountered. Random errors have a Gaussian distribution /13/. Systematic errors obey certain laws which can be found and taken into account when the test results are being processed. In order to estimate the correctness of the values of the aerodynamic coefficients, which are always obtained by indirect measurements, the accuracy of these measurements must be taken into account. This must be done both when setting up an experiment and designing the experimental equipment and after the experiment.

When setting up the experiment, it is necessary to consider the effects of random errors of the different measuring instruments on the accuracy of determining the required characteristic. This has already been mentioned in Chapter II. Here we shall consider specifically the influence

of errors of the measuring instruments on the accuracy of measuring the power coefficient of a propeller (see Chapter VII)

$$\beta = \frac{2\pi M}{\rho n_c^2 D^5}.$$

Comparison of results of tests in small and in full-scale tunnels permits many questions on the reliability of corrections to be solved. Such comparisons are made whenever possible.

In this formula the measured magnitudes are the propeller resistance torque M, the number of propeller revolutions per second n_c, and the air density ρ. Using the curve for the distribution of errors, we can express the standard deviation σ_β of the measurements of β through the standard deviations of the measurements of M, n_c, and ρ, which are respectively σ_M, σ_{n_c} and σ_ρ. We obtain

$$\frac{\sigma_\beta}{\beta} = \sqrt{\left(\frac{\sigma_M}{M}\right)^2 + \left(\frac{\rho_\rho}{\rho}\right)^2 + \left(2\frac{\sigma_{n_c}}{n_c}\right)^2}$$

or, noting that the density ρ is also determined indirectly by measuring the temperature T and the barometric pressure B (see § 15):

$$\rho = 0.125\frac{288B}{760T}.$$

(We are considering measurements in a low-speed tunnel where compressibility effects are neglected). We thus obtain

$$\frac{\sigma_\beta}{\beta} = \sqrt{\left(\frac{\sigma_M}{M}\right)^2 + \left(\frac{\sigma_T}{T}\right)^2 + \left(\frac{\sigma_B}{B}\right)^2 + \left(2\frac{\sigma_{n_c}}{n_c}\right)^2}.$$

In this expression the random errors are best considered to be the errors of single measurements, determined by static calibration of the respective instruments. This does not permit conclusions to be drawn on the accuracy of the experiment as a whole, which depends on the dynamic characteristics of the instruments, the number of measurements, the variation of β with λ, etc. Nevertheless, the last expression enables us to estimate the influence of errors of the different instruments on the total error σ_β. If all relative errors were equal, the influence of each on the error in measuring β would be the same, except for the influence of the error in measuring the number of revolutions, which would be double the influence of the other errors. Hence, the tachometer used for measuring the number of propeller revolutions must be more accurate than the other instruments. On the other hand, the relative error of each measurement increases when the measured magnitude itself decreases. The tests should therefore be carried out in such a way that the measured magnitudes are as large as is permitted by the instrument used. For instance, if a propeller is tested in a variable-density tunnel, the maximum possible measured torque can be obtained by varying the pressure in the tunnel. This method of experimentation is in this case permissible, since the influence of the Reynolds number on the propeller characteristics is small. The possibility of introducing corrections for systematic errors has to be considered before the experiment. The magnitude of the remaining systematic errors which are not taken into account and are later treated as random errors, has to be determined approximately. After the experiment, the accuracy of the results must be evaluated by the deviations of the experimental points from the most probable line drawn through them.

This line can be drawn by eye or better, by using the method of least squares (see § 29).

An important characteristic of the precision of the experiment is the accuracy of the "single test". Usually the test results are presented as a series of curves (e.g., $c_x = f(\alpha)$ for different Mach numbers; $\beta = f(\lambda)$ for different blade angles, etc.). It is very important to find the deviation of the points from the smoothed curves (which can arbitrarily be made by additional measurements of c_x, β, etc.) for one experiment (single test). This is usually done by additional tests, which are periodically carried out for methodological purposes and are included in multiple tests of any model.

Multiple tests of a model are usually performed after adjusting the tunnel and its equipment and developing the experimental method. In order to reduce the influence of systematic errors, these tests should be carried out under equal conditions as regards the tunnel, the measuring equipment, and the model, and at short intervals. The results of each test are processed by the same method, and curves plotted. For any value of the argument, the arithmetic mean of the ordinates is then found for each measured value. The deviation of the points (for a fixed value of the argument) on each curve from the mean value of the ordinate (for instance $\beta_{av} = \frac{\Sigma \beta_l}{n}$) determines the standard deviation of the measurement

$$\sigma_\beta = \sqrt{\frac{\Sigma (\beta_l - \overline{\beta_{av}})^2}{n-1}},$$

or the probable error

$$\rho_\beta = \frac{2}{3} \sigma_\beta.$$

A typical example of the variation of the probable relative error $\frac{\rho_\beta}{\beta_{av}} \%$ in propeller tests on a B-5 instrument is shown in Figure 8.24.

Multiple tests for determining the errors in single tests are in large aerodynamic laboratories performed on so-called control models, whose main purpose is to enable the reproducibility of test results to be verified. This is a criterion for the correctness of the experimental techniques and for the state of the measuring equipment and the tunnel. Periodically (usually once a month) the control model is tested under the same conditions at which the ordinary tests are performed. Deviations of the curves from the corresponding curves, obtained during previous tests of the model, indicate systematic errors whose causes can be established from the nature of the differences. Control models are usually made from steel or duraluminum, and they are very carefully maintained in a proper condition.

Results of multiple tests of geometrically similar airplane models in different wind tunnels yielded the following standard deviations of the measurements of the aerodynamic coefficients:

$$\sigma_{c_{x\,min}} = 0.0004 - 0.0005, \qquad \sigma_{c_z} = 0.001 - 0.0015,$$
$$\sigma_{c_y} = 0.004 - 0.005, \qquad \sigma_{m_x} = 0.0002 - 0.0003,$$
$$\sigma_{m_z} = 0.002 - 0.003, \qquad \sigma_{m_y} = 0.0003 - 0.0005.$$

The main sources of random errors in aerodynamic tests are inaccuracies, under static conditions, of the measuring equipment (about 20% of the errors), differences in the initial installation of the model in the tunnel (α_{inst}) (about 30% of the errors), and the nonsteady character of the aerodynamic loads (about 50% of the errors). The random errors also depend on the aerodynamic properties of the model: for high-lift models (large values of the derivative c_y^a) the values of σ_{c_y} and σ_{m_z} will be large,

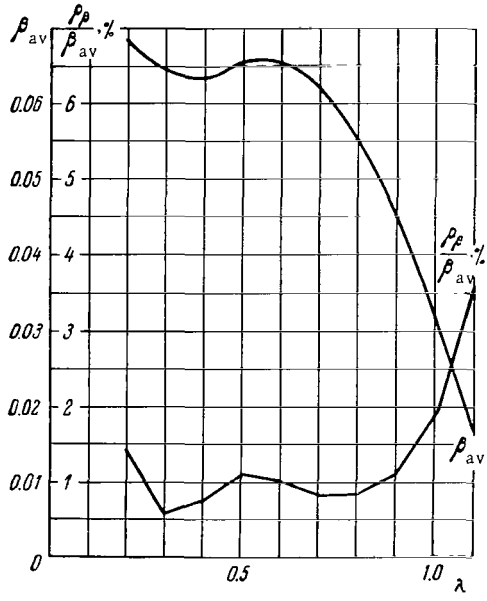

FIGURE 8.24. Probable relative error in measurements of the power coefficient of a propeller on a B-5 instrument.

especially in the region of $c_{y\,max}$. The value of σ_{c_x} increases with the angle of attack, usually in proportion to $\sqrt{c_x}$. The accuracy of determining the absolute values of the aerodynamic coefficients for airplanes, airfoils, etc. by multiple tests varies according to tunnel type and dimensions, flow velocity, relative dimensions of model and tunnel, and balances used. With correctly used equipment and appropriate test methods, the measuring errors should not exceed the values given on page 447.

Agreement between results of tests in different tunnels. Agreement between the results of tests of geometrically similar models in different wind tunnels is not only desirable as additional confirmation of the correctness of the experimental techniques applied in the tunnel considered, but is important for the continuity of tests in different tunnels at various ranges of **Re** and **M**. This applies especially to jet aircraft, rockets, etc.

Thus, production of a modern supersonic airplane is preceded by lengthy and systematic experimental research both in low-speed tunnels (conditions of take-off and landing, etc.) and in supersonic tunnels (conditions of maximum velocity, etc.). The analysis of the results of such tests

frequently requires comparison and compilation of the aerodynamic characteristics determined in different tunnels. Although such comparisons are mainly possible for overlapping conditions, (e.g., at a velocity which is the maximum possible in a low-speed tunnel, the minimum possible in a high-speed tunnel, or at equal Reynolds numbers when compressibility effects are neglected), agreement between the results of tests in different tunnels permits the range of investigations to be extended. The possibility of using results obtained in different tunnels permits superfluous expensive tests to be avoided in many cases.

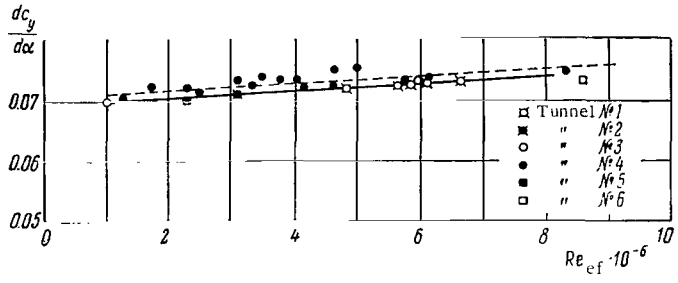

FIGURE 8.25. Values of $dc_y/d\alpha$ obtained in different tunnels.

Verifying the agreement between the results of tests in different tunnels is a complicated, lengthy, and expensive process; nevertheless, data are systematically collected in all aerodynamic laboratories for this purpose. For such comparative analysis, the specific conditions under which the tests are performed in each tunnel must be kept in mind

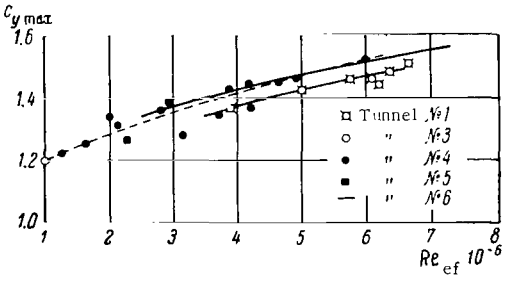

FIGURE 8.26. Values of $c_{y\,max}$ obtained in different tunnels.

(boundary-layer effects, interference between model and supports, errors in measuring loads and flow velocity, precision of model, etc.).

Figures 8.25 to 8.27 show the results of tests performed in six different wind tunnels, of the principal aerodynamic properties of a rectangular Clark-Y section wing having an aspect ratio λ-6 and a maximum relative thickness $\bar{c} = 11.7\%$. The comparison was made for the following

aerodynamic properties as functions of the effective Reynolds number:

$$\frac{dc_y}{d\alpha}, \qquad c_{y\,max} \text{ and } \alpha_{c_y=0}.$$

The effective Reynolds number

$$Re_{ef} = \frac{Vb}{\nu} T_F,$$

where b is the length of the chord, and

$$T_F = \frac{Re_{cr} \text{ for sphere in free atmosphere}}{Re_{cr} \text{ for sphere in tunnel}}$$

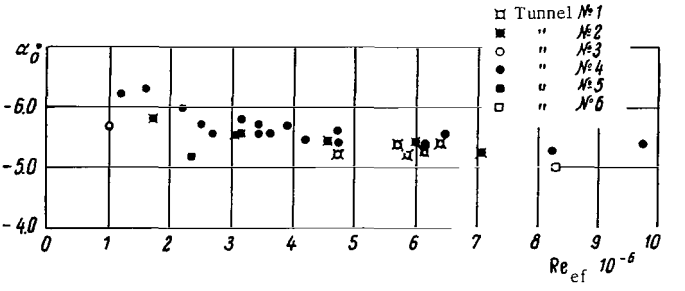

FIGURE 8.27. Values of angle of zero lift obtained in different tunnels.

The critical Reynolds number for a sphere in the free atmosphere is usually 385,000. Values of Re_{cr} and T_F for the tunnels compared are given in Table 15.

TABLE 15. Comparative characteristics of different tunnels

Number of tunnel	Type of tunnel	Dimensions of test section	Re_{cr}	T_F On tunnel axis
1	Open test section, closed circuit, two returns ducts	Elliptical	354.000	1.09
2	Ditto	Elliptical, dimensions one sixth of tunnel no. 1	348.000	1.11
3	Open test section, closed circuit, single return duct	Circular D = 7 m	365.000	1.06
4	Open test section, closed circuit, two returns ducts	Oval 18.3mX9.1m	350.000	1.10
5	Ditto	Circular D = 6.1 m	321.000	1.20
6	Open test section, closed circuit, single return duct	Circular D = 5.8 m	150.000	2.6

Figures 8.25 and 8.26 show that the values of $\frac{dc_y}{d\alpha}$ and $c_{y\,max}$ obtained in different tunnels agree with an accuracy of 2 to 3%.

Figure 8.28 shows comparative results of multiple tests of the same model in a tunnel with an open elliptical test section and in a tunnel with a closed circular test section. Noting the agreement between the aerodynamic properties determined in different tunnels, we can assume that the corrections introduced are sufficiently accurate. Thus, for instance,

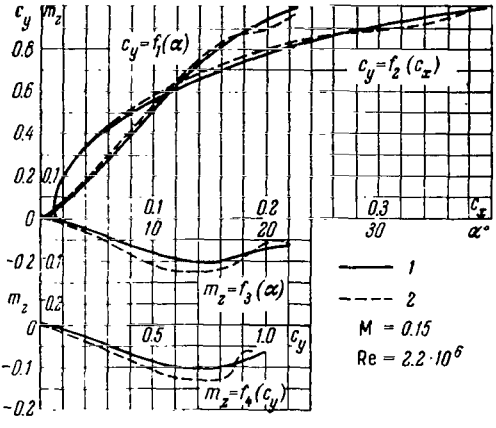

Figure 8.28. Multiple tests of an airplane model in two different tunnels. 1 — tunnel with open elliptical test section; 2 — tunnel with closed circular test section.

the agreement between the values of $\frac{dc_y}{d\alpha}$ shows that the corrections introduced in the velocity measurements for the lift effect and the blocking effect are appropriate, as are the corrections depending on the angle of attack, the receiver pressure, etc. Comparison of $\alpha_{c_y=0}$ as function of the Reynolds number for different tunnels shows that the errors in measuring the angles of attack and the flow inclination in these tunnels do not exceed ±0.1 to 0.15°. Comparisons of different tunnels are based not only on the results obtained in tests of models of airplanes, airfoils, propellers, etc., but also of spheres. This permits tunnels to be compared according to their turbulence level.

Agreement between tunnel and full-scale tests. The comparison of results of tunnel and full-scale tests is the final stage and the most effective method of evaluating the reliability of aerodynamic measurements in tunnels. The suitability of any experimental method must be finally proven by testing its results under natural conditions. On the other hand, modern developments in high-speed jet planes, rocket technology, etc., make it particularly important to ensure safety and flight stability of full-scale objects by preliminary testing in wind tunnels.

Figure 8.29 shows the results of tests of the NACA RM-10 model in different wind tunnels and in flight, as functions of the Mach number /14/. A 1860 mm long model was tested in a tunnel whose test section measured 2.44 m × 1.83 m. The total drag was measured by a balance. Two models, of 229 mm and 186 mm length were tested in a tunnel, whose test section measured 0.23 m × 0.19 m, by means of strain-gage balances located in the support outside the model. Nine models were tested in flight: five were 3720 mm and four were 1860 mm long. The total drag was determined

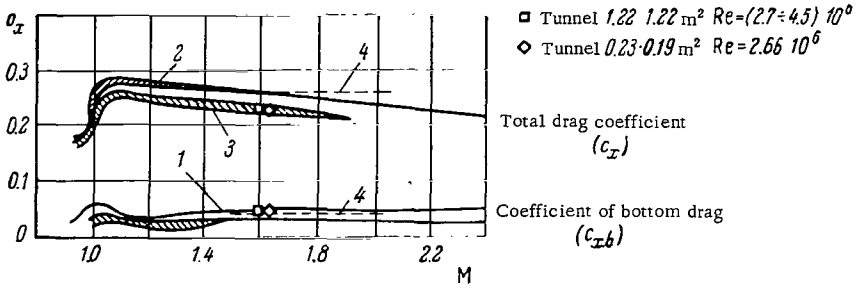

FIGURE 8.29. Comparative results of tests in tunnels and in flight of a NACA RM-10 model. 1 — model length 3720 mm, in tunnel; 2 — model length 3720 mm, in flight; 3 — model length 1860 mm, in flight; 4 — model length 1860 mm; in 2.44 m × 1.83 mm tunnel, Re = 30×10^6.

from the deceleration of the models (after burn-out of the gunpowder rockets inserted in them) by means of the Döppler effect, radar, and telemetering equipment. The ground pressure was determined as the difference between the pressure beneath the model and the static pressure in the nondisturbed flow, multiplied by the bottom area of the model. Despite the differences in tunnels, models, measuring devices, etc., comparison of the results of these experiments showed that tests of a model in a tunnel permit the aerodynamic properties of the full-scale object to be sufficiently accurately predicted under flight conditions.

BIBLIOGRAPHY

1. Pankhurst, R.C. and D.W. Holder. Wind Tunnel Technique (an account of experimental methods in low- and high-speed wind tunnels). — Pitman, London. 1952. [Russian translation. 1955.]

2. Glauert, H. Wind Tunnel Interference on Wings, Bodies and Airscrews. — R. and M. 1966. 1933.

3. Lock, C.N.H. The Interference of Wind Tunnel on a Symmetrical Body. — R. and M. 1275. 1929.

4. Glauert, H. The Interference of a Wind Tunnel on a Symmetrical Body. — R. and M. 1544. 1933.

5. Thom, A. Blockage Corrections and Choking in the RAE High-Speed Tunnel. — R. and M. 2033. 1943.

6. Allen, H. I. and W. G. Vincenti. Wall Interference in a Two-Dimensional Flow Wind Tunnel with Consideration of the Effect of Compressibility. — NASA, T. R. 782. 1944.

7. Vincenti, W. G. and D. I. Graham. The Effect of Wall Interference upon the Aerodynamic Characteristics of an Aerofoil Spanning a Closed Throat Circular Wind Tunnel. — NASA, A. C. R. 5D21. 1945; T. R. 849. 1946.

8. Batchelor, G. K. Interference on Wings, Bodies and Airscrews in a Closed Tunnel of Octagonal Section. — ASA 5. 1944.

9. Young, A. D. and H. B. Squire. Blockage Corrections in a Closed Rectangular Tunnel: Part I. Simple Approximate Formulae for General Application. — R. and M., 1984. 1945.

10. Prandtl, L. Der Einfluss des Kennwertes auf die Luftkräfte von Tragflügeln. — Ergebnisse der Aerodynamischen Versuchsanstalt zu Göttingen, Vol. 1, No. 54. 1920.

11. Glauert, H. Osnovy teorii kryl'ev i vinta (Fundamentals of the Theory of Wings and Airscrews) [Russian Title of Translator]. — GNTI, Moscow-Leningrad. 1931.

12. Mair, W. A. and H. E. Gamble. The Effect of Model Size on Measurements in the High-Speed Tunnel. Part I. Drag of Two-Dimensional Symmetrical Aerofoils at Zero Incidence. — R. and M. 2527. 1944.

13. Malikov, M. F. Osnovy metrologii, Ch. I. uchenie ob izmerenii (Fundamentals of Metrology. Part I. Theory of Measurements). — Komitet po delam mer i izmeritel'nykh priborov pri Sovete Ministrov SSSR, Moscow. 1949.

14. Evans, A. I. The Zero-Lift Drag of a Slender Body of Revolution (NASA RM-10 reserch model) as Determined from Tests in Several Wind Tunnels and a Flight at Supersonic Speeds. — Report NASA, 1160. 1954.

Chapter IX

AUTOMATIC DATA RECORDING AND PROCESSING OF WIND-TUNNEL MEASUREMENTS

After the Second World War many large wind tunnels for intermittent and continuous operation were constructed in a number of countries. Many of these tunnels are unique structures, requiring large capital outlay and taking up energy measurable from a few to thousands of kilowatts. To increase the number of experiments made in these tunnels, new methods had to be developed, for measuring different parameters. These methods enable the length of time required for the experiment to be considerably reduced.

However, the subsequent mathematical processing of the experimental results with the aid of simple desk calculators took up considerably more time than that taken up by the experiment, and very often it was found that the results of the experiment were available to the designer only many weeks after the end of the experiment itself. Furthermore, a considerable part of this time was connected with the reduction of the recorded (or hand-written) information into a form suitable for calculations. An example of such a labor-consuming operation is the making up of numerical tables from photographs of manometers, which record the distribution of pressure on the model.

Therefore, the necessity arose for using fast-operating automatic computers for speeding up the research and design operations connected with the development of aviation and rocket technology. The development of these computers paralleled the development of new methods of measuring in wind tunnels.

§ 43. METHODS OF AUTOMATICALLY PROCESSING MEASURED DATA

There are two types of automatic computers in modern computer technology, analog and digital. Analog computers receive signals from measuring instruments as continuous, changing, physical values, most often as electrical voltages. By operating on these values, called analog signals, the computers produce signals whose values are proportional to the sought function of the measured values and various parameters.

There are analog computers accepting signals from measuring instruments, and practically instantaneously processing and giving the computed results. In comparison with digital computers, analog computers are less accurate, but they are suitable for inserting initial data during

tests (for instance, inserting the values of aerodynamical coefficients from a balance test of the model without taking into account the influence of suspensions, interference, etc.).

During the last 10 years, electronic computers have been used for processing experimental data. Notwithstanding the fact that electronic digital computers are expensive and require complex systems for converting the measurements into digital form, they are used in most large modern aerodynamic laboratories.

As there is a large amount of literature on the use of electronic computers (see, for instance, /1/, /2/), only the main principles of their operation, necessary for understanding the methods of preparing the measured results for feeding to the computers, are explained here.

Electronic digital computers consist of the following main parts: 1) arithmetic unit, for operating on digits; 2) memory, for reception, storage, and output of the digits; 3) control unit, for controlling the automatic operation of the computer; 4) data input and output device, (Figure 9.1). The process of solving a problem on the computer, as with

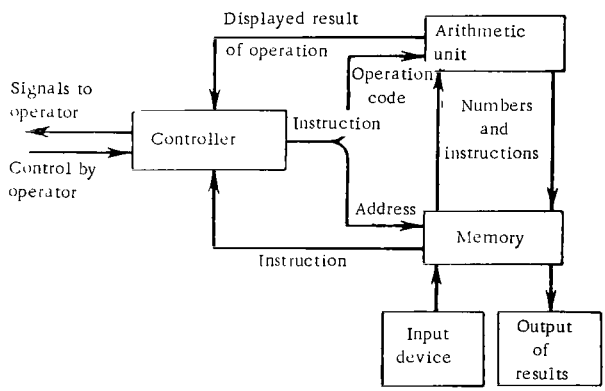

FIGURE 9.1. Block diagram of a digital computer.

manual calculations, consists of doing a certain series of operations on the initial digits. Each operation is carried out by the computer when acted upon by a special instruction signal. The sequence of the instruction signals is called the program of operation of the computer. The instructions of the program are put into the computer in code and are stored in the memory as words. Each instruction word is divided into several parts having different functional purposes. One part, called the operation, determines the type of operation which must be made by the computer. Another part, called the address, shows where the words are stored on which the operation must be made, and where the result must be sent In addition to arithmetic instructions, there are instructions necessary for the automatic operation of the computer. The program for each problem is made beforehand and is fed into the computer together with the basic data.

When processing basic data recorded on paper, the data are at first transferred by the operator (manually, with push-button devices), to punch cards, punch tape, or magnetic tape. From the latter, these data are automatically transferred to the computer memory.

Modern wind tunnels are equipped with instruments for recoring the measured data on punch cards, punch tapes, or magnetic tapes without the participation of the operator, and even for transferring them directly to the memory of the computer.

The output of the computed results from the computer is made in reverse order. A puncher connected to the computer records the result on punch cards or paper tapes. At the same time these data can be tabulated by special electric typewriters.

In electronic digital computers, the binary system is used to represent numbers and instructions. This system requires only two digits, 0 and 1. The main advantage of the binary system is the possibility of using a physical device having only two stable conditions, i.e., a device using the most simple principle of operation, on and off. Such devices are, for instance, electromechanical or electronic relays. One stable condition of the relay (for instance, energized) denotes a 1 and the other a 0. Each relay can store only one bit of a binary number. In order to store a number consisting of several bits, a corresponding number of relays is required. The main cell for short-term storage of a bit is a fast-acting electronic relay. Electromechanical relays are thousands of times slower than electronic relays but are used in devices which convert analog signals from the measuring instrument to digital values for recording them on punch cards or paper tape. The numbers (represented by the binary digits 0 and 1) are represented by definite punched holes on the card or tape. The punched position indicates a 1 in the number, whereas an unpunched position represents a 0.

In new wind tunnels, the measured data are processed both in series and parallel. When using the parallel method all the measured data are fed directly to the input of the computer. The final processed result comes in tabulated form or graphs, giving the aerodynamic coefficients on an $x-y$ plotter, referred to desired coordinate axes, and are obtained during the experiment. The serial method processes the measured results, at the end of the experiment, and is used in aerodynamical laboratories having computing centers equipped with general-purpose computers. Data processing on such computers, which are usually situated some distance from the wind tunnels take up only a very small part of the working time. However, the processed results from these computers become available to the experimenter only after a certain period of time. The output of the processed results is considerably speeded up when using the digital convertors described below.

In wind tunnels not equipped with digital computers operating during the experiments, simple analog computing devices are sometimes used, which give the operator the opportunity, during the experiment, to cancel bad measurements before they are fed to the complex computing process. When there are no methods of supervising the experiment, bad or unreliable data must be checked by additional experiments after the first series of experiments has veen processed. This causes considerable delays between the beginning of a series of experiments and the giving out of the results.

Wind-tunnel experiments consist of measuring a large number of different parameters. Thus, for instance, when testing an airplane model on six-component balances, the following values must be measured: three components of force, three components of moment, the full and static pressure in the working part, and the braking temperature. Sometimes, additional parameters are measured, for instance, the hinge moments of the control organs, and the pressure at different points on the model and walls of the tunnel. These are necessary for inserting suitable corrections when subsequetly computing the dynamic coefficients. One experimental point when testing the model is calculating a series of the above-mentioned values at the moment when these quantities are constant. Simultaneously, the parameters given by the experimenter must be calculated, for instance, the angle of attack and the angle of slip. The results of one test (or as is often said, one blowing of the model) consist of a number of experimental points received with one independent parameter, for instance, angle of attack or stream velocity. Testing an airplane or a rocket in a wind tunnel consists of several series of tests, for example: a series of tests according to velocity, according to the angle of installation of the control surfaces, with a model having different geometrical parameters, etc.

Thus, the full testing cycle of an airplane model consists of large numbers of measurements, whose total can reach thousands. Other types of experiments are no less labor-consuming as, for instance, testing a series of wing or propeller profiles. When testing turbojet engines in wind tunnels, the principal parameters measured are pressure and temperature. Sometimes hundreds of values are recorded in one read-off, and a full cycle of tests can contain several thousand measurements.

The manual recording of meter readings is connected with subjective errors and errors caused by nonsimultaneous read-downs from different instruments. To reduce errors and to speed up experiments, the indications of the separate balances and instruments are read down by different operators according to an audio or visual signal from the chief operator. This method is used at present only in wind tunnels with very low loads. To improve the utilization of modern powerful tunnels, the accuracy and speed of experiments are increased by automatically recording all the measured values.

There are two possible methods of automatically recording primary measurements: 1) graphically; 2) numerically.

By observing graphically recorded data, the senior experimenter can easily find any maladjustment in the measuring system or tunnel. From the tendency and shape of the curve, the experimenter can then plan the next part of the experiment.

The use of graphs for further computation is connected with additional errors and loss of time when measuring and recomputing the coordinates into digital form. For this reason, graphs are very seldom used for primary measurements in modern wind tunnels, but rather, digital forms of recording data. However, as the possibility of observing the process of the experiment from graphs is very important, many wind tunnels use, in addition to digital devices, all sorts of automatic graph recorders, placed on a panel before the senior experimenter. It is particularly useful

to use graphs if, instead of recording the primary measured data, the values of dimensionless coefficients automatically computed during the experiment are recorded.

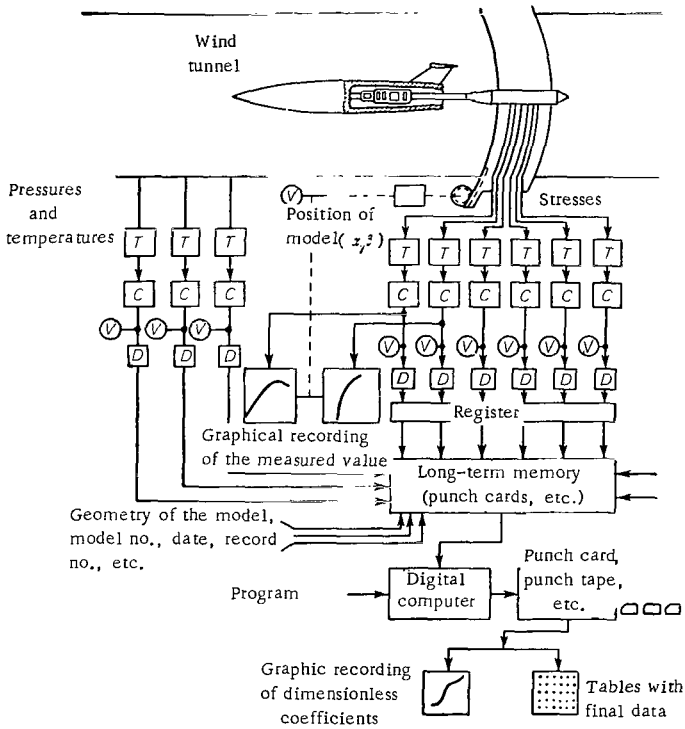

FIGURE 9.2. Typical arrangement for automatic data recording and processing in a wind tunnel. T — transducers; C — automatic compensators; D — digital converters; V — visual display.

Digital data in wind tunnels are recorded using two operations. The first operation is the conversion of the measured signals into digital or binary form; the second operation is the storing of the numbers representing the measured values in a short-term memory (register), from which the digits are rewritten onto special forms. Columns of decimal numbers are printed on these forms after passing through simple manual calculators. The primary data are recorded in digital code on punch cards, paper tapes, or magnetic tapes for processing in an electric computer. A simplified block diagram of a typical automatic data recording and processing system in a wind tunnel is shown in Figure 9.2. The physical data are measured by transducers with automatic compensators, converted by means of digital converters into digital form, and are then fed via a register to a long-term memory, which records these numbers on punch cards, paper tape, or magnetic tape.

In addition to the measured data, some auxiliary quantities are recorded (for instance, the point number, record number, model number, etc.). The punch cards are put into the computer which makes all the necessary computations according to a given program, which is usually recorded on punch cards. The computed data are punched out by the computer onto punch cards or paper tape. These data are transferred to a printer which prints the results in the tabulated form, or to a plotter.

Very often, the physical values measured during tests, such as linear and angular movements and voltages, must be converted into digital form. Thus, for example, compensating instruments (automatic lever-type balances, automatic bridges and potentiometers) have as the output signal the angular movement of a shaft. Strain gages, resistance thermometers, and thermocouples inserted into an unbalanced bridge produce signals in the form of voltages.

§ 44. DIGITAL CONVERSION OF MEASURED VALUES. DIGITAL CONVERSION OF ANGLES

The simplest device for continuously registering angular movements in digital form is a mechanical counter, consisting of a system of wheels numbered from 0 to 9. The lowest order wheel of the registered number is fixed directly to the shaft of the counter, and the digits on it represent

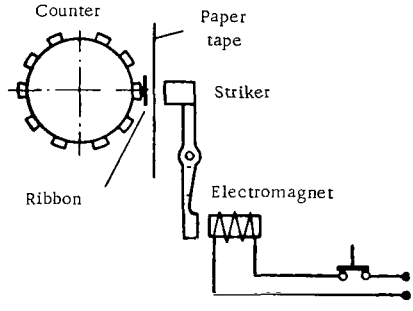

FIGURE 9.3. Recording counter indications with an electromagnet.

tenths of a turn of the shaft. When this wheel makes one rotation, the wheel of the next order is pushed ahead by a step change of 0.1 turn. Thus, the number of turns made can be read off the counter as a decimal number to 0.1 of a rotation.

Decimal counters are suitable, in most cases, for the maximum number of turns made by the balancing motor of an instrument. This can reach hundreds of turns, as in automatic lever-type balances.

The indications on the counters can be recorded using decimal wheels with protruding numbers and an electromagnetic device, as shown in Figure 9.3. Such a device is used for recording the indications of automatic bridges in stress balances.

A multichannel digital printer (Figure 9.4) is used for recording simultaneously the indications of all instruments when testing a model with mechanical wind-tunnel balances.

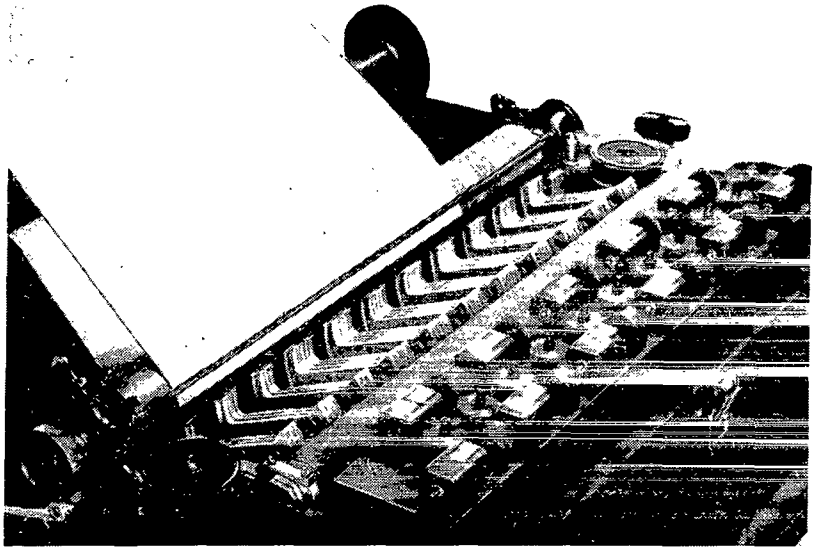

FIGURE 9.4. A printing mechanism for wind tunnels.

This device has 11 counters connected by selsyn transmitters to the balancing servomotors of the measuring instrument, and one counter for recording the read-down number. The recording is made by printing the digital indications of all 11 counters in one row on a wide paper tape. At the same time, electrical pulses can be fed to a puncher for storing the data on cards. The selsyn receivers are synchronized with the selsyn transmitters of the measuring instrument by visible counters installed in the upper part of the synchronizing mechanism and rotating synchronously with the built-in counters.

A device whose simplified diagram is shown in Figure 9.5 consists of special counters where the decimal wheels are replaced by spiral-type cams, a printing mechanism, a pulse feeding mechanism driving a puncher, and a distribution mechanism. The edge of the spiral-type can (1) is formed of 10 equidistant radial steps. During read-down, the ends of levers (2) are pressed onto these steps. The levers turn about point 0, through which passes a shaft common to all the levers.

The number of levers for each counter equals the number of decimal wheels on it. A printing sector (4), on whose periphery protrude numbers 0 to 9, is connected by hinged link (3) to each lever. When measuring, the shaft of the counter, with the aid of selsyn receiver (5), rotates synchronously with the shaft of the balancing device of the measuring instrument.

A read-down is made by depressing a print push-button switching on motor (6). The motor, via a cam distribution mechanism (7), first lowers all levers to the corresponding spiral cams (1). Simultaneously, the printing sectors (4) are turned by an angle corresponding to the radius of the protrusion on the spiral cam, on which is pressed the given lever. The digits of the sectors, equal to the digits in each of the decimal protusions of the counter, are placed opposite the center of rubber roller (8). As the levers (2) turn, the toothed sector (9) closes contact (10), which sends pulses to the puncher. The number of pulses equals the number recorded on the counter. The distribution mechanism then frees striker (11), which under the action of prestressed spring (12) strikes the base of all the printing sectors. The latter, moving by inertia, strike the rubber roller, making an impression by means of copying paper on paper tape (13). The registers are placed in one row, and therefore one strike of rod (11) on the tape prints the indications of all the measuring instruments as four digit numbers. The angle of attack and the read-down number are recorded by three-order counters. The read-down number on the counter changes automatically with each measurement.

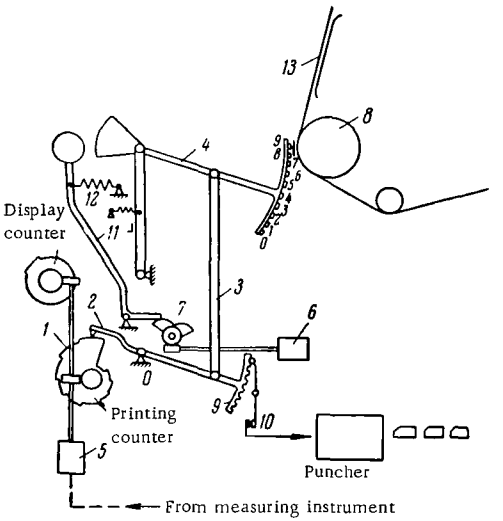

FIGURE 6.5. Arrangement of a printing device. 1 — spirals; 2 — counting levers; 3 — rods turning the printing sectors; 4 — printing sectors; 5 — selsyn receivers; 6 — motor; 7 — distributor; 8 — rubber roller; 9 — toothed sectors; 10 — contact; 11 — striker; 12 — force-spring; 13 — paper tape.

Figure 9.6 shows a block diagram of a system for recording measurements in a high-speed wind tunnel using mechanical balances with automatic lever-type balancing elements. A digital printer (2) is installed on the left side of the control panel (3). On the right hand side of the panel is concentrated the equipment controlling the units of the tunnel

and their operation. In the center is a graph recorder (5), an indicator displaying the Mach number of the stream (4), and an angle-of-attack indicator (6). This placing of the display instruments enables the experiment to be overseen by 2 operators, one for recording the measurements while the other changes the conditions in the tunnel. A panel (7), containing the selsyn receivers of the automatic balancing elements, is placed inside the desk, under the printer. The balancing elements measure six components of the forces on a wind-tunnel balance (1), the static pressure p in the working part of the tunnel, and the pressure drop Δp between the working part and the forechamber. In addition, the selsyn receivers of the automatic balance are installed on panel (7). This bridge measures the stream temperature with a resistance thermometer. Another selsyn receiver is connected to the mechanism changing the angle of attack.

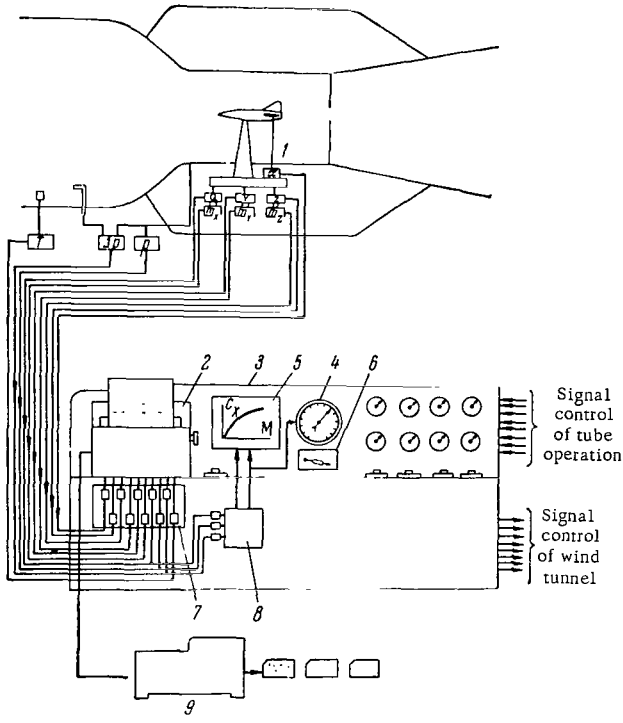

FIGURE 9.6. Recording measurements in a wind tunnel having mechanical balances. 1—wind-tunnel balance with lever-type balancing elements; 2—printer; 3—control panel; 4—visual display of the Mach number of the stream; 5—chart recorder; 6—angle-of-attack indicator; 7—selsyn receivers; 8—analog devices for measuring the Mach number of the stream; 9—puncher.

All the selsyns are connected with the input shafts of the cams and display counters of the printer. The analog computing device (8) for automatically determining, during the process, the Mach number of the stream, the velocity pressure Q, and one of the wind-tunnel coefficients

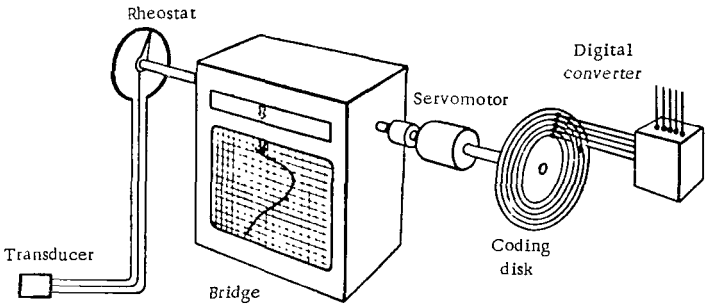

FIGURE 9.7. Diagram of an automatic bridge with a digital converter.

(for instance, c_x), is connected to the instruments for measuring p Δp and Q with the aid of parallel selsyns. The computed values of c_x are recorded on a graph recorder as a function of the computed values of the Mach number. The puncher (9) can be installed next to the desk or in the computing center.

Decimal number	Binary number	Reflected code	Number of path 6 5 4 3 2 1
00	000000	000000	
01	000001	000001	
02	000010	000011	
03	000011	000010	
04	000100	000110	
05	000101	000111	
06	000110	000101	
07	000111	000100	
08	001000	001100	
09	001001	001101	
10	001010	001111	
11	001011	001110	
12	001100	001010	
13	001101	001011	
14	001110	001001	
15	001111	001000	
16	010000	011000	
17	010001	011001	
18	010010	011011	
19	010011	011010	
20	010100	011110	
21	010101	011111	
22	010110	011101	
23	010111	011100	
24	011000	010100	
25	011001	010101	
26	011010	010111	
27	011011	010110	
28	011000	010010	
29	011101	010011	
30	011110	010001	
31	011111	010000	
32	100000	110000	
33	100001	110001	

FIGURE 9.8. Reflected binary code and the corresponding position of the path on the coding disk.

In fast-acting measuring compensation instruments electromechanical or electronic devices are used instead of mechanical registers. These convert the angle to a binary coded number, suitable for input to electronic digital computers. An example of a simple electromechanical converter for converting the angular position of a shaft is a device (Figure 9.7) used in English wind tunnels for reading down digitally the indications of strain-gage wind-tunnel balances /3/. The output shaft of the instrument bears a switching (coding) disk consisting of a number of concentric rings with conducting and non-conducting segments. A separate brush slides on each ring, and responds to a definite binary bit. The brush wiping a conducting segment produces an electrical pulse, representing a 1, while the brush wiping a non-conducting segment represents a 0 in the binary code. To obtain a read-out capability equal to 0.001 of a complete rotation of the shaft, it is necessary to have 10 rings, which allows the circumference to be divided by $2^{10} = 1024$ parts.

When a decimal number changes by one unit, the digits in a usual binary number change in several orders (see the first two columns of Figure 9.8).

To increase the operational reliability of the converter, the segments on the coding disk are placed so as to produce a reflected binary code, as shown in the third column of Figure 9.8. This code differs from the normal binary code in that in each subsequent number the digit changes in only one order, thus reducing the possibility of an error in read-down. The fourth column of Figure 9.8 shows the layout of a six-bit coding disk. The darkened segments are the conducting ones.

Numbers, read off from a coding disk, coded according to the reflected binary code, are not suitable for further use in electronic computers and must be converted to normal binary codes. For conversion, switching devices consisting of electromagnetic relays are switched into the brush circuits of the coding disk (Figure 9.9).

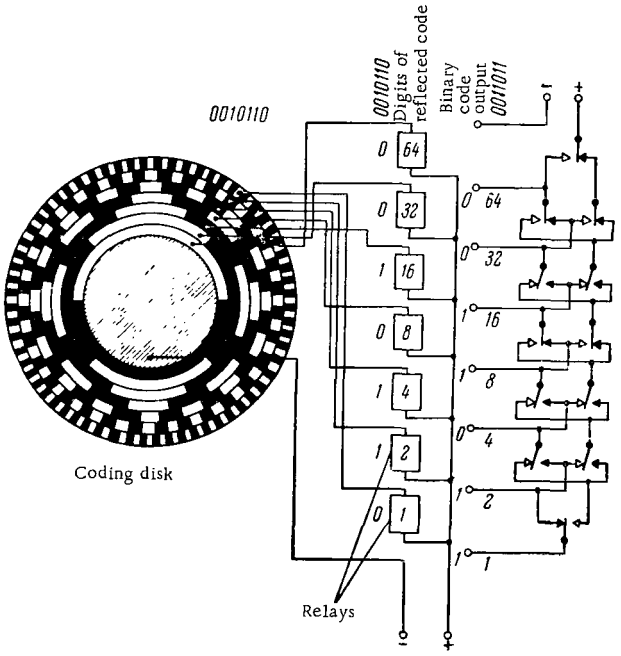

FIGURE 9.9. Reflected binary code to natural binary code converter.

When a brush makes contact with a conducting sector, corresponding to a 1 in the reflected binary code, the coil of the relay is energized, opening one contact and closing another. Each bit of the natural binary number has a definite output terminal. Binary ones in the natural binary number correspond to those output terminals where a positive voltage appears. Thus, for instance, when the position of the brushes corresponds to decimal number 27, the relays of the second, third, and fifth bits of the reflected code are energized, and this is read off from the disk in reflected code as 0010110. The contacts of these relays feed a positive voltage to the output terminals of the first, second, fourth and fifth bits of the natural binary numbers and from the relays is read off number 0011011 in the natural binary system, i.e., number 27 in the decimal system.

This relay converter serves at the same time as a short-term memory (register). The measured values are stored in a long-term memory (the machine for punching cards) during a period of time necessary for providing stabilized conditions in the stream before the next read-down. During the read-down of the register by the long-term memory, the balancing motors of the compensating instruments can be either stationary or rotating, watching the changing conditions. The second method is better, as it reduces measuring time. To make this method possible, the relay register is equipped with an additional blocking contact, which maintains the currents in the relay circuits until the next read-down.

Digital conversion of voltages

An example of the digital measurement of voltages is the decade a. c. compensator described in Chapter VI. The voltage measured across the diagonal of the transducer bridge (Figure 6. 58) is read off as a decimal

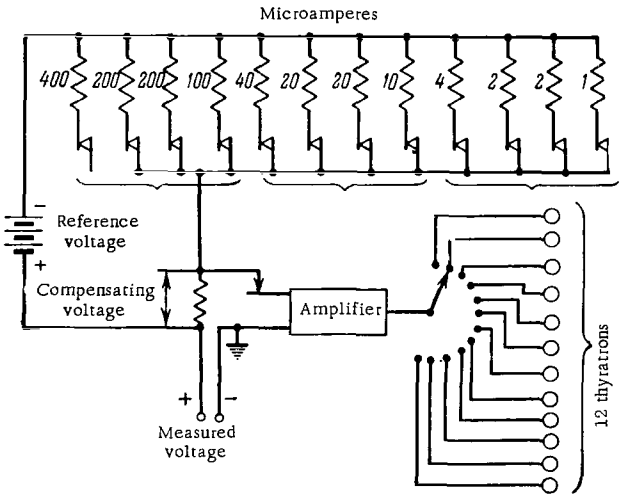

FIGURE 9. 10. Diagram of a high-speed digital potentiometer.

number with the aid of a mechanical counter connected to the shaft of the balancing motor of the compensator. In the system shown in Figure 9. 7 the measured voltage from the compensating instrument is first converted into an angular shaft position. The angular position is then converted by a coding disk into digital form.

There are systems where the voltages are digitally measured without conversion into angular motion. The advantage of these systems is their considerable increase in speed of operation. This is achieved by replacing the balancing motor by a system of electromechanical or contactless relays.

A circuit diagram of a high-speed digital potentiometer is shown in Figure 9.10. This system was developed by the Lewis Aeronautical Laboratory (NASA) for the multipoint measurement of thermocouple signals, but is also suitable for measuring signals from strain gages /4/. The instrument is designed for measuring voltages ranging from 0—10 and 0—40 millivolts in 72 channels during 48 seconds. The temperature is read by comparing a compensating voltage with the measured voltage. The difference between these voltages is amplified, and the output voltage from the amplifier is used for changing the compensating voltage until it equals the measured voltage. Twelve fast-acting relays switch on 12 resistors in the compensating circuit, for balancing the potentiometer. The figures in Figure 9.10 denote the current in microamperes passing through the corresponding resistors when the relay contacts, in series with the resistors, close. The sum of these currents pass through a 10 ohm resistor for producing the compensating voltage.

Different relay switching combinations give any compensating voltage between 0 and 9.99 millivolts in steps of 0.01 millivolts. To obtain the necessary voltage balance, the resistors are switched from left to right by a step selector incorporated in a circuit consisting of 12 thyratrons. Immediately after the first [selector] contact is closed, the relay contacts to the input of the amplifier are broken, giving a positive pulse if the balancing voltage is less than the unknown voltage, and a negative pulse if it is greater than the unknown voltage. A positive pulse fires the thyratron connected by the selector to the output of the amplifier, and switches in via an intermediate relay the first resistor. If the balancing voltage is greater than the unknown voltage, the first thyratron is not fired and as the switch passes to the next contact, the first relay remains de-energized. The same process takes place for each of the 12 steps. At the end of the cycle, some thyratrons are conducting, the contacts of the relays connected with them are closed, and the potentiometer is balanced. The voltage is read from the conducting or nonconducting condition of each of the 12 thyratrons, which serve as a register.

The relay in the plate circuit of the thyratron gives the information to a paper-tape puncher. For the puncher to be operated constantly, two thyratron assemblies are provided, one for obtaining the information from the potentiometer, and the second for simultaneously transmitting to the puncher the information received in the previous read-down. The thermocouples are switched successively into the circuit via a separate step selector switch. Figure 9.11 shows the simplified block diagram of the system. The moment the amplifier transmits the information to the upper thyratrons, the lower thyratron register transmits to the relay register the information recorded during the previous read-down. The information in the registers is erased by momentarily shorting the plate supply voltage of the thyratrons, thereby enabling the lower register to receive new information from the amplifier. The relay register decodes the information recorded on the thyratron register as a 1, 2, 2, 4 code into a natural binary code. The programmer transmits to the tape, in the necessary sequence, the information from the relay register and from the channel coder. The channel coder punches on the tape the number of the channel corresponding to the given read-down.

Method of dynamic compensation

Another method of digital conversion is to compare the measured value with a compensating value changing linearly with time. The compensating value is given as a sum of a certain number of pulses, each corresponding to a given interval of change in the measured value. Usually this interval is taken equal to the resolving capability of the measuring instrument. The number of intervals corresponding (to an accuracy of 1 interval) to the measured value are read off by an electronic pulse counter and recorded in a memory device (for instance on a magnetic tape or drum).

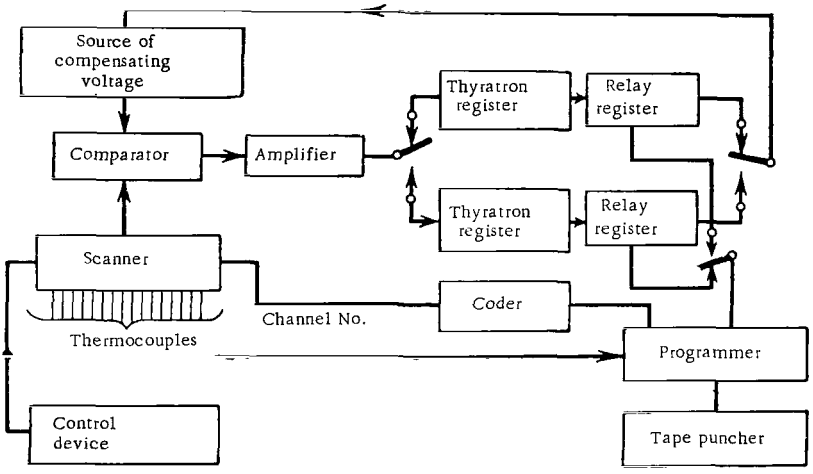

FIGURE 9.11. System for transmitting data from an automatic potentiometer to a puncher.

An example of a dynamic compensation system for measuring voltage is given in Figure 9.12. The voltage from one of the transducers (2) is fed through amplifier (3) to zero indicator (4), which is supplied with a saw-tooth voltage from saw-tooth voltage generator (10). The generator is started by a pulse from control circuit (1). Zero indicator (4) compares the amplified voltage u_1 from amplifier (3) with the momentary saw-tooth voltage u_2. When voltage u_1 and u_2 are equal, the zero indicator produces a pulse, which is fed to gate (5) and data output pulse generator (6). Until a pulse appears from the zero indicator (4), gate (5) is set by a control pulse to a state where clock pulses from generator (9) pass through the gate to binary counter (8). A pulse from the zero indicator (4) closes gate (5), inhibiting the passage of these pulses to counter (8). At the same time, the same pulse from zero indicator (4) starts data output generator (6) for transmitting the pulses recorded by counter (8) to the memory device (7), and subsequently resets the counter to zero. When the next control pulse appears the saw-tooth generator (10) starts again, gate (5) passes clock-pulses to counter (8), and the measuring cycle is repeated.

Thus the number of pulses recorded by counter (8) is proportional to the voltage from transducer (2). The recording in the long-term

memory (7) takes place between two measurements. Each pulse corresponds to a known small interval of voltage, and therefore knowing the total number of pulses, it is easy to determine the measured voltage.

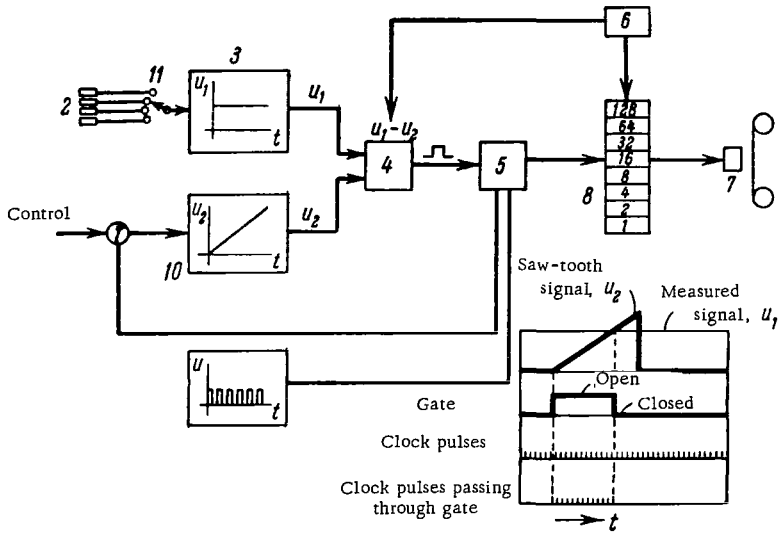

FIGURE 9.12. System for measuring a voltage as a number of pulses. 1 — control circuit; 2 — transducers; 3 — amplifiers; 4 — zero indicator; 5 — gate; 6 — data output pulse generator; 7 — long-term memory; 8 — electronic counter; 9 — clock-pulse generator; 10 — saw-tooth voltage generator; 11 — scanner.

The electronic binary counter consists of series-connected cells (triggers) each corresponding to a binary bit. The on condition of each cell represents a 1, while the off condition represents a 0. As pulses are fed to the input of the counter, they are transmitted from one cell to the other, changing their condition in a set sequence. The number of pulses sent to the counter can be read off from the state of the cells. Thus, for instance, if an on cell is represented by a dark rectangle and

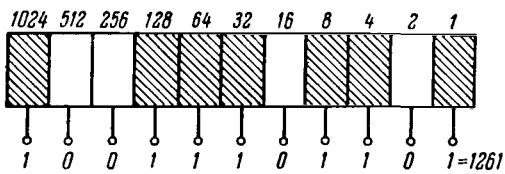

FIGURE 9.13. Electronic counter.

an off cell by a white one, then the display of the binary counter, as shown schematically in Figure 9.13, will be 10011101101, i.e., the decimal number 1261. For multipoint measurement, it is not required to count

the number of pulses in each measuring channel with separate electronic counters. Due to their high speed of operation, one counter can successively count the number of pulses in each channel and give this number as a binary code to a long-term memory for input to a computor. With a clock-pulse frequency of 10^6 cycles, it is possible by dynamic computation to record on magnetic tape, during one second, 1000 values to an accuracy of 0.1%. To accomplish this, a high-speed electronic switch (11) should be placed at the amplifier input (Figure 9.12). Electromechanical switches can be used for measuring up to 100 channels per second.

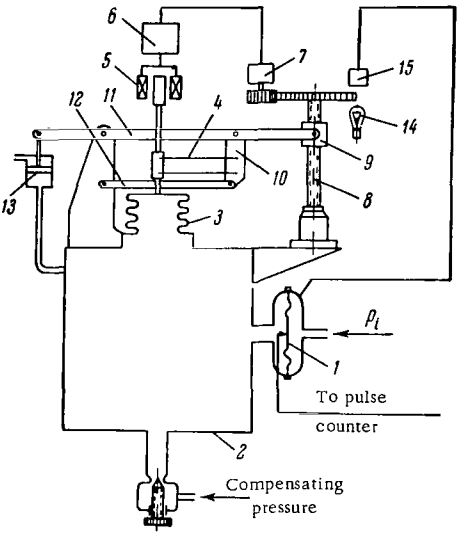

FIGURE 9.14. Converting compensating pressure into a pulse train. 1 — pressure-switch diaphragm; 2 — reservoir; 3 — bellows; 4 — spring; 5 — inductive pick-up; 6 — amplifier; 7 — servomotor; 8 — micrometric screw; 9 — nut; 10 — support for springs; 11, 12 — levers; 13 — unloading pistons; 14 — light source; 15 — photo element.

The pulse method was specially developed in the Lewis Aeronautical Laboratory, NASA (U.S.A.), where several thousand measurements are made daily in wind tunnels designed for testing turbojet engines. In this laboratory, multipoint measurements are made by comparing with one common compensating pressure, which is cyclically changed from zero to maximum. The compensating pressure, in its turn, is accurately measured by one of two methods: 1) with the aid of a compensating manometer producing a pulse train, each pulse corresponding to a fixed small interval of movement of the manometer balancing element, or, which is the same, to a fixed interval of change in pressure /5/; 2) by using equipment providing a pressure changing linearly with time. In this case, the number of pulses generated by a clock-pulse generator during

an interval of time are counted. These represent change in pressure from a fixed initial value up to the measured quantity /6/.

An arrangement for measuring pressure using the first method is shown in Figure 9.14. The primary pressure measuring element is pressure switch with a sensitive diaphragm (1) (Figure 5.56, Chapter V). For simplicity, only one switch is shown in the figure, but the actual number equals the number of pressures measured. The measured pressure p_i is applied to one side of the diaphragm. The other side of the diaphragm is connected with reservoir (2), in which is created a varying compensating pressure. Initially, a vacuum is created in reservoir (2). As the measured pressure is greater than the pressure in the reservoir, the diaphragm is deflected and closes an electrical contact. The reservoir is connected to an accurate manometer, which sends electrical pulses, with increasing pressure in the reservoir, to a circuit closed through the diaphragm. Each pulse corresponds to an increase in pressure of 0.25 mm Hg. The pulses are counted until the pressure in the reservoir equals the measured pressure. At this moment, the diaphragm opens its contact, and the pulses stop reaching the counter which is connected to the diaphragm. The measured pressure in mm Hg is eqaul to 0.25 n, where n is the number of recorded pulses. The pressure in the reservoir continues to rise to a value slightly higher than the highest measured pressure, after which a vacuum is again created in the reservoir. A measuring cycle lasts 10 seconds.

A null-instrument is used for measuring the compensating pressure and for sending pulses. It consists of a bellows (3), whose movable cover is connected with two flat cantilevered springs (4), and a differential transformer (5), sensitive to movements of up to 0.00025 mm. As the pressure increases in the reservoir, the cover of the bellows and the cantilevered springs move upward. As a result, a signal is induced in transformer (5), which is amplified in amplifier (6), giving a voltage to servomotor (7). The latter rotates micrometric screw (8). Nut (9) moves support (10), on which are fixed springs (4), until the force exerted by the springs equals the pressure on the cover of the bellows. This is carried out with the aid of levers (11) and (12), which form, together with the moving support (10), a parallelogram. This arrangement moves support (10) towards the bellows by about the amount of deformation of the spring, and prevents the bellows from moving sideways. A piston (13) relieves nut (9) from the forces acting on the bellows.

Servomotor (7) rotates the micrometric screw through a pair of gear wheels. The gear wheel on the axis of the screw has 180 teeth. The stiffness of springs (4), the area of bellows (3), the transmission ratio of lever (11), and the pitch of the screw are chosen in such a way that a turn of the screw by 2° corresponds to a change in pressure of 0.25 mm Hg. Each of the 180 teeth of the gear wheel, when turning, interrupts a ray of light between source (14) and photoelement (15).

Figure 9.15 shows a block diagram of a pressure recorder, the measured pressures $p_1, \ldots, p_n$ are fed by tubes to the diaphragm heads. The electrical pulses generated by the photoelements of pressure meter (3) are fed simultaneously via the closed contacts of all the diaphragm heads (2) to the recording heads (4) of a short-term magnetic memory. The latter is a bronze drum with an external diameter of 300 mm and a length of 100 mm. During the changing pressure cycle in the reservoir, the drum

rotates uniformly. Recordings are made by magnetizing the ferromagnetic coating on the surface of the drum which is at the given moment under the recording head. The clearance between the recording head and drum surface is 0.025 mm.

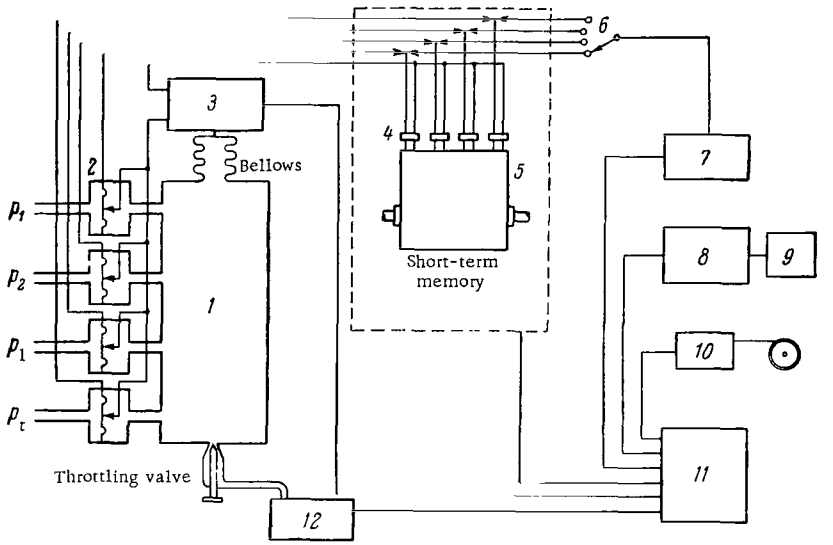

FIGURE 9.15. Diagram of a multipoint pressure measuring system. 1 — reservoir in which is created the compensating pressure; 2 — diaphragm pressure switch; 3 — pressure meter with pulse generator; 4 — magnetic recording heads; 5 — magnetic drum; 6 — scanner; 7 — electronic counter; 8 — coding and decoding; 9 — printer; 10 — tape puncher; 11 — control panel; 12 — pressure and vacuum control.

The recording head is an open permalloy core, wound with a coil having a small number of turns (to reduce inductance). During the passage of a pulse, a field is created in the core gap which magnetizes the ferromagnetic coating. The recording heads are uniformly placed around the drum in 21 rows with 5 heads in each row. Thus, the drum can record pressure from 105 measuring channels. The pulses are recorded on 85% of the circumference of the drum as separate tracks for each measured pressure. The maximum number of pulses is 400. The drum has two speeds: a low speed of one rotation per 12 seconds for recording pulses; a high speed of 1.5 sec per revolution for reading down the pulses from the drum to the electronic counter. The counter is in turn switched by a scanner to the recording head, which is switched beforehand for readings. The pulses are read down in reverse order from that in which they were recorded. As the magnetized sections of the drum pass under the head, a voltage pulse is induced in the head which is amplified and fed to an electronic counter.

The data from the electronic counters are fed to a special relay register, where the numbers are held for punching on paper tape and for being printed in a form suitable for a computer. At the same time,

such data as the channel number, computer instructions, experiment number, record number, date, and other necessary data are also recorded.

A characteristic example of using dynamic compensation methods is the centralized measuring system at the Lewis Aeronautical Laboratory (NASA) /6/. This system is the intermediate link between 9 wind tunnels and electronic computers. The data previously recorded on intermediate memory devices are transmitted as pulses over telephone wires to a central encoder and are recorded on magnetic tape during the time the necessary stream conditions are established for the next measurement.

Four types of data are recorded on the magnetic tape:

1) data common to the given job, e.g., read-down number, record, number, barometric pressure, date, etc.;

2) the pressure at 300 points measured with pressure switches;

3) voltages from 200 channels measured with thermocouples, and voltages from strain gages of wind-tunnel balances and potentiometers,

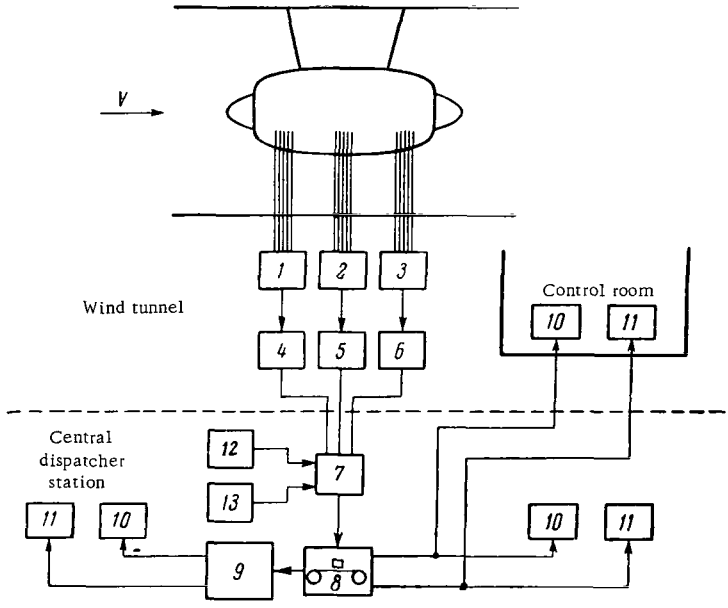

FIGURE 9.16. Centralized data collection system— Lewis Aeronautical Laboratory (NASA). 1—pressures; 2—voltages; 3—frequency pulses; 4—magnetic core matrix; 5, 6—electronic counters; 7—central encoder; 8—magnetic-tape recorder; 9—electronic computer; 10—printer; 11—graph plotter; 12—common information (model no., test no., etc.); 13—encoder control.

indicating shaft positions. The voltages are recorded at a speed of 20 channels/sec using a system similar to that shown in Figure 9.12;

4) pulse frequencies produced by magnetic pickups on tachometers measuring the r.p.m. of the tested engine, and magnetic pickups on flow meters measuring the amount of fuel entering the engine.

The block diagram of the connections between the measuring instruments, the central encoder, and output devices is shown in Figure 9.16.

The connections are made with relays, which automatically switch the different circuits during data recording. The dynamic compensation method used in the given system differs from the system shown in Figure 9.15 in that instead of using a manometric instrument for controlling the compensating pressure in the reservoir, a device providing a pressure changing linearly with time is used. A magnetic matrix is used for recording instead of a drum and the pulses recorded represent fixed intervals of time instead of fixed interval pressure. The linearly changing pressure is obtained by using a throttling nozzle which gives a constant critical flow.

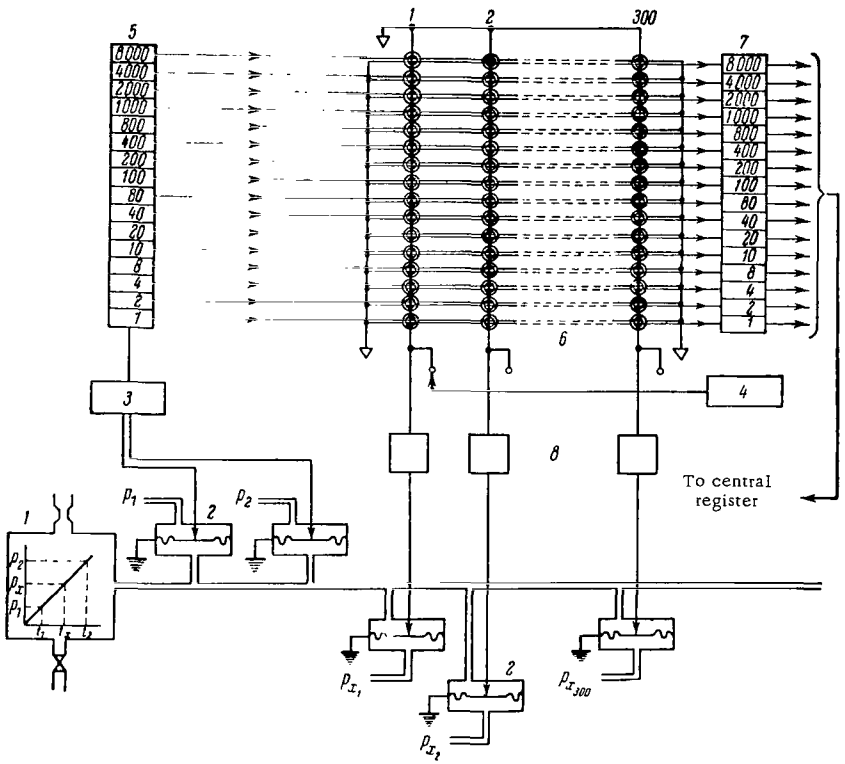

FIGURE 9.17. Arrangement for measuring pressure and recording the pulses in a magnetic core memory. 1 — reservoir with linearly changing pressure; 2 — diaphragm pressure switches; 3 — clock-pulse generator; 4 — readout-pulser; 5 — input from binary-decimal electronic counter; 6 — matrix; 7 — output register; 8 — gates.

By recording the moments corresponding to the known lowest pressure p_1, and the known highest pressure p_2, it is possible to determine the pressure p_{xi} at any intermediate moment. The time is measured using a 1000 cps clock-pulse generator. The number of pulses from the moment the pressure begins to change in the reservoir to moments t_1, t_{xi}, t_2 is counted by electronic counter (5) (Figure 9.17). A magnetic core matrix is used for storing the pulses

accumulated during time t_{xi} in each of the 300 measuring channels. Each magnetic core consists of a miniature ceramic bobbin wound with a tape of magnetic material 0.12 mm thick. Through a hole in the bobbin three wires pass for the voltage pulses.

The memory qualities of the cores are based on their magnetic rectangular hysteresis loop. A minimum current I through one of the wires is required to change the magnetic position of the core. With a current of $\pm\frac{1}{2}I$, the core remains in its initial magnetic condition. However, if two current pulses of $\frac{1}{2}I$ pass through two wires, the magnetic flux caused by these two currents is summed and the magnetic condition of the core changes. Thus, the core will remember the coincidence by changing its magnetic condition. The cores are placed in horizontal and vertical rows in the form of a matrix. Sixteen cores in one vertical column form one information channel and can store a 4 digit decimal number (a 16 digit binary number). To store the data of 300 channels, 300 vertical columns are required.

A vacuum tube is connected to each vertical column. The tube passes current only when a positive voltage is applied to the control grid. The tube is controlled by the diaphragm pressure switch of the given measuring channel. A horizontal wire passes through each of the 16 cores of one column, and the current through the wire is controlled by the 16 bits from the binary-decimal electronic counters. The function of each bit from the counter is to control the transmission of a pulse of $\frac{1}{2}I$ along the horizontal wire to the corresponding core. If the counter position contains a unit of information, it will pass a pulse of $\frac{1}{2}I$ into one core of each of the 300 channels.

At the moment the measuring cycle starts, the 1000 cps clock-pulse generator switches on. The generator sends pulses to the electronic counter and to each of the 300 tubes connected with the diaphragm pressure switches. When the pressure in the reservoir equals the pressure measured by the given pressure switch, the diaphragm opens its contact and a signal is transmitted to the tube connected to this pressure switch. With the next pulse from the generator, this tube passes a current pulse of $\frac{1}{2}I$ into the 16 cores of the corresponding channel. Simultaneously, the electronic counter sends pulses of $\frac{1}{2}I$ along the horizontal wires connected to those positions in the counter storing bits. Those cores of the given channel receiving coincident pulses along the horizontal and vertical wires change their magnetic condition, and thus remember the number of pulses stored by the electronic counter when the tube was switched on.

Those cores not receiving coincident pulses remain unchanged. After the contacts of all the diaphragm pressure switches have operated, a signal is automatically sent to read down the information stored in the matrix memory. The information is read down of a speed of 20 channels per second by sending a current pulse larger or equal to I through each vertical column via pulser (4). A second electronic counter (output register) (7) records the voltage pulses appearing on the third wire of each horizontal

row of the matrix. These pulses are induced by changes in the magnetic flux of the core and pass the recorded values to the central encoder. At the end of read-down the system is reset to its initial condition and is ready to receive the next measurement.

Engine r.p.m. and fuel output are recorded by electronic counters counting the number of pulses produced by magnetic tranducers from tachometers and flowmeters (Figure 9.18) during an interval of 10 seconds.

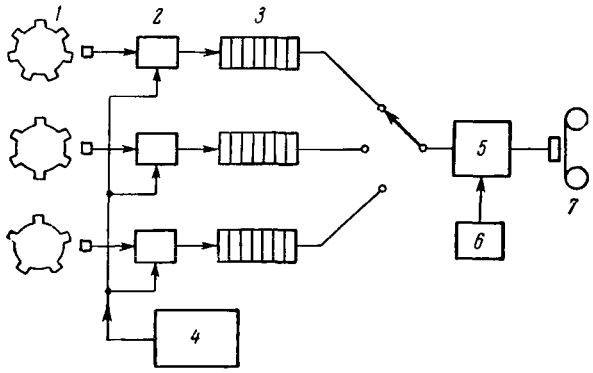

FIGURE 9.18. Measuring r.p.m. and flow.
1 — pulse transducers connected to a rotating element; 2 — gates; 3 — electronic counters; 4 — 10 sec interval generator; 5 — central register; 6 — read-down control; 7 — magnetic tape recorder.

All the instrument indications are recorded after establishing the conditions in the tunnel. When the operator presses a read-down button, all the instruments of the given tunnel are automatically switched to the corresponding output device for recording on magnetic tape. The cycle continues for 10 seconds, and when terminated, a light signal is switched on in the control room of the given wind tunnel, allowing conditions to be changed.

The time required to finish the recording cycle and prepare the necessary circuits for recording the next point is about 15 seconds. If during this time the operator of another wind tunnel presses a corresponding button, the beginning of recording signals from this tunnel is delayed until the end of recording from the first tunnel. Due to the short recording period, such delays remain unnoticed by the operator.

Depending on the type of experiment and the number of wind tunnels working simultaneously, the data measured can be either directly fed to electronic computers or accumulated on magnetic tape for further processing. In addition, the primary values recorded on magnetic tapes are printed on electric typewriters and recorded on high-speed graph plotters placed in the wind-tunnel control rooms.

§ 45. PROCESSING THE MEASURED DATA ON COMPUTERS

Data processing on an analog installation

Figure 9.19 shows a block diagram of an electronic analog installation at the Wright Brothers Scientific Research Center (U. S. A.) for automatically processing the data from strain gages used for measuring stresses and pressures /7/.

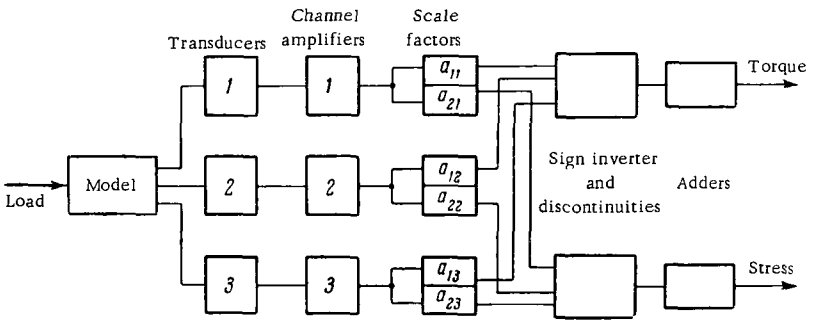

FIGURE 9.19. Block diagram of a system for continuously processing strain-gage indications at the Wright Brothers Research Center.

The least squares method is used to determine the torque M_{z_1} and the stress Y_1 acting on the model installed on pivoted strain-gage balances.

The device computes according to the formulas discussed in Chapter VI (page 409)

$$Y_1 = a_{11}\Delta u_1 + a_{12}\Delta u_2 + a_{13}\Delta u_3 + \ldots,$$
$$M_{z_1} = a_{21}\Delta u_1 + a_{22}\Delta u_2 + a_{23}\Delta u_3 + \ldots,$$

where Δu_1, Δu_2, ... are the voltages from the strain-gage bridges placed in different sections of the beam. The measuring system of each transducer operates with an a.c. carrier frequency. Filters at the output of the information channels filter out the carrier frequency and d.c. signals are received proportional to the measured values of Δu_i. The d.c. signals are summed in operational amplifiers. Before summation, the signals from different channels are multiplied by "weight" coefficients as determined by the constants of the equation. These coefficients depend on the design of the balances and the model, inserted by potentiometers at the input of the operational amplifiers, and are easily controlled. Correction factors are also inserted into the adders.

The pressure factor is determined by

$$c_p = \frac{\frac{p}{p_a} - \frac{p_\infty}{p_a}}{\frac{1}{2}\varkappa p_\infty / p_a M^2},$$

which is converted to

$$c_p = pm_1m_2m_3 - m_2,$$

where p is the measured pressure at a given point, p_∞ is the static pressure in the incoming stream, p_a is the barometric pressure. $m_1 = \frac{1}{p_a}$ can change during the day but is constant for the given test. $m_2 = \frac{2}{\varkappa M^2}$ is a constant for the given tunnel. $m_3 = \frac{p_a}{p_\infty}$ is a combination of variable values constant for the given series of tests.

The above equation is solved by modulating the voltage of the carrier with the amplitude of the signal from the pressure transducer. The modulated signal is rectified, multiplied by coefficients m_1 and m_3 in the information channel, and then summed in the operational amplifier with a voltage proportional to m_2. At the output of the adder, a voltage proportional to the pressure factor is obtained.

This system has an accuracy of about 1% and can test dynamic processes having a frequency up to 500 cps.

Processing the measured data on digital computers

The processing of data from wind-tunnel measurements differs by two specific characteristics. Firstly, the total amount of processed data is large. Consequently, the data input and output devices of the computer must have a large throughput capacity, and the internal memory must have a large storge capacity. Secondly, the necessary computations are simpler than those required by most analytical problems. Therefore, high computing speed is not a major requirement. Because of the above-mentioned reasons, in addition to universal electronic computers, special machines are found with fixed programs, adaptable for solving problems of a definite type. Special machines are usually simpler and less expensive.

The drawback of computers with fixed programs is that even small changes in the computing sequence (which are sometimes met when processing data from different types of measurements) call for readjusting the computer.

Where relatively simple computations are required, but the computing program cannot be given beforehand, small computers are used. Thus, for instance, in the Lewis Aeronautical Laboratory (NASA), a small IBM-604 computer is used for processing the data of multipoint pressure and temperature measurements of jet engines /8/. The basic data and instructions are fed from punch cards. The results are produced on punch cards at a speed of 100 cards per minute.

A property of the system is that the computer instructions are automatically fed in directly during the tests. With each read-down of temperature and pressure, separate instructions are given to the computer in the form of an operational code. Operational codes are automatically put into each measuring channel by means of a digital recorder, simultaneously with read-down. Thus, the computer can automatically change the computing sequence in accordance with the

instructions transferred to the computor following each read-down. This simplifies the processing of data obtained from different experimental objects and instruments.

The method of processing the measured data on an IBM-604 computer using punch cards can be seen in Figure 9. 20, where pressures are measured with the aid of a multipoint digital recorder.

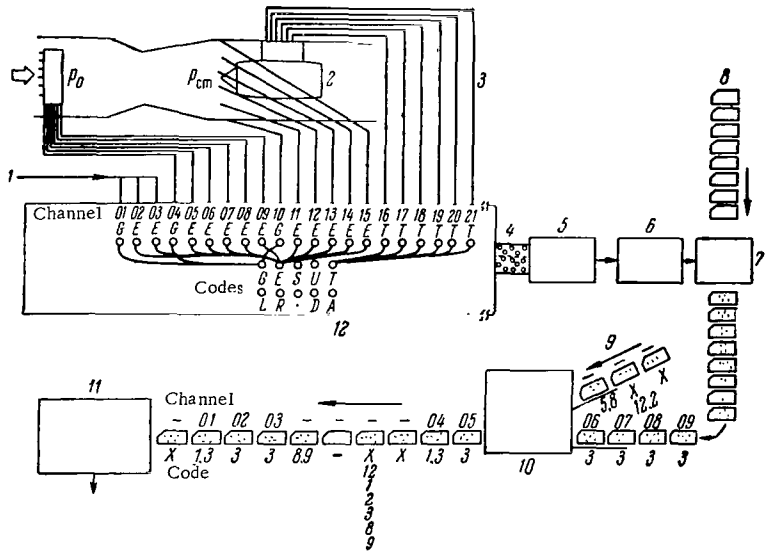

FIGURE 9. 20. Automatic data processing with a digital computer in the Lewis Aeronautical Laboratory. 1 — reference pressure; 2 — tested engine; 3 — pressure in engine; 4 — paper tape; 5 — reader; 6 — codex; 7 — puncher; 8 — blank punch cards; 9 — punch cards with additional punchings; 10 — sorter; 11 — computer; 12 — digital pressure recorder.

The recorder writes on a magnetic drum the digital values of the full pressure at 6 points in front of the engine, the static pressure at 6 points on the wind-tunnel walls, the pressure at 6 points on the engine, and 3 reference pressures against which the full pressure is compared.

The computer determines the average value of the full pressure, corrects for the losses between the sections where the pressure tranducers are placed and the input section to the engine, finds the average value of static pressure, and divides the static pressure and each of the pressures measured in the engine by the corrected full pressure.

The data from the digital recorder are punched onto paper tape and contain the coded digital values measured, the channel number, and the operating instructions. These data are transferred for each measurement from the puncher to a separate punch card. The punch cards are fed via a sorter to the computer.

Additional data, for instance, the calibration coefficients and corrections, are put into the computer with the aid of additional punch cards. The sorter compares the numbers punched on the main punch cards with the numbers in

the auxiliary punch cards and automatically puts the latter into the appropriate places between the main punch cards.

Figure 9.20 shows the sequence of feeding the main auxiliary punch cards to the computer and the marking of the code of the operational instructions. The first punch card is an auxiliary one and contains information on the calibration coefficient and support pressure. The code punched on this card instructs the machine as to the use of this information for further computation. The next punch card, referring to channel 01, is punched with a code 1, 3, and on those punch cards referring to channels 02 and 03, with code 3. Code 1, 3 instructs the machine to begin the summation of the computed pressure, while code 3 instructs this process to be continued. The card in channel 03 is followed by an auxiliary card, coded 8, 9. Code 8 instructs the machine to divide the summed pressures from channels 01, 02, and 03, by three, and to punch out the results. Code 9 instructs the machine to record the computed average pressure from all the following punch cards. This is necessary because at this point the complete limited capacity of the memory is used up.

The next card is an auxiliary card, coded X, 12, 1, 2, 3, 8, and 9. The machine does an operation corresponding to the logical sum of the instructions of this compound code. Code 12 instructs the machine to operate with the average pressure of channels 01, 02, and 03. The appropriate corrections are inserted into the average value, and the new pressure is kept for comparing with the subsequent pressure according to instruction code 2. The values of the full pressures are corrected by the corrected value of the support pressure as given on the punch card, and the next punch card with the code X gives a new calibration coefficient for channels 04 to 09. The code on subsequent cards instructs the machine on making further computations in the described order.

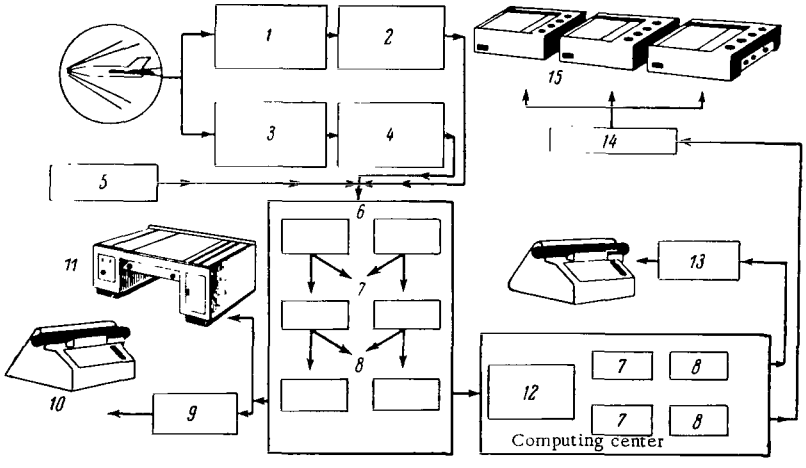

FIGURE 9.21. System for automatic data processing during an experiment. 1 — wind-tunnel balances; 2 — digital converters for wind-tunnel balances; 3 — multipoint manometer; 4 — digital converter for manometer; 5 — auxiliary data input; 6 — controller; 7 — punchers; 8 — readers; 9 — buffer memory; 10 — print-out of primary data; 11 — graph recorder of advance data; 12 — Datatron computer; 13 — print-out of processed data; 14 — distributor; 15 — graph plotter of final data.

Figure 9.21 shows an automatic system for processing data during the experiment intended for serving two supersonic wind tunnels at the California Institute of Technology (U. S. A.). In these tunnels, the forces acting on the model are measured by six-component hydraulic and strain-gage balances using automatic compensators. The output values of the balances represent the angular position of shafts. The angular positions are converted to digital form by relay converters.

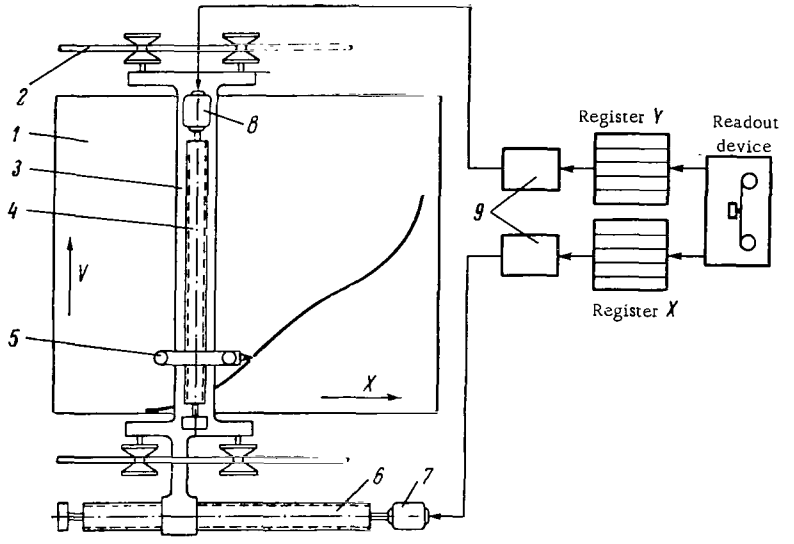

FIGURE 9.22. System for automatically plotting graphs from digital data. 1 — table with paper sheet; 2 — guide; 3 — carriage; 4 — lead screw for pen; 5 — pen; 6 — lead screw for carriage; 7, 8 — servomotors; 9 — analog-to-digital converters.

The distribution of pressures in the model is measured by a system described in Chapter V. Selector valves connect, in turn, all the openings in the drained model with one manometer, whose indications are measured by an automatic compensator and converted into digital form.

The values of the forces and pressures, together with data referring to the position of the model, the Mach number, experiment number, and the instructions for processing on the computer, are punched on paper tape at a speed of 60 digits per second. The punched tape is fed at once to the computer reader.

The control room of the wind tunnel is placed remotely from the computing center, and the data read from the punch tape are fed to the computer through wires. The data processed by the computer are recorded on punch tapes and fed back to the control room where they are tabulated. At the same time, graphs are plotted from the data. The readers, punchers, graph plotters, and printers can be interconnected by different methods depending on the test programs. For instance, with force measurements, when the amount of measured data is comparatively small, but the processing is more complicated, it is possible to prepare two identical

punch tapes with primary data. One is immediately fed to the computer, while the other is used for operating a tabulator or an X-Y plotter. With combined tests, where the forces and pressures are measured simultaneously, one tape records the indications of the balance, while the other records the indications of the manometer.

The printing of tables and plotting of graphs are operated by the given system during tests, thus allowing the senior engineer to monitor the experiment. This is very important when doing basic research of new phenomena.

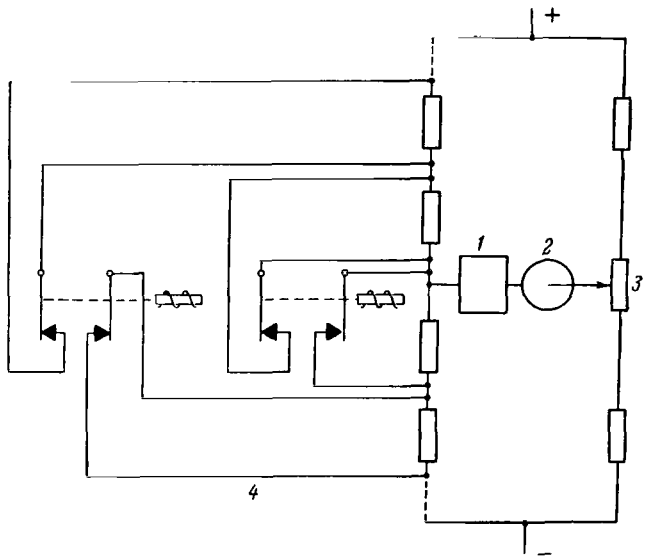

FIGURE 9.23. A digital-to-analog converter for an automatic X–Y plotter. 1 — amplifier; 2 — balancing motor; 3 — rheostat; 4 — potentiometer controlled by relays.

Figure 9.22 shows an arrangement of an automatic X-Y plotter for converting the digital numbers coded on paper tape to a continuous pen motion. The X-Y plotter can choose data from different measuring channels and plot several of them as a function of a parameter measured in any channel. Above the paper (1), parallel to the X-axis, a carriage (3) moves on guides (2). The carriage is driven by screw (6). The carriage moving along the Y axis, carries a pen (5), with an electromagnetic marker. The ruler and the pen are driven by balancing servomotors (7) and (8), connected to digital-to-analog converters (9). The digital values read from the paper tape are transmitted as pulses to the X-Y registers from where they are fed to the converters (9).

Each converter (Figure 9.23) consists of a balanced Wheatstone bridge, two branches of which are formed by a group of fixed resisters. The resisters are switched into the branches by a system of electromagnetic relays. The balancing motor of the bridge is connected with the corresponding lead screw of the X-Y plotter. When both bridges reach

balance, the electromagnetic marker frees the pen, which falls for a moment on the paper, making a dot. The pen is then raised, the *Y* relay register receives signals from the other channel, and the pen is moved to a new position, making another dot.

BIBLIOGRAPHY

1. Kitov, A.N. and N.A. Krinitskii. Elektronnye tsifrovie vychislitel'nye mashiny (Electronic Digital Computers). — Moskva, Fizmatgiz. 1961.
2. Lebedev, S.A. Elektronnye vychislitel'nye mashiny (Electronic Computers). — Izd. AN SSSR. 1956.
3. Scholes, J.F.M. The Automatic Handling of the Experimental Data in Wind Tunnels. — British Communications and Electronics, Vol. 4, No. 10. 1957.
4. Smith, R.L. A High-Speed Potentiometer for Recording on Punched Paper Tape, ISA Proc., Vol. 7. 1952.
5. Sharp, E.M. A Digital Multiple Point Pressure Recording System. - ISA Proc., Vol. 7, 1952.
6. Sharp, E.M. An Automatic Data Recording System for Aeronautical Research — IRE Trans. Instrum., Vol. 6, No. 7. 1957.
7. Haneman, V.S. Automatic Reduction of Wind Tunnel Data. — Aeron. Engns. Rev., Vol. 12, No. 2. 1953.
8. Rawlings, J.H. Mechanized Data Handling. — ISA Proc., Vol. 7. 1952.

$ 9.00

NASA TT F-346
TT 66-51026

Cover printed in Jerusalem, Israel